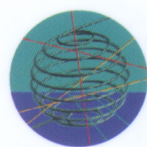


Volume II

The climate system

F I N A L R E P O R T S



SCIENTIFIC SUPPORT PLAN FOR A SUSTAINABLE DEVELOPMENT POLICY SPSD 1

This booklet is realised in the framework of the Scientific Support Plan for a Sustainable Development Policy (SPSD I).



D/2002/48

Published in 2004 by the
Belgian Science Policy

Rue de la Science 8
Wetenschapsstraat 8
B-1000 Brussels

Belgium

Tel : 32 (0)2 238 34 11 – Fax : 32 (0)2 230 59 12

<http://www.belspo.be> (FEDRA)

Contact person:

Mrs Martine Vanderstraeten (vdst@belspo.be)

Secretariat: 32 (0)2 238 36 13

Neither the Belgian Science Policy nor any person acting on behalf of the Belgian Science Policy is responsible for the use which might be made of the following information.

The authors of each contribution are responsible for the content of their contribution and the translation.

No part of this publication may be reproduced, stored in a retrieval system, or transmitted in any form or by any means, electronic, mechanical, photocopying, recording, or otherwise, without indicating the reference.

CONTENTS

Volume 2: Reducing uncertainties - The climate system

- ❑ Modelling the Climate and its Evolution at the Global and Regional Scales (CLIMOD) I
- ❑ Recent ENSO and paleo ENSO of the last 1000 years in lake Tanganyika II
- ❑ The global carbon cycle and the future level of atmospheric CO₂ III
- ❑ Natural Holocene climate variability and the recent anthropogenic impact IV
- ❑ Understanding the decadal-century-to- millennia climate variability by simulating extreme paleo-climatic situations V

MODELLING THE CLIMATE AND ITS EVOLUTION AT THE GLOBAL AND REGIONAL SCALES (CLIMOD)

UNIVERSITÉ CATHOLIQUE DE LOUVAIN (UCL)
INSTITUT D'ASTRONOMIE ET DE GÉOPHYSQUE G. LEMAÎTRE
ASTR-GCMG
Chemin du Cyclotron, 2
B-1348 LOUVAIN-LA-NEUVE
Thierry FICHEFET (coordinator CG/DD/09A)
Jean-Michel CAMPIN
Eric DELEERSNIJDER
Anne DE MONTETY
Hugues GOOSSE
Chantal PONCIN
Benoit TARTINVILLE

ASTR-RCMG
Jean-PASCAL VAN YPERSELE (promoter CG/DD/09B)
Hubert GALLÉE
Olivier BRASSEUR
Filip LEFEBRE
Philippe MARBAIX

INSTITUT ROYAL MÉTÉOROLOGIQUE
Avenue Circulaire, 3
B-1000 BRUXELLES
Christian TRICOT (promoter CG/DD/09C)
François FONTAINE
Pascal MORMAL
Marc VANDIEPENBEECK

VRIJE UNIVERSITEIT BRUSSEL (VUB)
GEOGRAFISCH INSTITUUT
Pleinlaan 2
B-1050 BRUSSEL
Philippe HUYBRECHTS (promoter CG/DD/09D)
Ives JANSSENS

TABLE OF CONTENTS

ABSTRACT	1
1. INTRODUCTION	2
2. THE AOGCM	6
2.1 Overview of the model	6
2.1.1 The AGCM	6
2.1.2 The CLIO model	8
2.1.3 Coupling technique	9
2.2 Improvements made to the model	9
2.3 Control experiment	11
3. THE GISM	18
3.1 Overview of the model	18
3.2 Improvements made to the model	18
3.2.1 Input datasets	19
3.2.2 Mass-balance model	21
3.2.3 Bedrock model	25
3.2.4 Calculation of the freshwater flux	27
3.3 Initialising the current ice-sheet evolution over the last two glacial cycles	28
4. THE MAR MODEL	30
4.1 Overview of the model	30
4.2 Improvements made to the model	30
4.2.1 Adaptations of the model with a view of enabling climate situations	30
4.2.2 Deep convection	33
4.2.3 Initialisation of the soil model	34
4.2.4 Snow model	35
4.2.5 Wind-gust estimation	35
4.3 Validation over Western Europe	36
4.3.1 Experimental design	36
4.3.2 Results	38
4.3.3 Important issues solved during CLIMOD and remaining questions	41
4.4 Validation over Belgium	42
4.4.1 Surface air temperature	43
4.4.2 Simulation of storms	44
4.4.3 Wind-gust estimation	45
4.5 Validation over Greenland	46
4.5.1 Model set-up	46
4.5.2 Comparison of model outputs with observations	47

5. COUPLING OF THE AOGCM WITH THE GISM AND NESTING OF MAR IN THE AOGCM	52
5.1 Validation/refinement of the mass-balance parameterisation of the GISM	52
5.2 Coupling of the AOGCM with the GISM	54
5.3 Nesting of MAR in the AOGCM	57
6. DEVELOPMENT OF A NEW CLIMATOLOGICAL DATABASE FOR BELGIUM	61
6.1 A regional climatological database for the recent past	61
6.1.1 Introduction	61
6.1.2 A corrected and completed climatological database	62
6.1.3 A homogenised climatological database	65
6.1.4 Normals for temperature and precipitation	71
6.1.5 Regional climatic evolution at the regional scale	73
6.2 100-yr-long climatic time series for Belgium	79
6.2.1 The longest climatic time series over the last century	79
6.2.2 Analysis of the reconstructed thermometric series	80
6.2.3 Analysis of the reconstructed pluviometric series	83
7. CLIMATE-CHANGE PROJECTIONS OVER THE 21ST CENTURY	85
7.1 Projections carried out with the global climate model	85
7.1.1 Experimental design	85
7.1.2 Global results	87
7.1.3 Resultsts related to the Greenland ice sheet	93
7.1.4 Comparison of the results over Belgium for the period 1970-1998 with observational data	98
7.2 Projections carried out with MAR	100
8. DEVELOPMENT OF A MORE ADVANCED AOGCM	101
8.1 Development and validation of a new version of the CLIO model	101
8.1.1 Improvement of the representation of physical processes	101
8.1.2 Enhancement of the resolution and validation	103
8.2 Development and validation of a new AOGCM	106
9. DISSEMINATION OF THE RESULTS	114
10. CONCLUDING REMARKS AND RECOMMENDATIONS	115
REFERENCES	117

ABSTRACT

The overall objective of the research project CLIMOD (CLimate MODelling) was to contribute to the international research effort leading to an improved understanding of the climate system and to a better assessment of the impact of human activities on the global and regional climates. Two main tools were employed to reach this goal: modelling and data analysis. Four Belgian research teams have pooled their expertise in this project: ASTR-GCMG (global climate modelling), GI (ice-sheet modelling), ASTR-RCMG (regional climate modelling), and RMI-GCS (climate data).

At the beginning of the project, members of the research network CLIMOD had at their disposal a coupled atmosphere–ocean general circulation model (AOGCM), the first and the only one in Belgium, a regional atmospheric model (called MAR), and a Greenland ice-sheet model (GISM). Each of these complex three-dimensional models was run by a different team in a different location. At the end of the project, a community model, to which each team has contributed a component, is accessible to all in a common computer environment.

The physics of each component has been improved to stay in line with the latest advances of the climate science. Radiation, clouds, and oceanic vertical mixing have received a particular attention in the AOGCM, with the specific goal of reducing the drift observed with similar models. The GISM has been improved in the areas of mass balance, iceberg calving, and bedrock isostasy. After a thorough validation over Greenland, the MAR model has been used to refine the meltwater-budget parameterisation utilised by the GISM. The refinements proposed did not improve significantly the mass-balance results. So, we decided to use the original formulation in the climate-change experiments conducted with the GISM. In parallel, a 50-km-resolution version of MAR has been validated over Western Europe for the present climate. This validation was carried out by nesting the model in the European Centre for Medium Range Weather Forecasts' (ECMWF) re-analyses. We also evaluated the ability of a finer-resolution-version of MAR limited to Belgium to reproduce extreme events.

The AOGCM and GISM have been coupled together. The coupled model has then been forced by the Intergovernmental Panel on Climate Change's (IPCC) scenario SRES B2 for both greenhouse-gas concentrations and sulphate-aerosol loading. By the end of the next century, the model simulates a global surface warming of 2.3°C and a global increase in precipitation of 3%, which fall within the range of estimates obtained with other models. The projected rise in sea-level due to thermal expansion reaches 22 cm in 2100. The partial melting of the Greenland ice sheet induces an additional rise in sea level of 4 cm. Greenhouse-gas-induced changes in meltwater flux

from the Greenland ice sheet do not seem to impact on the simulated climate, but this result must be taken with caution as the strength of the North Atlantic thermohaline circulation decreases with time in the control run performed with the model.

One of the initial objectives of CLIMOD was to perform with MAR a detailed assessment of the climate-change projections over Western Europe for the end of the 21st century. For several reasons explained in the main text, we were not able to reach this goal. We have however demonstrated that MAR is ready to carry out such a study.

We have also produced a high-quality (homogeneous) regional climatic database for Belgium from observational data covering the last few decades and characterised the regional patterns of the Belgium climate. Globally for Belgium, the extreme temperatures exhibit a warming trend of 2–2.5°C per century over the last 50 years, mainly in summer. A particularly warm period started abruptly after 1988. The most significant regional warming trends are observed in the coastal regions for the maximum temperature, and in the central part of the country and in regions of highest altitude for the minimum temperature. Regarding the annual mean precipitation, no significant trend was detected.

Furthermore, we have reconstructed and analysed long-term series of temperature and precipitation in order to improve our knowledge of the secular evolution of the Belgian's climate. The minimum temperature shows an overall warming trend over the country of 0.9°C per century, with an abrupt increase around 1988. The results for the maximum temperature are less clear. For precipitation, a positive trend over the century is generally detected over the country, mainly related to an increase during the 1900–1935 period. It should be noted that all these data constitute an invaluable tool to evaluate the performance of regional climate models over Belgium.

Finally, the transition towards a more advanced AOGCM has been prepared.

1. INTRODUCTION

Since the beginning of the industrial revolution, the amount of carbon dioxide (CO₂) in the atmosphere has increased by about 30%, an increase which is known to be in large part due to the combustion of fossil fuels and the removal of forests. In the absence of controls, projections are that future increases in CO₂ amount may accelerate and concentrations could double from pre-industrial values within the next 50–100 years. This gradual build-up of CO₂ leads to a perturbation of the natural greenhouse effect, tending to warm the Earth's surface and to produce other changes

of climate (IPCC, 1996, 2001). Several other greenhouse gases are also observed to be increasing in concentration in the atmosphere because of human activities (especially biomass burning, landfills, rice paddies, agriculture, animal husbandry, fossil fuel use, and industry). These include methane, nitrous oxide, and tropospheric ozone, and they tend to reinforce the change in radiative forcing from increased CO₂. The human-introduced halocarbons also produce an enhanced greenhouse effect although offset somewhat by the observed decrease in lower stratospheric ozone since the 1970s, caused principally by the halocarbons (IPCC, 2001). In parallel, human activities contribute to aerosol-particle formation mainly through injection of sulphur dioxide into the atmosphere (which results from fossil fuel combustion) and through biomass burning (IPCC, 1996, 2001). The main direct effect of these aerosols is the scattering of some solar radiation back to space, which tends to cool the Earth's surface. A further effect is that these particles act as nuclei on which cloud droplets condense. A changed concentration therefore tends to affect the number and size of droplets in a cloud, and hence alters the reflection and absorption of solar radiation by the cloud – the indirect effect.

To quantify the response of the climate system to these changes in the atmospheric composition, it is essential to account for all the complex interactions between the various components of the climate system (i.e., the atmosphere, the oceans, the ice masses, the upper Earth's mantle, and the living world). It is not possible to do this reliably using empirical or statistical models because of the complexity of the system, and because the possible outcomes may go well beyond any conditions ever experienced previously. Instead, the response must be found using numerical models of the climate system based upon sound physical principles.

The overall objective of the research project CLIMOD (CLimate MODelling) was to contribute to the international research effort leading to an improved understanding of the climate system and to a better assessment of the impact of human activities on the global and regional climates. Two main tools were used to reach this goal: modelling and data analysis. Four Belgian research teams have pooled their expertise in this project: ASTR-GCMG (global climate modelling), GI (ice-sheet modelling), ASTR-RCMG (regional climate modelling), and RMI-GCS (climate data).

The most comprehensive global climate models are coupled atmosphere–ocean general circulation models (AOGCMs). Despite the ability of these models to reproduce some of the features of today's climate, a significant number of shortcomings remain to be alleviated. The climate of an atmospheric general circulation model (AGCM) differs from the observed one, even when driven by observed sea-surface temperatures and sea-ice extents. The same is true for an oceanic general circulation model (OGCM) forced by observed atmospheric fluxes. In

an AOGCM where processes at the air–sea interface are allowed to reach their own equilibrium, systematic errors can amplify as the simulated sea-surface temperatures can differ substantially from the values normally observed. Several years ago, most of coupled models included a correction term for the surface fluxes to counter any climate drift. Locally, the flux correction was often as large as the fluxes themselves and one or two orders of magnitude larger than the radiative perturbation due to the increased concentrations of greenhouse gases and anthropogenic aerosols (e.g., Gates et al., 1993). This was a very unsatisfactory aspect of the modelling science (IPCC, 1996).

As part of the Belgian Impulse Programme "Global Change" (1990–1996), ASTR-GCMG has developed an AOGCM suitable for climate studies. Like the majority of AOGCMs in which flux adjustment was not implemented, it exhibited a significant climate drift. One of the specific objectives of CLIMOD was to reduce this drift by improving several aspects of the model physics.

The Greenland ice sheet constitutes an important component of the global climate system. First, this ice sheet contains the equivalent of about 7.2 m of global sea level. Today, about half of the ice-sheet annual mass loss is by extensive summer melting at the margin, and this fraction is likely to increase rapidly in a warming climate. The other half of the annual mass loss is by iceberg calving from outlet glaciers. In contrast to Antarctica, the increase of ablation rate in a warming climate is generally believed to dominate over the increase in accumulation rate. In recent assessments, the Greenland ice sheet is projected to be able to contribute up to 10 cm to the global sea-level rise by the end of the next century, with the potential of a larger contribution after that if the warming were sustained beyond the 21st century (IPCC, 2001). However, uncertainties remain large. Second, the Greenland ice sheet is located in a region of crucial importance for the global climate. Actually, the North Atlantic area is a region of intense heat and moisture exchanges from the ocean to the atmosphere, exchanges which are responsible for the formation of North Atlantic Deep Water (NADW). It has been suggested (see, e.g., Rahmstorf, 1994) that a sudden increase in the meltwater input in this area could trigger a rapid rearrangement of the oceanic thermohaline conveyor belt, leading to a general cooling of the North Atlantic.

The second specific objective of CLIMOD was to address these issues by coupling the ASTR-GCMG's AOGCM with an improved version of the three-dimensional (3-D) Greenland ice-sheet model (GISM) built at GI. This coupled climate model had then to be used for simulating the transient response of climate to the gradual accumulation of greenhouse gases and sulphate aerosols in the atmosphere during the past few decades and the 21st century. Compared to simulations of this type carried out with other models, the one we proposed had the peculiarity of being done with a model not utilising flux correction and including an interactive ice-sheet component. The latter

characteristic enabled to take into account the influence of the iceberg discharge and meltwater flow from the Greenland ice sheet on the World Ocean's thermohaline circulation, and thus on climate, and to produce a better estimate of the sea-level rise. In addition to this work, it was planned to start the development of a more advanced AOGCM.

Because of the limited computational power, the maximum horizontal resolution for long anthropogenic climate-change projections with AOGCMs is restricted to a few hundreds of kilometres, which is too coarse to adequately describe the regional climate details required for impact studies. One technique to obtain higher-resolution simulations consists in nesting in the AOGCM a regional atmospheric model over the region of interest (e.g., Giorgi, 1995). In this approach, the boundary conditions as well as the initial conditions of the regional atmospheric model are taken from the low-resolution AOGCM simulation. This method was pioneered by Dickinson et al. (1989), and was used in the first regional climate-change experiment for Europe by Giorgi et al. (1992).

Such a regional atmospheric model, called MAR (Modèle Atmosphérique Régional), has been developed at ASTR-RCMG within the framework of the Belgian Research Programmes on the Antarctic (1985–1996). This model has been validated for various situations over Antarctica and Greenland, but also over Belgium and Central Africa. As part of CLIMOD, we proposed to run MAR over Greenland under boundary conditions taken from a numerical weather-prediction model (usually referred to as perfect boundary conditions) in order to validate/refine the parameterisation of the surface mass balance used as interface between the GISM and the AOGCM, in anticipation of an improvement of the resolution of the AOGCM. Moreover, it was planned to thoroughly validate MAR over Western Europe and Belgium by carrying out simulations using perfect boundary conditions and by comparing the results to observations. The ultimate goal consisted in nesting MAR in the AOGCM–GISM with the purpose of refining the climate-change projections made with this global model over Western Europe.

Another important objective of CLIMOD was to produce a high-quality (homogeneous) regional climatic database for Belgium from observational data covering the last few decades and to characterise the regional patterns of the Belgium climate, with a particular emphasis on the frequency and intensity of extreme meteorological events. Furthermore, we intended to reconstruct and analyse long-term series of temperature and precipitation in order to improve our knowledge of the secular evolution of the Belgian climate at the regional scale. Such data should constitute an invaluable tool to evaluate the performance of regional climate models over Belgium.

In the present paper, we describe the improvements made to the models during the project together with the coupling and nesting techniques developed, we present the observational data collected, we discuss the scientific results obtained, we report on the dissemination of these results and on the degree of accomplishment of the initial objectives, and we end with some recommendations.

2. THE AOGCM

2.1 Overview of the model

The ASTR-GCMG's AOGCM is made up of two components: an AGCM based on version 5.2 of the AGCM developed at the Laboratoire de Météorologie Dynamique (LMD), Paris, and a three-dimensional ocean–sea-ice model, named CLIO (Coupled Large-scale Ice–Ocean), entirely built at ASTR-GCMG. A short description of the model components and coupling technique is given here. Further details can be found in Grenier et al. (2000) and references therein.

2.1.1 *The AGCM*

The AGCM solves the three-dimensional primitive equations of fluid dynamics with a finite-difference technique (Sadourny and Laval, 1984). For lateral diffusion, a bi-Laplacian for both the rotational part of the wind and potential enthalpy is employed, while a single Laplacian acts on the divergent part of the wind. The vertical velocity is diagnosed using the continuity equation and the hydrostatic approximation. The model incorporates a detailed gravity-wave-drag parameterisation (Boer et al., 1984) that accounts for the effect of the subgrid-scale orography. The horizontal resolution of the version utilised at ASTR-GCMG is of 64 regularly spaced points in longitude and 50 points spaced in a sinusoidal regular distribution from pole to pole (thus, the meridional resolution, which is of about 2° in the equatorial regions, decreases towards the poles). The vertical coordinate is the usual sigma (σ) coordinate. The model has 11 vertical levels. Four are located in the planetary boundary layer (PBL), where turbulent diffusion is parameterised following Sadourny and Laval (1984).

The solar radiation scheme is an updated version of the scheme proposed by Fouquart and Bonnel (1980), whereas the infrared radiation code is due to Morcrette (1991). The solar fluxes are calculated for two bands corresponding to the visible and near-infrared frequencies. The optical depth and single-scattering albedo of clouds are parameterised as a function of the cloud-water content (Stephens, 1978). The solar diurnal cycle is not resolved, and the effects of aerosols are not taken into consideration. The infrared radiation scheme computes the radiative transfer for six

spectral intervals which correspond to the absorption by water vapour (two intervals), by CO₂ and the rotational part of the water-vapour spectrum, by the water-vapour continuum only (two intervals in the atmospheric window), and by ozone. In accordance with Stephens (1978), clouds are treated as grey bodies in the infrared domain, with an emissivity depending on the liquid water path. Two kinds of clouds are considered: ice (or cold) clouds and liquid water (or warm) clouds. A cloud is supposed to be cold when its temperature drops below -15°C and warm when its temperature exceeds -5°C . The effective radius of cloud droplets used to determine the cloud optical depth and the absorption coefficient used in the cloud-emissivity formulation are different for both types of clouds. All clouds are assumed to overlap randomly along the vertical.

Condensation can occur according to three different schemes utilised sequentially: a moist adiabatic adjustment scheme (Manabe and Strickler, 1964), a Kuo-type scheme (Kuo, 1965), and a supersaturation scheme for non-convective precipitation. The cloud-water content is estimated by a prognostic budget equation (Le Treut and Li, 1991). It should be noted that the width of the prescribed distribution function of total water content within a given grid box has been made function of altitude. This, together with a reduction of the minimum allowable value for eddy diffusivity, enables a better simulation of low-level stratiform clouds (Grenier et al., 2000).

Theoretical as well as observational studies indicate that the precipitation processes for warm clouds and cold clouds are quite different. This is taken into account in the model. When the temperature in the cloud layer is below -15°C , the cloud precipitates following Heymsfield and Donner's (1990) scheme, in which the terminal fall speed of the ice crystals is parameterised in terms of the cloud-water content. For temperatures above -5°C , the rate of precipitation is given by Sundqvist's (1988) formula. At intermediate temperatures, both precipitation processes are supposed to exist, their relative importance depending linearly on the cloud temperature.

Hydrological exchanges between the soil-vegetation system and the atmosphere are determined by the parameterisation SECHIBA (Ducoudré et al., 1993). For each continental grid cell of the model, eight surface types (bare soil plus seven vegetation classes) are defined, each of them covering a fractional area of the grid cell. Over each of these covers, the following fluxes are computed: evaporation from soil, transpiration from plants through a resistance defined by the concepts of stomatal resistance and architectural resistance, and interception loss from the water reservoir over the canopy. These fluxes are then averaged over the grid cell to derive the total amount of water vapour that is transferred to the first level of the AGCM. The soil moisture is calculated by a two-layer model, the upper layer being the most reactive. When the soil-water

content exceeds some critical value, the excess is supposed to run off instantaneously into the ocean (26 drainage basins are considered).

Ground temperature is a prognostic variable of the model. A single snow layer is defined which can accumulate, melt, or sublimate snow (Chalita and Le Treut, 1994). The fraction of snow covering a given grid element is diagnosed from the snow depth. Precipitation falls in the form of snow whenever the temperature of the air above the ground is below the freezing point. Melting begins when the ground temperature rises above freezing. For the land grid cells, monthly values of the roughness length are prescribed from the climatology of Dorman and Sellers (1989). The drag coefficient is then computed from the value of the roughness length and the stability of the air above the ground using Louis et al.'s (1981) formulation.

2.1.2 The CLIO model

The CLIO model consists of a global OGCM coupled to a comprehensive thermodynamic–dynamic sea-ice model.

The OGCM is a primitive-equation, free-surface model that rests on the usual set of assumptions, i.e., the hydrostatic equilibrium and the Boussinesq approximation (Deleersnijder and Campin, 1995; Goosse et al., 1997a, 1997b). Vertical mixing is prescribed according to the parameterisation of Pacanowski and Philander (1981). Whenever the vertical density profile becomes unstable, the vertical diffusivity is enhanced to $10 \text{ m}^2 \text{ s}^{-1}$ to simulate convection. The horizontal eddy diffusivity and viscosity are set equal to $150 \text{ m}^2 \text{ s}^{-1}$ and $10^5 \text{ m}^2 \text{ s}^{-1}$, respectively.

The sea-ice model is that of Fichefet and Morales Maqueda (1997, 1999). Sensible heat storage and vertical heat conduction within snow and ice are determined by a three-layer model (one layer for snow and two layers for ice). The effect of the subgrid-scale snow- and ice-thickness distributions is accounted for through effective thermal conductivities, which are computed by assuming that the snow and ice thicknesses are uniformly distributed between zero and twice their mean value over the ice-covered portion of the grid cell. The storage of latent heat inside the ice resulting from the trapping of shortwave radiation by brine pockets is taken into account. The model also allows for the presence of leads within the ice pack. Vertical and lateral growth/decay rates of the ice are obtained from prognostic energy budgets at both the bottom and surface boundaries of the snow–ice cover and in leads. When the load of snow is large enough to depress the snow–ice interface under the water level, seawater is supposed to infiltrate the entirety of the submerged snow and to freeze there, forming a snow-ice cap. For the momentum balance, sea ice is considered as a two-dimensional

continuum in dynamical interaction with atmosphere and ocean. The viscous-plastic constitutive law proposed by Hibler (1979) is used for calculating the internal ice force.

The ocean–sea-ice model has a horizontal resolution of $3^\circ \times 3^\circ$, and there are 20 unequally spaced vertical levels in the ocean. To cope with the singularity at the North Pole associated with the geographical spherical coordinates, two spherical grids connected in the equatorial Atlantic are utilised: a grid with its poles situated on the geographical equator for the North Atlantic and the Arctic, and a classical latitude–longitude grid for the rest of the World Ocean (Deleersnijder et al., 1993).

2.1.3 Coupling technique

The AGCM and the CLIO model are coupled at a one-day frequency, which is the current time-step of the latter model. Fields are interpolated from one grid to the other by a procedure which preserves the average of the surface energy and water budgets. In order to avoid mismatch problems between non-overlapping land–sea masks, we have introduced subgrid continental and oceanic meshes into the AGCM, so that the World Ocean’s area is exactly the same in both models. This enables conservation of extensive quantities exchanged between the models through a simple interpolation procedure. The PBL scheme is applied separately over the continental, oceanic, and sea-ice portions of each grid cell. Mixing between the subgrid columns of air is accomplished by lateral diffusion. It is worth mentioning that no flux correction is employed.

2.2 Improvements made to the model

Within the framework of CLIMOD, a series of improvements have been made to the AOGCM in order to reduce its drift. These are the following.

The LMD has shown that the performance of its AGCM can be noticeably improved by increasing to 15 the number of vertical levels, by including an updated version of the longwave radiation scheme, which allows to treat the effect of each greenhouse gas separately and permits several types of cloud overlapping along the vertical, and by slightly lowering the transition criterion between cold and warm clouds. Therefore, all these changes have been implemented in the ASTR-GCMG’s version of the model.

As mentioned above, the AGCM simulates explicitly the cloud amount at each level. However, the radiative schemes need the total cloudiness as observed from the surface or from the top of the atmosphere. Two approaches have been tested at ASTR-GCMG: a random overlapping along the vertical (used in the previous version of the model), and a max/random overlapping (i.e., a random overlapping if there is a

clear sky level between two cloudy levels and a maximum overlapping for consecutive cloudy levels). The second formulation produces an overall decrease in cloudiness. The reduction of low-level stratiform clouds at mid-latitudes weakens the greenhouse effect there, which leads to sea-surface temperatures that are in better agreement with observations in those areas. In the tropical regions, the convective clouds are better stacked, but the net shortwave radiation at the surface is degraded. In view of these results, the second formulation was adopted.

The parameterisation of the direct effect of sulphate aerosols developed by Mitchell et al. (1995) has also been introduced into the AGCM and thoroughly tested. In this formulation the scattering of solar radiation by sulphate aerosols is crudely represented by an increase in surface albedo.

A sensitivity experiment has also been performed with CLIO in uncoupled mode to determine the influence of the water flow from the Arctic Ocean to Baffin Bay through the Canadian Archipelago on the water-mass properties of the Arctic Ocean and adjacent seas and, more generally, on the global ocean circulation (Goosse et al., 1997c). The results indicate that this flow plays a significant role in controlling the freshwater budget of the Arctic Ocean. When the Canadian Archipelago passage is open, the Arctic pycnocline experiences a noticeable increase in salinity. Furthermore, the flow of relatively fresh Arctic waters through the passage generates a pronounced decrease of surface salinity and density in the Labrador Sea, which leads to a diminution of convective activity there. Consequently, the NADW outflow in the model is reduced. Deep convection in the Norwegian Sea exhibits almost no change, despite a weakening of the inflow of relatively fresh Arctic waters through Fram Strait. Given these changes, we decided to keep open the Canadian Archipelago in CLIO, and the land–sea mask of the AGCM was modified accordingly.

In addition, a turbulence-closure scheme based on Kantha and Clayson's (1994) version of Mellor and Yamada's (1982) level-2.5 model has been incorporated in CLIO (Goosse et al., 1999). In order to evaluate the impact of this change on the model results, two quasi-equilibrium experiments were conducted with CLIO driven by observed atmospheric fluxes: one with the original parameterisation of vertical mixing and another with the comprehensive turbulence-closure scheme. We found that the new scheme allows a better representation of the wind-induced oceanic mixing. As the wind stirring is the major cause of mixing in summer, the mixed layer is generally deeper during this season. So, the surface warming penetrates deeper in the water column, yielding temperatures in the upper 100 m of the ocean that are in better agreement with observational data. Moreover, a strong salinity decrease was noticed in the top 60 m of the Southern Ocean. This enhances the stability of the water column

and reduces the deep convection taking place in this ocean. As a result, the Antarctic sea-ice extent increases and becomes closer to observations.

In parallel to this work, Campin and Goosse's (1999) parameterisation of density-driven downslope flows has been implemented in CLIO. This parameterisation is known for improving the representation of circulation and properties of deep water masses in coarse-resolution global ocean models.

Finally, a bug has been detected in the coupling procedure and has been subsequently corrected. The main effect of this bug was to produce too extensive a sea-ice cover in the model North Pacific. It contributed as well to the too intense open-ocean convection simulated in the Southern Ocean. The coupler has also been modified to enable the transfer of additional quantities, namely, the sea-ice albedo, the sea-surface albedo, and the sea-ice thickness, from CLIO to the AGCM. In the previous version of the model, these variables were calculated by the AGCM. This modification resulted in a better simulation of the melting of Arctic sea ice during summertime.

Once all these developments completed, a number of sensitivity experiments have been carried out with the revised AOGCM in order to define a set of parameter values that "minimise" the model drift. Those values were employed in the control run and climate-change experiments discussed below. It should be noted that completely eliminating the drift would require to employ a higher-resolution model and/or to design and implement new physical parameterisations, which was beyond the scope of the project.

2.3 Control experiment

A control simulation of 165-year duration (hereafter referred to as CONT) has been conducted with the new version of the AOGCM. The initial state consisted of outputs from equilibrium experiments performed with the stand-alone AGCM and CLIO model. In this run, the greenhouse-gas concentrations and sulphate-aerosol loading were prescribed to their 1970 values (Table I, Figure 1). The model which provided us with the geographical distribution of the sulphate-aerosol loading is described in Chuang et al. (1997) and Penner et al. (1998).

Table I: Greenhouse-gas concentrations for 1970.

	CO ₂ (ppm)	CH ₄ (ppb)	N ₂ O (ppb)	CFC-11 (ppt)	CFC-12 (ppt)
1970	323.774	1374.99	298.82	50.5	108.9

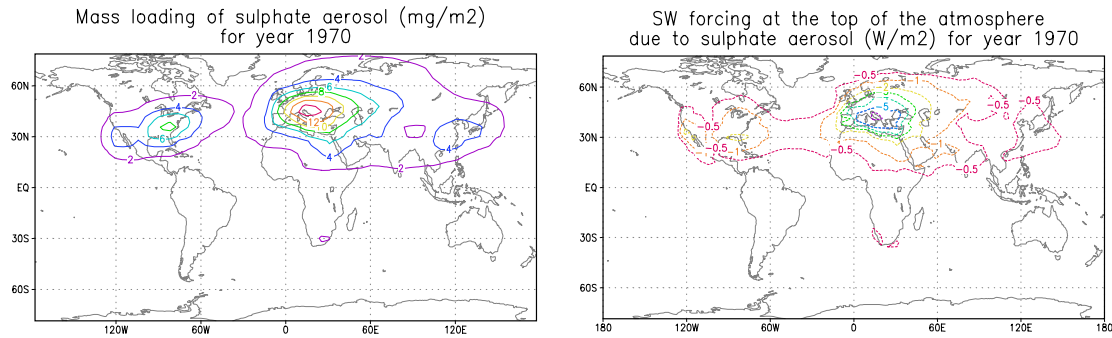


Figure 1: Geographical distributions of the sulphate-aerosol loading and associated radiative forcing for 1970.

As can be seen from Figure 2, the drift in annual mean, area-averaged sea-surface temperature (SST) amounts to $+1.3^{\circ}\text{C}$ after 10 years of integration and $+2.4^{\circ}\text{C}$ at the end of the experiment, which is quite reasonable for a coarse-resolution climate model including no flux adjustment. During the last 125 years, the mean warming rate is $0.003^{\circ}\text{C yr}^{-1}$.

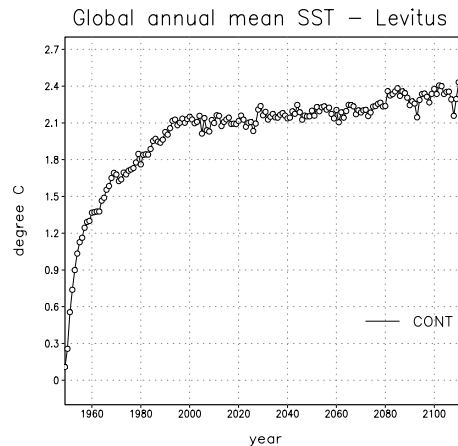


Figure 2: Temporal evolution of the difference between the annual mean, area-averaged SST computed by the AOGCM and the observed climatological value (Levitus, 1982).

Figure 3 shows the geographical distribution of the average error in annual mean SST over years 141–145 of CONT. Warm biases of up to 8°C are observed in the southern mid-latitudes. From about 50°S to the Antarctic continent, the deviation is maximum during austral winter and is attributable to a strong underestimation of the Antarctic sea-ice extent (see below). By contrast, the error around 40°S is largest during austral summer. One also notices much too high temperatures on the eastern sides of subtropical oceans. This error is due to the inability of the AGCM to correctly simulate marine stratocumulus clouds that form there. These low clouds, which strongly reflect solar radiation, are, at present, under-predicted by the majority of AGCMs (e.g., Gleckler et al., 1995). In addition, large warmings are visible in the regions of the Gulf Stream and Kuroshio. As these oceanic currents and their extension are associated

with high horizontal SST gradients, slight shifts in their position can lead to large local SST errors. The final major error is the cooling of the northern North Atlantic. This shortcoming mostly arises from a too intense river runoff into the Barents Sea. The overestimated runoff induces a strong freshening of the sea surface in the Barents and Norwegian Seas (Figure 4), which stabilises the water column. As a consequence, the rate of NADW production in the Norwegian Sea progressively decreases with time, and the North Atlantic thermohaline circulation and its upper limb, the North Atlantic Current and Norwegian Current, weaken accordingly (Figure 5). Less and less heat is therefore imported from equatorial regions into the northern North Atlantic, thus leading to a drop in SST there.

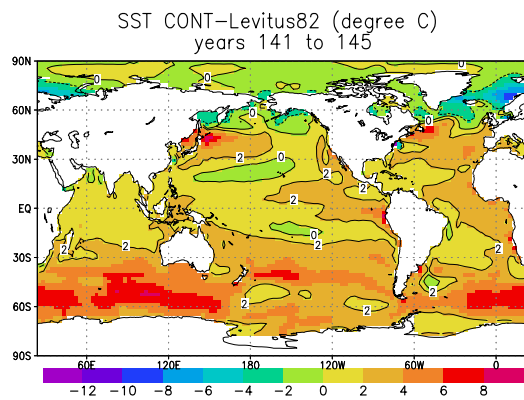


Figure 3: Differences between the annual mean SSTs averaged over years 141–145 of CONT and the observations of Levitus (1982). Units are °C.

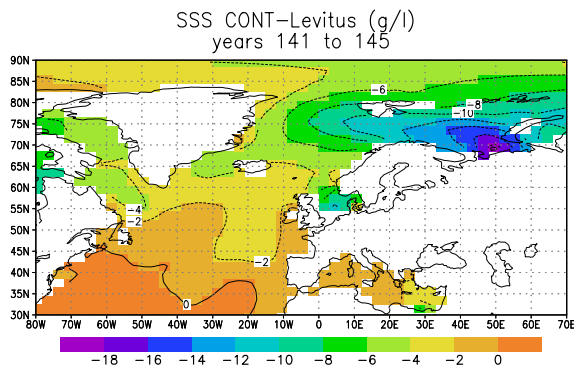


Figure 4: Differences between the annual mean sea-surface salinities averaged over years 141–145 of CONT and the observations of Levitus (1982). Units are psu.

The model does reasonably well in reproducing the observed amplitude of the seasonal cycle of the Arctic sea-ice extent (Figure 6), but the simulated extent appears overestimated throughout the year. Actually, the ice cover protrudes much too far southwards during all seasons in the Norwegian and Greenland Seas (Figure 7). This behaviour results from the too sluggish model North Atlantic and Norwegian Currents (see above) and from the very low latitudinal resolution of the AGCM in this region.

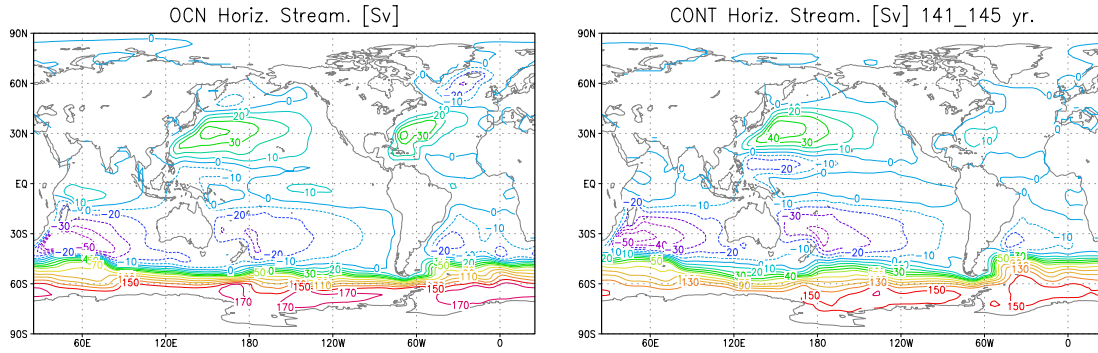


Figure 5: Annual mean mass-transport streamfunctions as simulated by the stand-alone CLIO model (left panel) and averaged over years 141–145 of CONT (right panel). Units are Sv ($1 \text{ Sv} = 10^6 \text{ m}^3 \text{ s}^{-1}$). Flow is clockwise around solid contours.

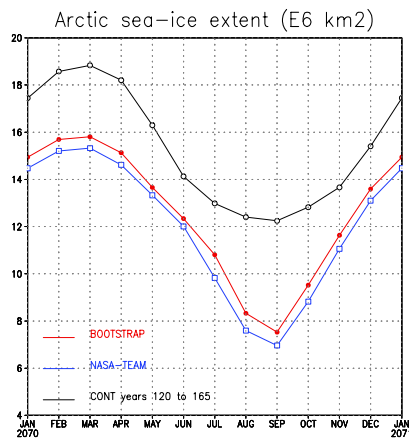


Figure 6: Seasonal cycles of the Arctic sea-ice extent (in 10^6 km^2) averaged over years 120–165 of CONT and observed following Gloersen et al. (1992) and Comiso et al. (1997).

Figure 8 indicates that the Arctic sea-ice volume increases substantially during the first 10 years of the run. Then, it remains nearly constant for 30 years before a new raise happens, which is caused by the above-mentioned progressive weakening of the North Atlantic and Norwegian Currents. After year 70, the model pack reaches a quasi-equilibrium state.

In the Antarctic, sea ice melts away during year 5. Afterwards, it reappears very sporadically in the Weddell and Ross Seas in wintertime, but its extent remains much lower than the observed one. The very intense, and unrealistic, open-ocean convection occurring in the model Southern Ocean is the main factor responsible for this underestimation.

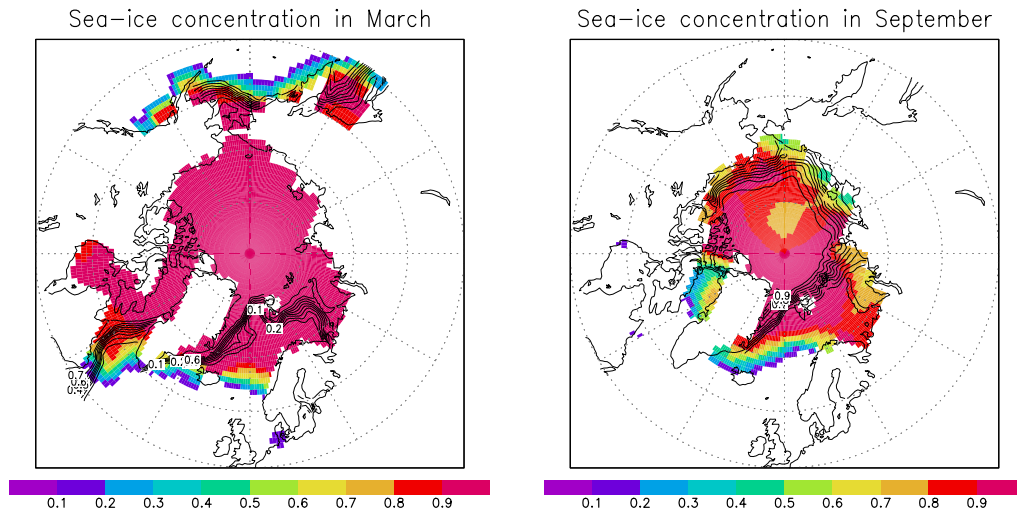


Figure 7: March and September sea-ice concentrations averaged over years 141–145 of CONT (colours) and observed following Comiso et al. (1997) (contours).

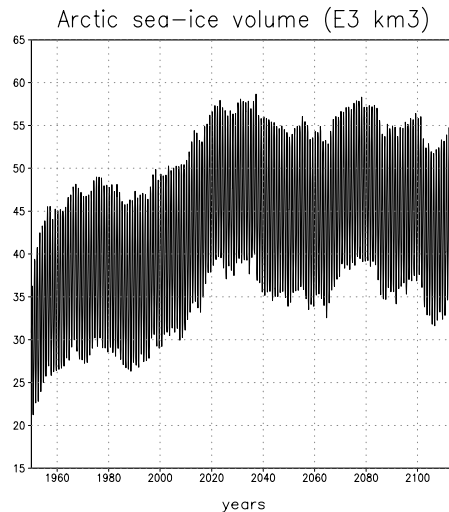


Figure 8: Temporal evolution of the Arctic sea-ice volume (in 10^3 km^3) during CONT.

Figure 9 depicts the vertical distribution in both the atmosphere and ocean of the drift in annual mean, zonally averaged temperature at the end of the experiment. In the atmosphere, the largest errors are confined in the near-surface layers, except between the tropics, where one observes a warm bias of 3 to 4°C near the tropopause. Regarding the ocean, the upper 850 m are overall too warm between 60° S and 50° N. By contrast, north of 50°N, the ocean undergoes a cooling near the surface and a warming at depth. This feature is a consequence of the weakening of the convective activity in the Norwegian Sea.

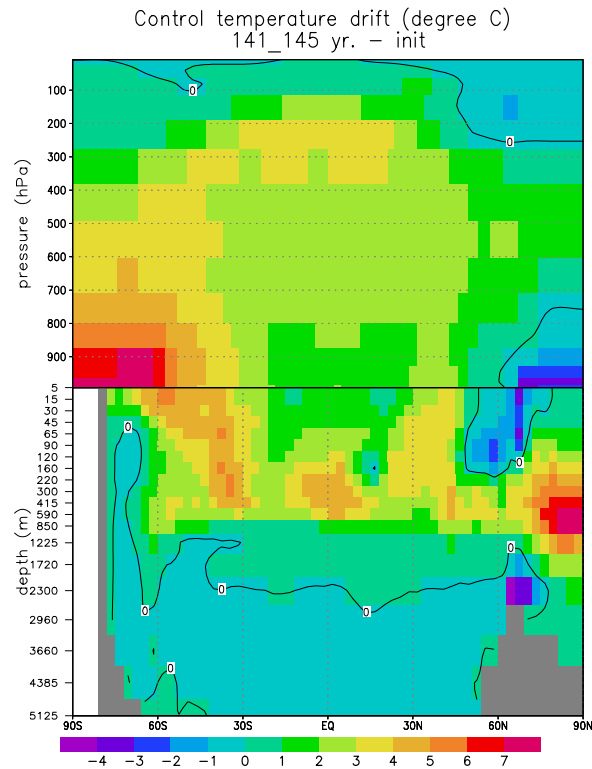


Figure 9: Vertical distribution of the drift in annual mean, zonally averaged temperature at the end of the experiment: years 141–145 of CONT minus the initial state.

From Figure 10, it can be seen that the simulated sea-level pressures, and thus winds, compare favourably with the National Centers for Environmental Prediction – National Center for Atmospheric Research’s (NCEP–NCAR) re-analysis data (Kistler et al., 2001). As in the data, the subtropical highs in the Northern Hemisphere are centred around 40° N during boreal summer, while they shift to 30° N in boreal winter. However, during the latter season, the Pacific subtropical high appears too pronounced, whereas the Atlantic one seems too weak. At the same period, low pressure centers prevail over the northern North Atlantic (Icelandic low) and North Pacific (Aleutian low). Compared to NCEP–NCAR’s re-analysis data, the model Aleutian low is located too far northwards. This is a consequence of the too intense Pacific subtropical high. This error leads to southwesterly winds near the Aleutian Islands, whereas they are in the opposite direction in the re-analysis. As a result, the modeled Kuroshio Current penetrates too far northwards (see Figure 5). Another area where some discordance is noted is the Arctic region, where the computed sea-level pressures are generally too low during winter and too high during summer. This error is partly due to the very coarse latitudinal resolution of the atmospheric model in that area. In the Southern Hemisphere, the model subtropical highs appear too weak both in austral summer and winter. However, the strong pressure gradient observed

between mid- and high latitudes is reasonably well simulated during the austral winter, although a bit too weak in the Pacific sector. The modelled Intertropical Convergence Zone (ITCZ) stays near 10° N in December–January–February, while it should be close to the equator. As for Trade winds, they are somewhat overestimated, especially in the Pacific basin. Finally, it is worth mentioning that the Indian monsoon is rather well reproduced by the model.

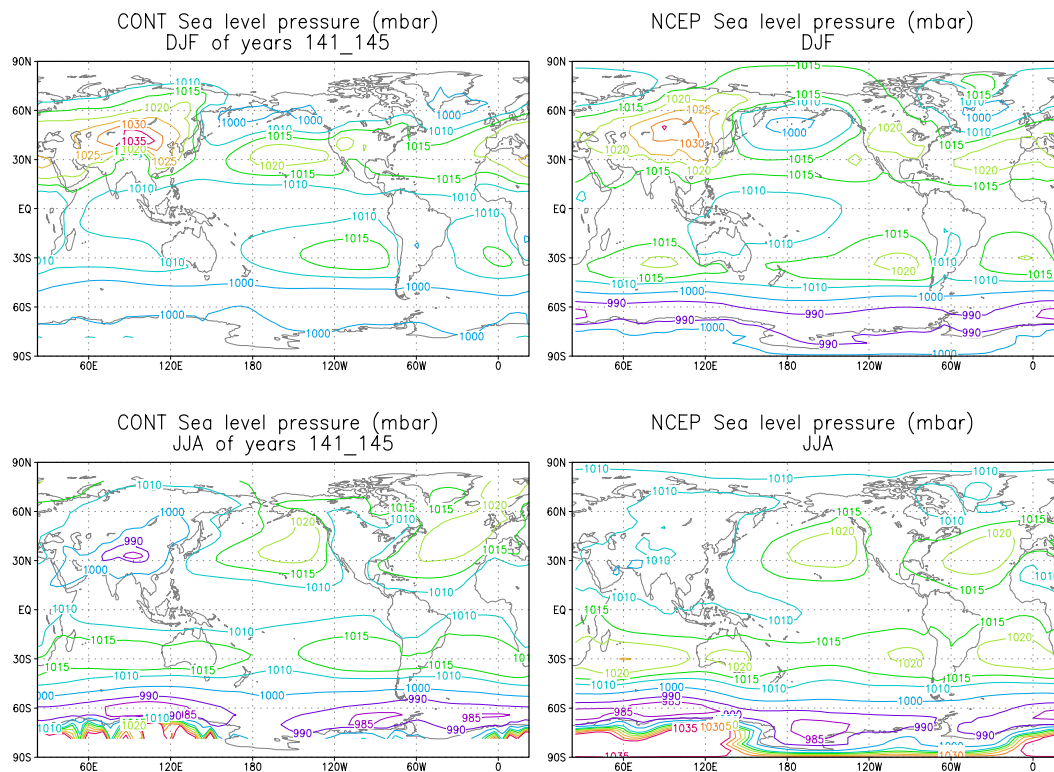


Figure 10: Geographical distributions of the sea-level pressure for December–January–February (DJF) (upper panels) and June–July–August (JJA) (lower panels) from years 141–145 of CONT (left panels) and from NCEP–NCAR’s re-analysis (Kistler et al., 2001) (right panels).

Although we have identified a number of inaccuracies in the results of the control experiment performed with the AOGCM, the discussion above demonstrates that the model shows sufficiently good agreement with enough aspects of the seasonal behaviour of the real climate to permit a sound study of the evolution of climate during the 21st century in response to human activities.

3. THE GISM

3.1 Overview of the model

The Greenland ice-sheet model (GISM) was originally developed at GI in the late 1980s (Huybrechts et al., 1991), and was upgraded during the course of the project. It consists of three main components which respectively describe the ice-sheet system, the solid Earth, and the surface mass balance, the latter of which represents the main driving force of the system. The ice-dynamics model solves the fully coupled thermomechanical equations for ice flow on a high-resolution three-dimensional mesh. It is time-dependent, and includes basal sliding and a temperature calculation within the bedrock. This basically involves the simultaneous solution of conservation laws for momentum, mass, and heat under appropriate simplifications, supplemented by Glen's flow law. The model has a free interaction between climatic input and ice thickness, and freely generates the ice-sheet geometry in response to prescribed changes in sea level, surface temperature, and mass balance.

The mass-balance model distinguishes between snow accumulation, rainfall, superimposed ice formation, and runoff, the components of which are all parameterised in terms of temperature. The melt-and-runoff model is based on the positive degree-day method and is similar to the method described in Reeh (1991). It takes into account ice and snow melt, the daily temperature cycle, random temperature fluctuations around the daily mean, liquid precipitation, and refreezing of meltwater.

The bedrock model describes the interaction between changes in the ice loading and the bed elevation. In the model version that was applied within this project, a two-layer isostasy model is employed. In this approach, the time-dependent response of the bed depression is given by the viscous properties of the asthenosphere (upper mantle), which is overlain by a rigid elastic lithosphere that determines the ultimate shape of the imprint. Further details on the models and a comprehensive outline of their formulations can be found in Huybrechts and de Wolde (1999).

3.2 Improvements made to the model

The GISM underwent a major overhaul within the project. This entailed the incorporation of new input datasets, the implementation of a more sophisticated mass-balance parameterisation that was recalibrated against recent mass-balance measurements, the coupling with more comprehensive isostasy models, and the reformulation of various freshwater components to enable coupling with the OGCM.

3.2.1 Input datasets

The main inputs to the model are bed topography, a mask specifying the coastline and the margin of the continental platform, the annual mean surface temperature, and the mass balance. The horizontal resolution of the model is of 20 km, resulting in a grid of $83 \times 141 = 11,703$ gridpoints.

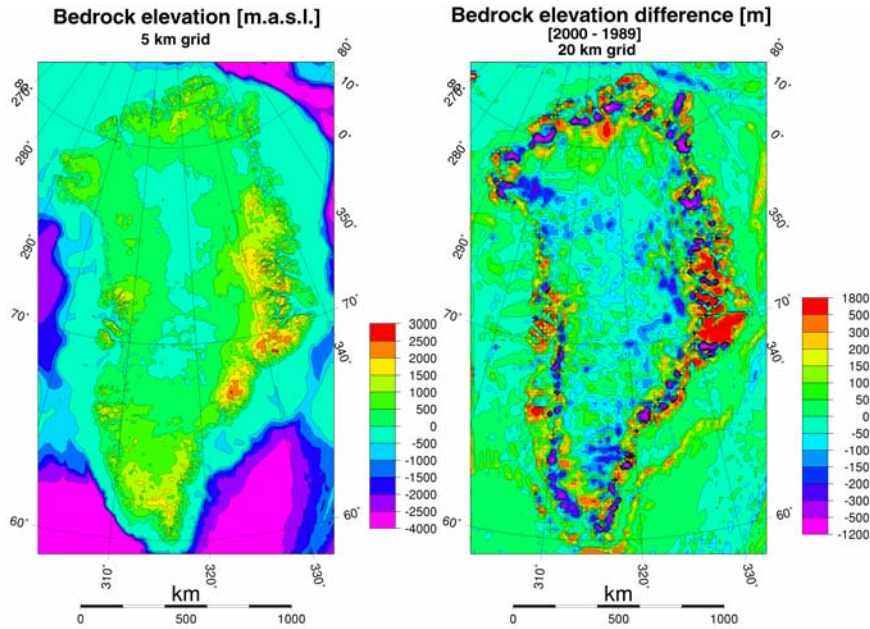


Figure 11: New dataset for bedrock topography obtained by subtracting the revised ice-thickness grid from high-accuracy surface-elevation data, shown for a grid resolution of 5 km (left panel). The right panel displays the changes with respect to the previous dataset ("1989 data") used in most of the older Greenland ice-sheet modelling studies (Letréguilly et al., 1991).

Much care was taken to derive a new gridded map for the bed topography, crucial to a correct geographical representation of the ice flow. This was done by subtracting an ice-thickness grid from highly-accurate surface-elevation data derived from GEOSAT and ERS-1 satellite altimetry, supplemented by airborne laser and radar altimetry and local terrestrial surveys (Ekholm, 1996). The surface-elevation dataset was initially provided at a $1.2' \times 3'$ resolution over the Greenland continent, and was merged with the ETOPO5 dataset for the ocean floor at the coastline. The ice-thickness grid basically stemmed from radio-echo soundings made by the Technical University of Denmark during airborne campaigns in the 1970s. One of the problems with the ice-thickness grid were missing values near to the ice-sheet margin, so that an artificial circular ridge around most of the Greenland ice sheet was created during the subtraction process. This problem was fixed by employing standard plastic flow theory to reconstruct ice thickness at the margin. This theory provides a relation (i) between ice thickness and distance to the margin, and (ii) between surface gradient and ice

thickness (Paterson, 1994). The first relation was used to select the grid points that needed to be revised, whereas the second property was used to compute a more acceptable ice thickness. Figure 11 shows the result. Hypsometrical curves of the surface elevation brought to light that the most important differences between the old and new data are located in the ablation zone, which results are also wrapped into the final bedrock topography. The final geometric data were derived for 4 different resolutions, namely 2.5, 5, 10, and 20 km, and thoroughly checked for internal consistency (Table II).

Table II: A comparison of ice-sheet statistics derived from the "old 1989 dataset" (Letréguilly et al., 1991) and from the new dataset which was developed within the project ("new 2000 dataset"). All averages are corrected for areal distortions of the map projection (Reeh and Starzer, 1996). The numbers represent new estimates of the physical characteristics of the Greenland ice sheet.

		Old 1989 dataset	New 2000 dataset	New 2000 dataset
		20 km	20 km	2.5 km
		(83 x 141)	(83 x 141)	(657 x 1121)
Land area	[km ²]	2187470	2131431	2211000
Ice-sheet area	[km ²]	1673466	1671500	1733842
Ice volume	[km ³]	2845522	2816971	2908882
Total precipitation over ice sheet	[km ³ /yr w.e]	538.665	527.0746	569.2578
Mean ice thickness	[m]	1700.4	1685.295	1677.436
Maximum ice thickness	[m]	3200.0	3235.202	3285.489
Mean bedrock elevation of total Greenland	[m]	410.8	458.6298	466.8966
Maximum bedrock elevation of total Greenland	[m]	2151.0	2446.620	3174.190
Mean surface elevation of ice sheet	[m]	2128.5	2123.337	2112.914
Maximum surface elevation of ice sheet	[m]	3261.0	3228.090	3239.000
Mean precipitation rate over ice sheet	[mm/yr w.e]	321.9	315.3304	328.3215
Maximum precipitation rate over ice sheet	[mm/yr w.e]	2548.0	2577.770	2647.190

A second important dataset that was updated within the project concerned precipitation. The precipitation dataset used in previous calculations was digitized from a map presented in Ohmura and Reeh (1991). Much more detailed information was obtained in the late 1990s from oversnow traverses by in particular the Alfred Wegener Institute, Bremerhaven. These new data have been embedded in the old Ohmura-Reeh datasets to produce new maps for accumulation and precipitation rates (Jung-Rothenhäusler, 1998), and were also interpolated on the various model grids. The new data show substantially drier conditions over northern and northeastern Greenland. This is important for, amongst other things, the ice-sheet mass balance and the delineation of zones of basal melting and basal sliding.

3.2.2 Mass-balance model

Several improvements were made in the way the mass-balance model treats ice and snow meltings and subsequent runoff. First, the sum of positive-degree days (PDDs), which represents a melt potential in the runoff model, is now derived in an exact analytical way using the mathematical properties of the standard normal density and distribution functions, whereas this was previously done with a rather coarse numerical integration. Second, the model calculates the fraction of precipitation falling as rain depending on the surface temperature, and treats the rainwater in a similar way as meltwater. Third, the meltwater retention is treated in a more comprehensive way taking into account both the refreezing process and the capillary suction effect of the snow pack (Pfeffer et al., 1991; Janssens and Huybrechts, 2000).

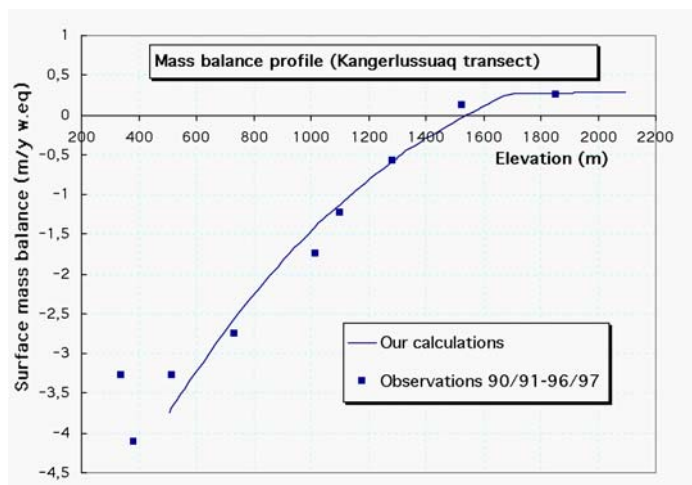


Figure 12: Comparison between the surface-mass-balance profile computed by the recalibrated mass-balance model and observations on the Kangerlussuaq transect averaged for the seasons 1990/91 to 1996/97 (Greuell, 1998).

The melt-and-runoff model was subsequently recalibrated by regionally matching the mass balance to a compilation of available observations of equilibrium-line altitude (ELA), mass-balance profiles, calving rates, and bottom melting rates. Particular attention was paid to obtaining a balance between runoff and accumulation in southwestern sectors, where iceberg calving is virtually absent, and to approximately matching runoff in the north with recent estimates of accumulation rates, bottom melting rates, and calving rates (Higgins, 1991; Rignot et al., 1997; Reeh et al., 1999). A detailed comparison with mass-balance data obtained between 1990 and 1997 along a transect near Kangerlussuaq, central West Greenland, shows that the mass-balance model is generally able to reproduce the field data within a reasonable accuracy (Figure 12). This generally acceptable agreement is further underlined from a comparison of calculated ELAs with observed altitudes (Figure 13). Here, the agreement is generally within 100 m or so. Nevertheless, it should be remarked that a comparison between calculated and observed ELAs should be reserved because the observations refer to different, sometimes short, time periods and because the observed interannual variability in the ELA position is large. In addition, the observed ELA of about 400 m in southeastern Greenland (65.5° N) is probably an outlier.

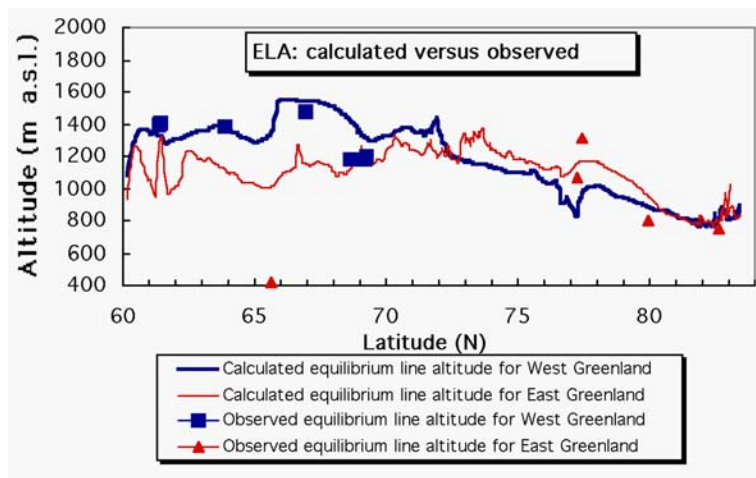


Figure 13: Comparison between the computed equilibrium lines at the west (blue) and east (red) sides of the Greenland ice sheet and available observations.

Another test of the mass-balance model entailed the comparison of the residual between total accumulation and total runoff with estimated calving fluxes from observations (mainly from iceberg production). These should agree in case of equilibrium and in case the calving flux can be equated with the mass flux across the grounding line. Although the total quantities over the entire ice sheet are roughly in agreement, there are substantial regional differences. This is shown in Figure 14. The excess mass balance found in the northern and northeastern regions can be explained by excessive melting below the ice shelves which form in the fjords and greatly reduce

calving rates (Rignot et al., 1997). The deficit in the western part probably indicates that the model overestimates runoff and/or that the derived calving flux is too large. The results also indicate the resolution dependence of the calculated fluxes. That is particularly the case for the runoff flux, which crucially depends on surface temperature, and thus on the ability of the digital elevation model to resolve the topography at the margin where the runoff takes place.

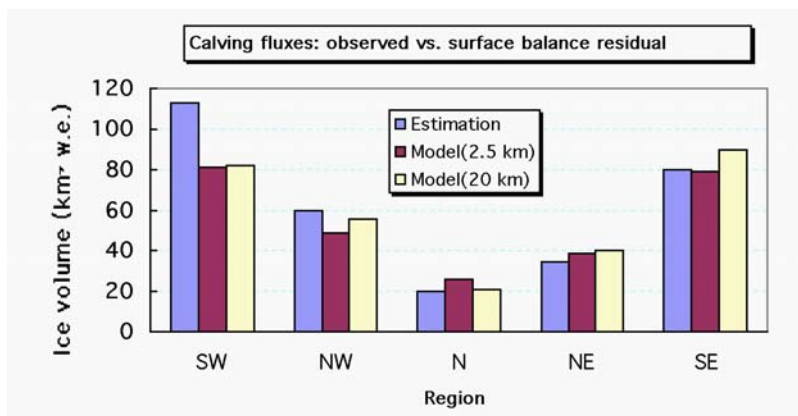


Figure 14: Comparison of calving fluxes derived from observations ("estimations") with regional mass-balance residuals (accumulation minus runoff) for model resolutions of 2.5 and 20 km. Results are shown for 5 Greenland ice-sheet sectors ("regions"). Units are km³ of water equivalent.

With the recalibrated mass-balance model, the total accumulation over the ice sheet was calculated to be 542.27 km³ yr⁻¹ of water equivalent, the runoff 261.98 km³ yr⁻¹, and the residual amount of ice being discharged into the ocean 280.29 km³ yr⁻¹ (assuming a steady state). Figure 15 shows some of the characteristics of this standard run. Under the assumption of a constant precipitation, the sensitivity of the mass balance for a +1°C warming corresponds to a sea-level rise of 0.335 mm yr⁻¹ °C⁻¹. This value is reduced to 0.246 mm yr⁻¹ °C⁻¹ if it is assumed that the precipitation increases by 5% °C⁻¹ in conjunction. These sensitivities are entirely in line with other studies (Church et al., 2001). It is also found that an annual mean temperature increase of 2.2°C is enough to reach a zero surface mass balance, that is, total runoff equals total accumulation. The implication is that the Greenland ice sheet cannot be sustained for a larger warming unless it is able to reorganise its area-elevation distribution to enlarge the accumulation zone at the expense of the ablation zone, e.g., by creating a steeper surface slope at the margin (Huybrechts and de Wolde, 1999).

An extensive parameter-sensitivity study revealed that the runoff-model results are most sensitive to the standard deviation of the surface temperature, σ , which represents the statistical spread of real daily temperature with respect to the monthly average temperature. Other sensitive parameters are the PDD factors for ice- and

snowmelt, the thickness of the thermally active layer, d , that absorbs the latent heat released by meltwater refreezing, and the surface temperature distinguishing between rain and snow. Figure 16 shows the parameter sensitivity of σ , snowmelt PDD factor, icemelt PDD factor, and d for relative changes of $\pm 25\%$, starting from a reference state with $\sigma = 4.2^\circ\text{C}$, snowmelt PDD factor = $2.7 \text{ mm } ^\circ\text{C}^{-1} \text{ day}^{-1}$, icemelt PDD factor = $7.2 \text{ mm } ^\circ\text{C}^{-1} \text{ day}^{-1}$, and $d = 1\text{m}$.

We also investigated the possibility to refine the mass-balance parameterisation by including spatial variation in the standard deviation of the surface temperature σ .

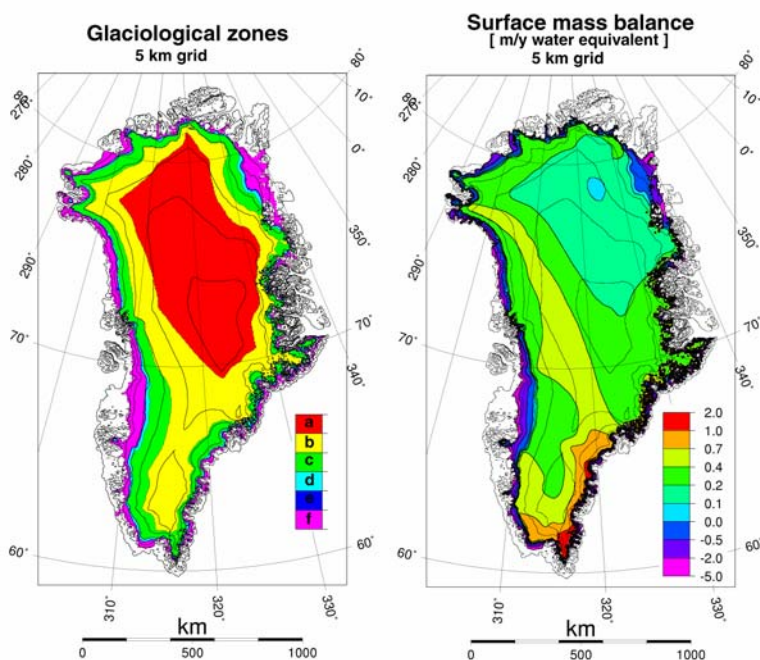


Figure 15: Characteristics of the surface mass balance of the Greenland ice sheet. The left panel displays the predicted zonation (facies) of the Greenland ice sheet. a = dry snow zone; b = percolation zone; c = wet snow zone; d = slush zone; e = superimposed ice zone; f = ablation zone. The right panel shows the corresponding surface mass balance values for the calibrated mass-balance model.

Relations derived from the ASTR-RCMG's regional atmospheric model MAR (see Section 5.1) for the period between September 1989 and August 1991, using the European Centre for Medium Range Weather Forecasts' (ECMWF) re-analyses as boundary conditions on a 50-km grid. For most catchment areas of the Greenland ice sheet, we found a positive relationship between σ and altitude with correlation factors r ranging between 0.62 to 0.98, but the correlation was weak for the crucial southwestern region. For the total ice sheet, we found an average σ of 4.35°C at an elevation of 1000 m, increasing with 0.06°C for each 100 m, but with a weak correlation

coefficient of 0.64. The relationship of σ with the latitude is rather weak for the total ice sheet ($r = -0.74$), but better if we divide the ice sheet in a northern part and southern part along 71° N. In the southern part, σ increases from about 4°C to 6°C , with 0.12°C for each degree ($r = 0.74$), while it decreases again from 6°C to 4°C in the northern part, with 0.14°C for each degree ($r = 0.73$). However, using this supplemental information did not improve significantly our mass-balance results, so we opted for a constant σ and used the PDD factors as tuning parameters.

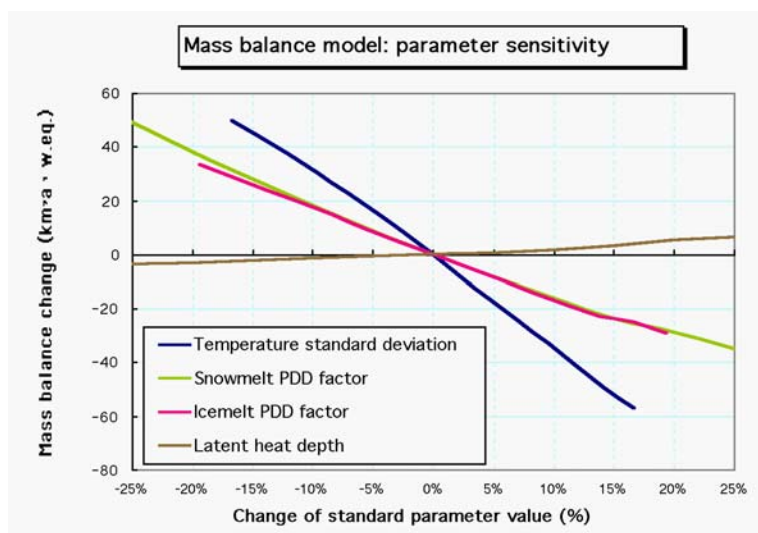


Figure 16: Sensitivity of the total surface mass balance (accumulation minus run-off) of the Greenland ice sheet for variations of crucial parameters by $\pm 25\%$. Mass-balance units are $\text{km}^3 \text{yr}^{-1}$ of water equivalent.

3.2.3 Bedrock model

The treatment of isostatic displacements are another important component of the GISM. That is because these also determine changes of surface elevation, which feed back on the surface temperature and, hence, on the surface mass-balance components, especially in the marginal ablation zone. It has been shown that the process of bedrock adjustment is sensitive to bedrock parameters and to the particular method applied (Le Meur and Huybrechts, 1996).

In the original version of the GISM (Huybrechts et al., 1991), the bedrock was treated with a two-layer model that assumed a relaxation-type viscous asthenosphere and a lithosphere obeying local isostatic compensation. In reality, however, the lithosphere is rigid, so that the compensation is non-local. Furthermore, the asthenosphere responds to different wavelengths of the load with a wide spectrum of relaxation times.

To investigate the consequences for the time-dependent behaviour of the Greenland ice sheet, the GISM was interactively coupled with a self-gravitating visco-elastic bedrock model (Le Meur and Huybrechts, 1998, 1999; Huybrechts and Le Meur, 1999). This coupling allows to fully account for the entire spectrum of time-space behaviour of the bedrock isostatic response.

A particular characteristic of the visco-elastic model is that it allows to split the rate of bedrock uplift into a long-term viscous part driven by the past loading history and an elastic instantaneous component related to the current load change. In the papers by Le Meur and Huybrechts (1998, 1999), this characteristic was used to present a framework to infer past and current loading changes. It was advocated to subtract the viscous evolution pattern from any observations to infer the residual elastic pattern. The resulting field could then be deconvolved to derive the present-day ice-loading change in an independent way. In another paper, the corresponding gravity-anomaly trends were analysed in more detail, with an emphasis on the various gravity corrections (free-air, Bouguer, terrain) required to interpret both surface and soon-becoming-available satellite-gravity data (Le Meur and Huybrechts, 2001).

This may provide a further constraint on the current evolution of the ice sheet. The present-day ice-sheet evolution is an important boundary condition to assess changes due to future anthropogenic forcing. Examples of relevant fields produced by the coupled Greenland ice-sheet–visco-elastic-bedrock model are displayed in Figure 17.

However, in view of the substantial computer resources required for the fully coupled approach, it was decided that the version of the GISM to be coupled to the ASTR-GCMG's AOGCM should employ a more simple approach for the bedrock isostatic response. Therefore, a two-layer model was introduced, consisting of a rigid elastic plate (lithosphere) overlying a viscous asthenosphere having only one characteristic response time-scale independent of the size of the load. It was found that this reduced model is able to reproduce the main characteristics of the full visco-elastic approach, but is much more efficient in its use.

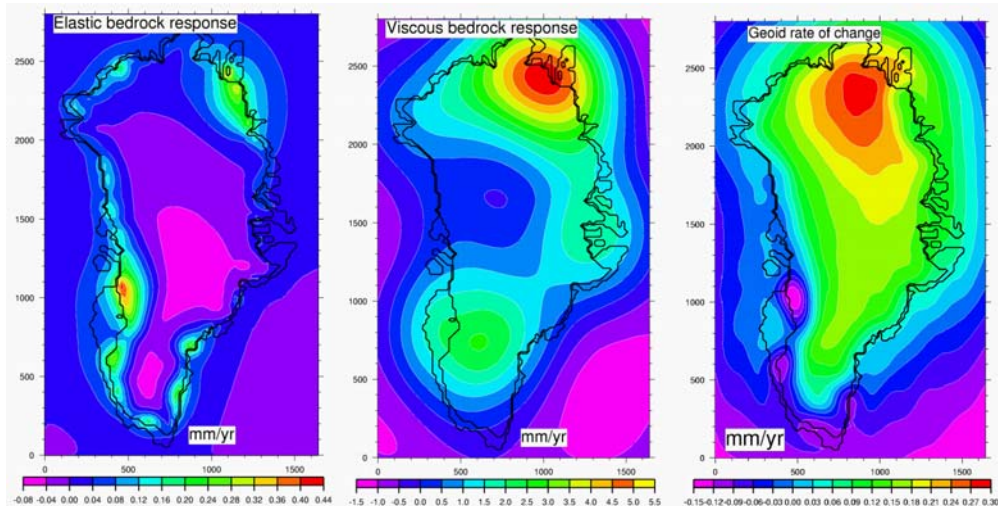


Figure 17: Present-day evolution patterns of bedrock elevation and geoid height of the Greenland ice sheet resulting from a coupled run over the last two glacial cycles. The displayed fields are to be understood as the average over the last 200 years. More details on these experiments and their significance can be found in Le Meur and Huybrechts (1998, 2001).

3.2.4 Calculation of the freshwater flux

To be able to close the hydrological cycle over Greenland in coupled runs with the AOGCM, new modules were written to determine the annual freshwater fluxes feeding into the ocean. This involved the separation of water fluxes in components of ice-sheet runoff, iceberg calving, runoff from the ice-free land, and melting below the ice sheet. Ice-sheet runoff is straightforwardly derived from the surface mass-balance model. The runoff from the tundra was set equal to the yearly precipitation, in effect assuming no sources or sinks for this component.

The determination of the calving flux needed more attention. In older versions of the model, this was simply calculated as the residual between the sum of all other mass-balance components (snow accumulation, surface runoff, basal meltwater), and the resulting total ice-volume change. Now, the calving flux is calculated more rigorously as the volume flux across the grounding line. This is computed as the sum of ice thickness multiplied by glacier width and depth-averaged horizontal velocity for all those gridpoints which border the coastline. This neglects melting above and below the ice shelves that locally form in embayments in North and Northeast Greenland, and which magnitudes can be substantial (Reeh et al., 1999; Mayer et al., 2000). However, from an oceanic point of view, these ice shelves can be considered as (melting) icebergs, with the difference that the freshwater flux is supplied locally rather than during the iceberg drift around Greenland. But most importantly, the newly adopted

treatment of calving allows to study the evolution of calving as an independent process, irrespective of the evolution of the other mass-balance components.

3.3 Initialising the current ice-sheet evolution over the last two glacial cycles

Because of the long response time-scales of the Greenland ice sheet (of the order of thousands of years), it is necessary to start the calculations early enough in the past to assess the current ice-sheet evolution that would occur irrespective of any future anthropogenic forcing. To that end, the GISM was first initialised over the last two glacial cycles. Figure 18 shows the results. The model forcing was derived from the GRIP $\delta^{18}\text{O}$ record (Dansgaard et al., 1993) to prescribe temperature and precipitation changes and from the SPECMAP stack (Imbrie et al., 1984) to prescribe sea-level changes, similar to the experiments described in Huybrechts and de Wolde (1999) and Huybrechts and Le Meur (1999). Large volume and bed-elevation changes are found to occur, especially during the Eemian, when climate was several degrees warmer than today. Of relevance for the greenhouse-warming experiment is the evolution for the present day, when the ice sheet is found to be near to a stationary state, corresponding to a mean ice-sheet thinning rate of -4 mm yr^{-1} , or a global sea-level contribution of $+1.8 \text{ mm century}^{-1}$.

Of interest is also the corresponding evolution of the total Greenland freshwater flux (Figure 18, panel c). For most of the glacial evolution, the largest part consists of the calving flux across the grounding line. Runoff from the ice sheet is of about the same order of magnitude than the calving flux for present conditions, but becomes dominant during the Eemian around 130,000 years before present. Basal melting from below the ice sheet is insignificant and about two orders of magnitude smaller. Runoff from the surrounding tundra is largely controlled by the size of the ice-free area around the Greenland margin, and is likewise largest during the Eemian, when the ice-sheet area was reduced by about half. During the Eemian, calving was minimal because only few parts of the ice sheet extended to the ocean.

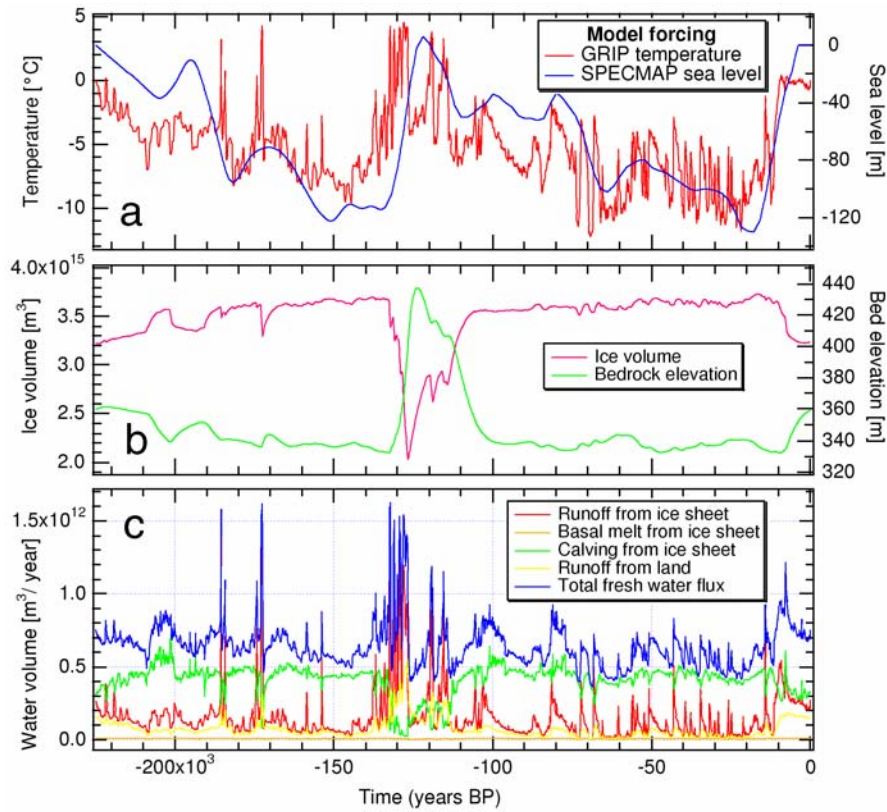


Figure 18: Results of the experiment conducted with the GISM over the last two glacial cycles to initialise the current evolution of the Greenland ice sheet. (a) Model forcing. (b) Ice volume and mean bedrock elevation calculated for the continental shelf area above about -300 m. For comparison, an ice volume change of $1 \times 10^6 \text{ km}^3$ corresponds to about 2.5 m of global sea-level change. (c) Components of the freshwater flux for the entire continent. $10^{12} \text{ m}^3 \text{ yr}^{-1}$ corresponds to about 0.03 Sv.

4. THE MAR MODEL

4.1 Overview of the model

The MAR model is described in detail in Gallée and Schayes (1994) and Gallée (1995). MAR is a hydrostatic primitive-equation atmospheric model in which the vertical coordinate is the normalised pressure. The subgrid-scale vertical fluxes are calculated by using the E- ϵ model of turbulence (Duynkerke, 1988) or the more simple model of Therry and Lacarrère (1982). The parameterisation scheme for the surface layer, where turbulent fluxes may be assumed constant, is based on the Monin-Obukhov similarity theory. The hydrological cycle includes a cloud-microphysics model of Kessler-type (Kessler, 1969), with conservation equations for cloud-droplet, raindrop, cloud-ice-crystal and snowflake concentrations. In particular, sublimation of snowflakes is a function of the air relative humidity. Sophisticated solar and infrared radiation schemes are utilised. The solar radiation scheme is from Fouquart and Bonnel (1980). The longwave radiation scheme follows a wide-band formulation of the radiative transfer equation (Morcrette, 1984), which was designed for use in AGCMs. Cloud properties are taken into account in the solar and infrared radiation schemes by computing the liquid-water path in each model layer from the hydrometeor concentrations. The horizontal resolution of MAR typically ranges between 2 and 50 km. Prior to the project, MAR has been coupled with a multi-layered thermodynamic snow model (Gallée and Duynkerke, 1997) and (separately) with the soil–vegetation–atmosphere interface (SVAT) of De Ridder and Schayes (1997). These couplings were a requisite for employing MAR in climate studies.

4.2 Improvements made to the model

4.2.1 Adaptations of the model with a view of enabling climate simulations

The domain size under consideration for climate simulations is relatively large. Unfortunately, the momentum equations of MAR have been written for a plane surface, so that the introduction of map projections is required when the domain is large (e.g., Anthes and Warner, 1978). Such a map projection is necessary to locate the model grid points on the Earth's sphere, in order to make use of geographical data such as topography, and to transfer large-scale meteorological fields to the lateral boundaries of MAR. Within the framework of CLIMOD, we have implemented in MAR two standard projections that were not available in previous versions of the model: the stereographic oblique projection and the Lambert conformal projection. It was also necessary to

somewhat modify the model equations in order to account for the curvature of the Earth. With these modifications, the model can now be adapted to domain sizes up to about 3000 km × 3000 km (and more in the zonal direction), with only minor changes in its equations (Marbaix, 2000). Test simulations have proved the validity of this approach.

The next step is the adaptation (or pre-processing) of the large-scale data prior to their use at the lateral boundaries of MAR. These data usually come from a relatively coarse-resolution GCM. A horizontal and vertical interpolation on the grid of MAR is therefore necessary, because of the enhanced resolution and the different coordinates, i.e., the map projection. For the horizontal interpolation, we selected the cubic spline interpolation (the implementation allows the use of stretched horizontal grids as input). The grid change implies a rotation of the wind vector. In addition, the topography associated with the large-scale data and that of the MAR model are generally different, because it is better represented in the latter due to its higher resolution. This complicates the problem of vertical interpolation.

The method utilised to solve this topography-difference issue is relatively basic. Indeed, it is generally accepted that simple procedures are adequate for regional climate modelling (e.g., Christensen et al., 1997). Our method is partly based on the work of Majewski (1985) in the context of numerical weather prediction. In the lower atmospheric levels, topography differences always imply some kind of extrapolation with inherent shortcomings. The implemented technique aims at conserving important atmospheric variables through the altitude-change process: potential temperature, specific humidity, and wind. The procedure uses a hybrid pressure/sigma coordinate for the interpolation (Marbaix, 2000). This means that the profiles of the atmospheric variables are stretched in the lowest 200 hPa of atmosphere (i.e., roughly in the boundary layer) to match the new topography, while the variables are simply linearly interpolated (in $\log(p)$) above that level. This is schematically illustrated in Figure 19.

The last step consists in the incorporation of the interpolated large-scale data at the lateral boundaries of the model. The numerical boundary condition which is widely accepted as standard in regional climate modelling, i.e., relaxation towards large-scale values (Davies, 1983), was already implemented in MAR at the start of CLIMOD. However, the choice of the relaxation coefficients is a matter of debate (e.g., Giorgi et al., 1993). The link between this empirical work and early theoretical investigations from Davies (1983) was clearly missing. Therefore, we made a synthesis and an extension of the theoretical work. On this basis, we were able to present an original comparison between the theoretical guidelines and empirical values from the regional climate-modelling literature (Marbaix et al., 2001).

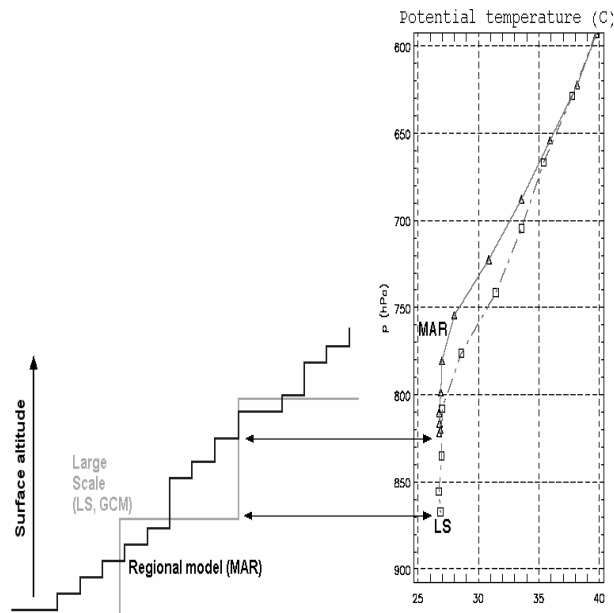


Figure 19: Schematic illustration of the adaptation to topography changes. Left-hand side: large-scale (e.g., GCM) and MAR surface heights. Right-hand side: potential temperature profiles (example). Dashed line: large-scale values; solid line: result of the interpolation to the MAR grid with adaptation to the topography.

The developed theory has limitations due to its simplicity in comparison with the numerical schemes employed in the models. However, there are indications that the main results may come from general principles. Broadly speaking, this means that the relaxation rate must increase smoothly when approaching the boundaries, with no abrupt change – specifically close to the boundary and close to the free model area.

The sensitivity tests performed with MAR are based on an evaluation of non-physical effects (noise) near the boundaries. This is mainly seen in the wind field and, especially, the meso-scale kinetic energy (MKE) (Giorgi et al., 1993), but we found that looking at small-scale changes in the surface pressure field may sometimes emphasize boundary-related noise which is not seen in the MKE field. An illustration of the sensitivity tests is given in Figure 20, where MKE peaks show that some of the tested relaxation configurations are less appropriate. Both theory and sensitivity tests reveal that the highest performant standard relaxation profile is the exponential decay, and that parabolic profiles also yield satisfactory results. We did not find any conflicting conclusion between the theoretical assessment and the sensitivity study. Two types of relaxation schemes are generally used: the simple Newtonian method (which progressively forces the model solution towards the large-scale values) and the diffusion-relaxation method (which diffuses the model/large-scale difference horizontally). Both the theory and empirical tests suggest that the diffusive relaxation

produces much less noise in the model domain than the Newtonian form. This confirms the choice already made in MAR.

A last remark on the model adaptations for climate simulations is that minor changes in the configuration or parameters may sometimes have large consequences on the model results; the most significant of these changes will be described in the sections dealing with validation.

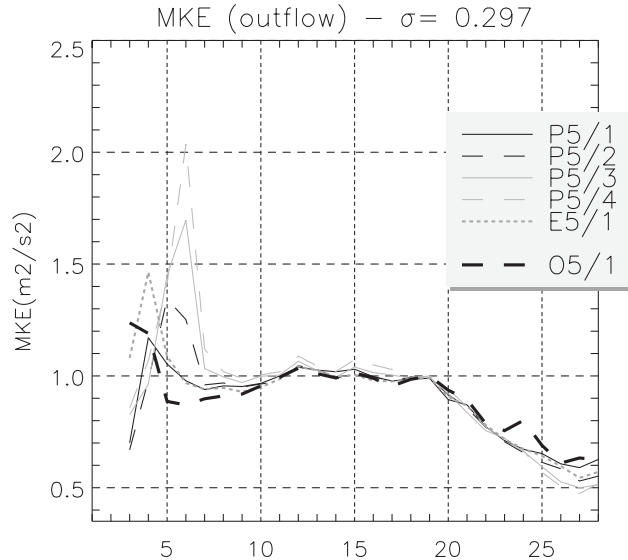


Figure 20: Sensitivity tests for the choice of the lateral boundary coefficients in MAR (see Marbaix et al. (2001) for details). Meso-scale kinetic energy (MKE) is given as a function of the distance to the domain boundary (in grid points). P5/1 to 4 correspond to relaxation coefficients that follow a parabolic decay from the boundary towards the interior domain, E5/1 corresponds to an exponential decay, and O5/1 is the theoretical optimum value from Davies (1983).

4.2.2 Deep convection

Moist convective instability can produce strong vertical motions which transport heat and moisture in the whole troposphere, a process called deep convection. The characteristic time-scale is about 1 hour and the horizontal extent is typically 10 km. Therefore, the deep-convection process is not explicitly represented in meso-scale models when the grid-cell size is larger than a few kilometres. It is thus important to introduce a parameterisation which mimics this phenomenon. Indeed, the convective activity is sometimes the dominant atmospheric motion, and can interact with the large-scale evolution. Moreover, this process is responsible for most of the summer precipitation at mid-latitudes.

Within CLIMOD, a sophisticated convection scheme has been developed and implemented in MAR (Brasseur, 1999). This scheme is based on the formulation of Fritsch and Chappel (1980) and Kain and Fritsch (1993), with some modifications. The retained approach is called hybrid: it is an intermediate solution between a fully explicit representation by the model and a simple global parameterisation of the entire convection phenomenon. The scheme includes a representation of updraft, downdraft, and environmental motions. The hybrid name refers to the fact that the detrained precipitation falling between the clouds is not parameterised, but represented explicitly by the model on the basis of a parameterised convective source term. This method is well suited for grid-cell sizes between 10 and 50 km, i.e., large enough to avoid an explicit representation of some convective clouds and small enough to resolve the meso-scale organisation. The adjusted profiles of temperature and moisture are computed in order to remove the available buoyant energy. The precipitation is parameterised as a function of the wind shear. One of the specific aspects of the scheme of Brasseur (1999) is that constraints have been added to ensure the conservation of the moist static energy and the equivalent water content. This scheme has been widely tested on idealised cases and real situations, in particular over Belgium.

4.2.3 *Initialisation of the soil model*

As already mentioned, a comprehensive soil–vegetation–atmosphere interface (SVAT) has been developed and implemented in MAR within the framework of other research projects (De Ridder and Schayes, 1997; De Ridder, 1998). This scheme determines the energy and water balances of the soil (5 levels) and vegetation. A particular feature of the radiation computation is the use of an effective leaf-area index, which accounts for the opening of leaves stomata. Other represented processes include plant transpiration and the interception by leaves of rainwater, which can then be re-evaporated. The canopy-water content is computed from a prognostic water-balance equation. Note that a recent development (and thus not available for the simulations presented here) is the coupling of this model with the snow model discussed below).

The initialisation of surface variables, specifically the soil-water content, is an important issue when performing simulations for periods ranging from months to seasons. These runs of intermediate duration are indeed very useful for validation purposes, but the state of the soil remains very dependent upon the initial conditions during most of the simulation time. Therefore, an off-line initialisation of the soil variables was implemented for the present project. This technique consists in conducting a separate run of the soil component, using surface air temperatures, precipitation, winds, and radiation fluxes from the ECMWF's re-analysis rather than from the regional model.

This work has been done in collaboration with the European project HIRETYCS (High RESolution Ten Year Climate Simulations; Dutrieux et al., 1998).

4.2.4 Snow model

The melting of snow and ice is a surface energy-balance problem. The sum of the radiative, turbulent, and diffusive ground fluxes determines the surface temperature evolution. Surface melting occurs when the surface temperature reaches 0°C, and the melt rate is proportional to the amount of energy available for melting. Melting is highly sensitive to the surface albedo because of the existence of a positive feedback. The stronger the melting at the surface, the lower the surface albedo, and conversely. The lowering of the surface albedo can be due to two mechanisms: growing of melting snow grains and meltwater accumulation on an ice surface (e.g., Greuell, 2000). Therefore, the already existing snow model (Gallée and Duynkerke, 1997) has been refined by adding parameterisations that represent the snow metamorphism processes which take place in the snow pack (Brun et al., 1992). From the simulated snow-grain form and size are calculated the snow albedo and solar radiation extinction parameters. The surface albedo has also been made dependent on the presence of ice or meltwater at the surface of the ice sheet in case all snow has melted away. This updated snow model has been validated at a well-documented site in Greenland (ETH-Camp: 69°N, 49°W, 1150 m above sea level) during the 1990 and 1991 summer seasons. Multiple experiments have been performed and an extensive sensitivity study has been carried out (Lefebvre et al., 2001a). Figure 21 compares the simulation results with observations during both ablation seasons. A good agreement is found for both the surface albedo and snow-pack depth at the surface of the ice sheet. The new snow model has been employed in all the simulations made with MAR over Greenland (see Section 4.5).

4.2.5 Wind-gust estimation

Another important improvement made to the model is the inclusion of the method for estimating wind gusts recently developed by Brasseur (2001). Contrary to most techniques utilised in operational weather forecasting, the determination of gusts in this approach is fully based on physical considerations. This new method assumes that surface gusts result from the deflection of air parcels flowing higher in the boundary layer, which are brought down by turbulent eddies. Thus, the method takes into account the mean wind and the turbulent structure of the atmosphere. Furthermore, it provides a range of likely gust magnitudes.

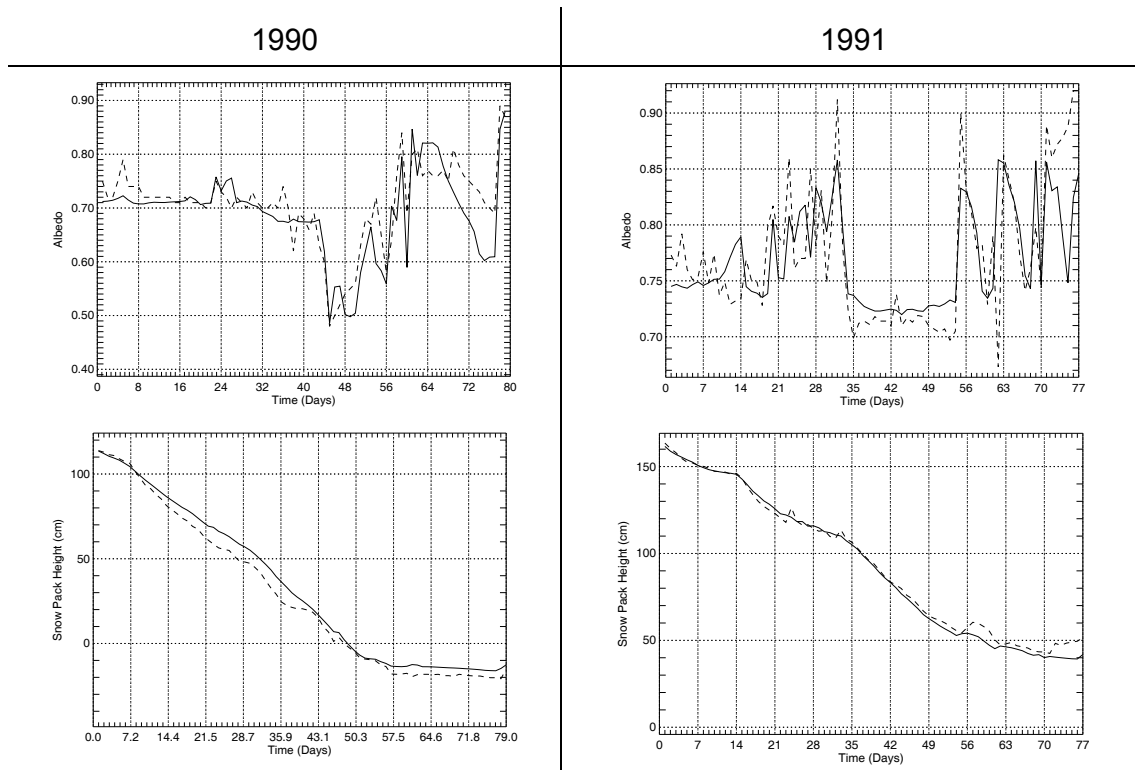


Figure 21: Comparison between the modelled (solid line) and observed (dashed line) albedos (upper panels) and snow-pack depth (lower panels) during the 1990 and 1991 melting seasons at ETH-Camp, West Greenland.

4.3 Validation over Western Europe

The MAR model has been tested on a variety of situations before the beginning of CLIMOD. However, the previous experiments were performed in the framework of process studies, so that the size of the model domain was often small and the integration time was rather short. In the present project, we made the first simulations with MAR over a long period (from 1 to 3 months) and analysed the results with the view of providing an overall assessment of the model performance over Western Europe.

4.3.1 Experimental design

The initial and lateral boundary conditions derive from the re-analysis of observations provided by the ECMWF. These so-called perfect boundary conditions enable a comprehensive evaluation of the model performance with limited simulation time. Indeed, it is not necessary to carry out simulations at the climatic time-scale for most

aspects of the validation task, because the lateral boundary forcing makes direct comparison to day-to-day observations possible.

The main period chosen for validating MAR over Western Europe was the month of October 1986, i.e., the same month as the one selected in the research project HIRETYCS. Choosing the month of October 1986 proved to be valuable because this month experienced both cyclonic (perturbed) and anticyclonic conditions. A high pressure area was located over Central Europe during the first days of the month, and it was extending to the west during the second week. Until October 17, the weather was rather dry over most of Western Europe, with a few small perturbations. In contrast, the two last weeks of the month were rainy, with pressure lows traveling from the Atlantic Ocean over the center and northern side of the area of interest.

The geographical domain is displayed in Figure 22. The domain size is 3000 km × 3000 km. This size is about the maximum possible with the current version of MAR. Studies with other models suggest that this domain is probably large enough to allow the development of meso-scale circulations which are not excessively constrained by the lateral boundaries. Much larger domains (e.g., 6000 km wide) are not desirable because this may lead to conflicts between the forcing and the regional model at the synoptic-scale, in the context of a one-way nesting. Furthermore, it was also suggested that the regional model must be highly constrained by the forcing from GCMs when climate-change experiments are performed, at least when the regional climate model/GCM nesting is unidirectional (Jones et al., 1995, 1997). The surface topography of MAR reproduces the main topographic features of Western Europe, significantly better than in the ECMWF re-analysis (not shown; see Marbaix (2000) for details and simulation parameters).

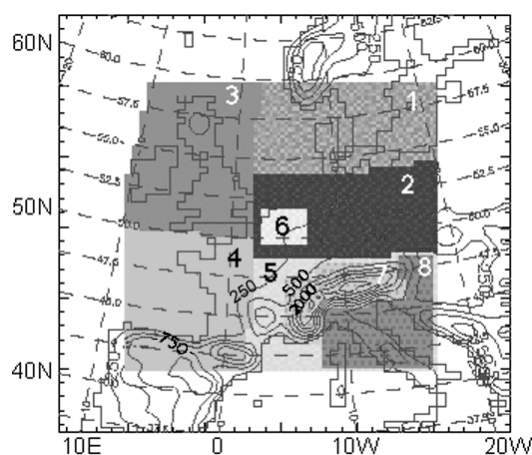


Figure 22: MAR domain over Western Europe. Shaded areas correspond to regions over which average values are computed. Solid lines refer to topography (altitude step between two lines: 250 m).

4.3.2 Results

An important requirement for a regional climate model is to obtain an accurate input from the external large-scale conditions and a regional simulation consistent with this forcing. An indication that MAR satisfies this requirement is that the difference in 500 hPa geopotential height between the model and re-analysis is low, for the mean values as well as for the changes from day to day (Figure 23). The correct reproduction of the synoptic variability is shown by the appropriate band-pass time-filtered 500 hPa height field for both the model and re-analysis (Figure 23, upper right panel), and by the continuously low root-mean-square model–re-analysis difference in 500 hPa height (rarely more than 20 m; see Marbaix (2000)). There is no spurious trend in the variables at the time-scale of one month and more (see, for example, the sea-level pressure time series in Figure 25). The experiments from this project were the first to demonstrate the capability of MAR to conduct three-dimensional simulations longer than the meteorological time-scale.

An additional verification of the lateral boundary-relaxation procedure is provided by analysing the MKE behaviour, as proposed by Giorgi et al. (1993). When a MKE peak is found near the boundaries, numerical noise due to inadequate treatment of the lateral boundaries should be suspected. This was not detected in our experiment (see Marbaix, 2000).

The observed temperatures (at all levels) and sea-level pressures are quite well reproduced in the northeastern part of the domain, where pressure lows are often present (Figure 23). These results confirm in particular that the lateral boundary scheme is working properly. However, the temperature (too low) and sea-level pressure (too high) are not as well simulated when (first half of the month) and where (center and southeastern part of the domain) a pressure high is present. This is probably related to weaker winds and reduced boundary inflow in these conditions, which are also known to cause higher biases during summer (e.g., Cress et al., 1995). Overall, the biases shown in these monthly mean fields demonstrate that the model is working appropriately, showing errors which do not exceed those obtained with other well-known regional climate models (a detailed comparison is available in Marbaix (2000)).

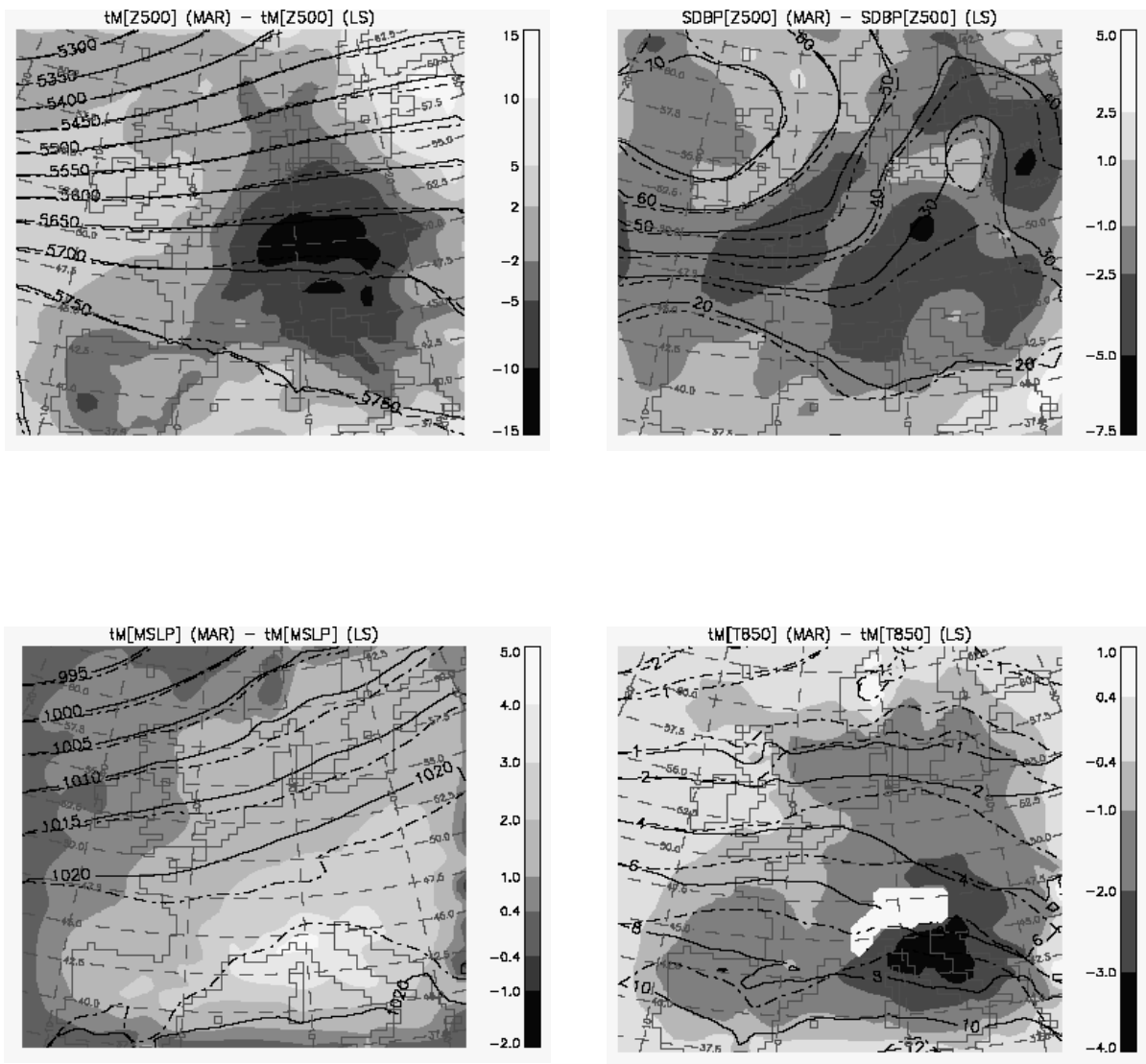


Figure 23: Monthly means of the 500 hPa geopotential height (Z500, upper left panel), the mean sea-level pressure (MSLP, bottom left panel), the 850-hPa temperature (bottom right panel). The synoptic variability is illustrated by the band-pass filtered (1.5 to 6 days) standard deviation of the 500 hPa geopotential height (upper right panel). Each panel shows the MAR results (solid lines), the ECMWF re-analysis values (dashed lines), and the MAR–ECMWF differences (shaded background).

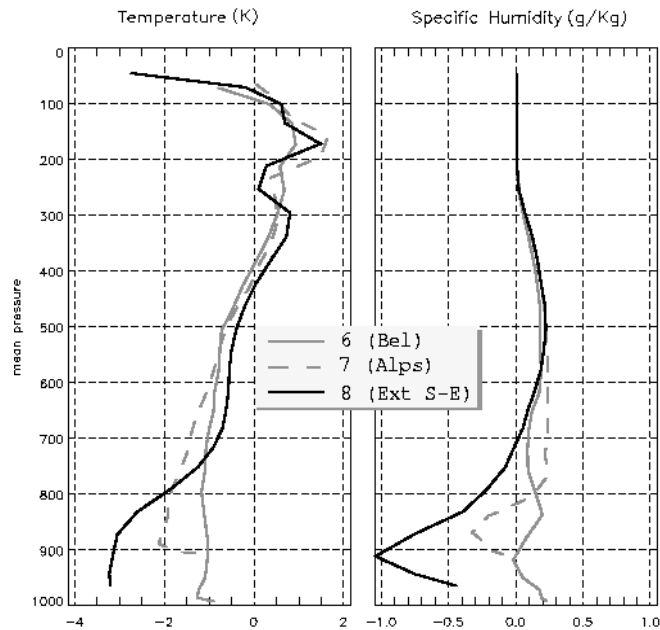


Figure 24: Mean vertical profiles of the bias (MAR-ECMWF's re-analysis) in temperature (left panel) and specific humidity (right panel) for some of the regions defined in Figure 22.

The biases are generally lower at higher levels (500 hPa) than at the surface (MSLP); this is likely a consequence of a more efficient lateral boundary forcing in the free atmosphere. The sea-level pressure bias is directly related to the cold bias in temperature. The temperature bias is indeed relatively high (more than 3°C; Figure 24) at the south-east of the Alps. However, the modelled temperatures remain within the range of acceptable values. The biases in MSLP which are found there and the idea that the mechanism is driven by the temperature error is consistent with the analysis of the results presented in Machenauer et al. (1998). In this report, a mechanism involving radiation is proposed as a possible explanation for the bias; although the radiation schemes utilised in MAR satisfy standard validation tests, further experiments are necessary to know if radiation is the cause of the obtained temperature bias.

By contrast, the biases in both temperature and humidity are low in the centre of the domain, in particular near Belgium (Figure 24, region 6).

The area-averaged precipitation rate simulated by the model amounts to about 80% of the observed value. The geographic distribution of precipitation is also quite good (Figure 25) as well as the day-to-day variability (Figure 26).

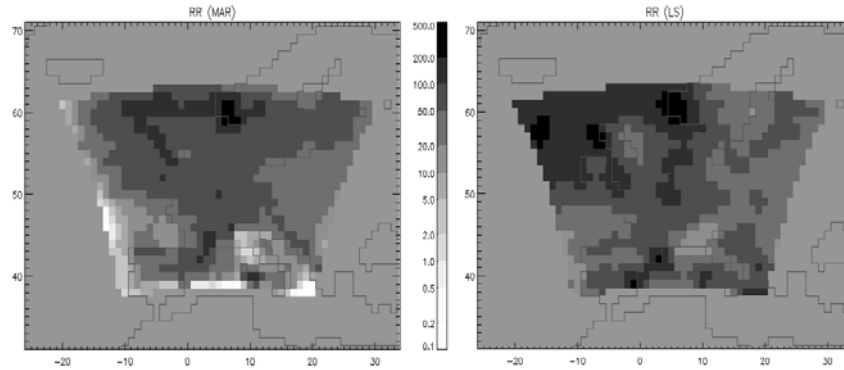


Figure 25: Cumulated rain for October 1986 (in mm): MAR simulation (left panel) and ECMWF's re-analysis (right panel). The re-analysis values are very similar to the gridded observations provided by the Global Precipitation Climatology Centre (GPCC, 1999).

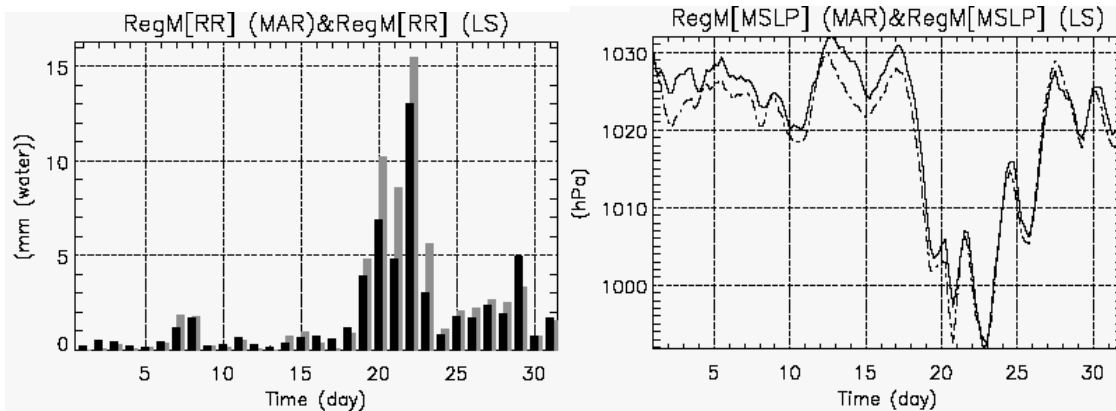


Figure 26: Time series for October 1986 in the Benelux/Germany area (region 2 in Figure 22) of the daily accumulated precipitation (left panel) and mean sea-level pressure (right panel). Black foreground or solid line: MAR model; grey background or dashed line: ECMWF's re-analysis.

4.3.3 Important issues solved during CLIMOD and remaining questions

The first experiments performed with MAR over Western Europe underestimated by half the amount of precipitation (Dutrieux et al., 1998; Marbaix, 2000). The cause of this problem was traced to excessive horizontal filtering. This filtering was necessary for the numerical stability of this model version, but led to an abnormally high horizontal diffusion – at least when the model resolution was 50 km, as in the present case (higher resolution may mitigate the problem, thus making it specific to our type of experiments). This problem has been solved, and all recent experiments used a lower horizontal filtering, thus providing a much better representation of precipitation (as shown above).

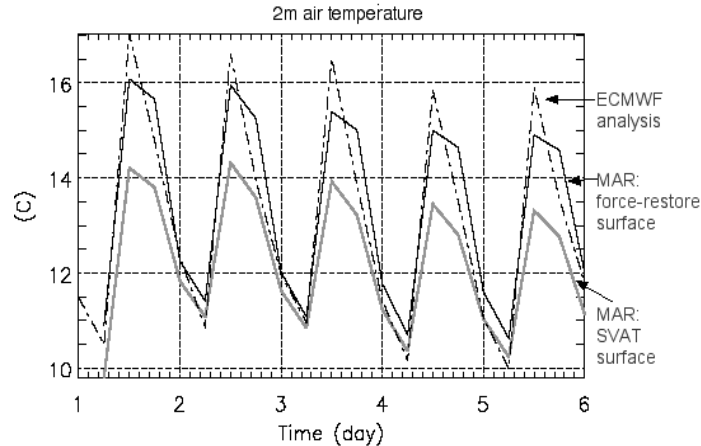


Figure 27: 2-m temperature during the first days of October 1986. Two simulations with MAR are illustrated, employing either the detailed SVAT scheme (grey solid line) or the simple force-restore formulation (black solid line).

We also found an abnormally weak diurnal cycle of surface air temperature when using the detailed SVAT scheme. Indeed, the daily temperature change amounted to about 50% of the expected diurnal variation in that case. As a temporary solution, we re-used the simple force-restore land-surface parameterisation in the simulations conducted within this project. As shown in Figure 27, this gives much better results. Since the land-surface model in itself was carefully validated, we think that the problem is due either to incorrect parameter values for the Western Europe domain or to SVAT–MAR coupling issues. The snow and SVAT models have been recently combined together (H. Gallée, personal communication, 2001), and this new version provides encouraging results, although its validation is still under way.

It should be also remembered that a cold temperature bias was sometimes found. Since the current radiation schemes were validated both in the MAR model and through experiments employing standard atmospheric profiles, they are clearly acceptable for climate simulations. However small inaccuracies in these schemes may be responsible for the cold bias, and thus improvements to the radiation schemes should be envisaged.

4.4 Validation over Belgium

The representation of extreme events at the regional scale is an important concern in the framework of climate change. With this aim in view, the ability of MAR to simulate such events was first investigated considering specific meteorological situations over Belgium.

4.4.1 Surface air temperature

The most severe frosts are favoured by clear sky conditions. In a more general view, the forecast of the diurnal temperature evolution is mainly influenced by four factors: radiative transfers, exchanges between surface and atmosphere, turbulence in the boundary layer, and three-dimensional dynamics at large-scale and meso-scale. In this section, the two last points are specifically studied.

Two particular situations have been treated: 16 March and 9 April 1990. Both of these are cloud-free and allow a maximum diurnal amplitude of temperature. They are respectively characterised by weak and dominant large-scale forcings.

The situation of 16 March (weak large-scale forcing) has shown the relevant impact of meso-scale circulations on the surface air temperature: katabatic winds during night-time, anabatic winds and sea breeze during daytime. Their role is particularly important on minimum temperature: katabatic winds produce a cooling reaching -4°C over Northeast Belgium. The maximum temperatures are less affected, with a difference of 1°C , essentially in reason of less intense circulations and active turbulent mixing. When the large-scale forcing leads to wind speed higher than about 3 m s^{-1} (situation of 9 April 1990), the meso-scale circulations are inhibited and the horizontal advection becomes a dominant process.

In 10-km MAR simulations, the mean temperature and the amplitude of the diurnal cycle are very well simulated for both cases. The error for both minimum and maximum temperatures is indeed around 1 to 2°C at most (Figure 28), while the amplitude of the diurnal cycle is between 10 and 20°C . However, the geographical temperature variations across Belgium are relatively small. Therefore, in spite of the good representation of the diurnal cycle, the temperature patterns given by the model cannot always fully capture the difference between regions in the country.

The role of the model resolution was investigated using mesh sizes of 20, 10, and 5 km. Increasing the resolution to 5 km has led to a slight improvement of the representation of meso-scale processes. For the particular case of 16 March 1990, we note a better prediction of the surface air temperature (about 25%). In contrast, when the large-scale forcing is dominant and prevents the development of local circulations, no significant improvement is noticed as the resolution increases. If the 5-km resolution improves the surface characteristics (topography, soil, vegetation) compared to 20-km resolution, this finest resolution remains insufficient to resolve properly local valley circulations in the Belgian Ardennes. A resolution of 1 km or less would be more appropriate to represent local effects. With a view of doing climate studies, the 20-km resolution appears to be the best choice for the highest resolution runs which may be achieved in the near future, at least with regard to temperature simulation.

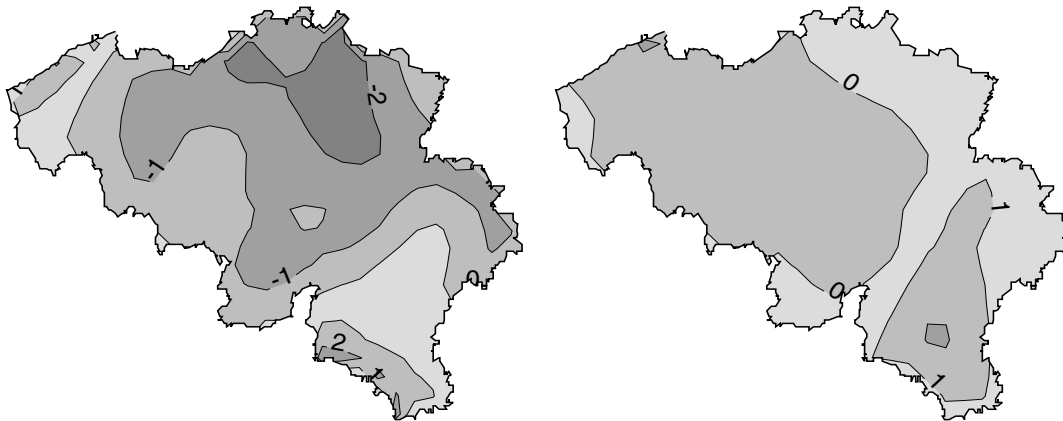


Figure 28: Errors in simulated minimum (left) and maximum (right) surface air temperature ($^{\circ}\text{C}$) over Belgium during 9 April 1990. The horizontal resolution of MAR is 10 km. The model is initialised and forced at its boundaries with the ECMWF's re-analysis data. Solid lines correspond to error isotherms. The contour interval is 1°C .

4.4.2 Simulation of storms

The beginning of year 1990 was marked by a succession of storms that battered the Northwestern Europe. The period of storms opened with the one of 25 January. It ended with the deep low and following wave depression on 26–28 February. These two situations were responsible for strongest damage over Belgium during the 1990 winter. Both are characterised by explosive cyclogenesis at the synoptic-scale, producing wind gusts reaching at least 45 m s^{-1} in Belgium. Since this involves scales much larger than the country, the simulation domain covered Western Europe (3500 km by 3500 km). Several simulations were performed with MAR. The most important in view of climate studies is a 3-month run starting on January 1, with an horizontal resolution of 50 km. The boundary forcing was provided by the ECMWF's re-analysis data.

MAR has been able to accurately reproduce the intense deepening of the explosive cyclogenesis (i.e., deepening rates exceeding 24 hPa per day). In particular, the difference between the simulated and observed central pressures at the end of the cyclone deepening is only 6 and 1 hPa for the storms of 25 January and 26 February, respectively. This is illustrated in Figure 29 for the 26 February case. While the minimum pressure was very well simulated, the trajectory path is less precisely represented but remains satisfying (the displacement is small at the scale of local pressure variations). In contrast, the storm track is almost perfectly simulated in the 25

January case (not shown; see Brasseur (2001)). The pressure and temperature fields generally appear in satisfying agreement with the observations. The location of the warm front matches well the ECMWF's re-analysis, while the simulated cold front is slightly less developed. Note that in some configurations, 25-km-resolution runs proved able to represent even better the deepening of the cyclones and of associated fronts.

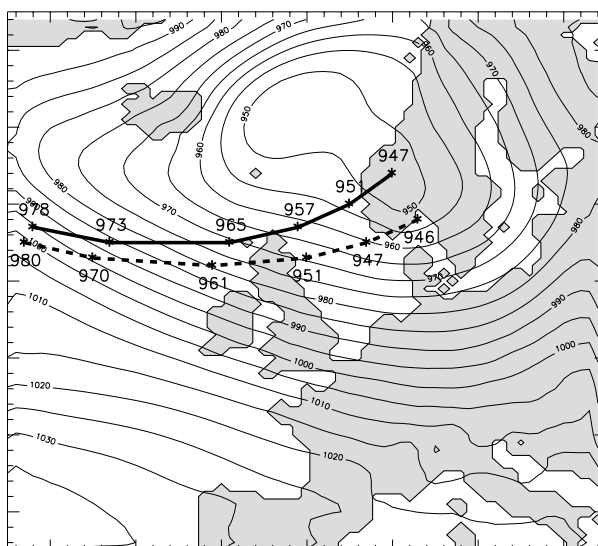


Figure 29: Simulated (thick solid line) and observed (dashed line) trajectory paths of the storm of 26 february 1990 obtained from the 3-month MAR simulation at 50-km resolution. The values correspond to the pressure (in hPa) in the center of the explosive cyclone. They are shown since 12:00 UTC 25 February 1990, and the time interval between two consecutive values is 6 hours. The simulated mean sea-level pressure field at 00:00 UTC 27 February 1990 is represented with solid contour lines.

4.4.3 Wind-gust estimation

The determination of maximum wind speed is of foremost importance for climatology and climate-change studies as well as for weather forecasting. However, the estimate of gusts is not an easy task due to the great variability of wind. There is no simple relation between the severity of surface wind gusts and amount of deepening of the storm depression. In operational weather prediction, a standard but simple method for the determination of wind gusts considers a constant ratio of maximum gust to hourly average surface wind speed (the ratio mainly depends on surface roughness). While such statistical or empirical approaches are often satisfying, we have developed a new physically-based wind-gust-estimation (WGE) method (Brasseur, 2001; see also Section 4.2.5). The main motivation for developing such an approach is to improve the knowledge of the physical processes that control the determination of gusts. However, our method has specific advantages, in particular for climate simulations because it is based on model variables, with no need for local parameters. The approach assumes

that gusts observed at the surface result from the deflection of air parcels flowing higher in the boundary layer. The trigger mechanism for the deflection is attributed to turbulent eddies. Compared to all other methods, an advantage of the WGE is that it computes a bounding interval for the gusts in addition to the estimate.

The WGE method was applied on the period from January to March 1990 on the basis of the above-described MAR simulation. The predicted 10-m wind speeds were compared with the observations from the Belgian synoptic network (provided by RMI-GCS). The WGE reproduces the main features of the climatology of gusts over Belgium very well. The statistics of estimated gusts tend to underestimate the observations (bias from 3 to 10%), but they appear able to reproduce the tendencies at different stations. An interesting aspect of the method is that the bounding interval has shown a reliability rate of at least 73% for the prediction of daily gusts. This is illustrated for the station Zaventem in Figure 30.

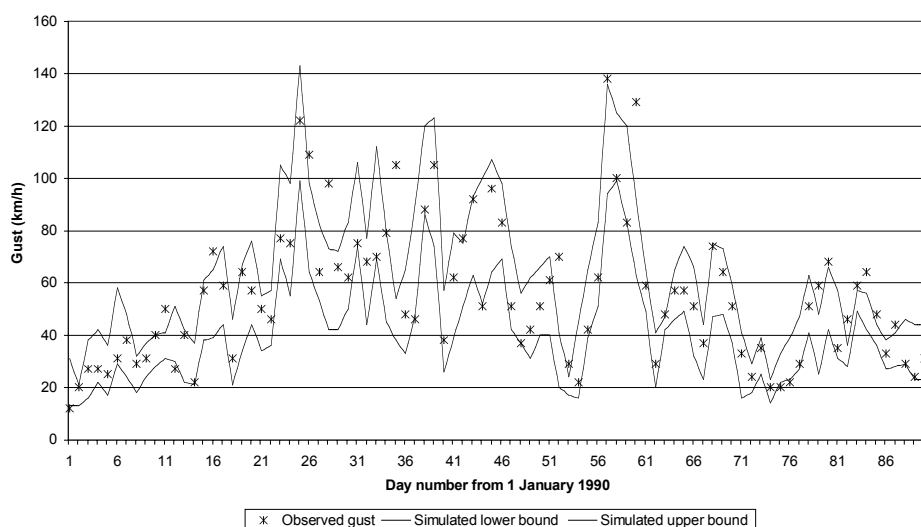


Figure 30: Estimated and observed daily gusts (units: km h^{-1}) for the period from January to March 1990. Solid lines represent lower and upper bounds of gust estimate, stars indicate observed gusts.

4.5 Validation over Greenland

4.5.1 Model set-up

MAR has also been validated over the southern part of Greenland. The simulated period starts the first of May 1991 and lasts until the end of August 1991. This period has been selected because of the availability of atmospheric and mass-balance measurements. Over the ice sheet, we used observations made along the GIMEX transect (Oerlemans and Vugts, 1993), at ETH-Camp (Ohmura et al., 1992), and by some automatic weather stations (AWS) located near the Greenland summit.

Additional data from some coastal stations operated by the Danish Meteorological Institute have also been utilised. We focused on the summer season as the computer time required to perform one simulation is on the order of 20 days on our fastest computers. This can be explained by the high horizontal resolution (20 km) needed to distinguish properly the various mass-balance zones of Greenland. Mass-balance models over Greenland are generally run at a 20-km resolution. Regional climate models, on the other hand, have typical horizontal resolutions of 40–50 km, which is insufficient for mass-balance predictions as well as for atmospheric modelling near the ice-sheet surface. Indeed, the exactness of the modelled katabatic downslope winds strongly depends on the accuracy of the surface slope parameter. At a 40-km resolution, the surface topography is smoother and slopes are reduced, especially near the ice-sheet border, where slopes are largest and katabatic winds dominate the local wind regime. Besides the high horizontal resolution, also the domain size must be sufficiently large so that clouds can be properly generated inside the domain as they are not entered at the lateral boundaries. Clouds are very important for the simulation of surface downward radiative fluxes (both solar and infrared) and near-surface air temperature. A horizontal domain size of 2000 km × 2000 km has been chosen. Sensitivity experiments with a reduced domain size showed important underestimations of cloud cover, precipitation, and surface infrared fluxes compared to simulations on a domain of 2000 km × 2000 km. The SST and sea-ice distributions were prescribed according to the ECMWF's re-analysis fields. The MAR fine-grid topography and soil types for Greenland were derived from Ekholm's (1996) Greenland topography and land masks. A complete description of the model, set-up, and initialisation can be found in Lefebre (2001). To date, no similar high-resolution climate simulation over Greenland have been reported in the scientific literature.

4.5.2 Comparison of model outputs with observations

The simulated vertical structure of the atmosphere over the ice sheet has been analysed through comparison with radiosonde measurements at ETH-Camp, West Greenland. ETH-Camp is some 40 km far from the ice-sheet margin, close to the long-term equilibrium line. Between 13 May and 21 August 1991, 294 radiosondes were launched to measure the vertical variations in air temperature, relative humidity, and wind components at this site. These radiosonde data are interesting because they are independent of the ECMWF's re-analysis data. Figure 31 shows the average observed, modelled, and re-analysed soundings for 8 July 1991 at ETH-Camp, which is a typical pure katabatic situation. MAR reproduces relatively well the temperature inversion and maximum in wind speed observed near the surface. By contrast, these features are absent in the ECMWF's re-analysis. This is mainly due to the poor vertical (the lowest level is situated at 40 m above the surface) and horizontal (spectral T106,

1.125°) resolution of the ECMWF's model that was employed to produce the re-analysis dataset.

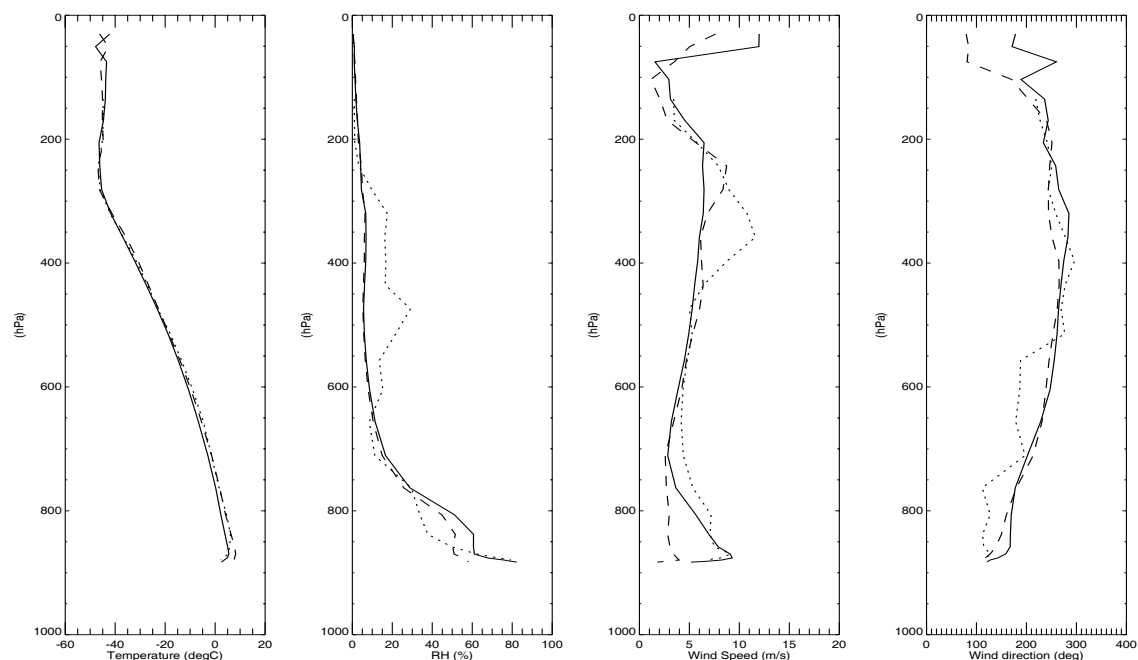


Figure 31: Comparison between the observed (dotted lines), MAR modelled, (solid lines), and ECMWF modelled (dashed lines) average vertical soundings of air temperature, relative humidity, wind speed, and wind direction at ETH-Camp for 8 July 1991.

The model results are average values for the whole grid-cell area and duration of the time step. Comparing those values with local instantaneous observations must be done carefully. The model grid cell closest to the observing site does not necessarily have the correct elevation. Moreover, subgrid topography roughness and obstacles can locally influence the air motion and thermodynamic characteristics. In the low ablation zone and tundra area which surrounds the ice sheet, these effects may be very important and should be kept in mind. Figures 32, 33, and 34 display the simulated and observed time series of a number of variables at the GIMEX-Mast 6, GIMEX-Mast 9, and AWS-Klinck sites, respectively. The first two sites are located in the ablation zone of West Greenland. AWS-Klinck is situated near the summit of the ice sheet at 3105 m above sea level in the dry snow zone. From these figures, it can be seen that the model results compare favourably with the observations. The too large simulated surface albedo at GIMEX-Mast 6 between 10 June and 30 June is due to the presence of an initial snow pack in the snow model. In reality, snow drift removes all the winter deposited snow in the low ablation zone close to the ice-sheet margin, and ice is observed from the beginning of the ablation season. At GIMEX-Mast 9, the computed albedo follows the observed one until 15 July. Afterwards, it drops to a too low value of 0.55, which corresponds to the model ice albedo. Clearly, the initial snow-pack height was underestimated. In-situ observations reveal that snow was

present during the whole duration of the melt season. At AWS-Klinck, the modelled values are overall in good agreement with the observational data. The too high air temperatures generated by MAR during May show up in combination with south-southwesterly winds, while the observations indicates east-southeasterly winds. The overestimated temperatures in May are probably also due to initialisation errors. The simulated and observed evolutions of surface pressure coincide during the whole duration of the experiment, which means that the large-scale circulation correctly penetrates into the model domain through the nesting scheme at the lateral boundaries.

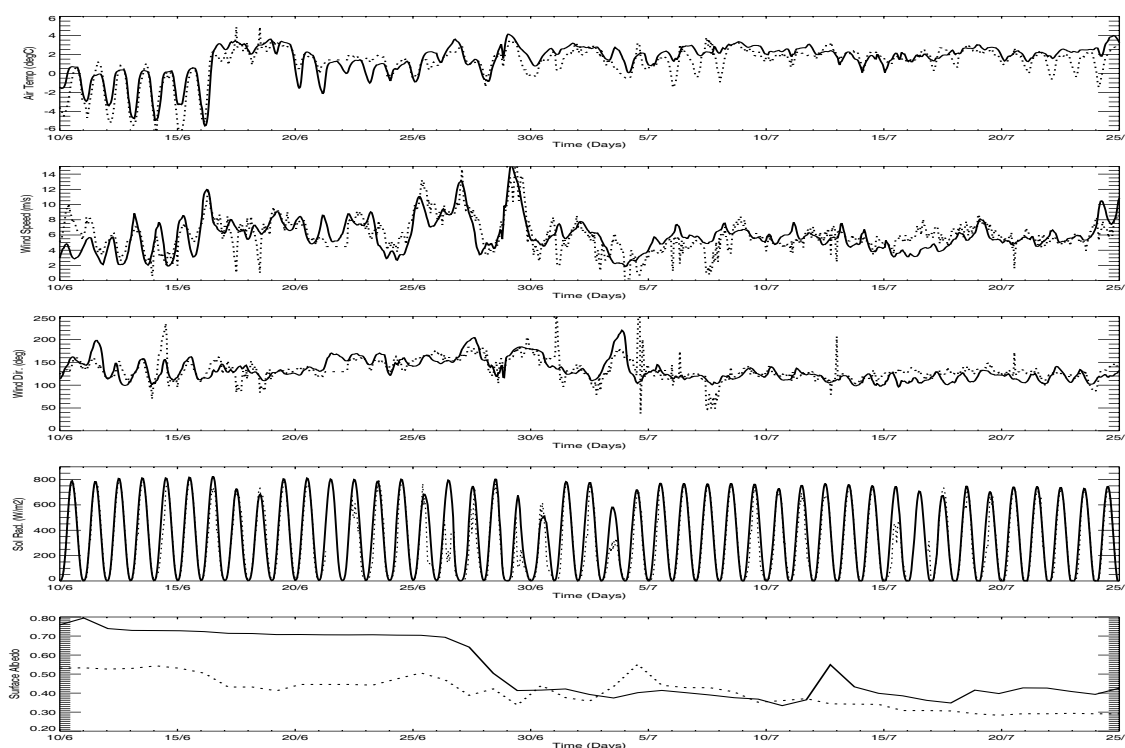


Figure 32: Simulated (solid lines) and observed (dashed lines) time series of surface air temperature, surface wind speed and direction, downward solar radiation, and surface albedo at the GIMEX-Mast 6 between 10 June and 25 July 1991.

Passive-microwave data can be used to delimit the melt area of the Greenland ice sheet. Abdalati and Steffen (1997) developed a method to detect melt regions based on the cross-polarised gradient ratio (XPGR). In Figure 35 are plotted the satellite-derived melt-extent evolution as determined by Abdalati and Steffen (1997) from SMM/I data and the modelled daily melt average as well as daily melt amplitude between 22 May and 30 August 1991. Melt is expressed in percentage of the Greenland ice sheet area that lies in the model area. The timing and amplitude of melt onset and offset are very well reproduced by the model. Moreover, the maximum melt

extent is similar in both MAR and SMM/I. The simulated underestimation after the melt maximum is possibly due to the homogeneous initial state of the snow pack in the MAR percolation zone. Ice lenses and other obstacles that could delay runoff or percolation and refreezing of meltwater are absent in the MAR snow pack.

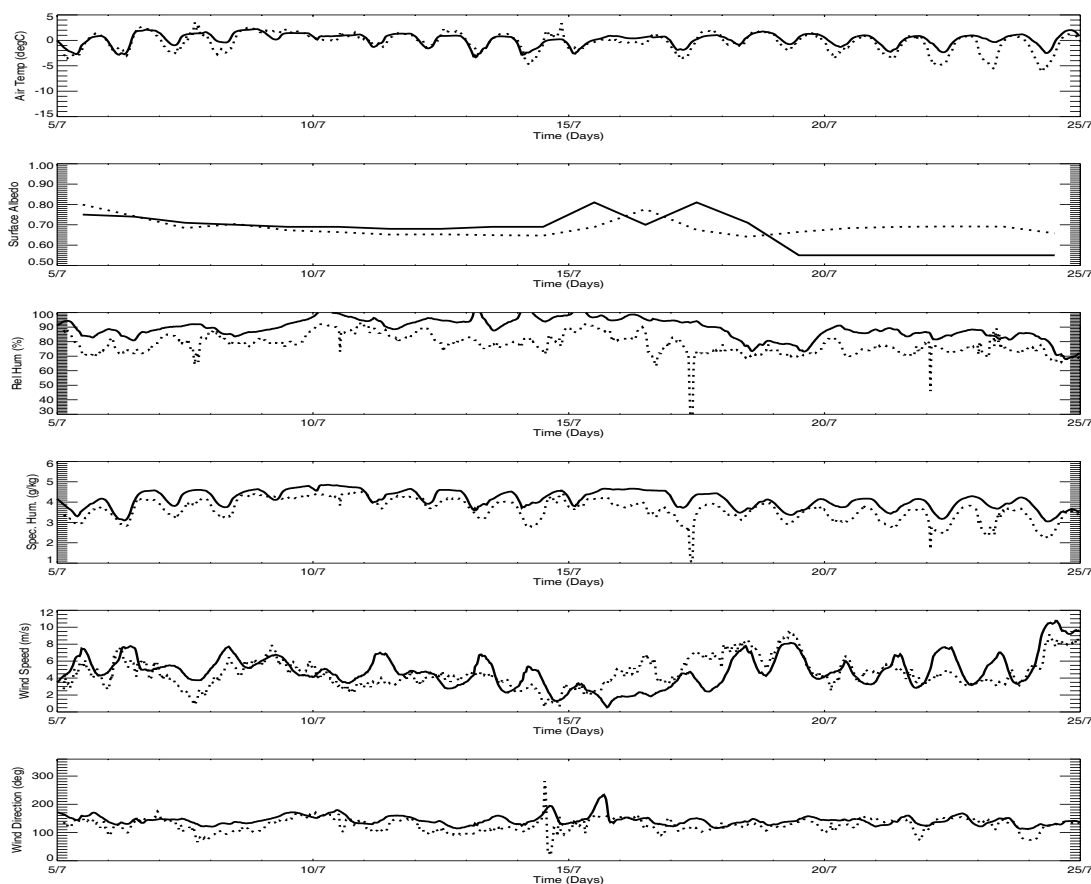


Figure 33: Simulated (solid lines) and observed (dashed lines) time series of surface air temperature, surface albedo, surface relative humidity, surface specific humidity, and surface wind speed and direction at GIMEX-Mast 9 between 5 and 25 July 1991.

In view of these results, we can conclude that the model does reasonably well in reproducing the atmospheric conditions and mass-balance over the southern part of the Greenland ice sheet, except in May because of initialisation errors. The use of a variable snow albedo improves significantly the simulation of the summer melt. This was expected as solar radiation is the primary source of energy for snow and ice melting. We also found that the radiation fluxes are highly sensitive to the presence of clouds and that a relatively large domain is needed.

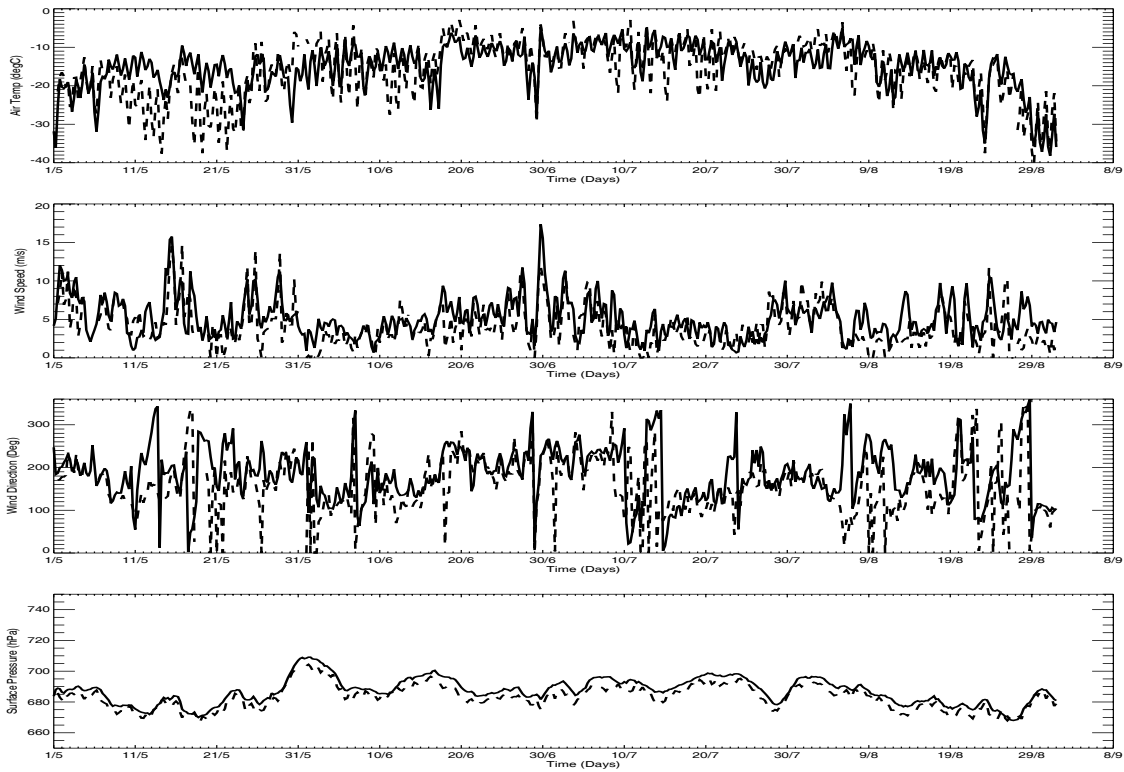


Figure 34: Simulated (solid line) and observed (dashed line) time series of surface air temperature, surface wind speed and direction, and surface albedo at AWS-Klinck between 1 MAY and 31 August 1991.

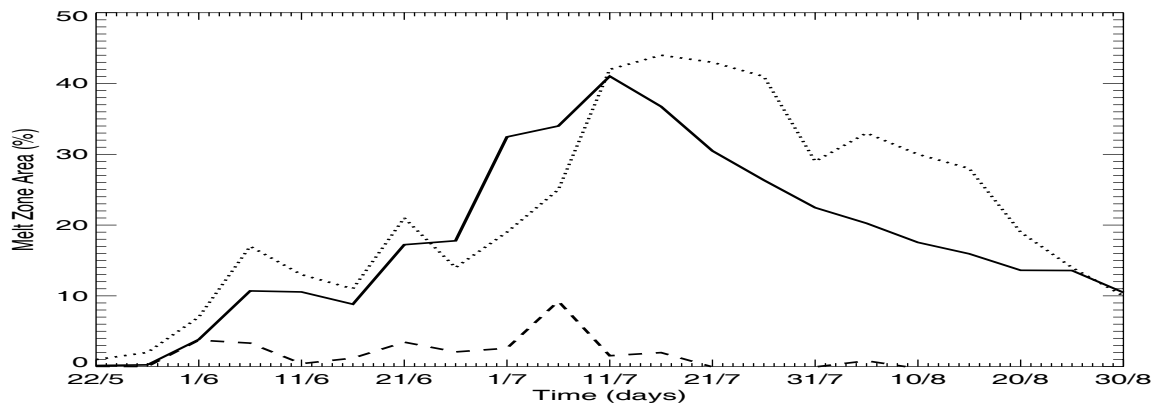


Figure 35: Evolution of the summer melt extent in 1991. The modelled daily average (solid line) and daily cycle amplitude (dashed line) is compared with the SMM/I (dotted) observed daily average.

5. COUPLING OF THE AOGCM WITH THE GISM AND NESTING OF MAR IN THE AOGCM

5.1 Validation/refinement of the mass-balance parameterisation of the GISM

Large-scale PPD-based melt parameterisations for the Greenland ice sheet are highly sensitive to their parameters such as the standard temperature deviation as well as the snow and ice PDD factors. In the literature, a wide range of values for these parameters can be found (e.g., Reeh, 1991; Huybrechts and de Wolde, 1999; Janssens and Huybrechts, 2000). We have explicitly modelled these large-scale melt parameters with the ASTR-RCMG's regional atmospheric model MAR. The equivalence between MAR and large-scale variables is not so straightforward because of the different vertical resolutions between the two models. The MAR multi-layer snow model has a time step of 6 minutes, while the large-scale PPD melt model can work with yearly time steps provided the PDD melt potential is calculated with sufficient accuracy. The large-scale PDD melt model uses vertically integrated quantities such as snow cover, superimposed ice, capillary water, and runoff. To discuss comparable variables, the MAR vertically integrated melt has been calculated. In the model, melt equals the difference between the amount of melted snow or ice and the amount of refrozen internal meltwater or surface meltwater. In case of snow melt at temperatures near the melting point, the amount of refreezing considerably lowers the net amount of melt. The modelled PDD factors for snow and ice at the GIMEX transect are shown in Figure 36. Both the net ablation and the melt without refreezing have been calculated. Near the ice-sheet margin, refreezing is of minor importance, but it becomes more important higher on the ice sheet. At the highest elevation point, the net ablation PDD factor reaches 43.57 mm of water equivalent $\text{day}^{-1} \text{C}^{-1}$. The increase with longitude, which actually corresponds to an increase with altitude because of the orientation and geometry of the ice sheet, is due to the growing relative importance of global radiation compared to the turbulent heat fluxes. Near the ice-sheet margin, half of the energy utilised to melt snow or ice comes from turbulent heat fluxes. Higher on the ice sheet, all the energy to melt snow or ice is provided by global radiation.

The computed PDD factors for the whole southern part of Greenland against altitude and latitude as well as their frequency distribution are displayed in Figure 37. The strongest variation can be seen as a function of surface height. In case of snow melt, a small decline is noticed as a function of latitude. Both the snow and ice histograms demonstrate that the most frequently simulated values agree with the generally accepted snow and ice PDD factors of 3 and 8 mm of water equivalent $\text{day}^{-1} \text{C}^{-1}$, respectively (Braithwaite and Zhang, 2000).

It should be noted that the measured net ablation PDD factors are not equivalent to the

PDD factors as used in the PDD melt models, where melt and refreezing are treated separately. If refreezing is excluded, higher simulated snow and ice PDD factors are obtained, which suggests that the current PDD melt models probably underestimate the amount of melt in the higher parts of the ice sheet. Close to the ice-sheet margin, refreezing is of minor importance.

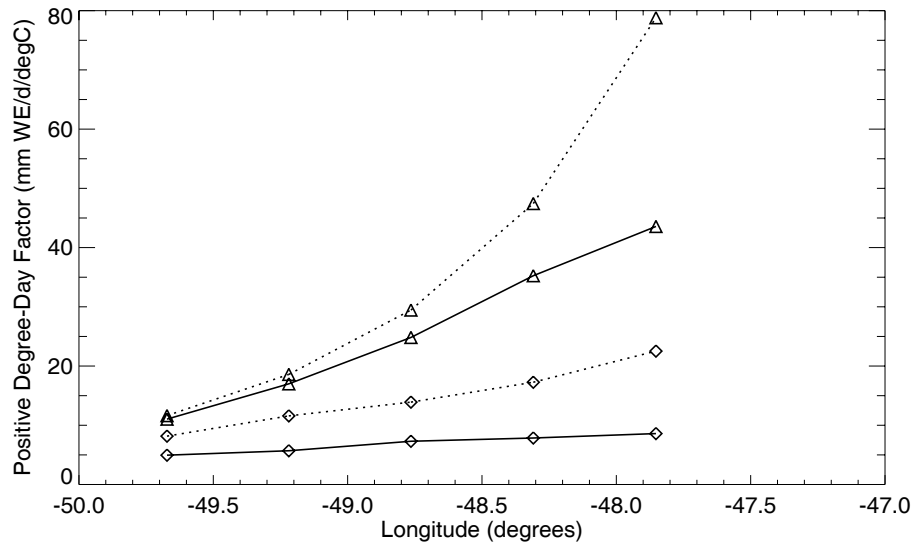


Figure 36: Modelled snow (diamonds) and ice (triangles) PDD factors for summer 1991 at the GIMEX transect ($\sim 67^\circ$ N), West Greenland. The dotted lines are for melt without subtracting refreezing.

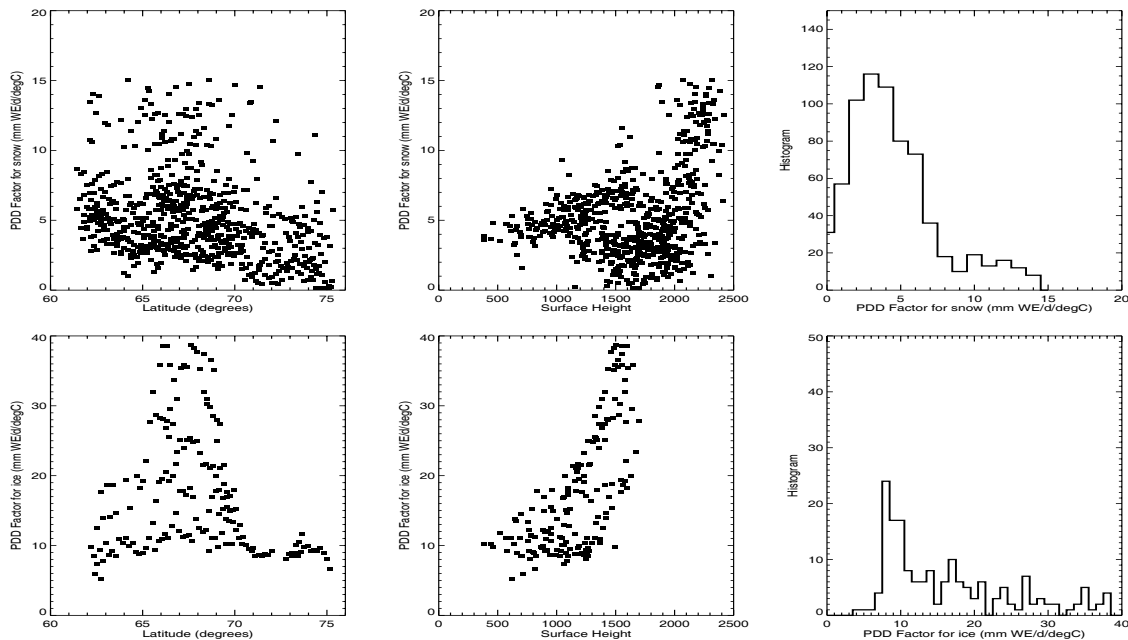


Figure 37: Modelled (from net ablation) snow (upper panels) and ice (lower panels) PDD factors during summer 1991 as a function of latitude and surface height. A histogram indicates 3 and 8 mm of water equivalent $\text{day}^{-1} \text{C}^{-1}$ as the most frequent values for snow and ice melt, respectively.

The temperature standard deviation has been determined by varying the daily temperature standard deviation σ in the following equation:

$$PDD = \frac{1}{\sigma\sqrt{2\pi}} \int_{year} \left\{ \int_0^{\infty} T \exp\left(-\frac{(T-T_d)^2}{2\sigma^2}\right) dT \right\} dt$$

where T_d is taken equal to the simulated monthly mean temperature that approaches best the simulated monthly PDD sum. The latter was calculated from hourly temperatures during the simulation. In May, the highest values are found in West Greenland (values between 3 and 5°C), and the lowest values are encountered in East Greenland. In June, the pattern is reversed, with lower values in West Greenland compared to East Greenland. The lowest seasonal values are found in July (below 3°C), when wide-spread surface melt reduces the near-surface air-temperature fluctuations and the standard temperature deviation is between 2 and 3°C (see Figure 6 in Lefebvre et al. (2001b)).

This seasonal cycle of temperature fluctuations is typical for northern latitudes where the highest daily temperature fluctuations occur in the transition months such as April, May, August, and September (see Section 3.2.2 for conclusions).

5.2 Coupling of the AOGCM with the GISM

The GISM is coupled with the AOGCM according to the scheme depicted in Figure 38. This coupling is fully interactive and quasi-synchronous if one takes into account the large spread of model time steps, which are at maximum 1 year for the slowest model components (the ice sheet and its underlying bedrock).

The key parameters needed as input for the GISM are the surface temperature and the precipitation rate. Climatic changes provided by the AGCM are downscaled in the perturbation mode by superimposing temperature anomalies and precipitation ratios (climate changes versus control) from the coarse AGCM grid onto the respective representations on the much finer ice-sheet-model grid. This procedure is preferred because the climatic patterns produced by the AOGCM differ from the observations and because the large difference in model resolution (the latitudinal resolution of the AGCM varies from 5° to more than 10° over Greenland, while that of the GISM is of 20 km) implies quite different surface topographies. Temperature perturbations are applied monthly, but precipitation ratios are only imposed annually because reliable information on their monthly distribution is missing for the reference climate.

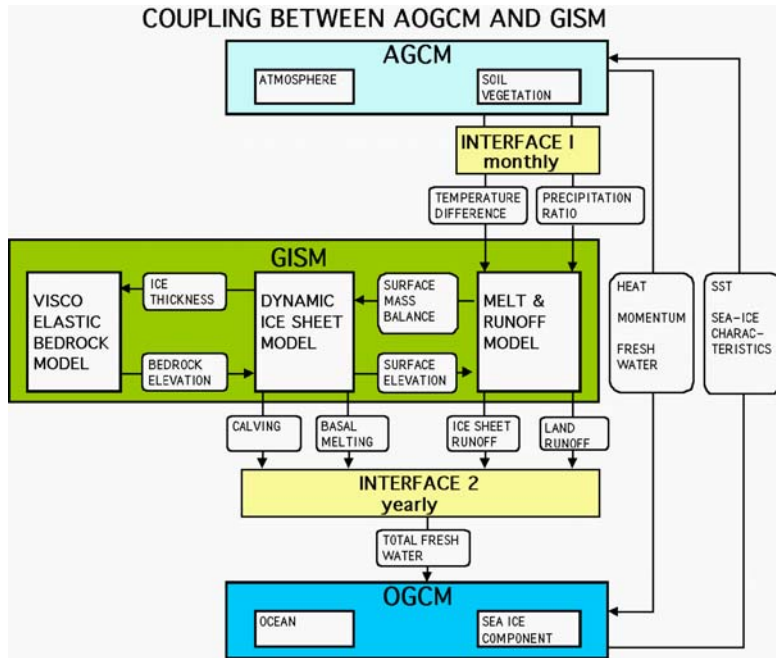


Figure 38: The scheme of the coupling between the AOGCM and the GISM.

For the interpolation of data from the AGCM grid to the GISM grid, we opted to first transform the GISM points in the AGCM grid and subsequently apply Lagrange interpolations. This procedure is more efficient than the reverse one as it avoids problems with search functions, choice of weights, and discontinuities that would otherwise be associated with the interpolation of the AGCM points which form a scarce and irregular system in the GISM grid. The procedure is shown in more detail in Figure 39a. It consists of finding the nearest southwestern AGCM point as reference point for the GISM point p and calculating the Lagrange coefficients $C_i(x)$ and $C_j(y)$ of p ($i, j = -3, \dots, 4$), being the weights, where (x, y) are the coordinates of p for the reference point:

$$C_i(x) = [(x-4)(x-3)\dots(x-i-1)(x-i+1)\dots(x+3)] / [(i-4)(i-3)\dots(-1)(+1)\dots(i+3)]$$

$$C_j(y) = [(y-4)(y-3)\dots(y-i-1)(y-i+1)\dots(y+3)] / [(j-4)(j-3)\dots(-1)(+1)\dots(j+3)]$$

During the coupling, a double summation in the neighborhood of the reference point is performed using a regular rectangular 8×8 point grid:

4

$$f(x,y)_{GISM} = \sum_{i,j=-3} C_i(x).C_j(y) f(i,j)_{AGCM} \quad \text{with } f = \text{the perturbation}$$

Note that we had to extend the AGCM grid to the North Pole, a singular point, by extrapolating and averaging climatic parameters in the vertical grid direction.

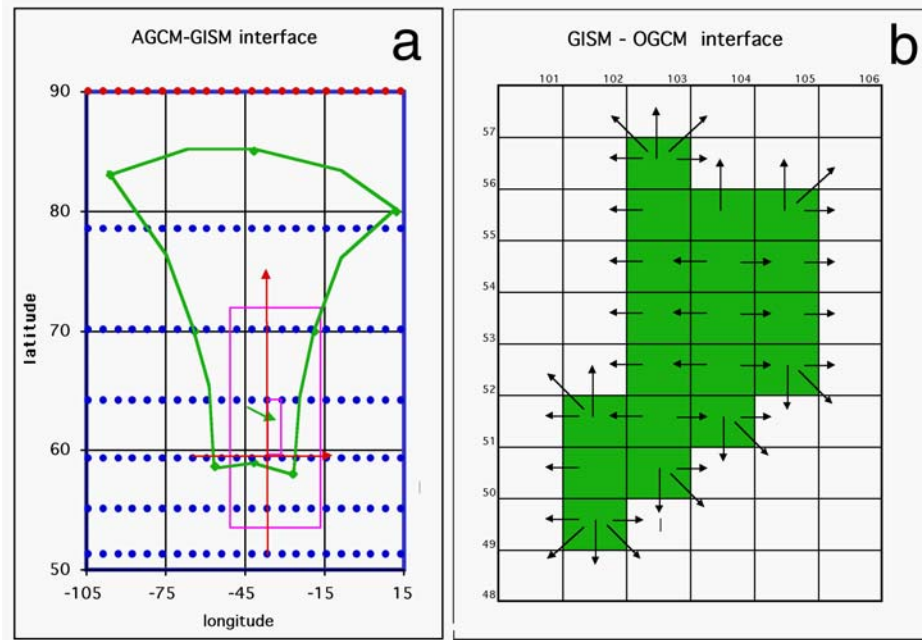


Figure 39: Schemes of the interfaces required to exchange information between the GISM and the AOGCM. (a) The interpolation scheme of the AGCM–GISM interface: the AGCM grid points are blue and the green arrow shows a GISM point. The left bottom point of the small purple rectangle is the reference AGCM point. The larger purple rectangle encloses the AGCM points used for the Lagrange interpolation of the GISM point value. The green figure is the boundary of the GISM points in the AGCM grid. (b) The GISM–CLIO interface. First the GISM freshwater-flux values are added up for each of the 6×10 CLIO grid cells, after which the "green Greenland CLIO values" are proportionally distributed into the adjacent "white CLIO grid cells" according to the black arrows.

For the coupling between the GISM and CLIO, a simple procedure was set up to allocate the total freshwater flux from the GISM to the respective oceanic grid boxes that border the Greenland continent, as illustrated in Figure 39b. The AGCM does not accommodate for changes in the geometry of the Greenland ice sheet (elevation and extent) as these would be hardly detectable on the coarse atmospheric grid on a century time-scale. The ice-dynamics model is only integrated forward after a net yearly surface mass balance has been established, meaning that the ice-sheet response and the associated freshwater fluxes are delayed by 1 year with respect to the climatic input. This is however not a serious problem considering the long response time-scales of the ice sheet and the ocean.

The GISM has first been run during the last two glacial–interglacial cycles before coupling with the AOGCM (see Section 3.3). At the end of this simulation, the GISM provides the AOGCM with the freshwater fluxes from the Greenland ice sheet under present-day conditions. These values are used in the control run and in the climate-

change experiment with no interactive ice-sheet component described below. But, in order to allow interannual and longer-term changes, anomalies computed by the AOGCM are added. In the climate-change experiment with the coupled AOGCM–GISM, the AOGCM supplies monthly temperature anomalies and annual mean precipitation ratios to the GISM, and gets back the freshwater fluxes (runoff and iceberg calving) at the oceanic grid points surrounding the Greenland Island.

5.3 Nesting of MAR in the AOGCM

It is generally admitted that regional climate models should preferably be validated on the basis of experiments using perfect boundary conditions, i.e., by nesting these models in re-analysis-data fields as presented in Section 4. This is indeed a straightforward method to evaluate the models and understand their behaviour without introducing GCM errors at the lateral boundaries. The next step consists in forcing the regional models with large-scale meteorological conditions corresponding to climatic forcings which can differ from the present-day conditions. This means that the prognostic variable must be provided by a GCM. In our case, this represents a relatively simple technical work, since both models are grid-point-based and use almost the same prognostic variables, except for a small change in the choice of the thermodynamic variable (temperature) and in the grid type.

As implied by the above-mentioned choice for the validation strategy and the relative simplicity of the technical aspects, there are no big differences between lateral boundary forcings based on re-analysis or on a GCM. One of the likely significant differences is the resolution change between the regional model and its forcing-data source. In the horizontal direction, the MAR/AOGCM resolution ratio is about 8. This is usual in the regional climate-modelling community, and we indeed did not find problems related to the interpolation process or to the resolution step between the models. However, the vertical resolution of the AOGCM is also lower than the one utilised for the re-analysis (from 30 levels to 19 levels), and this had an adverse consequence on our first results. The issue was traced back to an inaccuracy in a detail of the lower boundary-condition-data adaptation to the MAR grid (namely a computation of the height of the 600 hPa level in both MAR and the AOGCM coordinates, in order to obtain a closer agreement between the models in the free atmosphere). The issue was solved, but we noticed that the problem did only show up in the AOGCM–MAR experiments, not in the re-analysis–MAR validation. This suggests that moving from re-analysis-based experiments to GCM-based experiments can still bring surprises. Although we still agree that most of the validation work should be done on the basis of re-analysis, the results of the first AOGCM–MAR experiments must be carefully evaluated.

The main difference between the AOGCM–MAR nesting and the validation phase is that the AOGCM will normally provide a less accurate representation of the real atmosphere (because it is not continuously constrained by observations). Therefore, a good knowledge of the results of the AOGCM over the area of interest is necessary in order to have a detailed understanding of the regional model results. Since we started the regional-scale work with the AOGCM results only in the last months of this project, our conclusions are limited to a preliminary evaluation of the joined AOGCM–MAR system. Future experiments should involve a careful evaluation of the AOGCM fields, specifically those containing the synoptic information at the lateral boundaries (storm tracks and water-vapour amount are important, while precipitation is not, except for the consequences of potential hydrological cycle deficiencies in the atmospheric fields of the AOGCM).

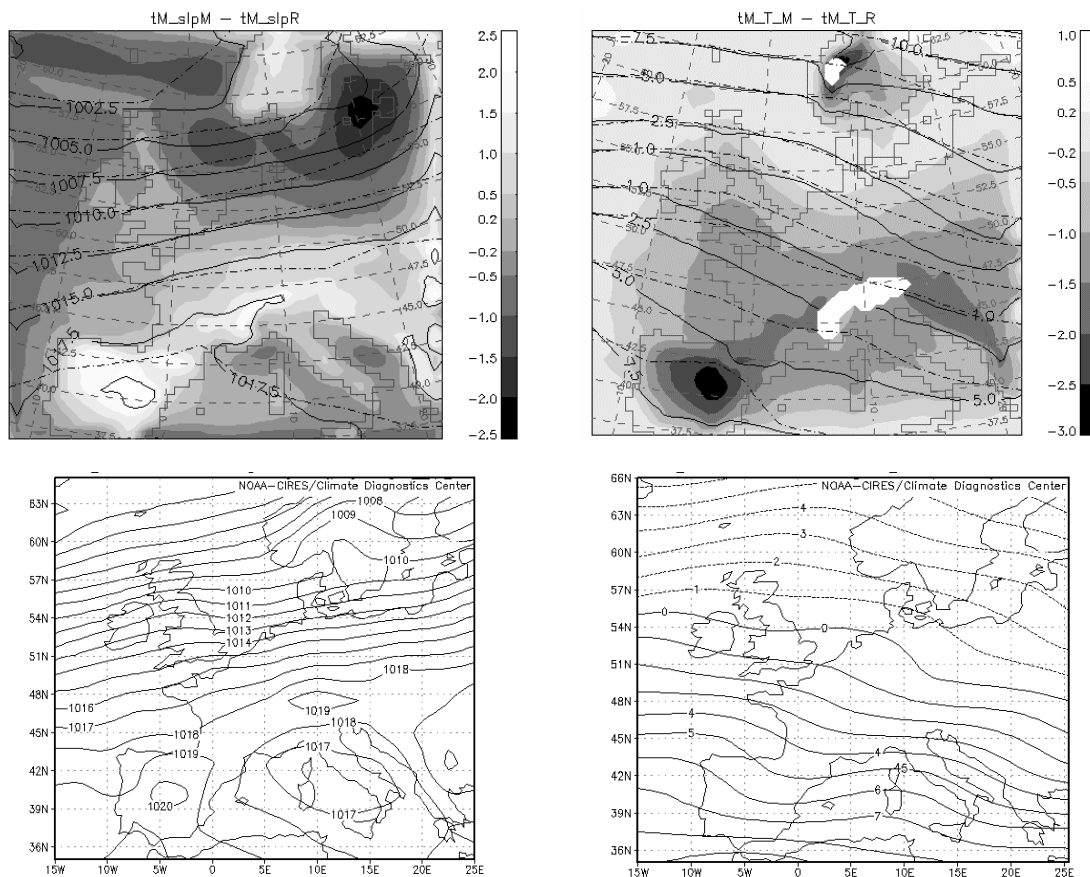


Figure 40: Nested AOGCM–MAR simulation. Left panels: mean sea-level pressure (in hPa). Right panels: 850 hPa temperature (in °C). Top: comparison of MAR and AOGCM results for the 5-month period (dashed lines: AOGCM; solid lines: MAR; shaded background: difference between the models). Bottom: National Centers for Environmental Prediction–National Center for Atmospheric Research’s re-analysis climatology for the month of November (Source: NOAA Climate Diagnostics Center).

To evaluate the performance of the AOGCM–MAR system, we performed a 5-month experiment on the basis of the month of November from each of the last 5 years of the AOGCM control run (CONT). Although this period is too short for a complete validation of the system, it provides a first insight into the ability of the present MAR version to work as a regional climate model.

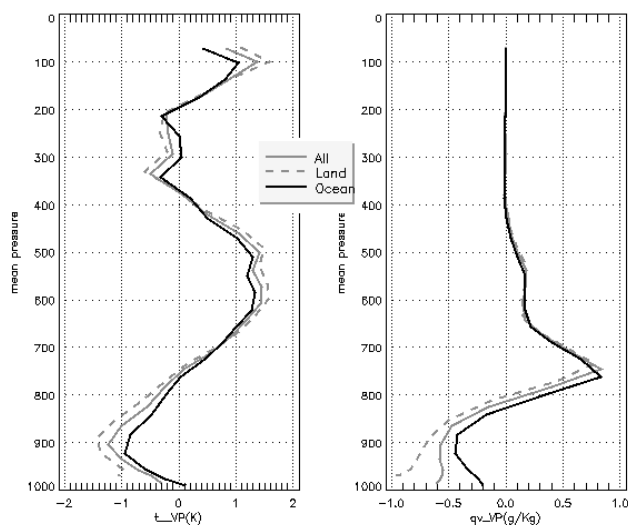


Figure 41: Vertical profiles of the 5-month, area-averaged difference between MAR and AOGCM temperatures (left; in °C) and specific humidity (right; in g kg^{-1}).

As a general rule, the MAR–AOGCM mean difference is moderate, as shown in particular by the area-averaged vertical profiles depicted in Figure 41. The maximum difference is somewhat more than 1°C for temperature and 0.5 g kg^{-1} for specific humidity. In comparison to other nested models, this represents a rather low difference for temperature, and a moderately high difference for humidity (see Marbaix (2000), Chapter 5 and references therein). However, we notice that similar differences in vertical profiles tend to be found at the one-month time-scale in the AOGCM–MAR experiment (not shown), and probably also in climate-change experiments. In contrast, such differences were not found in the re-analysis-driven experiments. This suggests that these differences are mainly caused by the AOGCM. Differences in the representation of convection probably contribute significantly to this discrepancy. This conclusion does not preclude however the use of the nested system.

The monthly (November) total precipitation over the domain is similar in the AOGCM (about 67 mm) and MAR (79 mm) simulations. The total amount and geographical repartition of the precipitation simulated by MAR seems rather satisfying in comparison to observations (Figure 42). However, further investigations involving longer runs are necessary to accurately evaluate the MAR ability to represent surface variables, and in

particular to know if the precipitation results are better than what might be expected by a simple desegregation of the AOGCM rainfall.

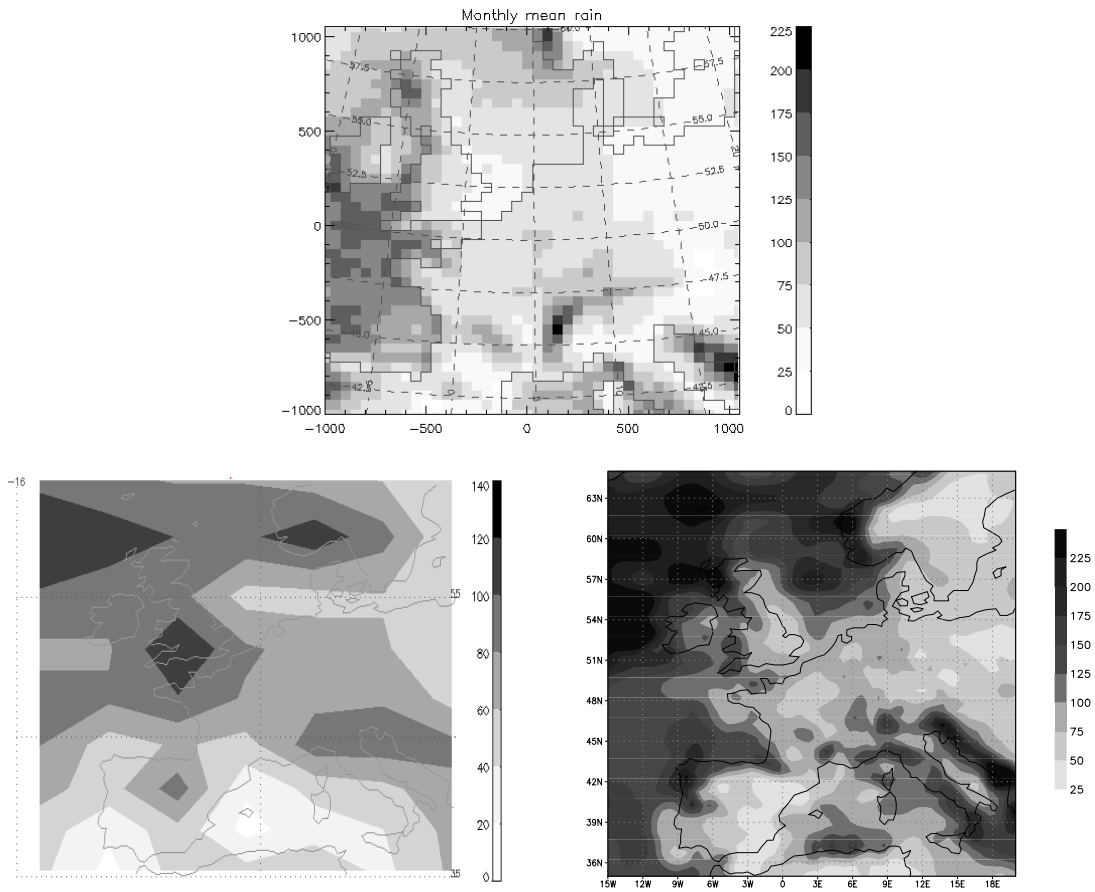


Figure 42: Monthly mean precipitation. Results averaged over the 5-month-simulation period are given for the MAR model (top) and for the AOGCM (bottom left). Climatological values based on Legates and Willmott (1990) are given in the last panel (bottom right).

6. DEVELOPMENT OF A NEW CLIMATOLOGICAL DATA-BASE FOR BELGIUM

6.1 A regional climatological database for the recent past

6.1.1 Introduction

In Belgium, the official climatic network started in the 1870s under the auspices of the former Observatory of Brussels located in St-Josse-ten-Noode, Brussels. In 1913, the Royal Meteorological Institute of Belgium was set up at Uccle-Ukkel, Brussels, and the climatic network was put under its responsibility. Mainly completed by voluntaries, the main climatic information collected across the time is the daily precipitation amount and the extreme maximum and minimum temperatures. Other climatic measurements or observations (snow thickness or state of the ground, for example) are available but not with the same regularity. At the present time, daily observations of precipitation and extreme temperatures have been coded in computer files for the 1951–2000 period. With a few exceptions for precipitation (Dupriez and Demarée, 1988), older data are only available in handwritten form.

Long-time series (at least 50 years of measurements at a same location) are not numerous. Figure 43 gives the temporal evolution of the number of operating stations in the country since 1883. Starting in 1911, an abrupt increase follows a call for collaboration published in the national newspapers. Also, the negative impact of the war periods on the climatological network is clearly visible.

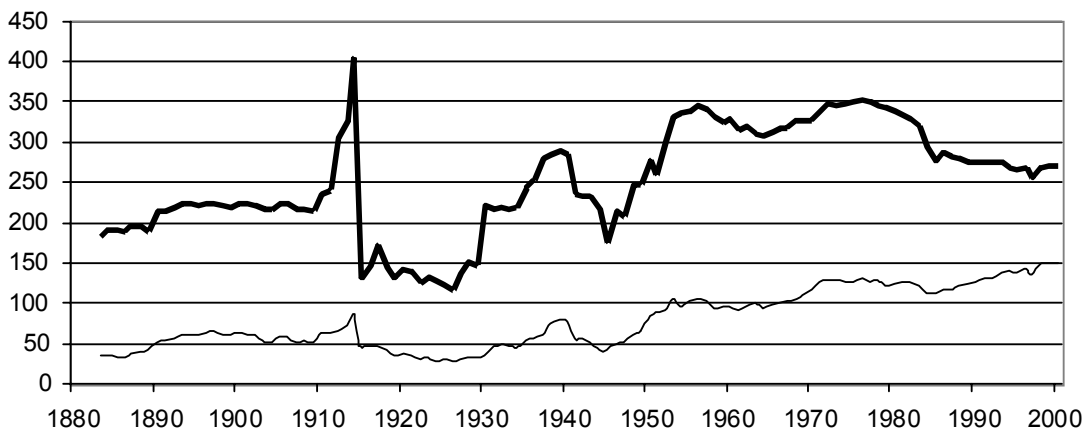


Figure 43: Temporal evolutions of the number of Belgian climatic stations measuring the daily precipitation amount (thick line) and extreme daily temperatures (thin line) from 1883 to 2000 (number of operating stations in January each year).

To characterise the regional climates or to study the climate evolution, artificial perturbations appearing in the measurements must be avoided as much as possible and possibly corrected. Station-location shift, gradual evolution of the environment around a measurement site, observer changes, instrumental modifications, changes in the observational procedure, measurement errors, missing data, ... are examples of perturbations which affect the overall quality of the climatological series. Such perturbations are the reasons of incomplete or heterogeneous series of data.

To construct an adequate climatological database over the last five decades, the following steps have to be considered. First, the quality of all existing data has to be controlled. Next, if not too numerous, missing data in the longest series have to be estimated by interpolation methods. The last step concerns the homogenisation of the longest series to eliminate as far as possible the non-climatic factors able to distort conclusions on the climate evolution.

6.1.2 A corrected and completed climatological database

The climatological database of RMI-GCS is made up of values of extreme temperatures (maximum and minimum) and precipitation amount measured at daily interval by the climatological network. At the start of the project, that information was accessible in computer files for the last 50 years approximately.

a) Historical and geographical check of data

For each climatological station having been operating after 1950, systematic examination of available data was undertaken at the monthly scale. For a lot of isolated months, data were assigned to erroneous stations and have been reassigned to correct stations. In parallel, search for available "metadata" (historical data useful for assessment of temporal homogeneity in observations) has been performed individually for the entire set of stations, and many unrecorded relocations of station have been discovered. Whenever possible, new exact geographical coordinates were attributed in relation with these location changes.

To avoid plethora of short time series, the usual solution is to combine successive time series available in a particular region in a single (longer) time series. The geographical relevance of the combinations carried out previously was systematically checked, taking account the newly discovered station relocations. As a first rough estimate, two stations less than 10 km apart (and, for temperature, with a difference of altitude of less than 100 m) have been considered as climatically equivalent. Consequently, successive time series of data attributed in the initial database to a single time series have been cut whenever distance (or altitude) criteria were not respected after station relocation. On the other hand, no overlapping time series (initially attributed to distinct

stations) have been joined whenever criteria were met. The main goal of these modifications was to reconstruct the longest possible climatically relevant time series at a local or regional scale over the 1951–2000 period.

b) Detection and correction of outliers

An improved knowledge of the past geographical location of the climatic stations is also useful for adequate spatial interpolation of climatic parameters. Such an interpolation was undertaken here to complete two tasks. The first one consists in detecting and correcting outliers (manifestly erroneous values) and the second one in estimating missing data. More generally, comparing systematically observations to their corresponding estimations can lead to detect other highly suspicious observations (called here also outliers).

These two tasks require choosing one or several interpolation methods. Many statistical methods can be found in the literature, and each can be preferred when working on a specific database. In the present work, seven spatial and temporal interpolation methods have been tested and compared for estimation of daily precipitation and temperature (Fontaine et al., 2001). Two have been chosen for their efficiency and their facility of use. The first method is the weighting of neighbouring measurements by the square of the distances (between the neighbouring stations and the candidate station).

For 100-yr-long climatic series, a temporal method is preferred for temperature estimation if neighbouring stations are too sparse. In the present work, the least squares regression with a correlated series will be used in that case to estimate daily temperatures. When daily precipitation data are too sparse, the chosen solution consists only in taking the measurements of the nearest station.

Errors of reading the instruments and errors of writing or coding them are usual errors in the measurements of the climatological network. Such errors have to be corrected for the false information they give, but also for the incorrect estimation of missing data they can induce. Detection and correction of outliers cannot be done across more than 10 millions of daily data without automatic procedures. Limits between possible and impossible values must be fixed from climatic knowledge for the considered variables in the studied regions.

In the present study, outliers have been detected in gradual steps. First, manifestly erroneous observations have been defined by fixing an interval of possible measurements. Maximum and minimum temperature values must be comprised between -30 and 45°C and daily precipitation must be a positive value less than

250 mm. Erroneous temperatures are also detected in a station when the minimum exceeds the maximum for the same date.

Next, other suspicious (probably erroneous) values can be found by the comparison of each observation with the neighbouring ones. For the rapidity of work, a computer program has compared each measured daily precipitation and extreme temperatures to their own estimation obtained using an interpolation method. The estimation is calculated here with the method of weighting data by the square of distance between stations. According to the difference between observed and estimated data, and taking into account the standard deviation between the measurements, daily values at the candidate station have been considered "possible" or "impossible".

The correction of outliers is facilitating by considering their most frequent origins. For temperature, it is well known that reading errors amounts frequently to -10°C , -5°C , $+5^{\circ}\text{C}$, or $+10^{\circ}\text{C}$, and propositions of correction are straightforward. For precipitation, outliers are mainly caused by rain accumulation in rain gauge during several days without measurement. The usual way to correct this kind of error is to redistribute the accumulated quantity on the several missing measurements using information from neighbouring stations. To avoid detection of spurious outlier for precipitation, special care has to be given to stormy situations often leading very locally intense rainfall.

Looking for outliers, special types of errors were discovered in the initial database. This concerns the considered daily interval for the extreme temperatures. The maximum temperature measured at 8.00 a.m. (local time) in the climatological network referred usually to the maximum of the previous afternoon. But, after consulting archives, we discovered that a few observers put already back the maximum to the correct date on their written monthly reports. The coding having the automatic instruction to put back the maximum, an upward shift in daily values was introduced in these time series. Another problem concerns the synoptic stations, which considered (for the period before 1968) the schedule 00.00–24.00 h (Universal Time) to determine the daily maximum and minimum temperatures. To detect the problem, daily data from synoptic stations were compared to those of several other stations in the surroundings. The monthly variance of the differences between both series was calculated considering the initial, moved forward (by one day) and put back (by one day) synoptic data (see example in Figure 44). By examination of the differences for the monthly variance, it was possible to adjust the synoptic data.

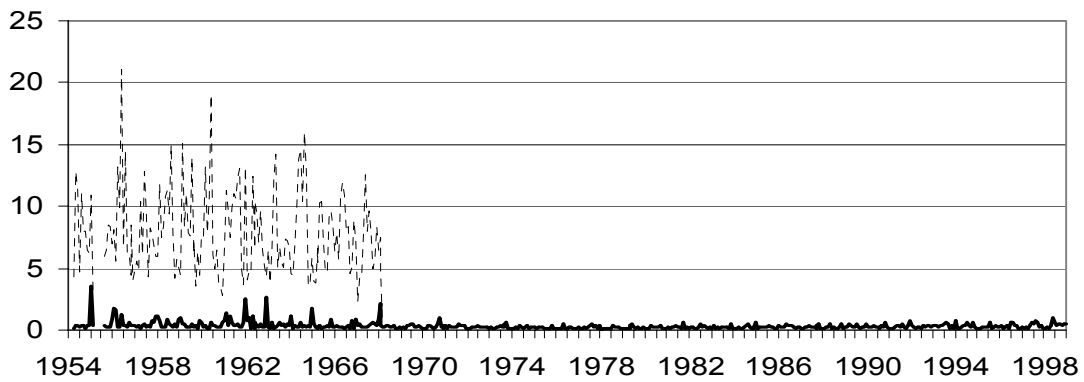


Figure 44: Time series of monthly variance (in $^{\circ}\text{C}^2$) of the daily difference for maximum temperature between the observations of Chièvres (synoptic) and Huissignies (climatic) over 1954–1998. The difference is calculated with the initial data of Chièvres (dashed line) and the moved forward data (solid line).

c) Estimation of missing data

The final step to obtain cleaned and complete climatic series consists in the estimation of missing data. This work has been accomplished for the most interesting time series according to the period they covered. When a rich density of observations was available, the estimation was performed by the weighting method by the square of distance between stations. Because they are very few available time series in computer files before 1950, missing data for the 100-yr-long time series were estimated by regression (for temperature) or replaced by the observations of the nearest station (for precipitation).

6.1.3 A homogenised climatological database

So far, the main outliers have been eliminated from the daily climatic database, and selected missing data have been replaced by estimations. Based on new metadata, several cuttings or combinations of successive time series have been done to guarantee spatial coherency for all data assigned to a single (regional) climatic time series. A set of cleaned and complete regional series of daily climatic data is thus available at this stage. The final step consists in the search and correction of temporal discontinuities affecting the time series. As mentioned before, changes of location, instruments, observational procedure, environment around the instruments, etc. can lead to artificial shifts when considering the temporal evolution of the variable studied. Whenever possible, the influence of these non-climatic factors must be taken into account before any study of climatic change from the time series analysis.

a) Statistical detection of break points in time series

Two types of artificial discontinuities can affect the observations through the time. The first case concerns instantaneous modifications – such as the change of instrument or a station relocation – which generally lead to abrupt discontinuities or shifts (called "break points") in the time series. In contrast, a progressive modification – like induced by the slow change of the environment around the instrument (e.g., the vegetation growing up) – will affect the measurements in a progressive and increasing way. These last discontinuities (called "trends") will not be corrected into our database, even if statistical methods exist to detect such kind of discontinuities. According to results of empirical tests, we could not find enough reliable procedure permitting their correction in the time series.

In principle, break points can be detected when comparing the time series of different stations in a homogeneous climatic region. Nevertheless, the following points have to be carefully taken into account:

- How to choose or to elaborate a reference series with which the candidate series will be compared? This reference series must be free of non-climatic influences and representative of the climate observed at the candidate station.
- Which statistical method must be used to detect and locate precisely in time the break points into the tested series?
- How to correct the discontinuities? What could be the relevant temporal scales of this correction?

Using a unique series as reference can be very dangerous because this one can be affected by discontinuities or can represent different climatic conditions. A more adequate method to create a reference series is given by Easterling and Peterson (1995). Let us consider the (daily) time series for a station j . Its temporal homogeneity will be tested by comparison with the reference series computed by averaging the data from surrounding stations. The average reference series is computed with weighting factors taken as the square of the correlation coefficients of surrounding stations. The effect of potential break points in time series utilised to elaborate the reference series is decreased by correlating not the raw data but rather the change in data per day:

$$(dT / dt)_i = T_{i+1} - T_i,$$

with i and $i+1$ stand for day (i) and day ($i + 1$), respectively.

In this way, discontinuities have an impact only on one element of the reference series, instead of over the whole considered period.

Concerning the method to detect break points, three main statistical procedures have been proposed: the first one analyses the mean distribution, the second one looks for breaks in the calculated regression, and the third one is based on the ranks order (non-parametric method). Many operational procedures have been proposed in the literature, and it is not straightforward to make a choice. In the present project, five statistical methods have been tested and compared theoretically and practically. Alexandersson's (1986), Alexandersson and Moberg's (1997), and Potter's (1981) methods are well-known methods in the analysis of the mean distribution. The common t-test is also a popular statistic in many fields. The method proposed by Easterling and Peterson (1995) has been chosen as a method based on regression. Concerning the non-parametric tests, the Pettitt's (1979) test is often mentioned in the literature and has been retained here.

These statistical methods have been tested on theoretically generated (i.e., perfectly controlled) series, similar to observed monthly time series of temperature or precipitation. Starting from two series (a candidate one and a reference one) strongly correlated and absolutely (statistically) homogeneous, discontinuities have been introduced artificially in the candidate series. The various methods of detection have been tested for several magnitudes of discontinuities introduced at different positions (from position 6 to 95 on a total of 100 elements) inside the candidate series. One hundred of couples of random simulated series have been tested following this procedure. The results of these tests show that Alexandersson's test is usually the most reliable method to detect break points (Fontaine et al., 2001). Potter's test presents also a good efficiency. On the contrary, the efficiency of the statistic t, of the Pettitt's test, and of Easterling and Peterson's test, is lower and too much dependent on the position of the discontinuity inside the candidate series. Those last three tests present also the disadvantage of detecting generally several non-existent discontinuities. The analysis of time series for precipitation and of temperatures leads to the same conclusions.

Alexandersson's test has also been shown the most efficient one in search of break points for actual climatic time series. That result was obtained by comparing the five methods for stations for which the metadata are (at least partially) known. As an example, Figure 45 shows the differences between the annual minimum temperature of the station Tienen and that calculated for the reference series (obtained by applying Easterling and Peterson's method). Two breaks of homogeneity can be observed in 1969 and 1996, resulting from known changes of location of instruments in 1970 and 1997. Alexandersson's test and Potter's test detect the two break points, even when different periods of data are considered. The results of other methods are influenced by the period considered for the test.

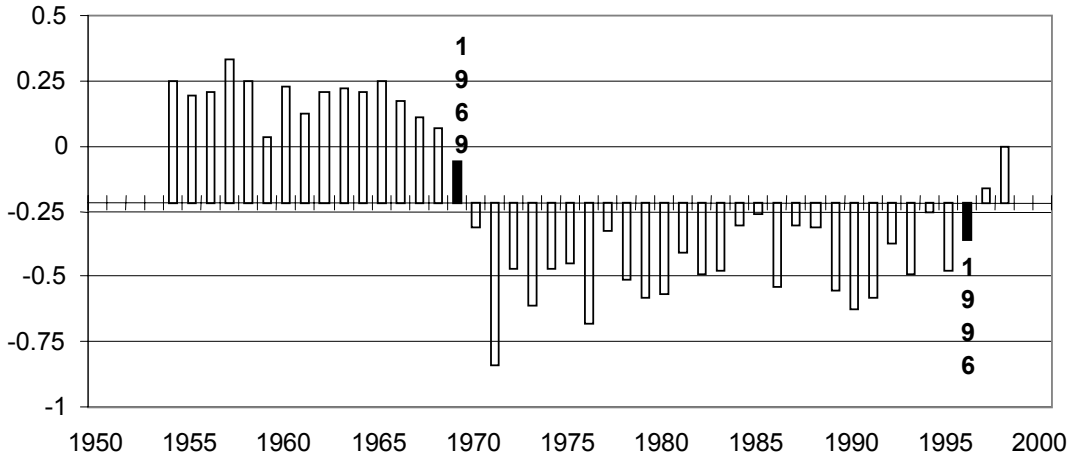


Figure 45: Differences (in °C) over the period 1954–1998 between the annually averaged minimum temperature observed at station Tienen and the corresponding one for the reference series. The annual difference is given as departure from its mean over the whole time period.

b) Correction of abrupt heterogeneities in the time series

In homogeneity analysis of a time series, the location of a break point is usually given by indicating the final element of the heterogeneous part of the series, comparing to the homogeneous part containing the most recent data. By definition, in each studied time series, the most recent observations have therefore been considered as reference data (correct data) before correction of heterogeneities. Secondly, for all the break-detection methods, the correction factor corresponds to the ratio (precipitation) or the difference (temperature) between the mean of the homogeneous and the mean of the heterogeneous elements.

Most results found in the literature deal with the identification of the discontinuities at the annual scale. Authors mention sometimes the possibility to look for them at a monthly scale. But they do not trust very much on these operations, which can lead to detect different years of breaks according to the month studied. An identification of discontinuities at smaller time-scales seems generally impracticable, because of the difficulty to separate unambiguously artificial perturbations from the natural and huge variation of the climatic conditions (e.g., at the daily time-scale).

However, to study the climatic evolution of daily extreme phenomena, homogenised daily data are ideally required. A rough solution could consist in applying a constant daily factor equal to the annual one. But, artificial perturbations are known to influence differently the observations according to the seasons (e.g., for extreme temperatures). So, a more relevant way to tackle the problem may be to detect annual breaks in a first step, then to estimate annually or monthly correction factors (to carry out

heterogeneities), and finally, to estimate daily correction factors. Vincent et al. (2000) have proposed such an approach, using the procedure elaborated by Sheng and Zwiers (1998). The following steps are defined:

- To detect the annual break point(s) and to calculate the annual correction factor(s).
- In respect of the year of a detected break, to calculate a monthly factor for each of the twelve monthly series. Each of these series considers thus the same month throughout the years.
- To calculate the "mid-month target values", which are resulting from a smoothing of the monthly factors.

Target values can be found by solving the following system of equations:

$$A T = M,$$

where T is a 12×1 vector of the target values, M is a 12×1 vector of the monthly factors, and A is a tridiagonal 12×12 matrix:

$$A = \begin{vmatrix} 7/8 & 1/8 & & & \\ 1/8 & 6/8 & 1/8 & & \\ & \cdot & \cdot & \cdot & \\ & & 1/8 & 6/8 & 1/8 \\ & & & 1/8 & 7/8 \end{vmatrix}$$

The mid-month target values can thus be obtained by solving the equation:

$$T = A^{-1} M$$

The target values are used as correction factors for the central day of the months. The other daily factors can be estimated by a linear interpolation between each target value to the following one. This method of correction has the advantage of providing daily factors representing the seasonal variability of the effect of the discontinuities. But, these daily factors respect also the monthly and annual correction factors.

As conclusion of our results from theoretical and practical comparisons between statistical methods, the following procedure has been applied to all complete time series of daily temperatures (over the 1954 – 1998 period) and precipitation (over the 1951 – 1998 period):

- The method of Easterling and Peterson is used to create reference series with which the candidate series will be compared. To construct the reference series, the data of a respective minimum and maximum number of 2 and 5 surrounding series have been used. When enough neighbouring stations were present, the correlated stations were searched in a maximum distance of 30 kilometres around the candidate series. To take benefit of the maximum of data available, all the completed series on at least 10 years were considered for the creation of the reference series.
- The break points were searched following Alexandersson's method applied to the annual and monthly series. All the discontinuities presenting a magnitude equal or up to 0.4°C (for temperature) and 10% (for precipitation) were systematically corrected. The breaks with a magnitude estimated between 0.2°C and 0.4°C or between 4% and 10% were only corrected when justified by a historical event. Breaks with a magnitude below 0.2°C and 4% were not considered. As proposed by Alexandersson, corrections were made only when a minimum of 5 successive years of homogeneous data was present.
- Daily correction factors were calculated according to Vincent's method for the temperatures. Because of the great spatial and temporal variability of precipitation, daily factors equal to the annual one were applied systematically for this parameter (without modifying the rainless days).

c) Final inventory of the new climatological database

Table III gives a summary of the number and completeness of time series available in the new climatological database (after cleaning, correction of outliers, and estimation of missing data). For temperature and precipitation, summaries are given for the longest possible period and for the 1961-1990 period (i.e., the standard reference period for computation of climatological normals).

Table III: Inventory of the new database of daily extreme temperature and precipitation.

	Precipitation		Temperatures	
	1951-1998	1961-1990	1954-1998	1961-1990
Complete series	125	172	45	52
Series with at least 80% of present data and without any missing sequence	34	19	7	8
Series with at least 80% of present data but with missing sequences of maximum 6 months	1	3	0	1
Series with at least 80% of present data but with missing sequences of minimum 7 months	45	25	6	6
Series with less than 80% of present data	293	207	187	130
Total number of series	498	426	245	197

The homogeneity of all available complete series has also been checked over the 1954–1998 period for temperature and over the 1951–1998 period for precipitation, and corrections have been made when necessary. The same work has been done for the complete series of extreme temperatures and precipitation over the 1961–1990 and 1971–1998 periods. The search of heterogeneities has also been undertaken for all the reconstructed 100-yr-long climatic time series. In spite of our extensive search of relevant metadata for the majority of stations, it is presently only possible to explain objectively 20% of the corrections introduced after detection of heterogeneities.

6.1.4 Normals for temperature and precipitation

To characterise the mean climatic conditions (called "normals"), a period of 30 years is usually considered (WMO, 1989). Consideration of such a long period decreases the impact of climate variability existing in the time series at the interannual time-scale. Presently, the 1961–1990 period is the standard time period usually chosen to calculate the monthly and annual climate normals. These normals for mean temperature and precipitation have been computed for all complete time series available in the database, i.e., for 172 pluviometric series and 52 thermometric series (see Table III). Using a kriging method, Figures 46 and 47 have been drawn from the normals computed at each station.

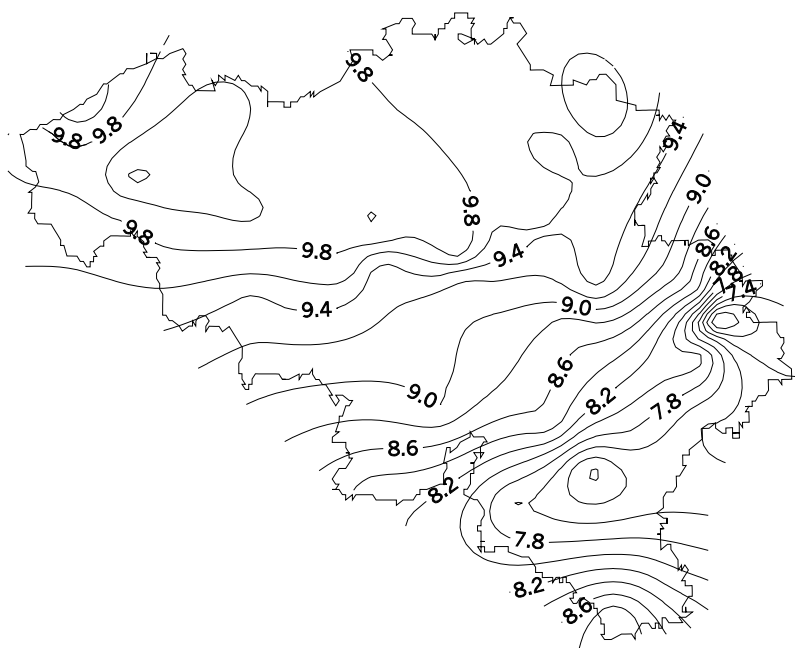


Figure 46: Annual normals of mean temperature (in °C). The contour interval is 0.2°C. The daily mean temperature is defined in the climatological database as the average between the daily maximum and minimum temperatures.

As expected, Figure 46 shows clearly that the annual normal of the mean temperature is decreasing with the altitude and with the distance from the sea. Figure 47 reveals that the annual normals of precipitation follow globally an inverse trend. Four stations (namely, Angleur, Liège, Malonne, and Houyet) have been excluded from the krigging for the mean temperature, because these stations induced a suspect perturbation in the plot of the iso-temperatures. The precise reasons for these local anomalies are not known, but probably related to an urban effect (warming) for the two first stations and to worse exposure of instruments for the last two stations.

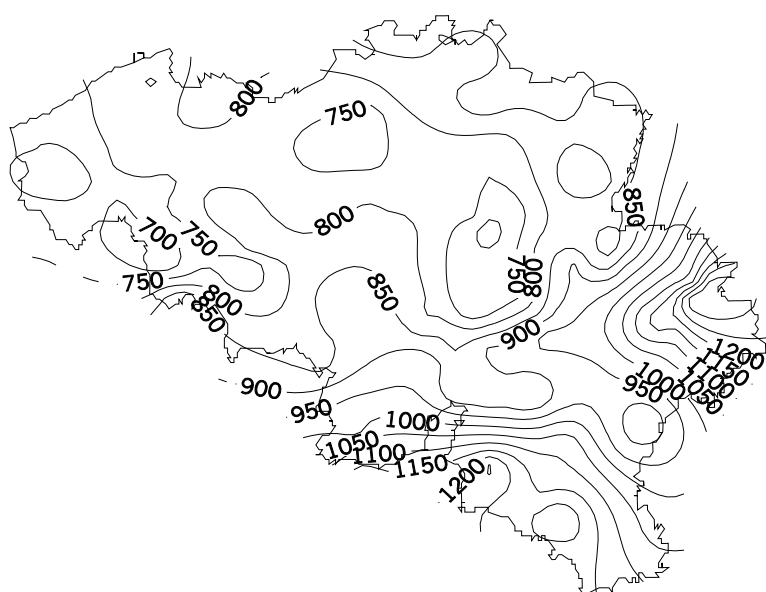


Figure 47: Annual normals of precipitation (in mm). The contour interval is 50 mm.

The map of normal annual temperature (see Figure 46) is roughly similar to that given in Poncelet and Martin (1947). The differences are attributable to the differences in the reference periods (1901–1930 for Poncelet-Martin) and in the station density (less than 40 stations for Poncelet-Martin) and spatial distribution. The map of normal annual precipitation (see Figure 47) shows similarities, but also significant differences, with the map published by Dupriez and Sneyers (1979). These authors have used pluviometric data from more than 350 stations over the 1951–1975 period. Many stations are incomplete during this period, and a statistical method was used to reduce monthly means of a particular station to estimated normals over a common reference period

(1833–1975) by comparing existing monthly data for the station with the data corresponding to station Uccle-Ukkel (Dupriez and Sneyers, 1978).

Spatial results from the two maps presented here are preliminary results. To increase the number of stations used for drawing the maps (and hoping so for improvement in spatial representation), it is planned in the future to estimate the normals also for incomplete series over the 1961–1990 period. The statistical methods described in Dupriez and Sneyers (1978) for precipitation and in Sneyers and Vandiepenbeeck (1989) for temperature could be used to carry out this task.

6.1.5 Recent climatic evolution at the regional scale

The new climatological database contains a huge amount of information potentially useful for the study of the Belgian regional climates and their evolution over the last half of the 20th century. To study the recent regional climates using data over the longest possible common time period, we will consider afterwards all complete series of temperature and precipitation, respectively over the 1954–1998 period and the 1951–1998 period (see Table III).

a) Regional classification for temperature and precipitation

Because some specific heterogeneities can still exist in particular time series, the climate evolution after 1950 will be tackled by considering averaged time series over homogeneous climatic regions. A climatic classification of climatological stations has been undertaken to determine a set of homogeneous climatic regions through the country. Separated classifications have been realised for temperature and precipitation from complete time series of daily mean temperature and amount of precipitation over the 1971–1998 period. This period has been chosen to take benefit of the maximal number of complete stations. Using the software STATISTICA, the classifications have been created according to the method described by Champeaux and Tamburini (1996). This method is a hierarchical classification based on the Euclidean distances between the series and optimised with the aggregation criterion of Ward. Figure 48 shows the homogeneous climatic regions resulting from the classification for the mean temperature and the amount of precipitation.

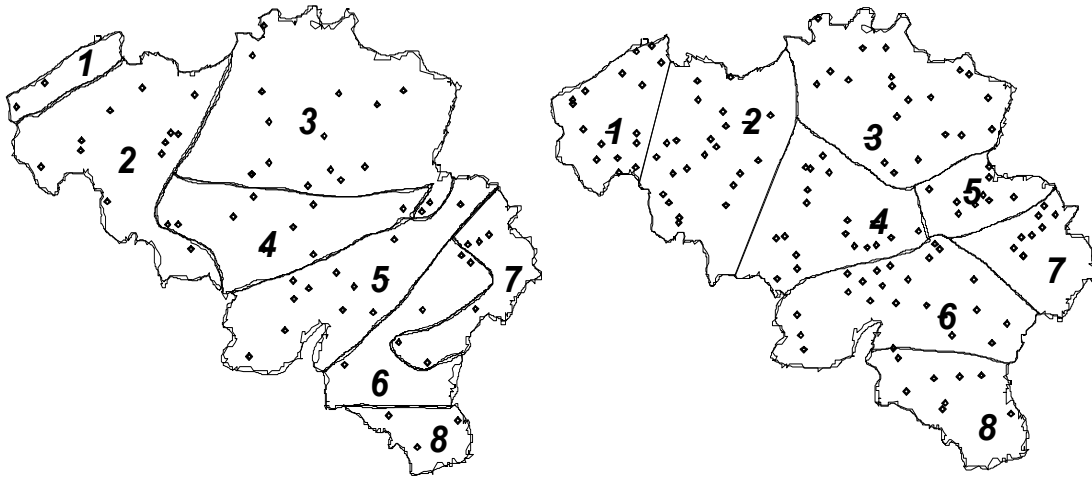


Figure 48: Representation of the classifications obtained for mean temperature (left) and precipitation (right) using daily data over the period 1971–1998. The locations of the stations used for the classifications are shown on the maps.

Based on the approximative geographical delimitations of the homogeneous regions depicted in Figure 48, these regions will be referred hereafter to as:

Temperature

Region 1 = Kust

Region 2 = Vlaanderen

Region 3 = Kempen

Region 4 = Brabant

Region 5 = Condroz

Region 6 = Ardenne

Region 7 = Haute Ardenne

Region 8 = Gaume

Precipitation

Region 1 = Polders

Region 2 = Vlaanderen

Region 3 = Kempen

Region 4 = Brabant

Region 5 = Pays de Herve

Region 6 = Ardenne

Region 7 = Haute Ardenne

Region 8 = Gaume

Using the results of classification for temperature and precipitation, a single daily time series has been obtained for each homogeneous region as the average of the data for all the stations located in the corresponding region. Only the stations with complete series over the 1954–1998 period for temperature and over the 1951–1998 period for

precipitation have been considered in the computations. These regionally averaged time series will be used afterwards to study the Belgian climatic evolution at the regional scale over the second half of the 20th century.

b) Method for determining the regional climatic evolution

The significant changes in regional time series have been studied for the second half of the 20th century at the annual, monthly, and daily time-scales. Two major statistical phenomena have been searched and analysed: break points and trends. Break points can be found using Alexandersson's test applied directly to the studied series (instead of to the difference series between candidate and reference series as used earlier in the homogeneity tests; see Section 6.1.3). As previously, break points found here are related to abrupt shifts (increase or decrease) in temperature or precipitation. Regarding the trends, Mann's test has been used to determine their statistical significance when considering globally the time series (Mann, 1945). The terms "significant", "very significant", and "very highly significant" applied to climatic changes will refer to the respective levels of statistical significance (α) equal to 0.05, 0.01, and 0.001. Only the major facts observed in the recent climatic evolution have been reported here.

c) Evolution of the minimum temperature (1954–1998)

Daily minimum temperature (TN) is defined as the minimum value reached by the air temperature at the surface over a period of 24 hours comprised between two successive periods of observations (done at 08.00 h in local time). Figure 49 displays the evolutions over the 1954–1998 period of the annual mean minimum temperature for the 8 homogeneous regions defined previously for temperature. An additional "national" time series (noted "Belgium") is also illustrated in the figure, defined by computing the average minimum temperature using all the stations. Over the concerned period, each region shows a warming trend amounting approximately to 2.5°C per century. This global trend is partly related to a general abrupt warming around 1988. The warming trend is (at least) statistically significant in each region (up to very highly significant in the regions Brabant and Ardenne).

Seasonally speaking, significant warming trends are observed in all regions in summer. Only the region Ardenne exhibits also a significant warming in winter.

For the whole country (region Belgium), the trends at the daily time-scale have also been studied. The warming trend induces an annual number of frost days (negative minimum temperature) which has decreased significantly during the second half of the 20th century.

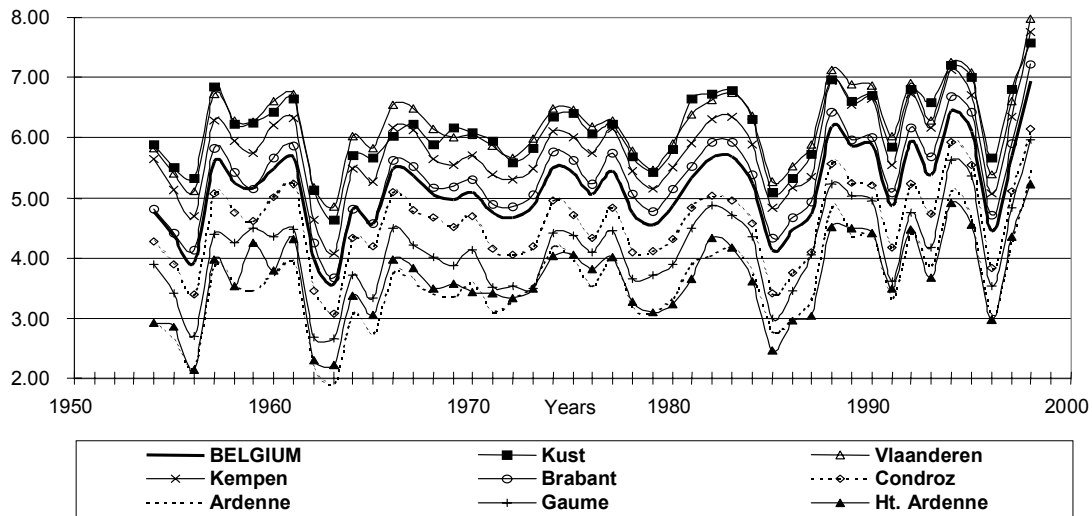


Figure 49: Evolutions of the annual mean minimum temperature (in °C) for the homogeneous climatic regions over the 1954–1998 period.

d) Evolution of the maximum temperature (1954–1998)

Daily maximum temperature (TX) is defined as the maximum value reached by the air temperature at the surface over a period of 24 hours comprised between two successive periods of observations. Similarly to the minimum temperature, the annual mean maximum temperature shows an overall increasing trend during the second half of the 20th century in the different homogeneous climatic regions, amounting to about 2.0°C per century (Figure 50). Around 1988, an abrupt warming is also clearly observed for this temperature and reaches about 1.0°C. A non-significant annual warming trend is observed in the regions Condroz and Kempen and a very significant one is present for the region Kust.

Seasonally speaking, the warming trend concerns principally the summer season. Only the region Kust experiences a significant trend in spring.

For the whole country (region Belgium), the trends at the daily time-scale have also been studied. As a direct consequence of the warming trend, the number of summer days (maximum temperature at least equal to 25°C) has increased significantly during the second half of the 20th century.

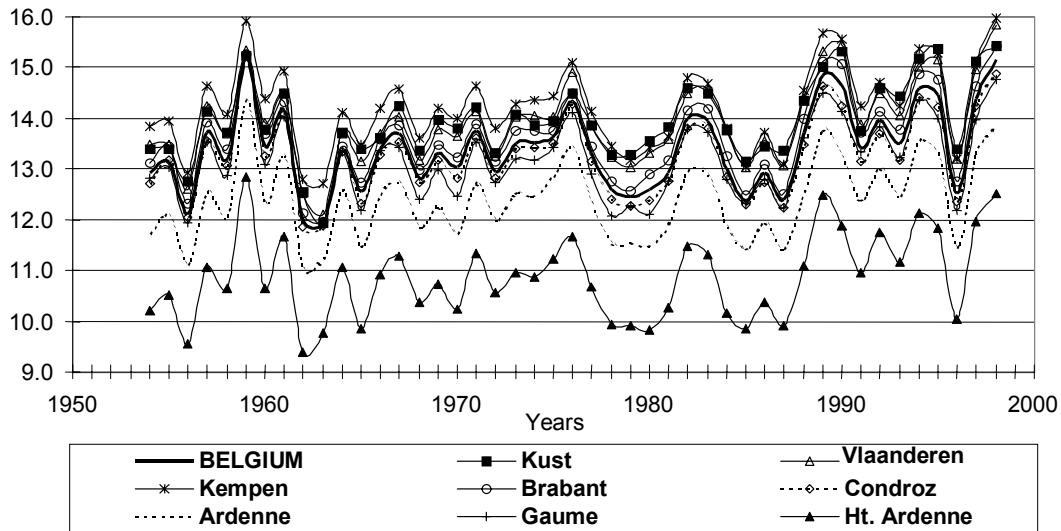


Figure 50: Evolutions of the annual mean maximum temperature (in °C) for the homogeneous climatic regions over the 1954–1998 period.

e) Evolutions of the mean temperature and of the daily range (1954–1998)

The daily mean temperature is defined here as the averaged value of the daily maximum and minimum temperatures. In the climatic regions, this temperature exhibits the same evolution as those shown by the minimum and maximum temperatures, i.e., an overall warming trend with an abrupt increase around 1988.

Seasonally speaking, the most significant warming trend is observed during summer. The abrupt warming after 1988 is especially strong in spring, except for the region Gaume. No trend or abrupt jump has been found in autumn, and the warming trend in winter is not statistically significant.

The evolution of the daily range of temperature (difference between the maximum and minimum temperatures) has also been analysed for the region Belgium. A small, not significant, negative trend in this climatic parameter is only noticed.

f) Evolution of the precipitation amount (1951–1998)

For each of the 8 homogeneous climatic regions delimited for precipitation (see above), daily mean series have been calculated for the 1954–1998 period using the complete precipitation series available for each region. A national mean series has also been constructed (region Belgium) using all the available complete daily series. Generally, estimating a daily mean regional amount of precipitation simply by averaging the values of all stations in the region is a questionable method. In the present case, we think that the high density of stations will give relatively good estimates, especially at long time-scales. In the future, we intend to make more

appropriate estimations of daily regional precipitation using more elaborated approaches (e.g., Thiessen's method).

As can be seen from Figure 51, no obvious trend is detected for the annual mean precipitation in any region. With the exception of the region Pays de Herve showing a small (not significant) negative trend, all other regions present a small (not significant) positive trend. No abrupt breaks have been detected in the precipitation time series.

From the seasonal time series, the following trends have been detected as significant : a decreasing trend in summer for the regions Pays de Herve and Haute Ardenne, and an increasing trend in spring for the regions Polders, Vlaanderen, and Brabant.

At the daily time-scale, the temporal evolutions of two parameters have been examined: the annual number of days with precipitation (defined here as days with mean regional precipitation of 1 mm at least) and the mean daily intensity of precipitation (defined as the total annual precipitation divided by the number of days with precipitation).

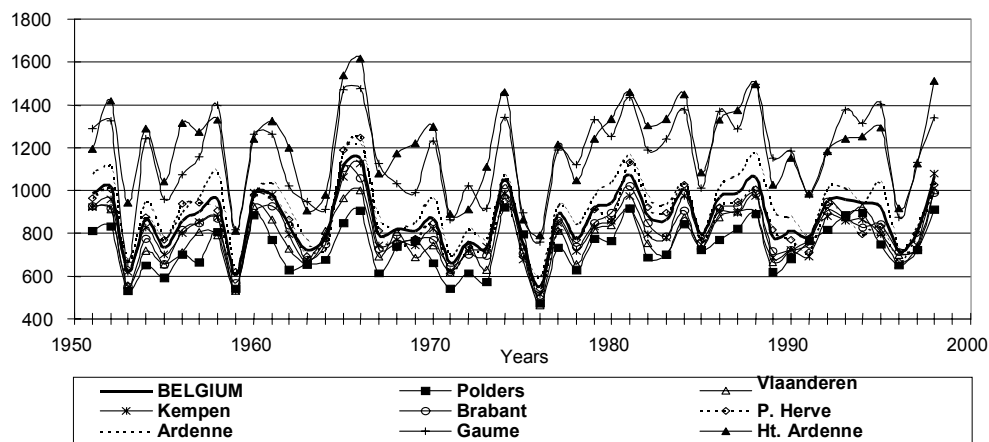


Figure 51: Evolutions of the annual mean precipitation (in mm) for the homogeneous climatic regions over the 1954–1998 period.

The annual number of days with precipitation shows a very highly significant decreasing trend over the considered time period. In parallel, the annual mean daily intensity of precipitation has also increased significantly over the whole country, with the exception of the region Pays de Herve. This increase is particularly significant in the regions Vlaanderen and Polders.

It is interesting to compare these results with those obtained by Gellens (2000) using the daily pluviometric data from the Belgian climatological network. This author analysed the time evolution for the k-day extreme precipitation events (i.e., the annual highest precipitation amount summed on $k = 1$ to 30 days) during the 1951–1995

period. He found no trend for small k (generally summer pluviometric events) and a significant positive trend for k larger than 7 (generally winter pluviometric events). Therefore, over the last 50 years, the mean daily intensity of precipitation shows a positive trend at the annual time-scale (this study), even though the daily extreme precipitation amount is stable at the same scale (Gellens, 2000).

6.2 100-yr-long climatic time series for Belgium

6.2.1 The longest climatic time series over the last century

100-yr-long daily time series have been coded for a selection of stations to analyse the regional climate evolution in Belgium during the 20th century. For the daily minimum and maximum temperatures, six daily time series have been reconstructed with complete data between 1900 and 1998 (Leopoldsburg, Uccle-Ukkel, Gembloux, Deneé-Maredsous, Thimister, and Stavelot). Because of the quality and regularity of their daily data, three other series have been coded on shorter periods: Baraque Michel (1928–1998), Chimay (1910–1998), and Rochefort (1912–1998). As shown in Figure 52, the reconstructed 100-yr-long time series are unfortunately located only in the eastern part of the Belgian territory. In the western part, no time series for temperature was found long enough to be coded and reliable enough to allow studying the regional evolution of the climate. Further, the small number of reconstructed 100-yr-long time series will not allow us to extrapolate directly the local analysis (with data of a single station) to the regional scale and certainly not globally for the entire country.

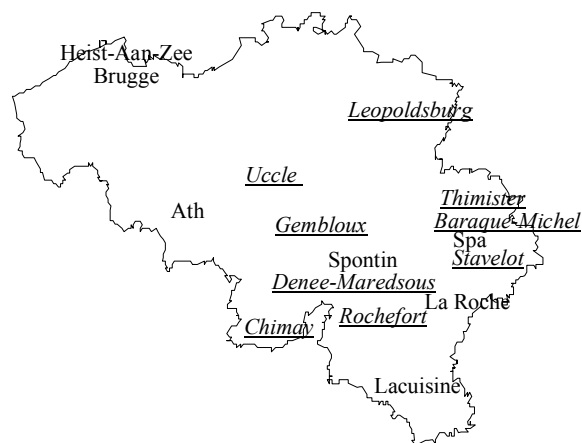


Figure 52: Geographical positions of the 100-yr-long daily time series coded for precipitation (all the stations) and for extreme temperatures (only underlined stations in italic).

To analyse the secular evolution of precipitation, 11 pluviometric series already existed at the daily time-scale in RMI's climatological database (Dupriez and Demarée, 1988). Five new long pluviometric series have been reconstructed at the daily time-scale in

the framework of the present project (Heist-aan-Zee, Gembloux, Spontin, Spa, and Baraque Michel). The climatological database includes now 16 long pluviometric time series (see Figure 52). All of these stations present complete daily pluviometric data from 1900 to 1998, with the exception of the station Baraque Michel, which is complete only for the 1931–1998 period.

6.2.2 Analysis of the reconstructed thermometric series

Analysing the regional climate evolution with only 9 long time series of temperatures is not straightforward. First, the study will be concentrated on punctual geographical points instead of regions. But, the main inconvenient was resulting from the difficulty to compare the different series in a direct way if no homogeneity control is first carried out.

More than the distance isolating the long time series of temperatures, the lack of information on the observation conditions in the course of time is a real obstacle to the homogeneity corrections. At the beginning of the century, only general information is available for the exposure of thermometers. As example, Poncelet and Martin (1947) mention the use of three different screens in the climatological network between 1900 and 1930 (see below). But, they also report the impossibility to know exactly when individual stations have been concerned by those changes. Use of different screens (large or small, partly or fully isolated from radiation) can influence in a significant way the measurement of temperature and especially the maximum temperature (particularly during calm, warm, and sunny weather).

a) Analysis of the non-homogenised long time series of temperature

Because of this lack of historical information about the stations, the analysis of the homogenised series of temperature must be considered carefully. It is hoped that the reliability of the homogenisation will increase in the future with coding of supplementary long time series (even if incomplete over the 20th century). Consequently, we have first analysed the time evolution of the non-homogenised series of temperature.

From the information contained in Table IV, the following trends can be underlined for the thermometric evolution during the 20th century:

- The minimum temperature follows a significant to very highly significant warming trend (0.1°C to 1.3°C per century, according to the station). This trend is partly due to the abrupt increase of temperature around 1988.
- By contrast (except for Uccle-Ukkel), the maximum temperature shows a cooling trend over the whole century. A huge trend of –1.6°C per century is

even reported for station Chimay (over the period 1910–1998). But, the year 1988 is still the starting point of an abrupt warming for all the stations.

Particular considerations lead us to consider carefully the results for the maximum temperature. For that temperature, the most reliable and well-known thermometric time series (station Uccle-Ukkel) exhibits indeed a warming trend over the century, contrary to the other stations. This station has undertaken thermometric observations with the same large half-open screen during all the century. On the other hand, the screens of all other stations have potentially changed in the course of the time, and especially during the first half of the century, as already mentioned. During this period, three screens could have been used (Poncelet and Martin, 1947) in the climatological network: a large half-open wood screen (approximately between 1901 and 1910), a little open screen in zinc (approximately between 1911 and 1920), and a little closed wood screen (approximately between 1921 and 1930).

Table IV: Analysis of the long-term evolutions of the annual maximum and minimum temperatures for the 9 100-yr-long non-homogenised series.

MAXIMUM TEMPERATURES	Global trend (°C/century)	Significant trend (*)	Date of brutal significant trend	Magnitude of the break (°C)	Date of brutal significant trend	Magnitude of the break (°C)
Leopoldsburg (1900-1998)	- 0.2					
Uccle (1900-1998)	+ 0.4		1987	+ 0.7		
Gembloux (1900-1998)	- 1.0	***	1953	- 0.8	1987	+ 0.9
Denee (1900-1998)	- 0.6	*	1949	- 0.5		
Thimister (1900-1998)	- 0.9	**	1953	- 1.0	1924	+ 1.1
Stavelot (1900-1998)	- 0.1		1988	+ 0.8	1949	- 0.5
Baraque-Michel (1928-1998)	- 0.6					
Chimay (1910-1998)	- 1.6	***	1949	- 1.0		
Rochefort (1912-1998)	- 1.3	***	1951	- 0.8	1987	+ 0.9
MINIMUM TEMPERATURES	Global trend (°C/century)	Significant trend (*)	Date of brutal significant trend	Magnitude of the break (°C)	Date of brutal significant trend	Magnitude of the break (°C)
Leopoldsburg (1900-1998)	+ 0.7	***	1909	+ 0.9		
Uccle (1900-1998)	+ 1.2	***	1965	+ 0.8		
Gembloux (1900-1998)	+ 0.6	**	1987	+ 0.7		
Denee (1900-1998)	+ 0.8	***	1965	+ 0.5		
Thimister (1900-1998)	+ 1.0	***	1942	+ 0.7	1921	- 0.6
Stavelot (1900-1998)	+ 1.1	***	1965	+ 0.9		
Baraque-Michel (1928-1998)	+ 1.3	**	1987	+ 1.0		
Chimay (1910-1998)	+ 0.6	*	1987	+ 0.7	1919	+ 0.6
Rochefort (1912-1998)	+ 0.1		1987	+ 0.7		

(*) *, ** and *** refer to the levels of statistical significance 0.05, 0.01 and 0.001

The last two kinds of screen are known to exaggerate the maximum temperature, in comparison with the actual standard large closed screen or with the large half-open screen, both in operation at Uccle-Ukkel. If that succession of screens is relevant for the 100-yr-long time series included in the database, it could explain the large differences in trend between Uccle-Ukkel and the other stations. In the same way, the abrupt breaks appearing close to 1951, except again for Uccle-Ukkel, could be explained by a (more or less) simultaneously change of screen in the climatological network. The middle of the 20th century corresponds indeed to an important restructuration of the climatological network.

b) Analysis of the homogenised long time series of temperature

To assess the impact of the heterogeneities in the thermometric time series, discontinuities have been searched and corrected for all the reconstructed long thermometric series. As already mentioned, the regional analysis of climatic change with homogenised series must be considered very carefully. Therefore, only main results at the annual time-scale are reported here.

Compared to the non-homogenised series, the procedure of homogenisation for minimum temperature has only induced a slight smoothing between the various time series. The stations show now a global warming trend between $+0.5^{\circ}\text{C}$ per century (for Rochefort) and $+1.1^{\circ}\text{C}$ per century (for Uccle-Ukkel and Thimister, very highly significant). The year 1988 is yet the abrupt beginning of a warm period.

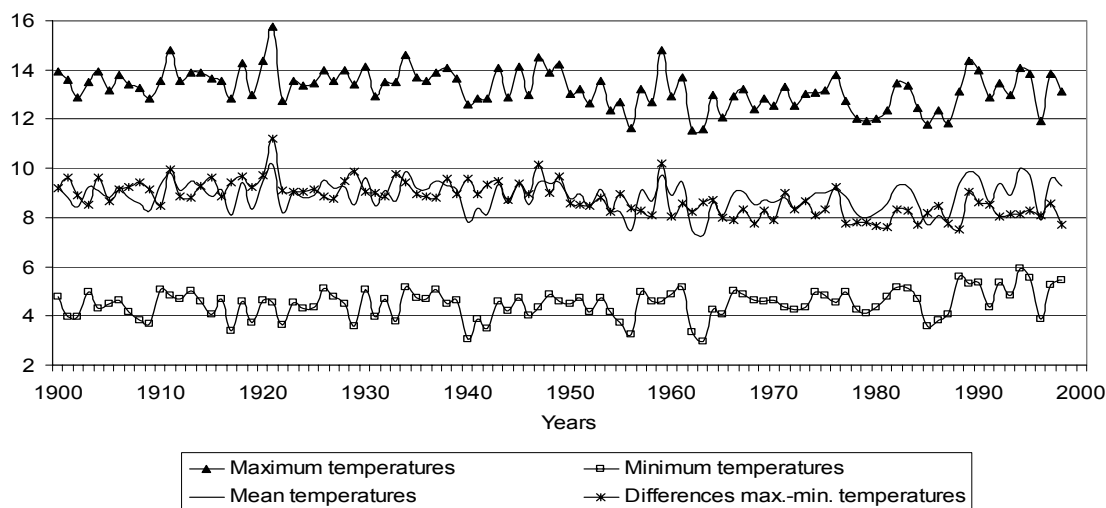


Figure 53: Representative time series for Belgium of the minimum (TN), maximum (TX), mean (TM), and range (TX-TN) temperatures (in $^{\circ}\text{C}$), computed by averaging the data from the 9 long series.

In contrast, the procedure of homogenisation has led to a total inversion of the trend for the maximum temperature at Uccle-Ukkel. From an initial warming trend of $+0.4^{\circ}\text{C}$ per century, this station shows now a cooling trend of -0.5°C per century, similarly to the other stations. The 1950–1954 period and the year 1988 are still the starting points of an abrupt cooling and warming, respectively.

As conclusion, the main fact observed for the homogenised series is the overall large decrease of the long-term difference between the (decreasing) maximum temperature and the (increasing) minimum temperature. This is clearly visible in Figure 53, which displays results for the average of the 9 long thermometric series (the similarity of the trends for all the stations allows us to consider averaged data over the 20th century).

6.2.3 Analysis of the reconstructed pluviometric series

Contrary to the maximum temperature, the homogenisation of the precipitation has almost not modified the trend evolution for individual stations. Therefore, a study of the pluviometric evolution over the last century is undertaken with the homogenised series.

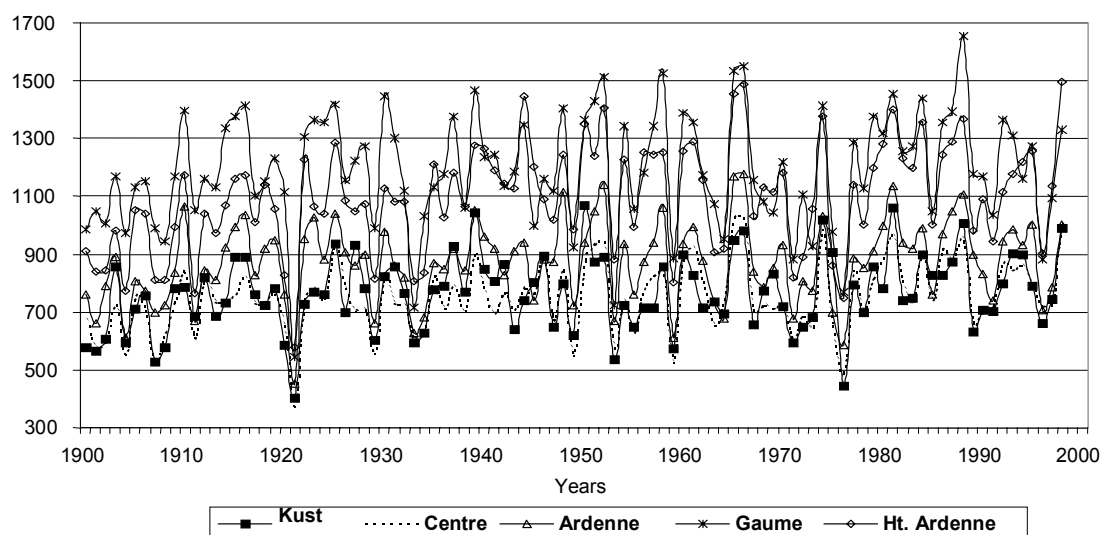


Figure 54: Evolutions of the annual precipitation (in mm) for 5 regions over the 1900–1998 period.

To clarify and to make easier the study of the evolution of precipitation, the 16 long series have been classified into 5 regions (referring approximately to existing geographical regions): Kust (Brugge and Heist-aan-Zee), Centre (Ath, Uccle-Ukkel, Gembloux, and Leopoldsburg), Ardenne (Denée-Maredsous, Spontin, Rochefort, and La Roche), Gaume (Lacuisine and Chimay), and Haute Ardenne (Thimister, Spa,

Stavelot, and Baraque Michel). In this way, it was possible to consider the evolutions of precipitation for a few regions instead of only for isolated stations. Anyway, the results given here cannot be considered as necessarily relevant for particular location somewhere in the country.

The analysis of the homogenised long series for the annual precipitation over the last century reveals a positive trend in precipitation for all the series (Figure 54). This trend has been particularly rapid during the 1900–1935 period, and became progressive over the rest of the century. The increase is the most significant in the region Haute Ardenne, reaching a trend of 240 mm per century. The lowest and non-significant trend is found for the region Gaume (100 mm per century). The region Centre presents a very significant increase, followed by the regions Polders and Ardenne with a significant trend. Seasonally speaking, the increasing trend is especially apparent in winter, spring, and autumn.

The evolution of the mean daily intensity of precipitation is very fluctuating during the 20th century. This variable experiences no significant regional trend, in contrast to the result (increase) mentioned above for the 1951–1998 period. Finally, the annual number of days with precipitation is also very fluctuating over the century, without coherent trend between the different regions.

7. CLIMATE-CHANGE PROJECTIONS OVER THE 21ST CENTURY

7.1 Projections carried out with the global climate model

7.1.1 Experimental design

Figure 55 presents a schematic overview of the various experiments that were performed to investigate the response of the global climate to human activities during the 21st century. All results were obtained for a time window stretching from 1970 to 2100, with the year 1970 taken as the reference state. Allowance was made for the inertia of the different subcomponents by starting simulations at a time early enough to alleviate the effects of specific start-up conditions. In addition to the control run (CONT) discussed previously (see Section 2.3), two climate-change experiments were conducted with the AOGCM: one with the AOGCM alone (SRESb2), in which Greenland freshwater fluxes did not take into account ice-sheet changes, and another one with the AOGCM coupled to the GISM (SRESb2G). This set of simulations allowed us to forecast climate changes and to estimate the role of changes of the Greenland ice sheet in modifying the climate during the 21st century. The climate-change simulations used a mid-range IPCC's (2001) scenario (SRES B2) for greenhouse-gas concentrations and sulphate-aerosol loading (Figures 56 and 57). These runs started at year 20 of CONT. An additional control run performed with the GISM in uncoupled mode with climate conditions fixed at the unperturbed 1970 initial state enabled to establish the background evolution of the ice sheet in the absence of anthropogenic climate changes.

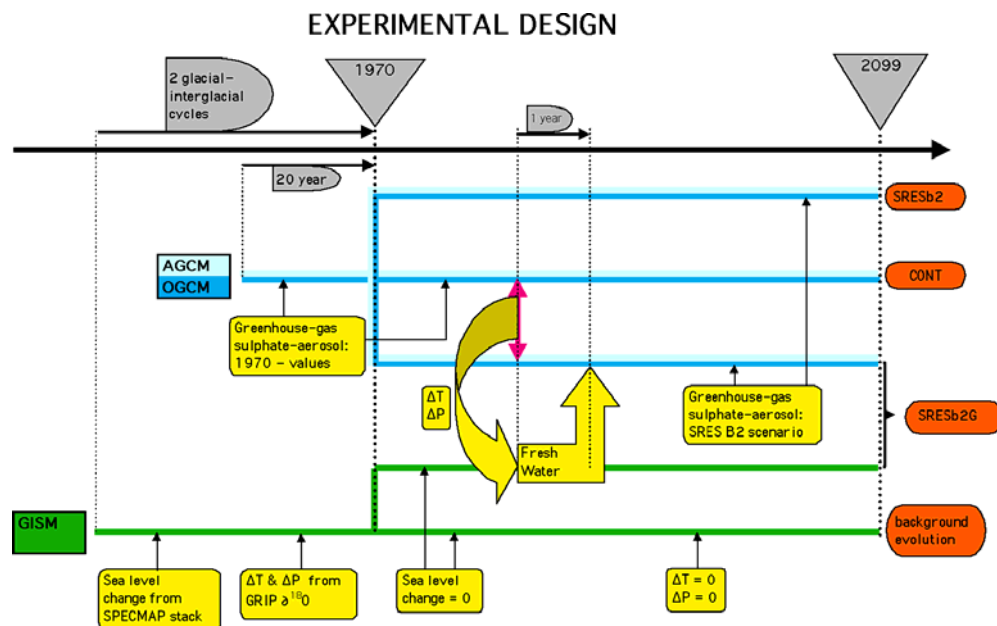


Figure 55: Schematic overview of the climate-change experiments.

SRESb2 scenario GHG concentration

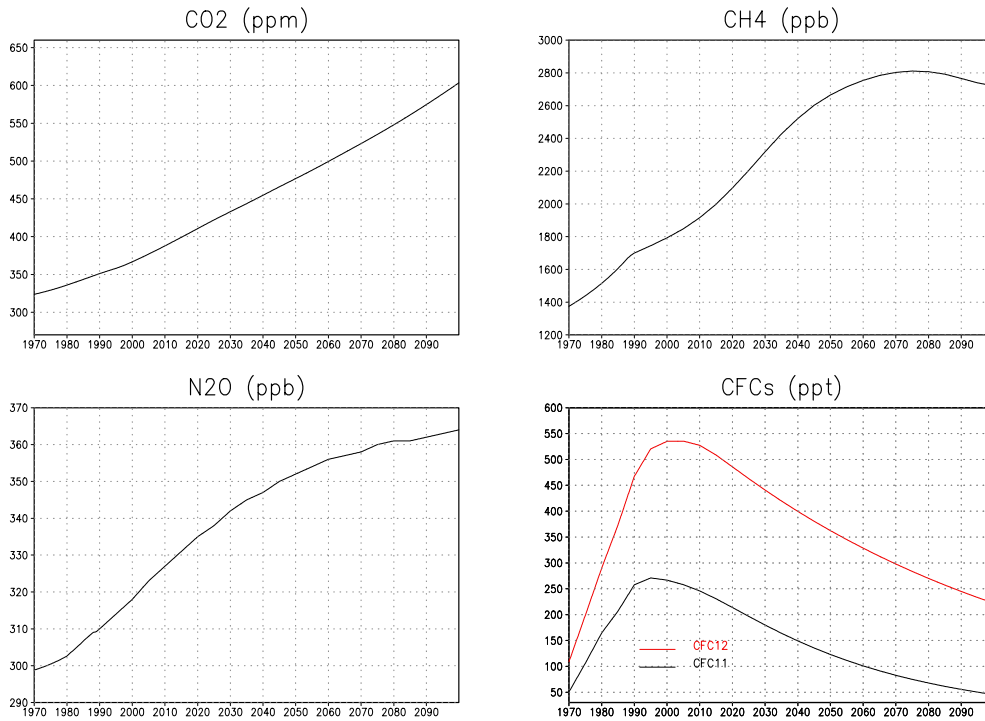


Figure 56: Greenhouse-gas concentrations following the scenario SRES B2.

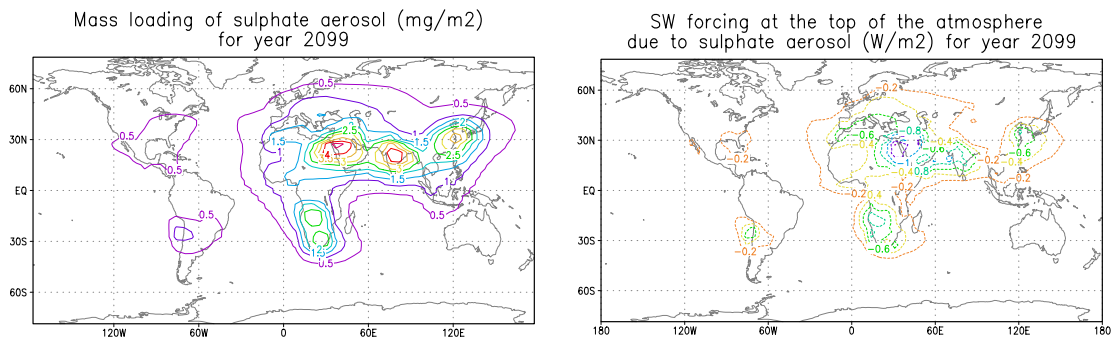


Figure 57: Sulphate-aerosol loading and radiative forcing in 2099 according to the scenario SRES B2.

7.1.2 Global results

Figure 58 shows that the annual mean, area-averaged SST increases progressively with time in both SRESb2 and SRESb2G. By the end of the experiments, the model sea-surface has warmed by 1.5°C globally. With the exception of some regions of the Southern Ocean, where sea ice becomes a bit more extensive than in CONT, the warming is global (Figure 59). The largest SST increases are found at mid-latitudes in the Northern Hemisphere.

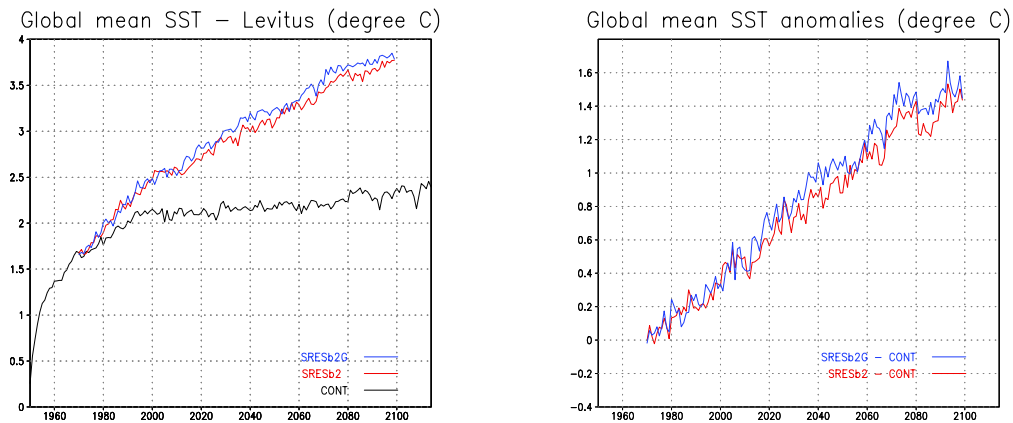


Figure 58: Temporal evolutions of the differences between the annual mean, area-averaged SST from CONT, SRESb2, and SRESb2G, and the observed value of Levitus (1982) (left panel). Temporal evolutions of the difference in annual mean, area-averaged SST between the climate-change experiments and CONT (right panel).

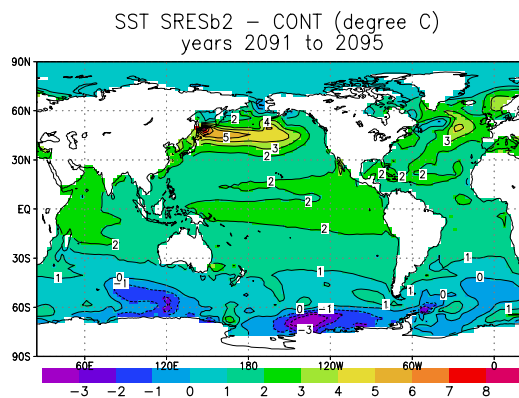


Figure 59: Changes in annual mean SST as simulated in SRESb2 at the end of the 21st century.

From Figure 60, it can be seen that the troposphere experiences an overall warming. At least three factors contribute to this feature:

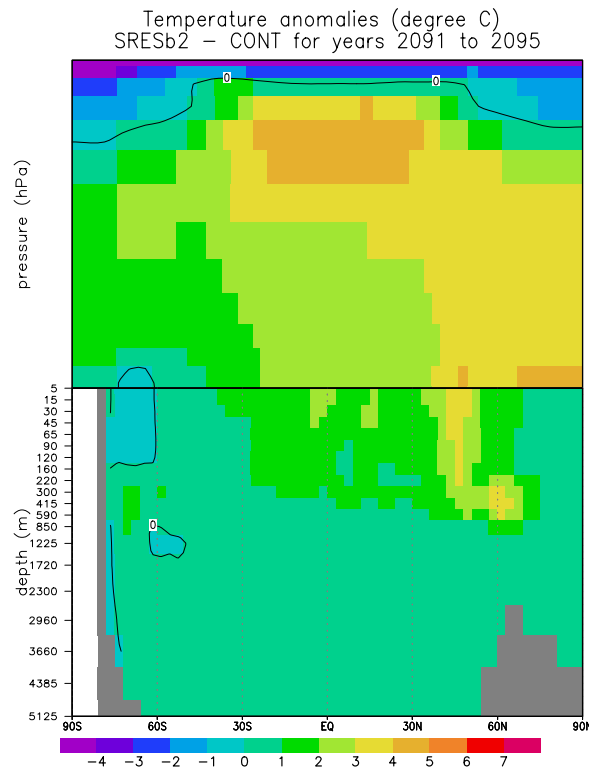


Figure 60: Changes in annual mean, zonally averaged temperature in the atmosphere and ocean as simulated in SRESb2 at the end of the 21st century.

- According to Stefan-Boltzmann's law, more longwave radiation is emitted by the surface in the climate-change experiments. But, as the greenhouse-gas (including water vapour) concentrations are enhanced, this energy flux is more efficiently absorbed. Therefore, the air warms and more longwave radiation is re-emitted back to the surface. As a result, the net (upward minus downward) longwave radiation at the surface is reduced in the climate-change experiments (Figure 61).
- The hydrological cycle is strengthened (see below), releasing more latent heat in the atmosphere by condensation. This process explains probably the maximum warming observed in the tropics just below the tropopause (see Figure 60).
- The other maximum located near the surface in the Arctic (see Figure 60) is partly attributable the albedo–temperature feedback. Under warmer conditions,

the sea-ice pack becomes less extensive. As sea ice reflects more efficiently solar radiation than open water, the mean surface albedo decreases. Consequently, more solar energy is caught at the surface, leading to a further sea-ice melting. This is a positive feedback. Furthermore, the temperature rise is stronger during winter. In summer, the additional energy available in the climate-change experiments is used to thaw sea ice as its temperature is already near the freezing point, while in winter, this energy brings about a temperature response.

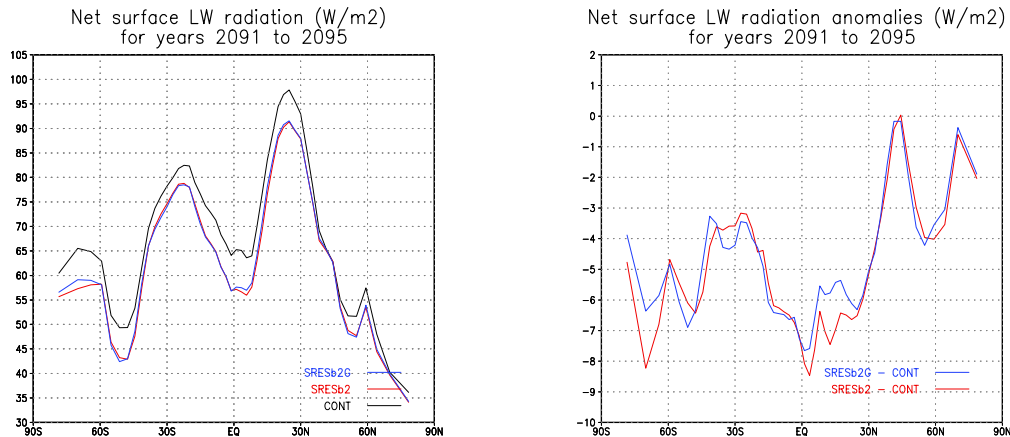


Figure 61: Net (upward minus downward) longwave radiation at the Earth’s surface. On the left, the annual mean, zonally averaged values are shown for the three simulations. On the right, are depicted the anomalies between the climate-change experiments and the control run.

Regarding the stratosphere, it undergoes a cooling as more longwave radiation is emitted by the greenhouse gases towards space. Indeed, at those altitudes, since temperature decreases with height, the atmospheric layers radiate more upwards than downwards.

The ocean interior also gets warmer. The thermal expansion associated with this heating reaches 22 cm in 2100 (Figure 62). The warming is mainly confined in the surface boundary layer, where water properties are strongly influenced by the surface heat fluxes. The temperature changes in the ocean are weaker than those in the atmosphere, but we must keep in mind that liquid water has a specific heat of about $4.2 \times 10^6 \text{ J K}^{-1} \text{ m}^{-3}$, while only about 1000 J are needed to warm 1 m^3 of air by 1°C . Under sea ice, the oceanic temperature response is small as water stays near the freezing point until the whole sea ice has disappeared.

In the Arctic, we observe a significant reduction in sea-ice extent and concentration, especially during summertime (Figure 63). Ice also gets thinner by more than 1 meter over the whole Arctic basin. The thinning can reach 2.5 meters near the ice margin in summer. The thickness maximum is still located north of Greenland. By contrast, the

Antarctic sea-ice extent is slightly larger at the end of SRESb2 and SRESb2G than in CONT. But, as the ice areal coverage in CONT is strongly underestimated compared to observations, it is hard to draw any reliable conclusion.

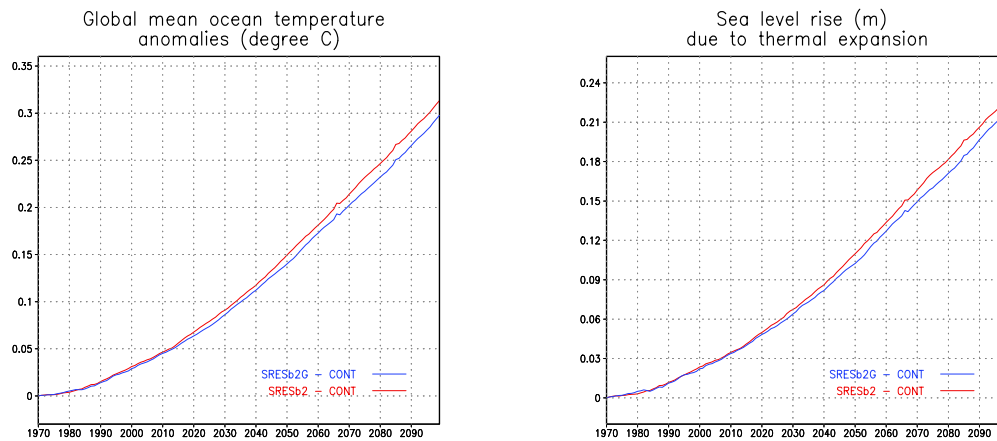


Figure 62: Temporal evolutions of the anomalies in global mean ocean temperature (left panel) and sea-level rise due to thermal expansion (right panel) as simulated in SRESb2 and SRESb2G.

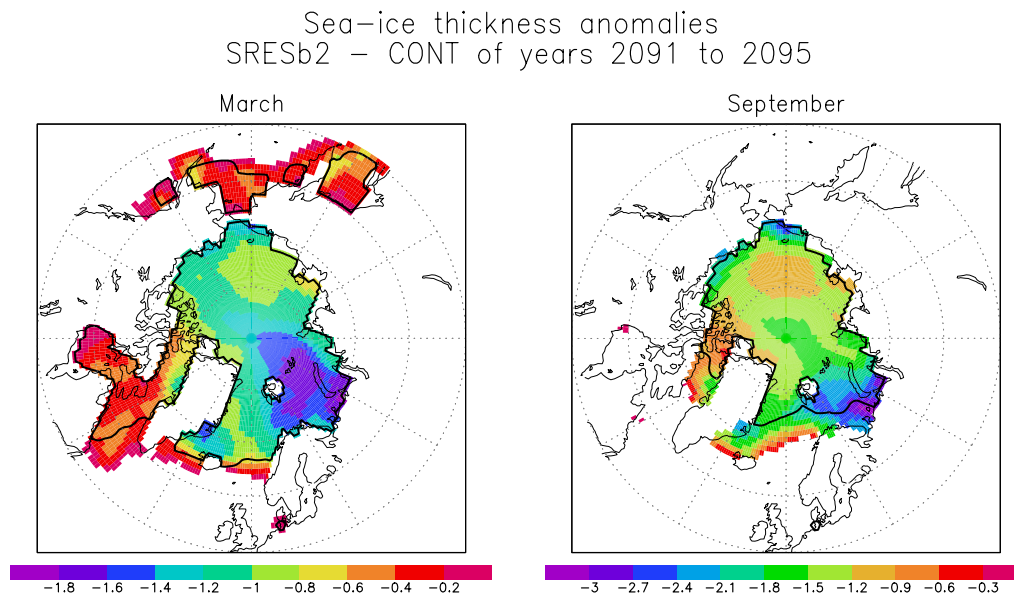


Figure 63: March (left panel) and September (right panel) changes in Arctic sea-ice thickness (in m) as simulated in SRESb2 at the end of the 21st century. The thick black line indicates the location of the sea-ice margin in SRESb2.

The modelled global mean surface air warming in 2100 reaches about 2.3°C in both experiments (Figure 64, left panel). This value falls within the range of estimates obtained with other climate models (IPCC, 2001). As in other modelling studies, the warming is larger in the Northern Hemisphere than in the Southern Hemisphere (Figure 64, right panel), because the latter contains a much greater oceanic area. In

the Northern Hemisphere, the magnitude of the warming increases towards the pole as a result of the snow- and ice-albedo–temperature feedback.

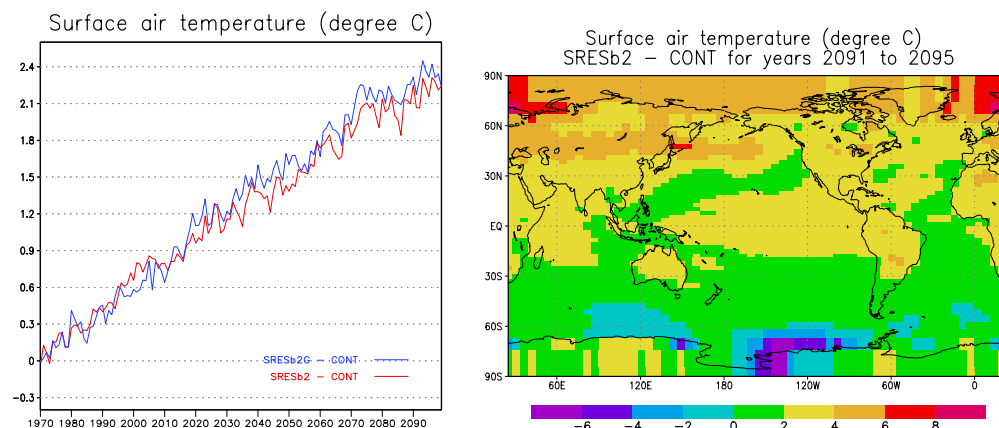


Figure 64: Temporal evolutions of the changes in annual mean, area-averaged surface air temperature as simulated in SRESb2 and SRESb2G (left panel). Geographical distribution of the change in annual mean surface air temperature as simulated in SRESb2 at the end of the 21st century (right panel).

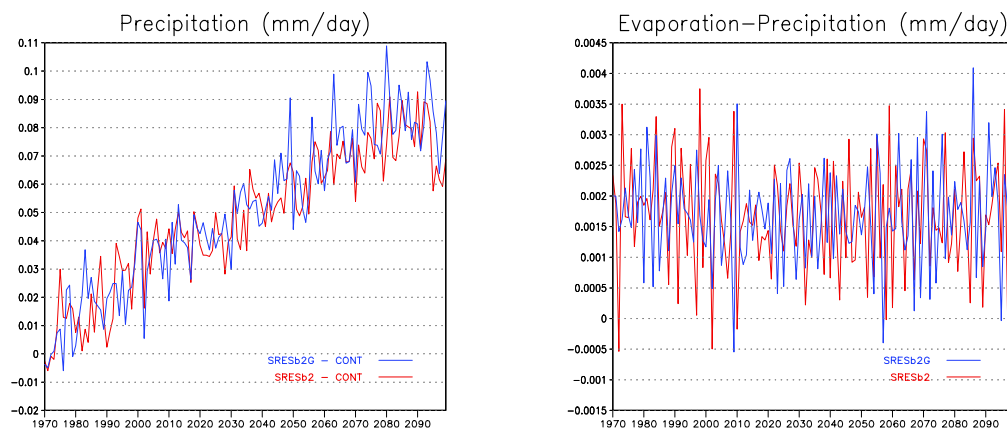


Figure 65: Temporal evolutions of the annual mean, area-averaged anomalies in precipitation as simulated in SRESb2 and SRESb2G (left panel). Temporal evolutions of the annual mean, area-averaged net surface freshwater fluxes as simulated in SRESb2 and SRESb2G (right panel).

At the end of both climate-change experiments, the annual mean, area-averaged evaporation and precipitation are enhanced by 3% (+1 mm day⁻¹) compared to CONT (Figure 65), an increase which falls within the range of current uncertainty (IPCC, 2001).

The left panel of Figure 66 reveals that the atmosphere contains more water vapour in the climate-change experiments. Indeed, according to Clausius-Clapeyron's relationship, as temperature rises, the amount of water vapour in saturated air increases. This leads to a very powerful positive feedback because water vapour, being a greenhouse gas, traps longwave radiation, thus enhancing the warming. The liquid water content is also enlarged in SRESb2 and SRESb2G just below the tropopause between 15° S and 30° N in good agreement with the utmost temperature warming (Figure 66, right panel). Furthermore, these changes together with modifications in the cloud distribution indicate that more vigorous convective motions lift up the tropical tropopause in the climate-change simulations.

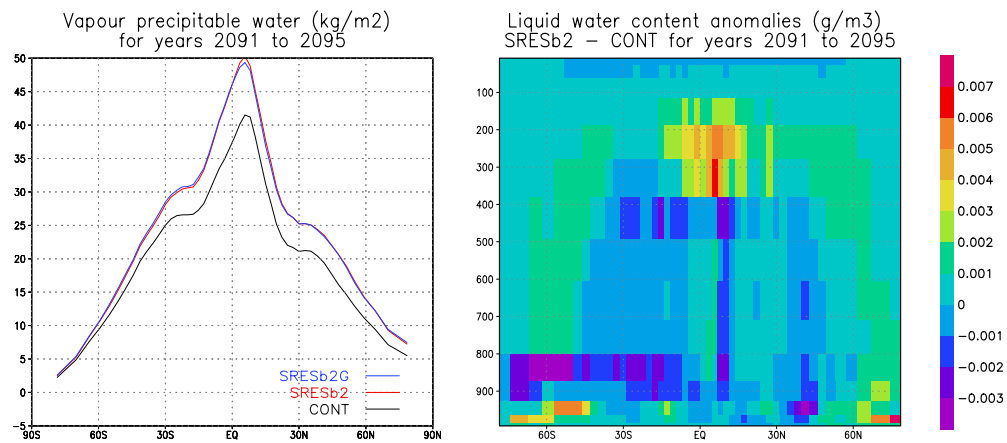


Figure 66: Annual mean, zonally averaged total precipitable water amounts as simulated in CONT and at the end of SRESB2 and SRESb2G (left panel). Annual mean, zonally averaged anomalies in liquid water content at the end of SRESb2. The Y axis is pressure (in hPa), while the X axis is latitude.

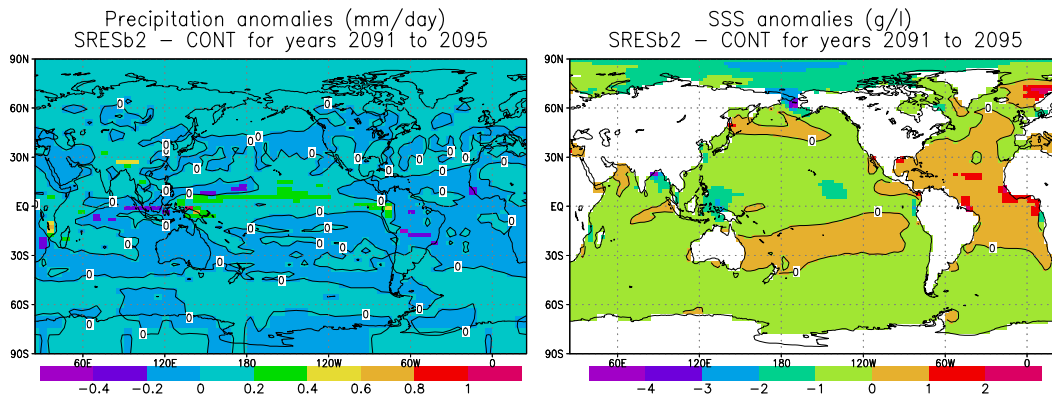


Figure 67: Geographical distributions of the change in annual mean precipitation (left panel) and sea-surface salinity (right panel) as simulated in SRESb2 at the end of the 21st century.

Moreover, as the Asian monsoon is stronger in SRESb2 and SRESb2G, more precipitation occurs over the Tibetan plateau in June–July–August (Figure 67, left panel). This additional water runs off into the Gange and Brahmaputra, thus leading to a salinity decrease in the Bay of Bengal, or in the Hwang Ho and the Yangtze Kiang, producing a freshening of the Yellow and East China Seas (Figure 67, right panel). The convective activity strengthens over New Guinea and in the Pacific ITCZ. As precipitation increases more than evaporation there, the freshwater flux towards the ocean is enhanced, yielding a significant decrease in sea-surface salinity in this region. One also notices a strong decrease in salinity in the Arctic basin. This feature is caused by the release of nearly freshwater into the ocean associated with the melting of sea ice.

7.1.3 Results related to the Greenland ice sheet

a) Climate changes over Greenland

Figure 68 displays the climate changes for the final two decades of SRESb2G over the region that encompasses the Greenland ice sheet and the North Atlantic Ocean, including Northwestern Europe. Averaged over the Greenland ice sheet, the annual mean precipitation intensifies by 30–40% by the end of the 21st century, and the annual mean surface air temperature increases by 4 to 5°C (Figure 69a). The latter indicates a polar amplification of temperature that is in the mid range of values obtained with other AOGCMs (Church et al., 2001). Incidentally, these climate-change results correspond to an average precipitation sensitivity over the Greenland ice sheet of 6–7% °C⁻¹, very similar to the sensitivities found by Kapsner et al. (1995) and Cuffey and Clow (1997) for the entire GRIP/GISP2 ice-core records using a transfer coefficient of 0.42 ‰ δ¹⁸O °C⁻¹. These precipitation increases are larger than the 0 to 5% °C⁻¹ employed in most older work in which precipitation was made a direct function of temperature (e.g., Huybrechts et al., 1991; De Wolde et al., 1997).

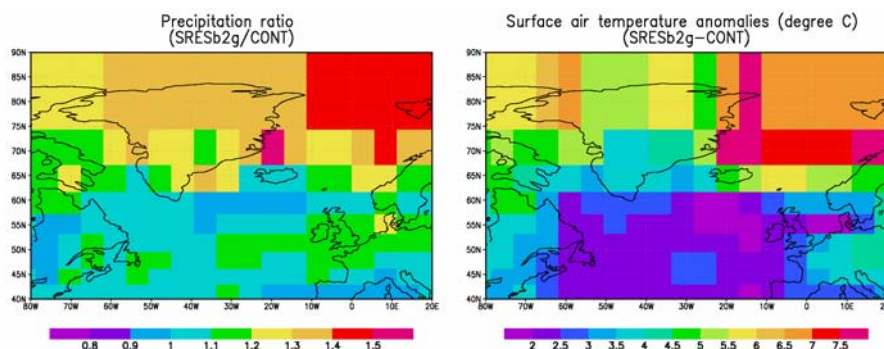


Figure 68: Climate changes over Greenland and its surroundings predicted by the coupled AOGCM–GISM for the last two decades of the simulation SRESb2G compared to the control run for the same time period (CONT).

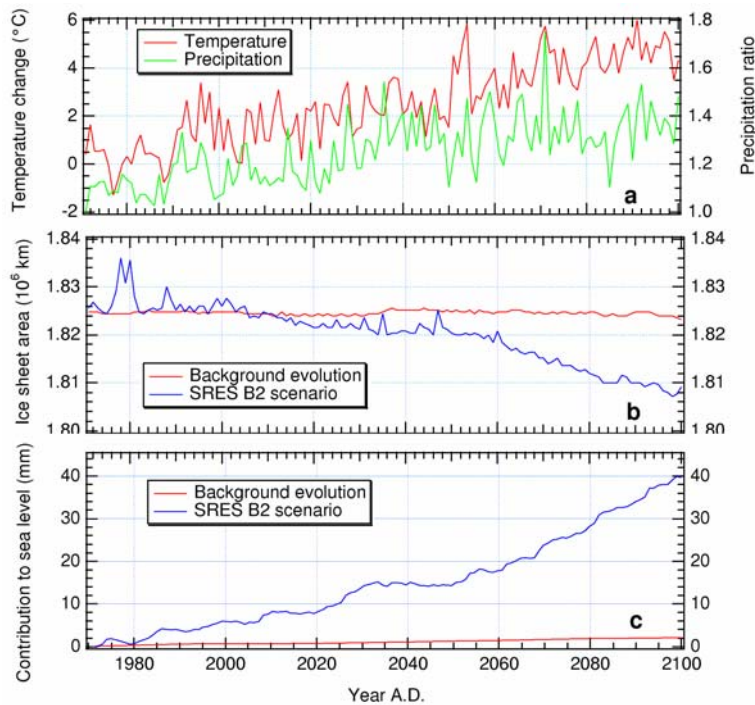


Figure 69: Response of the Greenland ice sheet for the period 1970–2100 driven by climatic outputs from the AOGCM in coupled mode. The climatic perturbations shown in panel a are annually and spatially averaged over the entire ice sheet. In panel c, 1 cm of global sea-level change corresponds to an ice-volume change of $3.98 \times 10^{12} \text{ m}^3$.

Actual precipitation changes over Greenland scale with the pattern shown in Figure 68 and the present observations, and are therefore largest in the southeastern part of the ice sheet, where present-day precipitation is up to 2 m year^{-1} . Further inspection of the climate-change patterns over Greenland (results not shown) brought to light substantial regional and seasonal differences. Summer temperature rise, which largely controls runoff, is about $2\text{--}3^\circ\text{C}$ by the end of the simulation, whereas winter values peak at 7°C or more, especially in October and November. These are also features seen in most other AOGCMs, and are related to such features as sea-ice extent and vertical stratification of the atmosphere. Summer temperature increases are largest in the south and over the central plateau, but close to zero in the northern part. At the regional scale, the patterns of precipitation and temperature changes are poorly related, and local and seasonal precipitation sensitivities were found to range anywhere between 0 and $10\% \text{ }^\circ\text{C}^{-1}$.

b) Greenland ice-sheet response

The ice-sheet response during the 21st century shows a clear reduction in area and volume. Total area shrinks by about 1%, and total volume varies by an amount equivalent to 4 cm of global sea-level rise (Figure 69, panels b and c). These changes are about half of those found in older works for a comparable temperature forcing (De Wolde et al., 1997; Huybrechts and de Wolde, 1999), but more in line with the 1–4 cm reported in recent studies that used AOGCM results to drive 21st century mass-balance changes (Bugnion, 2000; Church et al., 2001; Van de Wal et al., 2001). This is attributed to the smaller temperature rises predicted by AOGCMs in summer and the larger precipitation increases which partly compensate the increased runoff, and which effect is found to be more important than assumed in previous studies that derived precipitation changes directly from temperature changes. We also found that the background evolution (with constant 21st century climate) is very weak compared to the anthropogenically induced response, causing a sea-level change of only 2 mm between 1970 and 2100, or $+0.015 \text{ mm year}^{-1}$.

The plots shown in Figure 70 enable to distinguish between the static mass-balance effect and the ice-dynamics response. The latter has a component due to both the longer-term background trend, as the ice sheet is still adjusting to past changes in boundary conditions as far back as the last glacial–interglacial transition, and to the direct ice-dynamics response to the imposed surface mass-balance changes between 1970 and 2100. The average surface mass-balance changes over the simulation period are displayed in Figure 70a. These are negative in a narrow strip that forms the ablation zone all around the ice sheet and go up to $1\text{--}2 \text{ m year}^{-1}$ in the southwestern ablation area, where melting is most pronounced. Central areas above the runoff line generally exhibit a larger surface mass balance. Those patterns are typical signatures of climatic warming, giving rise to increased runoff and increased snow accumulation that respectively dominate the response in the lower and higher reaches of the ice sheet.

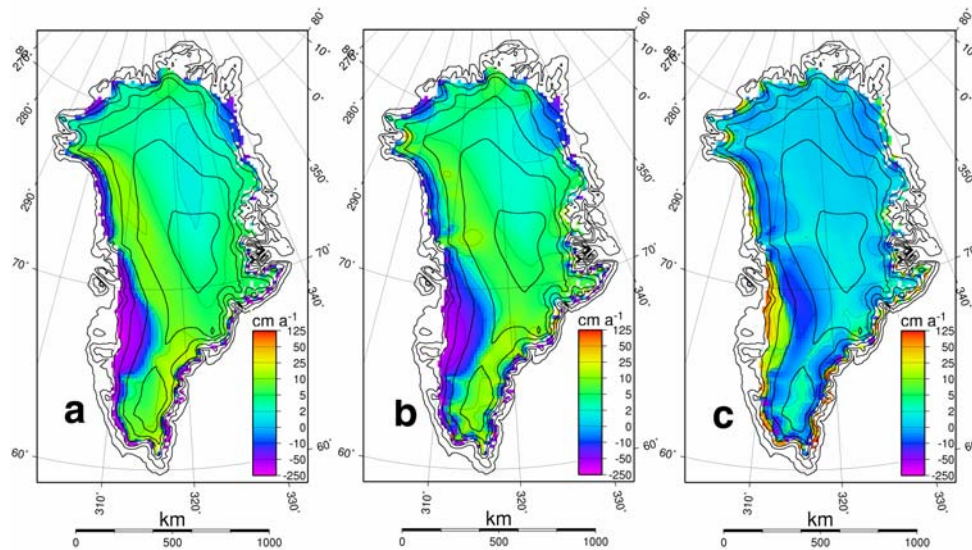


Figure 70: Time-averaged response patterns of Greenland evolution for the period 1970–2100. (a) Static mass-balance response obtained as the mean cumulative mass-balance perturbation with respect to the initial state at 1970. (b) Average ice-thickness evolution having a component due to the background trend and the ice-sheet evolution for 1970–2100. (c) Ice-dynamics response obtained as the difference between (b) and (a). Values are in ice equivalent. The contour lines are for surface elevation and are spaced 500 m apart.

The pattern for the actual ice-thickness changes over the same time period is quite similar to the imposed surface mass-balance changes (Figure 70b), indicating that surface mass-balance variations dominate the response. The difference between panels b and a yields the ice-dynamics response proper (Figure 70c). Wrapped into this pattern is the longer-term background trend (Huybrechts and Le Meur, 1999) of the order of some cm year^{-1} at most, but the most conspicuous feature is the thinning of $\sim 10 \text{ cm year}^{-1}$ in the southwest just above the equilibrium line and the thickening of up to 1 m year^{-1} further down in the ablation zone. This is a nice demonstration of the ice-dynamics effect described in Huybrechts and de Wolde (1999), and which typically reduces the overall static mass-balance response by 10–20% for simulations spanning the 21st century. The reason is the increased mass-balance gradient in a warmer climate, which is matched by a larger ice-flux across the equilibrium line and thus increased transfer of ice mass from the accumulation zone into the melting zone. It leads to a thinning above the equilibrium line and a dynamic thickening below it. The higher surface level of the ablation zone in turn leads to somewhat less melting than would be the case when ice dynamics were not included, hence the counteracting effect.

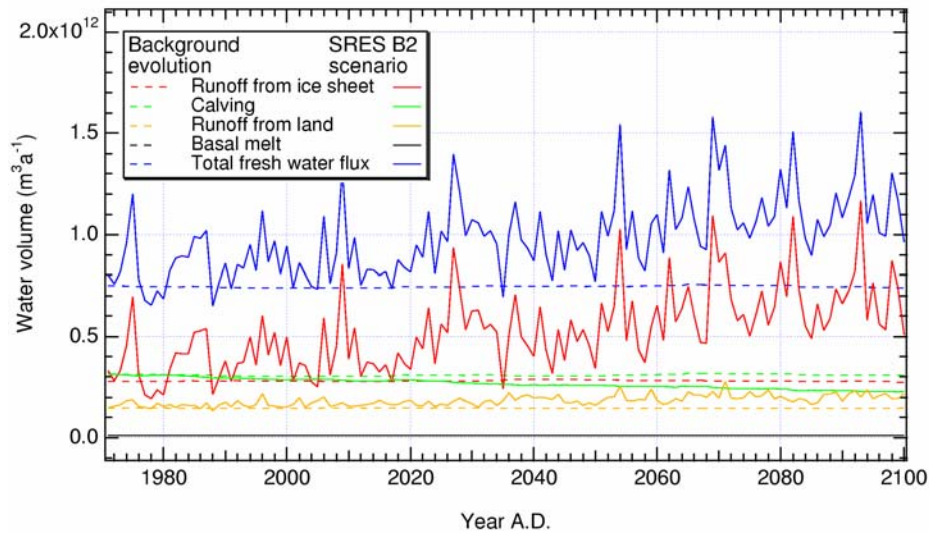


Figure 71: Freshwater-flux components from the Greenland continent for the period 1970–2100 shown for the climate-change experiment (full lines) and for the background evolution with zero climatic perturbation (dashed lines). Values are in water equivalent. $1 \times 10^{12} \text{ m}^3$ corresponds to 0.03 Sv.

c) Greenland freshwater fluxes and climatic impact

Between 1970 and 2100, the total freshwater flux increases by more than 50%, mainly due to the doubled runoff from the ice-sheet surface (Figure 71). The runoff from land also increases in line with the increased precipitation, but is counterbalanced by a 25% reduction in the ice flux transported across the grounding line (~calving flux). The latter is due to a thinning of the ice at the margin, so that less ice is able to flow out to the ocean. While the calving flux is for present-day conditions twice the runoff from land and about equal to the ice-sheet runoff, it is after 130 years about one third of the ice-sheet runoff and equal to the runoff from land. The water flux resulting from basal melt is negligible and hardly varies during the simulation. For comparison, also the freshwater components for the unperturbed run are shown (dashed lines), but these remain almost constant during the simulation.

The maximum increase of freshwater input from the Greenland ice sheet never exceeds $1 \times 10^{12} \text{ m}^3 \text{ year}^{-1}$, or about 0.03 Sv. As demonstrated in Figure 72, this meltwater pulse is insufficient to cause significant additional changes in the climate of the North Atlantic region. The evolutions of surface air temperature and precipitation rate are not significantly different between an experiment with interactive Greenland freshwater fluxes (SRESb2G) and a simulation without freshwater feedback from Greenland (SRESb2). This is in agreement with simple model studies which indicate that a freshwater perturbation of at least 0.075 Sv would be required to reach the threshold value to critically weaken the thermohaline circulation in the North Atlantic

(Rahmstorf, 1995). Such a flux is at least 2.5 times larger than the one obtained in this study, but not unattainable if climatic warming over Greenland were more pronounced than evident from the scenario SRES B2. Furthermore, as the NADW formation progressively decreases in the AOGCM control simulation, the model sensitivity to an enhanced freshwater flux is modified.

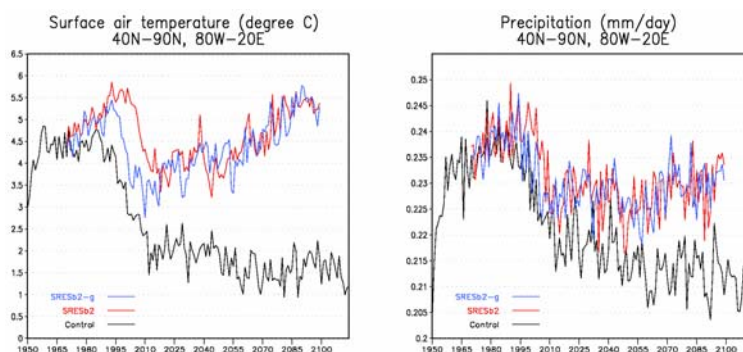


Figure 72: Spatially and annually averaged changes in surface air temperature and precipitation rate for the rectangle displayed in Figure 68. The blue line is for the fully coupled experiment driven by IPCC's scenario SRES B2 (SRESb2G); the red line refers to a run excluding oceanic feedback from increased Greenland ice-sheet melting (SRESb2).

7.1.4 Comparison of the results over Belgium for the period 1970–1998 with observational data

As described in Section 6, a large number of thermometric time series have been corrected, completed, and homogenised before inclusion in the new climatological database of RMI-GCS. From those series, a monthly mean temperature series averaged over Belgium has been calculated for the 1970–1998 period and has been used to make comparison with the results of CONT and SRESb2 over the same time interval.

The precise locations of the model grid points is not directly relevant because the model resolution is finite. Several grid points have been selected to potentially represent Belgium. In the model, one grid point (called here "central point") is located near the centre of the country. Three other continental grid points were also chosen around the Belgian territory. After comparison of the temperature outputs at these grid points, the central point has been finally conserved for the model validation. The outputs extracted from that central point follow indeed the same global evolution than those at the other points.

For comparison with observations, the monthly thermometric outputs of SRESb2 at the central grid point have been subtracted from the monthly mean values of CONT over

the 1970–1998 period. To allow more relevant comparison, the monthly simulated and observed thermometric values have been reduced afterwards by considering their difference with their respective mean values over the whole 1970–1998 period.

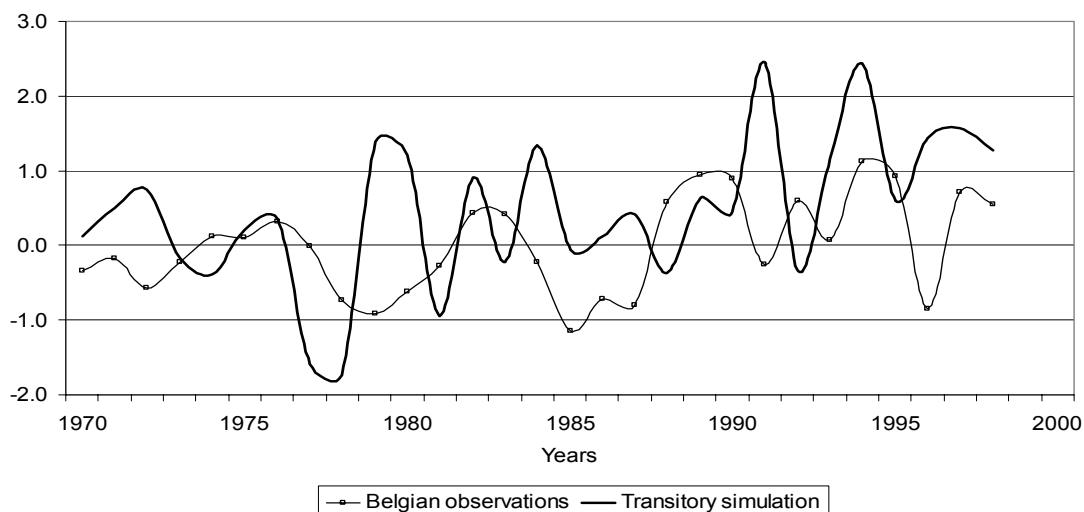


Figure 73: Temporal evolutions of the anomalies in annual mean temperature as simulated in SRESb2 and as observed over Belgium for the 1970–1998 period.

At the annual time-scale, Figure 73 shows a warming trend greater for the model than for the observations. Over the considered period, linear regression indicates a global increase of $+5.5^{\circ}\text{C}$ per century for the simulation and of $+3^{\circ}\text{C}$ per century in the observations averaged over Belgium. The standard deviation of the simulated climate is also higher.

The same study of the trend and the standard deviation has been made for the four seasons. In each case, the standard deviation of the model outputs is greater than the deviation of the observations. This is particularly true for winter and autumn. As revealed by Table V, the difference in trend also depends on seasons. In comparison with observations, the simulated warming trend is double for summer and much larger for autumn. On the other hand, the simulated warming trend in winter is smaller, and a very similar trend with observations is obtained in spring.

Table V: Regression coefficient (in °C/period) and standard deviation (in °C) of the seasonal mean temperatures over the 1970–1998 period. The values are given for observations averaged over Belgium and for SRESb2.

	Standard deviation	Regression coefficient
WINTER		
Belgian observations	1.491	0.020
SRESb2 simulation	2.062	0.003
SPRING		
Belgian observations	0.886	0.059
SRESb2 simulation	1.057	0.066
SUMMER		
Belgian observations	0.957	0.032
SRESb2 simulation	1.025	0.063
AUTUMN		
Belgian observations	0.793	0.013
SRESb2 simulation	1.956	0.076

7.2 Projections carried out with MAR

The validation of MAR and the tests of the nesting procedure took more time than expected. Moreover, the results of the climate-change experiments conducted with the AOGCM were obtained during the last few months of the project, partly because of an overload of our computers. As a consequence, we have not been able to perform with MAR a detailed climate-change assessment over Western Europe, as initially planned. Nevertheless, a one-month (November) test has been made with MAR nested in the outputs of the last few years of the SRESb2 experiment carried out with the AOGCM. The results for precipitation are illustrated in Figure 74. We insist that these results cannot be used to make a climate-change assessment. They only prove that MAR is technically ready to perform such simulations.

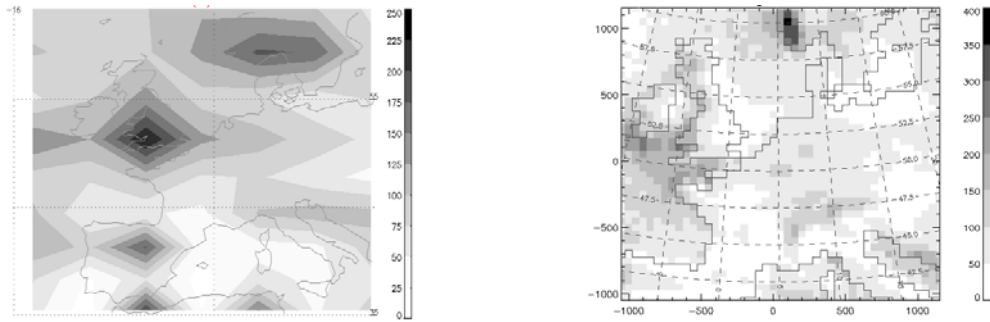


Figure 74: Precipitation for November over Western Europe as simulated by the AOGCM in SRESb2 at the end of the 21st century (left panel) and as computed by MAR nested in the AOGCM outputs (right panel).

8. DEVELOPMENT OF A MORE ADVANCED AOGCM

8.1 Development and validation of a new version of the CLIO model

Several developments could be made in primitive-equation ocean models so as to improve the representation of oceanic processes (Griffies et al., 2000). An efficient solution might be to increase the model resolution. However, the performance of available computers is still a limiting factor for long-term simulations with high-resolution models. As far as OGCMs are not eddy-resolving, a tremendous work has to be performed on the representation of physical subgrid-scale processes. Therefore, the developments carried out within CLIMOD in the CLIO model were along two main axes: a better representation of physical processes and an increased resolution.

8.1.1 Improvement of the representation of physical processes

In the real ocean, a major part of the total kinetic energy is associated with meso-scale eddies that have a characteristic size of about a few kilometres, far below the horizontal resolution of OGCMs used in climate studies. To account for the effect of these unresolved eddies, a scheme of mixing along isopycnal surfaces and the parameterisation of Gent and McWilliams (1990) have been included in CLIO. The latter scheme has been adapted to the high resolution utilised at the top of the water column (the thickness of the uppermost oceanic grid box is 10 m) following the formulation of Large et al. (1997). The isopycnal mixing scheme improves noticeably the properties of intermediate waters (e.g., the high-salinity Mediterranean water in the Atlantic and the low-salinity Antarctic Intermediate Water). As in other OGCMs, the inclusion of the parameterisation of Gent and McWilliams (1990) impacts on the ocean stratification and leads to a drastic reduction in open-ocean convection at high southern latitudes. This has an effect on the formation rate of Antarctic Bottom Water

and on the thermohaline circulation (Goosse et al., 2001). Furthermore, the need for a more sophisticated parameterisation, including a spatially varying mixing coefficient, has been enlightened.

In parallel to these tests at global scale, more conceptual studies on the numerical representation of the isopycnal mixing operator in z-coordinate models have been carried out. Indeed, the algorithm originally proposed by Cox (1987) is unstable when applied to temperature and salinity because it induces a non-zero isoneutral diffusive flux of potential density (Griffies et al., 1998). Furthermore, when applied to passive tracers, this method induces a non-monotonic behaviour (Beckers et al., 1998; Mathieu and Deleersnijder, 1998). In order to correct the latter drawback, various numerical methods have been tested. All linear schemes produce strong diapycnal mixing and do not preserve monotonicity. The more complex and expensive flux-corrected method satisfies the monotonicity principle and produces only a small diapycnal diffusion (Beckers et al., 2000).

Despite its important role in the climate system (Webster, 1994), little attention has been paid to the treatment of the surface freshwater flux in OGCMs. Since the pioneering rigid-lid model of Bryan (1969), the freshwater flux at the sea surface has been usually parameterised as an equivalent salt flux: salt is removed/introduced at the sea surface in order to take into account the dilution effect. Though unphysical, this representation has been maintained in more recent models. As an improvement, a more physical representation of this atmospheric flux could be introduced by taking into account the vertical velocity at the air–sea interface (Huang, 1993; Beron-Vera et al., 1999). This new surface boundary condition has been tested, together with other surface boundary conditions, within a rigid-lid model of the Atlantic Ocean by Wadley et al. (1996). According to this study, at short time-scales, it produces a much more realistic pattern of the sea-surface salinity, temperature, and current than the equivalent salt-flux method. It has also been tested within an OGCM on time-scales ranging from seasons to decades by Roulet and Madec (2000). They conclude that the formulation has an impact on the salinity distribution near river mouths and also in the ocean interior.

Because sea ice plays an important role on the water storage and freshwater transport at high latitudes, it seems necessary to implement and test this formulation within a coupled ice–ocean general circulation model. This has been done, for the first time, in the CLIO model. This formulation allows to represent the Goldsbrough-Stommel circulation and the meridional pathway of the freshwater at the ocean surface. Contrary to the old formulation, the calculation of the meridional freshwater transport is simpler and does not drastically depend on an arbitrary reference surface salinity. Furthermore, since it does not include the meridional salt transport due to sea-ice

formation/melting, the meridional freshwater transport derived from the new formulation appears to be more directly comparable with atmospheric water-vapour transport (Tartinville et al., 2001).

Other improvements of the model physics have been tested. A new advection scheme for passive tracers based on the Piecewise Parabolic Method of Colella and Woodward (1984) was introduced in the model. For transient tracers such as chlorofluorocarbons, this method does not significantly improve the model results with respect to the additional computer time required. Moreover, a model study has highlighted how sensitive are the Antarctic ice pack and the thermohaline circulation to the insulating effect of the snow cover (Fichefet et al., 2000).

8.1.2 *Enhancement of the resolution and validation*

Several studies have shown that OGCM results are improved by increasing the resolution (e.g., Washington et al., 1994; Covey, 1995; Gent et al., 1998). Washington et al. (1994) and Covey (1995) pointed out that a horizontal resolution of the order of 1° provides a great improvement over coarser-resolution models, and includes most features of higher-resolution models. Such a resolution appears to be a good compromise between accuracy and computer capability. Thus, a new version of CLIO at a horizontal resolution of 1.5° in latitude and longitude has been set-up. The vertical resolution has also been increased and is now of 30 uneven levels. The maximum vertical grid size is 350 m instead of 750 m for the previous model version. The bathymetry has been adapted to the higher resolution. Those improvements lead to a better representation of straits, passages, and sills, which are of importance for the global ocean circulation. It should be noted that this new version also includes the refinements of the model physics described above.

A series of 200-year numerical experiments have been carried out in order to evaluate the performance of this new model version and to define the best set of parameters so as to represent the effect of meso-scale eddies. For these simulations the model was forced by climatological surface air temperatures and wind velocities taken from the the NCEP–NCAR re-analysis (Kalnay et al., 1996). It appears that the model is able to reproduce the main characteristics of the real ocean and of the sea-ice packs. However, the rate of NADW formation is weak in all these experiments: less than 10 Sv of NADW are exported out of the Atlantic Ocean. This is mainly caused by a too weak northward transport of salty waters by the Gulf Stream that induces a relatively low formation rate of deep waters in the Greenland–Iceland–Norwegian Seas.

Nonetheless, the model accurately represents the formation of deep waters in the Labrador Sea.

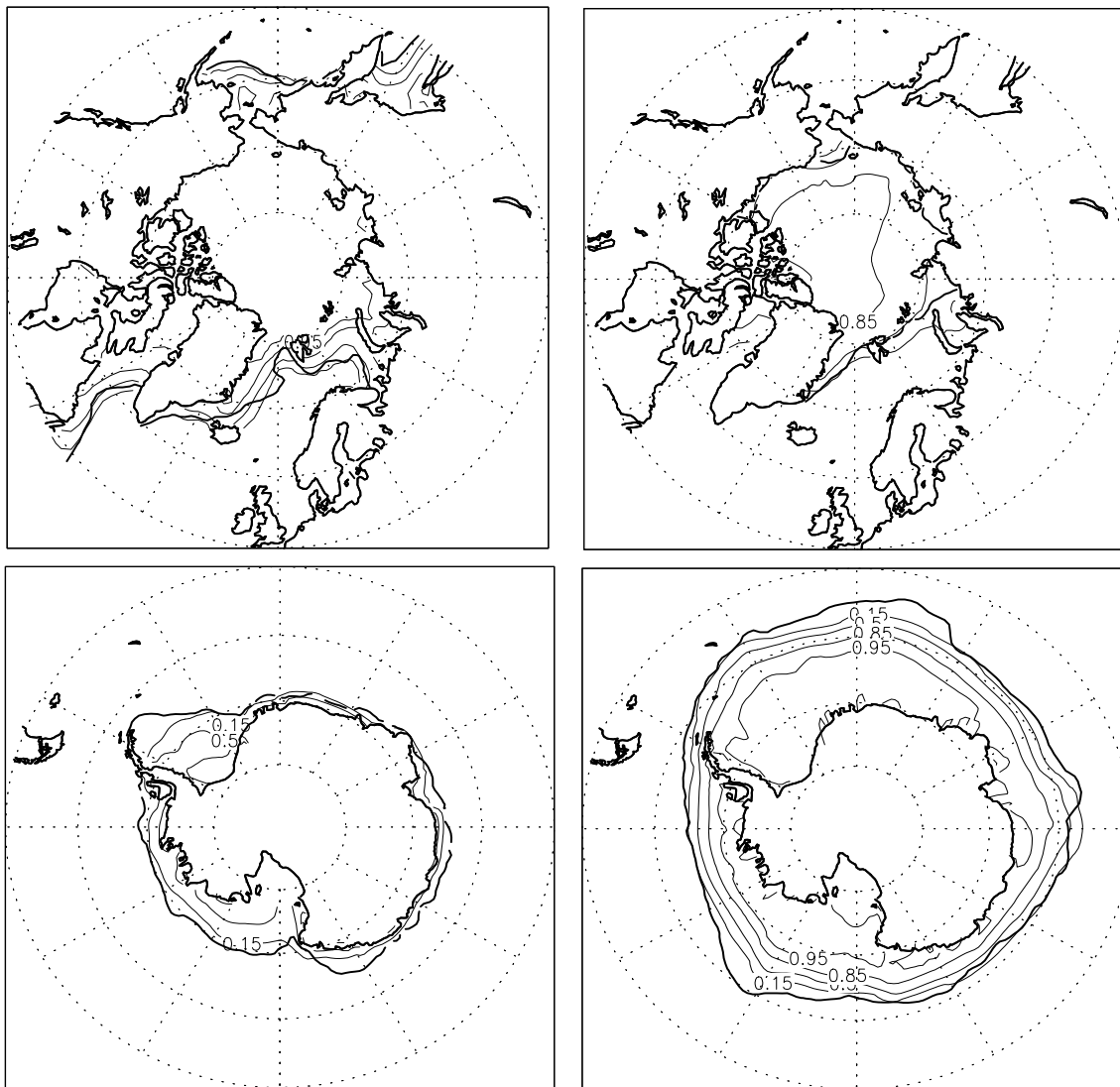


Figure 75: Average March (left) and September (right) sea-ice concentrations as simulated by the new version of CLIO. Contour lines are 0.15, 0.50, 0.85, and 0.95 (thin lines). The 0.15-ice-concentration contours derived from passive-microwave data are superimposed (thick lines).

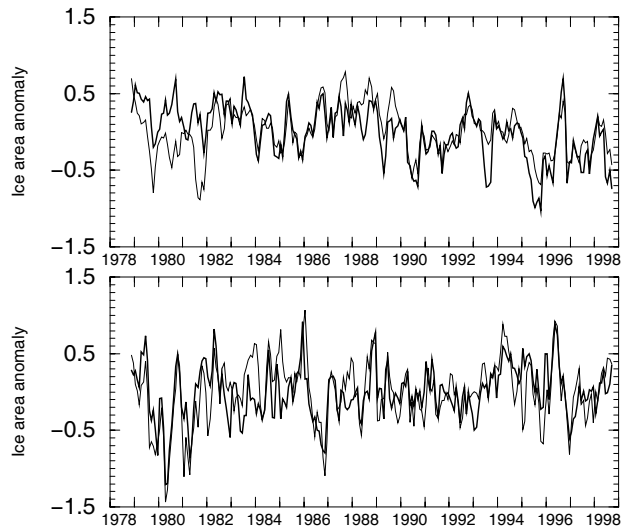


Figure 76: Monthly anomalies in sea-ice area (10^6 km^2) for the period November 1978–September 1998 derived from passive-microwave data (thick lines) and calculated by the model (thin lines) for the Northern Hemisphere (upper panel) and the Southern Hemisphere (lower panel).

Furthermore, a hindcast simulation has been performed using daily variable surface air temperatures and wind velocities from the NCEP–NCAR re-analysis for the period 1948–1999, so as to test the ability of the model to reproduce the observed interannual and longer-term variability of the high-latitude ice–ocean system. In polar regions, model results were verified against remote-sensing-ice-concentration estimates, observed buoy drifts, remote-sensing-ice-drift estimates, and in-situ ice-draft and -transport measurements for the last 20 years (Tartinville et al., 2001; Fichefet et al., 2001). The model does reasonably well in reproducing the observed mean seasonal cycles of ice area and extent in both hemispheres. As displayed in Figure 75, the location of the ice edge is accurately represented by the model. Except at the beginning of the 1980s, when a warm bias is identified in NCEP–NCAR winter surface air temperatures in the Beaufort and Laptev Seas, the model reproduces the observed interannual variability of the ice area for both hemispheres as deduced from remote-sensing observations (Figure 76). Simulated ice drifts have also been favourably compared to observed drifts from the International Arctic Buoy Program and to ice velocities derive from remote-sensing observations. In addition, the model ice thicknesses have been compared to upward-looking-sonar measurements in the Weddell Sea (Strass and Fahrbach, 1998). Whereas the simulated formation rate of deep waters in the Greenland–Iceland–Norwegian Seas is too weak, the modelled interannual variability of the deep-water-formation rate in the Labrador Sea is similar to the one inferred from observations. The simulated increase of the March mixed-layer depth in the Labrador Sea since the beginning of the 1970s is consistent with the observed progressive cooling of the Labrador Sea Water since 1970 (Dickson et al.,

1996). In the Southern Ocean, the model also exhibits a strong interannual variability. The formation rate of bottom waters on the Antarctic continental shelf is minimum at the end of the 1970s, when the annual mean ice area is also minimum.

8.2 Development and validation of a new AOGCM

A new AOGCM has also been set up at ASTR-GCMG within CLIMOD. This model is made up of the new AGCM LMDZ developed at LMD, the new version of the CLIO model described in the previous section, and the Ocean–Atmosphere–Sea-Ice–Soils (OASIS) coupler built at the Centre Européen de Recherche et de Formation Avancée en Calcul Scientifique (CERFACS), Toulouse (Terray, 1995).

The LMDZ model has the peculiarity that it can be used with different horizontal grids (regular or in sine of latitude) and can even utilise a zoom over specific regions. At the beginning of CLIMOD, the model sensitivity to the horizontal resolution was assessed. The observed patterns of surface temperature and sea-level pressure at high latitudes were much better reproduced with the regular grid compared to the sine-of-latitude one, without modification of the results at low latitudes. Therefore, a regular grid with 45 points along the latitude and 72 points along the longitude has been selected. 19 levels were considered along the vertical. Most of the physical parameterisations of LMDZ are similar to those used in the previous version of the LMD's AGCM (see Section 2). However, deep convection is now represented by the mass-flux scheme of Tiedke (1989). Furthermore, a parameterisation for shallow convection has been recently introduced by the LMD to improve the exchanges within the PBL. In order to couple the atmospheric model to the CLIO model, each surface mesh was divided into four subsurfaces: ocean, sea ice, land, and ice sheet.

The CLIO version coupled to this AGCM is the same as the one described in Section 8.1, except that a low-resolution ($3^\circ \times 3^\circ$, 20 vertical levels) has been employed for testing more easily the coupled system.

The OASIS coupler orchestrates the exchange of fields between the two models once a day. Different interpolations are available as well as some analyses, which can be performed on the fields. The OASIS version chosen in our coupling utilises the message-passing technique (PVM).

The fields transferred from LMDZ to CLIO are: the solar fluxes over ocean and sea ice, the non-solar fluxes (composed of the net longwave flux and the sensible and latent heat fluxes) over ocean and sea ice, the sensitivity of turbulent fluxes to sea-ice temperature, the freshwater flux, the snowfall, the runoff, and the three components of

the wind stress over ocean and sea ice. The SST and the sea-ice concentration, surface temperature, and albedo are transferred from CLIO to LMDZ.

In order to set up this coupled model several developments were required. First, the spatial interpolation used is a weighted sum according to the overlapped areas between the atmospheric and oceanic grid cells. These weights have been calculated besides the OASIS coupler, because none of the interpolations available in the coupler conserves energy or water. Also, the oceanic surface in the atmospheric model has been modified in order to be the same as that of CLIO. Second, the heat fluxes are transferred separately over each subsurface instead of using an average flux. They are indeed drastically different over sea ice and leads. The separation of radiative and turbulent fluxes has been implemented in the atmospheric model. Third, a runoff scheme, which is necessary so as to conserve the total water content of the system, has been introduced. The atmospheric model computes an amount of water that is discharged by runoff. In a coupled model, this water has to reach the oceanic basins. Thus, a correspondence table between atmospheric meshes and oceanic ones had to be determined. This work has been done thanks to the use of observed drainage basins. Fourth, wind stresses are the only fields that have to be interpolated with bicubic interpolation. In this case, it is more important to avoid strong discontinuities between two cells, because this creates non-physical movements in the ocean. The interpolation used is one of those available in OASIS. But, this interpolation does not treat the vector direction in a general manner. So, some modifications had to be made in each model. Finally, in order to compute the sea-ice temperature in the CLIO model, which is the most accurate model to do it, the sensitivity of turbulent heat fluxes are required. This parameter is calculated by the atmospheric model in addition to the other heat fluxes.

The design of the experiments conducted with the coupled model is the following. The AGCM is initialised with outputs from a 4-year run conducted in uncoupled mode with prescribed SSTs and sea-ice extents. Regarding the CLIO initial state, it is derived from a quasi-equilibrium run of 1000-year duration carried out also in uncoupled mode. Afterwards, the two models run in coupled mode. It is important to notice that no flux correction is applied. After a long period of calibration where many sensitivity experiments were performed, a 100-year control simulation has been made with the best set of parameters. In this report, we focus on the results of this control experiment.

The control run shows an initial drift during the first 10 years. This behaviour is present in all our coupled simulations. This drift affects several sea-ice characteristics: volume, area, and thickness. This medium is indeed particularly sensitive to small changes in atmospheric fluxes and in the oceanic vertical density profile. The annual mean, area-

averaged SST and the annual mean, globally averaged ocean temperature do not exhibit greater drifts during the beginning of the simulation compared to the whole period. The SST drift is about -1.2°C over 100 years, whereas it amounts to -0.26°C for the global mean ocean mean temperature. Figure 77 shows the temporal evolution of the annual mean, zonally averaged SST relatively to the initial state. Two distinct periods can be detected. During the first 10 years, a strong warming occurs at high latitudes, with a SST anomaly of $+1.5^{\circ}\text{C}$ at 65°N and $+2.5^{\circ}\text{C}$ at 65°S . This warming is associated with a decrease in sea-ice extent. By contrast, the tropics are getting colder. During the rest of the simulation, the global climate gets colder, and the temperature decreases by up to 4°C at about 60°N . The cooling can be partly explained by the loss of energy at the ocean/sea-ice surface. Indeed, the net surface heat flux over the ocean/sea-ice surface experiences a deficit of 1 W m^{-2} in global average during the first 30 years. At the end of the simulation, this feature tends to disappear.

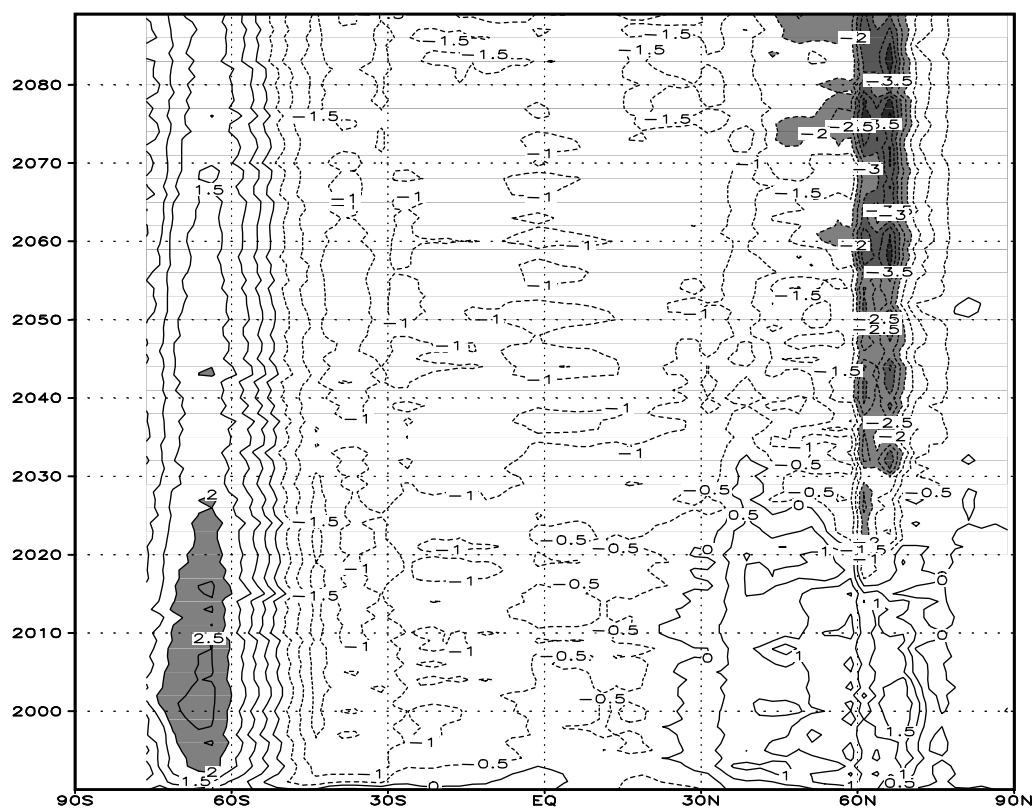


Figure 77: Temporal evolution of the annual mean, zonally averaged SST relatively to the initial state as simulated in the control experiment. The latitudes from 90°S to 90°N are shown on the horizontal axis, and the temporal evolution on the vertical axis. The contour interval is 0.5°C , with dotted lines denoting negative values. Values greater than 2°C or lower than -2°C are shaded.

A comparison between the simulated annual mean SSTs at the end of the experiment and the observations of Da Silva (1994) is given in Figure 78. The model climate is too cold nearly everywhere, except around Antarctica, in the Arctic (near the Bering Strait), and close to the west coast of America. The tropics are relatively stable, only 1°C too cold in the Pacific and Indian Oceans and about 2°C too cold in the Atlantic. This low drift is very reasonable compared to other coupled model results. At higher latitudes, the maximum bias reaches 4°C in the North Pacific and between 30 and 40° S. The cold biases between 30 and 40° S have been improved compared to a previous version by increasing the solar radiation absorbed at the surface. The maximum cooling of 8°C is located in the North Atlantic. It is due a shift in the areas of deep convection (which implies less warm deep water brought up to the surface at this location) and to the presence of sea ice.

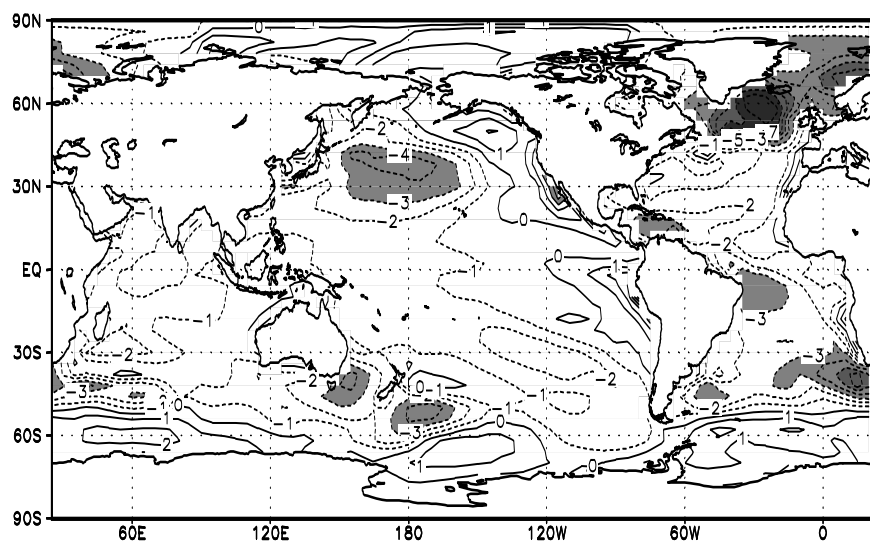


Figure 78: Differences between the annual mean SSTs simulated by the new AOGCM at the end of the control experiment and the observations. The contour interval is 1°C, with dotted lines denoting negative values. Values greater than 3°C or lower than -3°C are shaded.

The sea-level pressure is an important variable for the coupling, because it shows the way the atmospheric model dynamically drives the oceanic one. In Figure 79 is presented the geographical distribution of the sea-level pressure at the end of the simulation for the winter season. The observed low and high pressures in both hemispheres are relatively well simulated. However, in the Southern Hemisphere, the intensity of the troughs around Antarctica and the high pressures over the subtropical oceans are slightly underestimated compared to the NCEP–NCAR re-analysis data. By contrast, in the Northern Hemisphere, both low and high pressures are too intense. The Aleutian low is located at the right place, but its intensity is about 10 hPa too high compared to the re-analysis data. Therefore, the flux of cold air from the Arctic Ocean

to the northwestern Pacific is larger than in the observations. This can partly explain the cold SST anomaly simulated in the Northwest Pacific. Over the North Atlantic, the Icelandic low pressure is shifted eastwards and is located over the Norwegian Sea. This implies a northerly surface wind in this region instead of the observed southerly wind. Thus, warm waters from the North Atlantic Current cannot be transported into the Norwegian Sea, and sea ice is exported out of the Arctic Ocean east of Spitzberg. The presence of sea ice in the North Atlantic could be linked to this sea-level pressure anomaly. This point will be discussed later.

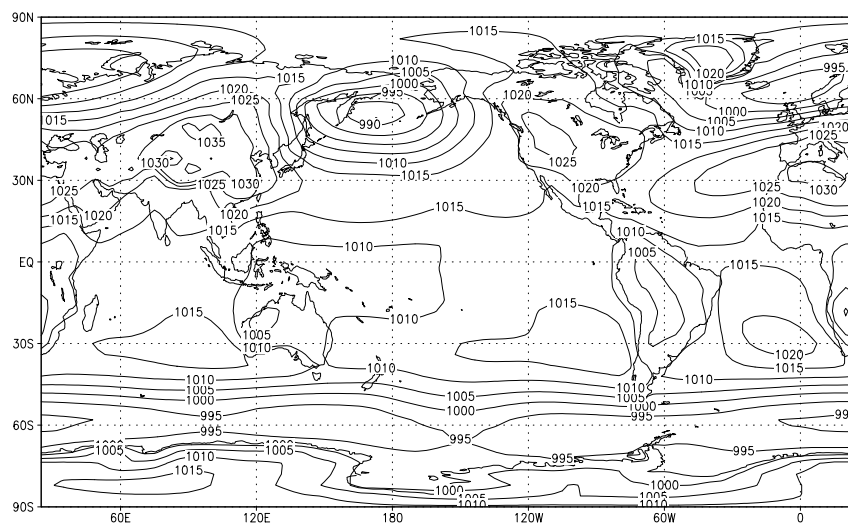


Figure 79: Geographical distribution of the sea-level pressure for DJF as simulated by the new AOGCM at the end of the control experiment. The contour interval is 5 hPa.

During the first 30 years of the experiment, sea-ice extent is relatively low in both hemispheres (see Figures 81 and 83). This is associated with an increase in the rates of production of NADW and Antarctic Bottom Water (AABW). In the Northern Hemisphere, after 30 years of simulation, sea ice forms over the northwestern part of the Atlantic. The deep-convection areas then shift to lower latitudes. Indeed the presence of sea ice isolates the oceanic surface from the cold atmosphere during winter and prevents instabilities. After 40 years, both the NADW formation rate and the amount of NADW exported out of the Atlantic Ocean stabilise. Figure 80 depicts the annual mean Atlantic meridional overturning streamfunction at the end of the simulation. The NADW overturning is well simulated even after 100 years of simulation. The amount of NADW exported at 20° S is about 14 Sv, which is within the range of current estimates. The behaviour of the NADW is a very positive point of this simulation. In the Southern Hemisphere, the stabilisation of the AABW produced and exported occurs after 50 years of simulation. The amount of AABW formed is close to that obtained with CLIO in uncoupled mode. However, the amount of water exported

appears overestimated by about 15 Sv compared to a simulation in uncoupled mode. Most of this excess goes into the Indian and Pacific Oceans.

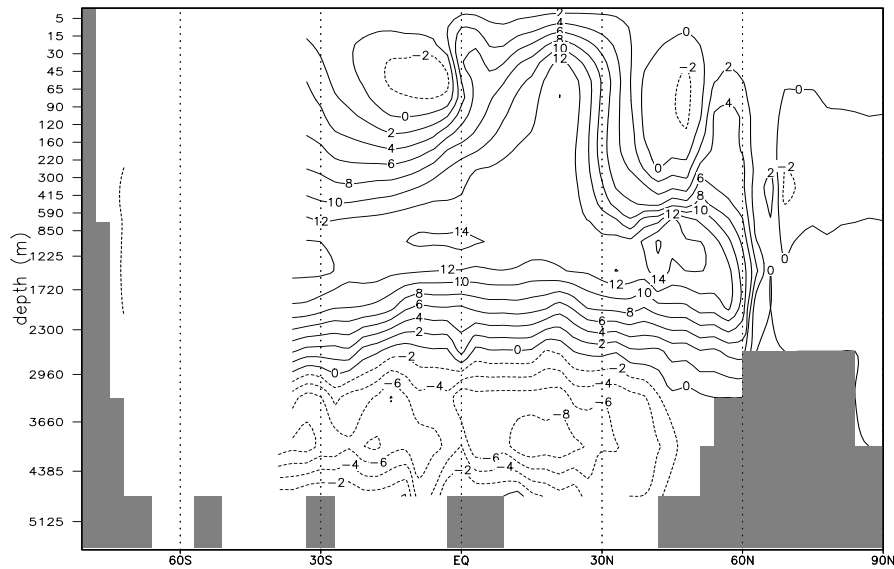


Figure 80: Annual mean meridional overturning streamfunction in the Atlantic Ocean as simulated by the new AOGCM at the end of the control experiment. The contour interval is 2 Sv, with dotted lines denoting negative values. Flow is clockwise around solid contours.

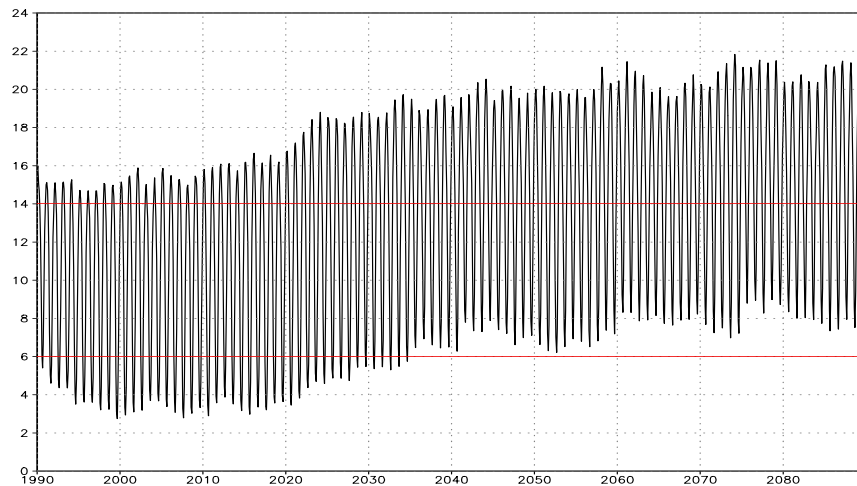


Figure 81: Temporal evolution of the Northern Hemisphere's sea-ice area (in 10^6 km^2) as simulated by the new AOGCM. Red lines represent the observed maximum and minimum.

We now focus on polar regions. In the Northern Hemisphere, the sea-ice volume rapidly decreases by about $20 \times 10^3 \text{ km}^3$ in 5 years (not shown). This is mainly due to a decrease in sea-ice thickness. Only the summer minimum ice area is reduced, the winter area being not affected by this initial drift (Figure 81). Afterwards, the sea-ice

volume remains stable for 25 years. Then, it rapidly increases and seems to reach an equilibrium state. In Figure 81, a jump in sea-ice area can be seen after 30 years of simulation and corresponds to the appearance of sea ice in the western part of the North Atlantic in winter. During the rest of the simulation, the sea-ice area grows very slowly.

The simulated March sea-ice thicknesses at the end of the simulation are displayed in Figure 82. The observed geographical distribution is reasonably well reproduced. As in the observations, it exhibits a maximum of about 5.5 m north of the Greenland ice sheet and off the Canadian Archipelago. Simplified climate GCMs (e.g., Goose et al., 2000) or GCMs with the same complexity as ours (e.g., Weatherly et al., 1997; Boville et al., 2000) do not succeed in reproducing this feature. However, an unobserved maximum is noticed in Baffin Bay. Two processes are responsible for this feature. First, Greenland seems to diffuse its cold climate in neighbouring regions. After 100 years, the sea-ice temperature in Baffin Bay is too cold by more than 15°C in comparison to the initial state. This could be caused by the cohabitation of continental ice and sea ice in the same atmospheric meshes.

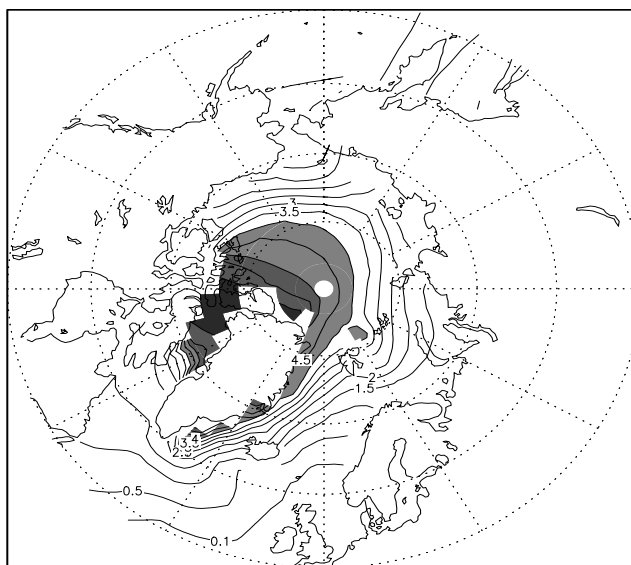


Figure 82: March sea-ice thicknesses in the Northern Hemisphere as simulated by the new AOGCM at the end of the control experiment. The contour interval is 0.5 m for values above 0.5 m, and the 0.1 m contour is added. Values greater than 4 m are shaded.

This explanation will be checked thanks to a sensitivity experiment. Second, the sea ice in Baffin Bay should be flushed out forced by northerly winds. Due to the coarse resolution of the CLIO model, Baffin Bay is only two-grid-cell wide. Thus, only one ice velocity is computed there. When sea ice thickens, the internal sea-ice stress slows down the drift. However, the most important problem is the presence of sea ice in the western part of the North Atlantic and south of Iceland after 30 years of simulation.

This feature could be due to the increase in the amount of sea ice exported out of the Arctic. As explained previously, the atmospheric circulation, and in particular the center of the Icelandic low pressure, is shifted eastwards. Then, the wind, which should blow northwards between Iceland and the Norwegian coast, is in the opposite direction. The same amount of sea ice is exported through Fram Strait (between Greenland and Spitzberg) and between Spitzberg and Norway. The total amount of sea ice exported is then twice the observed value. During summer, the CLIO model succeeds in melting nearly all the sea ice over the North Atlantic, thanks to the warm water advected by the model Gulf Stream and North Atlantic Current.

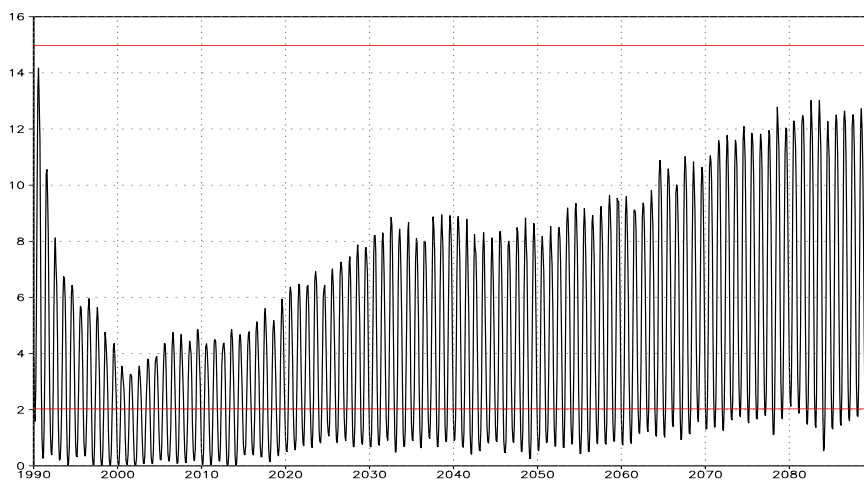


Figure 83: Temporal evolution of the Southern Hemisphere's sea-ice area (in 10^6 km^2) as simulated by the new AOGCM. Red lines represent the observed maximum and minimum.

The temporal evolution of the Antarctic sea-ice area simulated by the model over the 100 years of the control experiment is illustrated in Figure 83. A strong melting of sea ice takes place during the first 10 years. Afterwards, the sea ice grows progressively, and at the end of the simulation, the ice pack reaches a maximum area of $13 \times 10^6 \text{ km}^2$ in winter, to be compared to $15 \times 10^6 \text{ km}^2$ in the observations. The minimum area is similar to the observed value ($2 \times 10^6 \text{ km}^2$). After the melting period, the sea-ice extent is considerably reduced. The convection around Antarctica then intensifies and deepens. This convection is located nearly all around the continent at places where the sea ice was present at the beginning of the simulation. This is due to an increase in surface density, mainly caused by an increase in salinity. The atmospheric freshwater fluxes do not seem to be responsible for this increase. However, the decrease in freshwater release during the melting period can create this salinity change. Indeed, sea-ice melting tends to stabilise the water column and to suppress convection. The strong mixing induced by convection modifies the properties of the surface water. After the melting period, when convection sets off, the sea-surface salinity and temperature increase by 0.4 psu and 0.5°C , respectively, at areas where strong mixing takes place.

Because of the homogenisation of the density profile during a convective event, a small perturbation can enhance another convective event. At the end of the experiment, the ice edge reaches more or less its initial location, and the ice melting stabilises the region where convection acted. Convection remains only in the Indian Ocean sector. The amount of deep water created around Antarctica behaves in the same way: 25 Sv are produced during the first 10 years of the simulation; afterwards, this amount increases until 35 Sv after 30 years and then progressively returns to its initial value.

We can conclude this section by saying that the new model does reasonably well in reproducing the observed present-day climate. The tropics remain stable. The sea-ice volume and area after an initial drift reach realistic values in both hemispheres. Furthermore, the thermohaline circulation remains stable in both hemispheres after 50 years of simulation. The amount of NADW exported at 20° S is close to the observational estimates. The sole problem is the presence of sea ice in the northwestern part of the Atlantic Ocean. Further analyses will be performed in order to circumvent this problem.

9. DISSEMINATION OF THE RESULTS

The results discussed above have been presented in a number of international scientific meetings and have led to about 45 papers published in, under press in, or submitted to peer-reviewed scientific journals. Dissemination took also place via the training of young researchers. In particular, 4 PhD theses related to CLIMOD were defended during the project, and 3 others are still under way.

The research network CLIMOD consisted of scientists deeply involved in the activities of the IPCC and in international research programmes on climate change such as CLIVAR (Climate Variability and Predictability) and ACSYS/CliC (Arctic Climate System Study / Climate and Cryosphere), which are two subprogrammes of the World Climate Research Programme. In particular, two members were lead authors of two different chapters of the IPCC's Third Assessment Report (TAR), and a third one was contributing author of another chapter. This has enabled the dissemination of the CLIMOD results both to scientists involved in studying climate change and to the communities involved in impact studies. Note, however, that the climate-change projections conducted within CLIMOD are not included in the IPCC's TAR because they have been completed too late. It is also noteworthy that one of us contributed actively to the work of the Belgian Federal Council for Sustainable Development.

Furthermore, members of the research network CLIMOD were engaged in vulgarization activities such as (1) conferences in universities, schools, and societies, (2) publication of articles in the non-specialized press, (3) printed press, television, and radio interviews, and (4) participation to several documentaries produced by the RTBF, the French-speaking Belgian television, about the climate-change issue. In addition, they contributed to the exhibition "Vivre ou survivre" organised by the Royal Institute for Natural Sciences in collaboration with the Belgian Federal Office for Scientific, Technical, and Cultural Affairs (OSTC). Results of CLIMOD were also disseminated through meetings, symposia, and other activities organised by the OSTC in the course of the project.

Finally, we would like to stress here that most of the model outputs generated during CLIMOD are stored in a database and are available upon request.

10. CONCLUDING REMARKS AND RECOMMENDATIONS

All the initial objectives of the research project CLIMOD, that are recalled in Section 1 of the present report, have been reached, except that, for the reasons explained in Section 7.2, we were not able to perform with MAR a detailed assessment of the climate-change projections over Western Europe for the end of the 21st century. We have however demonstrated that MAR is ready to carry out such a study.

The global climate model developed within CLIMOD is, to our knowledge, the first of this type including an interactive ice-sheet component. It has been used to investigate the evolution of climate during the 21st century in response to the increase in greenhouse-gas concentrations and sulphate-aerosol loading projected by the IPCC's scenario SRES B2. By 2100, the model simulates a global surface warming of 2.3°C and a global increase in precipitation of 3%, which fall within the range of other model estimates. By the end of the 21st century, the projected rise in sea-level due to thermal expansion reaches 22 cm. The partial melting of the Greenland ice sheet induces an additional rise in sea level of 4 cm. Greenhouse-gas-induced changes in meltwater flux from the Greenland ice sheet do not seem to affect the simulated climate, but this result must be taken with caution as the strength of the North Atlantic thermohaline circulation decreases with time in the control run performed with the model. Reduction of uncertainties like this one will require to improve significantly the model physics and/or to enhance the model resolution, which was beyond the scope of CLIMOD.

The work made within the framework of CLIMOD is a contribution to the ongoing international scientific effort to better understand how human activities impact the climate system at the global and regional scales. This is needed in order to provide a

sound basis for policies designed to address the challenge of climate changes. The problem will not go away quickly, and is most likely to become more and more important. Each Party to the United Nations Framework Convention on Climate Change (UNFCCC) has committed itself to "promote and cooperate in scientific (...) research (...) related to the climate system and intended to further understand and reduce the remaining uncertainties (...)." (UNFCCC Article 4.1(g)).

The sustained funding of this kind of research is required both at the international and national levels, so that the appropriate scientific capacity is available in as many countries as possible. Two areas that require particular attention are (1) the improvement of the representation of physical processes in global climate models and (2) the downscaling of global climate-model results to the European and Belgian scales through nested regional models and increased spatial resolution at these scales. This will allow addressing the specificity of the European and Belgian climates, while improving the overall quality of climate simulations at the global scale and reducing the remaining uncertainties. So that the Belgian research effort becomes better integrated in the European and international research programmes, the appropriate support should be given to facilitate participation in the existing and planned model-intercomparison programmes. These allow the different modelling laboratories to confront their methods and results to each other, so that the origin of differences can be better understood. This will lead to better models, enhance capacity building, and help integrate the Belgian research efforts. For the same reasons, participation of Belgian modellers to interdisciplinary research dealing with the impacts and mitigation of climate change is of high value, and collaboration to the work of the IPCC should be encouraged.

REFERENCES

- Abdalati, W. and Steffen, K. 1997. Snowmelt on the Greenland ice sheet as derived from passive microwave satellite data. *J. Clim.* 10: 165-175.
- Alexandersson, H. 1986. A homogeneity test applied to precipitation data. *J. Climatol.* 6: 661-675.
- Alexandersson, H. and Moberg, A. 1997. Homogenization of Swedish temperature data. Part I : Homogeneity test for linear trends. *Int. J. Climatol.* 17: 25-34.
- Anthes, A. and Warner, T. 1978. Development of hydrodynamic models suitable for air pollution and other mesometeorological studies. *Mon. Wea. Rev.* 106: 1045-1078.
- Beckers, J.-M., Burchard, H., Campin, J.-M., Deleersnijder, E. and Mathieu, P.-P. 1998. Another reason why simple discretizations of rotated diffusion operators cause problems in ocean models: Comments on "Isoneutral diffusion in a z-coordinate ocean model". *J. Phys. Oceanogr.* 28: 1552-1559.
- Beckers, J.-M., Burchard, H., Deleersnijder, E. and Mathieu, P.-P. 2000. Numerical discretization of rotated diffusion operators in ocean models. *Mon. Wea. Rev.* 128: 2711-2733.
- Beron-Vera, F.J., Ochoa, J. and Ripa, P. 1999. A note on the boundary conditions for salt and freshwater balances. *Ocean Modell.* 1: 111-118.
- Boer, G.J., McFarlane, N.A., Laprise, R., Henderson, J.D. and Blanchet, J.-P. 1984. The Canadian Climate Centre spectral atmospheric general circulation model. *Atmos.-Ocean* 22: 397-429.
- Boville, B.A., Kiehl, J.T., Rasch, P.J. and Bryan, F.O. 2000. Improvements to the NCAR CSM-1 for transient climate simulations. *J. Clim.* 14:164-179.
- Braithwaite, R.J. and Zhang, Y. 2000. Sensitivity of mass balance of five Swiss glaciers to temperature changes assessed by tuning a degree-day model. *J. Glaciol.* 46: 7-14.
- Brasseur, O. 1999. Mesoscale modeling of extreme meteorological events over Belgium. Dissertation doctorale. Fac. des Sci. Appl., Univ. catholique de Louvain, Louvain-la-neuve.
- Brasseur, O. 2001. Development and application of a physical approach to estimating wind gusts. *Mon. Wea. Rev.* 129: 5-25.
- Brun, E., David, P., Sudul, M. and Brunot, G. 1992. A numerical model to simulate snowcover stratigraphy for operational avalanche forecasting. *J. Glaciol.* 38:13-22.
- Bryan, K. 1969. A numerical method for the study of the circulation of the World Ocean. *J. Comp. Phys.* 4: 347-376.

- Bugnion, V. 2000. Reducing the uncertainty in the contribution of Greenland to sea-level rise in the 20th and 21st centuries. *Ann. Glaciol.* 31: 121-125.
- Campin, J.-M. and Goosse, H. 1999. Parameterization of density-driven downsloping flow for a coarse-resolution ocean model in z-coordinate. *Tellus* 51A: 412-430.
- Chalita, S., and Le Treut, H. 1994. The albedo of temperate and boreal forest and the Northern Hemisphere climate: A sensitivity study using the LMD GCM. *Clim. Dyn.* 10: 231-240.
- Champeaux, J.-L. and Tamburini, A. 1996. Zonage climatique de la France à partir des séries de précipitations (1971–1990) du réseau climatologique d'Etat. *La Météorologie Série 8, N°14*: 44-55.
- Christensen, J.H., Machenhauer, B., Jones, R.G., Schär, C., Ruti, P.M., Castro, M. and Visconti, G. 1997. Validation of present-day regional climate simulations over Europe: LAM simulations with observed boundary conditions. *Clim. Dyn.* 13: 489-506.
- Chuang, C., Penner, J., Taylor, K., Grossman, A. and Walton, J. 1997. An assessment of the radiative effects of anthropogenic sulfate. *J. Geophys. Res.* 102: 3761-3778.
- Church, J.A., Gregory, J.M., Huybrechts, P., Kuhn, M., Lambeck, K., Nhuan, M.T., Qin, D., and Woodworth, P.L. 2001. Changes in sea level. In: *Climate Change 2001: The Scientific Basis: Contribution of Working Group I to the Third Assessment Report of the Intergovernmental Panel on Climate Change*. Houghton, J.T., Ding, Y., Griggs, D.J., Noguer, M., Van der Linden, P.J., Dai, X., Maskell, K. and Johnson, C.A. (Eds.). Cambridge University Press, Cambridge: 639-694.
- Colella, P. and Woodward, P.R. 1984. The piecewise parabolic method (PPM) for gas-dynamical simulations. *J. Comput. Phys.* 54: 174-210.
- Comiso, J.C., Cavalieri, D.J., Parkinson, C.L., and Gloersen, P. 1997: Passive microwave algorithms for sea ice concentration: A comparison of two techniques. *Remote Sens. Environ.* 60: 357-384.
- Covey, C. 1995. Global ocean circulation and equator-pole heat transport as a function of ocean GCM resolution. *Clim. Dyn.* 11: 425-437.
- Cox, M.D. 1987. Isopycnal diffusion in a z-coordinate ocean model. *Ocean Modell.* 74: 1-5 (unpublished manuscript).
- Cress, A., Majewski, D., Podzun, R. and Renner, V. 1995. Simulation of European climate with a limited area model. Part I: Observed boundary conditions. *Beitr. Phys. Atmos.* 68: 161-178.
- Cuffey, K.M. and Clow, G.D. 1997. Temperature, accumulation, and ice sheet elevation in central Greenland through the last deglacial transition. *J. Geophys. Res.* 102: 26,383-26,396.

- Dansgaard, W., Johnsen, S.J., Clausen, H.B., Dahl-Jensen, D., Gundestrup, N.S., Hammer, C.U., Hvidberg, C.S., Steffensen, J.P., Sveinbjornsdottir, A.E., Jouzel, J. and Bond, G.C. 1993. Evidence for general instability of past climate from a 250-kyr ice-core record. *Nature* 364: 218-220.
- Da Silva, A.M., Young, C.C., and Levitus, S. 1994. Atlas of surface marine data 1994. Volume 1: Algorithms and procedures. NOAA Atlas NESDIS 6.
- Davies, H.C., 1983. Limitations of some common lateral boundary schemes used in regional NWP models. *Mon. Wea. Rev.* 111: 1002-1012.
- Deleersnijder, E. and Campin, J.-M. 1995. On the computation of the barotropic mode of a free-surface World Ocean model. *Ann. Geophysicae* 13: 675-688.
- Deleersnijder, E., van Ypersele, J.-P. and Campin, J.-M. 1993. An orthogonal, curvilinear coordinate system for a World Ocean model. *Ocean Modell.* 100: 7-10 (unpublished manuscript).
- De Ridder, K. 1998. Land surface-induced regional climate change in southern Israel. *J. Appl. Meteor.* 37: 1470-1485.
- De Ridder, K. and Schayes, G. 1997. The IAGL land surface model. *J. Appl. Meteor.* 37: 167-182.
- De Wolde, J., Huybrechts, P., Oerlemans, J. and van de Wal, R.S.W. 1997. Projections of global mean sea level rise calculated with a 2D energy-balance climate model and dynamic ice sheet models. *Tellus* 49A: 486-502.
- Dickinson, R.E., Errico, R.M., Giorgi, F. and Bates, G.T. 1989. A regional climate model for the Western United State. *Clim. Change* 15: 383-422.
- Dickson, R., Lazier, J., Meincke, J., Rhines, P. and Swift, J. 1996. Long-term coordinated changes in the convective activity of the North Atlantic. *Prog. Oceanog.* 38: 241-295.
- Dorman, J.L. and Sellers, P.J. 1989. A global climatology of albedo, roughness length and stomatal resistance for atmospheric general circulation models as represented by the Simple Biosphere model (SiB). *J. Appl. Meteor.* 28: 833-855.
- Ducoudré, N., Laval, K. and Perrier, A. 1993. SECHIBA, a new set of parameterizations of the hydrologic exchanges at the land/atmosphere interface within the LMD atmospheric general circulation model. *J. Clim.* 6: 248-273.
- Dupriez, G.L. et Demarée, G. 1988. Totaux pluviométriques sur des périodes continues de 1 à 30 jours. I. Analyse de 11 séries pluviométriques de plus de 80 ans. *Miscellanea Série A., N°8*, Institut royal météorologique de Belgique Brussels, 53 p.
- Dupriez, G.L. and Sneyers, R. 1978. Les normales du réseau pluviométrique belge. *Publications, Série A, N°101*, Institut royal météorologique de Belgique, Brussels, 69 p.

- Dupriez, G.L. and Sneyers, R. 1979. Les nouvelles cartes pluviométriques de la Belgique. Publications, Série A, N°103, Institut royal météorologique de Belgique, Brussels, 17 p.
- Dutrieux, A., Tricot, C., Vandiepenbeeck, M., Brasseur, O., Gallée, H. and Marbaix, P. 1998. The Belgian contribution to the HIRETYCS project. Task C11: Validation of the simulated climate over Belgium. Task D2: Driving the MAR LAM with GCM boundary conditions. Final report of HIRETYCS project. EC Environment and Climate Programme.
- Duynkerke, P.G. 1988. Application of the E-e turbulence closure model to the neutral and stable atmospheric boundary layer. *J. Atmos. Sci.* 45: 865-880.
- Easterling, D.R. and Peterson, T.C. 1995. A new method for detecting undocumented discontinuities in climatological time series. *Int. J. Climatol.* 15: 369-377.
- Ekholm, S. 1996. A full coverage, high-resolution, topographic model of Greenland computed from a variety of digital elevation data. *J. Geophys. Res.* 101: 21,961-21,972.
- Fichefet, T. and Morales Maqueda, M. 1997. Sensitivity of a global sea ice model to the treatment of ice thermodynamics and dynamics. *J. Geophys. Res.*, 102: 12,609-12,646.
- Fichefet, T. and Morales Maqueda, M., 1999. Modelling the influence of snow accumulation and snow-ice formation on the seasonal cycle of the Antarctic sea-ice cover. *Clim. Dyn.* 15: 251-268.
- Fichefet, T., Tartinville, B. and Goosse, H. 2000. Sensitivity of the Antarctic sea ice to the thermal conductivity of snow. *Geophys. Res. Lett.* 27: 410-404.
- Fichefet, T., Tartinville B. and Goosse, H. 2001. A numerical simulation of the Antarctic sea ice variability, 1958–1999. Submitted to *J. Geophys. Res.*
- Fontaine, F. et al. 2001. La nouvelle banque de données climatologiques de l'IRM. Institut royal météorologique de Belgique, Brussels, in preparation.
- Fouquart, Y. and Bonnel, B. 1980. Computation of the solar heating of the Earth's atmosphere: A new parameterization. *Beitr. Phys. Atmos.* 53: 35-62.
- Fritsch, J. M. and Chappell, C.F. 1980. Numerical prediction of convectively driven mesoscale pressure systems. Part I: Convective parameterization. *J. Atmos. Sci.* 37: 1722-1733.
- Gallée, H. 1995. Simulation of the mesocyclonic activity in the Ross Sea, Antarctica. *Mon. Wea. Rev.* 123 2051-2069.
- Gallée, H. and Schayes, G. 1994. Development of a three-dimensional meso-gamma primitive equations model. *Mon. Wea. Rev.* 122: 671-685.

- Gallée, H. and Duynkerke, P.G. 1997. Air–snow interactions and the surface energy and mass balance over the melting zone of West Greenland during the Greenland Ice Margin Experiment. *J. Geophys. Res.* 102: 13,813-13,824.
- Gates, W.L., Cubasch, U., Meehl, G.A., Mitchell, J.F.B. and Stouffer, R.J. 1993. An intercomparison of selected features of the control climates simulated by coupled ocean–atmosphere general circulation models. WMO/TD-No. 574, World Meteorological Organization, Geneva, 46 p.
- Gellens, D. 2000. Trend and correlation analysis of k-day extreme precipitation over Belgium. *Theor. Appl. Climatol.* 66: 117-129.
- Gent, P.R., Bryan, F.O., Danabasoglu, G., Doney, S.C., Holland, W.R., Large, W.G. and McWilliams, J.C. 1998. The NCAR climate system model global ocean component. *J. Clim.* 11: 1287-1306.
- Gent, P.R. and McWilliams, J.C. 1990. Isopycnal mixing in ocean general circulation models. *J. Phys. Oceanogr.* 20 : 150-155.
- Giorgi, F. 1995. Perspectives for regional earth system modeling. *Global and Planetary Change* 10: 23-42.
- Giorgi, F., Marinucci, M.R., Bates, G.T. and De Canio, G. 1993. Development of a second-generation climate model (RegCM2). Part II: Convective processes and assimilation of lateral boundary conditions. *Mon. Wea. Rev.* 121: 2814-2832.
- Giorgi, F., Marinucci, M.R. and Visconti, G. 1992. A $2 \times \text{CO}_2$ climate change scenario over Europe generated using a limited area model nested in a general circulation model. 2. Climate change scenario. *J. Geophys. Res.* 97: 10,011-10,028.
- Gleckler, P.J., Randall, D.A., Boer, G., Colman, R., Dix, M., Galin, V., Helfand, M., Kiehl, J., Kitoh, A., Lau, W., Liang, X.-Z., Lykossov, V., McAveney, B., Miyakoda, K. and Planton, S. 1995. Cloud-radiative effects on implied oceanic energy transports as simulated by atmospheric general circulation models. *Geophys. Res. Lett.* 22: 791-794.
- Gloersen P., Campbell, W.J., Cavalieri, D.J., Comiso, J.C., Parkinson, C.L. and Zwally, H.J. 1992. Arctic and Antarctic sea ice, 1978–1987: Satellite passive-microwave observations and analysis. NASA Spec. Publ., SP-511, 290 p.
- Goosse, H., Campin, J.-M. and Tartinville, B. 2001. The sources of Antarctic Bottom Water in a global ice–ocean model. *Ocean Modell.* 3: 51-65.
- Goosse, H., Campin, J.-M., Fichet, T. and Deleersnijder, E. 1997a. Sensitivity of a global ice–ocean model to the Bering strait throughflow. *Clim. Dyn.* 13: 349-358.

- Goosse, H., Campin, J.-M., Fichefet, T. and Deleersnijder, E. 1997b. The impact of sea-ice formation on the properties of Antarctic Bottom Water. *Ann. Glaciol.* 25: 276-281.
- Goosse, H., Deleersnijder, E., Fichefet, T. and England, M. 1999. Sensitivity of a global coupled ocean–sea ice model to the parameterization of vertical mixing. *J. Geophys. Res.* 104: 13,681-13,695.
- Goosse, H., Fichefet, T. and Campin, J.-M. 1997c. The effects of the water flow through the Canadian Archipelago in a global ice–ocean model. *Geophys. Res. Lett.* 24: 1507-1510.
- Goosse, H., Selten, F.M., Haarsma, R.J. and Opsteegh, J.D. 2000. Decadal variability in high northern latitudes as simulated by an intermediate-complexity climate model. *Ann. Glaciol.* 33: in press.
- GPCC, 1999. Global Precipitation Climatology Centre homepage: [HTTP://www.dwd.de/research/gpcc](http://www.dwd.de/research/gpcc).
- Grenier, H., Le Treut, H. and Fichefet, T., 2000. Ocean–atmosphere interactions and climate drift in a coupled general circulation model. *Clim. Dyn.* 16: 701-717.
- Greuell, W. 1998. In: *Fluctuations of glaciers 1990–1995*. IAHS-UNESCO Publication.
- Greuell, W. 2000. Melt-water accumulation on the surface of the Greenland ice sheet: Effect on albedo and mass balance. *Geogr. Ann.* 82A: 489-498.
- Griffies, S.M., Böning, C., Bryan, F.O., Chassignet, E.P., Gerdes, R., Hasumi, H., Hirst, A., Treguier, A.-M. and Webb, D. 2000. Developments in ocean climate modelling. *Ocean Modell.* 2: 123-192.
- Griffies, S.M., Gnanadesikan, A., Pacanowski, R.C., Larichev, V.D., Dukowicz, J.K. and Smith, R.D. 1998. Isoneutral diffusion in a z-coordinate ocean model. *J. Phys. Oceanogr.* 28: 805-830.
- Heymsfield, A.J. and Donner, L.J. 1990. A scheme for parameterizing ice-cloud water content in general circulation models. *J. Atmos. Sci.* 47: 1865-1877.
- Hibler, W.D., III, 1979. A dynamic thermodynamic sea ice model. *J. Phys. Oceanogr.* 9: 815-846.
- Higgins, A.K. 1991. North Greenland glacier velocities and calf ice production. *Polarforschung* 60: 1-23.
- Huang, R.X. 1993. Real freshwater flux as a natural boundary condition for the salinity balance and thermohaline circulation forced by evaporation and precipitation. *J. Phys. Oceanogr.* 23: 2428-2446.

- Huybrechts, P. and de Wolde, J. 1999. The dynamic response of the Greenland and Antarctic ice sheets to multiple-century climatic warming. *J. Clim.* 12: 2169-2188.
- Huybrechts, P. and Le Meur, E. 1999. Predicted present-day evolution patterns of ice thickness and bedrock elevation over Greenland and Antarctica. *Polar Res.* 18: 299-308.
- Huybrechts, P., Letréguilly, A., and Reeh, N. 1991. The Greenland ice sheet and greenhouse warming. *Palaeogeogr., Palaeoclim., Palaeoecol.* (Global and Planetary Change Section) 89: 399-412.
- Imbrie, J.Z., Hays, J.D., Martinson, D.G., MacIntyre, A., Mix, A.C., Morley, J.J., Pisias, N.G., Prell, W.L. and Shackleton, N.J. 1984. The orbital theory of Pleistocene climate: Support from a revised chronology of the marine $\delta^{18}\text{O}$ record. In: Milankovitch and Climate. Berger, A., Imbrie, J.Z., Hays, J.D., Kukla, G. and Saltzman, B. (Eds). D. Reidel: 269-305.
- IPCC. 1996. Climate change 1995: The science of climate change. Contribution of Working Group I to the Second Assessment Report of the Intergovernmental Panel on Climate Change. Houghton, J.T., Meira Filho, L.G., Callander, B.A., Harris, N., Kattenberg, A. and Maskell, K. (Eds). Cambridge University Press, Cambridge, 572 p.
- IPCC. 2001. Climate change 2001: The scientific basis. Contribution of Working Group I to the Third Assessment Report of the Intergovernmental Panel on Climate Change. Houghton, J.T., Ding, Y., Griggs, D.J., Noguer, M., van der Linden, P.J., Dai, X., Maskell, K. and Johnson, C.A. (Eds). Cambridge University Press, Cambridge, 881 p.
- Janssens, I. and Huybrechts, P. 2000. The treatment of meltwater retention in mass balance parameterizations of the Greenland ice sheet. *Ann. Glaciol.* 31:133-140.
- Jones, R.G. , Murphy, J.M. and Noguer, M. 1995. Simulation of climate change over Europe using a nested regional-climate model. I: Assessment of control climate, including sensitivity to location of lateral boundaries. *Quat. J. Royal Meteor. Soc.* 121: 1413-1449.
- Jones, R.G., Murphy, J.M., Noguer, M. and Keen, A.B. 1997. Simulation of climate change over Europe using a nested regional-climate model. II: Comparison of driving and regional model responses to a doubling of carbon dioxide. *Quat. J. Royal Meteor. Soc.* 123: 265-292.
- Jung-Rothenhäusler, F. 1998. Remote sensing and GIS studies in North-East Greenland. *Berichte zur Polarforschung* 280, 161 p.
- Kain, J.S. and Fritsch, J.M., 1993. Convective parameterization for mesoscale models: The Kain-Fritsch scheme. The representation of cumulus convection in numerical models. *Meteor. Monogr.* 46: 165-170.

- Kalnay, E., Kanamitsu, M., Kistler, R., Collins, W., Deaven, D., Gandin, L., Iredell, M., Saha, S., White, G., Woollen, J., Zhu, Y., Chelliah, M., Ebisuzaki, W., Higgins, W., Janowiak, J., Mo, K.C., Ropelewski, C., Wang, J., Leetmaa, A., Reynolds, R., Jenne, R. and Joseph, D. 1996. The NCEP/NCAR 40-years reanalysis project. *Bull. Amer. Meteor. Soc.* 77: 437-470.
- Kantha, L. and C. Clayson, 1994. An improved mixed layer model for geophysical applications. *J. Geophys. Res.* 99: 25,235-25,266.
- Kapsner, W.R., Alley, R.B., Shuman, C.A., Anandakrishnan, S. and Grootes, P.M. 1995. Dominant influence of atmospheric circulation on snow accumulation in Greenland over the past 18,000 years. *Nature* 373: 52-54.
- Kessler, E. 1969. On the distribution and continuity of water substance in atmospheric circulation. *Meteor. Monogr.* 32: 84 p.
- Kistler, R., Kalnay, E., Collins, W., Saha, S., White, G., Woollen, J., Chelliah, M., Ebisuzaki, W., Kanamitsu, M., Kousky, V., van den Dool, H., Jenne, R. and Fiorino, M. 2001. The NCEP–NCAR 50-year reanalyses: Monthly means. CD-ROM and Documentation. *Bull. Amer. Meteor. Soc.* 82: 247-267.
- Kuo, H. 1965. On formation and intensification of tropical cyclones through latent heat release by cumulus convection. *J. Atmos. Sci.* 22: 40-63.
- Large, W.G, Danabasoglu, G., Doney, S.C. and McWilliams, J.C. 1997. Sensitivity to surface forcing and boundary layer mixing in a global ocean model: Annual-mean climatology. *J. Phys. Oceanogr.* 27: 2418-2447.
- Lefebvre, F. 2001. Validation of MAR over South Greenland during the summer of 1991. Scientific Report 2001/1, Institut d’Astronomie et de Géophysique G. Lemaître, Université catholique de Louvain, Louvain-la-Neuve.
- Lefebvre, F., Gallée, H., van Ypersele, J.-P. and Greuell, W. 2001a. Modelling of snow and ice melt at ETH-Camp (West Greenland, 1155 m a.s.l.) during the summers of 1990 and 1991. Submitted to *J. Geophys. Res.*
- Lefebvre, F., Gallée, H., van Ypersele, J.-P. and Huybrechts, P. 2001b. Modelling of large-scale melt parameters with a regional climate model in South Greenland during the 1991 melt season. Submitted to *Ann. Glaciol.*
- Legates, D.R. and Willmott, C.J. 1990. Mean seasonal and spatial variability in gauge-corrected, global precipitation. *Int. J. Climatol.* 10: 111-127.
- Le Meur, E. and Huybrechts, P. 1996. A comparison of different ways of dealing with isostasy: Examples from modeling the Antarctic ice sheet during the last glacial cycle. *Annals Glaciol.* 23: 309-317.

- Le Meur, E. and Huybrechts, P. 1998. Present-day uplift patterns over Greenland from a coupled ice-sheet/visco-elastic bedrock model. *Geophys. Res. Lett.* 25: 3951-3954.
- Le Meur, E. and Huybrechts, P. 1999. Correction to: Present-day uplift patterns over Greenland from a coupled ice-sheet/visco-elastic bedrock model. *Geophys. Res. Lett.* 26: 139-140.
- Le Meur, E. and Huybrechts, P. 2001. A model computation of surface gravity and geoidal signal induced by the evolving Greenland ice sheet. *Geophys. J. Internat.* 145: 1-21.
- Legates, D.R. and Willmott, C.J. 1990. Mean seasonal and spatial variability in gauge-corrected, global precipitation. *Int. J. Climatology*, 10, 111-127.
- Letréguilly, A., Huybrechts, P. and Reeh, N. 1991. Steady-state characteristics of the Greenland ice sheet under different climates. *J. Glaciol.* 37: 149-157.
- Le Treut, H. and Li, Z.-X. 1991. Sensitivity of an atmospheric general circulation model to prescribed SST changes: feedback effects associated with the simulation of cloud optical properties. *Clim. Dyn.* 5: 175-187.
- Levitus, S. 1982. Climatological atlas of the World Ocean. NOAA Prof. Pap. 13, U.S. Gov. Print. Office, Washington, D.C., 173 p.
- Louis, J.F., Tiedtke, M. and Geleyn, J.-F. 1981. A short history of the PBL parameterisation at ECMWF. In: *Proceedings of Workshop on Boundary Layer Parameterisation*. ECMWF, Reading: 59-79.
- Machenhauer, B., Windelband, J., Botzet, M., Christensen, J.H., Deque, M., Jones, R., Ruti, P.M. and Visconti, G. 1998. Validation and analysis of regional present-day climate and climate change simulations over Europe. MPI report No. 275, Hamburg.
- Majewski, D. 1985. Balanced initial and boundary values for a limited area model. *Beitr. Phys. Atmos.* 58: 147-159.
- Manabe, S. and Strickler, R. 1964. Thermal equilibrium of the atmosphere with a convective adjustment. *J. Atmos. Sci.* 21: 361-385.
- Mann, H.B. 1945. Non parametric test against trend. *Econometrika* 13: 245-259.
- Marbaix, P. 2000. A regional atmospheric model over Europe: Adaptation for climate studies and validation. Dissertation doctorale. Fac. des Sci., Univ. catholique de Louvain, Louvain-la-Neuve, 174 p.
- Marbaix, P., Gallée, H., Brasseur, O. and van Ypersele, J.-P. 2001. Lateral boundary conditions in regional climate models: A detailed study of the relaxation procedure. To be submitted to *Mon. Wea. Rev.*

- Mathieu, P.-P. and Deleersnijder, E. 1998. What is wrong with isopycnal diffusion in World Ocean models? *Appl. Math. Model.* 22: 367-378.
- Mayer, C., Jung-Rothenhäusler, F., Reeh, N., Huybrechts, P. and Oerter, H. 2000. The subglacial cavity and implied dynamics under Nioghalvfjerdingsfjorden Glacier, NE-Greenland. *Geophys. Res. Lett.*
- Mellor, G. and Yamada, T. 1982. Development of a turbulence closure model for geophysical fluid problems. *Rev. Geophys. Space Phys.* 20: 851-875.
- Mitchell, J., Cavis, R., Ingram, W. and Senior, C. 1995. On surface temperature, greenhouse gases, and aerosol: Models and observations. *J. Clim.* 8: 2364-2386.
- Morcrette, J. 1984. Sur la paramétrisation du rayonnement dans les modèles de la circulation générale atmosphérique. Thèse de Doctorat d'Etat. Univ. des Sci. et Tech. de Lille, Lille.
- Morcrette, J.-J. 1991. Radiation and cloud radiative properties in the ECMWF operational weather forecast model. *J. Geophys. Res.* 96: 9121-9132.
- Oerlemans, J. and Vugts, H. 1993. A meteorological experiment in the melting zone of the Greenland ice sheet. *Bull. Amer. Meteor. Soc.* 74: 355-365.
- Ohmura, A. and Reeh, N. 1991. New precipitation and accumulation maps for Greenland. *J. Glaciol.* 37:140-148.
- Ohmura, A., Steffen, K., Blatter, H., Greuell, W., Rotach, M., Konzelmann, T., Laternser, M., Ouchi, A. and Steiger, D. 1992. Energy and mass balance during the melt season at the equilibrium line altitude, Paakitsoq, Greenland ice sheet: Progress Report 1. Dept. of Geography, Swiss Federal Institute of Technology, Zürich.
- Pacanowski, R.C. and Philander, S.G.H. 1981. Parameterization of vertical mixing in numerical models of tropical oceans. *J. Phys. Oceanogr.* 11: 1443-1451.
- Paterson, W.S.B. 1994. *The physics of glaciers*, 3rd edition. Pergamon Press, Oxford.
- Penner, J., Chuang, C. and Grant, K. 1998. Climate forcing by carbonaceous and sulfate aerosols. *Climate Dyn.* 14: 839-851.
- Pettitt, A. N. 1979. A non-parametric approach to the change-point problem. *Appl. Statis.* 28: 126-135.
- Pfeffer, W.T., Meier, M F. and Illangasekare, T.H. 1991. Retention of Greenland runoff by refreezing: Implications for projected future sea level change. *J. Geophys. Res.* 96: 22,117-22,124.
- Poncelet, L. and Martin, H. 1947. *Esquisse climatographique de la Belgique*. Mémoires, Vol. 27, Institut royal météorologique de Belgique, Brussels: 265 p.

- Potter, K.W. 1981. Illustration of a new test for detecting a shift in mean in precipitation series. *Mon. Wea. Rev.* 109: 2040-2045.
- Rahmstorf, S. 1994. Rapid climate conditions in a coupled ocean-atmosphere model. *Nature*. 372: 82-85.
- Rahmstorf, S. 1995. Bifurcations of the Atlantic thermohaline circulation in response to changes in the hydrological cycle. *Nature* 378: 145-167.
- Reeh, N. 1991. Parameterisation of melt rate and surface temperature on the Greenland ice sheet. *Polarforschung* 59: 113-128.
- Reeh, N., Mayer, C., Miller, H., Thomsen, H.H. and Weidick, A. 1999. Present and past climate control on fjord glaciations in Greenland: Implications for IRD-deposition in the sea. *Geophys. Res. Lett.* 26: 1039-1042.
- Reeh, N. and Starzer, W. 1996. Spatial resolution of ice-sheet topography: Influence on Greenland mass-balance modelling. *Rapport Grønlands Geologiske Undersøgelse*: 85-94.
- Rignot, E.J., Gogineni, S P., Krabill, W.B. and Ekholm, S. 1997. North and Northeast Greenland ice discharge from satellite radar interferometry. *Science* 276: 934-937.
- Roullet, G. and Madec, G. 2000. Salt conservation, free surface and varying levels: a new formulation for ocean general circulation models. *J. Geophys. Res.* 105: 23,927-23,942.
- Sadourny, R. and Laval, K. 1984. January and July performance of the LMD general circulation model. In: *New perspectives in climate modeling*. Berger, A. and Nicolis, C. (Eds). Elsevier Press, Amsterdam: 173-197.
- Sheng, J. and Zwiers, F. 1998. An improved scheme for time-dependent boundary conditions in atmospheric general circulation models. *Clim. Dyn.* 14: 609-613.
- Sneyers, R. and Vandiepenbeeck, M. 1981. *Les normales du réseau thermométrique belge*. Publications, Série A, N°106, Institut royal météorologique de Belgique, Publications, Brussels: 34 p.
- Stephens, G.L. 1978. Radiation profiles in extended water clouds. II. Parameterization schemes. *J. Atmos. Sci.* 35: 2123-2132.
- Strass, V.H. and Fahrback, E. 1998. Temporal and regional variation of sea ice draft and coverage in the Weddell Sea obtained from upward looking sonars. In: *Antarctic sea ice: physical processes, interactions and variability*, *Antarc. Res. Ser.*, vol. 74. Jeffries, M.O. (Ed). Amer. Geophys. Union, Washington, D.C.: 123-139.
- Sundqvist, H. 1981. Prediction of stratiform clouds: Results of a 5-day forecast with a global model. *Tellus* 33: 242-253.

- Tartinville, B., Campin, J.-M., Fichefet, T. and Goosse, H. 2001. Realistic representation of the surface freshwater flux in an ice–ocean general circulation model. *Ocean Modell.* 3: 95-108.
- Tartinville, B., Cavanié, A., Ezraty, R. and Fichefet, T. 2001. Arctic multiyear ice coverage: A model study. Submitted to *J. Geophys. Res.*
- Terray, L., Sevault, E., Guilyardi, E. and Thual, O. 1995. Ocean–Atmosphere–Sea-Ice–Soil user’s guide and reference manual OASIS 2.0. CERFACS, Toulouse.
- Therry, G. and Lacarrère, P. 1982. Improving the eddy kinetic energy model for the planetary boundary-layer description. *Bound. Layer Meteor.* 25: 63-88.
- Tiedke, M. 1989. A comprehensive mass flux scheme for cumulus parameterization in large-scale models. *Mon. Wea. Rev.* 117:1179-1800.
- Van de Wal, R.S.W., Wild, M. and de Wolde, J. 2001. Short-term volume changes of the Greenland ice sheet in response to doubled CO₂ conditions. *Tellus* 53B: 94-102.
- Vincent, L.A. et al. 2000. Homogenized daily temperatures for trend analyses in extremes over Canada. 12th Conference on Applied Climatology, Ashville, N.C., May 8–11, 2000.
- Wadley, M.R., Bigg, G.R., Stevens, D.P. and Johnson, J.A. 1996. Sensitivity of the North Atlantic to surface forcing in an ocean general circulation model. *J. Phys. Oceanogr.* 26: 1129-1141.
- Washington, W.M., Meehl, G.A., VerPlank, L. and Bettge, T.W. 1994. A World Ocean model for greenhouse sensitivity studies: Resolution intercomparison and the role of diagnostic forcing. *Clim. Dyn.* 9: 321-344.
- Weatherly, J.W., Briegleb, B.P. and Large, W.G. 1997. Sea ice and polar climate in the NCAR CSM. *J. Clim.* 11: 1472-1486.
- Webster, P.J. 1994. The role of hydrological processes in ocean-atmosphere interactions. *Rev. Geophys.* 32: 427-476.
- WMO 1989. Calculation of monthly and annual 30-year standard normals. Report of a WMO meeting of experts, Washington D.C., March 1989, WMO-TD N°341, World Meteorological Organization, Geneva, 11 p.

RECENT ENSO AND PALEO ENSO OF THE LAST 1000 YEARS IN LAKE TANGANYIKA

MUSÉE ROYAL D'AFRIQUE CENTRALE
SECTION DE GÉOLOGIE GÉNÉRALE
Leuvensesteenweg 13
B-3080 TERVUREN
Jean KLERKX (coordinator, promoter CG/DD/10A)
Pierre-Denis PLISNIER

UNIVERSITÉ CATHOLIQUE DE LOUVAIN (UCL)
INSTITUT GÉOLOGIQUE - UNITÉ PAGE
Place L. Pasteur 3
B-1348 LOUVAIN-LA-NEUVE
Eric LAMBIN (promoter CG/DD/10B)
Suzanne SERNEELS

UNIVERSITÉ CATHOLIQUE DE LOUVAIN (UCL)
DÉEP. DE GÉOGRAPHIE ET DE GÉOLOGIE
LAB. DE TÉLÉDETECTION ET D'ANALYSE RÉGIONALE
Place Louis Pasteur 3
B-1348 LOUVAIN-LA-NEUVE
Guy SERET (promoter CG/DD/10C)
Pierre FRANCUS

UNIVERSITEIT GENT - LAB. PLANTKUNDE
VAKGROEP MORFOLOGIE, SYSTEMATIEK EN ECOLOGIE
K.L. Ledeganckstraat 35
B-9000 GENT
Wim VYVERMAN (promoter CG/DD/10D)
Christine COCQUYT

TABLE OF CONTENTS

ABSTRACT	1
1. INTRODUCTION	5
2. RESEARCH TEAMS	6
3. STRATEGY AND STEPS FOLLOWED BY THE PROJET	6
4. BACKGROUND: ENSO TELECONNECTIONS IN AFRICA	7
5. MATERIAL AND METHODS	9
5.1 Multidisciplinary database	9
5.2 Pre-processing for recent climate data	10
5.3 Lake temperature	11
5.4 Recent climate- stability relationships	12
5.5 ENSO-fisheries relationships	13
5.6 Search for recent El Niño signal in AVHRR time series	14
5.6.1 Remote sensing time series	14
5.6.2 Preliminary analyses	14
5.6.3 Final methodology for remote sensing analysis	15
5.6.4 Pre-processing for teleconnection	15
5.6.5 Teleconnection with climatic variables	16
5.6.6 Teleconnection with remote sensing variables	16
5.6.7 Testing the spatial coherence in teleconnection	16
5.6.8 ENSO effect on lake surface temperature	17
5.6.9 Analysis of land-use changes around the lake	18
5.7 Sampling of the sediment cores	18
5.8 Sub-sampling and core description	18
5.9 Dating	21
5.9.1 210Pb dating	21
5.9.2 14C dating	22
5.10 Methods for thin-sections	22
5.10.1 Core description	22
5.10.2 Thin-sections preparation	22
5.10.3 Thin-section observation	24
5.10.4 Electron microscopy	24
5.11 Methods for paleo-diatoms analysis	27
5.11.1 Subsampling of the sediment cores	27
5.11.2 Preparation of the permanent diatom slides	27
5.11.3 Diatom analysis	28
5.11.4 Analysis of the diatom data set	28
5.12 Other micro-paleontological analysis	28

5.13	Phytoplankton research	29
6.	RESULTS	30
6.1	Recent ENSO	30
6.1.1	Lake Tanganyika	30
6.1.1.1	<i>Teleconnection with climate data</i>	30
6.1.1.2	<i>Teleconnections with lake stability</i>	32
6.1.1.3	<i>ENSO effect on lake surface temperature and NDVI</i>	37
6.1.1.4	<i>Teleconnections with fisheries catches</i>	38
6.1.1.5	<i>Recent trend in climate, limnology and fisheries</i>	41
6.1.2	Eastern African region	45
6.1.2.1	<i>Preliminary analyses</i>	45
6.1.2.2	<i>Teleconnections with climate data</i>	47
6.1.2.3	<i>Teleconnections with remote sensing data</i>	50
6.1.2.4	<i>Spatial coherence in teleconnections</i>	52
6.1.2.5	<i>Clustering of stations based on their pattern of teleconnections with SST4</i>	56
6.1.2.6	<i>Analysis of land-use changes around the lake</i>	56
6.1.2.7	<i>Teleconnections with Indian Ocean data</i>	58
6.2	Sedimentology and algology	58
6.2.1	Description of the sediment cores	58
6.2.1.1	<i>Sediment cores taken near Kasaba</i>	59
6.2.1.2	<i>Sediment cores taken near Kapembwa</i>	61
6.2.1.3	<i>Sediment core taken near Msamba at 1000m water depth</i>	66
6.2.1.4	<i>Sediment core taken near Kipili at 1200m water depth</i>	66
6.2.2	Dating	67
6.2.2.1	<i>²¹⁰Pb dating</i>	67
6.2.2.2	<i>¹⁴C dating</i>	67
6.2.3	Thin-section analyses	68
6.2.3.1	<i>Sediment core taken near Kipili at 1200 m water depth</i>	68
6.2.3.2	<i>Sediment of the Kalemie Ridge taken at 430 m water depth</i>	72
6.2.4	Paleo-diatom analyses	74
6.2.4.1	<i>Sediment core TAN 98/9, taken near Kasaba in 500m water depth</i>	75
6.2.4.2	<i>Sediment core TAN 98/15, taken near Kipili in 1200m water depth</i>	86
6.2.4.3	<i>Sediment core TAN 98/7, taken near Kapembwa in 330m water depth</i>	89
6.3	Other micro-paleontological analyses	89
6.3.1	Sponges	89
6.3.2	Cysts of Chrysophytes and Dinophytes	92
6.3.3	Remains of Cyanobacteria	92
6.4	Recent phytoplankton research	94

7. DISCUSSION	95
7.1 Recent teleconnections	95
7.1.1 Teleconnections with ENSO near Lake Tanganyika	95
7.1.2 Recent trend in climate, limnology and fisheries at Lake Tanganyika	96
7.1.3 Hypothesis on Lake Tanganyika variability and ENSO conditions	99
7.1.4 East African region area and ENSO teleconnections	100
7.2 Sedimentology and algology	103
7.2.1 Sedimentation rate	103
7.2.2 Thin-sections analyses	103
7.2.2.1 <i>Sediment core TAN 98/15, taken near Kipili in 1200m water depth</i>	103
7.2.2.2 <i>Sediments of the Kalemie Ridge</i>	105
7.2.2.3 <i>Concluding remarks</i>	105
7.2.3 Diatom analyses	106
7.2.3.1 <i>Sediment core TAN 98/9, taken near Kasaba in 500m water depth</i>	106
7.2.3.2 <i>Sediment core TAN 98/15, taken near Kipili in 1200m water depth</i>	111
7.2.4 Other micro-paleontological analyses	111
7.2.5 Recent phytoplankton	112
7.2.6 Concluding remarks	112
8. CONCLUSIONS	113
9. ACKNOWLEDGEMENTS	116
10. BIBLIOGRAPHY	117
11. LIST OF FIGURES	126
12. LIST OF TABLES	131
13. LIST OF PAPERS PUBLISHED DURING THE PROJECT	132
14. APPENDIX	134

ABSTRACT

Lake Tanganyika is one of the oldest lakes in the world. Its present limnological cycle shows that it is very sensible to climate variability (Coulter, 1991; Plisnier *et al.*, 1999). The winds and the air temperature fluctuations influence the mixing of the lake, allowing access of nutrient-rich deeper water toward the surface where biotic production takes place. When organisms die, they accumulate into layers at the bottom of the lake, where some of them may be identified and related to the lake conditions prevailing at the time of their deposit.

Global signals of oceanic/atmospheric origin affect the local climate in East Africa and probably the hydrodynamic and the biotic environment of Lake Tanganyika. Its sediments could thus archive paleoclimatic variability partially related to world climatic variability such as ENSO (El Niño/Southern Oscillation). ENSO is a major climatic/oceanographic event characterised by the apparition every 2-10 years of a warm current in the Pacific Ocean and numerous climatic anomalies around the Pacific Ocean and in many other areas of the world. The influence of El Niño stretches across the Indian Ocean to southern Africa where it brings droughts and to equatorial Africa where it brings flooding (WMO-UNDP, 1993; IPCC, 1990).

The objective of the project was to check the possible influence of climate variability on Lake Tanganyika at two scales of time: the recent period (+/- last 50 years) and the last 1000 years. For the recent period, the project studied the teleconnections (correlation with remote climatic or proxy data) between ENSO and various data (oceanic, climatic, remote sensing, hydrological, fisheries catches...) in the Lake Tanganyika area. For the last 1000 years, paleo-signals were studied in the sediments of the lake. The finely laminated sediments were studied particularly using diatom composition and thin sections analysis to detect variability of organisms as possibly related to limnological and climatic variability.

For the study of the recent period, available climate data in the Lake Tanganyika area (Tanzania, Burundi, Zambia and R.D.Congo), were processed using various statistical methods for the 1981-94 period at different time lags. The results of teleconnections with climate data were compared with remote sensing data from NOAA/AVHRR (National Oceanic and Atmospheric Administration / Advanced Very-High Resolution Radiometer) using the same procedures.

Significant ENSO teleconnections were found with average air temperature, maximum and minimum air temperature, humidity, rainfall, winds, pressure and radiation. The strongest teleconnections were found between monthly air temperature anomalies with the sea surface temperature anomalies in the west

equatorial Pacific Ocean. A time lag of 4-6 months generally gave the strongest correlation (e.g. in the range of $R=0.6$). ENSO events were characterised by average air temperature increase ($+0.26^{\circ}\text{C}$) while extreme air temperature could reach $\pm 0.8^{\circ}\text{C}$ as observed during a strong El Niño event for the recent period. During ENSO events, winds decreased but air pressure and radiation increased. The stability of the water column was reconstructed for the last 40 years using water temperature profiles and air temperature data. The results suggested a $\pm 20\%$ variability range of stability for the upper 100 m of the lake. Catches per unit of effort of the main pelagic fishes were partially correlated with ENSO for the last 30 years in two stations of Lake Tanganyika. Hypotheses of changes in hydrodynamic and upwelling intensity have been presented to explain this. More winds and lower temperature seem favourable for clupeids fishes (and possibly phytoplankton and zooplankton) while *Lates stappersi* catches are lower maybe because of lower transparency unfavourable to this visual predator.

One of the major findings of this project is that several climate and land surface attributes show a partial correlation with the fluctuation of the Pacific sea surface temperature (SST) index. These different variables are not all teleconnected to ENSO in the same way, which leads to a complex impact of ENSO on the ecosystem. The SST anomalies in the Pacific Ocean induce changes in climate variables. These ENSO-driven changes in climate induce changes in vegetation activity, as measured by changes in several remote-sensing measured variables (a vegetation index, the surface temperature etc...). The exact response of the vegetation to the ENSO-induced climate variations depends on the land cover type.

The project showed that the ENSO impact is highly differentiated in space in the investigated East African area. Many previous studies have postulated a single, region-wide impact of ENSO. It appears that the direction, magnitude and timing of this impact is controlled by the climate system at a regional scale and at a more local scale – e.g. as influenced by the presence of large lakes, local topography or proximity to the coast. Surface attributes, as determined by geology, soil and vegetation might also influence the magnitude and the time lag of the ENSO impact. Hence different zones are recognised in the East African area studied, each subject to different combinations of ENSO induced climate variations.

ENSO is however not the only source of inter-annual variability in climate conditions in the region. The changes of the variables studied, not taken into account by ENSO, could be related to the variability of neighbouring oceans as well (Saji et al., 1999). Beside ENSO, a warming was observed in the recent decades in the air temperature at Lake Tanganyika ($>0.7-0.9^{\circ}\text{C}$). This was apparently linked to a water temperature increase and a higher stability of the lake. Decreased winds and changes in fish

catches were observed during the same period for the clupeids fishes and *Lates stappersi*. Those observations suggest that the lake is sensitive to other climate variability such as the recent global temperature increase besides ENSO.

In order to study the sediments of Lake Tanganyika, an expedition was organised in collaboration with the EAWAG-team from Switzerland (Dr. M. Sturm). During this expedition, 16 cores were retrieved in the southern basin of the lake, between 330 and 1200m water depth. All cores were taken in deep water where permanent anoxic conditions exist and where bioturbation is minimal.

Thin section analysis was performed on parts of the sediments of the two cores taken on the Kalemie Ridge in 424 and 428m water depth and of one core taken in the southern basin in 1200m water depth. Both laminated as well as homogeneous layers are present in all cores. The laminated layers result from the settling of alternating organic sedimentation and terrigenous sediments. Homogeneous parts in the sediment cores probably correspond to periods with a steady settling of a continuous rain of debris.

The results of the thin section analyses support the hypothesis that the laminated sediment, present in the sediments of Lake Tanganyika, reflects a varying biogenic production. More intense winds prevailing apparently in La Niña years could possibly have favoured this increased production. Because the laminations were not continuous in the entire core and are difficult to count reliably, we do not expect them to provide a comprehensive annual reconstruction of the ENSO-signal. However, it seems possible to produce a reconstruction of the primary productivity related to the strongest ENSO events. An accurate chronology for the sedimentary records is necessary to test this hypothesis.

Sediment material for dating was taken from a core recovered near Kasaba in 500m water depth and from a core taken near Kipili in 1200m water depth. The results for the Kasaba core are the only one available at the moment. ^{14}C AMS dating indicates that the sediments between 10.5 and 11.5cm are from the historical period (830 (± 40) BP), corresponding to a sedimentation rate of about 0.134mm/y during recent periods. The sediments between 48 and 52cm depth are much older (8060 (± 60) BP), which would correspond with a very low sedimentation rate of 0.06mm/y. It is known that sedimentation rates in Lake Tanganyika have not been constant and vary considerably in the sedimentary record (Coulter, 1991). Mean reported sedimentation rates in Lake Tanganyika vary between 0.4 and 0.6mm/y (Haberyan and Hecky, 1987; Tiercelin et al., 1988; Coulter, 1991). Extremely low sedimentation rates (± 0.05 -0.25mm/y) were only reported from the Kalemie Ridge, a bathymetric high that separates the northern and southern basin (Cohen and Palacios-Fest, 1999).

The extremely low sedimentation rate, calculated for deeper parts of core taken near Kasaba and the absence of a layer rich in *Aulacoseira* (*Melosira*) species, a layer reported earlier for sediment cores from the southern basin of Lake Tanganyika (Tiercelin et al., 1988), may suggest that part of the sediment is missing, possibly because of sediment-sliding events.

High-resolution diatom analyses were performed on the upper parts of both of the above-mentioned cores. The upper 11cm of the Kasaba core consist of dark finely laminated sediments; the laminations in the upper 18cm of the Kipili core are mostly diffuse. These upper layers were analysed at a vertical resolution of 100µm and 500µm, respectively. Deeper parts of the Kasaba core were also studied at a lower resolution.

Although 230 diatom taxa were observed in the two cores studied, only a few taxa were relatively abundant. In the upper finely laminated sediments “long” *Nitzschia*’s and *Gomphonema clevei* were relatively the most important diatoms, followed by *Nitzschia lancettula*, *N. vanoyei*, *N. frustulum*, *N. fonticola* and *Gomphonitzschia spp.* The high species diversity was due to the numerous benthic taxa; although individual abundancies were generally low, these benthic taxa dominated the fossil assemblage in certain layers.

The diatom record revealed a cyclicity, with a provisionally estimated period of about 200 years, in the Kasaba core. This might be related to a 200 years cycle in the sun activity but this needs to be confirmed by data from longer or more time series. Among the diatoms, “long” *Nitzschia spp.* most clearly demonstrate this cyclicity. They are pennate, planktonic species which can replace *Cyclostephanos spp.* (centricate planktonic diatoms) in the plankton of East African lakes when Si/P ratios decrease (Haberyan and Hecky, 1987).

Benthic diatoms are potentially good indicators of lake level fluctuations, indicating the presence of nearby littoral zones (Barker, 2001). In the Lake Tanganyika cores the significant changes in the proportion of benthic diatoms may likewise indicate lake level changes. In addition, our data suggest that the interpretation of the benthic diatom assemblages might be more complicated. A notable change in the benthic assemblage was the dominance of *Gomphonema clevei* in the lower part of the sediment section studied for the Kasaba core, while in the upper layers other species were abundant. Although this pattern may reflect changes in the littoral environments in Lake Tanganyika, more needs to be known about the ecology of key taxa. Similarly, further investigation of the ecology of planktonic and facultative planktonic key-taxa, e.g. “long” *Nitzschia*’s, *Nitzschia lancettula*, *N. vanoyei*, *N. frustulum*, *N.*

fonticola and *Gomphonitzschia* spp., is needed to permit a detailed interpretation of the L. Tanganyika sediments.

The present data and work in progress illustrate the unique potential of these cores. It seems feasible to infer records of historical changes in paleo-ENSO intensity, as well as longer-term variation in regional and global climatic conditions.

The recent ENSO signal confirms thus the hypothesis that ENSO may impact significantly the climate in the Lake Tanganyika area and the mixing conditions of the lake in the actual period. It is recommended that a multidisciplinary database using recently collected information in various fields (climate-hydrodynamics-phytoplankton-fisheries) at regular sampling intervals, could provide the required information to interpret the various sediments signals and decrypt the coded information stored in the sediments.

1. INTRODUCTION

ENSO (El Niño/Southern Oscillation) is one of the major driving forces of the interannual natural variability of earth climate. Correlation with ENSO has been established world-wide including in Africa (Cane *et al.*, 1994).

Lake Tanganyika, one of the oldest lake in the world, is very sensible to climate variability. Its sediments might prove to be real archives of paleoclimatic variability. The interannual phytoplanktonic variations could to be recorded into the laminated sediments (Degens *et al.*, 1971) which constitute proxies of world interest. The IDEAL program (International Decade for the East African Lakes) has suggested that ENSO records might be found in African lakes sediments (Johnson *et al.*, 1990).

To investigate possible ENSO impact on Lake Tanganyika during the recent period and the recording of past environmental variability possibly teleconnected to ENSO, the present multidisciplinary research project was launched mainly during the period 1997-2001.

The objectives of the project were mainly:

a) to compile a database built with climatologic, limnological, remote sensing, sedimentological and agricultural data, and to study correlation with recent ENSO. The local climatic pattern would be characterised in relation with ENSO events (El Niño, La Niña). Those data would be used to study recent teleconnection in the Lake Tanganyika area.

b) to test climatic/hydrodynamic relations to describe some physical links between climatic conditions linked to ENSO variability and the lacustrine environment.

c) to analyse the sediments for the last 1000 years in relationships to paleoclimatic conditions with a high resolution.

Annually resolved tropical paleoclimatic reconstruction of the upper Holocene are of direct relevance to understanding the longer period modulation of the ENSO and monsoon phenomena (Duplessy and Overpeck, 1996). ENSO could possibly be forecasted with one or two years prediction. The aim of this study is to investigate the actual variability of climate in the Lake Tanganyika area and to retrieve sediments cores possibly able to record signals of this variability linked to paleo-climatic conditions. The aim is thus to reduce uncertainty on climatic variability and predictability thanks to the unique environmental conditions found at Lake Tanganyika.

2. RESEARCH TEAMS

Four teams were involved:

- Recent ENSO

Section de Géologie Générale (GG), Musée Royal de l'Afrique Centrale (MRAC)

Laboratoire de Télédétection et d'Analyse Régionale (GEOG), UCL

- Paleo-ENSO:

Vakgroep Biologie, Afdeling Protistologie en Aquatische Ecologie, UG

Unité de Paléontologie et Paléogéographie (PAGE), UCL

3. STRATEGY AND STEPS FOLLOWED BY THE PROJECT

The steps followed by the project during the 4 years were:

Year 1:

- Collecting data and database organisation
- Pre-processing for teleconnection
- Collecting and pre-processing of temporal series of AVHRR (NOAA)
- Preparation mission for the sampling expedition
- Bibliographic study of algologic data published on Lake Tanganyika

Year 2:

- Analyse of teleconnection for recent ENSO for the Oceanic and climate data
- Extraction of “Normalized Difference Vegetation Index” (NDVI) and surface temperature (Ts) for the Lake area
- Statistical analyse of temporal series
- Characterisation of climatic regimes (El Niño, La Niña).
- GIS analyse of teleconnection
- Sediments sampling and pre-analyse
- Description of some of the cores
- Preparation and analyse of diatoms
- Analyse of some phytoplankton samples

Year 3:

- Teleconnection with extended time series
- Map representation of teleconnection results (GIS)
- Integration (recent ENSO) of teleconnection from climate and remote-sensing data
- Statistical analyse of climatic variability (recent)
- Diatoms analyse

Year 4:

- Physical impacts of climate regimes on Lake Tanganyika
- Dating the cores
- Description of the rest of the cores
- Statistical analysis of paleo signals variability
- Integration RECENT ENSO recent and PALEO-ENSO
- Synthesis and interpretation of results

4. BACKGROUND: ENSO TELECONNECTIONS IN AFRICA

Global climate anomalies linked to the El Niño/Southern Oscillation are a major topic of scientific investigation. Since the mid-1970's, the ENSO frequency is accentuated with more intense El Niños. Recently, El Niño returned for four consecutive years between 1991 and 1994. Throughout Africa, droughts have been associated with ENSO and a number of studies using standard meteorological data have shown that south-eastern and southern Africa are major centres of ENSO teleconnection over

Africa. Most of the previous investigations on the climate teleconnection in East Africa were based on rainfall data (Nicholson and Entekhabi, 1986; Ropelewski and Halpert, 1987; Ogallo, 1987; Farmer, 1988). Nicholson (1996) used time series of rainfall data from 1901 to 1985. This study revealed that most of the peaks in rainfall in East Africa correspond to warm ENSO years in the Pacific Ocean, e.g. 1941, 1951, 1957, 1963, 1968, 1972 and 1982. During warm ENSO events, wetter conditions are observed near the equator while drier conditions are observed in southern Africa (Rasmusson and Arkin, 1985; Ropelewski and Halpert, 1987).

Besides rainfall, teleconnection studies with other climatic variables such as air temperature and air pressure have generally been included in studies at a global scale. Those studies have shown that, during warm ENSO events, air temperature is higher in most of the tropics (Diaz and Kiladis, 1992) while air pressure is higher in East Africa (Trenberth and Shea, 1987). There is no detailed study of teleconnection with ENSO in the East African region dealing with air temperature and humidity, although those are important factors for agriculture (directly or through their influence on pests). Inter-annual and seasonal variations in these climatic variables may have an impact on crop yields. Regions situated at the boundary between two biomes or ecosystems, such as semi-arid regions, are particularly sensitive to small changes in air temperature or humidity. Small changes in air temperature may also affect the thermal stability of water columns of lakes. For the Great Lakes of the African Rift, this may have a significant impact on the mixing conditions of the waters and on the primary production patterns that might then affect fish productivity (Gucinski *et al.*, 1990).

Over the past few years, several authors have studied time series of satellite images to assess the response of vegetation to inter-annual climatic variability. To investigate the existence of an ENSO signal, authors have correlated a vegetation index (the normalised difference vegetation index, NDVI) with ENSO indicators measured in the southern Pacific Ocean. Anyamba and Eastman (1996) used standardised principal component analysis to demonstrate a link between time series of NDVI data in Africa and the ENSO phenomena. Anyamba and Eastman (1996) have found a positive correlation between the 8th principal component of the African NDVI time series, and both Pacific southern oscillation index (SOI) and outgoing long-wave radiation (OLR) anomalies. They found the effect to be most pronounced in Southern Africa. However, the 8th principal component accounts for less than 1% of the total variance of the NDVI time series. Note that several authors have indicated that a relation exists between NDVI values for African vegetation and rainfall (Richard and Pocard, 1998, Eklundh, 1998, Davenport and Nicholson, 1993).

Recently, global scale vegetation index data were linked with sea surface temperature (SST) anomalies for warm and cool ENSO events (Myneni *et al.*, 1996). The similarity between the monthly SST and NDVI anomalies time series was determined by calculating the correlation coefficient at a fine spatial resolution. Three areas in Africa were identified as having a strong correlation between Pacific SST and coincident NDVI anomalies: (i) parts of eastern Africa extending towards the Horn of Africa, (ii) south-eastern Africa, and (iii) central southern Africa. Eastern Africa and the Horn of Africa showed a tendency towards wetter conditions with tropical Pacific SST warming, whereas the other areas experienced drought conditions with the ENSO warming. In another tropical region, Batista *et al.* (1997) recently found evidence of the influence of El Niño phenomena on the vegetation cover in the Amazonian region of northern Brazil. These authors state that ENSO has a multi-year impact on the vegetation. A decrease in vegetation due to ENSO-related droughts requires two years for full recovery to pre-ENSO NDVI values in northern Brazil.

Several scientists have recently adopted a more mathematical approach towards analysis of time series. Menenti *et al.* (1993) used temporal Fourier analysis of AVHRR/NDVI (Advanced Very-High Resolution Radiometer/ Normalised Difference Vegetation Index) observations for vegetation monitoring in southern Africa. They conclude that the Fourier spectra are well correlated with the ratio of net radiation to precipitation (Budyko ratio) and with vegetation types as mapped by White (1983). This approach was refined by Olsson and Eklundh (1994) who used the Fourier Series and the derivatives to depict the seasonality of the vegetation and to calculate the growing season.

5. MATERIAL AND METHODS

5.1 Multidisciplinary database

A database of 1784 **climatic stations** has been built for the countries of Central and East Africa. It contains names (official or local names), geographic coordinates, altitudes, world meteorological identification code, origin of data, CIDAT reference number.

The main climatic stations used for the teleconnection analysis are listed in appendix 1 with their geographical coordinates.

Climatic and fisheries data have been gathered for the 4 countries bordering Lake Tanganyika (Congo, Burundi, Tanzania and Zambia). Those data originate from

several sources: SERDAT, CIDAT, NOAA, MRAC, University of East Anglia (UK), Central Library of Dar Es Salaam, Tanzanian and Zambian Ministries dealing with meteorological or fisheries data. The data are general monthly average and cover mainly the period from 1960 to 1995. Older sets of data are sometimes available such as for Zambia (since the 1930's or 1940's).

Some **agricultural data** were also collected for Tanzania, Zambia and Congo. However, it was observed that those data were not exploitable due to poor quality during several periods. So, it was decided not to deal with those data and to concentrate on more reliable sets of data such as for climate and industrial fisheries.

Oceanic data: ENSO data (original data and anomalies of SST in NIÑO 1+2, NIÑO 3 and NIÑO 4 area, Southern Oscillation Index data) were acquired thanks to the Climate Prediction Centre in Washington. A set of COADS data (Comprehensive Oceanographic and Atmospheric Data Sets) was acquired through the Jet propulsion Laboratory, California.

El Niño years are defined here for mean annual SST superior to 0.5°C, and La Niña years for mean annual SST inferior to 0.5°C compared to the reference period 1963-93. The Southern Oscillation Index (SOI) is the normalised difference between the standardised anomalies of sea level pressure between Tahiti (French Polynesia) and Darwin (Australia) (Philander, 1990). SOI is negative during El Niño and positive during La Niña.

Cartographic data: a digital map of the world (CVG Map) was converted to GIS Map Info format. The layers of needed information (political boundaries, hydrographic network, main cities...) were extracted for the East African region using Arc Info before importation into Map Info format. It allowed to access and display data as needed for the analysis of teleconnection.

5.2 Pre-processing for recent climate data

Data of air temperature (max. and min.), evaporation, and humidity in Congo (1950-1959) were checked and digitized (40 to 60 stations depending on the parameters). A same work was done for the Tanzanian stations (22 stations between 1965 and 1990). Those data were added to an existing database of Zambian data (35 from 1950 to 1995 generally). They were organised in a standard way (Excel) for statistical processing.

The meteorological stations for which 90% of the data were missing for the studied periods have not been used.

Monthly anomalies for each time series were calculated using the z-score $((x_i - \mu)/std)$ with x_i being the data value for a given month in year i , μ the mean data value for that month across all years and std the standard deviation of the data value for that month across all years. Further calculations were performed on anomalies rather than on the original data.

A preliminary teleconnection study was performed. The temperature data of SST from 3 different areas in the Pacific Ocean (Niño-1+2, Niño-3 and Niño-4) and the SOI have been processed for teleconnection with a first set of climatic data in East Africa (max T°, min T° and humidity) for the 1981-94 period. It was observed that teleconnection with SST from Niño-3 and Niño-4 areas gave the strongest correlation. Further analyses were performed mainly with those data sets.

A preliminary study with 0 to 60 months time lags was first performed on a set of data from stations close to Lake Tanganyika. Further analysis used time lags between 0 and 12 months. A spatial study integrating remote-sensing and climatic data in many stations in East and South East Africa was performed with an average time lag of 6 months.

Two automatic procedures of calculations were set up. The first procedure calculates standardised anomalies for the period considered (such as 1981-94). The second procedure calculated the Pearson correlation coefficient with a step of 1 month and a time lag of 0 to 12 months between Oceanic data and the climatic series in Africa.

The Comprehensive Oceanic and Atmospheric Data Set (COADS) have been converted to smaller size files using a Fortran procedure (with F. Mercier, UCL). The period 1940-1990 has been targeted. For the preliminary analyses, we used data from the Indian Ocean.

5.3 Lake temperature

Water temperature profiles presented were acquired during the FAO-LTR project (Plisnier *et al.*, 1999). Water samples were collected every 6 weeks in 1993-94 down to 300m in the frame of 24h cycle (sampling at 12h, 18h, 24h and 06 h) using 7.4 litre capacity Limnos sampler. Bottles were lowered and raised with a hand winch. Water temperature (accuracy ± 0.1 °C) was first measured with a thermometer placed inside the water bottle. The thermometer was read as soon as the bottle reached the deck. This method was replaced in April 94 with *in situ* measurements taken down to 80 m using a digital thermometer, coupled to an oxygen meter (made by Yellow Springs Instrument Co.), with the same accuracy as before. For deeper water, the probe was

placed in the sampling bottle and read when the bottle reached the surface. Median values used the "box and whiskers" representation (Tuckey, 1977).

5.4 Recent climate- stability relationships

Stability is the work or mechanical energy in joules required to mix the entire volume of water to a uniform temperature without addition or subtraction of heat. It has been calculated to obtain the stability per unit of area (Hutchinson, 1957). Since data are available only for the first 100m for series at Lake Tanganyika (3 periods of 1 or 2 years since 1962), the stability of this layer only was calculated. As most of the temperature gradient is observed there, the changes during the year mainly concern this upper layer.

Stability is calculated as:

$$\Delta E = g \int_{-h}^0 (\bar{\sigma} - \sigma) z A(z) \delta z \quad \text{where the average density was calculated as:}$$

$$\bar{\sigma} = \frac{\int_{-h}^0 \sigma(z) A(z) \delta z}{\int_{-h}^0 A(z) \delta z}$$

The volume was calculated as:

$$V = \sum_{k=0}^K \frac{A_k + A_{k+1}}{2} (Z_k - Z_{k+1})$$

To computerise the average density, we used:

$$\bar{\rho} = \frac{1}{V} \sum_{k=0}^K \frac{\rho_k + \rho_{k+1}}{2} \frac{A_k + A_{k+1}}{2} (Z_k - Z_{k+1})$$

Finally the stability is equal to:

$$\Delta E = g \sum_{k=0}^K \left[\bar{\rho} - \frac{\rho_k + \rho_{k+1}}{2} \right] \frac{(Z_k + Z_{k+1})}{2} \frac{A_{(z_k)} + A_{(z_{k+1})}}{2} (Z_k - Z_{k+1})$$

The units are:

$$\begin{aligned} V &: \text{m}^3 \\ \Delta E &: \text{Joule} \\ \bar{\rho} &: \text{kg m}^{-3} \\ A &: \text{m}^2 \end{aligned}$$

The stability units were standardised to the surface area (joule/m²). Standardised anomalies were used for Lake Tanganyika stability (LTS) (no units). They were calculated as: (data of month x - average data for all months x) / stand. dev. of data of all months x. This is the usual way for the teleconnection data processing as anomalies are calculated for each month and variability taken into account proportionally.

First, stability of the 0-100 m layer was calculated from all the water temperature profiles available (Coulter and FAO, pers. comm.). Relationships with air temperature at Mbala for 3 sets of data of stability at Mpulungu were:

- for the period 1960-62: $R^2 = 0.46$
- for the period 1964-65 : $R^2=0.63$
- for the period 1993-95 : $R^2=0.36$

The pair of data for the 3 periods above were considered together and the relationship obtained was: $y = 1211.5x - 18681$ where y is stability (J/m²) at month m+1 and x is air temperature at month m (°C) ($R^2 = 0.45$).

5.5 ENSO-fisheries relationships

Amongst the various type of fishing (Plisnier, 1995), catches per unit of effort (CPUE) for industrialised fishermen are the most reliable and were used here (Pearce, 1992, Coenen, pers. com.). CPUE are defined for catches done by one unit of fishermen during one night of fishing. One unit of fishermen is one boat with the average number of gears and crew used by industrialised units on the lake (Coenen, 1995). Time series processing involved calculation of anomalies from the 1963-93 base period means and normalisation by the standard deviations. In addition, we have smoothed the time series using a 3 or 12 month running average as indicated.

5.6 Search for recent El Niño signal in AVHRR time series

5.6.1 Remote sensing time series

Preliminary analyses were carried out with the NOAA-AVHRR-GAC (Global Area Coverage) data set over Africa, kindly made available by the Monitoring Tropical Vegetation Unit (Joint Research Centre, Ispra, Italy). The data set is composed of daily images from January 1982 to December 1991 covering the entire African continent. The data have a spatial resolution of 5x5 km and contain six georeferenced channels from which we derived two biophysical indicators: NDVI calculated from AVHRR channels 1 and 2 and Ts computed from AVHRR channels 4 and 5. More detailed information on the processing of GAC is available in Vogt (1990) and Malingreau and Belward (1994). Maximum value compositing was applied to the data (Holben, 1986), selecting independently the maximum value of daily NDVI and Ts over a one month period (Cihlar *et al.*, 1994).

Results obtained with the GAC data set showed that the time series was not sufficiently long to detect the ENSO signal. It was therefore decided to acquire and process the NOAA/NASA Pathfinder AVHRR 8-km Land Data Set. Although the spatial resolution of this database is slightly inferior to the GAC data set, it covers the time period 1981–1994, thus including the ENSO events of 1991–1994. The data set contains 12 parameters from which we derived two biophysical indicators: NDVI (calculated from channels 1&2) and Ts computed from AVHRR channels 4 and 5 brightness temperatures. Brightness temperatures are derived by inverting the Plank equation and surface temperature is then derived through the split window method for land surfaces (Price, 1984), assuming a constant emissivity. More detailed information on the processing of PAL data is available in Smith *et al.* (1997).

The data are archived as daily grids. We applied monthly maximum value compositing to the data (Holben, 1986), selecting independently the maximum value of daily NDVI and Ts over a one month period (Cihlar *et al.*, 1994). By compositing Ts data, some part of the dynamic nature of this variable is removed while the seasonal pattern of temperature change is retained. Thus, while the compositing of NDVI data mainly removes the atmospheric contamination from time series, the compositing of Ts data also removes the information on surface dynamics related to daily variations in weather and soil moisture conditions.

5.6.2 Preliminary analyses

For a first series of analyses, based on the GAC time series, 3 areas surrounding Lake Tanganyika were selected (Plisnier *et al.*, 2000). The first area is situated near

Kigoma, the second one is north of Kalemie and a third one was selected in the south-western area of the lake basin, just south of Moba. On the time series of the 3 study areas, a principal component analysis (PCA) was performed on the monthly NDVI and Ts composites and the first 10 components were kept for further analysis. Subsequently, within these areas, sites of 65x65 km were selected and spatially averaged per month. The resulting time series of mean PCA coefficients for NDVI and Ts data were exported to a spreadsheet for further processing. Besides the PCA, two other types of analyses were performed: the averaged NDVI time profiles for the 3 study sites were detrended for the mean and seasonal variability with the program SYSTAT, before embarking on the statistical analysis. The same processing was applied to the ENSO indicators.

The averaged NDVI and Ts anomalies time series for the 3 study sites (only corrected for the mean) were used in a Fourier analysis.

Cross-correlation plots were made for all PC's of the 3 study sites with SOI, OLR, SST 1&2, SST3, SST4 and SST3&4 anomalies. Analogous to the PC data, cross-correlation plots were calculated for the NDVI time profiles and ENSO indicators.

The periodograms for the NDVI and Ts anomaly series were plotted. The periodogram shows the % of variance that is explained by each harmonic of the Fourier series. The most important harmonics are selected and compared with the Fourier series that are obtained from SOI, OLR, and the different SST anomaly time series.

5.6.3 Final methodology for remote sensing analysis

Based on the results of these preliminary analyses, a final methodology was developed, which is based on linking teleconnection between satellite derived indices (NDVI and Ts) and SST anomalies with teleconnection between climate data and SST anomalies. Besides temporal correlation, also spatial correlation patterns within the study area are examined. The satellite data used with this methodology was the AVHRR-PAL data set.

5.6.4 Pre-processing for teleconnection

Prior to the statistical analyses, all time series were standardised. Further calculations were performed on anomalies rather than on the original data. Monthly anomalies for each time series were calculated using the z-score $((x_i - \mu) / \text{std})$ with x_i being the data value for a given month in year i , μ the mean data value for that month across all years and std the standard deviation of the data value for that month across all years. The time series of all variables were smoothed using a moving

average filter over a three months period. As rainfall data were only available as total values per season for Tanzania, these data were standardised per season. The analysis of teleconnection with the rainfall data was performed separately for each season.

5.6.5 Teleconnection with climatic variables

Pearson correlation coefficients between the time series of anomalies of each of the climatic variables in East Africa and SST in the Niño 4 zone in the Pacific were calculated for each meteorological station in the study area. As it was expected that changes in Pacific SST anomalies would have an effect on the climate in eastern Africa with a delay of several months, the correlation between time series of Pacific SST anomalies and climate anomalies in East Africa was calculated for lags of one to twelve months. Critical values for the correlation were calculated at the 0.95 and 0.99 level of significance.

5.6.6 Teleconnection with remote sensing variables

Pixel-wise correlation coefficients were calculated between, on the one hand, East African NDVI and T_s anomalies and, on the other hand, Pacific SST anomalies. Lagged correlation was also used, with SST observed at steps from one to twelve months prior to the observations in East Africa. Correlation coefficients were also analysed at the 0.95 and 0.99 level of significance. The zones with a high positive or high negative correlation between NDVI or T_s anomalies in East Africa and Pacific SST anomalies were represented in a map. An additional variable combining remote sensing measurements and ground observations was computed: infrared remote sensing data combined with maximum air temperature data can be used to assess water conditions of the vegetation on a regional scale. The deviation between the mid-afternoon surface temperature (measured by satellite) and the maximum air temperature (obtained from the meteorological ground network), $(T_s - T_a)$, is related to the latent heat flux (Seguin *et al.*, 1991). The cumulative $\Sigma(T_s - T_a)$, named stress-degree-day (Jackson *et al.*, 1977), has been proven to well describe water stress of the vegetation. In this study, monthly values for $(T_s - T_a)$ were calculated for each of the stations. For T_s , the average value of 2x2 pixels at the location of the meteorological station was calculated. The average monthly maximum air temperature was used for T_a values.

5.6.7 Testing the spatial coherence in teleconnection

The analyses of teleconnection were performed independently for each variable and for each location (i.e. meteorological stations for the climate variables and AVHRR

pixels for the remote sensing variables). To understand the combined effect on the ecosystem of the ENSO-induced inter-annual variability in the climate variables, we tested the spatial coherence in the response of these different variables to ENSO.

The location of each meteorological station was identified on the remote sensing data. Hence, the correlation coefficients between Pacific SST anomalies, and each of the remotely sensed variables were extracted for the locations corresponding to a meteorological station. Then, the spatial correlation between the strength of the teleconnection at every station was computed for all pairs of climate and remote sensing variables. These spatial correlation coefficients represent the relationships in space between site-specific teleconnection and ENSO. They measure the level of spatial coherence in the response of the different ecosystem variables to ENSO. While these variables are mechanically linked, (e.g. rainfall causes green vegetation growth which leads to an increase in vegetation index; green vegetation growth is associated with an increase in evapotranspiration which leads to a decrease in surface temperature) their patterns of teleconnection are not necessarily in phase and of the same magnitude. Different time lags were used to test whether there is a delayed response to ENSO in the remotely sensed variables as compared to the climate variables measured on the ground.

The above mentioned analysis will only test the spatial coherence in the way pairs of climate and/or remote sensing variables are teleconnected to ENSO. It is also interesting to identify spatial patterns of teleconnections based on the combination of all climate and remote sensing variables. For that purpose, we applied a multivariate clustering technique to regroup the stations according to the patterns of teleconnections with SST4 for all the ecosystem variables examined in this study.

5.6.8 ENSO effect on lake surface temperature

Temperature profiles in Lake Tanganyika are apparently increasing since a few years (Plisnier, 1997 and in press). This process can either be due to a warming up related to higher air temperatures in the lake zone, or, in the south of the lake, to a decrease in the upwelling, due to decreased wind velocities (Plisnier, 1997). Tuomainen *et al.* (1997) tested the capability of AVHRR-1km data for measuring lake surface temperatures. They found that the lake surface temperature calculated with the split window technique correlated very well with the temperatures measured in the lake. NOAA-AVHRR 1km data can therefore be suitable to follow the evolution of lake surface temperature throughout the year and also allow comparison of Ts maps for the lake from different years. Working with Ts for an "El Niño" year and a normal year, might allow to analyse the impact the ENSO phenomenon has on the lake surface temperature and thus indirectly at the fisheries in Lake Tanganyika.

A series of NOAA-AVHRR 1km data from 1996 was used to interpret the evolution of lake surface temperature at a monthly interval. 1996 can be considered to be the reference year. For each of the images, the lake was isolated and a pseudo-colour image created, depicting the temperature range for the lake. The temperature scale had an accuracy of 0.2 °C. Subsequently, the images were overlaid to allow analysis of the temperature pattern throughout the year.

5.6.9 Analysis of land-use changes around the lake

Changes in land-use around Lake Tanganyika were studied for a 10-year period, based on the time series of NOAA-AVHRR data covering 1981-1991. Based on the NDVI and Ts values, a change vector magnitude (ChM) image per year was calculated (procedure see Lambin and Ehrlich, 1997). The yearly ChM values represent the deviation from the optimal vegetation conditions for a certain pixel during that year. To eliminate the influence of the climatic variability, the mean ChM per image was calculated and the image was threshold at the mean + 1 std. Pixels with a change vector magnitude higher than the threshold value were considered to have been subject to change for that particular year. The resulting set of binary images (changed-no change) was classified according to the number of times each pixel has undergone changes. The resulting map shows the change hotspots as well as the unchanged areas.

5.7 Sampling of the sediment cores

An expedition was organised to the southern basin of Lake Tanganyika in collaboration with the Swiss EAWAG team during September/October 1998. Sixteen gravity cores were taken successfully near Kasaba, Kapembwa, Msamba and Kipili (Figure 1, table I).

A second set of cores, provided by Dr. C. Scholz (previously University of Miami, currently University of Syracuse), has been retrieved from the Kalemie Ridge, a bathymetric high which separates the northern and southern basin of the lake (Figure 2) The cores were collected in 1997 using a gravity corer (TG48) and a piston corer (TG50).

5.8 Sub-sampling and core description

The sixteen cores were not opened all at the same time. In December 1998, a first series of cores were opened in collaboration with the EAWAG team, supervised by Dr. M. Sturm. Five sediment cores were cut longitudinally and photographed by the EAWAG team. The description and the sampling for sedimentological studies and for

diatom analysis were done at Kastanienbaum by the Belgian team. Sampling of the upper part of the cores was very difficult due to the rather liquid state of its sediments.

A second series of cores were cut longitudinally in October 2000, one half was kept at EAWAG, the other one was taken to Gent. All opened cores were photographed and described in Kastanienbaum by the EAWAG team. Samples for diatom analysis were taken at Gent, samples for sedimentological analysis were taken from the halves kept at EAWAG.

Table 1: List of the cores taken in the southern basin of Lake Tanganyika during the September/October 1998 expedition with indication on the location, the water column depth and the core depth.

Core number	Date	Location	Water column Depth (m)	Latitude (° S)	Longitude (° E)	Core depth (cm)
TAN 98/1	01/10/1998	Kasaba 1	300	8.332865	30.66392	105
TAN 98/2	01/10/1998	Kasaba 1	300	8.332865	30.66392	55
TAN 98/3	01/10/1998	Kasaba 2	400	8.332400	30.66118	37
TAN 98/4	01/10/1998	Kasaba 2	400	8.332400	30.66118	40
TAN 98/8	01/10/1998	Kasaba 2	400	8.332400	30.66118	73
TAN 98/6	01/10/1998	Kasaba 3	500	8.333330	30.66666	42
TAN 98/9	01/10/1998	Kasaba 3	500	8.333330	30.66666	107.7
TAN 98/13	01/10/1998	Kasaba 3	500	8.333330	30.66666	71.5
TAN 98/7	02/10/1998	Kapembwa	330	8.534780	30.77159	72
TAN 98/10	02/10/1998	Kapembwa	330	8.534780	30.77159	110
TAN 98/11	02/10/1998	Kapembwa	330	8.534780	30.77159	112
TAN 98/12	02/10/1998	Kapembwa	330	8.534780	30.77159	105.5
TAN 98/16	02/10/1998	Kapembwa	330	8.534780	30.77159	107
TAN 98/14	02/10/1998	Kapembwa	330	8.534780	30.77159	73
TAN 98/5	29/09/1998	Msamba	1000	7.843700	30.61160	33.5
TAN 98/15	27/09/1998	Kipili	1200	7.442460	30.44164	113

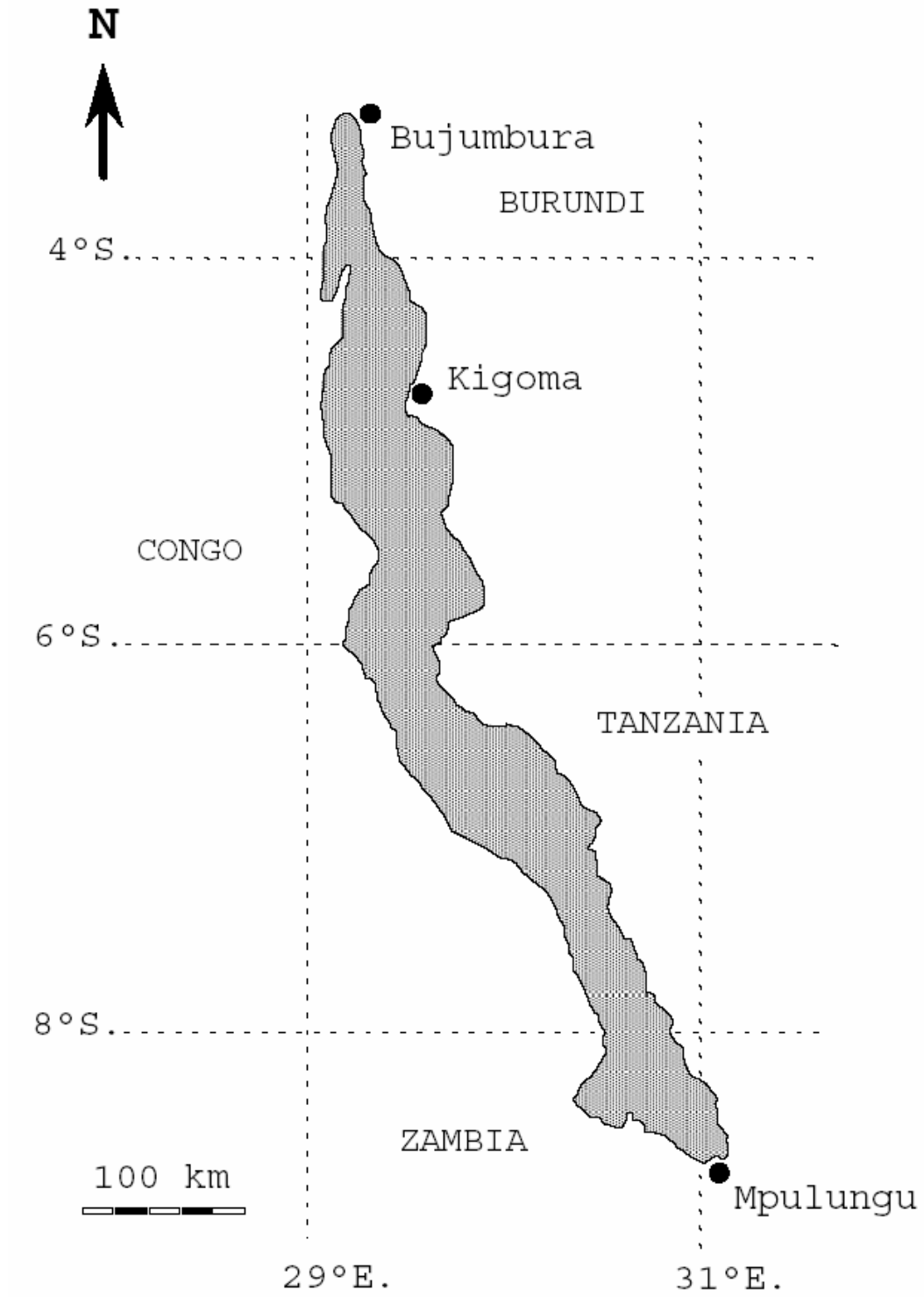


Figure 1: Map of Lake Tanganyika showing the sediment core sample stations. Code names of sediments cores analysed are shown.

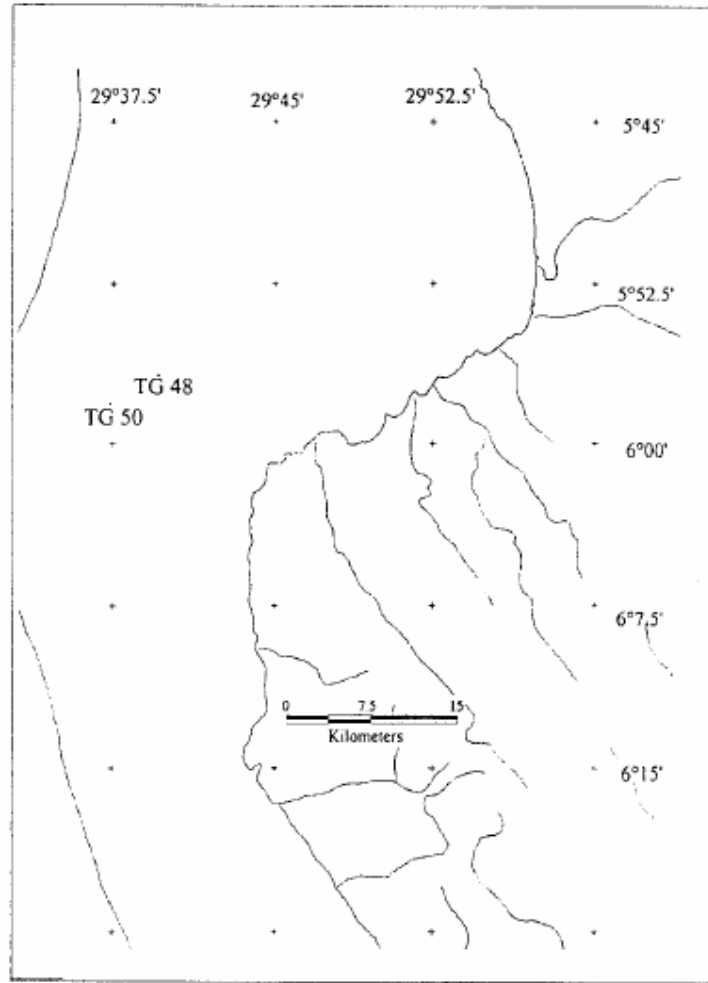


Figure 2: Map of Lake Tanganyika showing the sediment core sample stations on the Kalemie Ridge TG48 and TG 50.

5.9 Dating

5.9.2 ^{210}Pb dating

^{210}Pb is an unstable by-product of a long series of radiogenic decay processes originating from the decay of the long lived radio-isotope ^{238}U . The flux of ^{210}Pb to the lakes is influenced by several factors such as the atmospheric input, particle size to which it is bound, etc. The short half-life (22.3 years) of ^{210}Pb makes it ideal for dating of material from the recent past (100-200 years) (Appleby, 1997).

^{210}Pb profiles of the upper 10cm of five cores (TAN 98/5, TAN 98/7, TAN 98/9, TAN 98/12, TAN 98/13) were measured in the EAWAG laboratory (Switzerland) under supervision of Dr. M. Sturm.

5.9.3 ¹⁴C dating

The radiogenic isotope of carbon, ¹⁴C, is produced in the atmosphere by the interaction of cosmic radiation with ¹⁴N. In the atmosphere the free carbon oxidises to CO₂ which is taken up by plants via photosynthesis. With a rather long half-life (5730 year), ¹⁴C is ideal for dating of organic matter from the late Quaternary lake sediments.

In case fossil plant fragments are absent in the sediment cores, dating can be done by ¹⁴C Accelerator Mass Spectrometry (AMS). This involves the direct counting of the relative proportions of ¹⁴C, ¹³C and ¹²C in rather small amounts of organic matter (mg) in core material.

Two samples of core TAN 98/9 were dated with ¹⁴C AMS, the first sample being taken between 10.5 and 11.5cm, the second between 48 and 52cm depth. Material from core TAN 98/15 was also sent for dating, taken between 2.5 and 3.0cm sediment core depth.

All AMS dating were done at the Institute of Particle Physics at the Swiss Federal Institute of Technology Zurich, Switzerland. All ¹⁴C dates are reported both as uncorrected radiocarbon years BP and as corrected calendar dates (AD and BC). The last mentioned dates were used in the graphics and for the sedimentation rate calculations.

The calibration dates are in the 2 σ range (95% confidence limit) and are calculated using the Program CalibETII (Niklaus et al., 1992). Due to the variation in the date range of the calibration curve, several possible date variations are possible. Only the variations with the greatest probability are given (as percentage in table 7).

5.10 Methods for thin-sections

5.10.1 Core description

Sediment cores have been described using standardised protocols (PALE, 1993). Among other, the structure and texture of the sediment, and the Munsel chart colour were noted. Colour photographs have been taken on fresh cut sections.

5.10.2 Thin-sections preparation

Subsampling for thin-section has been performed using the method described in Francus and Cosby (in press). Sub-sampling boxes were constructed in-house from aluminium sheeting, which have been acquired from a local printing company at a

nominal cost, as the material is a waste product in the production of newspaper. Holes were punched along the bottom of the box to aid the impregnation process, which is the final step in chip preparation. The final product was a 0.2 mm-thick disposable aluminium box, 18 cm long x 2 cm wide x 0.7 cm deep. The boxes were placed on the surface of the sediment and without difficulty pushed by hand into the sediment (Figure 3).

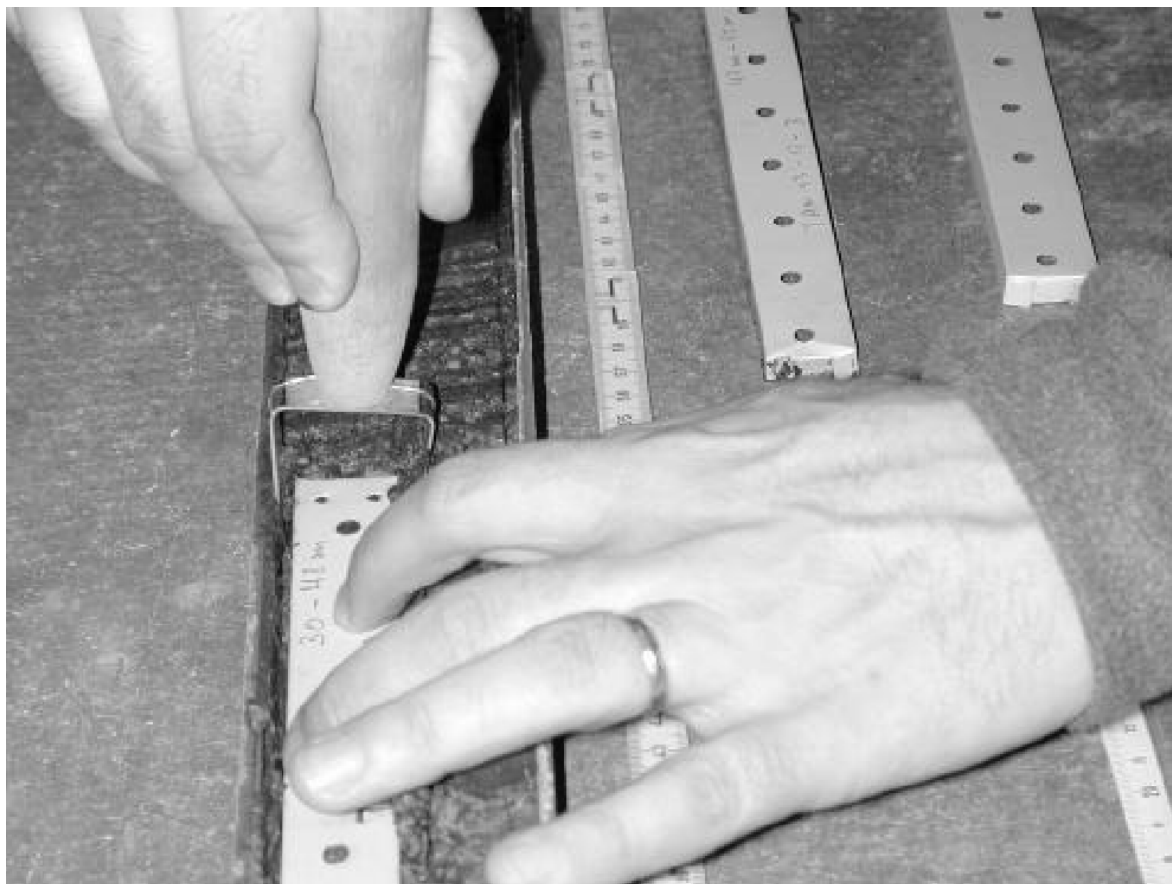


Figure 3: Sampling operation for core TAN98/9, in EAWAG Duebendorf (Switzerland). Here is displayed the simple cheese-cutter-like subsampling device cutting the sediment underneath the sampling aluminium box.

Boxes were positioned with a ~ 1 cm overlap for continuous sub-sampling. A simple, cheese-cutter-style device was used for sub-sampling sediment with little clay and water content, and using the newly developed electro-osmosis technique for the more clayey sediments. Then impregnation was performed using a freeze-drying technique (von Merkt, 1971; Lotter and Lemcke, 1999). Thin-sections have been cut right through the middle of the impregnated chip to avoid any disturbance to the upper and lower faces due to the sub-sampling cut or core opening cut, respectively. From the 18 cm long impregnated slabs, three ~ 7 cm long chips are cut with a 45° angle to the bedding to insure the recovery of an entire sedimentary succession. This

technique does not impart any orientation to the sediment fabric (Kuehl et al. 1988), although cracks may develop (Pike and Kemp, 1996). Cracking, however, does not significantly affect the primary depositional fabrics, and, where present, the cracks can easily be recognised.

5.10.3 Thin-section observation

Thin sections were digitised at 1440 dpi using the transparency capabilities of an Agfa DuoScan™ flat bed scanner (De Keyser, 1999). Large-scale prints of the thin-sections were used as a location map for subsequent work at the scanning electron microscope (SEM), and for illustration purpose. Large prints and petrographic microscope observations were used for the construction of sedimentary logs of the studied sections. Views of interest under the microscope have been digitised using a Fuji™ HC-300Z Digital camera, at a resolution of 1280 x 1000 pixels.

5.10.4 Electron microscopy

Thin sections were uncovered and carbon-coated for electron microscope examination, using a SEM equipped with a Backscattered Electron (BSE) detector. The microscope was operated at 20 kV and a working distance of 19 mm. Images of 512 x 512 pixels were digitised using the video output of the microscope. Latest work has been done using a 4Pi™ acquisition system that allows images to be retrieved at a resolution up to 4000 x 4000 pixels. The epoxy resin used for impregnation of thin sections has a light atomic weight, and therefore a lower backscattered electron coefficient. The interacting volume between the beam and the specimen is only 1—2 µm deep (Krinsley *et al.*, 1998), limiting the occurrence of object superposition. Digitised pictures were processed on Power Macintosh computers (G3 and G4), using the public-domain NIH Image program, v 1.61 (developed at the U.S. National Institutes of Health and available on the Internet at <http://rsb.info.nih.gov/nih-image/>). First, the Region of Interest (ROI) was manually selected to ensure the measurement of a single sedimentary unit. Then, contrast was enhanced using the built-in function of NIH-Image. This operation consists of stretching the grey-level-value histogram to completely fill the range of 256 grey levels. Because settings remained constant during the acquisition of most of the images used in this study, this operation makes grey intensities of BSE images comparable. An image-analysis processing layout is applied to the 256 grey-scale BSE images. The image processing was conducted almost automatically by a specifically designed macro (Figure 4) filtering to reduce noise (median filter/contrast/hybrid median filter), thresholding, and binary image edition (fill interior blanks/suppress less than 20 pixel objects/watershed segmentation) (Francus 1998; Russ 1999; <http://www.geo.umass.edu/climate/francus/>).

Processing produces black-and-white images, where white pixels represent the clay-rich sedimentary matrix and black pixels represent objects (i) to be measured (e.g. clastic grains, organic debris, diatoms) (Francus, 1998). On each object, i , the following are measured (Figure 5): (1) the area (A), calculated by counting the number of contained pixels; (2) lengths of the major (L) and the minor (l) axes; and (3) angle (α) between the horizontal and the major axis L , measured counter-clockwise. Data are exported to a spreadsheet for further processing.

In detrital sediments, beds, layers or laminae result from variations of the composition, size, shape orientation and packing of elements of the sedimentary structure. Indices are defined to estimate quantitatively all those parameters. They are extensively discussed in Francus (1999).

The size of the grains is estimated by the equivalent disk diameter, D_0 [as 1]:

$$D_0(\mu m) = 2\sqrt{\frac{A(\mu m^2)}{\pi}} \quad [1]$$

where A is the area of the object (Francus, 1998).

The shape is estimated from [2]:

$$R_i = \frac{4A}{\pi L^2} \quad [2]$$

Quantified information about the orientation could also be obtained computing the resultant vector Θ [3] and its strength S [4]. Doing so, one casts off pre-established limits that are orientation classes.

$$\tan\Theta = \frac{\sum_i^n p_i \sin \alpha_i}{\sum_i^n p_i \cos \alpha_i} \quad [3]$$

$$S = \frac{\sqrt{\left(\sum_i^n p_i \sin \alpha_i\right)^2 + \left(\sum_i^n p_i \cos \alpha_i\right)^2}}{\sum_i^n p_i} \quad [4]$$

$$\text{where } p_i = \left(\frac{l}{L} - 1\right)D_0 \quad [5]$$

$P\%$ is a phase percentage as:

$$P\% = \left(\frac{\# \text{ black pixels}}{\# \text{ image pixels}}\right) \times 100 \quad [6]$$

H_i index measures the "horizontality" of the objects [7] and is discussed extensively in Francus (2001).

$$H_i = \left(\frac{l}{L} - 1\right) \left(\left(\frac{l}{L} \cos(2\alpha) \right) \cos(2\alpha) \right) \left(\frac{D_0 - MD_0}{s} \right) \quad [7]$$

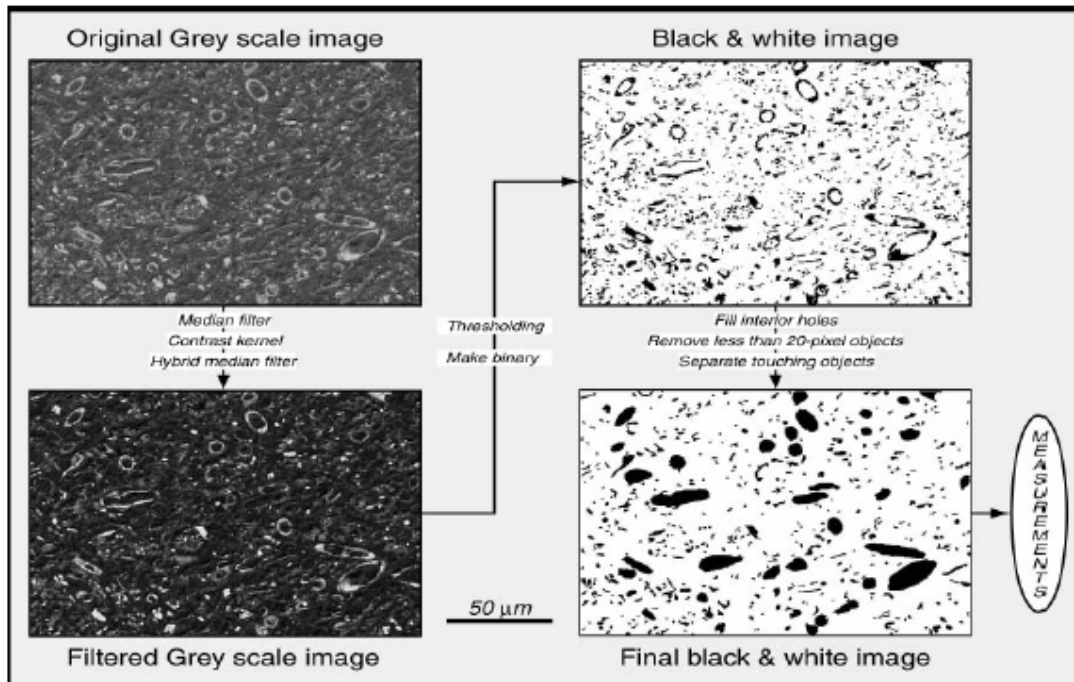


Figure 4: Image processing steps used to obtain measurable images. Example from a BSE image, Lake Tanganyika. Resolution is 1.7 pixels/ μm for regular image, but using the high resolution 4pi system, and high magnification (X500), the resolution can reach up to 20 pixels/ μm . Processing images and computing indices takes about 1 minute/image.

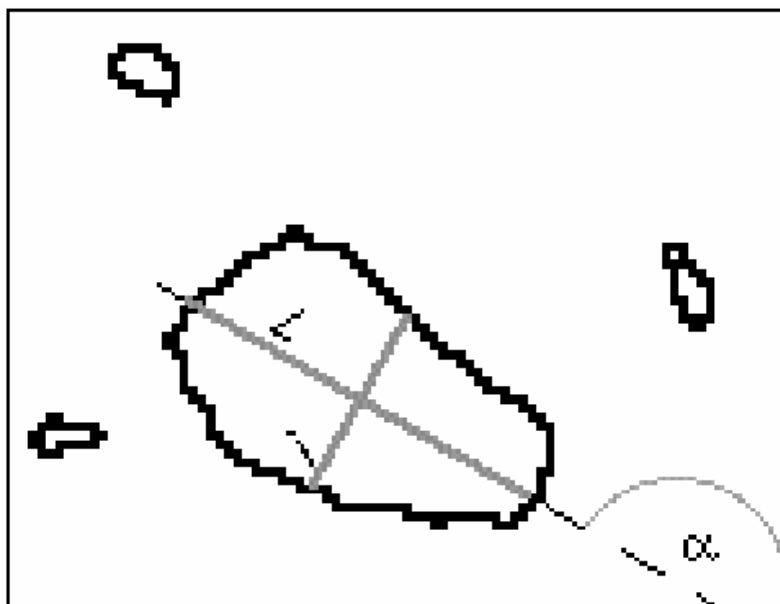


Figure 5: Detail of a binary image. Measurements on each object i : major (L) and minor (l) axes and angle α between horizontal and major axis L .

5.11 Methods for paleo-diatoms analysis

5.11.1 *Subsampling of the sediment cores*

Core material, sampled from the longitudinally opened cores by means of small Al-boxes, was subsampled for diatom analysis by means of a “microtome”, specially designed for this purpose.

Core TAN 98/9, taken near Kasaba in 500 m water depth, was chosen to be first studied; the upper rather fluid part of the core was sampled successfully. Because of its fluidity, the subsampling was done in a cold chamber. Every 100 µm was sampled for the upper 11 cm using the “microtome”. As the aim of the Paleo-part of the ENSO project was the study of sediments of the last 1.000 year, deeper layers of the core were not so finely sampled. A small amount of sediment material (mg) from each visible lamination was taken using a small spatula.

Core TAN 98/15, taken near Kipili in 1200 m water depth was the second studied core. The subsampling for diatom analysis was done every 500 µm for the upper 15 cm using the “microtome”.

Core TAN 98/7, taken near Kapembwa at 330 m water depth was also sampled every 100µm for the upper 2.5 cm using the “microtome”. As the black, finely laminated sediments of upper part of this core almost entirely lacking, with exception of 1.5cm, we decided not to continue the subsampling of this core in the ENSO project.

5.11.2 *Preparation of the permanent diatom slides*

The sediment material was put in small glass tubes (8x40 mm), after measuring the weight of these tubes. Wet weight was calculated; for dry weight material was sampled at regular intervals and was put during 24 h in an oven at 60 °C.

Depending on the amount of sediment material, a known number of aqua destillata was added. Using a micro-pipette, a known volume (40-400 µl) was put on a cover glass. After evaporation, the material was amounted in NAPHRAX, a traditional imbedding resin for diatom analysis (refraction index: 1.710).

No treatment of the sediment material was done. Usually an oxidation (with peroxide and acetic acid) is performed on core material for diatom analysis. We choose not to treat the material for two reasons:

- Firstly the amount of organic matter was relative low and the amount of material for the diatom analysis was very small, sometimes not even one mg. The chance to loose material during the oxidation and the rinsing process was too high.
- Secondly by not treating the material, the slides can also be used to observe remains of non-siliceous organisms, e.g. heterocysts of Cyanobacteria.

5.11.3 Diatom analysis

For each investigated permanent slide, a total of 500 diatom valves were counted. The counts were transferred to percentage data.

As all permanent slides were made quantitatively, and as for each investigated slide the counted area was noted, all counts could be converted to numbers of cells per dry/wet weight.

5.11.4 Analysis of the diatom data set

The percentage abundance of major diatom taxa and ecological/functional groupings were represented in a diagram using the program TILIA, a program specially designed for analysis of pollen (and diatoms) of sediment core material. With this program, a cluster analysis (CONISS), taken into account the depth sequence of the samples, can be performed and different zones in the sediment core can be determined.

The data were also analysed by a PCA (principal component analysis) and DCA (detrended correspondence analysis) using the program CANOCO (Jongman *et al.*, 1987).

Time series analyses were performed on the data set, using a Fourier analysis.

5.12 Other micro-paleontological analyses

Fresh-water sponges are abundant in the littoral zone of Lake Tanganyika. Several endemic taxa, erected as well as encrusting species are known from the lake. Little is known, however, of their ecology. The abundance of siliceous skeletal sponge-elements (spicules) in sediment material might reflect turbidity, wave activity and/or grazing intensity in the littoral of the lake. Counting of sponge spicules was done during the diatom analysis. The abundance of sponges, expressed as number of spicules per 500 diatom valves, in relation to the diatoms was analysed.

As mentioned in paragraph 5.11.2. permanent slides were made of untreated sediment material. This allows also the investigation of other rests from micro-organisms. Resting stages of Chrysophytes, Dinophytes and Cyanobacteria belong to the possible expected remains of micro-organisms.

Cysts of Chrysophytes: Studies on seasonal variations in Lake Tanganyika have revealed that Chrysophytes are important with a maximum at the end of the wet season, beginning of the dry season (April-May) in the pelagic of the northern basin (near Bujumbura and near Kigoma) (Hecky *et al.*, 1978; Hecky and Kling, 1981). In the littoral zone, Chrysophytes seems to be less important and were never abundant (Cocquyt *et al.*, 1991).

Cysts of Dinophytes: No references to the importance of Dinophytes in the pelagic of Lake Tanganyika can be found. In the littoral of the northern basin, Dinophytes were not very important during the sampling period of 1986-1987 (Cocquyt *et al.*, 1991). However, blooms of these algae were regularly observed in the littoral of the southern basin (near Mpulungu, 17 October 1995, Plisnier, pers. obs., and observed also by G. Cronberg, pers. comm.).

As for the sponges, the abundance of cysts was calculated during the diatom analysis and expressed as number per 500 diatom valves.

Cysts of Cyanobacteria: Cyanobacteria are very important in Lake Tanganyika. Blooms were already described in the middle of the 20th (Symoens, 1955). As above, the abundance of Cyanobacteria remains was studied during the diatom analysis.

5.13 Phytoplankton research

Seasonality in the phytoplankton composition and productivity was described by Hecky *et al.* (1978) and Hecky and Kling (1981) for the pelagic zone of Lake Tanganyika and for the littoral zone along the Burundian coast (Cocquyt *et al.*, 1991, Cocquyt 1999a, Cocquyt 1999b). For both zones, successions on higher taxonomic levels (Cyanobacteria/Chlorophyta/Diatoms) were observed.

Phytoplankton samples were taken monthly, from 25 February till 15 June 1998, 2 km off Kigoma by C. O'Reilly (U.S.A.). Samples were fixated in situ with a lugol solution and investigated with an inverted-microscope, at a magnification of 400 x.

The location of the sample station was chosen off Kigoma to be able to compare these data with the data of Hecky *et al.* (1978) and Hecky and Kling (1981). Although the locations of the 1975 and the 1998 campaign were not exactly the same by lack of precise information of the sample station and by the restricted possibility C.

O'Reilly had to execute the sampling. The 1998 sampling was probably done somewhat more nearshore (2 km off the shore), which may cause a greater influence of littoral zone on species composition in the samples.

6 RESULTS

6.1 Recent ENSO

6.1.1 Lake Tanganyika

6.1.1.1 Teleconnection with climate data

The lagged correlation with several climatic variables for different periods has first been explored for a 60 months time lag with a 3 month running average processing. The results are presented in figure 6. The teleconnection of air temperature at Bujumbura (Figure 6), for the period from 1963 to 1987, reached a maximum after 3-4 months and then decreased until non significant values were obtained after one year. The strongest correlations were obtained with data from NIÑO-3 area (SST3) and NIÑO-4 area (SST4). The inverse correlation is significant with SOI for the same periods as could be expected from the inverse relationship between SST and SOI (Philander, 1990). In Mbala, at the South of the Lake, the correlations with air temperature were strong during 15 months. Further analysis, with data processed for running average of 12 month, for the period 1981-94 confirmed the positive correlation between air temperature and sea surface temperature in the Niño-4 area significant for a time lag up to 12 months (table II). The variation of these values was not wide. The most significant time lag also appeared to be around 4 months in the North of the lake and 7 months in the South. The close relationships between air temperature at Bujumbura and Mbala and SST4 may be well observed at figure 7. The El Niño events are clearly observed in this figure.

On average air temperature was between 0.24°C (Mbala) and 0.54°C (Bujumbura) higher during El Niño years than during La Niña years for the period 1952-94. Increase of annual average air temperature for years corresponding to El Niño events could reach 1.0°C in Bujumbura and 0.83 °C in Mbala, as during the strong 1982-83 El Niño. These rises are remarkable when compared with monthly fluctuations at these near-equatorial latitudes; e.g. they correspond to 59 % at Bujumbura and 24 % at Mbala of the amplitude of monthly air temperature during an average annual cycle. Such an average annual cycle is presented at figure 8.

Table II: Correlation (*r*) between air temperature at Bujumbura and Mbala and SST in Niño-4 area (running average of 12 months) at different time lags for the period 1981-1994.

Time lag (months)	AAir T°-SST4	
	Bujumbura	Mbala
0	0.62	0.40
1	0.66	0.44
2	0.68	0.48
3	0.69	0.51
4	0.70	0.54
5	0.69	0.56
6	0.68	0.57
7	0.66	0.58
8	0.63	0.58
9	0.59	0.57
10	0.54	0.56
11	0.50	0.54
12	0.44	0.53

The max. and min. air temperature at Kigoma and Mbala also show positive correlation as it could be expected from the average air temperature. More details are given appendices 2 and 3.

At both stations (Bujumbura and Mbala), the teleconnection with air pressure was positive with ENSO warm event (from 0 to 4 months time lag in the north and 9 months in the south for SST4). This means that higher pressure in this area could influence the wind pattern in a way significantly related to ENSO variability as confirmed below (Figure 6).

The teleconnection with precipitation was weak and non significant in the north of the lake (period 1963-87). It was not significant at Mbala for the period 1963-94 (Figure 6).

The wind data showed inverse teleconnections with each SST set of data at Bujumbura for the period 1963-87 (best correlations from no lag until 4 months later) and Mbala (significant from 5 to 23 months time lag and higher correlation with a 12 month time lag) (Figure 6). However, several years of data are missing for Mbala and this needs supplementary data. The existence of those data is doubtful given the very few stations in the Lake Tanganyika area. Those preliminary results show however that ENSO event seem tied with decreased wind speed in the Lake Tanganyika area.

Solar radiation at Bujumbura is positively correlated with air temperature ($r= 0.46$) and with SST4 ($R= 0.57$ to 0.60) with a 0 to 3 months time lag for the 1963-1988 period for which data were available (Figure 9).

Those preliminary analyses with data from stations neighbouring the lake showed that all climatic variables gave significant teleconnections with ENSO. The El Niño years appear significantly correlated with higher air temperature, radiation, higher atmospheric pressure and lower wind speed.

6.1.1.2 *Teleconnections with lake stability*

Lake temperature profiles, as recorded in 1993-94 and 1994-95, show that by far the largest part of annual temperature variation occurs in the 0-100 m layer for three stations of the lake (Figure 10).

Temperature accounts for 95% of the density variation in Tanganyika (Tietze, 1982) and at the high water temperatures (range 24 - 28°C; average difference 2.3°C between epilimnion and hypolimnion) stratification is in fact stable and apparently permanent. Stability of stratification in the upper 100m, where the thermocline is situated, was calculated for available water temperature profiles (Dubois, 1958; Coulter, 1968, 1991; Plisnier *et al.*, 1999) and compared with climatic conditions prevailing in those years. Since only a few years of lake temperature (hence stability) data are available, and given the close correlations between air temperature and lake stability (table III), we used air temperature at Bujumbura and Mbala as a proxy for stability in the upper 100m in order to investigate the continuous nature of overall trends over a period of about 40 years.

Table III: Correlation between monthly average of water stability and air temperatures at the south and north ends of the lake for different time periods for a time lag of 1 month.

Stability (0-100m) vs air temperature			
Site	Period	R ²	Signif.
South End	1960-62 (1)	0.456	p<0.01
	1964-65 (2)	0.634	p<0.01
	1993-95 (3)	0.360	p<0.05
	sets (1) to (3)	0.418	p<0.01
North End	1972-73	0.292	NS
	1993-95	0.211	p<0.05

Stability of Lake Tanganyika appears linked to ENSO phenomena. This is expressed by correlations between LTS (Lake Tanganyika Stability) and SOI ($R^2 = 0.30, p < 0.01$) in figure 11 (using SOI as an index of ENSO). Stability increased significantly during El Niño periods (eg. +8.9 % during the 1982-83 El Niño) and decreased by -12.8 % during the 1989 La Nina) (Figure 11). More field data on the lake collected during various ENSO events and a 3D ECO-HYDRO model could detail this in further studies.

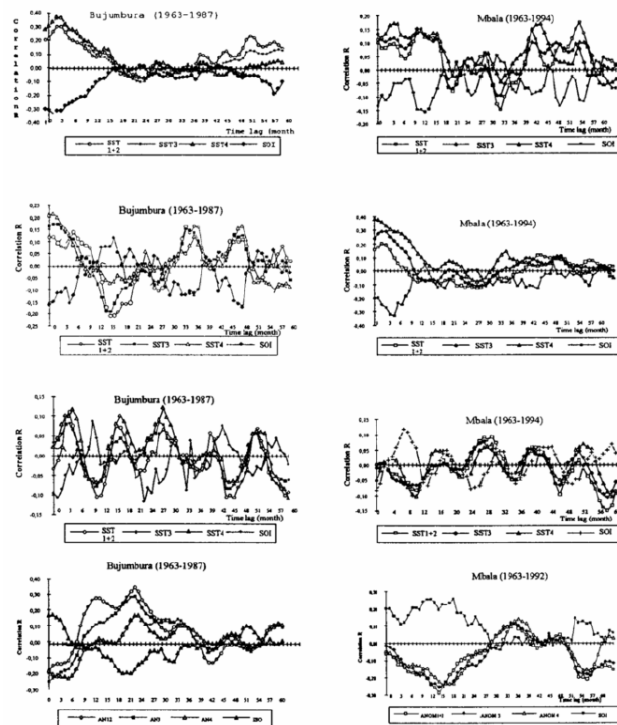


Figure 6: Teleconnections between anomalies of air temperature (A), air pressure (B) and precipitations (C) and wind speed (D) with SST anomalies in Niño1+2; Niño3, Niño4 and the SOI at time lags from 0 to 60 months.

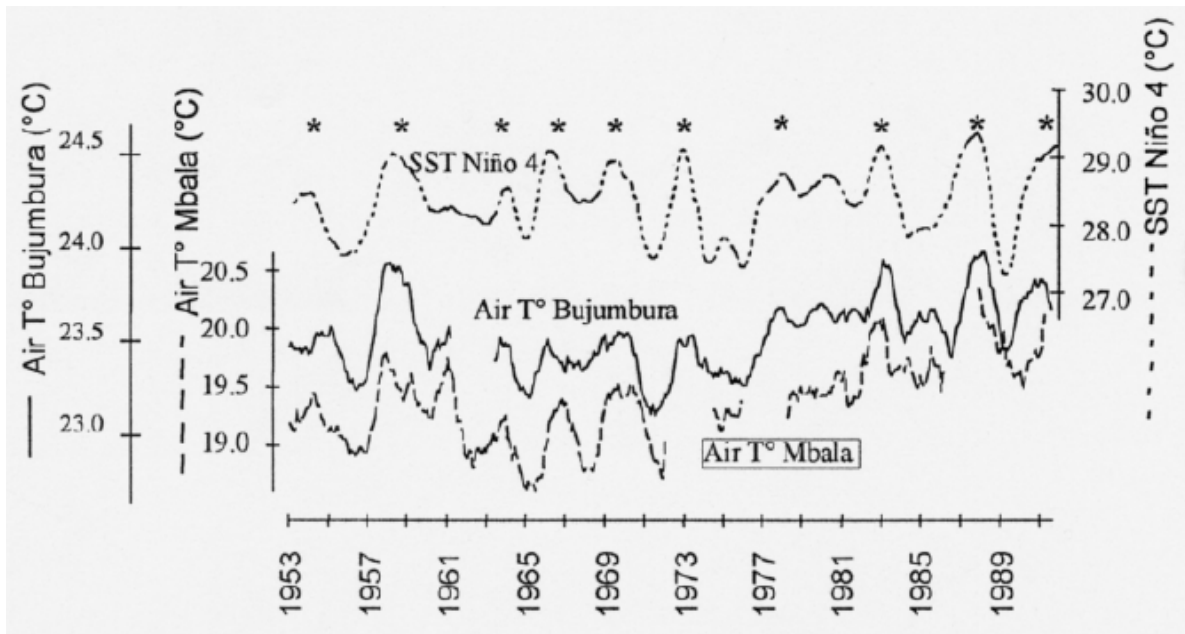


Figure 7: Teleconnections between anomalies of air temperature (A), air pressure (B) and precipitations (C) and wind speed (D) with SST anomalies in Niño1+2; Niño3, Niño4 and the SOI at time lags from 0 to 60 months.

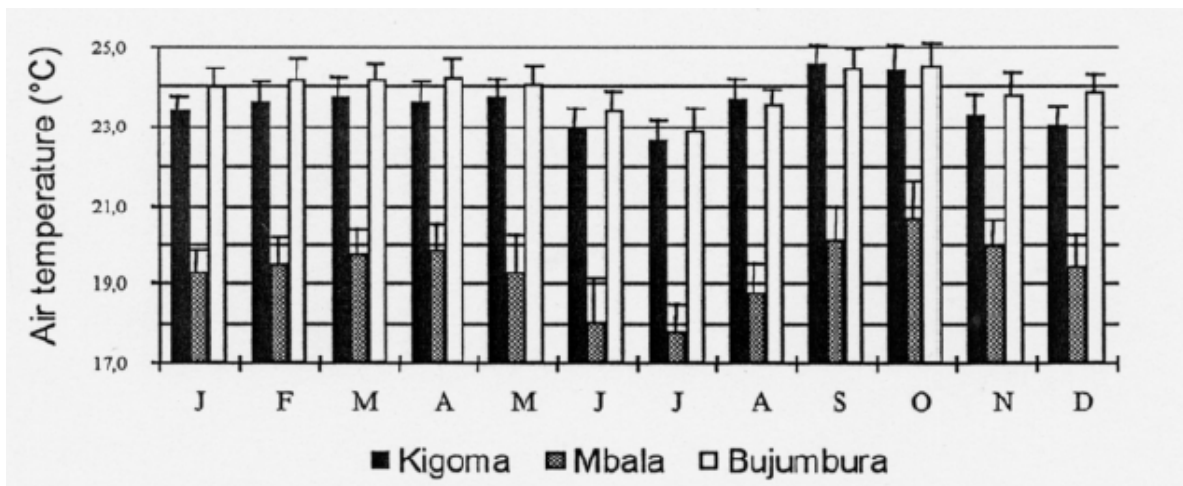


Figure 8: Monthly average air temperature at three stations near Lake Tanganyika for the 1965-1993 period (standard deviations are shown).

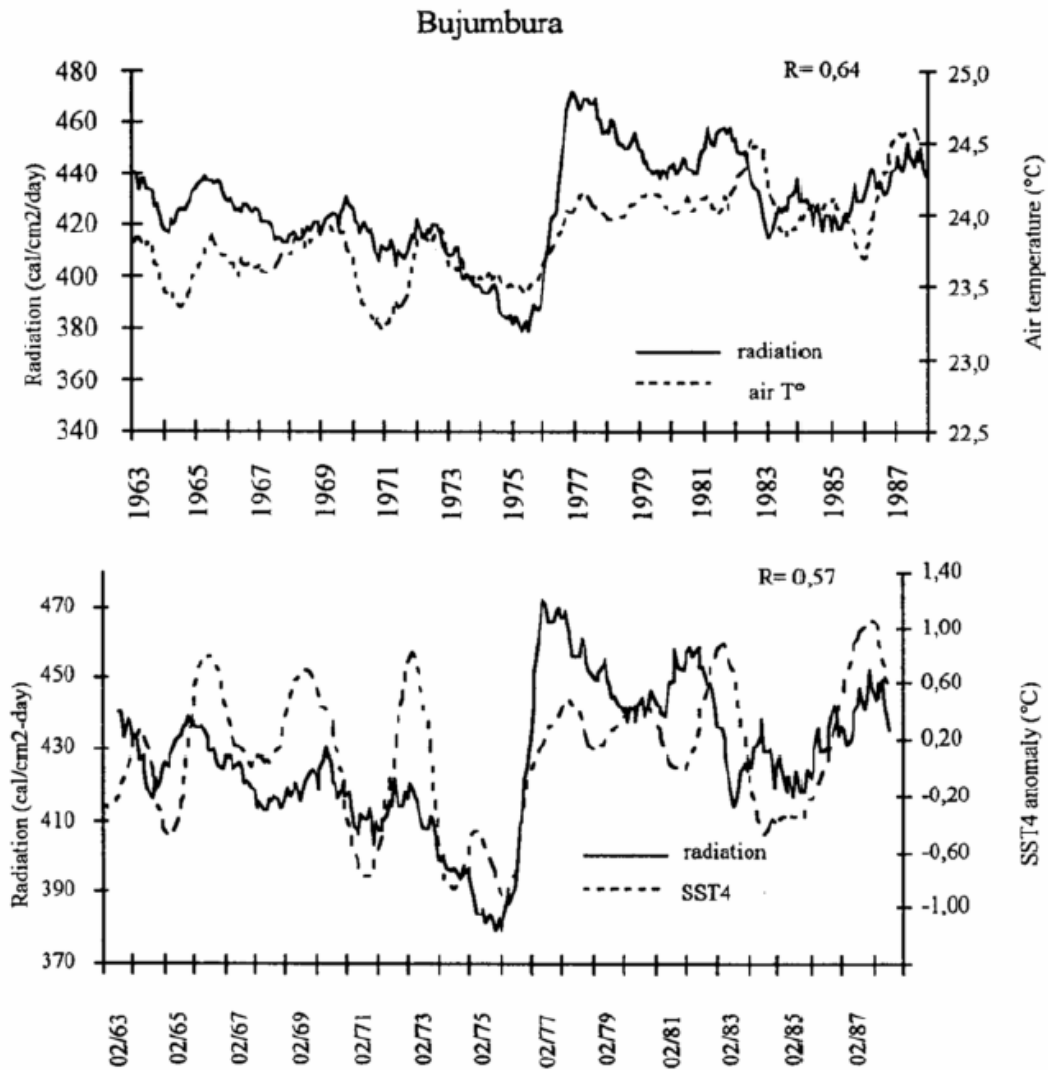


Figure 9: Time series of (A) radiation and air temperature in Bujumbura (no time lag) and (B) radiation in Bujumbura and SST4 (7 months time lag).

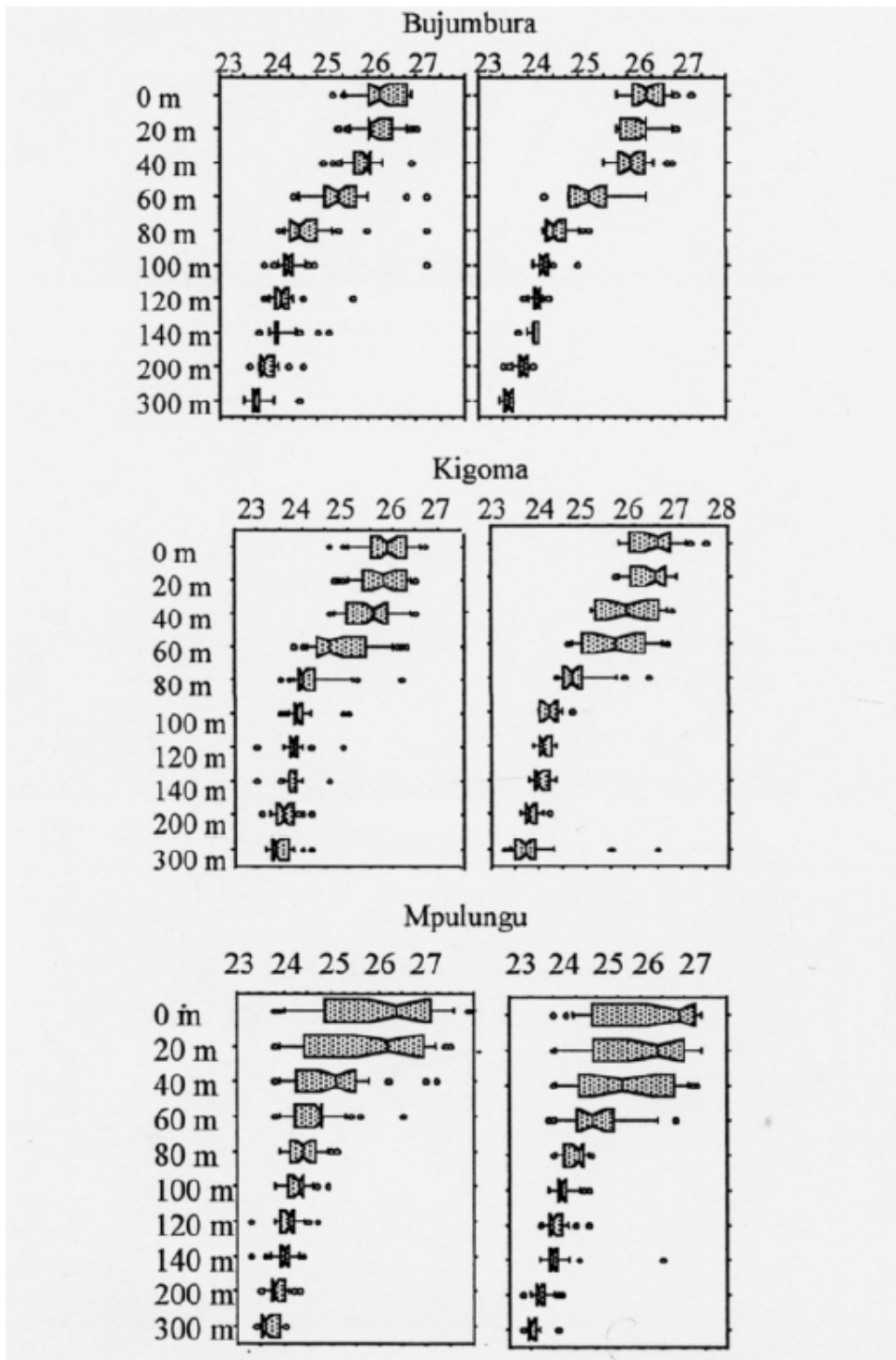


Figure 10: Median vertical profile of water temperature from bi-weekly sampling in 1993-94 at three stations of Lake Tanganyika.

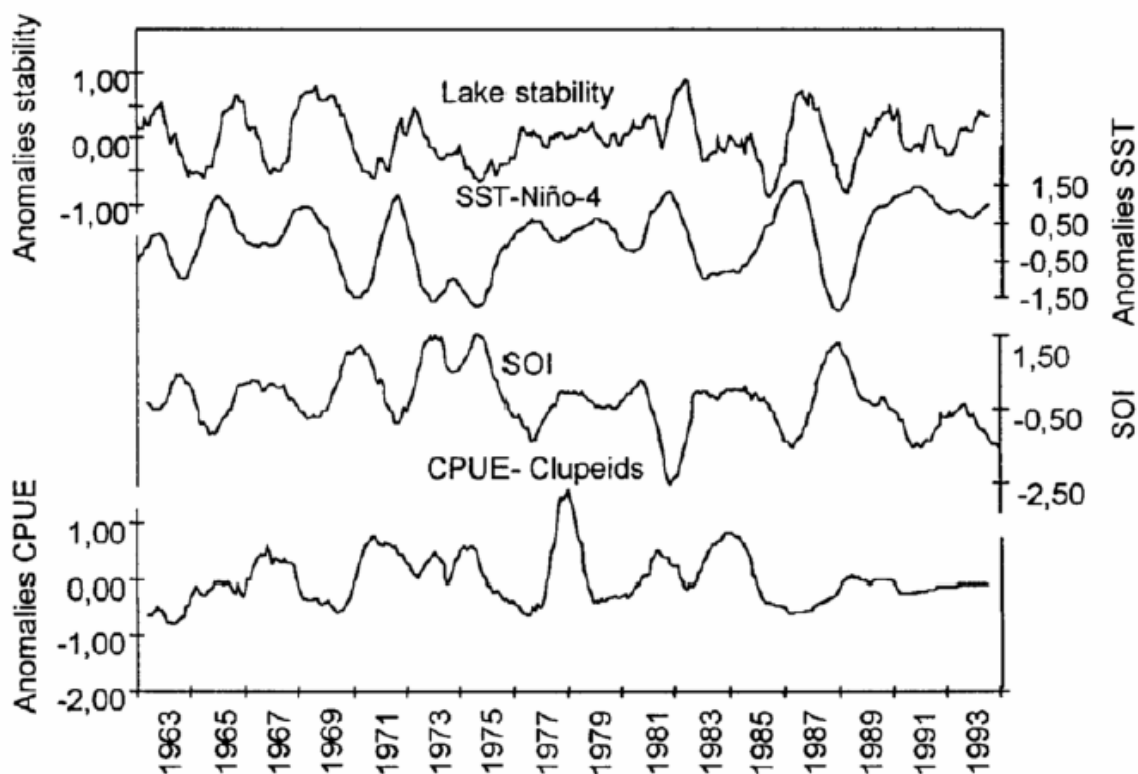


Figure 11: Twelve month running mean of (a) standardized stability anomalies near Mpulungu (b) standardized SST anomalies in NINO4 area (c) Southern Oscillation Index (SOI) (d) standardized catches per unit of effort (CPUE) of clupeids fishes at Mpulungu. Anomalies are departure from the 1993-94 base period means and are normalized by the mean annual standard deviation. The series have been de-trended.

6.1.1.3 ENSO effect on lake surface temperature and NDVI

Data analysis has shown that in April, just before the arrival of the SE monsoon winds and the start of the dry season, the water temperatures in the northern half of the lake are colder than temperatures measured in the southern half. As the monsoon winds start blowing, warm epilimnion water accumulates in the north, causing an upwelling of deep cold waters in the southern part of the lake. By the end of September at the end of the monsoon winds, areas of cold and warm water can be found all over the lake. In November, there is again a slow built up of warm waters in the southern tip of the lake. Towards the north, the water gradually gets colder.

To study the impact of ENSO on lake surface temperature from NOAA-AVHRR, data at 1km resolution had to be acquired for a typical El Niño year. Readily available products are tailored for land observations but water bodies are masked in these products. Hence the need to buy data which were processed particularly for water applications. Due to limited funds, this has not been feasible.

NDVI data could theoretically be used to estimate chlorophyll concentration in Lake Tanganyika. However, other researchers (Huttula and Podsetchine, 1997; Tuomainen *et al.*, 1997) found that the daytime concentration of chlorophyll is zero in the water column at the thin surface of the lake, while satellite data only measures the water column at this thin surface. It is thus not possible to measure chlorophyll concentrations based on AVHRR-NDVI data.

6.1.1.4 *Teleconnections with fisheries catches*

The catches of clupeids in the south and north of the lake are positively correlated ($p < 0.01$) to the southern oscillation index (SOI) linked to El Niño from 1963 to 1993 (Figure 12). The most significant relationship ($r = 0.58$) was found in the south between the mean SOI for February and March and the yearly difference in the CPUE from the 1963 to 1993 mean for clupeids caught between June and September (3 to 6 months later than the SOI). This is also presented in figure 11 showing not only relationships between CPUE of clupeids in the south of the lake and SOI but also the SST4 and the reconstructed stability curve of the lake during the 1963-94 period.

In the north, the relationship was significant ($r = 0.62$) between the mean SOI for February and March and the yearly difference in the CPUE from the 1976 to 1994 mean for clupeids caught from November to January, 8 to 10 months later than the SOI values (Figure 13 B).

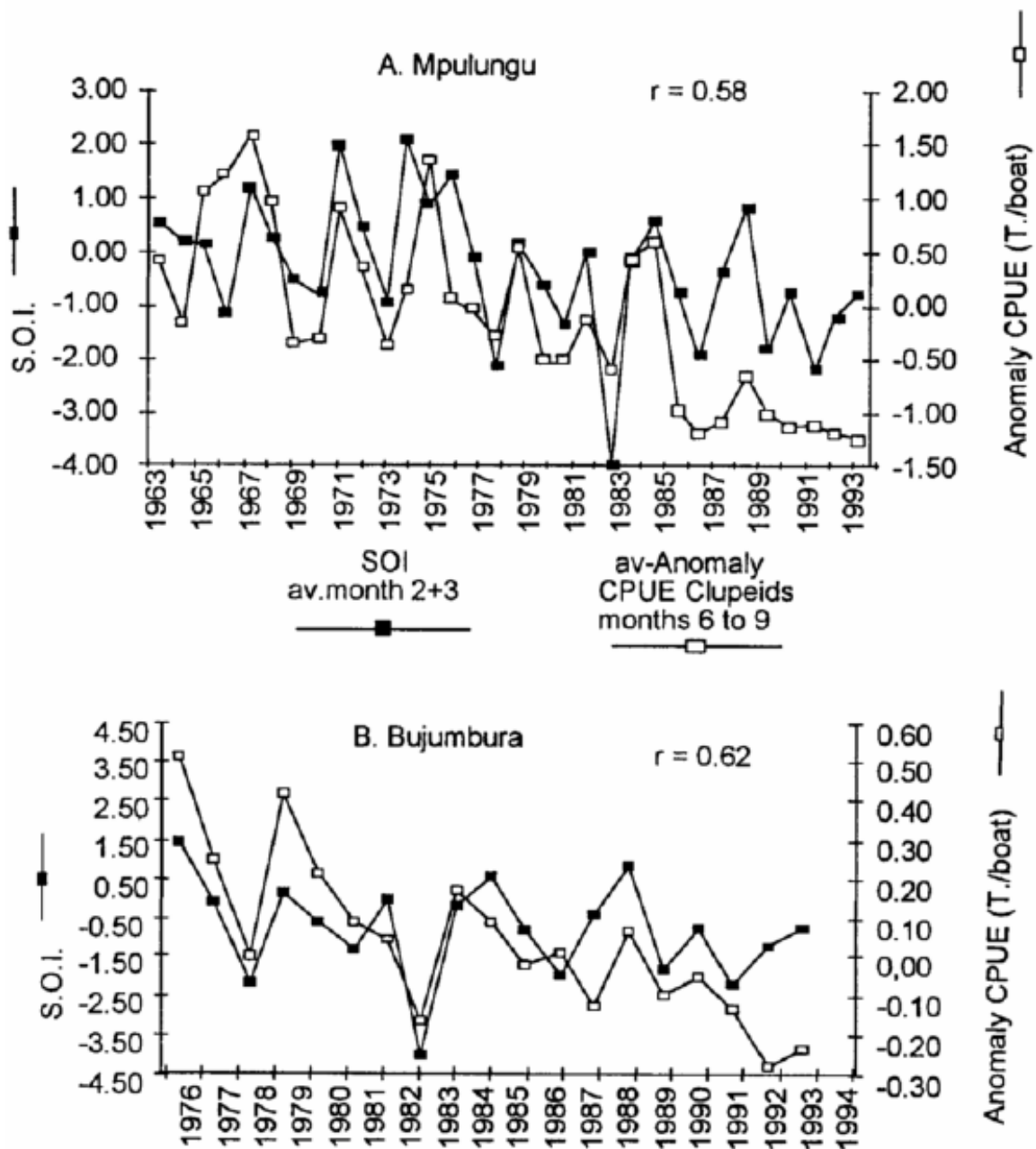


Figure 12: Teleconnection between the southern oscillation index (SOI, mean for February and March) and anomalies of catches per unit of effort (tonnes) of clupeids in (A) Mpulungu, CPUE for June to September, 1963-94. (B) Bujumbura, CPUE for November to January, 1976-94 (All correlations are statistically significant ($p < 0.01$). (Month 11 is November of year 0, month 13 is January of year 1).

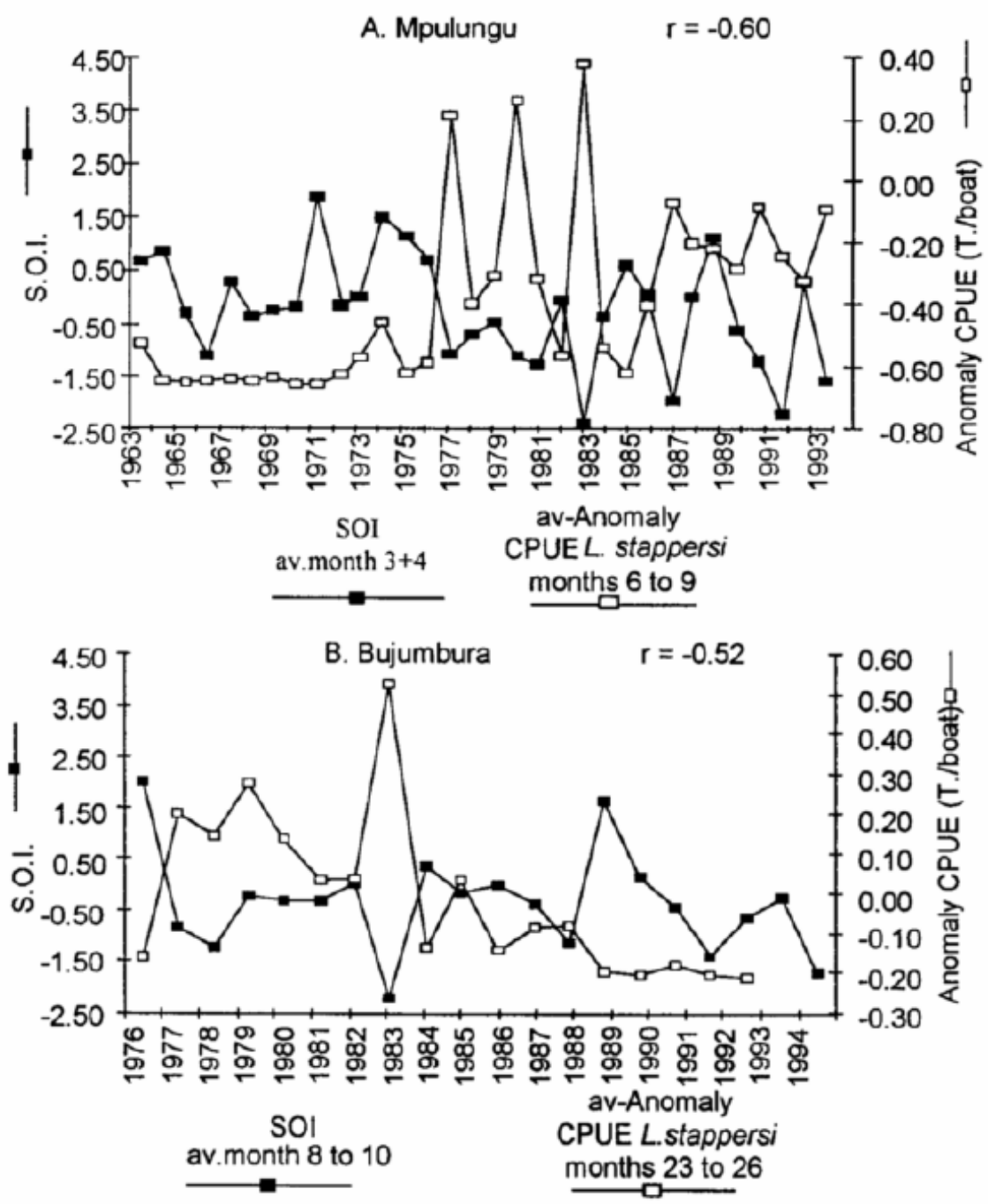


Figure 13: Teleconnection between the southern oscillation index (SOI, mean of March to April in the south and August to September in the north) and anomalies of catches per unit of effort (tonnes) of *L. stappersi* in (A) Mpulungu, CPUE for June to September (month 6 to 9), 1963-94. (B) Bujumbura, CPUE for November to February (month 23 to 26), 1976-94. (All correlations are statistically significant $p < 0.01$ at Mpulungu and $p < 0.05$ at Bujumbura) (month 11 is November of year 0, month 26 is February of year 3).

The CPUE of *Lates stappersi* was negatively correlated with the Southern Oscillation Index (Figure 13). The most significant relationship ($r=-0.60$) was found in the south (Figure 13 A) between the mean SOI for March and April and the yearly difference in the CPUE from the 1963 to 1994 mean for fish caught between June and September (3 to 6 months later than the SOI). In the north the relationship was significant ($r=-0.52$) between the mean SOI for August to October and the yearly difference in the CPUE from the 1976 to 1994 mean for fish caught from November to February, 13 to 16 months later than the SOI (Figure 13 B).

It is interesting to note that in 1983, a very strong El Niño year, the catches of clupeids were particularly low near Bujumbura (low also at Mpulungu) while inversely, CPUE of *L. stappersi* showed strongest peaks at Bujumbura and Mpulungu.

6.1.1.5 Recent trend in climate, limnology and fisheries

For air temperature, a recent trend could be identified. It showed a strong increase in average air temperature from 1961 to 1994; specifically $0.87\text{ }^{\circ}\text{C}$ ($r^2 = 0.552$) at the north of the lake (Bujumbura) and $0.95\text{ }^{\circ}\text{C}$ ($r^2 = 0.627$) at the south of the lake (Mbala). The increase was well marked since the end of the 70's as can be observed at figure 14. The mean increase, based on this linear regression of monthly data, was $0.7\text{ }^{\circ}\text{C}$ at Bujumbura Airport and $0.9\text{ }^{\circ}\text{C}$ at Mbala Airport.

Lake Tanganyika's position and geographical orientation make it particularly dependent upon regular unidirectional SE trade winds from May to September. This has an important effect on the tilting of the epilimnion. Water movements (progressive wave and reactivation of internal waves) follow the shift in direction of the monsoons. Wind speed has decreased in recent years in the Lake Tanganyika area (Plisnier, 1997). The monthly mean wind speed at Bujumbura fluctuated between 1.4 and 2.5 m/s on average from 1964 to 1979. Between 1986 and 1990 the range was between 0.5 to 1.5 m/s. At Mbala the mean wind also decreased from the end of the 1970's to a minimum in 1983. The winds increased afterwards but not to the previous levels. However data were incomplete. Although subjective, it is interesting to note that local fishermen at the south of the lake have reported wind strength diminishing from the late 1970's (pers. comm.).

The temperature profiles in the upper part of Lake Tanganyika (0-100m) near Bujumbura were significantly ($p<0.01$) warmer in 1993-94 than in 1956-57 (Dubois, 1958). The mean surface temperature near Bujumbura was $25.99\text{ }^{\circ}\text{C}$ in 1956-57 compared to $26.33\text{ }^{\circ}\text{C}$ in 1993-94. The difference in temperature between the above time periods was greater during the dry season, 0.40°C , than during the wet season, 0.28°C . In the south of the lake, Coulter (1968) recorded a range in surface temperatures from 23.3°C to 24.0°C and mentioned that the water column was

frequently homothermal at c. 23.5°C. During the dry season of 1993-94, the FAO/LTR project has recorded all surface temperature >23.90 °C in the south.

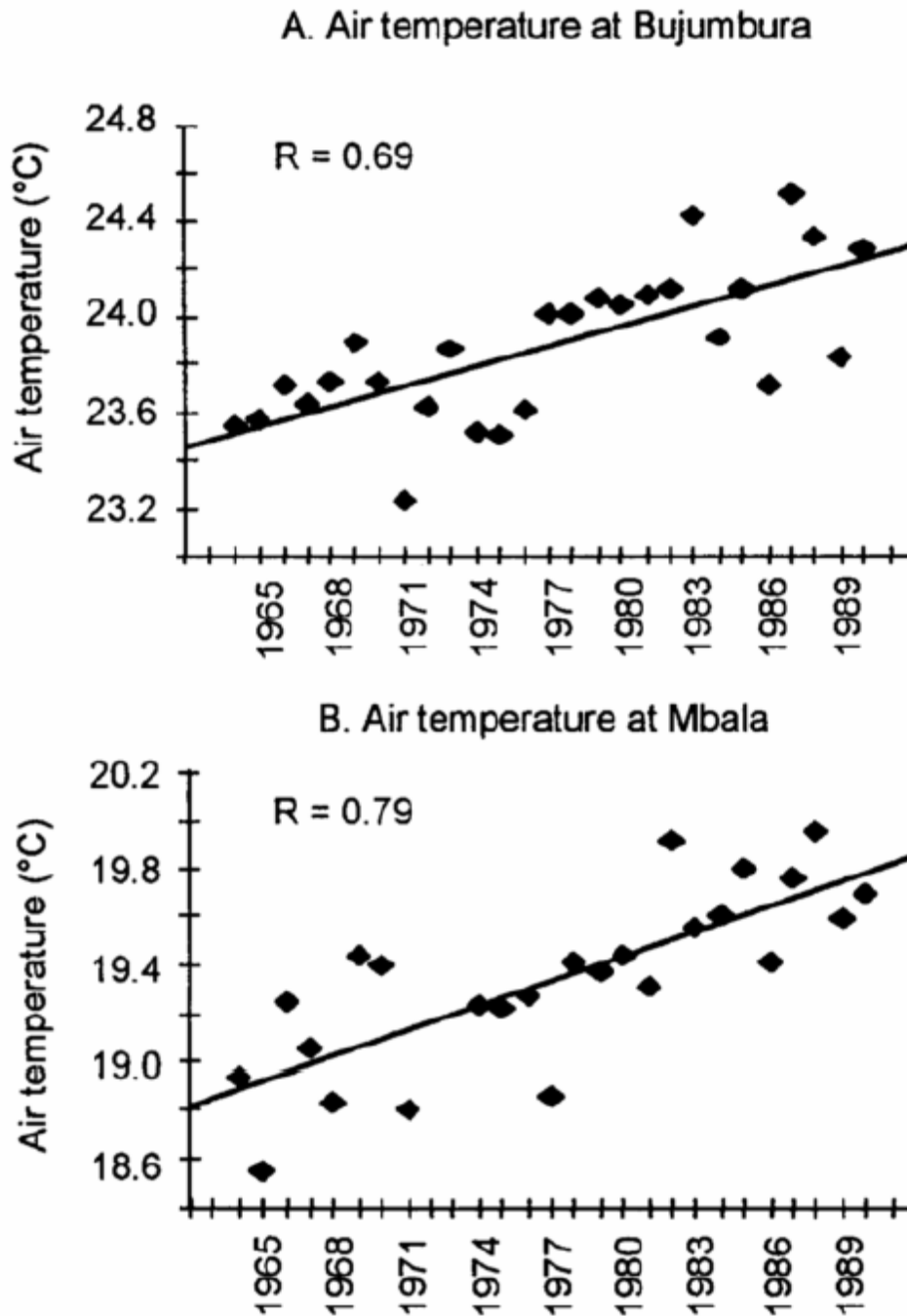


Figure 14: Linear regressions of yearly mean air temperature from 1964 to 1990 in (A) Bujumbura and (B) Mbala.

There are also indications of deeper warming (table IV). However, the number of observations published from the early period is not sufficient for statistical tests and

their accuracy is questionable. We may only remark that reported measurements for water temperature of Lake Tanganyika are all showing an increase with time.

Table IV: Mean temperature (°C) (100-300 m) for 1946-47 (Van Meel, 1987), 1973 (Craig et al., 1974) and 1993-94 (FAO, pers. comm).

Depth(m)	1946-47 (VAN MEEL 1987)	1973 CRAIG et al. 1974)	1993-94FAO
100	23.88	24.02	24.18
150	23.52	23.71	23.85
200	23.42	23.55	23.67
250	23.40	23.44	23.54
300	23.32	23.38	23.46

The mean thermocline depth in the north of the lake was 68m in 1955-57 (Dubois, 1958) and 55m in 1993-94 (Plisnier, 1997). The difference is particularly important when comparing the main dry season (June to September). The thermocline depth was similar in 1994-95 and 1995-96 compared to 1993-94. In the recent period the nutrient rich layers are closer to the euphotic zone.

Water in the pelagic zone in the north of the lake was not as clear (9m) in 1993-94 as in 1955-57 (13.6m) (Dubois, 1958). The transparency was different mainly during the dry season of each period (Plisnier, in press). In 1955-57, the transparency showed particularly well an increase with thermocline depth. In the south, the water was clearer in the recent period, mean Secchi depths 12.1m in 1993 and 9.6m in 1994 compared to 8.0m in 1961 (Coulter, 1991). It is not known if this reflects a general trend or if it was due to interannual variability.

The oxygenated layer in the north was shallower in 1993-94 compared to 1946-47 and 1955-57 particularly during the dry season (the oxycline depth was c. 60m in 1993-94 and 80-100m in 1946-47). Anoxic conditions (<1 mg/l DO) in the north were measured at 100m during the dry season in 1993-94 compared to 130m in 1946-47. A lower tilting of the epilimnion during the dry and windy season and increased stratification could explain the shallow oxygenated layer in the north. The seasonal differences in surface oxygenation were well marked in 1946-47 and 1955-57 but much less so in 1993-94.

In 1993-94 a higher zooplankton density was measured in the north of the lake than in the south (Kurki, pers. comm.). However, shrimps and adult *Lates stappersi* are

actually more abundant in the south. *Lates stappersi* is feeding heavily on shrimps there (Mannini, pers. com.) rather than on *Stolothrissa tanganicae*, rare in the catches since several years.

A general decrease in CPUE of offshore catches of the pelagic clupeids *Stolothrissa* and *Limnothrissa* occurred over the last two decades of the data series in Mpulungu and Bujumbura while CPUE of *Lates stappersi* decreased also in Bujumbura but increased at Mpulungu, coincidental with an apparent general increase in stratification stability in the upper 100m.

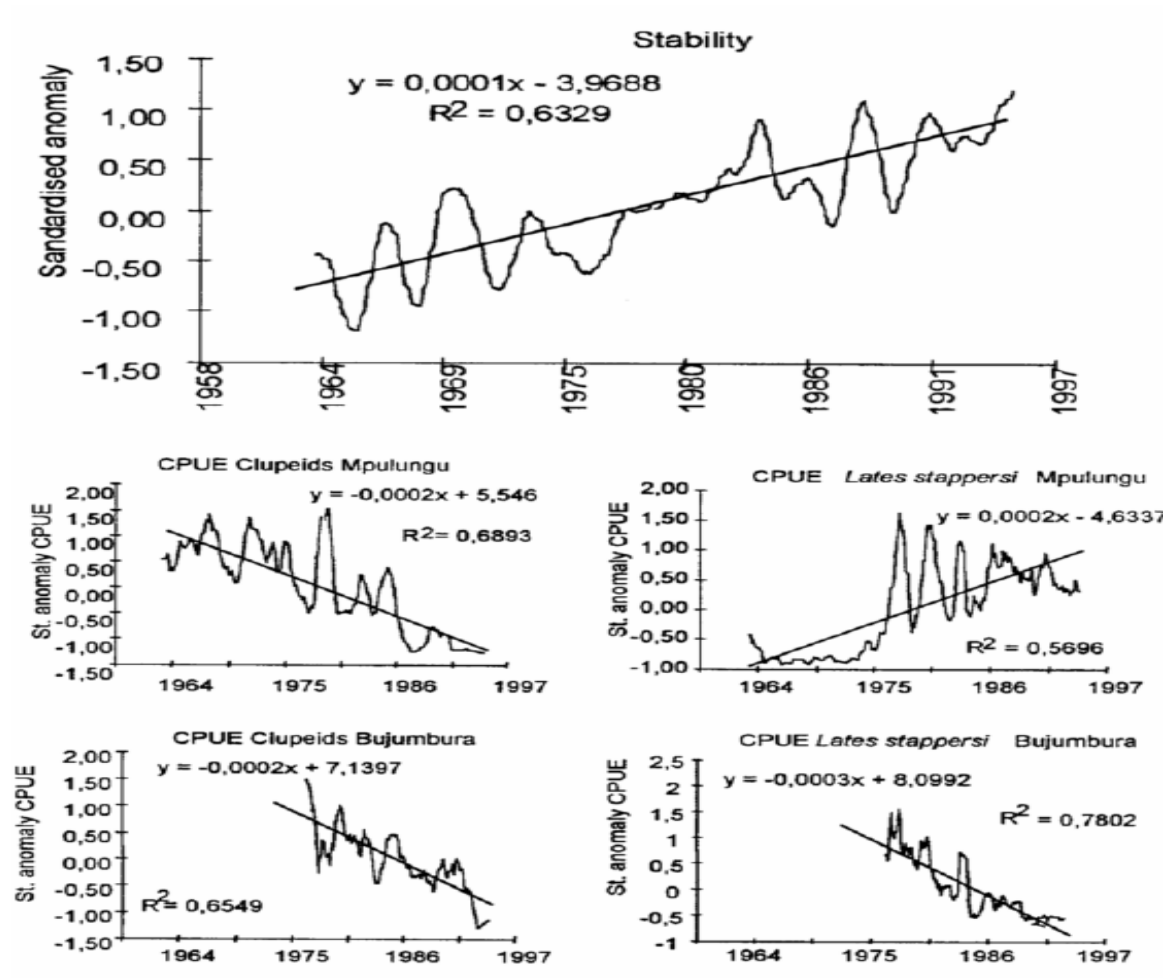


Figure 15: Recent trend in stability of water at Mpulungu and catches per unit of effort of the main pelagic fish species made by industrial fishermen (standardized anomalies smoothed with 12 months running average). This suggests recent possible links between abiotic and biotic changes at Lake Tanganyika.

6.1.2 Eastern African region

6.1.2.1 Preliminary analyses

In remote sensing, the principal components analysis is known to depict the spatial variations in vegetation cover in the first component, whereas the second component is related to the spatial variations in seasonality of the vegetation. Changes in vegetation cover and anomalies related to the satellite system are present in the lower PC's. Herewith one can state that minor changes that affect large areas will be picked up in higher components, whereas strong changes over small areas will be accounted for in lower components.

Following correlations were found (table V):

Table V: Preliminary results of cross-correlations between principal components and ENSO indices.

Site	variables	delay (months)	Ccf	% variance for PC
NW	NDVI PC7 and SOI	10	0.348	2.62
	Ts PC7 and SOI	10	-0.457	3.44
	Ts PC7 and Anom3	12	0.34	3.44
	Ts PC7 and Anom1&2	4	0.364	3.44
NE	Ts PC6 and SOI	9	0.477	2.65
	Ts PC6 and Anom3	10	0.338	2.65
SW	NDVI PC6 and SOI	0	0.421	3.57
	NDVI PC6 and Anom3	1	-0.338	3.57
	Ts PC4 and SOI	10	0.49	4.81
	Ts PC6 and Anom1&2	5	0.29	4.20

The correlations with ENSO indicators are always found amongst the lower PC's. However, as compared to the results found by Anyamba and Eastman (1996) the amount of explained variance is considerably higher. There seems to be a higher degree of correlation between surface temperatures and ENSO indicators than with the NDVI.

The rather long time lag between observations of ENSO phenomena and the response of either Ts or NDVI is not understood at present (table VI). As PC's are

used rather than the physical data, the mechanism at work is even more difficult to trace.

Table VI: Preliminary results of cross-correlations between NDVI anomalies and ENSO anomalies.

site	variable	delay (months)	Ccf
NW	NDVI and SOI	10	0.364
	NDVI and Anom1&2	7	-0.368
	NDVI and Anom 3	11	-0.340
	NDVI and Anom 4	11	-0.316
NE	NDVI and Anom 3	11	-0.236
SW	NDVI and SOI	10	0.263
	NDVI and Anom 3	6	-0.286
	NDVI and Anom 3&4	6	-0.263

Correlations of NDVI anomalies with SOI are mostly characterised by a delay of about 10 months and a positive correlation coefficient. Apparently, the effects of changing Sea Surface Temperatures in the Pacific are negatively correlated with NDVI, again with a considerable delay. As the PCA analysis suggests that Ts might be more sensible to ENSO indicators than the NDVI, the same analysis as presented above is to be repeated with the Ts data.

The Fourier analysis periodograms of the study sites all show similar profiles. The most important component is the annual one, with a less pronounced peak depicting the seasonality. A third signal, which is found back in all periodograms, is the peak at 64 months, showing the interval between the 2 Niño occurrences in 1982-83 and 1987. About 45 to 50% of the total variance is explained by the annual and seasonal peak in the NDVI Fourier series. The 5 year peak (ENSO) represents an average of about 5% variance in the NDVI series.

The annual component is split over 2 waves in the Ts data, representing an average of 40-45% of the variance. The seasonal peak is much stronger in the Ts series as compared to the NDVI series, representing about 10% of the variance. The ENSO signal is found back more clearly in the Ts series and explains about 8% of the total variance of the signal.

The periodograms of the ENSO anomalies also show a similar course, with the most important component occurring at 42 or 32 months explaining about 20-30% of the total variance. A less pronounced peak is sometimes found at 64 months, accounting for about 8% of the total variance. The annual component hardly shows in this data, but a small seasonality related component was found (< 2% of variance).

Although Fourier analysis allows decomposing the complex signal into its most important components, it is not an ideal technique for the detection of the ENSO signal. As the calculation of Fourier transforms is quite complicated, most software are restricted to the calculation of the simplified Fast Fourier transforms, limiting the data set to contain a number of samples which equals a power of 2. As we only had 108 observations, we had to add zero's to complete the data set. This causes interruption of the wave signal and implies that the Fourier series are only an approximation of the original signal. Also, the decomposition in harmonics depends on the number of samples. The frequency estimation between adjacent estimates of the spectrum is constrained to be $1/2M$, where M is the total width of the spectrum. Thus harmonics are only available at points $1/2M\pi$, $2/2M\pi$ up to $1/2\pi$ (Bennett, 1979). This implies that multiples of 12 (the periodicity of the data) will not be found back, as $M=128$. So the harmonics will have periods which are only an approximation of the real period in the signal. Additionally, as the ENSO signal is not periodic over time, it will emerge in several harmonics and is thus more difficult to detect.

6.1.2.2 *Teleconnections with climate data*

Sea surface temperature (SST) in the Pacific has been used in this part of the study because it displays less noise than the southern oscillation index (SOI). We performed a first round of analyses using anomalies in SST for the four Niño zones. Generally, we found a stronger correlation between climate variables (air temperature, humidity) or remote sensing variables (NDVI and Ts), and anomalies in SST for the Niño4 region (SST4 = 150°W-160°W, 5°N-5°S). The SST4 indicator was therefore used for the analyses in this study. The same indicator also showed the higher correlation in the PCA analysis by Anyamba and Eastman (1996). Note that the SST for the Niño3 zone has been used in studies analysing rainfall-ENSO teleconnections such as in Zimbabwe (Cane *et al.*, 1994).

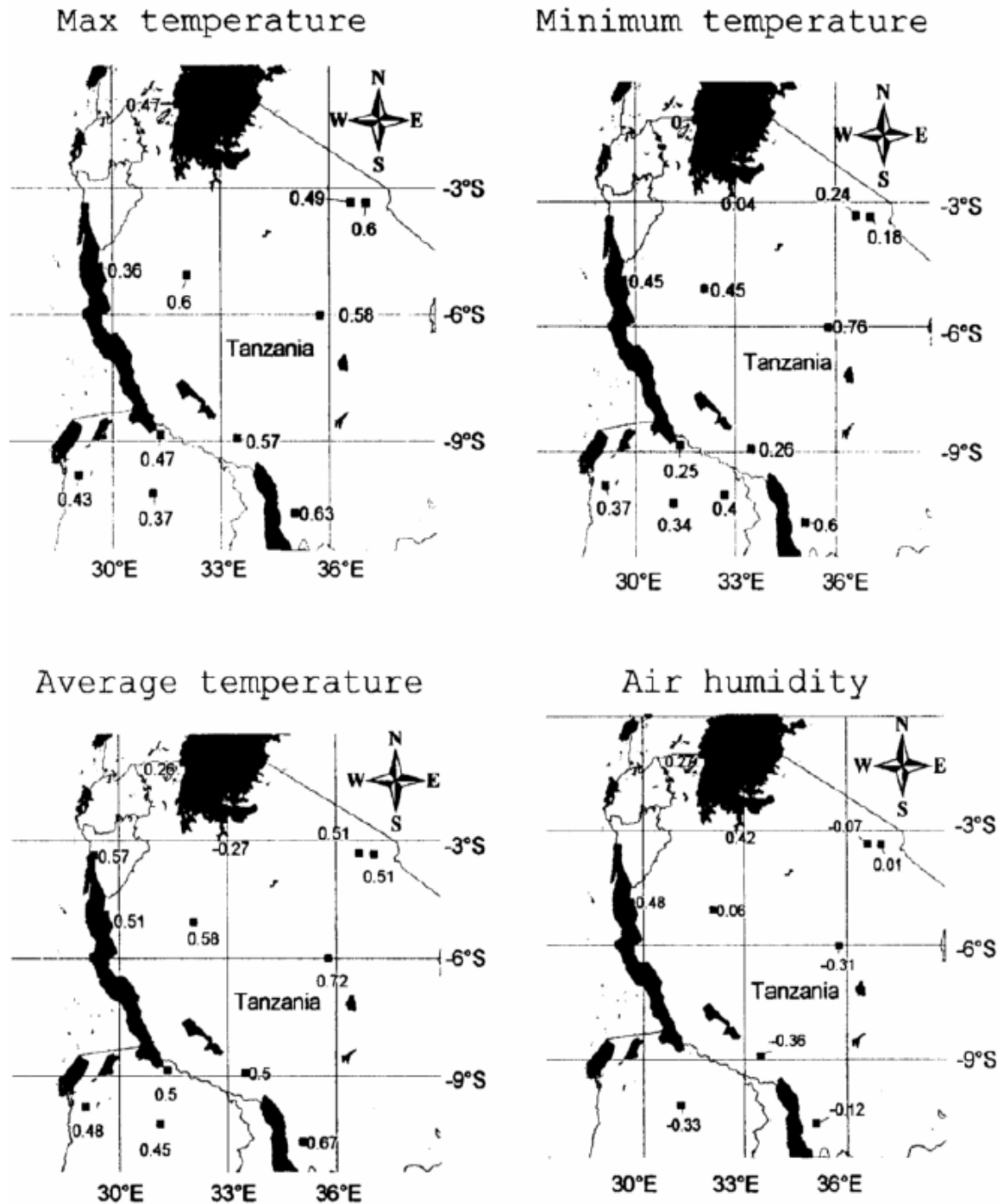


Figure 16: Correlation coefficients (R) for teleconnections between, on one hand, T_{max} , T_{min} , T_{avg} and relative air humidity in Zambia (1981-1994) and Tanzania (1981-1991) and, on the other hand, sea surface temperature (SST4) of the Pacific Ocean, for a 6-month time lag.

Most correlation values between Pacific SST anomalies and air temperature (maximum, minimum and average) measured at the East African stations are positive and highly significant ($P < 0.005$) (Figure 16 a, b, c). For all three temperature variables, the highest correlation with SST4 anomalies is found in central Tanzania. The correlation between each of the air temperature variables and SST4 is maximal for a time lag of 4 to 8 months. For T_{\min} , two stations do not show a significant correlation with SST4: the stations of Bukoba and Mwanza bordering Lake Victoria (Figure 16 b). For the twelve meteorological stations in the study area, during the 1981-1994 period, the three air temperature variables had higher values when SST4 anomalies were positive (with a 6 months time lag) as compared to the values for the years when SST4 anomalies were negative. Temperatures rose with on average 0.31°C (T_{\max}), 0.28°C (T_{avg}) and 0.26°C (T_{\min}) during warm ENSO events. The correlation between SST4 anomalies and air humidity is significant and positive in northern Tanzania (Mwanza, Bukoba) and north-western Tanzania (Kigoma), while it is negative for all the other areas (Figure 16 d). Moreover, the lag of the teleconnections between the SST4 anomalies and humidity is different for the two regions. In the first region (north-western Tanzania: Mwanza, Bukoba and Kigoma), the positive correlation is maximum for a 6 months time lag while, in the second region (south-eastern Tanzania and northern Zambia) the correlation reach the highest negative values for a 10 months time lag. This is probably related to differences in rainfall patterns between the north and the south of the study area. Thus, contrary to air temperature, there is not a single, region-wide effect of ENSO for the variable “air humidity”, but rather different effects for different locations. The increase in humidity in the north-western stations during ENSO warm events is 2 to 3 %. However, this increase is not statistically significant as there are only a few meteorological stations in this region.

For Tanzania, teleconnections between SST4 and rainfall are analysed per season. For a number of stations with a bimodal rainfall pattern, the correlation between SST4 anomalies and anomalies for the main rainy season (March to May) is statistically significant and negative, which suggests that a warm ENSO event is associated with drier conditions during that season. The time lag involved was shorter than found for other variables. Rainfall during the main wet season seems to be influenced by ENSO with a delay of 3-4 months. For the short rainy season, the teleconnection is not significant in Tanzania, but tends to be positive with a shorter time lag.

The results are presented for an extended area (including all of Zambia and Tanzania) for teleconnections with T_{\max} (appendix 2), with T_{\min} (appendix 3) and

with humidity (appendix 4). Values of teleconnections with SST4 are presented for different lag of time (0,2,4,6,8 and 10 months).

Table VII: Correlation coefficients for teleconnections with SST4 anomalies for all stations. The lag is indicated between brackets. In bold: correlation values with $p < 0.01$ (R= rainfalls).

	Ts (6M)	NDVI (6M)	Tmax (6M)	Tmin (6M)	Tavg (6M)	Humi- dity (6M)	(Ts-Ta) (6M)	Roct- dec (1M)	Rdec- feb (5M)	Rmar- may (4M)
Arusha	-0.09	-0.24	0.49	0.24	0.51	-0.07	-0.37	0.23		-0.51
Bukoba	-0.49	0.07	0.47	0.00	0.26	0.27	-0.72	0.19		0.19
Dodoma	-0.10	-0.24	0.58	0.76	0.72	-0.31	-0.44		-0.10	
Kigoma	-0.52	-0.08	0.36	0.45	0.51	0.48	-0.57	0.63		-0.79
Mbeya	-0.30	-0.22	0.57	0.26	0.50	-0.36	-0.66		0.14	
Moshi	-0.17	-0.12	0.60	0.18	0.51	0.01	-0.49	0.30		-0.30
Mwanza	-0.49	0.24	0.14	0.18	0.18	0.42	-0.53	0.27		
Songea	-0.22	-0.01	0.63	0.60	0.67	-0.12	-0.62		0.02	
Tabora	-0.43	-0.13	0.60	0.45	0.58	0.06	-0.77			
Isoka	-0.21	-0.11		0.40				0.01	-0.30	-0.08
Kasama	-0.34	0.04	0.37	0.34	0.45	-0.33	-0.47	0.01	0.52	-0.35
Kawamba	-0.32	-0.21	0.43	0.37	0.48		-0.47	0.04	0.01	0.20
Mbala	-0.45	-0.10	0.47	0.25	0.50		-0.58	0.27	0.29	-0.32
Bujumbura	-0.42	0.01			0.57			-0.21	-0.71	-0.57

6.1.2.3 Teleconnections with remote sensing data

Correlation coefficients between both NDVI and Ts anomalies and the ENSO index were found to be strongest for a time lag of 6 to 8 months. Correlation values for the NDVI-SST4 teleconnections vary in space between -0.70 and $+0.55$. 30% of the values are negative and statistically significant ($P < 0.005$) and 0.6% of the correlations are positive and significant (Figure 17 a). For the teleconnections between Ts and SST4, 65% of the area shows a significant negative correlation, but only 0.02% of the pixels have a significant positive correlation (Figure 17 b). Again, for these two variables, there is not a single, region-wide effect of ENSO but rather different effects for different locations.

To better understand the pattern of teleconnections between Pacific SST4 and the remotely sensed land surface variables, a land cover map for Africa was used to determine the different vegetation types in the area. We used the global land cover map at 1 km² resolution produced by the IGBP (Loveland and Belward, 1999). In the northwestern part of the study area, there is a strong negative correlation between NDVI and SST4 (Figure 17 A), meaning that warm ENSO events are associated with a lower-than-usual NDVI, thus suggesting a lower net primary production. Towards the south of this area, on the western side of Lake Tanganyika, the negative correlation values are smaller, but still significant. The north-western area is covered by evergreen tropical forest, gradually changing into woody savannah towards the south. Another area with pronounced negative correlation values for the NDVI-SST4 teleconnections is found in the Maasai steppe, south of Arusha (Figure 17 A). This is a relatively flat area dominated by savannah and some grassland vegetation. There is a small area south of Lake Victoria and close to Mwanza, characterised by a strong positive correlation between NDVI and SST4, suggesting that warm ENSO events are associated with an increase in net primary production of the vegetation. Other areas with a positive but weak teleconnections between NDVI and SST4 are found west of Lake Victoria and near Lake Tanganyika, north-east of Kigoma, in areas supporting grassland vegetation or a mixture of cropland and natural vegetation. We see in this case that there is no perfect correspondence between land cover types and the pattern of ENSO teleconnections of NDVI as different grassland areas are affected by both positive and negative correlations with SST4. In the remaining areas, the teleconnections between NDVI and SST4 is not significant and no clear impact of ENSO events on vegetation can be observed.

The correlation coefficients for Ts-SST4 teleconnections are largely negative (Figure 17 b), implying that a positive Pacific SST4 anomaly will cause lower than usual surface temperatures (Ts) in East Africa about 6 to 8 months later. The area that shows the strongest teleconnections between Ts and SST4 is found in the north-western part of the study area, in the evergreen broad-leaved forest. Further to the south, the teleconnections are weaker, but significant negative correlation values are found for the area around Lake Victoria, around Lake Tanganyika and down to Lake Rukwa. In the centre and towards the east of the study area, correlation values are insignificant. For a few pixels in the eastern part of the study area, covered by woody savannah, significant but weak positive teleconnections for Ts are found.

Teleconnections with Pacific SST for the (Ts - Ta) variable are negative for all stations and are strongest for a time lag of 6 months. Thus, for years with positive ENSO anomalies, (Ts - Ta) values are smaller than usual, suggesting that evapotranspiration is increased for all meteorological stations.

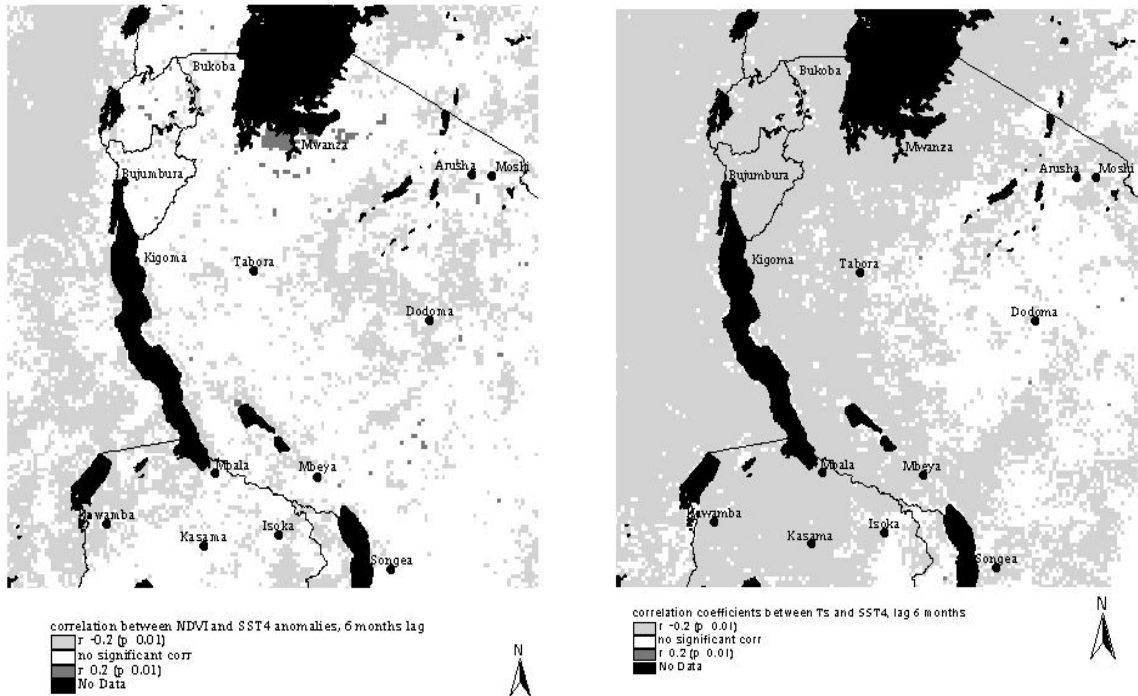


Figure 17: Maps showing pixel wise correlation coefficients for the teleconnections between SST4 anomalies and: (a) NDVI anomalies and (b) Ts anomalies, with a 6-month time lag. Only the values of the correlation coefficients that are significant at the level 0.01 are represented.

6.1.2.4 Spatial coherence in teleconnections

In general, the teleconnections with Pacific SST of the different climate and remotely sensed variables are spatially coherent (table VII), with notable exceptions concerning the NDVI teleconnections, which measures the response of vegetation to the ENSO-induced climate variability. Firstly, the spatial correlation values for teleconnections of pairs of climate variables have been examined. Secondly, the spatial correlation between the teleconnections for the two remotely sensed variables has been analysed; and thirdly, the spatial correlation between the teleconnections for pairs of one climate and one remote-sensing variable has been examined. Results are presented in table VIII. These analyses were conducted using teleconnections data from all the stations.

Table VIII: Spatial correlation coefficients between teleconnections values for pairs of variables. Lag of 6 months for all variables. In *Italics*: $p < 0.05$; in **bold**: $p < 0.01$.

	Ts	NDVI	Tmax	Tmin	Tavg	humidit v	(Ts-Ta)
Ts	1	-0.595	0.567	0.391	0.569	-0.697	0.598
NDVI		1	-0.643	-0.379	-0.656	0.547	-0.239
Tmax			1	0.343	0.753	-0.570	-0.228
Tmin				1	0.820	-0.374	0.158
Tavg					1	-0.580	0.132
humidity						1	-0.238
(Ts-Ta)							1

As it could be expected, the three variables related to air T° (maximum, minimum and average air T°) are teleconnected to SST4 in the same way, with the spatial correlations being positive and significant at $P < 0.005$ (fig18 a). These three air T° variables and air humidity are also teleconnected with ENSO in a similar way but with the opposite sign in the case of air humidity - spatial correlations significant and negative (fig18 b). Two areas may be distinguished: the stations in the north-eastern part of the study area (Bukoba, Mwanza) which have high teleconnections with humidity and lower teleconnections with air T° , and the stations in the south-western part of the study area (Dodoma, Songea, Mbeya) which show the inverse combination. Note that the teleconnections in Kigoma between SST4 and T_{min} , T_{avg} and relative air humidity are all particularly high compared to the other stations. A significant spatial correlation was also found between teleconnections for rainfall during the period March-May and teleconnections for average air temperature.

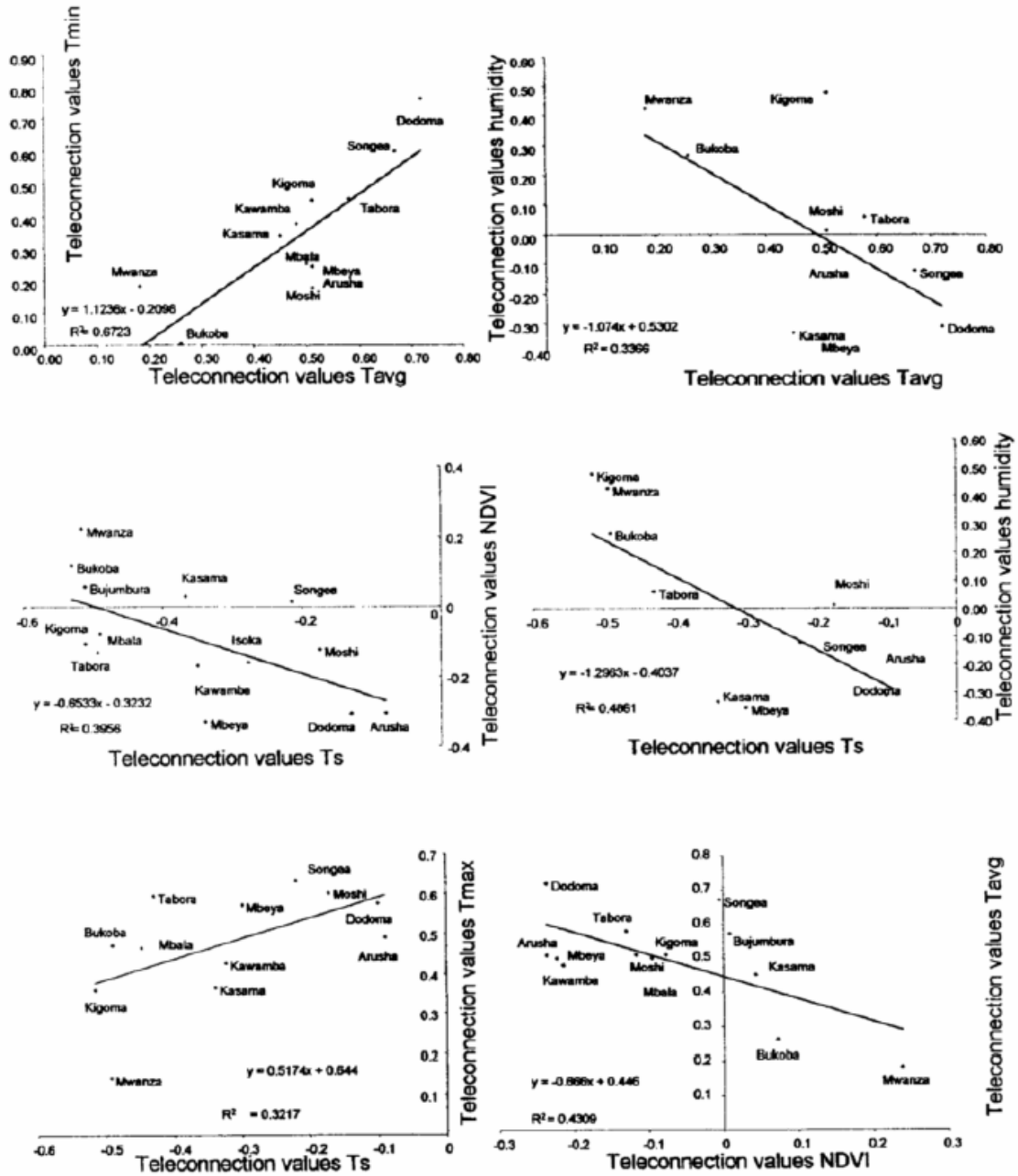


Figure 18: Scatterplots of the teleconnection values (i.e. correlations between Pacific SST4, and climate and remote sensing variables for each station) for pairs of climate and remote sensing variables for all stations: (a) T_s and NDVI, (b) NDVI and average air temperature, (c) T_s and air humidity, (d) average air temperature and air humidity, (e) average and minimum air temperatures, and (f) NDVI and maximum air temperature.

The spatial correlation between the NDVI-SST4 and T_s -SST4 teleconnections is significant and generally negative (Figure 18 c). The negative value for the spatial correlation between NDVI and T_s teleconnections is expected as, in water-limited ecosystems, an increase in photosynthetically active green biomass is associated

with a reduction in surface resistance to evapotranspiration, a larger latent heat flux and, therefore, a lower surface temperature (Lambin and Ehrlich, 1996). Accordingly, a positive teleconnection between NDVI and SST4 is expected to be associated with a negative teleconnection between Ts and SST4. This is verified for most of our study area, except for the north-western part of the region, which is dominated by evergreen tropical forests (Figure 17 a, b). Over evergreen tropical forests, where there is no moisture availability constraint, both the NDVI-SST4 and Ts-SST4 teleconnection values are strongly negative. Thus depending on land cover and ecosystem constraints, the sign of the relationship between the NDVI and Ts teleconnections may be inverted. Accordingly, it is difficult to identify a unique relationship for the entire study area between the teleconnections of NDVI and Ts with SST4. As for the climate variables discussed above, there is generally a difference between the northwestern stations of the study area (Mwanza, Bukoba, Bujumbura, and Kigoma) and the southeastern stations (Dodoma, Arusha, Moshi, and Songea) in the NDVI and Ts teleconnections with SST4 (Figure 18 c).

Teleconnections between SST4 and Ts measured by remote sensing show, in general, a good spatial correlation with the SST4 teleconnections with the climate variables. The teleconnection patterns for Ts and air humidity correlate best, with a negative sign (Figure 18 D). Thus, during a positive ENSO event, air humidity is higher in regions that have lower Ts – e.g. in regions characterised by a high surface evapotranspiration. The north-eastern stations are again well separated from the south-western stations. As could be expected, there is a good spatial correlation between Ts and (Ts-Ta). Spatial correlation between the SST4 teleconnections with Ts and air temperature (T_{max} and T_{avg}) variables is strong and positive (Figure 18 E), while NDVI teleconnections are negatively correlated with air temperature variables (Figure 18 F). Rainfall data show a negative spatial correlation for teleconnections with Ts in December-February. Only stations that have a unimodal pattern are taken into account here. Increase in rainfall increases surface moisture, which increases evapotranspiration and therefore decreases surface temperature. The station of Bujumbura does not comply with this correlation pattern. The spatial patterns of SST4 teleconnections of NDVI and air humidity seem to be positively correlated for all stations except for Kigoma, Kasama and Songea. The overall relationship is not statistically significant. Against the expectations, no overall spatial correlation was found between NDVI and rainfall teleconnections. Meteorological stations with a bimodal rainfall pattern in the northeast of the study area display a weak (not significant) positive correlation with NDVI teleconnections for the main rainy season in March-May. For the stations with a unimodal rainfall season in Zambia, the spatial correlation between NDVI and rainfall teleconnections (March-May) is significant ($p < 0.05$) and negative.

6.1.2.5 *Clustering of stations based on their pattern of teleconnections with SST4*

A multivariate clustering technique allows regrouping the stations according to their teleconnection values for the entire set of climate and remote sensing variables. A 6 months time lag was used for teleconnections with all the variables. Teleconnections for rainfall data were not used in this analysis due to the coarse temporal resolution of the rainfall data. A first separation in two clusters of stations is made between all lakeside stations (Mwanza, Bukoba, Bujumbura and Kigoma) and the remaining stations. All lakeside stations have a strong positive teleconnection between SST4 and air humidity. Air humidity was not available for Mbala, but teleconnections with other variables follow the same pattern as the other lakeside stations. The lakeside stations are further characterised by strong negative teleconnections with Ts and no teleconnection with NDVI (except Mwanza). Moderate positive teleconnection values were found for air temperature variables for the stations situated near Lake Tanganyika, but the stations near Lake Victoria do not have a clear teleconnection with the temperature variables (particularly T°min). Thus, ecosystems located near the great east African lakes display a specific pattern of teleconnections compared to other locations. This reveals the importance of the lakes on local climate conditions. The stations in the dryer part of the study area, lying on the central plateau or in the south (Kasama, Songea, Kawamba, Mbeya and Dodoma), are also grouped together. The area has a unimodal rainfall pattern and naturally supports a savannah vegetation which, in certain zones, is converted to cropland. The stations are characterised by a strong negative teleconnection between SST4 and air humidity. Furthermore, the stations display a negative teleconnection with NDVI and a negative teleconnection with Ts (moderate values). The remaining stations of Arusha, Moshi, and Tabora are grouped together based on the absence of any teleconnections with air humidity. Teleconnections with remote sensing variables are also insignificant, while teleconnections with maximum and average air temperature are consistently high and positive. Arusha and Moshi are both situated in the north-east of the study area, at the footslopes of Mount Meru and Mount Kilimanjaro respectively. Rainfall pattern is bimodal and the area supports a woody savannah vegetation (Plisnier et al, 2000).

6.1.2.6 *Analysis of land-use changes around the lake*

The map in figure 19 displays areas that have been subject to change once or several times over the 10-year period under study. The grey scale ranging from black to white depicts no change (black) to substantial changes (white). A few big hotspots can be localised, one area lies east of Kigoma and another lies south of Moba. At the eastern side of the lake, several small hotspots are found that are probably related to increased human activities in rural settlements. Hotspots of change can indicate

several processes. Either an area with a high frequency of high change vector magnitude can be subject to a gradual decrease in vegetation, caused by the expansion of human settlement, or human impact leading to land degradation. It can however also indicate natural vegetation types, such as semi-arid savannahs, which are very sensitive to inter-annual climate variability, without really being converted to a different vegetation type, or without being degraded by human activities. Such vegetation types are very resilient and will recover rapidly in years of above average rainfall. The map produced here can be used to select areas for in-depth study of vegetation changes, based on interpretation of high-resolution satellite data and aerial photographs. It was envisaged in the project to link those study sites to the areas in the lake where sediment cores would be taken. However, due to problems with the organisation of the expedition, the cores were taken after funding for the remote sensing part of the project was finished and we could thus not perform the detailed land-cover change analysis, nor the estimation of the effect of these land-cover changes on erosion and sediment loads in the lake.

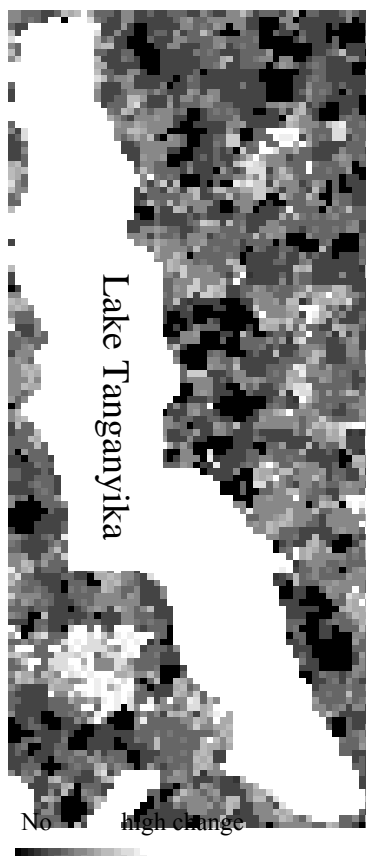


Figure 19: Change map for the Lake Tanganyika region.

6.1.2.7 Teleconnections with Indian Ocean data

Preliminary teleconnections found in the Indian Ocean were less important compared than those with the Pacific ocean data (max correlation R of 0.45 between SST (9° S., 46-48° E.) and air temperature data at Bujumbura for example (Figure 20). A comprehensive study of the Indian Ocean should be undertaken in the future particularly because recent results have been showing a dipole mode there that could have some significant impact on East African climate (Saji *et al.*, 1999).

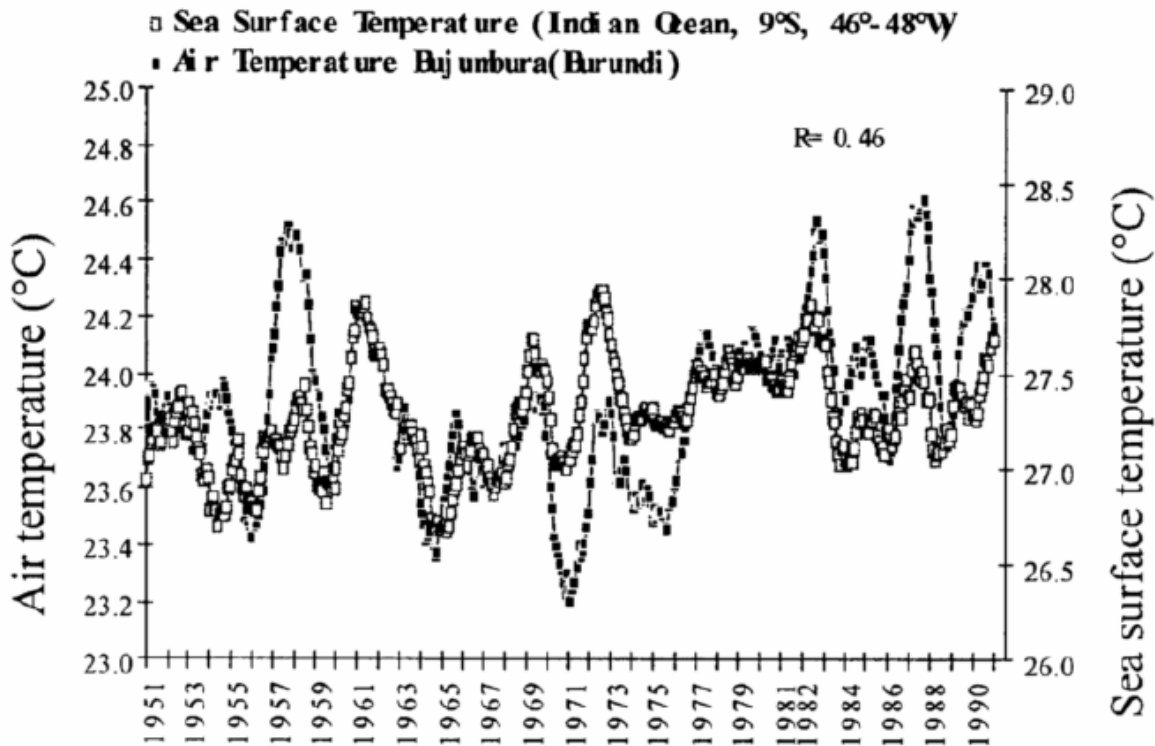


Figure 20: Air temperature at Bujumbura and Sea surface temperature (°C) (Indian Ocean, 9°S, 46°-48°E). Running average of 12 month are shown for the 1951 to 1991 period. (time lag: 4 months).

6.2 Sedimentology and algology

6.2.1 Description of the sediment cores

Photographs of all the cores were taken just after opening the cores by the team of Dr. M. Sturm (EAWAG, Kastanienbaum, Switzerland). Photographs of some selected cores are given in Figure 21. As the ENSO project aimed to study the last 1000 years, the description of the entire cores will be kept brief. The uppermost part of almost all cores is a rather well-defined finely laminated black zone.

6.2.1.1 *Sediment cores taken near Kasaba*

TAN 98/1 (Figure 22)

Core TAN 98/1 was collected in 300m water depth. Total length of the core is 105cm, measured in the field just after the coring.

By opening of the core mid October 2000, the sediments had compacted, and the total length of the core was compressed to 93 cm. The sediment material from the upper first centimetre was oxidised, visible as a brown colouring.

The upper 8.5cm of the core consists of black, finely laminated sediments, followed by a more homogeneous zone up to 32cm. Two black oblique veins interrupt this zone at 14/17 and 17/18cm. A more sandy layer, of which a part is missing, lies between the above mentioned homogeneous zone and a next, more dark, homogeneous zone between 32 and 38cm. The following zone, from 49 to 54cm, is coarsely laminated with alternating yellow-greenish and greyish-green layers. Between 54 and 65.5cm is a more homogeneous zone is followed by a yellow-greenish layer up to 66.5cm. The rest of the core consists of dark, laminated sediments with again a yellow-greenish layer between 92 and 93cm.

TAN 98/2 (Figure 22)

Core TAN 98/2 was collected in 300m water depth. Total length of the core is 55cm. The upper 2cm of the sediments were coloured brownish, by opening of the core mid October 2000, due to oxidation of the sediment.

The upper 10 (11) cm of the core consists of black, finely laminated sediments, followed by a more homogeneous zone up to 26cm. The lower part of this zone is somewhat lighter coloured. Between 26 and 38 cm, the core consists of two different layers, divided vertically (fig 22). One part is homogeneous, with a sandy layer from 32 to 38cm, the other part contains coarse laminated sediments, alternating yellow-greenish and more dark sediments. From 38cm to the end of the core, yellow-greenish and greyish-green layers are alternating.

TAN 98/3 (Figure 22)

Core TAN 98/2 was collected in 400m water depth. Total length of the core is 37cm. The upper 0.5cm of the sediment was coloured brownish, by opening of the core mid October 2000, due to oxidation of the sediment.

Laminated yellow-greenish and greyish-green sediments were present in the upper 6cm only in a well vertically delimited a part of the core; the other part consists of sandy material. Dark greyish-green laminated sediments builds up between 6 and

13cm depth. A yellow-greenish layer at 13-14.5cm is followed by a more homogeneous greyish-green zone. From 14.5 up to 22.5cm the sediment consists of dark laminated layers, with a dark band at 15.5-16.5cm. The end of the core, between 22.5 and 37cm is coarsely laminated, with alternately yellow-greenish and dark layers.

TAN 98/4 (Figure 22)

Core TAN 98/4 was collected in 400m water depth. Total length of the core is 40cm. Unfortunately the material of this core was lost due to technical problems.

TAN 98/8 (Figure 22)

Core TAN 98/8 was collected in 400m water depth. Total length of the core is 73cm.

The upper 12.5cm of the core consists of black, finely laminated sediments, followed by a more homogeneous zone up to 18cm. A sandy layer is present between 18 and 22cm. The zone between 22 and 50cm consists of coarsely laminated, alternately greyish, dark-greyish, yellow-greenish layers. A sandy light greyish sand layer is present at 50-50.2cm, followed by a dark laminated zone up to 53cm. Between 53 and 73cm the sediment is coarsely laminated, with alternating yellow-greenish and greyish-green layers.

TAN 98/6 (Figure 22)

Core TAN 98/6 was collected in 500m water depth. Total length of the core is 42cm. By opening of the core mid October 2000 the upper 1cm was coloured brownish due to oxidation of the sediment.

The upper 21cm of the core consist of black, finely laminated sediments, followed by a light greyish layer between 21 and 21.5cm. From 21.5cm to the end of the core, coarse lamination of yellow-greenish and greyish-green is present, interrupted by sand lenses between 28 and 31.5 cm. Shell material from molluscs was present between 31.5 and 32.5cm.

TAN 98/9 (Figure 22)

Core TAN 98/9 was collected in 500m water depth. Total length of the core is 107.7cm.

The upper 12cm of the core consist of black, finely laminated sediments, followed by a homogeneous layer between 12 and 25.3cm. The zone from 25.3 to 32cm consists of coarse lamination of yellow-greenish and greyish-green layers. Between 32 and 36cm lays a homogeneous layer. The rest of the core is principally coarsely laminated, alternating of yellow-greenish and greyish-green layers, interrupted at 58-

62cm, 73.5-80.4cm and 82.5-84.5cm by fine dark laminations and several thin homogeneous bands.

TAN 98/13 (Figure 22)

Core TAN 98/13 was collected in 500m water depth. Total length of the core is 71.5cm.

The upper 12cm of the core consist of black, finely laminated sediments, followed by a homogeneous zone up to 29cm. The zone between 29 and 37cm consists of coarse lamination of yellow-greenish and greyish-green layers. Between 37 and 43cm a more homogeneous zone, followed by a zone of coarse lamination of yellow-greenish and greyish-green layers up to 57cm. Between 57 and 59cm a homogeneous layer followed by a zone of coarse lamination of yellow-greenish and greyish-green layers up to the end of the core, but interrupted at 68.5-69cm by a band of sandy, light orange coloured sediment.

6.2.1.2 Sediment cores taken near Kapembwa

TAN 98/7 (Figure 23)

Core TAN 98/7 was collected in 330m water depth. Total length of the core is 72cm.

The upper 1.5cm of the core consists of black, finely laminated sediments, followed by a sandy zone up to 6cm. Between 6 and 29cm a homogeneous zone followed by black, finely laminated sediments up to 33cm. A homogeneous zone between 33 and 34cm is followed by a zone of coarse lamination of yellow-greenish and greyish-green layers up to 40cm. The rest of the core consists of alternating zones of sandy bands and coarse laminated zones of yellow-greenish and greyish-green layers.

TAN 98/10 (Figure 23)

Core TAN 98/7 was collected in 330m water depth. Total length of the core is 110cm.

The upper 0.5cm of the sediment was coloured brownish, by opening of the core mid October 2000, due to oxidation of the sediment. Up to 21cm the core consists of black, finely laminated sediments, followed by a lighter laminated band at 21-23cm. Between 23 and 34cm coarse lamination of yellow-greenish and greyish-green layers interrupted at 29.5-31cm by a sandy, pink coloured band. A homogeneous zone, between 34 and 57cm, is interrupted by a zone of coarse laminations of yellow-greenish and greyish-green layers at 46-48cm. Between 57 and 59.5cm the sediment is vertically split in two parts, one part contains more sandy material. Dark laminated bands between 59.5 and 62.5cm, followed by a zone of coarse lamination of yellow-greenish and greyish-green layers up to end, interrupted by sandy bands.

TAN 98/11 (Figure 23)

Core TAN 98/11 was collected in 330m water depth. Total length of the core is 112cm.

The upper 1.5cm of the sediment was coloured brownish, by opening of the core mid October 2000, due to oxidation of the sediment. Up to 19cm the core consists of black, finely laminated sediments, followed by a homogeneous zone up to 23.5cm. Several sandy bands between 23.5 and 35cm, followed by a homogeneous zone up to 42 cm. Coarse lamination of yellow-greenish and greyish-green layers between 42 and 54.5cm, interrupted by a sandy band at 47-49cm. A homogeneous zone between 54.5 and 60cm is followed by coarse lamination of yellow-greenish and greyish-green layers interrupted by a small number of sandy bands and a sand lens at 94-95cm.

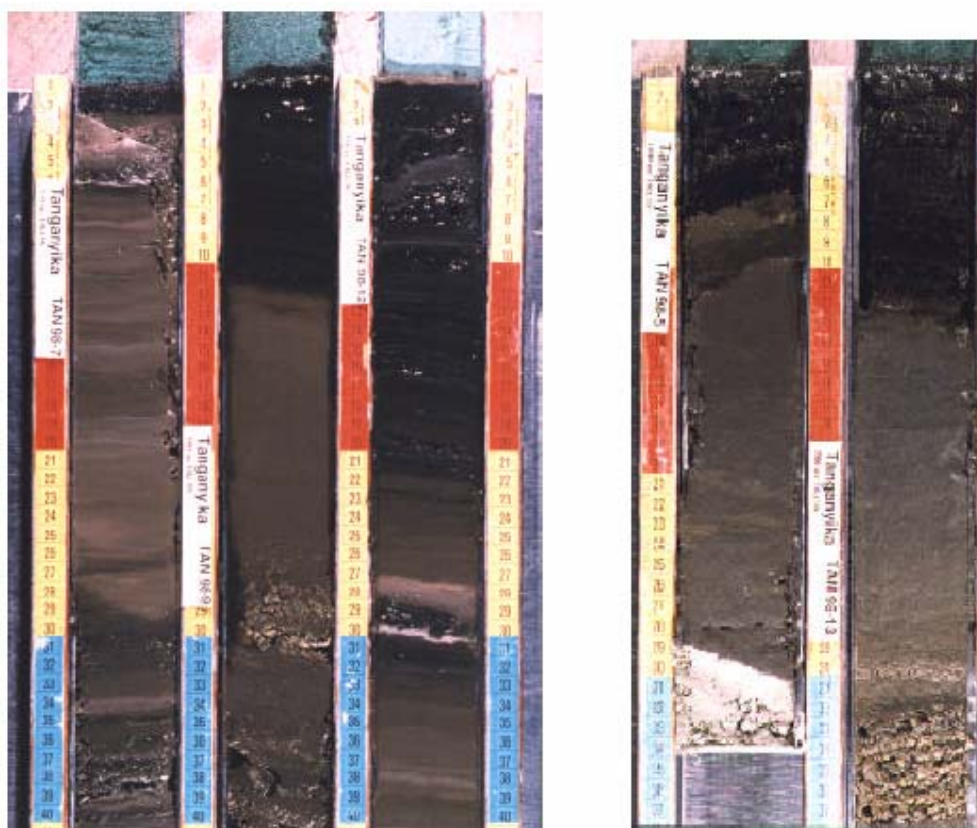


Figure 21: Photographs of the upper layer of some sediments cores taken in the Southern Basin of Lake Tanganyika: core TAN 98/12 taken near Kapembwa in 330m water depth.; core TAN 98/9, taken near Kasaba in 500m water depth.; core TAN 98/7, taken near Kapembwa in 330m water depth.; core TAN 98/13, taken near Kasaba in 500m water depth.; core TAN 98/5, taken near Msamba in 1000m water depth.

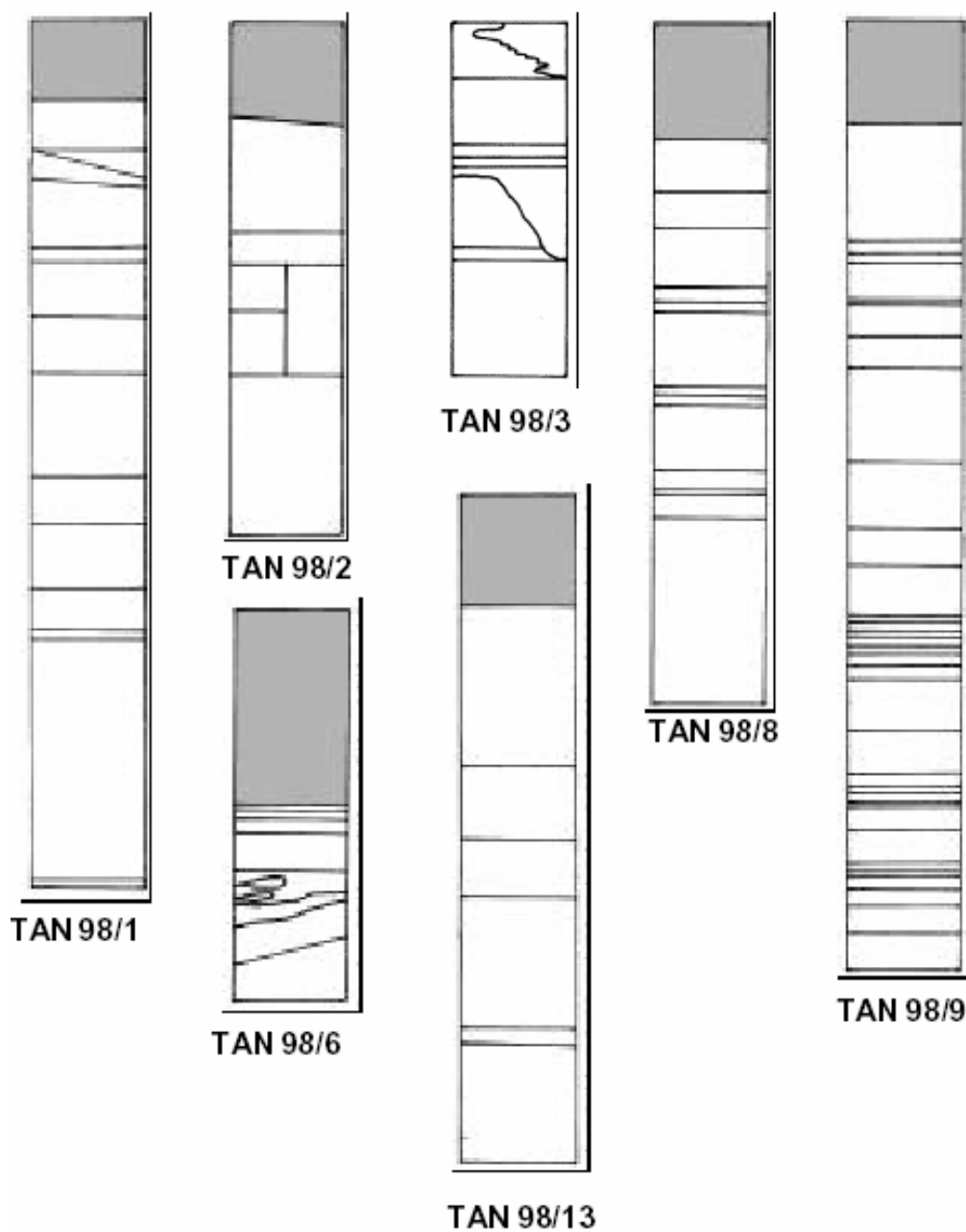


Figure 22: Schematic presentation of the sediment cores taken near Kasaba: cores TAN 98/1 and TAN 98/2 taken in 300m water depth; cores TAN 98/3, TAN 98/4 and TAN 98/8 taken in 400m water depth; cores TAN 98/6, TAN 98/9 and TAN 98/13 taken in 500m water depth.

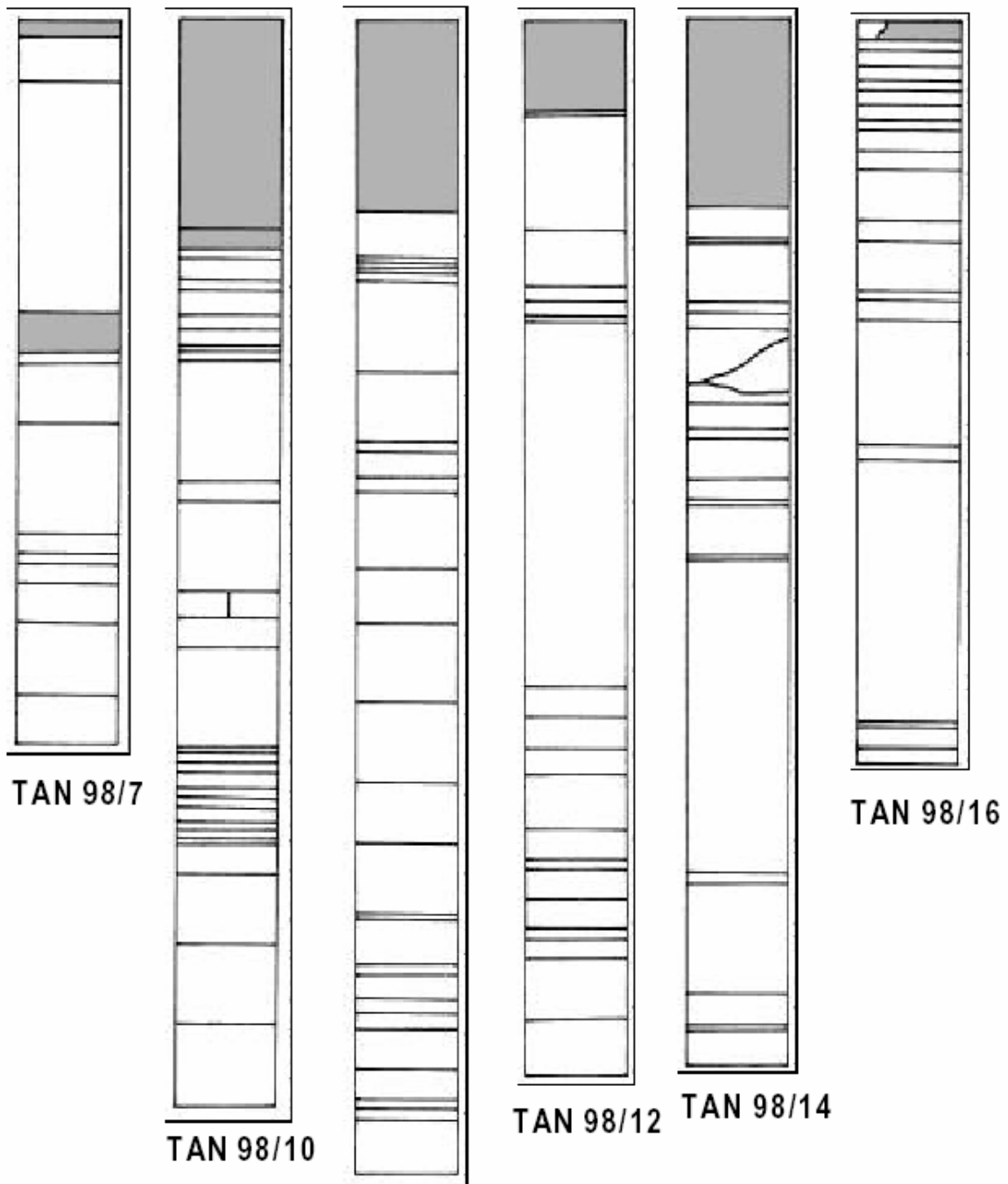


Figure 23: Schematic presentation of the sediment cores taken near Kapembwa taken in 330m water depth: cores TAN 98/7, TAN 98/10, TAN 98/11, TAN 98/12, TAN 98/14 and TAN 98/16.

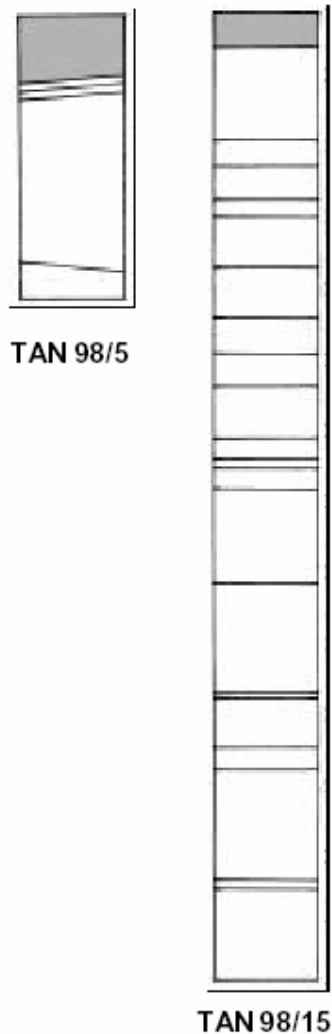


Figure 24: Schematic presentation of the sediment cores taken near Msamba (core TAN 98/5) and near Kipili (core TAN 98/15) in 1000m and 1200m water depth respectively.

TAN 98/12 (Figure 23)

Core TAN 98/12 was collected in 330m water depth. Total length of the core is 105.5cm.

The upper 21cm of the core consist of black, finely laminated sediments, interrupted at 9cm by a lighter band, and followed by a homogeneous zone up to 26.5cm. A sandy layer between 26.5 and 28cm followed by a dark sediment layer between 28 and 29.5cm, then a light grey band up to 30cm. From 30 to 66.5cm a zone of alternating grey and light grey bands is present. Dark sediment layer between 66.5 and 69.5cm, followed by a Grey homogeneous band. From 69.5cm up to the bottom of the core alternating coarse laminations of yellow-greenish and greyish-green layers interrupted by grey homogeneous layers.

TAN 98/14 (Figure 23)

Core TAN 98/14 was collected in 330m water depth. Total length of the core is 107cm.

The upper 19cm of the core consist of black, finely laminated sediments, followed by a homogenous zone up to 29.5cm interrupted by a sandy layer at 22-22.5cm. From 29.5 to 31cm a laminated light grey band followed by a homogeneous zone interrupted by a sandy band. From 38.5 to 42cm a dark laminated layer, followed by a zone of alternating coarse laminations of yellow-greenish and greyish-green layers interrupted by several sandy bands.

TAN 98/16 (Figure 23)

Core TAN 98/16 was collected in 330m water depth. Total length of the core is 73cm. The upper 2cm of the core consists of black, finely laminated sediments, followed by a light grey sandy band. From 3 to 28cm a zone of alternating coarse laminations of yellow-greenish and greyish-green layers interrupted by light grey sandy bands. From 28 to 30cm a homogeneous zone followed by a zone of alternating coarse laminations of yellow-greenish and greyish-green layers.

6.2.1.3 *Sediment core taken near Msamba at 1000m water depth***TAN 98/5** (Figure 24)

Core TAN 98/16 was collected in 1000m water depth. Total length of the core is 33.5cm.

The upper 7cm of the core consist of black, finely laminated sediments, followed by a homogeneous zone up to 30cm interrupted by number of lighter Grey bands. From 30cm down to the end of the core a zone of light grey sediments is present.

6.2.1.4 *Sediment core taken near Kipili at 1200m water depth***TAN 98/15** (Figure 24)

Core TAN 98/15 was collected in 1200m water depth. Total length of the core is 113cm.

The upper 2cm of the sediment was coloured brownish, by opening of the core mid October 2000, due to oxidation of the sediment. Up to 4cm the core consists of black, finely laminated sediments, followed by a homogeneous zone up to 15cm. From 15 to 67cm a zone of alternating coarse laminations of yellow-greenish and greyish-green layers, interrupted between 53.5 and 56cm by a grey sandy band of laminated

sediment. From 37cm down to the bottom of the core alternating bands of dark and greyish-green layers.

6.2.2 Dating

6.2.2.1 ²¹⁰Pb dating

The ²¹⁰Pb profiles obtained on five cores (TAN 98/5, TAN 98/7, TAN 98/9, TAN 98/12, TAN 98/13) were difficult to interpret. Two main hypotheses might explain the difficulties of dating the upper sections of the sediment cores retrieved in this project:

- recent sediments (last 200 years) are lacking in the cores;
- chemical reactions in the sediments (Appleby, 1997).

6.2.2.2 ¹⁴C dating

Dating were performed on the cores which were selected for diatom research.

The results of the ¹⁴C AMS dating are given in table IX.

Table IX. Results of the ¹⁴C AMS dating for core TAN 98/9, taken near Kasaba at 500m water column depth.

Sample	AMS ¹⁴ C Date (years BP)	δ ¹³ C (‰)	Calibration Date (BC/AD)
TAN 98/9 – 10.5-1.5cm	830 ± 40	-18.9 ± 1.1	1158 - 1285 (96.8%)
TAN 98/9 – 48-52cm	8.060 ± 60	-22.1 ± 1.1	7100 - 6706 (89.8%)

The first dating corresponds to the base of upper, dark laminated part of core TAN 98/9. Assuming a constant accumulation rate, which is supported by the more or less continuous lamination of the upper sediments, the sedimentation rate is about 0.134 mm/y. The sedimentation rate, calculated from the dating at 48-52 cm sediment depth is 0.06 mm/y.

6.2.3 *Thin-section analyses*

6.2.3.1 *Sediment core taken near Kipili at 1200 m water depth*

Introduction

Because of the high water content of the sediment of Lake Tanganyika, several attempts to subsample other cores for thin-sections have been done. A new subsampling technique, using electro-osmotic effect has been implemented (Francus and Cosby, in press). In core TAN98/15 (1200 m deep) a continuous series of thin-sections were sampled along the entire core (0-113.5cm). According to previous studies (Gasse et al., 1989; Degens et al., 1971), the sedimentation rate in the Southern basin is about 0.6 mm/yr. This core could therefore span a ~ 1900 yr long period. Core TAN98/13 (500m deep) has been sampled between 30 and 65 cm.

Sediment description

Macroscopically, the upper sediments have a black colour and show well defined fine laminations. The black zone is lying on a non laminated grey-greenish layer, followed by repetitive zones of laminated green-yellowish and more homogeneous section. Petrographic microscope and SEM observation of the sediment allowed us to establish a detailed sedimentary log description (Figure 25) of core TAN 98/15.

Four sedimentary types have been recognised. They are:

a) Homogeneous sediment:

The sediment is mainly biogenic. It is mainly made of diatom frustules, rather large black organic debris (wood, leaves), and ostracodes shells. The silt fraction only represents between 1.29 to 2.35 percents. The median grain-size MD_0 of the detrital fraction is fine, 3.8 μm , and P99 D_0 (percentile 99 of apparent grain size) is 14 μm . The mean H index for this massive sedimentary facies is 0.52. Mean shape index R_m of the silt grains is 0.59. One have to mention that H indices have been measured on silt grains only. Because they are round grains, it lowers the value of the H index (Francus, 2001). Further measurements of horizontality will be performed including diatoms. We expect to find stronger H indices values, because the diatoms appear to be horizontal and have a much more elongated shape.

b) Diffuse laminations:

The laminations are not visible macroscopically and barely visible in thin-sections. This facies is characterised by horizontally disposed diatom frustules (Figure 26). It is not possible to establish a count of those laminations because they are not continuous across a thin-section. The silt fraction only represents between 0.75

percents. The median grain-size MD_0 of the detrital fraction is fine, about 3.74 μm , and P99 D_0 is 12 μm . Mean shape index R_m of the silt grain is 0.59.

c) *Fine laminations:*

Laminations are visible macroscopically and microscopically. In thin-sections, they are a succession of light and dark very fine layers (Figure 27). A dark layer together with a white one is about 150 μm thick. By analogy with the coarse laminations (see next section), the dark layer is terrigenous, while the light layer is biogenic. A count of those laminations is difficult to obtain because some of the couplets fade away laterally. The silt fraction only represents between 0.75 percents. The median grain-size MD_0 of the detrital fraction is fine, about 3.62 μm , and P99 D_0 is 10.5 μm . Mean shape index R_m of the silt grain is 0.64.

d) *Coarse laminations:*

The sediment present laminations that are composed of the following two head members (Figure 27):

- Dark lamina: amorphous organic material, diatoms and terrigenous material. MD_0 of the silt fraction is 3.5 μm .
- Light lamina: amorphous organic material, and diatoms. No diatoms were visible at the petrographic microscope. However, observations at the SEM reveal that the amorphous layers are generally composed of very fine elongated pennates diatoms (Figure 28), *Nitzschia*. Some of the light layers do not contain diatoms; even when a careful SEM examination at high magnification is performed. Because no visible structure or chemical component (EDS) is detected, we assume that in such a case, the light laminae are made of algal or bacterial mat.

The thickness of the couplets range between 0.3mm and 2mm.

Carbonate:

The portion of the core between 57 and 70 cm depth show significant occurrences of carbonate. Carbonate appears as micritic grains, most probably very fine grained calcite, less than 2 μm in diameter. Micrite is dispersed in the sedimentary matrix. There are few 1mm thick beds, e.g. at 63.5 cm, strongly enriched in carbonates. The occurrence of carbonates is not related to a particular sedimentary facies.

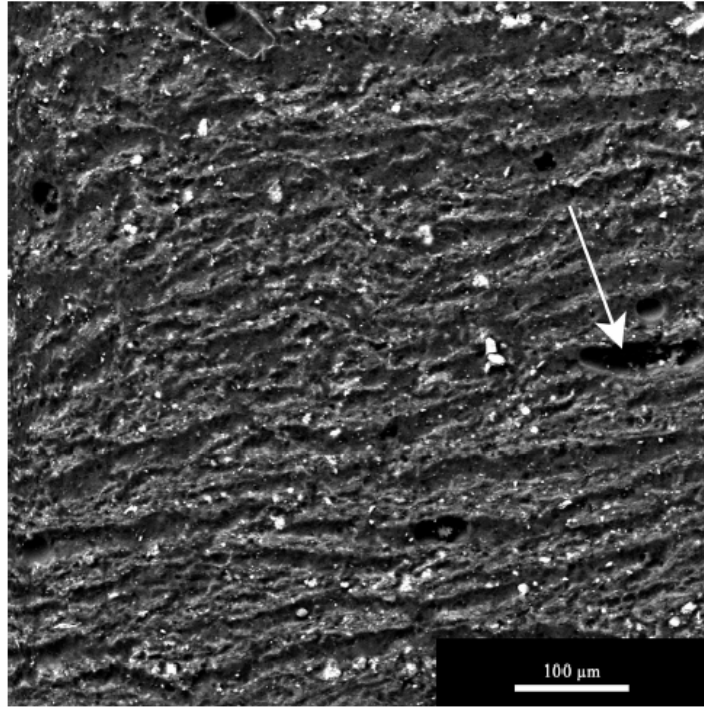


Figure 26: SEM view in BSE of core TAN98/15, 20 cm depth, Lake Tanganyika. Features, as diatoms, are horizontally disposed, but it is not possible to spot laminations limits. The white arrow points hole left by ostracodes shells. White spots are silts grains.

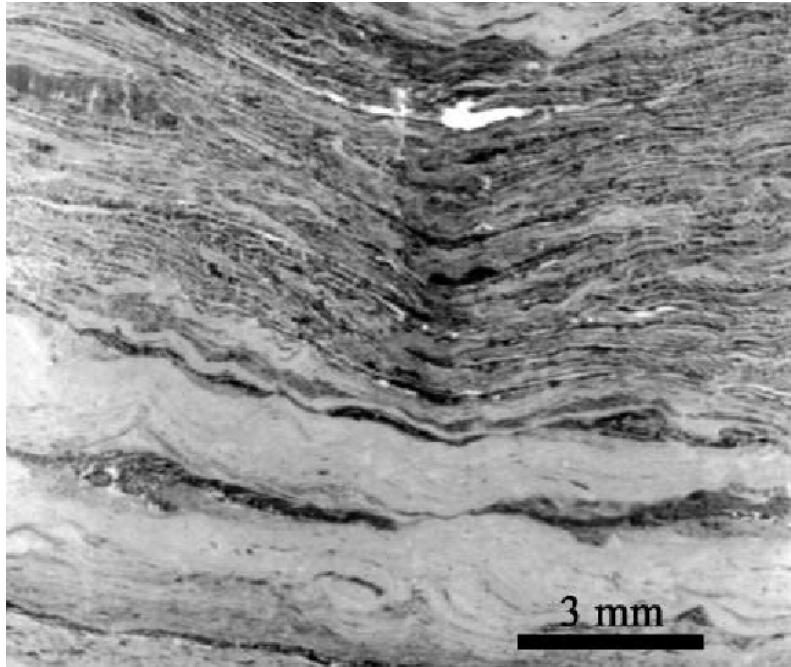


Figure 27: Flatbed scans of a thin-section, core TAN98/15, 20 cm depth, Lake Tanganyika. The upper part is an example of fine laminations. It is possible to follow some of them across the thin-section, but a lamination count would be very difficult to perform. The lower part is made of two coarse couplets.

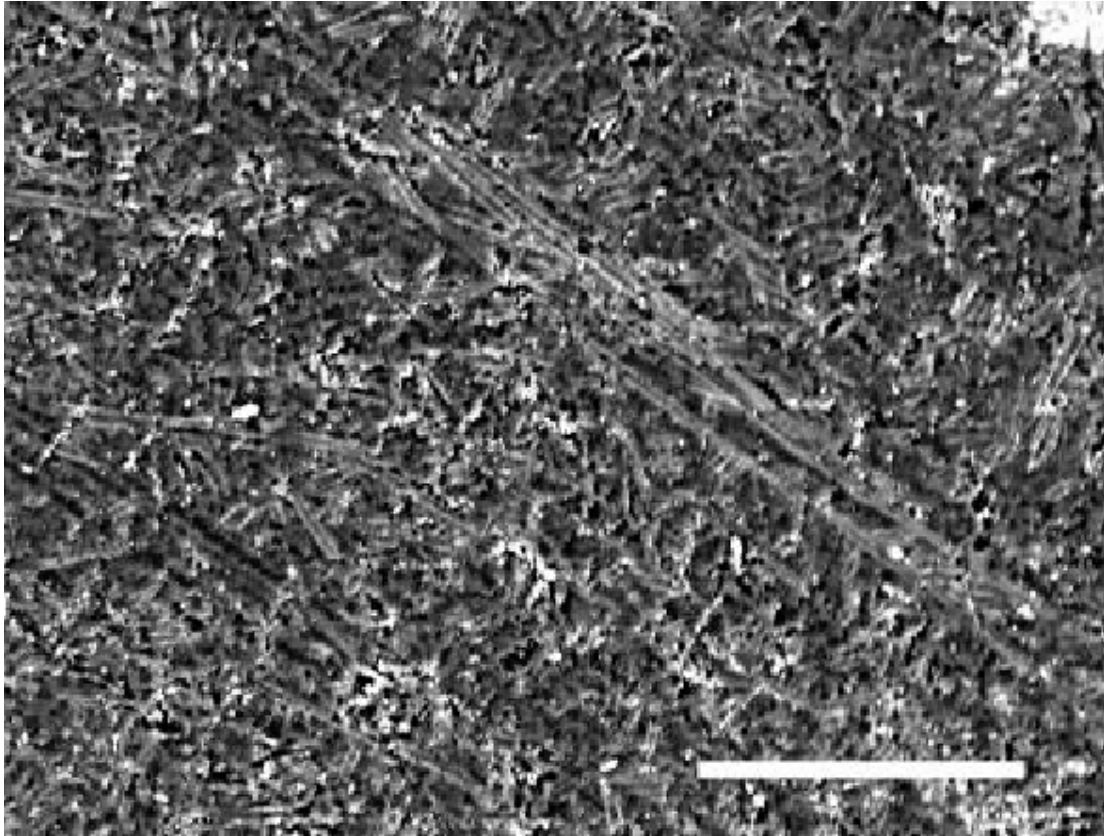


Figure 28: SEM view of long *Nitzschia* in BSE. Lake Tanganyika, core TAN98/15, 47 cm depth. Scale bar: 20µm.

Coarse sandy layer:

A coarse grained bed (grains > 63µm are 53 %), with a sharp lower and upper boundary occur at 55cm depth. It might be an ash layer, but further investigation is needed.

6.2.3.2 Sediment of the Kalemie Ridge taken at 430 m water depth

Introduction

Cores TG48 and TG50 were located on Kalemie ridge. Sedimentation rates at this bathymetric high are low, ~0.05 mm/yr according to Degens et al. (1971). Despite the fact that those locations are less suitable for high-resolution studies, they remain of interest because it is possible to recover longer records of environmental history. Though, because of potential particle winnowing typical for bathymetric highs (Hohman et al., 1997), one must keep in mind the possibility of sedimentary hiatus. Our goal here is to investigate whether the same sedimentary patterns than the one

recovered in modern periods have also occurred in older time periods. Unfortunately, no precise chronology has been established yet: 14C dates are pending (Scholz, pers. comm.). However, it is possible to estimate *grosso modo* the time window recovered by the studied sections based on published sedimentation rates for this area:

- TG48 section 93.1 -111 cm: ~ 18 ka - 22 ka
- TG50 section 150.8-233 cm: ~ 30 ka - 46 ka
- TG50 section 14-26 cm: ~ 2.8 ka - 5.2 ka

Sediment description

Core TG48: 93.5 - 111cm depth

The sediment is terrigenous, clay-rich with some silt grains and contains little black organic debris (wood, leaves), and shows a homogeneous structure. There are some yellow blebs that have been interpreted as faecal pellets. We investigated the chemical composition of the pellets under SEM using an Energy Dispersive Spectrometer (EDS). Their composition is similar to the sedimentary matrix, allowing us to disregard the interpretation of those structures being neoformed minerals.

Core TG 50, 150.8-233cm

150.8-163 cm

The sediment presents laminations that are composed of the following two head members (Figure 29):

- Dark lamina clay rich lamination slightly enriched in silts.
- Light lamina amorphous (organic?) material.

No diatoms were visible at the petrographic microscope. The thickness of the couplets range between 300µm and 2mm.

Some beds (up to 1/2 cm thick) are clearly bioturbated (Figure 30) and include numerous fecal pellets (Figure 31). Organic debris, fish scales, and wood debris are visible.

163 -178 cm depth

Sediment is composed of thin laminations. This interval differs from the previous one by its content of carbonate. This section indeed displays some beds made of micrite (very fine-grained calcite, less than 2 µm), usually concentrating in at the base of the clay-rich lamina. Micritic grains can also be widespread into both laminae.

There is a bed very rich in organic debris at 176 cm.

178-191 cm depth

Sediment is alike the previous section but the without calcite.

191-215.2 cm depth

The sediment is massive and homogenous.

215.2 –221 cm depth

The sediment is massive and homogeneous. They are some levels of diatom enrichment, and a bed of corresponding to a massive diatom bloom

221-233 cm depth

The sediment is massive and homogenous.

Core TG 50, 14-26cm:

Sediment is homogeneous, with a silt concentration of about 3 % instead of 1 % in deeper samples. It contains a lot of large organic debris.

6.2.4 Paleo-diatom analyses

Diatom analyses were performed on several cores, taken at different locations and water depth in the southern basin of the lake. The results of the most dominant diatom taxa, expressed as percentage of total counted valves, are depicted using the TILIA program. For each investigated sample the relative portion of planktonic, facultative planktonic, benthic and aerophytic taxa was calculated as well as the percentage of unbroken valves. The diatom productivity, expressed as number of frustules (=diatom cell; valve=1/2 frustule) per mg wet and dry weight were calculated.

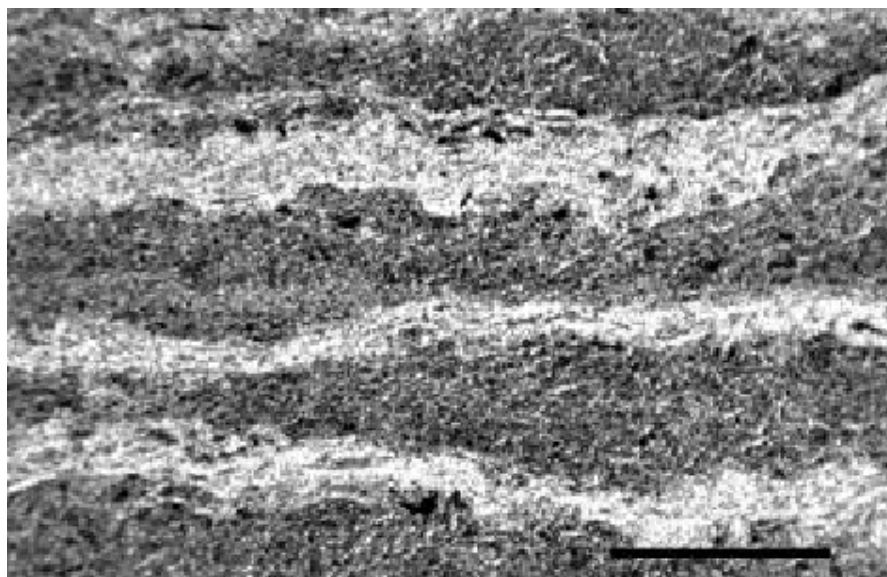


Figure 29: Laminated couplet at Kalemie Ridge. The clear lamina is made of organic debris. The dark lamina is made of terrigenous material. Scale bar is 500 μm .

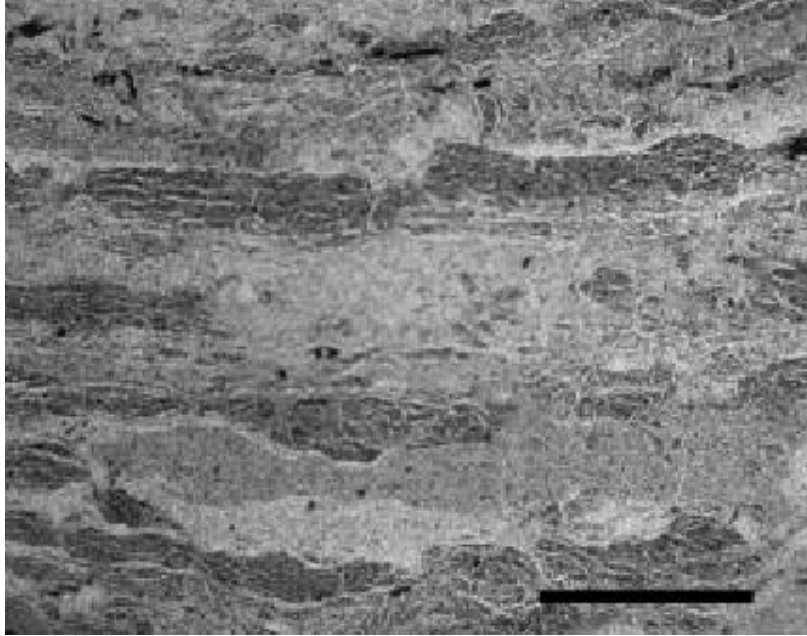


Figure 30: View at the petrographic microscope of bioturbated couplets. Lake Tanganyika, Kalemie Ridge, TG50, 155 cm depth - scale bar is 500 μ m.

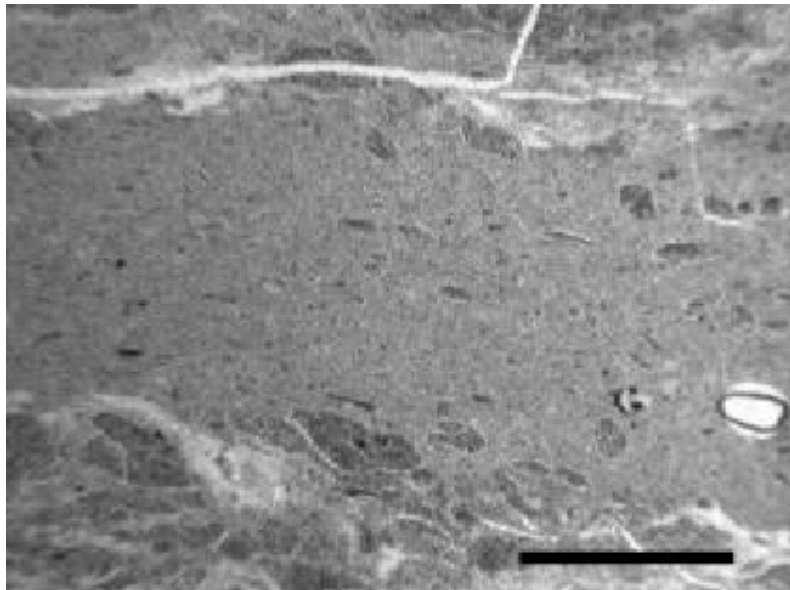


Figure 31: View at the petrographic microscope of faecal pellets. Lake Tanganyika, Kalemie Ridge, TG50, 158 cm depth - scale bar is 500 μ m.

6.2.4.1 Sediment core TAN 98/9, taken near Kasaba in 500m water depth

Sampling was done every 100 μ m for the upper 11cm and from each visible lamination of the rest of core TAN 98/9. Between 2.8 and 3.8cm sediment depth all slides (= 100 slides) were counted. The rest of the dark, finely laminated upper part

of the core was counted at regular intervals of 0.5 or 1mm. The results of the most dominant diatom taxa were expressed as percentage of total counted valves. The relative portion of planktonic, facultative planktonic, benthic and aerophytic taxa was calculated as well as the percentage of unbroken valves and the diatom productivity, expressed as cells per mg.

Results of the high-resolution diatom analysis of the upper 11.5cm of the core

Throughout this section of the core, layers dominated by planktonic species alternated with layers with a greater proportion of benthic species (Figure 32). “Long” *Nitzschia* spp. (e.g. *N. asterionelloides*, *N. spiculum*, *N. nyassensis*, *N. gracilis*, *N. lacustris*) (Figure 33) are the dominant planktonic species in the studied material. The “long” *Nitzschia* spp. were mostly broken which is reflected in the low portion of unbroken frustules at in these layers. The planktonic centricate diatoms (e.g. *Cyclostephanos* spp. (Figure 33) seldom reached more than 10%, but were dominant in the non-laminated part of the core beginning at 11cm sediment depth.

A peak of long *Nitzschia*'s appears at 0.99cm (20% of the total diatom abundance), at 1.50cm (20% of the total diatom abundance), between 2.30 and 2.48cm (up to 50% of the total diatom abundance), between 2.75 and 3.70cm (up to 80% of the total diatom abundance), between 4.89 and 5.29cm (up to 60% of the total diatom abundance), between 5.79 and 7.49cm (40% of the total diatom abundance), between 7.90 and 8.10cm (77% of the total diatom abundance), at 8.40cm (77% of the total diatom abundance), between 9.10 and 9.50cm (up to 42 % of the total diatom abundance), at 9.80cm (41% of the total diatom abundance), between 10.10 and 10.30cm (up to 70% of the total diatom abundance) and a smaller peak (26% of the total diatom abundance) at 10.70cm. After this smaller peak, *Cyclostephanos* spp. become more important in the sediment; 35% of the total diatom abundance at 11.20cm, 75% of the total diatom abundance at 17.70cm.

Small planktonic *Nitzschia* spp. also showed maximal relative abundance at different levels. A small peak of 7% of the total diatom abundance at the top of the core, between 0.82 and 0.99cm depth, of *Nitzschia vanoyei* and *N. lancettula*. The next peaks of these two related taxa appear between 3.50 and 3.70cm depth (up to 14% of the total diatom abundance), at 4.89cm and at 7.49cm depth. The last two peaks are very small and only account for about 5% of the total diatom abundance.

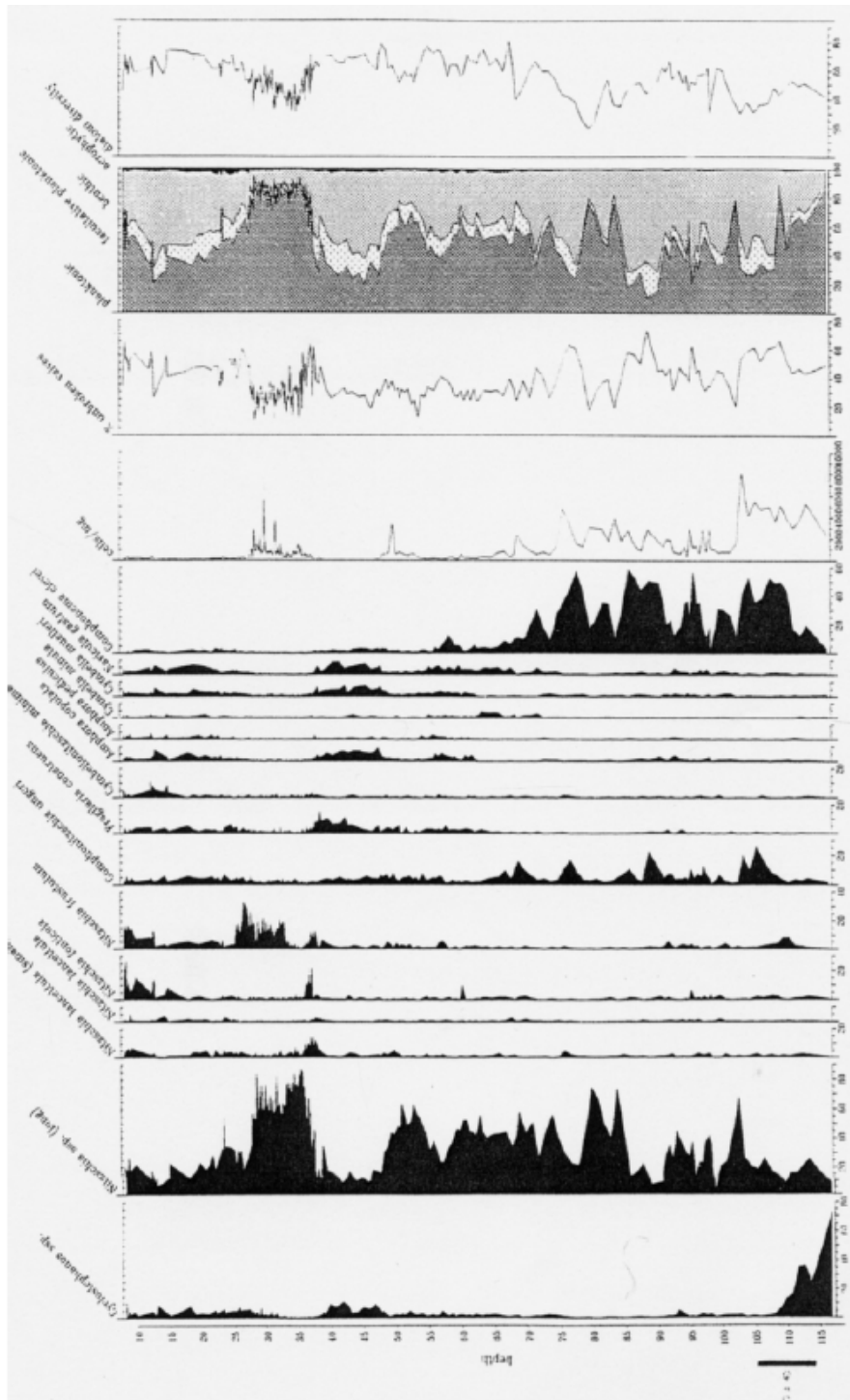


Figure 32: Major diatom taxa, percentage of unbroken valves, productivity (cells/mg dry sediment), percentage of planktonic, facultative planktonic, benthic, aerophytic diatoms and species diversity in the upper 11.5cm of sediment core TAN 98/9 taken near Kasaba in 500m water depth, Lake Tanganyika, Southern Basin.

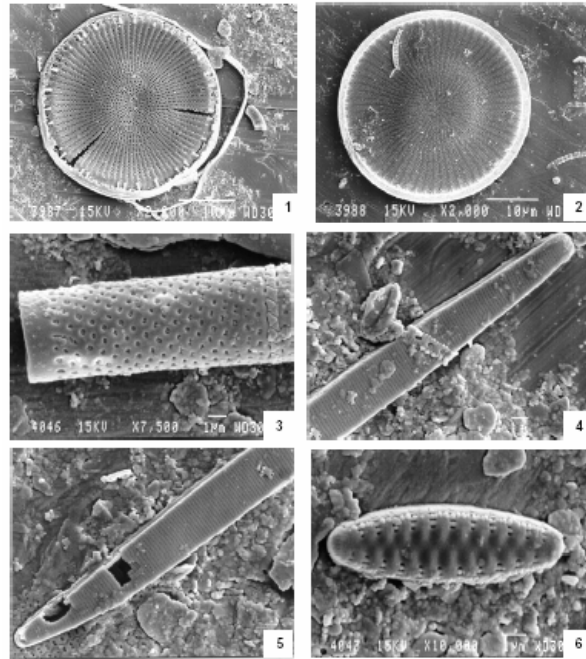


Figure 33: SCAN photographs of some diatom taxa observed in the sediment cores taken in the Southern Basin of Lake Tanganyika. 1, 2: *Cyclostephanos* sp.; 3: *Aulacoseira* cf. *granulata*; 4,5: “long” *Nitzschia* sp.; 6: *Fragilaria* sp.

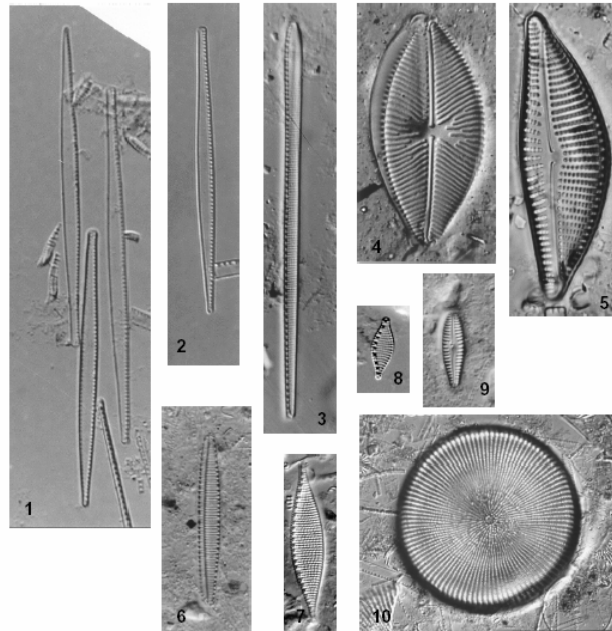


Figure 34: Light microscopic photographs of some diatom taxa observed in the sediment cores taken in the Southern Basin of Lake Tanganyika: 1, 2: “long” *Nitzschia* spp., 3: *Gomphonitzschia ungeri*; 4: *Navicula gastrum*; 5: *Cymbella muelleri*; 6: *Nitzschia frustulum*; 7: *Nitzschia lancettula*; 8: *Nitzschia vanoyei*; 9: *Gomphonema cleveii*; 10: *Cyclostephanos* sp.

A peak of *Nitzschia fonticola*, up to 25% of the total diatom abundance, appears between 0.50 and 1.07cm, followed by a smaller peak (up to 15% of the total diatom abundance) at 1.29cm and at 1.50cm. Other small peaks occur between 3.6 and 3.7cm a peak 20% of the total diatom abundance, at 5.59cm (10% of the total diatom abundance), at 9.51 cm (5% of the total diatom abundance), between 10.40 and 10.80cm and at 11.30cm (less than 5% of the total diatom abundance).

A peak of *Nitzschia frustulum*, up to 15% of the total diatom abundance, appears between 0.50 and 1.29cm, followed by a more important peak between 2.48 and 3.29cm (up to 30% of the total diatom abundance), a smaller peak between 3.60 and 3.70cm (up to 10% of the total diatom abundance) and some less important peaks (around 5% of the total diatom abundance) at 3.80cm, 5.59cm, 9.10cm, 9.90 cm and between 10.80 and 10.90cm.

The peaks of all these small *Nitzschia*'s appears in the core just before the arrival of the abundance of the "long" *Nitzschia*'s.

Gomphonitzschia ungeri is a relatively important taxon (around 5% of the total diatom abundance) for the entire sequence, up to 6.50cm sediment depth. Between 6.50 and 11.00cm, several more important peaks were observed: at 6.70cm (up to 12% of the total diatom abundance), at 7.60cm (up to 15% of the total diatom abundance), 8.90cm (up to 22% of the total diatom abundance), at 10.30cm (up to 20% of the total diatom abundance) and 10.50cm (up to 25% of the total diatom abundance). Five smaller peaks (10% or less than 10% of the total diatom abundance) are observed in between at 8.55cm, 9.10cm, 9.45cm, 9.70cm and 9.95cm.

The ecology of *Gomphonitzschia ungeri* is, however, not well known. Ross (1983) described it as an attached taxon, Gasse (1986) recorded this taxon from the plankton as well as epiphytic and Cocquyt (1998) mentioned it as a tychoplanktonic species. After the observation of a lot of specimens, the possibility that this taxon is heterogeneous, and consists of a cluster of several taxa (at least two, maybe three) with potentially different ecology, is realistic. Further observations are needed to confirm this hypothesis.

Fragilaria construens, a facultative planktonic species, has its maximal relative abundance (between 5 and 10% of the total diatom abundance) between 3.75 and 4.4cm sediment depth. Some smaller peaks are observed in the upper 2.5cm.

Gomphonema clevei (Figure 34) is the most important benthic diatom. This taxon has its maximal relative abundance between 7.50 and 11.50cm with up to 55% of the total diatom abundance, interrupted by layers where this species attains only 10% of

the total diatom abundance. From 7.50cm up to 3.70cm depth the importance of *G. clevei* decreases, to become quasi nihil in the zone between 3.70 and 2.70cm depth. Between 2.6 and 0cm it is present again, but with less than 5% of the total diatom abundance.

Cymbellonitzschia minima, *Amphora copulata*, *A. pediculus*, *Cymbella minuta*, *C. muelleri* and *Navicula gastrum* were some of the most important other benthic taxa. The benthic fraction, exclusive of *G. clevei*, never accounted for more than 20% relative abundance.

The highest productivity was observed just after the transition zone of *Cyclostephanos* and the zone with alternating dominance of “long” *Nitzschia*'s and benthic diatoms (10.2-11.0cm depth). The highest obtained peak is 5200 frustules/mg dry sediment (6000 frustules/mg wet weight) at 10.4cm depth. Smaller peaks were observed between 10.20 and 6.50cm. Productivity is very low between 6.5 and 5.5cm. A small peak occurred between 5.49 and 4.80cm, with a maximum of 3400 frustules/mg dry sediment (2500 frustules/mg wet weight) at 5.00cm. Between 4.80 and 3.90cm, there was quasi no productivity at all. Productivity increased again from 3.90 up to 2.30cm with a maximum of 1500 frustules/mg dry sediment (8.000 frustules/mg wet weight). Productivity was very low in the upper 2.30cm of the sediment.

The percentage of unbroken valves varies between 10 and 70%. The percentage of unbroken valves was highest when the lowest abundance of “long” *Nitzschia*'s was observed and vice versa. The layers with a high relative abundance of *Gomphonema clevei* have a higher percentage of unbroken valves. Valves of *Gomphonema clevei*, *Nitzschia fonticola* and *N. frustulum* were mostly observed unbroken; valves of *Navicula gastrum* were mostly broken. The benthic taxa belonging to the genera *Amphora* and *Cymbella* were observed as broken as well as unbroken valves. Besides parts of valves, dissolution of the diatoms was sometimes observed within the “long” *Nitzschia*'s. In those cases, the valves were compactly clustered together.

The relative abundance of planktonic diatoms varies between 10 and 95%. Most planktonic specimens occur during the highest relative abundance of “long” *Nitzschia*'s: between 2.75 and 3.70cm, between 4.90 and 5.30cm, between 5.80 and 7.50cm, between 7.90 and 8.40cm, at 10.20cm, at 10.70cm and between 11.00 and 11.70cm.

Facultative planktonic diatoms obtained their highest relative abundance in layers where *Fragilaria construens* has his highest relative abundance (between 3.75 and 4.40cm sediment depth) and at 10.60cm. Other facultative plankton diatoms, such as *Cyclotella* spp. (most of which are confined to the littoral zone of the lake), were observed only sporadically and always in very small, negligible, percentages.

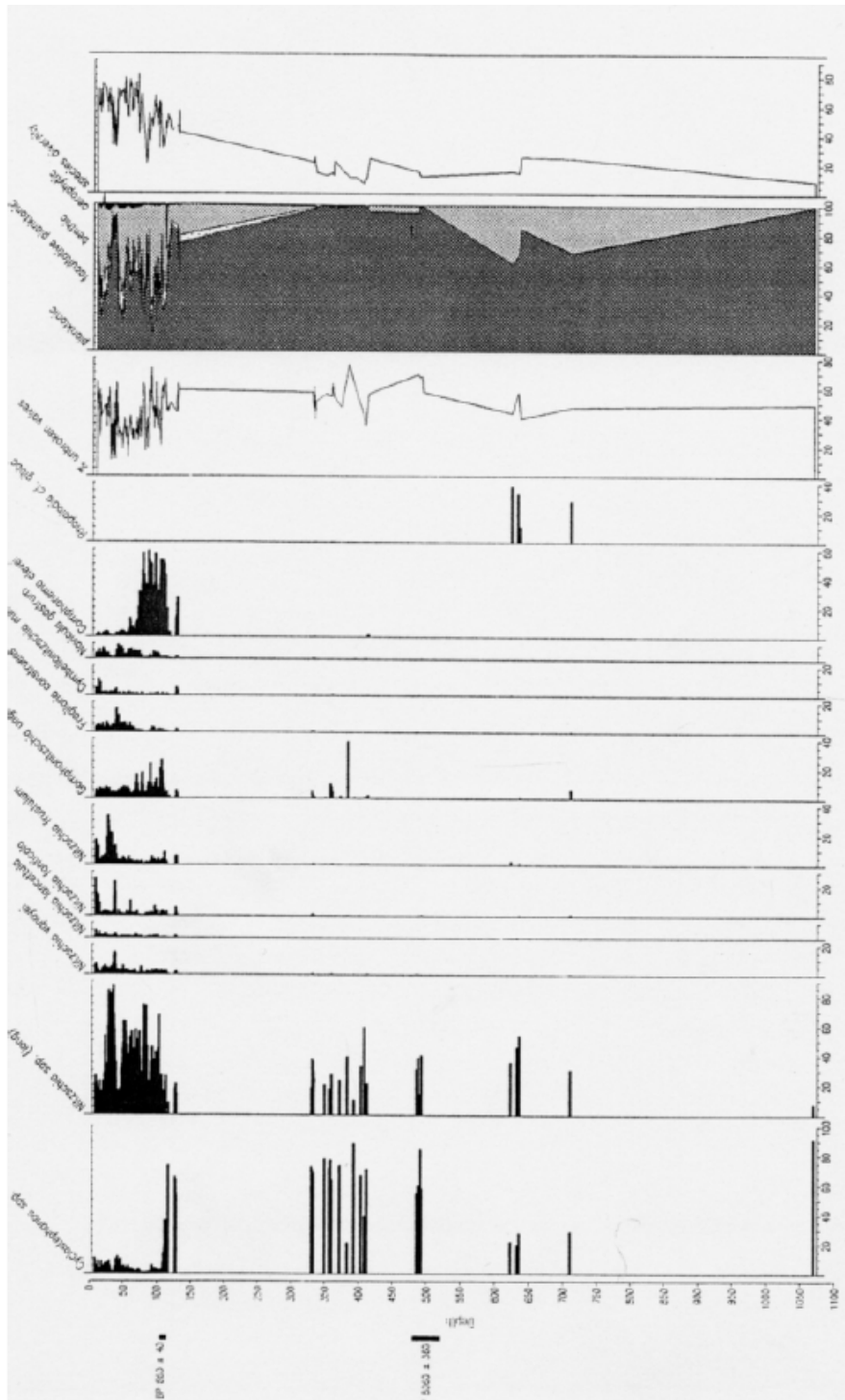


Figure 35: Major diatom taxa, percentage of unbroken valves, productivity (cells/mg dry sediment), percentage of planktonic, facultative planktonic, benthic, aerophytic diatoms and species diversity in core TAN 98/9 taken near Kasaba in 500m water depth, Lake Tanganyika, Southern Basin.

The relative abundance of benthic diatoms varies between 10 and 68%. Most benthic specimens were observed in the zone between 7.00 and 11.70cm when *Gomphonema clevei* obtained its highest relative abundance and in the zone between 0 and 7 cm when the other benthic taxa (e.g. *Cymbellonitzschia minima*, *Amphora copulata*, *A. pediculus*, *Cymbella minuta*, *C. muelleri* and *Navicula gastrum*) obtained their highest relative abundance. The relative abundance of areophytic taxa (e.g. *Hantzschia amphioxys*, *Pinnularia* spp.) is negligible. Species richness decreases slightly from the top of the sediment core to 11.70cm depth. Three zones of higher species richness can be distinguished: from the top to 2.53cm; between 3.95 to 6.75cm, between 9.15 and 10.00cm. Zones with lower species richness correspond to layers with higher proportions of long *Nitzschia*'s.

Results of the diatom analysis of the entire core

As the aim of the ENSO project was the study of the sediments of the last 1000 year, only a small number of samples, taken deeper than 12 cm were analysed (Figure 35).

Alternating zones rich in *Cyclostephanos* spp. and "long" *Nitzschia*'s are observed in the deeper part of the sediment core. Besides these planktonic taxa, a small number of benthic species were observed. Most important are *Gomphonitzschia ungeri* (37% at 38 cm depth) and *Rhopalodia* cf. *gibba* (40% at 62cm depth).

The percentage of unbroken valves varies between 35 and 72%. The lowest percentage of unbroken valves correspond with layers rich with "long" *Nitzschia*'s; the highest percentage of unbroken valves with layers rich with *Cyclostephanos* spp., *Gomphonitzschia ungeri* and *Rhopalodia* cf. *gibba*.

Planktonic species are the most abundant group of diatoms, even up to 100%. The lowest relative abundance was observed at 62cm and 71cm, where benthic species (particularly *Rhopalodia* cf. *gibba*) accounted for 40% and 30% of diatom abundance respectively.

Facultative planktonic and aerophytic taxa were almost absent in most of the core, with exception of the upper 13cm.

Species diversity is very low beneath 11cm depth, between 9 and 25 taxa. The "highest" diversity was observed when the relative abundance of benthic species was highest (at 13cm depth and between 62 and 71cm depth).

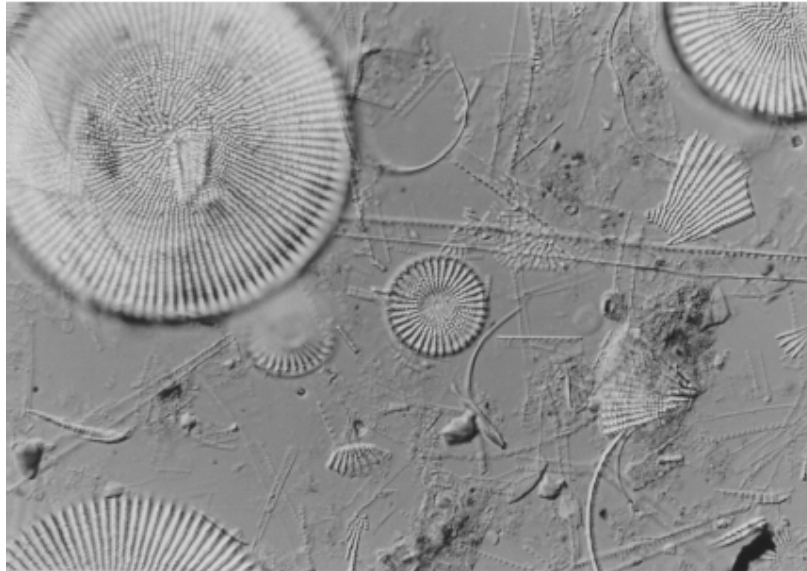


Figure 36: *Cyclostephanos* spp. and broken valves of “long” *Nitzschia* spp. as observed in deeper layers of sediments (37cm sediment depth) of core TAN 98/9, taken near Kasaba in 500m water depth.

Analysis of the diatom data set

Four major groupings were delimited in the upper dark finely laminated sediments of core TAN 98/9, using the CONISS cluster analysis program.

- Zone A: situated between 11.70 en 7.39cm. *Gomphonema clevei* and “long” *Nitzschia* spp. are relatively the most dominant diatom taxa. *Gomphonitschia ungeri* reached its highest relative abundance.
- Zone B: situated between 7.39 and 3.65cm. This grouping is characterised by “long” *Nitzschia* spp. *Gomphonema clevei* and *Gomphonitschia ungeri* became less important. *Fragilaria construens* and *Navicula gastrum* reached their highest relative abundance.
- Zone C: situated between 3.65 and 2.73cm. This grouping is characterized by “long” *Nitzschia* spp. and *Gomphonema clevei*, *Gomphonitschia ungeri*, *Fragilaria construens* and *Navicula gastrum* are relatively not important. *Nitzschia frustulum* became relatively more important.
- Zone D: is situated between 2.73 cm and the top of the core. This zone is characterised by the relative abundance of the “long” *Nitzschia*’s at the expense of benthic taxa.

The data-set of the high resolution diatom analysis of the upper 11.5cm of the sediment core was submitted to a PCA (figs 38 and 39). The fluctuations in the diatom community of the sediment core are given in Figure 37. The second axis represent the residual values of the PCA analysed, which are plotted against depth. The fluctuations in this diagram correspond with the fluctuations observed in the “long” *Nitzschia* spp.

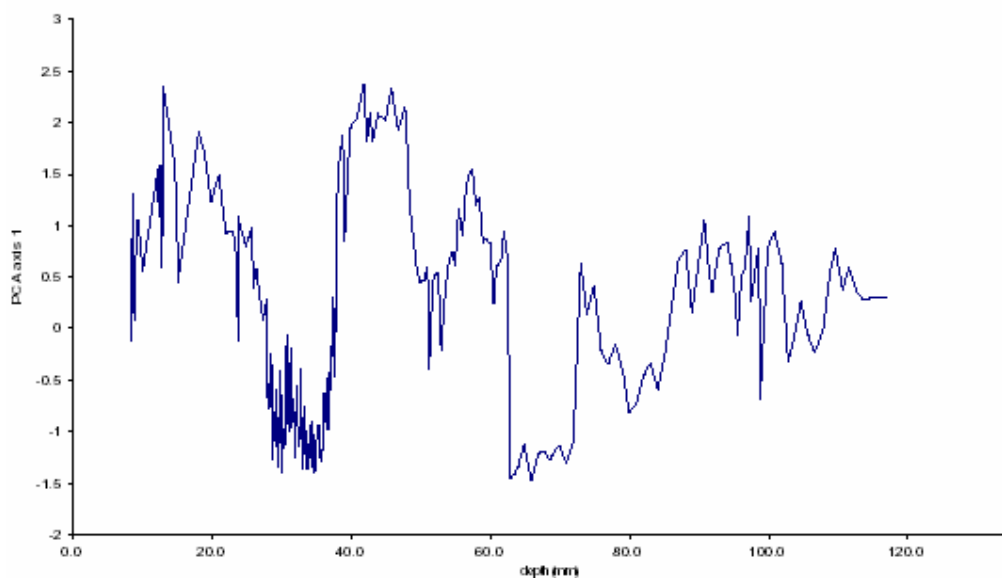


Figure 37: First axis of the PCA of the upper 11.7cm sediments of core TAN 98/9, taken near Kasaba in 500m water depth, representing the entire diatom community.

The four groupings, delimited in the CONISS cluster analysis, can be found also in the Principal Component Analysis executed on the same data set (Figure 38). Samples belonging to Zone A, characterised by “long” *Nitzschia* spp. and *Gomphonema clevei* are distinctly separated from the rest of the samples along the second axis. Samples belonging to Zone C, characterised by “long” *Nitzschia* spp., are separated from the rest of the samples along the first axis. The delimitation of Zones B and C is more diffuse. “Long” *Nitzschia* spp. and *Gomphonema clevei* are also clearly separated from the other taxa in the species ordination (Figure 39).

These results correspond well with the results of the PCA species ordination: “long” *Nitzschia* spp. and *Gomphonema clevei* are distinctly separated from the other taxa.

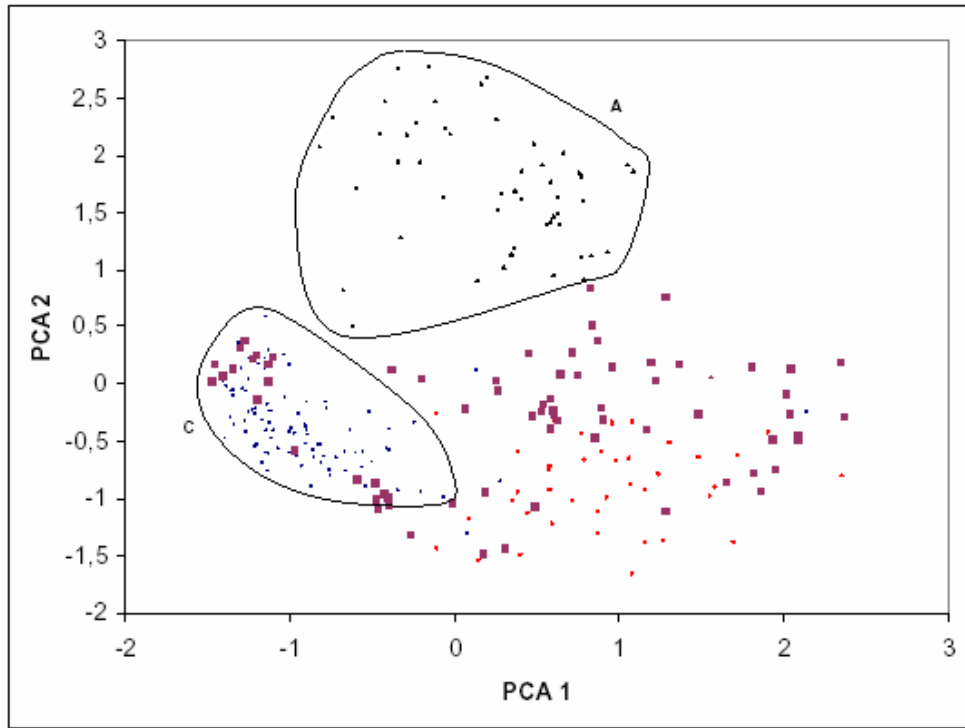


Figure 38: PCA ordination of the samples of core TAN 98/9, taken near Kasaba in 500m water depth, with indication of the groupings A and C, delimited in the CONISS cluster analysis.

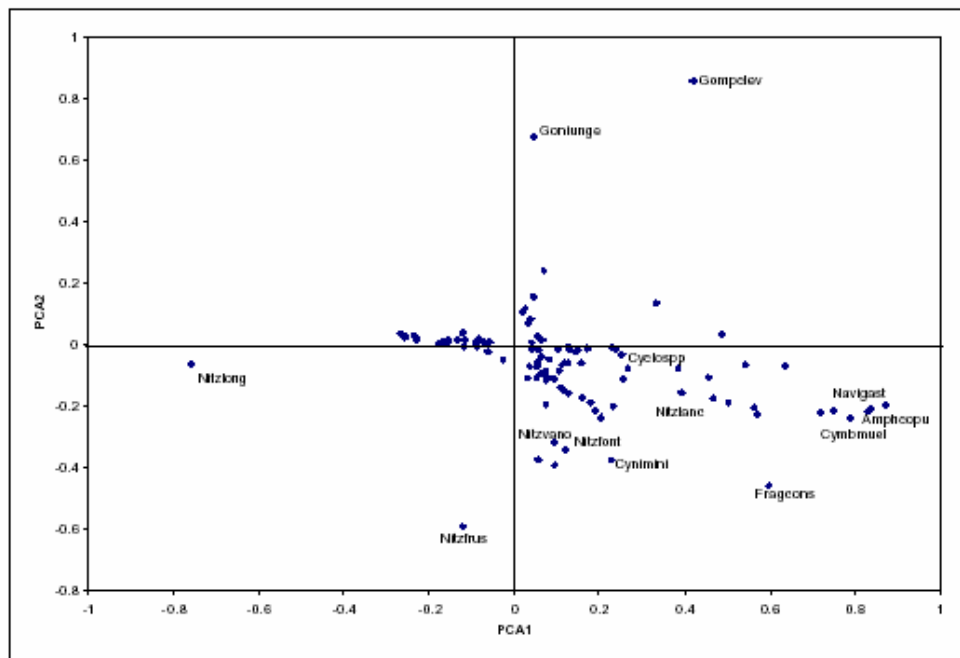


Figure 39: PCA ordination of the diatom taxa of core TAN 98/9, taken near Kasaba in 500m water depth, with indication of the most important diatom taxa.

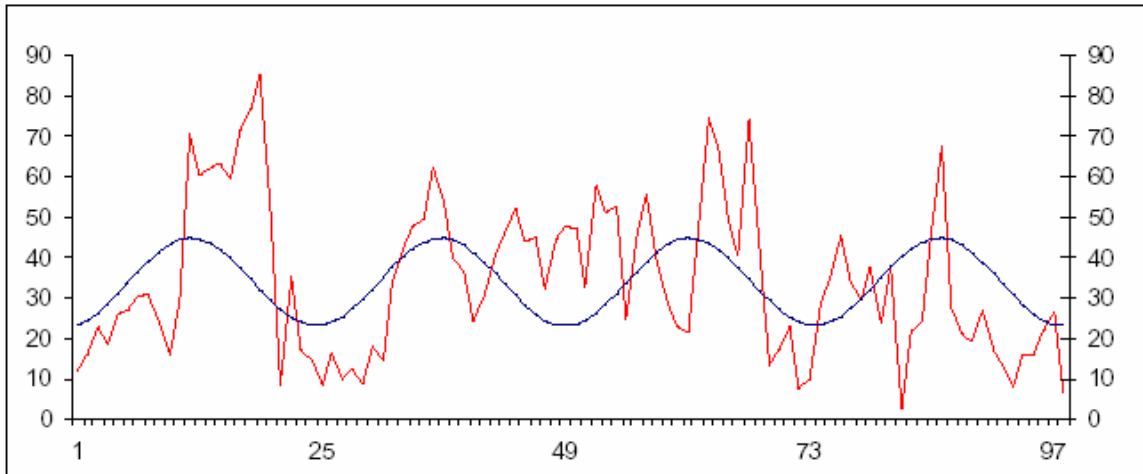


Figure 40: Core TAN 98/9: time series analysis of “long” *Nitzschia* ssp. for the upper sediments (1.8–11.7cm).

A time series analysis was performed on the relative abundance data of the “long” *Nitzschia*’s for the upper 11cm. Four repeating periods could be distinguished (Figure 40). These periods could correspond with a periodicity of 200 year based on the ¹⁴C dating at 10.5-11.5cm depth (830 years old, see 2.2.2.).

6.2.4.2 Sediment core TAN 98/15, taken near Kipili in 1200m water depth

Sampling was done every 500 μm for the upper 18 cm of core TAN 98/15. The results of the most dominant diatom taxa, expressed as percentage of total counted valves, the relative portion of planktonic, facultative planktonic, benthic and aerophytic taxa, the percentage of unbroken valves and the diatom productivity, expressed in cells/mg dry sediment, are given in figure 41.

“Long” *Nitzschia* spp are the dominant planktonic species in the studied material with up tot 98% of the total diatom abundance at 17.0cm sediment depth and a peak (75% of the total diatom abundance) at 3.0cm. The lowest abundance (10%) was observed between 8.5 and 9.0cm. The “long” *Nitzschia* spp. were mostly broken which is reflected in the low portion of unbroken frustules at these layers. The planktonic centricate diatoms (e.g. *Cyclostephanos* spp.) reached more than 10% of the relative diatom abundance only twice: between 16.5 and 14.5 cm and between 7.5 and 4.5cm. *Nitzschia vanoyei* and *N. lancettula* never reached a relative abundance above the 5% of the total diatom abundance.

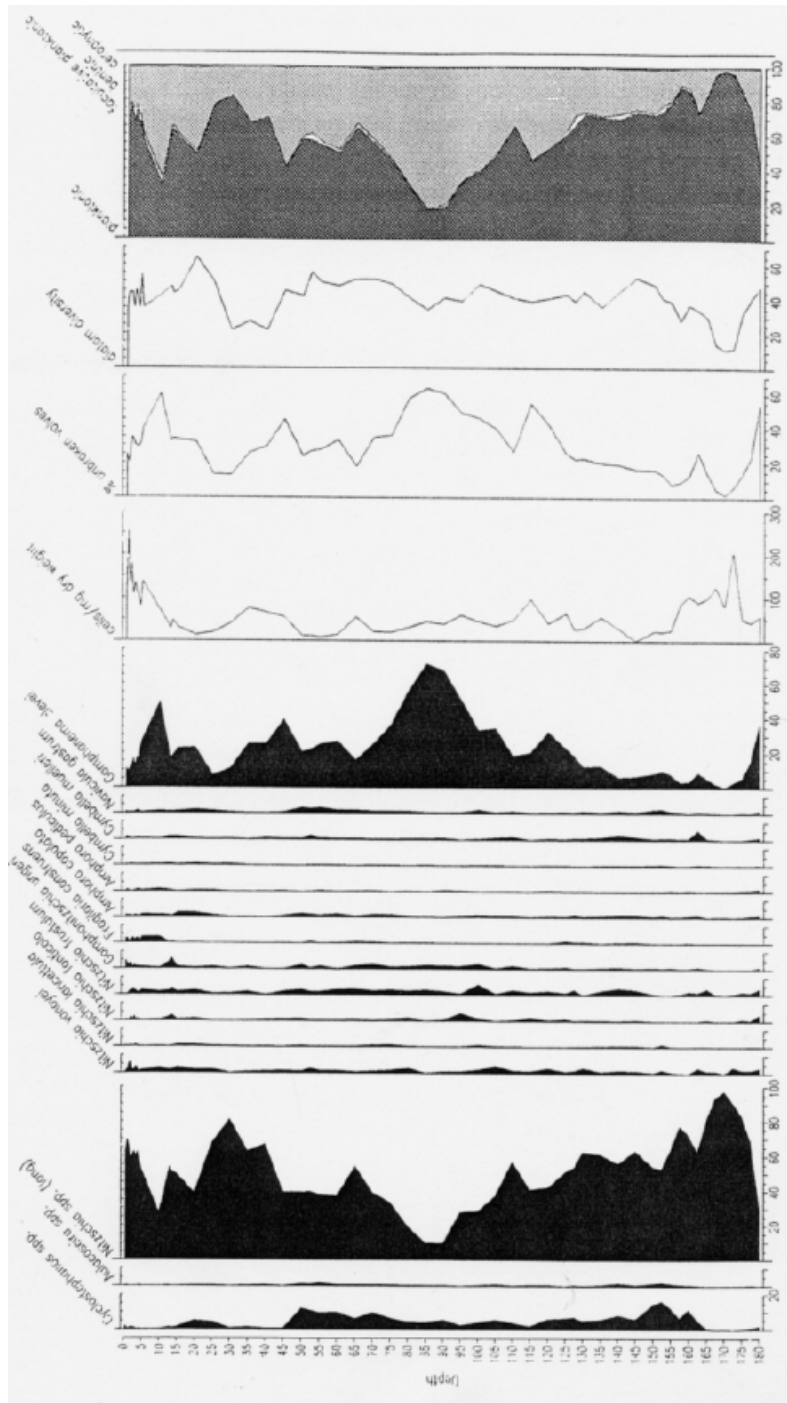


Figure 41: Major diatom taxa, percentage of unbroken valves, productivity (cells/mg dry sediment), percentage of planktonic, facultative planktonic, benthic, aerophytic diatoms and species diversity in the upper 18cm of sediment core TAN 98/15 taken near Kipili in 1.200m water depth, Lake Tanganyika, Southern Basin.

One small peak of *Nitzschia fonticola* and one of *Nitzschia frustulum* (5% of the total diatom abundance) appears at 9.5cm and at 10.0cm respectively. *Nitzschia frustulum* was observed along the entire investigated part of the core in very low percentage (1% of the total diatom abundance), in contradiction with *Nitzschia fonticola*.

Fragilaria construens is the only important facultative planktonic diatom. A small peak of this taxon was observed between 0.5 and 1cm (only 5% of the total diatom abundance).

Gomphonema clevei is the most important benthic diatom. This taxon has its highest relative abundance between 7.5 and 9.5cm depth with up to 70% of the total diatom abundance. A smaller peak was observed at 10.0cm (50% of the total diatom abundance), at 4.5cm (40% of the total diatom abundance), at 18.0cm (35% of the total diatom abundance) and at 12.0cm (30% of the total diatom abundance). Only at one depth (17.0cm) the percentage of *Gomphonema clevei* drops to about zero.

Beside *Gomphonema clevei*, most important other benthic taxa are: *Amphora copulata*, *A. pediculus*, *Cymbella minuta*, *C. muelleri* and *Navicula*. However, these species never reach more than 5% of the total diatom abundance. A peak of *Nitzschia paleacea* was observed at 11.5cm depth (up to 15.3% of the total diatom abundance).

The percentage of unbroken valves varies between 2 and 60%. The percentage of unbroken valves was lowest when the highest abundance of “long” *Nitzschia*'s was observed (17.0 and 3.0cm) and highest when *Gomphonema clevei* has its highest relative abundance (between 7.5 and 9.5cm). As mentioned for core TAN 98/9, dissolution of the diatoms was sometimes observed within the “long” *Nitzschia*'s; the valves were than compactly clustered together.

The relative abundance of planktonic diatoms varies between 17 and 98%. Most planktonic specimens were observed when the “long” *Nitzschia*'s obtained their highest relative abundance.

Facultative planktonic diatoms have their highest relative abundance at the top of the core (between 0.5-1.0cm) (4.4%). Besides *Fragilaria construens*, which obtained a very small peak at 12.5cm, a small number of *F. africana*, *F. pinnata* and facultative planktonic *Cyclotella* spp. were observed.

The relative abundance of benthic diatoms varies between 2 and 82.5%. Most benthic specimens were observed in the zone between 7.5 and 9.5cm depth when *Gomphonema clevei* obtained its highest relative abundance.

The relative abundance of aerophytic taxa (e.g. *Hantzschia amphioxys*, *Pinnularia* spp.,) is negligible.

Species diversity was highest, 64 taxa per 500 valves, at 2.0cm. Periods with low diversity were observed at 17.0cm (11 taxa per 500 valves) and between 3.0 and 4.7cm (22 taxa per 500 valves) when “long” *Nitzschia* spp. reached their highest relative abundance.

6.2.4.3 Sediment core TAN 98/7, taken near Kapembwa in 330m water depth

Sampling of core TAN 98/7 was done every 100 µm for the upper 2.5cm. Four samples were analyzed but investigation of this core was not carried out further because the upper, dark laminated sediments, were lacking in the core, and the aim of the present project was the study of sediments from the last 1000 years in Lake Tanganyika (Figure 42). The most important diatoms were “long” *Nitzschia* spp. (between 56.1% and 80.2%) and *Gomphonema clevei* (2.3% and 24.6%) (Figure 40).

6.3 Other micro-paleontological analyses

6.3.1 Sponges

In core TAN 98/9, taken in 500m water depth near Kasaba, the highest number of spicules per 500 diatom valves (with a maximum of 66 spicules) was observed between 4 and 4.5cm sediment depth (Figure 43). Between 5.4 and 6.9cm the spicules were somewhat more abundant with a maximum of 29 spicules per 500 diatom valves and at 10.5cm depth with 14.6 spicules per 500 diatom valves.

In core TAN 98/15, taken in 1200m water depth near Kipili, the highest number of spicules per 500 diatom valves was observed at 5cm sediment depth; two smaller peaks between 6 and 7cm and two between 15 and 16cm (Figure 44). Four other levels where the sponges spicules were somewhat more abundant could be distinguished at 2.5cm, 8.5cm, 10cm and 12.5cm depth.

Noteworthy is that sporadically gemmascleres were observed. These sponge elements have not yet been reported from Lake Tanganyika.

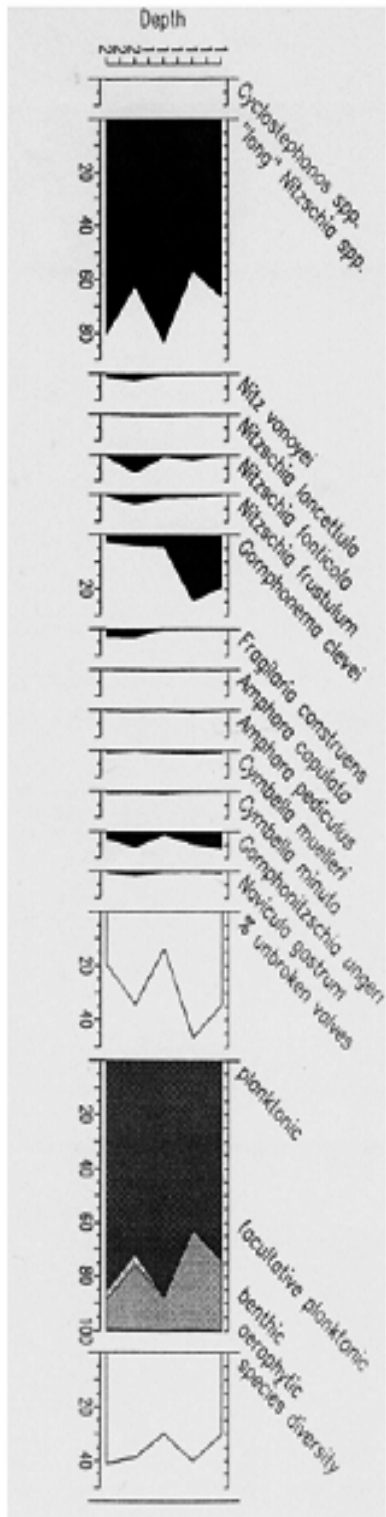


Figure 42: Major diatom taxa in the upper 2 cm of sediment core TAN 98/7 taken near Kapembwa in 330m water depth, Lake Tanganyika, Southern Basin.

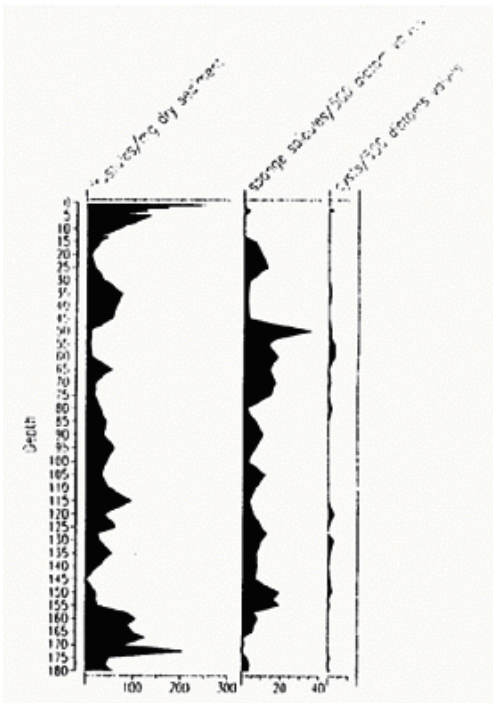


Figure 43: Number of sponge spicules and cysts per 500 diatom valves, observed in the sediment core TAN 98/9 taken near Kasaba in 500m water depth, Lake Tanganyika, Southern Basin.

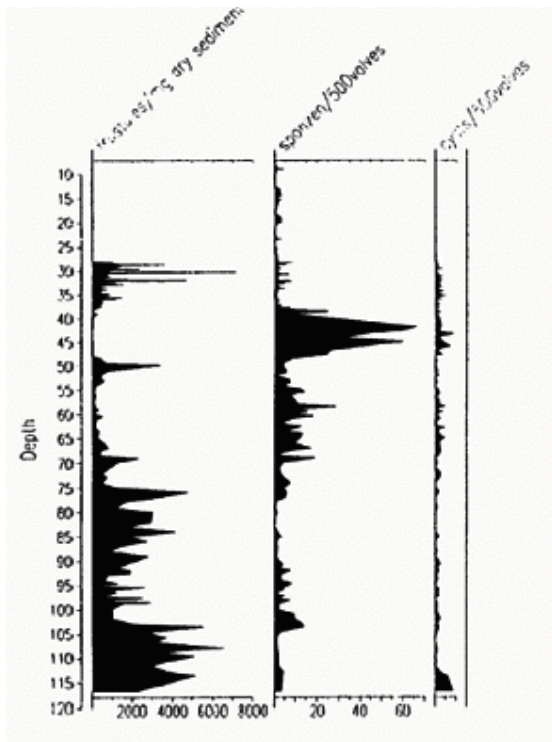


Figure 44: Number of sponge spicules and cysts per 500 diatom valves, observed in sediment core TAN 98/15 taken near Kipili in 1200m water depth, Lake Tanganyika, Southern Basin.

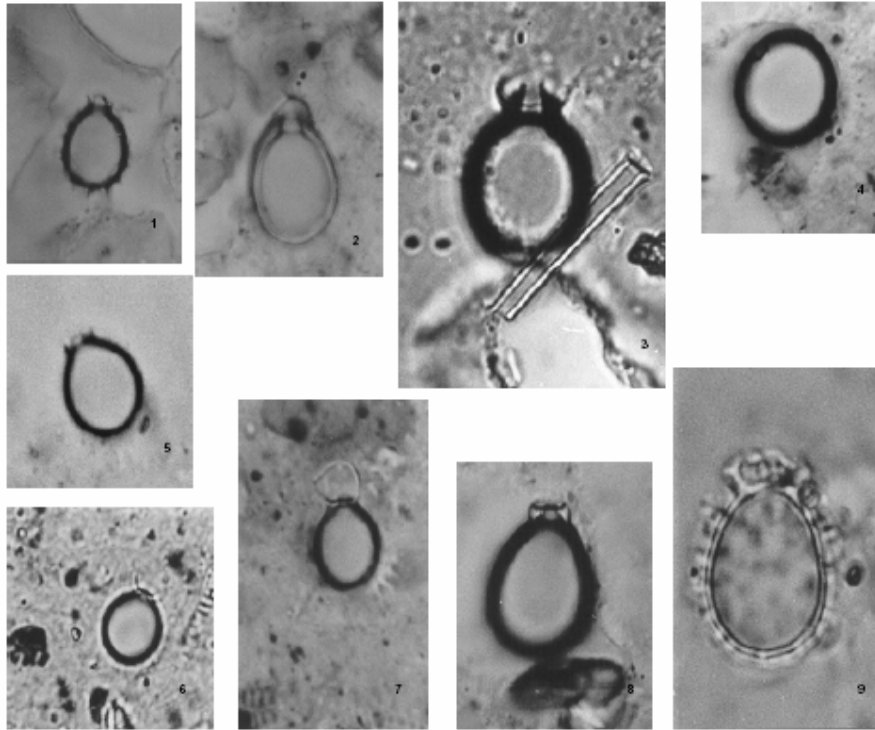


Figure 45: Light microscopic photographs of some stomatocysts observed in the sediment cores taken in the southern basin of Lake Tanganyika.

6.3.2 Cysts of Chrysophytes and Dinophytes

During the investigation the cysts of these two higher taxonomic groups (Figure 45) were treated together.

The number of observed cysts of Chrysophytes and Dinophytes was very low in the investigated core material. In core TAN 98/9, the number of observed cysts during the investigation was never higher than 9 (at 4.3cm depth) and in one third of the samples no cysts were observed (Figure 43). In core TAN 98/15 the observed cysts never exceeded 6 per 500 diatom valves (at 13.6cm depth) and in one third of the samples no cysts were observed (Figure 44).

6.3.3 Remains of Cyanobacteria

No remains of Cyanobacteria were observed during the analysis of the sediment cores.

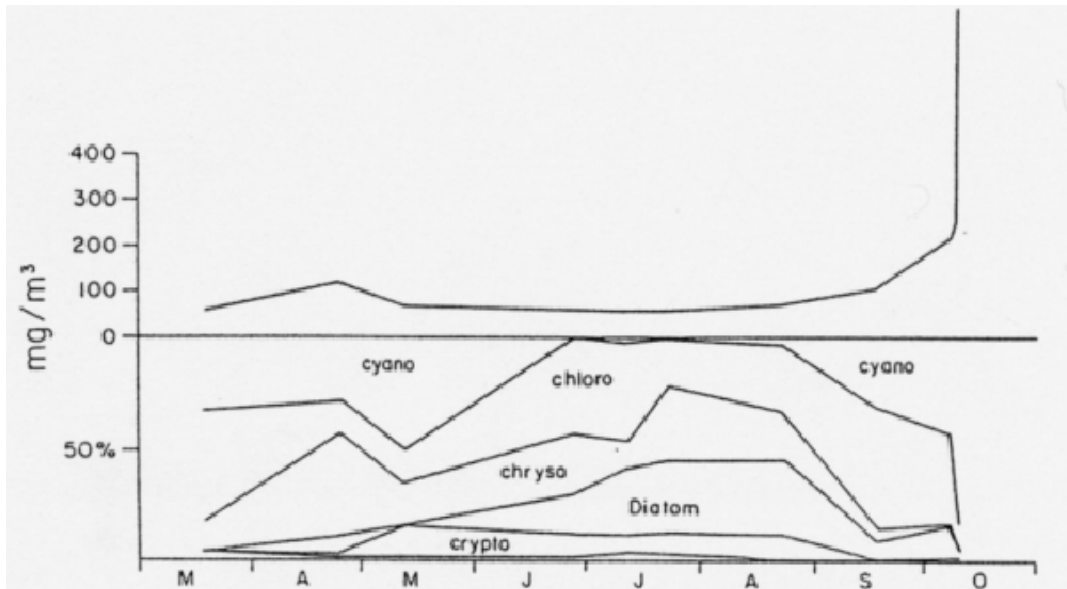


Figure 46: Seasonal variation in phytoplankton biomass and composition off Kigoma in 1975 (after Hecky et al. 1978).

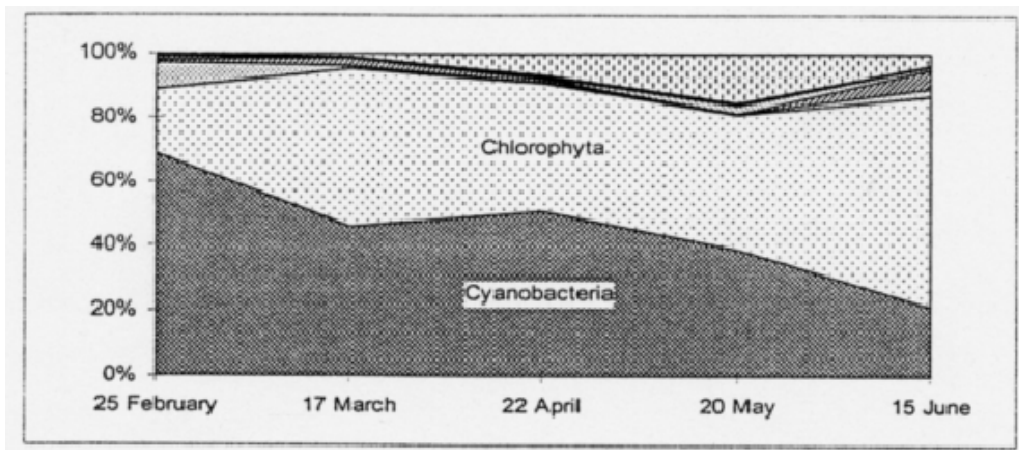


Figure 47: Seasonal variation in phytoplankton composition 2 km off Kigoma in 1998.

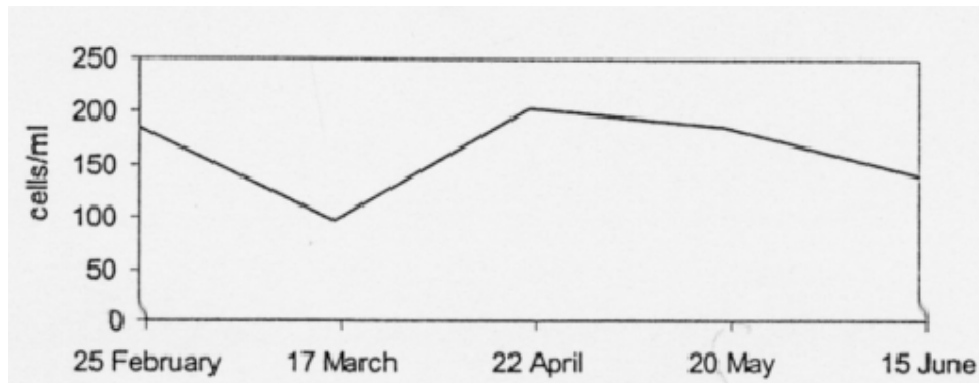


Figure 48: Seasonal variation in phytoplankton density, expressed as cells/ml, 2km off Kigoma in 1998.

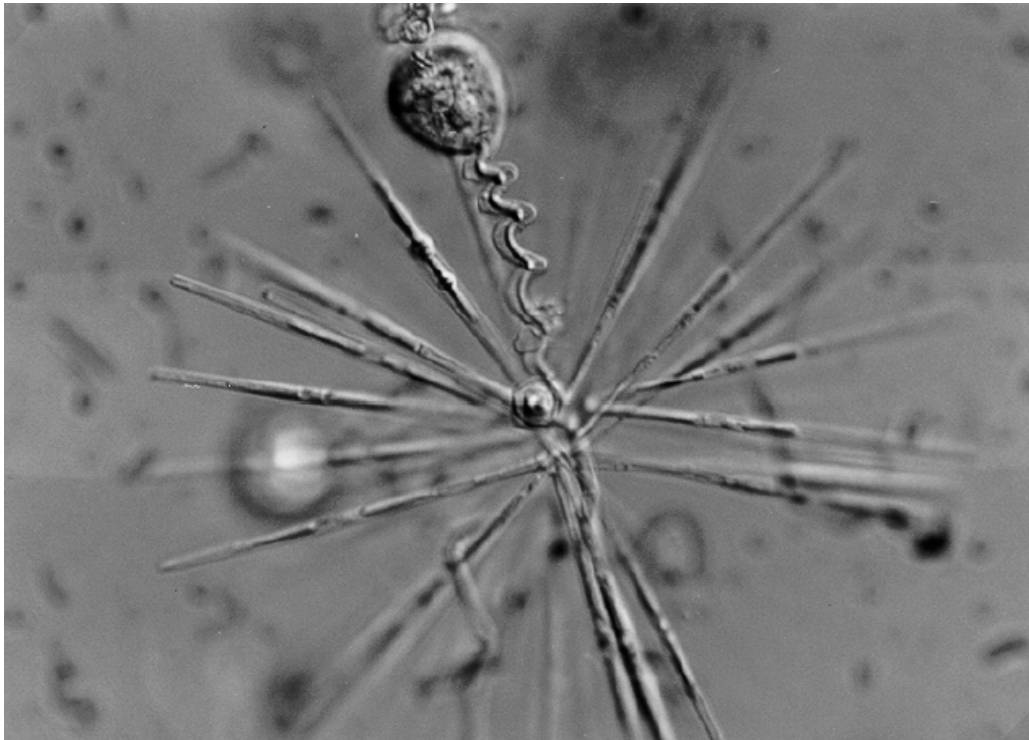


Figure 49: Colony of *Nitzschia asterionelloides*, observed in recent phytoplankton samples of Lake Tanganyika, taken near Kigoma in July-August 1998 and 1999.

6.4 Recent phytoplankton research

Seasonality as described by Hecky *et al.* (1978) and Hecky and Kling (1981) in the pelagic of Lake Tanganyika was also observed in the pelagic samples taken monthly in 1998, from February till June, 2km offshore Kigoma (Figure 46).

The same succession of higher taxonomic groups (Cyanobacteria/Chlorophyta) as described by Hecky *et al.* (1978) and Hecky and Kling (1981) was observed in 1998. Cyanobacteria were the most important group, followed by green algae. Diatoms were less important during the time of the sampling while Dinophyta and Euglenophyta were more important.

The importance of the Cyanobacteria decreased from 70% end of February to 24% mid June, the Chlorophyta increased from 20% to 60%. (Figure 47). Recent samples, taken in the pelagic zone off Kigoma in July 1998 and July 1999 by P.-D. Plisnier, were examined for their diatom content. *Nitzschia asterionelloides*, a colony building diatom (Figure 46), was the dominant taxon in both samples. However, in the 1999 sample, a large number of a small *Vorticella* species (Protozoa), feeding on bacteria, were epiphytic on the colonies of this *Nitzschia* sp. (Figure 49). *Vorticella* specimens

were also present in July 1975 (Hecky *et al.*, 1978), when the greatest productivity in the Protozoa was observed.

7. DISCUSSION

7.1 Recent teleconnections

7.1.1 Teleconnections with ENSO near Lake Tanganyika

During El Niño, air T° is significantly greater in the intertropical area (Bradley *et al.*, 1987). This is well observed at Lake Tanganyika and was quantified for the first time apparently in the east African region during the project. Although the increase does not appear very important (0.28°C on average, 0.24 °C at Mbala and 0.54 °C at Bujumbura), during strong El Niños, this reached 1.0°C in Bujumbura and 0.83 °C in Mbala, as in the strong 1982-83 El Niño. Those increases are proportionally important compared with monthly fluctuations during an average yearly cycle. The impact on the stability of the lake may therefore be significant, particularly since data available show that the winds decrease also during El Niños events.

Air temperature is only one of the several variables that were found to be correlated to the ENSO phenomena near Lake Tanganyika. Other significant correlations were found with air pressure, precipitation, humidity, total radiation and wind speed. In some cases, however, the number of meteorological data near Lake Tanganyika is too small to be very affirmative on the conclusions. The general trend observed in East African teleconnections partially fills this gap for available variables such as air temperatures (average, max. and min.) and humidity.

The study suggests significant teleconnections between the ENSO phenomena and the thermic stability of Lake Tanganyika. This is important as it supports the hypothesis that climate variability acts upon the physical structure of the lake, its mixing (more nutrient-rich deep waters able to reach the photic area) and possible varying abundance in phytoplankton. This supports thus the hypothesis that not only recent ENSO impact Lake Tanganyika but also that paleo ENSO or other paleo-climatic signals could be recorded in the sediments of the lake e.g. by sedimentation of diatom frustules.

More field data from a multidisciplinary study (climate, physico-chemistry and phytoplankton data) collected during an extended period ideally including various ENSO events could quantify the relationships suggested by the statistical approach.

A 3D ecological and hydrological (ECO-HYDRO) model could detail this in further studies.

It is possible that similar processes as for Lake Tanganyika could also be observed for other deep tropical lakes such as Lakes Malawi, Kivu, Eduard and Albert. Those lakes have a south-north orientation making them particularly sensitive to the unidirectional South-East winds during several months each year. The increase of air temperature during ENSO event seems global (Bradley *et al.*, 1987) and this appears clearly in East Africa as observed here for the great majority of stations.

As for air temperature, it is observed that the statistical relationship between SST4 and clupeids fishes in the south is strongest 4-7 months later than the lower SST. The catches of clupeids are higher every year from June to September. This is the period for which the correlation shows higher values. This corresponds with the upwelling period, which is the main period for the capture for clupeids attracted probably by the abundant zooplankton at this time of the year. A correlation with low catches of clupeids implies probably weaker upwelling with its likely consequences: less primary and secondary production, less attraction for fishes, decrease of abundance in the catches...

The difference of time lag for teleconnections between air temperature and SST4 at the North (4 months) and the South (7 months) of the lake is probably linked to the latitudinal difference and the different yearly cycle of air temperature showing a comparable delay between the two stations.

7.1.2 Recent trend in climate, limnology and fisheries at Lake Tanganyika

Although the warming (0.34°C for the upper 100 m) of Lake Tanganyika should be confirmed through several years of sampling, it may be noted that it is similar to the warming noted in Lake Victoria: 0.3°C compared to the first part of the century (Hecky *et al.*, 1994). The productivity of African Great Lakes is determined to a large extent by the strength of stratification and the amount of the hypolimnion water brought to the surface. A warming of Lake Tanganyika would probably enhance the thermic stratification since density differences are increasing non linearly with temperature.

The increase of air temperature since the end of the 70's is probably linked with the global warming. Available data on radiation in Lake Tanganyika area have shown also an increase at the end of the seventies. This resulted probably in the increase of stability of the lake as observed through the reconstruction of stability.

In the past, cooler conditions may have caused not only important quantities of nutrient rich waters but also larger quantities of deep anoxic water containing hydrogen sulphide or ammonia to rise up to the surface. Fishermen in the south of the lake reported that fish kills were more frequent in the 1960's and 1970's than during the last decades.

The changes in thermocline depth, transparency and depth of the oxygenated layer are coherent with a change in wind forcing leading to a decreased tilting of the epilimnion. This could have led to a decreased hydrodynamic state of the lake in the recent years.

Clupeids have strongly decreased in the south of Lake Tanganyika since the early 80's. It could be argued that this has been caused mainly by the increased fishing effort in the 80's. However, in the north of the lake, catches of clupeids have also decreased although industrial fishing effort has decreased there. A fast recovery should have been observed considering the fast turnover and high resilience of the clupeids. This has not been observed. Although more arguing could take place taking the artisanal fisheries into account (for which reliable data are missing), it is suggested that the fishing effort is not the main cause for the decreased catches of the clupeids. One strong reproductive (or larval survival) peak each year gives rise to the dominant annual cohort. The life span of *Stolothrissa tanganicae* Regan, 1917 can conveniently be regarded as a year (Coulter, 1991). As Lasker (1985) pointed out, with the clupeids, there may be an important year class success arising from small to virtually non-existent population. There may always be enough fertilised eggs produced, no matter how small the population (because of overfishing for example), to produce a good year if the conditions are favourable. Tentative estimates of fishing mortality for *S. tanganicae* have recently been obtained (Mannini *et al.*, 1996) and a mean value of 0.4 was derived for the whole lake. This confirmed that currently the *S. tanganicae* stock is on a lake-wide basis, exploited within safe limits.

There are close links between pelagic plankton cycles and the feeding regime and life history of *S. tanganicae* (Coulter, 1991). Catches of clupeids in the pelagic area of southern Lake Tanganyika are probably strongly correlated to upwelling intensity. The clupeid catches in the South are positively linked with the winds during the dry season from May to September. During this period, upwellings are tied with increased inputs of nutrients in the epilimnion and phytoplankton peaks of abundance. Clupeids are more appreciated by consumers during this period as they contain more fat (Sililo, pers. comm.). *Limnothrissa miodon* (Boulenger, 1906) invades the pelagic waters probably from the shores while *S. tanganicae* probably migrates from a more distant location (Pearce, 1992). During an annual cycle,

average *L. miodon* CPUE increase simultaneously with an increase of the wind ($r = 0.77$, $p < 0.01$) while *S. tanganyicae* CPUE show the strongest correlation with the wind ($r = 0.87$, $p < 0.01$) with a time lag of 2 months (Plisnier, 1997).

Air temperature fluctuations influence the limnology of the lake and possibly also indirectly contribute to the fluctuation of the clupeids. The increase of air temperature was almost simultaneous with the decrease of the wind and the decrease of the clupeids CPUE during the last decades. From data between 1963 and 1991, an inverse relationship between clupeid catches and air temperature was observed ($r = -0.73$) (Plisnier, 1997). As there are ENSO teleconnections with air temperature, this suggests direct links between ENSO and CPUE of clupeids. Positive correlation with SOI of February-March and following catches of clupeids (from April to July) indicate teleconnections with ENSO ($r = 0.58$, $P < 0.01$). Similar relations have been found with CPUE of clupeids at the north of the Lake and with fluctuations of *Lates stappersi* CPUE. Fluctuations in monsoon of the Indian Ocean tied with ENSO (Tourre and White, 1994) and interannual differences in climate could affect Lake Tanganyika's ecosystem and the abundance of pelagic fishes.

Contrary to the clupeids, since the mid 70s, the catches per unit of *Lates stappersi* in the South show an important increase. They represented 96 % of the total catches of the industrial fisheries in 1994 (Plisnier, 1995). While this is probably tied with the decrease of the other *Lates* species, environmental changes could also be involved. During an average year in the south of the lake, it was observed that the catches per unit of effort of *L. stappersii* are inversely related to the wind speed (Plisnier, 1997). *L. stappersi* is seldom caught during the dry and windy season (from May to September) in the South. It seems that the decreased transparency during the upwelling is a main cause for this. *L. stappersi* is a visual predator, hence transparency could be one of the key factors to explain its distribution in the lake. The transparency was highly correlated with the Zambian monthly catches in 1993-1994 ($r = 0.75$, $p < 0.01$). *L. stappersi* is seldom caught in the north of the lake, an area that actually shows a reduced transparency (annual average of 9m in 1993-94 instead of 13.6m in 1995-57) (Plisnier *et al.*, 1996; Dubois, 1958). *Lates stappersi* seems actually more abundant in the South compared to the northern end. The decrease of the winds in the mid 70's and the increase of the temperature coincided with the increase of the catches of *L. stappersi* especially in the South. More stable conditions of the lake and possible increased transparency in the South could favour visual predation and increase catchability by light fishing. An increase of shrimps may also have favourably influenced *L. stappersi* in the South. Pearce (1985) recorded during a three years period that shrimps were the main food item of adult *L. stappersi* while *S. tanganyicae* came second in importance. Recent observations also have shown that shrimps were a major food item for *L. stappersi* (Milindi and Mannini, pers.

com.). In the North, *L. stappersi* CPUE have much decreased. Industrial fishing effort may not explain this trend since it has decreased there. Those changes might be tied to climatic changes leading to changes in the ecosystem such as a reduced transparency in the north of the lake.

7.1.3 Hypothesis on Lake Tanganyika variability and ENSO conditions

On the basis of the various teleconnections found with ENSO and the local climate (this project) and the previous results on the limnological cycle at Lake Tanganyika (Plisnier *et al.*, 1999), some preliminary hypothesis linking the ENSO conditions, the local climate and possible effect on the lake hydrodynamic could schematically be drawn:

- "windy and cold year at Lake Tanganyika " (Niña conditions)": during a year of strong winds, the SE wind piles up more epilimnion water in the northern part of the lake. The thermocline is deeper near Bujumbura. The return currents in the deeper layers generate during this season from May to September a strong upwelling in the southern part of the lake. The SE monsoon shows its annual inversion of direction around September and SE winds stop. Movements of water to re-equilibrate tilted layer of water are important. The intense hydrodynamic events (currents, oscillations of layers, internal waves, turbulence...). positively influence productivity of the epilimnion by allowing important mixing of nutrients in the euphotic zone. Productivity of phytoplankton and zooplankton is favoured. Internal waves induce a pulse production whose amplitude may be well observed in those years. Algal blooms and fish kills are likely to be well marked. Turbulence level may favourably influence pelagic fishes. For the oceans, it has been demonstrated theoretically that even a small increase in the turbulence level may greatly increase the contact frequency between fish larvae and food particles. The turbulence intensity may play a decisive part in the establishment of the magnitude of year classes for fish (Furnes, 1992). During those years, the decreased stability of the water would add to the positive effect of the high turbulence on the increased mixing and higher phytoplankton production. Some algae such as diatoms might be favoured under those conditions.
- "calm and warm year at Lake Tanganyika" (El Niño conditions): during a year of weaker winds, particularly from the SE, the dynamic of the whole ecosystem could be reduced linked to less tilting of epilimnion. Less potential energy being accumulated in the north of the lake, hydrodynamics of the lake could have a decreased intensity (including weaker upwelling). Higher air temperature during those years favours also the lake stability. However, the thermocline depth being closer from the surface in the North during the dry season could positively

influence primary production since the nutricline is closer to the surface than during a "windy and cold year". During this season and in this area, primary production may be favoured since mixing through turbulence or pulse production induced by internal waves for example has a higher probability to reach the euphotic zone. These conditions would however not be favourable to clupeids in the north because of the reduced layer of oxic waters.

A multidisciplinary study of the lake including climate, physico-chemistry and plankton is necessary to quantify the multiples effects of climate on the lake limnology and investigate further the advanced hypothesis.

7.1.4 East African region area and ENSO teleconnections

Teleconnections with ENSO are observed for all climate and land surface variables analysed in this project. This confirms the ENSO impact on the climatic and ecological variability in East Africa. However, the pattern of teleconnections is much more complex than generally assumed, both in terms of spatial distribution and impact on different ecosystem variables. Air temperature is clearly positively linked with ENSO in the entire study area. The average temperature increase in this area during warm ENSO events was +0.28°C during the 1981-1994 period. The correlation with Pacific SST4 is particularly strong for air temperature in eastern Tanzania. This could be linked to the proximity of East Tanzania to the Indian Ocean where SST warming is also observed during ENSO events (Monastersky, 1994; Toure, pers. com.). Significant teleconnections between rainfall and SST in the Pacific Ocean were found for very few stations in this study. The weak teleconnections with rainfall can be linked to the high spatial and temporal variability of rains, which are strongly influenced by local conditions, and to the short period considered here (1981-1994) compared to previous studies dealing mainly with rainfall for longer periods (Nicholson, 1996). Our results suggest that the relative air humidity could be a more sensitive and more easily detectable indicator of climate teleconnections than rainfall.

Most of the previous studies mainly have dealt with one climate variable at a time, mostly rainfall. One of the major findings of this study is that several other climate and land surface attributes show a partial correlation with the fluctuation of the Pacific SST4 index. These different variables are not all teleconnected to ENSO in the same way, which leads to a complex impact of ENSO on the ecosystem. The sea surface temperature anomalies in the Pacific Ocean induce changes in climate variables such as air temperature, air humidity and rainfall. These ENSO-driven changes in climate induce changes in vegetation activity, as measured by changes in NDVI and changes in T_s and $(T_s - T_a)$, which indicate changes in surface moisture and

evapotranspiration. The exact response of the vegetation to the ENSO-induced climate variations depends on land cover. There were no clear indications that there is an additional time lag for the teleconnections of remote sensing variables as compared to the teleconnections of climate variables (except rainfall), which suggests a rapid response of the vegetation to changes in climate conditions. The few results obtained with rainfall data suggest that the response of rainfall to SST4 anomalies is more rapid (3-4 months) than is the case for other climate variables.

The second major finding of this part of the project is that the ENSO impact is highly differentiated in space. Many previous studies have postulated a single, region-wide impact of ENSO. In reality, the direction, magnitude and timing of this impact is controlled by the climate system at a regional scale and at a more local scale – e.g. as influenced by the presence of large lakes, local topography or proximity to the coast. Surface attributes, as determined by geology, soil and vegetation might also influence the magnitude and the time lag of the ENSO impact. Hence different zones are recognised in the East African area studied, each subject to different combinations of ENSO induced climate variations. The lake's region in the north-west is one zone, the plateau in the centre and south-east of the study area is a second one and the more temperate stations in the north-east form a third zone. For example, during warm ENSO phases, the Lake Victoria area showed warmer and more humid conditions with an increased vegetation activity while the central and southern part of the study area showed warmer, but drier conditions with a decreased vegetation activity. The area west of Lake Tanganyika is characterised by poor vegetation conditions during warm ENSO events. Our study area is situated at the interface between main centres of teleconnections between climate variables and SST of the Pacific Ocean. These centres have opposite signs for the teleconnections between SST4 and rainfall: a positive correlation in the east-equatorial area and a negative correlation in southern Africa (Rasmusson and Arkin, 1985; Ropelewski and Halpert, 1987). Within each of these broad zones, different weather systems interact on finer spatial scales. The main weather system in East Africa is associated with the Intertropical Convergence Zone (ITCZ), a belt of low pressure following six weeks behind the sun as it moves south and north of the equator. The southward movement brings relatively dry north-easterly prevailing winds to Tanzania in November, followed by the wetter, south-easterly winds coming from the Indian Ocean in March until May. From June to September, the south-west monsoon brings relatively cool, dry weather. The wetter climate of Congo is influenced by the eastern winds from the Atlantic Ocean. These patterns are influenced by local phenomena, such as rain shadow areas created in the vicinity of mountain ranges. Lake Victoria, for example, produces its own convergence zone and affects certain areas by increasing precipitation in the dry season. The difference in time lag for the maximum correlation between relative air humidity and SST4 in the north and the south of the study area is

probably linked to the Intertropical Convergence Zone that drives the rainy season in both areas with a lag of a few months.

A third finding for the recent signals study is that ENSO is not the only source of inter-annual variability in climate conditions in the region, as none of the correlation coefficients measured were very high (in the range of 0.3-0.6). The mechanisms behind the teleconnections with SST are still hypothetical. The SST4 index is measured in the part of the Pacific that is geographically closer to Africa. Only SST fluctuations in the Pacific Ocean have been considered here although it could be argued that ENSO induced SST fluctuations in the Indian and Atlantic Ocean might be more strongly teleconnected with climate variability in Africa (Trenberth, 1991; Nicholson, 1996; Charles *et al.*, 1997). Preliminary work has not found in this project stronger relationships with the Indian Ocean. However, a great amount of data recently obtained still needs to be processed, particularly in the frame of recent finding about the Indian Ocean Dipole (Saji et al, 1999). The changes of the variables studied, not taken into account by ENSO in the Pacific Ocean, could well be related to the variability of those neighbouring oceans as well.

As modelling and forecasting efforts of global phenomena such as ENSO are underway, the detailed study of teleconnections between regional African climate variables and ENSO improves the prospect for partial forecasting of ENSO impacts on agriculture, fisheries or health. Although the results on rainfall teleconnections in the study area do not allow to make firm statements on the usability of rainfall teleconnections for the forecasting of ENSO impacts, it is shown that other variables such as air temperature, air humidity or vegetation activity, are significantly correlated to ENSO. These teleconnections have a potential for forecasting as, for some resources, small changes in climate conditions have an important effect on ecosystem functioning. For example, small changes in air temperature may have a significant impact on the thermic stratification of tropical lakes. Vegetation response to ENSO integrates the impact of several climate variables.

Considerable work remains to be done on the identification of teleconnections in Africa for many other climate variables such as wind patterns, cloudiness or radiation. Comprehensive time series for weather variables for a large number of stations, widely distributed in Africa, are often lacking. Remote sensing data may partially fill this gap for the recent years and for land surface attributes. A better understanding of the mechanisms of the teleconnections would however have to rely on comprehensive climate data, including several extreme ENSO phases.

7.2 Sedimentology and algology

7.2.1 Sedimentation rate

The average sedimentation rate for the upper 12cm of core TAN 98/9 is about 0.134 mm/y based on ^{14}C dating. This sedimentation rate is lower than reported in the literature for the southern basin of Lake Tanganyika, about 0.6 mm/yr (Tiercelin *et al.*, 1988; Gasse *et al.*, 1989). Description of the cores investigated by the above mentioned authors, let suppose that the upper, most recent sediments, are lacking in there cores. These cores were taken to study long term changes in Lake Tanganyika, and not focused on the historical time as the ENSO project.

Recently, extremely slow rates of sediment accumulation ($\pm 0.05\text{-}0.25$ mm/y), with a small increase after ± 1100 AD, were reported for offshore-sills of Lake Tanganyika. Nearshore sediments, taken for studies of the influence of sediment discharge on the lake, showed a much higher sedimentation rate (0.7-2.3 mm/y). The upper portions of the cores showed an increasing up to 3.5-9.0 mm/y (Cohen and Palacios-Fest, 1999).

The sedimentation rate calculated from the ^{14}C dating in deeper parts of core TAN 98/9 would be very low (0.06 mm/y). This can be an indication that a part of the sediment is missing. In paragraph 7.2.3.1 other arguments are discussed that points to the probability that a part of the sediments are lacking in the upper 50cm of this core. More dating on core material in the future could help to check this hypothesis.

7.2.2 Thin-sections analyses

7.2.2.1 Sediment core TAN 98/15, taken near Kipili in 1200m water depth

All the sedimentary facies (section 6.2.3.1.2) encountered here are the results of the accumulation of settling of mainly biogenic material and little terrigenous input. The very fine grain-size of the terrigenous fraction reveals that no turbidite activity has occurred at this location. All the described facies can be considered as hemipelagic. The diffuse lamination, fine lamination and coarse lamination facies have been deposited in anoxic conditions because their primary horizontal disposition has not been disrupted by benthic activity. Horizontality indices H measured on the homogeneous facies do not allow alone to decipher whether its massive appearance is due to bioturbation or to the lack of variability in the sedimentary input. Indeed, H values of 0.52 are typical of the transition zone between bioturbated and non-bioturbated massive facies as described in Francus (2001). However, because this core has been taken in a very deep location in the lake (1200m) it is very unlikely that

oxic conditions ever prevailed here. Currently, the anoxic monimolimnion begins at about 150 m deep. To bring the lake floor to oxic conditions, it should imply a substantial lowering of the water level. This is not supported by recent evidences of Cohen *et al.* (1997), reporting that the lake level has been stable for the last 2800yr, with fluctuation of 10 meter at the most. Other sedimentological arguments support the permanent anoxia scenario. In the case of a lowering of the lake level, one should expect to see in the sedimentary sequence the following succession of the sedimentary facies: coarse or fine laminations, then diffuse lamination and finally massive facies, and inversely for a transition back to anoxic conditions. This is not the case: for instance, at 43cm depth, the facies switch directly from laminated to massive. This observation also supports the hypothesis that oxygen content does not control the sedimentary facies at this location.

The occurrence of lamination is better explained by the variability of the biogenic input. Laminations are due to massive algal blooms. This is supported by our image analysis measurements. (1) The phase percentage $P\%$ of the silt fraction is twice smaller in the laminated facies, pointing out for a dilution of the terrigenous input. (2) The grain size of the silt fraction is similar in laminated facies and the homogeneous one, pointing out that terrigenous input remained stable. The cycle may be annual: diatom blooms are known to occur in October, and terrigenous input can correspond to the rain season. According to estimated sedimentation rate, the couplet thickness of coarse laminations can potentially represent a year of lamination.

The occurrences of carbonate grains can result from several phenomena. The first possibility is that the enrichment is due to more intense photosynthetic activity. Indeed, photosynthesis decreases the amount of dissolved CO_2 , and therefore increases the pH of the water. The saturation with respect to carbonate is then reached and triggers the precipitation of neoformed carbonates grains in the epilimnion (Lami *et al.*, 1994). It is unlikely that the saturation is reached because of fluctuations of water temperature because the temperature fluctuation is very small during the year. A third triggering mechanism could be an increase of the salinity of the lake as already pointed out by Haberyan and Hecky (1987). One must also take into account for the interpretation of the presence of calcite grains, the differential dissolution of calcite in the water column. Because of the small size of the calcite grain, it is very difficult to detect dissolution traces on the grains. It is tempting to correlate the increase in micrite occurring in our core in between 57 and 70 cm depth, with the carbonate layer found throughout the lake (Degens *et al.*, 1971 - fig5). In the southern basin, this layer has been located at $\sim 71\text{cm}$ depth in their core. If the correlation is correct, it might confirm the roughly estimated sedimentation rate, but the correlation must be confirmed with our pending radiometric date.

7.2.2.2 *Sediments of the Kalemie Ridge*

The sediment at Kalemie Ridge is due to hemipelagic sedimentation. The large majority of the sequence is made of homogeneous sediments (Scholz, comm. pers.). The steady settling of a continuous rain of debris can produce the massive facies. However it might be a laminated facies being bioturbated after the sedimentation. The presence of undoubtedly bioturbated facies and faecal pellets in the same sediment core point out for oxic condition at the water/sediment interface. A lowering of the lake level can trigger oxygenated bottom water. The Kalemie ridge is more prone to be oxygenated, because of its relative shallow location. Large fluctuations of the lake level have been reported (Gasse et al., 1989), up to 350 to 400m below present level for the period between 21.700 and 12.700 years BP. Lake fluctuations must have been very fast because sections of the cores shows fluctuations between the two facies (laminated/massive/laminated) on very short intervals, ~ 2cm. Because of its bioturbated nature, this facies has not recorded fine variations of the environmental conditions.

The laminated sections result from the settling of alternating organic sedimentation, mainly diatoms blooms, and terrigenous sedimentation. Based on published mean sedimentation rates of 0.05mm/yr, the lamination thickness is here too thick for being the result of 1 year of sedimentation. However, because of its location on a bathymetric high, the sedimentation might be very episodic, with period of no sedimentation because of intense winnowing due to under currents, and with periods of high sedimentation, like during algal blooms. In these conditions, laminations can potentially represent a yearly cycle, but cannot be used for establishing a chronology because of the episodic character of the sedimentation.

7.2.2.3 *Concluding remarks*

Preliminary sedimentation rate estimations and sedimentary structure observations of the sediments of southern basin support our hypothesis that ENSO conditions have been recorded in the Lake Tanganyika. More precisely, we believe now that laminated sediments are reflecting an increased biogenic production that are likely to have been favoured by more intense wind prevailing in La Niña years. However, because the sediment is not completely laminated, and because laminations are difficult to count reliably, we do not expect to provide a comprehensive annual reconstruction of the ENSO signal, although this might be possible partially and for other climatic variations during longer periods.

In the southern basin, the massive sections of the sediment are probably due to a lack of variability in the sedimentary input. On the Kalemie Ridge, the massive aspect

of the sediment is due to a steady sedimentation and to bioturbation. Bioturbation is most probably triggered by lake-level fluctuations.

The establishment of the accurate chronology for the records is necessary to test our hypothesis. Correlation with other published records seems possible. A coarse bed that is believed to be an ash layer is also a very good candidate to provide a very accurate time frame.

7.2.3 Diatom analyses

Studies undertaken earlier on sediments of Lake Tanganyika covering the Holocene had shown distinctly laminated parts in the cores and fluctuations in the diatom composition. Periods with dominance of *Stephanodiscus* (=Cyclostephanos) alternated with periods dominated by “long” *Nitzschia* species, interrupted by a period with dominance of *Aulacoseira* (Haberyan and Hecky 1987, Tiercelin et al., 1988).

The period with dominance of *Aulacoseira* (=Melosira) began at 9.200 (\pm 180) BP and ended around 6700 BP (Haberyan and Hecky, 1987 and Tiercelin et al., 1988 respectively). This period was followed by a shorter period dominated by *Cyclostephanos* (= *Stephanodiscus*). “Long” *Nitzschia* species became important in more recent sediments (1390 BP \pm 190). *Aulacoseira* and *Cyclostephanos*, however, were still quantitatively very important.

7.2.3.1 Sediment core TAN 98/9, taken near Kasaba in 500m water depth

In core TAN 98/9, taken near Kasaba in 500m water depth, a zone with dominance of *Cyclostephanos* spp. ends rather abruptly around 11.5cm sediment depth. A dating was executed on the sediments just above this zone, between 10.5 and 11.5cm. The result of this ¹⁴C AMS dating indicates that the sediments of this zone are about 830 BP \pm 40 years old. This is too young compared with the investigated cores by Haberyan and Hecky (1987) and Tiercelin *et al.* (1988).

The *Cyclostephanos* zone is very well delimited at its top (figs 32 and 35); it is very probable that a part of the upper sediment may have been washed out. A number of facts support this hypothesis:

- In other sediments of the Lake Tanganyika, the most recent *Cyclostephanos* zone is situated deeper in the sediment, between 2.45-1.95m (Haberyan and Hecky, 1987). In the core studied by Tiercelin et al. (1988), the *Cyclostephanos* zone is situated at 25cm depth; but we must remark that the upper, most recent sediment is lacking in that study (Figure 50).

- The second dating, executed on core TAN98/9 had an age of 8.060 BP \pm 60 at 48-52cm sediment depth. A comparable age corresponds to about 75cm sediments in the study of Tiercelin et al. (1988) and to about 4m sediments studied by Haberyan and Hecky (1987). As mentioned above the upper, most recent sediment lacks in the first mentioned study.
- A layer, rich in *Rhopalodia* sp., was observed in core TAN 98/9 at 62 and 71cm depth. Dominance of *Rhopalodia* sp. was also described in the studies of Haberyan and Hecky (1987) and Tiercelin et al. (1988), up to 6.8m and up to 2.5m respectively.
- The absence of a zone with dominance of *Aulacoseira*. In both sediments cores studied by Haberyan and Hecky (1987) and Tiercelin et al. (1988), a zone with *Aulacoseira* was observed between 4.65 and 2.45m depth and between 1.6 and 0.4m depth respectively. (The upper, most recent sediment lacks in last mentioned study).
- In core Tan 98/15, at 18cm depth, the *Cyclostephanos* zone was not yet observed. The same alternations pattern of “long” *Nitzschia* species and benthic diatoms, as observed in the upper 11 cm of core TAN 98/9 was still present.

“Long” *Nitzschia*’s are dominant during periods of higher Si/P ratio concentration in the water, compared to *Cyclostephanos* (after Haberyan and Hecky, 1987).

The importance of the benthic diatom *Gomphonema clevei* in the lower part of the sediment section studied, is not yet clear. This taxon is known as a common periphytic diatom (Gasse, 1986; Barker, 2001). Further investigations on the autoecology of this taxon, however, are needed. Benthic diatoms are potentially good indicators of lake level fluctuations, indicating the presence of nearby littoral zones (Barker, 2001). In the studied cores the significant changes in the proportion of benthic diatoms may likewise indicate lake level changes. In addition, our data suggest that the interpretation of the benthic diatom assemblages might be more complicated. Notheworthy is the good conservation of the specimens of *Gomphonema clevei* in contrast to the mostly broken frustules of the many other benthic littoral. Epipsammic taxa, e.g. *Cymbellonitzschia minima* (Cocquyt and Jewson, 1994), are also present in the investigated material. The sponge spicules originating from the littoral, however, never reached their highest relative abundance when *Gomphonema clevei* was most abundant.

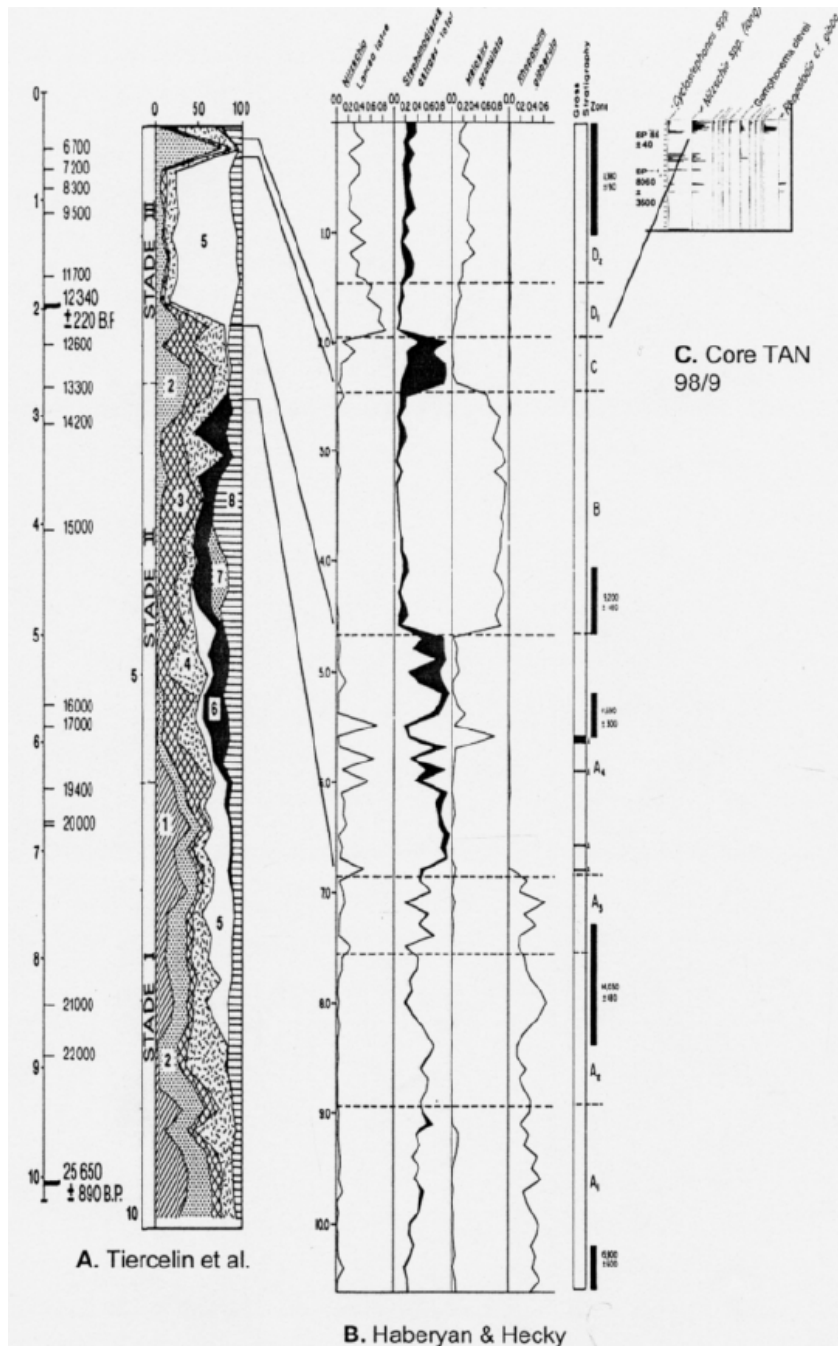


Figure 50: Diatom analysis of sediment cores of Lake Tanganyika. A. after Tiercelin et al. (1988) (1: *Cyclotella ocellata*, 2: *Cyclostephanos damasii*, 3: *Stephanodiscus rotula* & *S. minutus*, 4: *Nitzschia* "long", 5: *Aulacoseira* sp., 6: *Rhopalodia gracilis*, 7: *Gomphonema clevei*, 8: others); B: after Haberyan & Hecky (1987); C: core TAN 98/9 taken near Kasaba in 500m water depth.

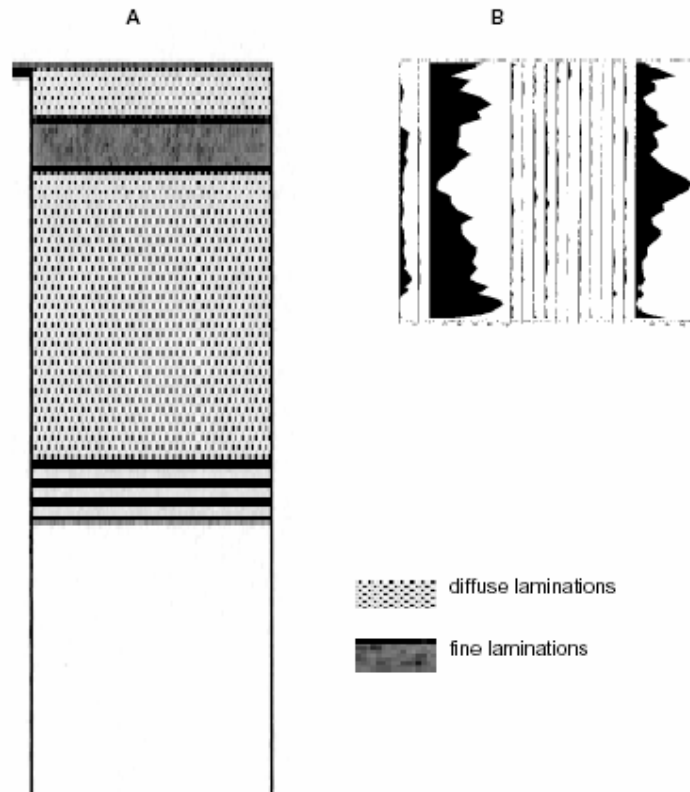


Figure 51: Results of thin-section (for the entire core) and diatom analysis (for the upper 18cm of the sediments) of core TAN 98/15, taken near Kipili in 1200m water depth.

Nitzschia fonticola is known to be more abundant during periods of very stable water column conditions and can grow epiphytic on *Microcystis* (Cyanobacteria) under stratified conditions (Haberyan and Hecky, 1987, Stager *et al.*, 1997).

The periodical trend, found in the first PCA axis for the last 830 years (the upper part) in core TAN 98/9, is principally due to fluctuations in the “long” *Nitzschia* species. Periods with the greatest productivity correspond with dominance of “long” *Nitzschia*’s; periods with lowest productivity with *N. fonticola*, *N. lancettula*, *N. vanoyei* and *Cyclostephanos*.

Time series analysis resulted in a 200 year cycle during the historical period (upper sediments of core TAN 98/9), based on the ¹⁴C dating at 10.5 -11.5cm sediment depth of core TAN 98/9. This could be related to a 200 year solar cycle. In Antarctica, a similar cyclicity (about 200-300years) was described by Bárcena *et al.* (1998) and Domack and Mayewski (1999). The Little Ice Age, between 600-200 year BP, appears as a cool, arid signal in African records (Hamilton, 1982, Bonnefille and Mohammed in Stager *et al.*, 1997).

During warm ENSO events (El Niño) the air temperature in the area of Lake Tanganyika is significantly higher than normal (see 6.1.1.1). The temperature and the stability of the water column should probably be higher than normal (see 6.1.1.1), resulting in less mixing of the oxic water layer above the thermocline.

During cold ENSO events (La Niña) the air temperature in the area of Lake Tanganyika is significantly lower than during normal years. The temperature and the stability of the water particularly in the hypolimnion should probably be lower than normal. This induces probably deeper mixing of the water column. Water of the nutrient enriched anoxic hypolimnion is mixed with the oxic epilimnion. Algal productivity will increase, including the diatoms. The benefit of the growth of “long” *Nitzschia* species at the expense of *Cyclostephanos*, let suppose that the Si/P ratio must have become lower during the historical time. Changes in Si/P ratio may have taken place during the historical time. As *Cyclostephanos* was never present in great quantities in the upper part of the sediment, other factors must have greater impact on the lake system during historical time. Higher nutrient input due to erosion can only have had an important impact during the 20 century, when deforestation in Central Africa increased enormously.

Changes in diatom composition in Lake Victoria, especial changes in *Aulacoseira*, *Cyclostephanos* and *Nitzschia acicularis* (a “long” *Nitzschia* species) covering the last decades of the 20th century were studied together with biogenic silica analyses. Progressive enrichment with essential nutrients other than Si, such as P and N, first led to increased diatom production. Later, however, the combination of excess Si demand and greater losses of diatom-Si to the sediments resulted in depletion of the dissolved-Si reservoir and a transition to Si-limited diatom growth (Verschuren et al., 1998).

Human impact cannot totally rule out during the last 4 Kyr in Central Africa and could have modified the composition of the forest. Pollen analysis of peat-sediment cores taken in Burundi between 1850 and 2240m altitude (Kashiru and Gitanga) showed declines in forest pollen at 5.8 and 3.8 ky BP and that a drastic decrease in forest pollen started 1ky ago (Bonnefille and Chalié, 2000). Other declines in forest pollen was observed 5.8 and 3.8 ky BP. Nutrient enrichment of the lake through the catchment area could than have taken place favoring the grown of “long” *Nitzschia* spp. at the expense of *Cyclostephanos*. Further analyses of deeper parts of the sediment cores (TAN 98/15 and other, not TAN 98/9 because a part of the sediments are probably lacking) are needed. The cores studied by Haberyan and Hecky (1987) and Tiercelin et al. (1988) showed a changes between these diatoms between 1.380 and 9.200 BP and after 6.700 BP respectively.

7.2.3.2 Sediment core TAN 98/15, taken near Kipili in 1200m water depth

Dates are not yet available for core TAN 98/15, taken near Kipili in 1200m water depth. Black, finely laminated sediments were only present in the upper first cm of the core. The diatom composition of this part of the core corresponds well with results obtained in the upper sediments of core TAN 98/9, from 7cm depth. Alternating layers with dominance of “long” *Nitzschia* spp. and *Gomphonema clevei* were observed. The total diatom abundance was also higher when “long” *Nitzschia* spp. were most abundant.

The presence of the alternating layers with dominance of “long” *Nitzschia* spp. and *Gomphonema clevei* in the entire investigated part (18 cm) of the sediment core let us suppose that the probably missing sediments of core TAN 98/9 are maybe present in core TAN 98/15. As core TAN 98/15 is taken in the central, deepest part of the lake the average sedimentation rate should be suspected to be the same or lesser than in core TAN 98/9 which is located more near-shore and is more influenced by the littoral zone. Further studies on deeper layers of the core are needed to detect if the *Aulacoseira*-zone, described by Haberyan and Hecky (1987) and Tiercelin et al. (1988), is present. This would support the hypothesis of the missing sediments in core TAN 98/9 below 11.5cm depth.

The zone with diffuse laminations and the zone with fine laminations, as described after the thin-section analysis of the same core (Figure 25) in the upper sediments of core TAN 98/15 could be distinguished using the results of the diatom analysis (Figure 51). The layer with the lowest relative abundance of “long” *Nitzschia* spp. and the highest relative abundance of *Gomphonema clevei* (between 8.5 and 9cm sediment depth), can be situated just before the transition of diffuse lamination into fine laminations.

7.2.4 Other micro-paleontological analyses

The presence of sponges spicules in the sediments of the investigated cores, taken in the pelagic of the lake, can point to influence of the benthic zone. The highest number of spicules per 500 diatom valves was always found when diatom production was low and when benthic taxa, other than *Gomphonema clevei* were relative somewhat more abundant.

Cysts of Dinophytes were only observed sporadically. Dinophytes were not to be a very important group in the plankton of the lake (see 6.3.). When they appear in greater numbers, they form spherical blooms with very strict local distribution. Chrysophytes form an important group within the plankton of Lake Tanganyika (see 6.3. and Hecky et al. 1978, Hecky and Kling 1981).

Most of the known Chrysophyte species of the lake are heterotrophic, which form no cysts (e.g. *Bicoeca*, *Cercoboda*, *Desmarella*, *Erkenia*, *Kephyrion*). The autotrophic species (e.g. *Mallomonas*) are known to form cyst. The conditions in the pelagic and even in the littoral of Lake Tanganyika are not such that Chrysophytes need cyst formation.

7.2.5 Recent phytoplankton

Changes in species composition were observed between the samples taken in 1975 and in the 1998 campaign:

- Diatoms: *Nitzschia asterionelloides* O. Müller was less important in the sampling of 1975 but present in great quantities during the period February-March-April in 1998.
- Cyanobacteria: *Anabaena circinalis* Rabh. Ex Born. & Fl. was the most abundant species in 1975, while *Anabaena* spp. were only observed in small quantities in 1998. On the other hand the Chroococcales, especially small species belonging to the genera *Chroococcus* and *Synechococcus*, were very well represented in 1998.

Small changes in the algal abundance, expressed as cells/ml, could be observed during the 1998 campaign (February- June) (Figure 48). Abundance was very low during the whole period, with a maximum of about 200 cells/ml in April. These results fit with the observation by Hecky et al. (1978) and Hecky and Kling (1981); they also found a small increase in abundance during April. Unfortunately, we had only samples from February till June at our disposal, so we could not detect the plankton bloom during October, at the beginning of the wet season, as described by Hecky et al. (1978) and Hecky and Kling (1981).

Changes in species composition have taken place since the sampling campaign of 1975. The abundance of a small *Vorticella* sp., epiphytic on *Nitzschia asterionelloides*, in the recent plankton (July-August 1999) was not observed in 1975 nor any references to this phenomenon was found in the literature. *Strombidium*, the most abundant ciliate in 1975, with its symbiotic Chlorophyte (Hecky et al., 1978; Hecky and Kling, 1981) was not observed in the plankton of the last year (February-June sampling 1998; July-August 1998 and 1999).

7.2.6 Concluding remarks

Cyclicity was found in the laminated sediments of the historical time in Lake Tanganyika, southern basin. "Long" *Nitzschia* ssp. are the driving forces for this cyclicity in the sediments.

To interpret the presence of the periphytic *Gomphonema clevei* in the sediments, more research is needed on the auto-ecology of this taxon. Certain layers in the sediments had undergone influence from the littoral: higher percentage of benthic diatoms and increased number of sponge spicules. In these, *G. clevei* was relatively less important.

8. CONCLUSIONS

During the recent period, it was found that ENSO was significantly correlated with higher air temperature, radiation, higher atmospheric pressure and lower winds speed in the Lake Tanganyika area. Because of the impact on the thermic stratification of the lake, higher air temperature and radiation and lower wind would imply that the lake is much less dynamic during an El Niño year. A preliminary study has quantified the probable theoretical impact of El Niño and temperature changes on the lake stability. Partially linked to ENSO conditions, the preliminary results (last 40 years) suggested that the lake stability (upper 100 m) had a 20% variability range during this period (positively correlated with the Pacific Ocean sea surface temperature anomalies). It is possible that this figure would be higher if more wind data were available. It became clear during the study that quantification of climate impacts on the hydrodynamics of the lake needs recent limnological and simultaneous meteorological data.

The time lag between ENSO events and climate at Lake Tanganyika are depending on the variables and the regions. Generally, the correlation is significant up to one year after an ENSO event. It is observed that ENSO may explain only a part of the variability and supplementary explanative factors are certainly involved in the variability of the ecosystem. A preliminary investigation showed significant teleconnections with SST in some areas of the Indian Ocean. This needs more investigations with the recently discovered Indian Ocean Dipole (Saji *et al.*, 1999).

Teleconnections between ENSO and the catches per unit of effort of three species of fishes (2 clupeids and *Lates stappersi*), the main pelagic species of Lake Tanganyika, have been detailed and hypothesis linking the observed ENSO conditions in the Lake Tanganyika area with possible hydrodynamic states of the lake have been presented. This is important as it suggest that a physical and biological link between ENSO, the local climate, the hydrodynamics, the limnology, the biology of fishes and the abundance in the north and south of the lake linked to the fisheries. Available data make it possible to link ENSO and climate in one hand and ENSO and fisheries on the other hand. Limnological data may provide part of the explanations.

The absence of long series of data particularly for phytoplankton has made it impossible however to check further the impact of climate on the planktonic environment. The suggested hypothesis need now to be confronted with new field data since the lake holds strong evidence of its high sensibility to climate and global environmental signals.

At a wider geographical scale in East Africa, the results of the present study confirm the ENSO impact on the climatic and ecological variability. However, the pattern of teleconnections is more complex than generally assumed, both in terms of spatial distribution and impact on different ecosystem variables. Not all climate and land surface variables are teleconnected to ENSO in the same way, which leads to a complex impact of ENSO on the ecosystem. Moreover, the ENSO impact is highly differentiated in space, as the direction, magnitude and timing of this impact is controlled by the local climate system, the presence of large lakes, the proximity to the coast and, possibly, the local topography and land cover.

A recent trend in several variables at Lake Tanganyika was detected. It showed an increase in air temperature, water temperature, water stability and recent changes in fisheries. The possible impact of global warming was discussed. It showed that other signals than ENSO could be recorded in Lake Tanganyika sediments given the very high sensibility of the lake for physical reasons and the answer to this being could be translated into varying biological productions.

Thin-section analyses of cores taken on the Kalemie Ridge and in the Southern Basin of Lake Tanganyika support the hypothesis that laminated sediments could reflect an increased biogenic production, that are likely to have been favoured by more intense wind prevailing in La Niña years. The laminated layers result from the settling of alternating organic sedimentation, mainly diatom blooms, and terrigenous sediments while steady settling of a continuous rain of debris can produce a homogeneous facies. However, because the sediment is not completely laminated, and because laminations are difficult to count reliably, we do not expect them to provide a comprehensive annual reconstruction of the ENSO signal. However, it seems possible to produce a reconstruction of the primary productivity related to strong ENSO events. The establishment of an accurate chronology for the sedimentary records is necessary to test our hypothesis.

In the southern basin, the massive, non-laminated layers of the sediment are probably due to a lack of variability in the sedimentary input. On the Kalemie Ridge, the homogeneous aspect of the sediment is due to a steady sedimentation and to bioturbation. Bioturbation is most probably triggered by lake-level fluctuations.

Seasonal variations of higher taxonomic algal groups (Cyanobacteria, Chlorophyta, Chrysophyta, Diatoms) and productivity in recent phytoplankton are known from the pelagic and the littoral zone of Lake Tanganyika. These variations result in a sedimentation of alternating layers with increased and with lesser biogenic production. Changes in plankton composition could be diagnosed during the last decades. *Nitzschia asterionelloides*, a colony building diatom became the dominant diatom species. *Strombidium* sp., the dominant protozoan taxon during the 70's was not observed in recent pelagic plankton while another protozoan species, a *Vorticella* sp. growing epiphytically on the *Nitzschia asterionelloides* colonies, was very abundant in the pelagic samples of 1999.

The present data and work in progress illustrate the unique potential of these cores as archives of historical changes in paleo-ENSO intensity, as well as longer-term variation in regional and global climatic conditions.

The study has strengthened the hypothesis that the recent ENSO may impact significantly the climate in the Lake Tanganyika area and the mixing conditions of the lake in the actual period. A preliminary quantification of this impact has been presented for the area of East Africa and for the Lake Tanganyika itself. A multidisciplinary study (climate-hydrodynamic-phytoplankton-fisheries) during regular sampling at Lake Tanganyika could provide the information needed to interpret the various sediments signals and decrypt the coded information stored in the sediments. Such a comprehensive multidisciplinary data set does not exist actually. The integration and quantification of those data into a 3D model based on hydrodynamics and ecological relationships should provide the necessary tool to decrypt the recent and past climate impacts archived in its sediments.

9. ACKNOWLEDGEMENTS

This project was financed by the Prime Minister's Office-Federal Office for Scientific, Technical and Cultural Affairs, Belgium. M. Vanderstraeten has supervised the administration of the project at SSTC. The following foundations have supported the sampling expedition: The Leopold III Foundation and the FFRSA (Foundation to Favour the Scientific Research in Africa).

We thank various persons at EAWAG, Switzerland for their participation in the sampling and analysis of sediments: M. Sturm, R. Kipfer and M. Hoffer. C. Scholtz (University of Syracuse) has helped in providing cores from the central part of Lake Tanganyika. O'Reilly and H. Kling have participated in the recent plankton study with samples and/or advises. A. Cohen has helped in various ways, including sampling and discussions. Y. Israel has realised the designing and construction of the "microtome" used for the sediment sub-sampling for the high-resolution diatom analysis. Eric Deleersnijder has provided advises in stability calculations. C. Brone (MRAC) has helped for the expedition. A. Dierickx has digitalised various data at MRAC. C. Blignaut and the late J. Blignaut have provided appreciated logistical support for the expedition. Dr Kilembe and the TPDC have provided much assistance for the expedition as well as the Geological Survey Department in Zambia. We thank G. Coulter and K. Martens for their appreciated advises. J.P Descy and J.-C. Micha of the Facultés Notre-Dame de la Paix in Namur have provided help at various occasions. The Department of Meteorology in Burundi (IGEBU) and Zambia (ZMD) provided meteorological records. Data from the Pacific Ocean were provided by the Climate Prediction Centre in Washington. Limnological sampling was realised in 1993-1995 during the FAO/FINNIDA project "Research for the Management of the Fisheries on Lake Tanganyika" (LTR project, GCP/RAF/271/FIN). P. Francus has been supported by the University of Massachusetts during the last 2 years of the project.

10. BIBLIOGRAPHY

Anyamba, A. and R. Eastman, 1996. Interannual variability of NDVI over Africa and its relation to El Niño/Southern Oscillation. *Int. J. Remote Sensing* 17(13): 2533-2548.

Appleby, P.G, 1997. Sediment records of fallout radionuclides and their application to studies of sediment-water interactions. *Water Air and Soil Pollution* 99 (1-4): 573-585.

Bärcena, M.A., R. Gersonde, S. Ledesma, J. Fabrés, A.M. Calafat, M. Canals, F.J. Sierro and J.A. Flores, 1998. Record of Holocene glacial oscillations in Bransfield Basin as revealed by siliceous microfossil assemblages. *Antarctic Science* 10(3): 269-285.

Barker, P., 2001. A new view of Lake Malawi at the LGM. *Quaternary International* 2001: 1-2.

Batista, G.T., Y.E. Shimabukuro and W.T. Lawrence, 1997. The long-term monitoring of vegetation cover in the Amazonian region of northern Brazil using NOAA-AVHRR data. *Int. J. Remote Sensing* 18(15): 3195-3210.

Bennett, R. J. (1979). *Spatial time series*. Pion Ltd, London: 674 p.

Bonnefille, R. and F. Chalié, 2000. Pollen-inferred precipitation time-series from equatorial mountains, Africa, the last 40 kys BP. *Global and Planetary Change* 26: 25-50.

Bradley, R.S., H.F. Diaz, G.N. Kiladis and J.K. Eischeid, 1987. ENSO signal in continental temperature and precipitation records. *Nature* 327: 427-501.

Cane A.C., G. Eshel and R.W. Buckland, 1994. Forecasting Zimbabwean Maize Yield Using Eastern Equatorial Pacific Sea Surface Temperature. *Nature* 370: 204-205.

Charles, C.D., D.E. Hunter and G. Fairbanks, 1997. Interaction between the ENSO and the Asian monsoon in a coral record of tropical climate. *Science* 277: 925-928.

Cihlar, J., D. Manak and M. D'lorio, 1994. Evaluation of compositing algorithms for AVHRR data over land, I.E.E.E. *Transactions on Geoscience and Remote Sensing* 32: 427-437.

- Cocquyt, C., 1998. Diatoms from the northern basin of Lake Tanganyika. *Bibliotheca Diatomologica* 39: 1-276.
- Cocquyt, C., 1999a. Seasonal dynamics of diatoms in the littoral zone of Lake Tanganyika, Northern Basin. *Archiv für Hydrobiologie*, series: Algological Studies 92: 73-85.
- Cocquyt, C., 1999b. Seasonal variations in periphytic diatom communities in the northern basin of Lake Tanganyika. *Systematics and geography of Plants* 69: 265-273.
- Cocquyt, C., A. Caljon and W. Vyverman, 1991. Seasonal and spatial aspects of phytoplankton along the north-eastern coast of Lake Tanganyika. *Annales de Limnologie* 27(3): 215-225.
- Cocquyt, C. and D. Jewson, 1994. *Cymbellonitzschia minima* Hustedt (Bacillariophyceae), a light and electron microscopic study. *Diatom Research* 9(2): 239-247.
- Coenen, E. J., 1995. LTR's Fisheries Statistics Subcomponent: March 1995 update of results for Lake Tanganyika. FAO/FINNIDA Research for the Management of the Fisheries on Lake Tanganyika. GCP/RAF/271/FIN-TD/32 (En): 38p.
- Cohen A., Talbot M., Awramik S., Dettman D. and Abell P., 1997. Lake level and paleoenvironmental history of Lake Tanganyika, Africa, as inferred from late Holocene and modern stromatolites. *GSA Bulletin* 109: 444-460.
- Cohen, A. S. and M. R. Palacios-Fest. 1999. Paleo-limnological investigations. UNDP/GEF Pollution Control and Other Measures to Protect Biodiversity in Lake Tanganyika (RAF/92/G32): 165 p.
- Coulter G.W., 1968. Hydrological processes and primary production in Lake Tanganyika. *Proceedings 11th Conference Great Lakes Research International Association of Great Lakes Research*: 609-626.
- Coulter G.W., 1991. *Lake Tanganyika and its life*. Oxford University Press, London Oxford and New York: 354 p.
- Craig H., Dixon F., Craig V., Edmond J. and G. Coulter, 1974. Lake Tanganyika geochemical and hydrographic study: 1973 expedition. *Publication Scripps Institution of Oceanography Series* 75(5): 1-83.

- Davenport, M.L. and S.E. Nicholson, 1993. On the relation between rainfall and the normalised difference vegetation index for diverse vegetation types in East Africa. *Int. J. Remote Sensing* 14: 2369-2389.
- Degens, E.T., R.P. Von Herzen, R.P. and H.-K. Wong, 1971. Lake Tanganyika: water chemistry, sediments, geological structure. *Naturwissenschaften* 58: 229-241.
- De Keyser, T.L., 1999. Digital scanning of thin-sections and peels. *Journal of Sedimentary Research* 69 (4) : 962-964.
- Diaz H.F. and G. Kiladis, 1992. Atmospheric teleconnections associated with the extreme phases of the Southern Oscillation. In: *El Nino. Historical and Paleoclimatic Aspects of the Southern Oscillation*. Diaz H.F. and V. Markgraf (eds): 2-28.
- Domack, E.W. and P.A. Mayewski, 1999. Bi-polar ocean linkages: evidence from late-Holocene Antarctic marine and Greenland ice-core records. *Holocene* 9(2): 247-251.
- Dubois J. Th., 1958. Evolution de la température de l' oxygène dissous et de la transparence dans la baie nord du Lac Tanganika. *Hydrobiologia* 10: 215-240.
- Duplessy J.C. and J. Overpeck, 1996. The PAGES/CLIVAR Intersection. Report of a joint IGBP-WCRP Workshop, Venice, Italy, November 1994.
- Eklundh, L., 1998. Estimating relations between AVHRR NDVI and rainfall in East Africa at 10-day and monthly time scales. *Int. J. Remote Sensing* 19: 563-568.
- Farmer, G., 1988. Seasonal forecasting of the Kenya coast short rains, 1901-84. *J. Climatology* 8: 489-497.
- Francus, P., 1998. An image analysis technique to measure grain-size variation in thin sections of soft clastic sediments. *Sedimentary Geology* 121: 289-298.
- Francus, P., 1999. Using image analysis to estimate quantitatively some microstructural parameters of detrital sediments. *Geologica Belgica* 2/3-4: 173-180.
- Francus, P., 2001. Quantification of bioturbation in hemipelagic sediments via thin-sections image analysis. *J. Sedimentary Research* 71(3): 501-507.
- Francus, P. and C. Cosby. Sub-sampling unconsolidated sediments: a solution for the preparation of undisturbed thin-sections from clay-rich sediments. *J. Paleolimnology*: in press.

Francus, P. and Karabanov E., 2000. A computer-assisted thin-section study of lake Baikal sediments: a tool for understanding sedimentary processes and deciphering their climatic signal. *International Journal of Earth Sciences. Geologische Rundschau* 89(2): 260-267.

Furnes, G.K., 1992. Climatic variations of oceanographic processes in the North European Seas. A Review of the 1970s and 1980s. *Cont. Shelf Res.* 12 : 2-3.

Gasse, F., 1986. East Africa Diatoms. Taxonomy, ecological distribution. *Bibliotheca Diatomologica* 11: 1-202 + 44 pl.

Gasse, F., V. Ledee, M. Massault and J.C. Fontes, 1989. Water-level fluctuations of Lake Tanganyika in phase with oceanic changes during the last glaciation and deglaciation. *Nature* 342: 57.

Gucinski, H., Lackey, R.T. and B. C. Spence, 1990. Global Climate Change: Policy Implications for Fisheries. *Fisheries* 15(6): 33-38.

Haberyan, K.A. and R.E. Hecky, 1987. The late Pleistocene stratigraphy and paleolimnology of Lakes Kivu and Tanganyika. *Palaeogeography, Palaeoclimatology, Palaeoecology* 61: 169-197.

Hecky R.E., F.W.B. Bugenyi, P. Ochumba, J.F. Talling, R. Mugidde, M. Gophen and L. Kaufman, 1994. Deoxygenation of the deepwater of Lake Victoria, East Africa. *Limnol.Oceanogr.* 39(6): 1476-1481.

Hecky, R.E., E.J. Fee and H.J. Kling, 1978. Studies on the planktonic ecology of Lake Tanganyika. *Fisheries and Marine Service Techn. Rep.* 816: 1-51.

Hecky, R.E. and H.J. Kling, 1981. The phytoplankton and zooplankton of the euphotic zone of Lake Tanganyika: species composition, biomass, chlorophyll content, and spatio-temporal distribution. *Limnol. Oceanogr.* 26: 548-564.

Hohman, R., R. Kipfer, F. Peeters, G. Piepke, D.M. Imboden and M.N. Shimaraev, 1997. Processes of deep water renewal in Lake Baikal. *Limnol. Oceanogr.* 42: 841-855.

Holben, B.N., 1986. Characteristics of maximum-value composite images from temporal AVHRR data. *Int. J. Remote Sensing* 7: 1417-1434.

Hutchinson, G.E., 1957. A treatise on limnology. I Geography, Physics and Chemistry. John Wiley and Sons Inc., New York: 1015 p.

- Huttula, T. and V. Podsetchine, 1994. Hydrological modelling on Lake Tanganyika. FAO/FINNIDA Research for the Management of the Fisheries on Lake Tanganyika. GCP/RAF/271/FIN-TD/20 (En), 13p.
- Jackson, R.D., R.J. Reginato and S.B. Idso, 1977. Wheat canopy temperature: a practical tool for evaluation water requirements. *Water Resour. Res.* 13: 651-656.
- Johnson, T., M. Talbot, K. Kelts, A. Cohen, J. Lehman, D. Livingstone, E. Odada, A. Tambala, J. McGill, A. Arquit and J.-J. Tiercelin, 1990. IDEAL. An International Decade for the East African Lakes. Workshop Report 1 on the Paleoclimatology of African Rift Lakes, Bern 29-31 March 1990: 39 p.
- Jongman, R.H.G., C.J.F. Ter Braak and O.F.R. Van Tongeren, 1987. Data analysis in community and landscape ecology. Pudoc, Wageningen, 299 p.
- Krinsley, D.H., K. Pye, S. Boggs and N.K. Tovey, 1998. Backscattered Scanning Electron Microscopy and Image Analysis of Sediments and Sedimentary Rocks. Cambridge University Press, Cambridge, U.K., 193 p.
- Kuehl, S.A., C.A. Nittrouer and D.J. DeMaster, 1988, Microfabric study of fine-grained sediments: observations from the Amazon subaqueous delta. *J. Sedimentary Petrology* 58: 12-23.
- Lambin, E.F., and D. Ehrlich, 1996, The surface temperature-vegetation index space for land cover and land-cover change analysis. *Int. J. Remote Sensing* 17: 463-487.
- Lambin, E.F., and D. Ehrlich, 1997, Land cover changes in sub-Saharan Africa (1982-1991): application of a change index based on remotely sensed surface temperatures and vegetation indices at a continental scale. *Remote Sensing of Environment* 61: 181-200.
- Lami A., F. Niessen, P. Guilizzoni, J. Masferro and C.A. Belis, 1994. Palaeolimnological studies of the eutrophication of volcanic Lake Albano (Central Italy). *J. Paleolimnology* 10: 181-197.
- Lasker R., 1985. What Limits Clupeoid Production ? *Can. J.Fish. Aquat. Sci.* 42: 31-37.
- Lotter, A.F. and G. Lemcke, 1999. Methods for preparing and counting biochemical varves. *Boreas* 28: 243-252.
- Loveland, T.R. and A.S. Belward, 1999. The IGBP-DIS global 1km land cover data set, DISCover: first results. *Int. J. Remote Sensing* 18: 3289-3296.

Malingreau, J.P. and A.S. Belward, 1994. Recent activities in the European Community for the creation and analysis of global AVHRR data sets. *Int. J. Remote Sensing* 15: 3397-3416.

Mannini, P., E. Aro, I. Katonda, B. Kassaka, C.G. Mambona, G. Milindi, P. Paffen and P. Verburg, 1996. Pelagic fish stocks of Lake Tanganyika: biology and exploitation. FAO/FINNIDA. GCP/RAF/271/FIN, TD/53, Bujumbura

Menenti, M., S. Azzali, A. de Vries, D. Fuller, and S. Prince, 1993. Vegetation monitoring in southern Africa using temporal Fourier analysis of AVHRR/NDVI observations. In: *Proceedings of international symposium on remote sensing in arid and semi-arid regions*, Lanshou, China: 287-294.

Monastersky, R., 1994. Twin of El Niño found in Indian Ocean. *Science News* 146: 442.

Myneni, R.B., S.O. Los and C.J. Tucker, 1996. Satellite-based identification of linked vegetation index and sea surface temperature anomaly areas from 1982-1990 for Africa, Australia and South America. *Geophysical Research Letters* 23(7): 729-732.

Nicholson, S.E., 1996. A review of Climate Dynamics and Climate variability in Eastern Africa. In: *The limnology, climatology and paleoclimatology of the East African Lakes*. Johnson, T.C. and E.O. Odada (Eds): 25-56.

Nicholson, S.E., and D. Entekhabi, 1986. The quasi-periodic behaviour of rainfall variability in Africa and its relationship to the Southern Oscillation. *Journal of Climate and Applied Meteorology* 34: 311-348.

Niklaus, T.R., G. Bonani, M. Simonius, M. Suter and W. Wölfli, 1992. CalibETII. *Radiocarbon* 34(3): 483-492.

Ogallo, L. 1987. Relationships between seasonal rainfall in East Africa and the Southern Oscillation. *J. Climatology* 7: 1-13.

Olsson, L. and Eklundh, L., 1994, Fourier Series for analysis of temporal sequences of satellite sensor imagery. *Int. J. Remote Sensing* 15(12): 3795-3741.

PALE steering committee, 1993. Research Protocols for PALE, Paleoclimates of Arctic Lakes and Estuaries. PAGES workshop report series 94 (1).

Pearce, M. J. 1985. A description and stock assessment of the pelagic fishery in the south-east arm of the Zambian waters of Lake Tanganyika. Report of the Department of Fisheries, Zambia, 74p.

Pearce M.J., 1992. The development of the pelagic fisheries since 1980 and its effect on the pelagic fish stocks in the South of Lake Tanganyika. Final Report, Department of Fisheries, Zambia, August 1992, Mpulungu, 129 p.

Philander S.G., 1990. El Niño, La Niña, and the southern Oscillation. Acad. Press Inc., San Diego, 281p.

Pike, J., and A.E.S. Kemp, 1996. Preparation and analysis techniques for studies of laminated sediments, In: Palaeoclimatology and Palaeoceanography from Laminated Sediments. Kemp, A.E.S. (Ed). Geological Society of London, Special Publication 116: 37-48.

Plisnier, P.-D., 1995. Catch Assessment Survey in Zambian Waters of Lake Tanganyika in 1994. FAO/FINNIDA Research for the Management of the Fisheries on Lake Tanganyika GCP/RAF/271/FIN-TD/41 (En), 26 p

Plisnier, P.-D., 1997. Climate, limnology and fisheries changes of Lake Tanganyika. FAO/FINNIDA Research for the Management of the Fisheries on Lake Tanganyika GCP/RAF/271/FIN-TD/73(En), 50 p.

Plisnier P.D. Recent climate and limnology changes in Lake Tanganyika. Verh. Internat. Verein. Limnol.: in press.

Plisnier, P.-D., D. Chitamwebwa, L. Mwape, K. Tshibangu, V. Langenberg and E. Coenen, 1999. Limnological annual cycle inferred from physical-chemical fluctuations at three stations of Lake Tanganyika. Hydrobiologia 407: 45-58.

Plisnier P.-D., V. Langenberg, L. Mwape, D. Chitamwembwa and E. Coenen, 1996. Limnological Sampling During an Annual Cycle at Three Stations of Lake Tanganyika (1993 - 1994). FAO/FINNIDA Research for the Management of the Fisheries on Lake Tanganyika. GCP/RAF/271/FIN-TD/46 (En), 136 p.

Plisnier P.-D., S. Serneels and E.F. Lambin, 2000. Impact of ENSO on East African ecosystems: a multivariate analysis based on climate and remote sensing data. Global Ecology and Biogeography 9 (6): 481-497.

Price, J.C. 1984. Land surface temperature measurements from the split-window channels of the NOAA 7 Advanced Very High Resolution Radiometer. J. Geophysical Res. 85 (D5): 7231-7237.

Rasmusson, E.M. P.A. and Arkin, 1985. Inter-annual climate variability associated with the El Niño/Southern Oscillation. In: Coupled Ocean-Atmosphere Models. Nihoul, J.C. (Ed). Elsevier Oceanographic Series 40: 697-725.

Richard, Y. and I. Pocard, 1998. A statistical study of NDVI sensitivity to seasonal and interannual rainfall variations in Southern Africa. *Int. J. Remote Sensing* 19: 2907-2920.

Ropelewski, C.F. and M.S. Halpert, 1987. Global and regional scale precipitation and temperature patterns associated with El Niño-Southern Oscillation. *Monthly Weather Reviews* 15: 1606-1626.

Ross, R. 1983. Endemism and cosmopolitanism in the diatom flora of the East African Great Lakes. In: *Evolution, time and space*. Sims, R.W., Price, J.H. and Whalley, P.E.S. (Eds). Academic Press, Systematics Ass. Special 23: 157-177.

Russ, J.C., 1999. *The Image Processing Handbook*, 3rd Edition: Boca Raton, Florida, CRC Press, 771 p.

Saji N.H., B.N. Goswami, P.N. Vinayachandran and T. Yamagata, 1999. A dipole mode in the tropical Indian Ocean. *Nature* 401: 361-362.

Seguin, B., J.P. Lagouarde and M. Savane, 1991. The assessment of regional crop water conditions from meteorological satellite thermal infrared data. *Remote Sens. Environ.* 35: 141-148

Smith, P. M., Kalluri, S. N. V., Prince, S. D. and R. De Fries, 1997. The NOAA/NASA Pathfinder AVHRR 8-km Land Data Set. *Photogrammetric Engineering and Remote Sensing* 63(1): 12-32.

Stager, J.C., 1982. The diatom record from Lake Victoria (East Africa): the last 17.000 years. In: *Proceedings of the 7th international diatom symposium 1982*, Philadelphia. Mann D.G. (Ed). Strauss and Cramer, Koenigstein: 455-476.

Stager, J.C., B. Cumming and L. Meeker, 1997. A high-resolution 11.400-yr diatom record from Lake Victoria, East Africa. *Quaternary Research* 47: 81-89.

Symoens, J.-J., 1955. Sur la formation de "fleurs d'eau" à Cyanophyceae (*Anabaena flos-aquae*) dans le bassin nord du lac Tanganyika. *Bull. Acad. Sci. Colon. Belg.* 2: 414-419.

Tiercelin, J.-J., A. Mondeguer, F. Gasse, V. Hillaire-Marcel, M. Hoffert, P. Larqué, V. Lédée, P. Marestang, C. Ravenne, J.-F. Raynaud, N. Thouveny, A. Vincens and D. Williamson, 1988. 25.000 ans d'histoire hydrologique et sédimentaire du lac tanganyika, Rift Est-Africaine. *C. r. Acad. Sci. Paris* 307, s. 2: 1375-1382.

Tietze, K.L., 1982. Results of the Lake Tanganyika investigation in December, 1981. Bundesanstalt für Geowissenschaften und Rohstoffe, 93356, Hannover.

- Tourre Y.M. and W.B. White, 1994. Indian Ocean may have El Niño of its own. EOS, Dec 13.
- Trenberth, K.E., 1991. General characteristics of El Niño-Southern Oscillation. In: Teleconnections linking worldwide climate anomalies. Glantz M.H. (ed): 13-42
- Trenberth, K.E. and D.J. Shea, 1987. On the evolution of the Southern Oscillation. Monthly Weather Review 115: 3078-3096.
- Tuckey I.W., 1977. Exploratory data analysis. Addison Wesley Publ. Co., Massachusetts, 688 p.
- Tuomainen, V., H. Mölsä J. Parkkinen, L. Patomäki, and O. V. Lindqvist, 1997, The NOAA series' AVHRR radiometer's capability of revealing water features in Lake Tanganyika. FAO/FINNIDA Research for the Management of Fisheries on Lake Tanganyika. GCP/RAF/271/FIN-TD/77 (En), 29p.
- Van Meel L., 1987. Contribution à la limnologie de quatre grands lacs du Zaïre oriental: Tanganyika, Kivu, Mobutu Sese Seko (ex Albert), Idi Amin Dada (ex Edouard). Les paramètres chimiques. Fascicule A: Le lac Tanganyika Institut Royal des Sciences Naturelles de Belgique, Document de travail 41, 118 p.
- Verschuren, D., D.N. Edgington, H.J. Kling and T.C. Johnson, 1998. Silica Depletion in Lake Victoria: sedimentary signals at offshore stations. J. Great Lakes Res. 24(1): 118-130.
- Vogt, J., 1990, Calculation of a T-o-A albedo, NDVI, surface temperature and precipitable water content of the atmosphere from NOAA AVHRR data. Technical Note 1.90.72, Commission of the European Communities, Joint Research Centre, Ispra, Italy.
- von Merkt, J., 1971, Zuverlässige Auszählungen von Jahresschichten in Seesedimenten mit Hilfe von Grob-Dünnschliffen. Arch. Hydrobiol. 69: 145-154.
- White, 1983. The vegetation of Africa. A descriptive memoir to accompany the UNESCO/AETFAT/UNSO vegetation map of Africa. Courvoisier, Paris, 356 p.

11. LIST OF FIGURES

Figure 1: Map of Lake Tanganyika showing the sediment core sample stations. Code names of sediments cores analysed are shown.

Figure 2: Map of Lake Tanganyika showing the sediment core sample stations on the Kalemie Ridge.

Figure 3: Sampling operation for core TAN98/9, in EAWAG Duebendorf. Here is displayed the simple cheese-cutter-like subsampling device cutting the sediment underneath the sampling aluminium box.

Figure 4: Image processing steps used to obtain measurable images. Example from a BSE image, Lake Tanganyika. Resolution is 1.7 pixels/ μm for regular image, but using the high resolution 4pi system, and high magnification (X500), the resolution can reach up to 20 pixels/ μm . Processing images and computing indices takes about 1 minute/image.

Figure 5: Detail of a binary image. Measurements on each object i : major (L) and minor (I) axes and angle a between horizontal and major axis L .

Figure 6: Teleconnections between anomalies of air temperature (A), air pressure (B) and precipitations (C) and wind speed (D) with SST anomalies in Niño1+2; Niño3, Niño4 and the SOI at time lags from 0 to 60 months.

Figure 7: Teleconnections between anomalies of air temperature (A), air pressure (B) and precipitations (C) and wind speed (D) with SST anomalies in Niño1+2; Niño3, Niño4 and the SOI at time lags from 0 to 60 months.

Figure 8: Monthly average air temperature at three stations near Lake Tanganyika for the 1965-1993 period (standard deviations are shown).

Figure 9: Time series of (A) radiation and air temperature in Bujumbura (no time lag) and (B) radiation in Bujumbura and SST4 (7 months time lag).

Figure 10: Median vertical profile of water temperature from bi-weekly sampling in 1993-94 at three stations of Lake Tanganyika (FAO, pers. comm.).

Figure 11: Twelve months running mean of (a) standardized stability anomalies near Mpulungu (b) standardized SST anomalies in Niño-4 area (c) Southern Oscillation Index (SOI) (d) standardized catches per unit of effort (CPUE) of clupeids fishes at

Mpulungu. Anomalies are departure from the 1993-94 base period means and are normalized by the mean annual standard deviation. The series have been de-trended.

Figure 12: Teleconnection between the southern oscillation index (SOI, mean for February and March) and anomalies of catches per unit of effort (tonnes) of clupeids in (A) Mpulungu, CPUE for June to September, 1963-94. (B) Bujumbura, CPUE for November to January, 1976-94) (All correlations are statistically significant ($p < 0.01$). (Month 11 is November of year 0, month 13 is January of year 1).

Figure 13: Teleconnection between the southern oscillation index (SOI, mean of March to April in the south and August to September in the north) and anomalies of catches per unit of effort (tonnes) of *L. stappersi* in (A) Mpulungu, CPUE for June to September (month 6 to 9), 1963-94. (B) Bujumbura, CPUE for November to February (month 23 to 26), 1976-94. (All correlations are statistically significant $p < 0.01$ at Mpulungu and $p < 0.05$ at Bujumbura) (month 11 is November of year 0, month 26 is February of year 3).

Figure 14: Linear regressions of yearly mean air temperature from 1964 to 1990 in (A) Bujumbura and (B) Mbala.

Figure 15: Recent trend in stability of water at Mpulungu and catches per unit of effort of the main pelagic fish species, by industrial fishermen (standardized anomalies smoothed with 12 months running average).

Figure 16: Correlation coefficients (R) for teleconnections between, on one hand, T_{max} , T_{min} , T_{avg} and relative air humidity in Zambia (1981-1994) and Tanzania (1981-1991) and, on the other hand, sea surface temperature (SST4) of the Pacific Ocean, for a 6-month time lag.

Figure 17: Maps showing pixel wise correlation coefficients for the teleconnections between SST4 anomalies and: (a) NDVI anomalies and (b) T_s anomalies, with a 6-month time lag. Only the values of the correlation coefficients that are significant at the level 0.01 are represented.

Figure 18: Scatterplots of the teleconnection values (i.e. correlations between Pacific SST4, and climate and remote sensing variables for each station) for pairs of climate and remote sensing variables for all stations: (a) T_s and NDVI, (b) NDVI and average air temperature, (c) T_s and air humidity, (d) average air temperature and air humidity, (e) average and minimum air temperatures, and (f) NDVI and maximum air temperature.

Figure 19: Change map for the Lake Tanganyika region.

Figure 20: Air temperature at Bujumbura and sea surface temperature (°C) (Indian Ocean, 9°S, 46°-48°E). Running average of 12 months are shown for the 1951 to 1991 period. (time lag: 4 months).

Figure 21: Photographs of the upper layer of some sediments cores taken in the Southern Basin of Lake Tanganyika: A: core TAN 98/7, taken near Kapembwa in 330m water depth; B: core TAN 98/9, taken near Kasaba in 500m water depth; C: core TAN 98/12 taken near Kapembwa in 330m water depth; D: core TAN 98/5, taken near Msamba in 1000m water depth; E: core TAN 98/13, taken near Kasaba in 500m water depth.

Figure 22: Schematic reproduction of the sediment cores taken near Kasaba: cores TAN 98/1 and TAN 98/2 taken in 300m water depth; cores TAN 98/3, TAN 98/4 and TAN 98/8 taken in 400m water depth; cores TAN 98/6, TAN 98/9 and TAN 98/13 taken in 500m water depth.

Figure 23: Schematic reproduction of the sediment cores taken near Kapembwa taken in 330m water depth: cores TAN 98/7, TAN 98/10, TAN 98/11, TAN 98/12, TAN 98/14 and TAN 98/16.

Figure 24 : Schematic reproduction of the sediment cores taken near Msamba (core TAN 98/5) and near Kipili (core TAN 98/15) in 1000m and 1200m water depth respectively.

Figure 25: Sedimentary log of core TAN98/15 retrieved from a water depth of 1200 meters in southern basin.

Figure 26: SEM view in BSE of core TAN98/15, 20cm depth, Lake Tanganyika. Features, as diatoms, are horizontally disposed, but it is not possible to spot laminations limits. The white arrow points hole left by ostracodes shells. White spots are silts grains.

Figure 27: Flatbed scans of a thin-section, core TAN98/15, 20 cm depth, Lake Tanganyika. The upper part is an example of fine laminations. It is possible to follow some of them across the thin-section, but a lamination count would be very difficult to perform. The lower part is made of two coarse couplets.

Figure 28: SEM view of “long” *Nitzschia* in BSE. Lake Tanganyika, core TAN98/15, 47cm depth. Scale bar: 20µm.

Figure 29: Laminated couplet at Kalemie Ridge. The clear lamina is made of organic debris. The dark lamina is made of terrigenous material. Scale bar is 500 µm.

Figure 30: View at the petrographic microscope of bioturbated couplets. Lake Tanganyika, Kalemie Ridge, TG50, 155 cm depth. Scale bar is 500µm.

Figure 31: View at the petrographic microscope of faecal pellets. Lake Tanganyika, Kalemie Ridge, TG50, 158 cm depth. Scale bar is 500µm.

Figure 32: Major diatom taxa, percentage of unbroken valves, productivity (cells/mg dry sediment), percentage of planktonic, facultative planktonic, benthic, aerophytic diatoms and species diversity in the upper 11.5cm of sediment core TAN 98/9 taken near Kasaba in 500m water depth, Lake Tanganyika, Southern Basin.

Figure 33: SCAN photographs of some diatom taxa observed in the sediment cores taken in the Southern Basin of Lake Tanganyika. 1, 2: *Cyclostephanos* sp.; 3: *Aulacoseira* cf. *granulata*; 4,5: “long” *Nitzschia* sp.; 6: *Fragilaria* sp.

Figure 34: Light microscopic photographs of some diatom taxa observed in the sediment cores taken in the Southern Basin of Lake Tanganyika: 1, 2: “long” *Nitzschia* spp., 3: *Gomphonitzschia ungeri*; 4: *Navicula gastrum*; 5: *Cymbella muelleri*; 6: *Nitzschia frustulum*; 7: *Nitzschia lancettula*; 8: *Nitzschia vanoyei*; 9: *Gomphonema clevei*; 10: *Cyclostephanos* sp.

Figure 35: Major diatom taxa, percentage of unbroken valves, productivity (cells/mg dry sediment), percentage of planktonic, facultative planktonic, benthic, aerophytic diatoms and species diversity in core TAN 98/9 taken near Kasaba in 500m water depth, Lake Tanganyika, Southern Basin.

Figure 36: *Cyclostephanos* spp. and broken valves of “long” *Nitzschia* spp. as observed in deeper layers of sediments (37cm sediment depth) of core TAN 98/9, taken near Kasaba in 500m water depth.

Figure 37: First axis of the PCA of the upper 11.7cm sediments of core TAN 98/9, taken near Kasaba in 500m water depth, representing the entire diatom community

Figure 38: PCA ordination of the samples of core TAN 98/9, taken near Kasaba in 500m water depth, with indication of the groupings A and C, delimited in the CONISS cluster analysis.

Figure 39: PCA ordination of the diatom taxa of core TAN 98/9, taken near Kasaba in 500m water depth, with indication of the most important diatom taxa.

Figure 40: Core TAN 98/9: time series analysis of “long” *Nitzschia* ssp. for the upper sediments (1.8 – 11.7cm).

Figure 41: Major diatom taxa, percentage of unbroken valves, productivity (cells/mg dry sediment), percentage of planktonic, facultative planktonic, benthic, aerophytic diatoms and species diversity in the upper 18cm of sediment core TAN 98/15 taken near Kipili in 1.200m water depth, Lake Tanganyika, Southern Basin.

Figure 42: Major diatom taxa in the upper 2cm of sediment core TAN 98/7 taken near Kapembwa in 330m water depth, Lake Tanganyika, Southern Basin.

Figure 43: Number of sponge spicules and cysts per 500 diatom valves, observed in the sediment core TAN 98/9 taken near Kasaba in 500m water depth, Lake Tanganyika, Southern Basin.

Figure 44: Number of sponge spicules and cysts per 500 diatom valves, observed in sediment core TAN 98/15 taken near Kipili in 1200m water depth, Lake Tanganyika, Southern Basin.

Figure 45: Light microscopic photographs of some stomatocysts observed in the sediment cores taken in the southern basin of Lake Tanganyika.

Figure 46: Seasonal variation in phytoplankton biomass and composition off Kigoma in 1975 (after Hecky *et al.*, 1978).

Figure 47: Seasonal variation in phytoplankton composition 2 km off Kigoma in 1998.

Figure 48: Seasonal variation in phytoplankton density, expressed as cells/ml, 2km off Kigoma in 1998.

Figure 49: Colony of *Nitzschia asterionelloides*, observed in recent phytoplankton samples of Lake Tanganyika, taken near Kigoma in July-August 1998 and 1999 with an epiphytic protozoan (*Vorticella* sp.).

Figure 50: Diatom analysis of sediment cores of Lake Tanganyika. A. after Tiercelin *et al.* (1988) (1: *Cyclotella ocellata*, 2: *Cyclostephanos damasii*, 3: *Stephanodiscus rotula* and *S. minutulus*, 4: *Nitzschia* "long", 5: *Aulacoseira* sp., 6: *Rhopalodia gracilis*, 7: *Gomphonema clevei*, 8: others); B: after Haberyan and Hecky (1987); C: core TAN 98/9 taken near Kasaba in 500m water depth.

Figure 51: Results of thin-section (for the entire core) and diatom analysis (for the upper 18cm of the sediments) of core TAN 98/15, taken near Kipili in 1200m water depth.

12. LIST OF TABLES

TABLE I: List of the cores taken in the southern basin of Lake Tanganyika during the September/October 1998 expedition with indication on the location, the water column depth and the core depth.

TABLE II: Correlation (r) between air temperature at Bujumbura and Mbala and SST in Niño-4 area (running average of 12 months) at different time lags for the period 1981-1994.

TABLE III: Correlations between monthly average of water stability and air temperatures at the south and north ends of the lake for different time periods for a time lag of 1 month.

TABLE IV: Mean temperature (100-300 m) for 1946-47 (VAN MEEL 1987), 1973 (CRAIG et al. 1974) and 1993-94 (FAO, pers. comm.).

TABLE V: Preliminary results of cross-correlations between principal components and ENSO indices.

TABLE VI: Preliminary results of cross-correlations between NDVI anomalies and ENSO anomalies.

TABLE VII: Correlation coefficients for teleconnections with SST4 anomalies for all stations. The lag is indicated between brackets. In bold: correlation values with $p < 0.01$.

TABLE VIII: Spatial correlation coefficients between teleconnection values for pairs of variables. Lag of 6 months for all variables. In Italics: $p < 0.05$; in bold: $p < 0.01$.

TABLE IX: Results of the ^{14}C AMS datings for core TAN 98/9, taken near Kasaba at 500m water column depth.

13. LIST OF PAPERS PUBLISHED DURING THE PROJECT

Cocquyt, C and D. Schram, 2000. Diatom assemblages in surface sediments along the eastern coast of Lake Tanganyika. *Hydrobiologia* 436: 59-71.

Cocquyt, C. , 1999. Seasonal variations in periphytic diatom communities in the northern basin of Lake Tanganyika. *Systematics and geography of Plants* 69: 265-273.

Cocquyt, C. ,1999. Diatoms from a hot spring in Lake Tanganyika. *Nova Hedwigia* 68: 425-439.

Cocquyt, C., 1999. Seasonal dynamics of diatoms in the littoral zone of Lake Tanganyika, Northern Basin. *Arch. Hydrobiol. series: Algological Studies* 92: 73-85.

Cocquyt, C., 2000. Biogeography and Species Diversity of Diatoms in the Northern Basin of Lake Tanganyika. *Advances in Ecological Research*, 31, 2000, 125-150.

Cocquyt, C., 2001. Notes on *Cymatopleura calcarata* Hustedt (Bacillariophyceae), an endemic diatom from Lake Tanganyika. *Festschrift für H. Lange-Berlalat*: in press.

Cocquyt, C., 2000. A light and microscopic investigation of *Surirella brevicostata* O. Müller (Bacillariophyceae), an endemic Tropical African diatom. *Systematics and Geography of Plants* 70: 245-254.

Francus P. & Karabanov E., 2000. A computer-assisted thin-section study of lake Baikal sediments: a tool for understanding sedimentary processes and deciphering their climatic signal. *International Journal of Earth Sciences, Geologische Rundschau*, 89, 2, 260-267.

Francus P., 1999. Using image analysis to estimate quantitatively some microstructural parameters of detrital sediments. *Geologica Belgica*, 2/3-4, 173-180. (published in 2000).

Francus P., 2001. Quantification of bioturbation in hemipelagic sediments via thin-sections image analysis. *Journal of Sedimentary Research*, 71, 3, 501-507.

Plisnier P.D. Climate impacts on Lake Tanganyika Limnology and Fisheries *Verhandlungen Internationale Vereinigung für theoretische und angewandte Limnologie*. In press.

Plisnier P.-D. Limnological profiles and their variability in Lake Tanganyika. IDEAL, Proceedings of the second International symposium on East African Lakes at Lake Malawi, Makakola 01/2000. In press.

Plisnier P.-D., 1997. Lake Tanganyika Research seeks evidence of the El Niño-Southern Oscillation during the past 1000 years. Bulletin of the International Decade for the East African Lakes (IDEAL), Spring issue: 4.

Plisnier P.-D., 1998. Lake Tanganyika: Recent climate changes and teleconnections with ENSO. Proceedings of the International Conference "Tropical Climatology, Meteorology and Hydrology" (Brussels, 22-24 May 1996). G. Demarée, J. Alexandre and M. De Dapper (ed.): Royal Academy of Overseas Sciences and Royal Meteorological Institute of Belgium: 228-250.

Plisnier P.-D., 1998. Limnologische Untersuchungen am Tanganjikasee. DATZ, 09/1998: 594-600.

Plisnier P.-D., D. Chitamwebwa, L. Mwape, K. Tshibangu, V. Langenberg and E. Coenen, 1999. Limnological annual cycle inferred from physical-chemical fluctuations at three stations of Lake Tanganyika. *Hydrobiologia* 407: 47-61.

Plisnier P.-D., S. Serneels and E.F. Lambin, 2000. Impact of ENSO on East African ecosystems: a multivariate analysis based on climate and remote sensing data. *Global Ecology and Biogeography* 9 (6): 481-497.

Plisnier P.-D. and E.C. Coenen, 2001. Pulsed and dampened annual limnological fluctuations in Lake Tanganyika. In: *The Great Lakes of the World (GLOW): Food-web, health and integrity*. Munawar M. and Hecky R. (Eds). *Ecovision World Monograph Series*, Leiden, The Netherlands: 81-94.

Sarvala J., K. Salonen, M. Järvinen, E. Aro, T. Huttula, P. Kotilainen, H. Kurki, V. Langenberg, P. Mannini, A. Peltonen, P.-D. Plisnier, I. Vuorinen, H. Mölsä and O. V. Lindqvist, 1999. Trophic structure of Lake Tanganyika: carbon flows in the pelagic food web. *Hydrobiologia* 407: 155-179.

14. APPENDIX

Appendix 1: Geographical coordinates of main climatic stations used.

Appendix 2: Teleconnections between SST4 and max air Temperature at 0,2,4,6,8 and 10 months time lag in East and south East Africa.

Appendix 3: Teleconnections between SST4 and min air Temperature at 0,2,4,6,8 and 10 months time lag in East and south East Africa.

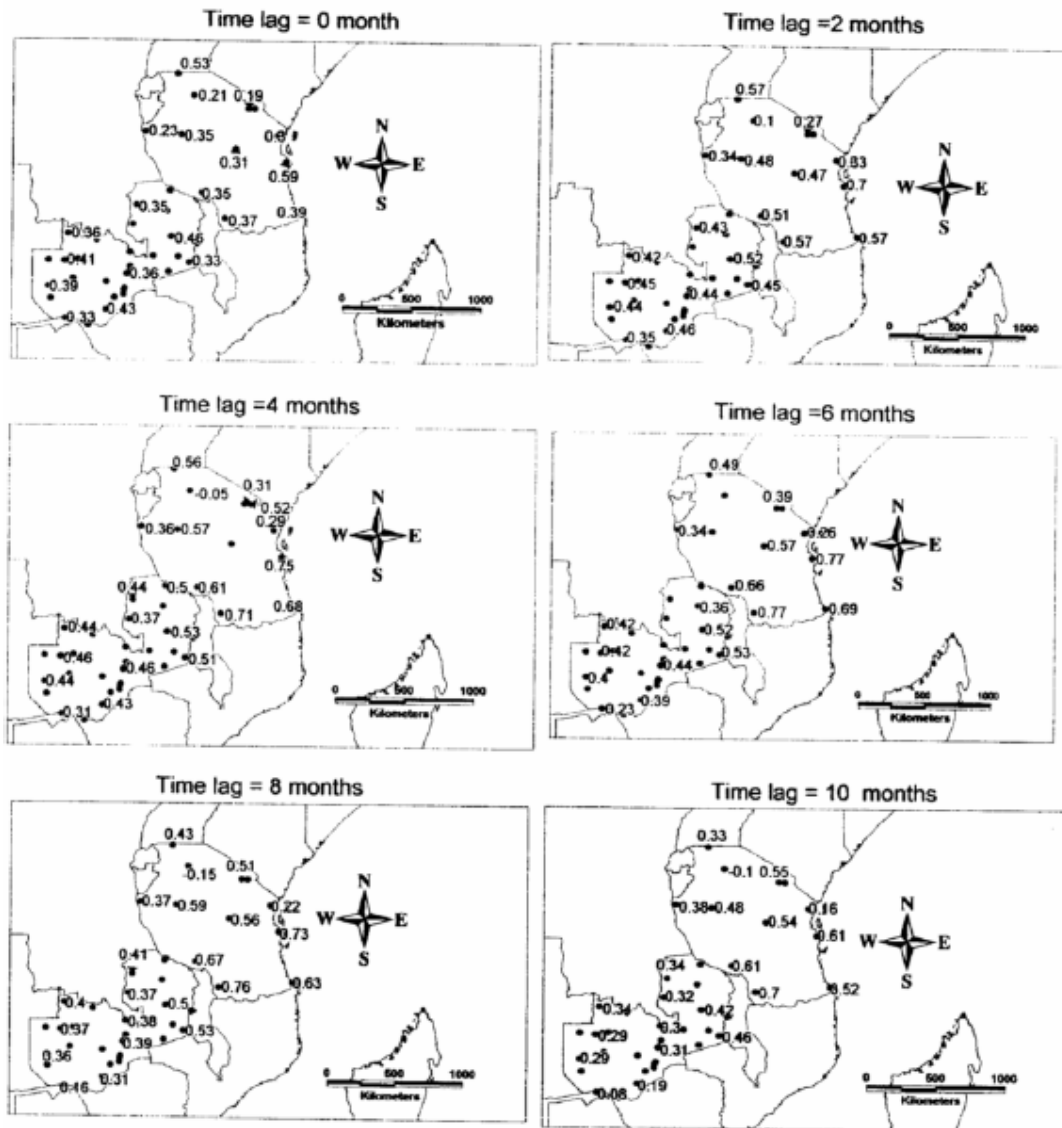
Appendix 4: Teleconnections between SST4 and air humidity at 0,2,4,6,8 and 10 months time lag in East and south East Africa.

Appendix 5: List of diatoms observed during the investigation of sediment cores TAN 98/9, taken near Kasaba in 500m water depth and TAN 98/15, taken near Kipili in 1200m water depth.

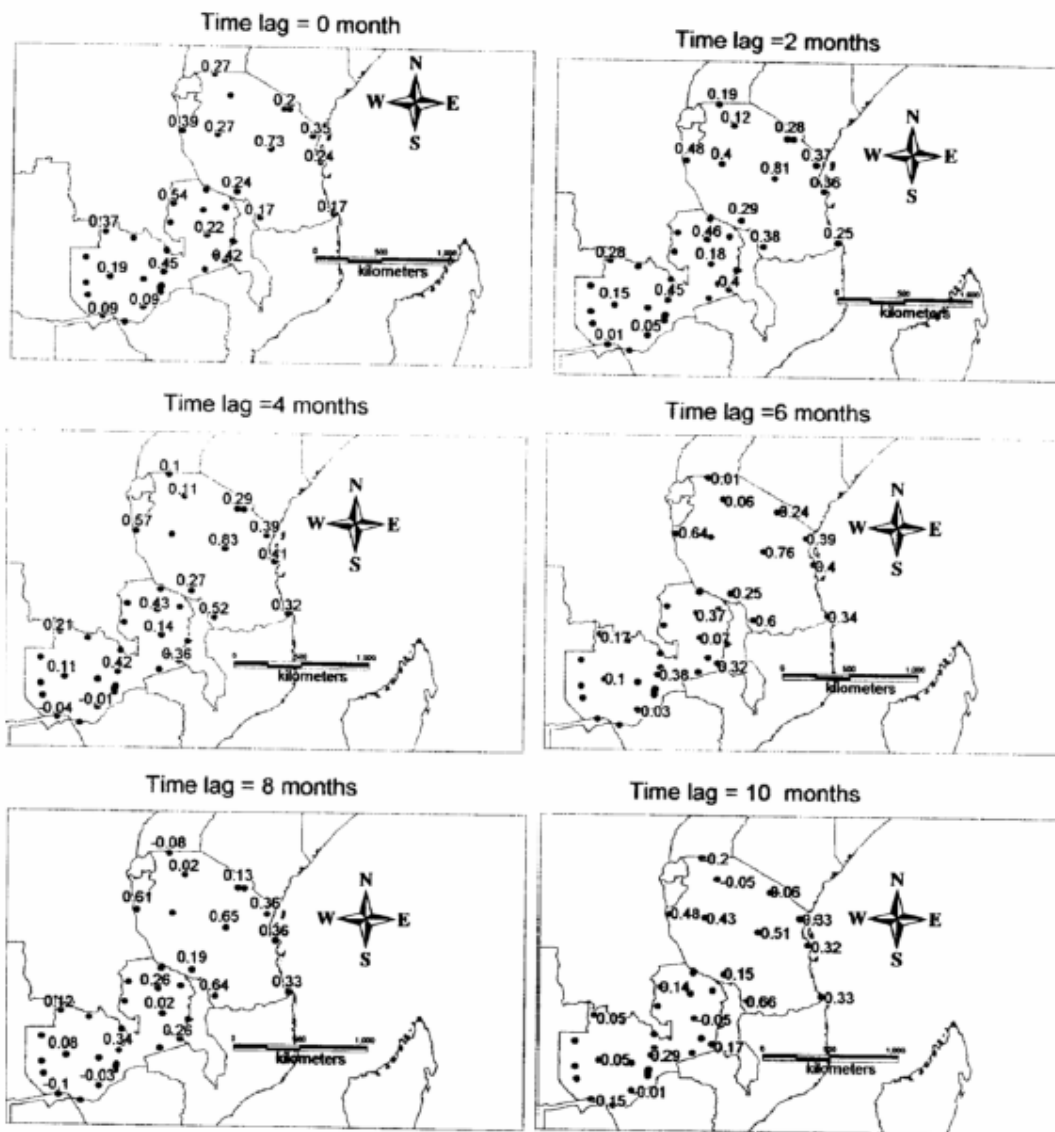
Appendix 1: Geographical coordinates of main climatic stations used.

Country	Station name	IWMO	lat(°dec)	long(°dec)	Alt.(m)
Zambia	Chipata	6758100	-13.63	32.65	1032
	Choma	6775300	-16.85	27.07	1267
	Isoka	6748100	-10.02	32.68	1360
	Kabompo	6754300	-13.60	24.20	1075
	Kabwe	6766300	-14.45	28.47	1207
	Kabwe Agr.	6766200	-14.40	28.50	1165
	Kafironda	6756300	-12.63	28.17	1243
	Kafue	6765900	-15.77	27.92	978
	Kalabo	6763304	-14.95	22.70	984
	Kaoma	6764100	-14.80	24.80	1213
	Kasama	6747500	-10.22	31.13	1384
	Kasempa	6754100	-13.47	25.08	1134
	Kawamba	6740300	-9.80	29.08	1324
	Livingstone	6774300	-17.87	25.85	907
	Lundazi	6758300	-12.30	33.20	1140
	Lusaka	6766705	-15.40	28.30	1279
	Lusaka m.		-15.42	28.32	1283
	Magoye	6775100	-16.03	27.63	1018
	Mansa	6746100	-11.10	28.85	1259
	Mbala	6741300	-8.85	31.33	1672
	Mfuwe	67585	-13.27	31.93	570
	Misamfu	67476	-10.10	31.48	1536
	Mongu	6763300	-15.27	23.13	1061
	Mpika	6747700	-11.90	31.43	1400
	Mskera		-13.65	32.57	
	Mt Makulu	67667	-15.55	28.25	
	Mumbwa	6765500	-14.98	27.07	1189
	Mwinilunga	6744100	-11.75	24.43	1361
	Ndola L.		-12.98	28.72	
	Petauke	6767300	-14.25	31.28	1036
	Samfya	67469	-11.35	29.53	1172
	Senanga	6773100	-16.10	23.27	1019
	Serenje	6757100	-13.23	30.22	1382
Sesheke	6774100	-17.47	24.30	1333	
Solwezi	6755100	-12.18	26.38	1383	
Zambezi	6753100	-13.53	23.12	1077	
Mpulungu		-8.75	31.12		
Tanzania	Amania	6384402	-5.10	38.63	911
	Arusha	6378900	-3.33	36.62	1387
	Bukoba	6372900	-1.03	31.82	1137
	Dar Es Salaam	6389400	-6.88	39.20	55
	Dodoma	6386200	-6.02	35.77	1119
	Kigoma	6380100	-4.88	29.63	882
	Mbeya	6393200	-8.93	33.47	1704
	Moshi	6379001	-3.35	37.03	854
	Mtwara	6397100	-10.35	40.18	113
	Mwanza	6375600	-2.47	32.92	1140
	Songea	6396200	-10.68	35.07	1153
	Tabora	6383200	-5.08	32.08	1181
Burundi	Bujumbura	6439000	-3.38	29.35	800

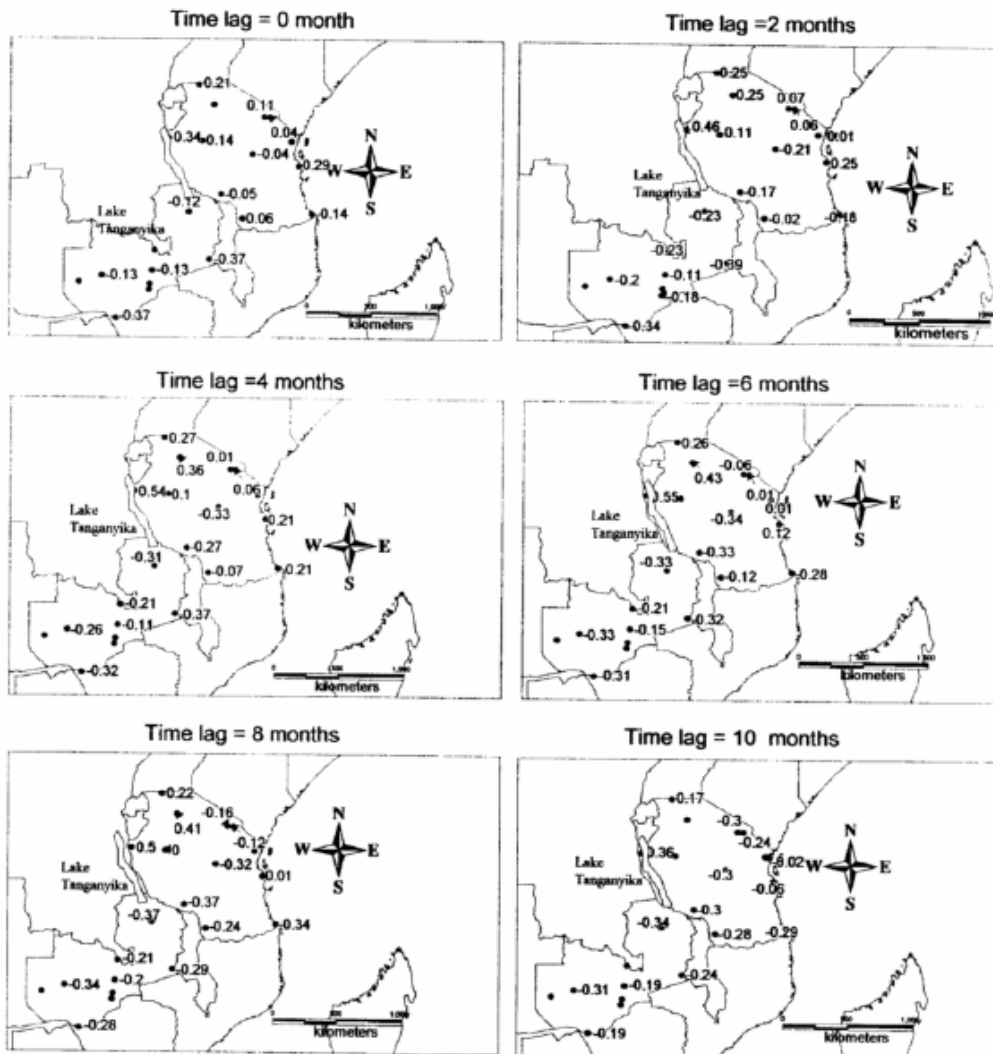
Appendix 2: Teleconnections between SST4 and max air Temperature at 0,2,4,6,8 and 10 months time lag in East and south East Africa.



Appendix 3: Teleconnections between SST4 and min air Temperature at 0,2,4,6,8 and 10 months time lag in East and south East Africa.



Appendix 4: Teleconnections between SST4 and air humidity at 0,2,4,6,8 and 10 months time lag in East and south East Africa.



Appendix 5: List of diatoms observed during the investigation of sediment cores TAN 98/9, taken near Kasaba in 500m water depth and TAN 98/15, taken near Kipili in 1200m water depth.

<i>Achnanthes affinis</i> Grun.	<i>minuta</i> Hilse ex Rabh.
<i>buccula</i> Chol	<i>muelleri</i> Hust.
cf. <i>exigua</i> Grun.	cf. <i>silesiaca</i> Bleich ex Rabh.
<i>lanceolata</i> (Bréb.) Grun.	sp.
<i>lanceolata</i> var. <i>rostrata</i> Hust.	<i>Cymbellonitzschia minima</i> Hustedt
cf. <i>linearis</i> (W. Smith) Grun.	<i>Diploneis</i> cf. <i>finnica</i> (Ehr.) Cl.
<i>minutissima</i> Kütz.	<i>ovalis</i> (Hilse) Cl.
cf. <i>trinodis</i>	sp.
sp.	<i>Epithemia adnata</i> (Kütz.) Bréb.
<i>Amphora copulata</i> (Kütz.) Schoeman & Archibald	<i>Eunotia flexuosa</i> Bréb. ex Kütz.
<i>copulata</i> var. <i>tallingae</i> Gasse	<i>incisa</i> W. Smith ex Greg.
<i>ovalis</i> (Kütz.) Kütz.	cf. <i>monodon</i> Ehr.
<i>pediculus</i> (Kütz.) Grun.	<i>pectinalis</i> (O.F. Müll.) Rabh.
<i>tanganyikae</i> Caljon	<i>pectinalis</i> var. <i>minor</i> (Kütz.) Rabh.
<i>tanganyikae</i> var. .	<i>pectinalis</i> var. <i>rostrata</i> Germain
<i>thromboliticola</i> Cocquyt	<i>pectinalis</i> var. <i>undulata</i> Ralfs
sp.	spp.
<i>Aulacoseira ambigua</i> (Grun.) Sim.	<i>Fragilaria africana</i> Hust.
cf. <i>distans</i> (Ehr.) Sim.	cf. <i>africana</i>
<i>distans</i> var. <i>africana</i> O. Müll.	<i>construens</i> (Ehr.) Grun.
cf. <i>goetzeana</i> (O. Müll.) Sim.	<i>construens</i> var. <i>subsalina</i> Hust.
<i>granulata</i> (Ehr.) Sim.	<i>construens</i> var. <i>venter</i> (Ehr.) Grun.
<i>granulata</i> var. <i>angustissima</i> (O. Müll.) Sim.	<i>heidenii</i> Østrup
cf. <i>granulata</i>	<i>pinnata</i> Ehr.
<i>nyassensis</i> (O. Müll.) Sim.	<i>pinnata</i> var.
<i>nyassensis</i> [var. <i>victoriae</i> O. Müll.]	<i>Frustulia rhomboides</i> (Ehr.) De Toni
sp.	<i>vulgaris</i> (Thwaites) De Toni
<i>Brachysira brebissonii</i> Ross	sp.
<i>serians</i> (Bréb.) Round & Mann	<i>Gomphocymbella beccarii</i> (Grun.) Forti
<i>Caloneis bacillum</i> (Grun.) Cl.	<i>gracilis</i> Hust.
<i>hyalina</i> Hust.	sp.
<i>limosa</i> (Kütz.) Patrick	<i>Gomphonama aequatoriale</i> Hust.
<i>ventricosa</i> (Ehr.) Meister	<i>affine</i> Kütz.
<i>Capartogramma amphoroides</i> Ross	<i>africanum</i> G.S. West
<i>crucicula</i> (Grun. Ex Cl.) Ross	cf. <i>clavatum</i> Ehr.
<i>karstenii</i> (Zanon) Ross	<i>clevei</i> Fricke
<i>rhombicum</i> Ross	cf. <i>clevei</i>
<i>Cocconeis</i> cf. <i>disculus</i> (Schumann) Cl.	<i>gracile</i> Ehr.
<i>hustedtii</i>	Kilhamii Kociolek & Stoermer
<i>pediculus</i> Ehr.	cf. <i>olivaceum</i> (Hornemann) Bréb.
<i>placentula</i> Ehr.	<i>paddockii</i> Kociolek & Stoermer
<i>placentula</i> var. <i>euglypta</i> (Ehr.) Cl.	<i>parvulum</i> (Kütz.) Kütz.
<i>placentula</i> var. <i>rouxii</i> (Brun & Héribaldi) Cl.	spp.
<i>Coscinodiscus</i> sp.	<i>Gomphonitzschia ungeri</i> Grun.
<i>Cyclostephanos</i> spp.	sp.
<i>Cyclotella</i> cf. <i>krammeri</i> Håkansson	<i>Gyrosigma attenuatum</i> (Kütz.) Rabh.
<i>meneghiniana</i> Kütz.	<i>nodiferum</i> (Grun.) Reimer
<i>ocellata</i> Pantocsek	sp.
<i>steiligeri</i> Cl. & Grun.	<i>Hantzschia amphioxys</i> (Ehr.) Grun.
<i>Cymatopleura calcarata</i> Hust.	<i>amphioxys</i> var. <i>africana</i> Hust.
<i>solea</i> (Bréb.) W. Smith	<i>Navicula</i> cf. <i>agrestis</i> Hust.
<i>solea</i> var. <i>apiculata</i> (W. Smith) Ralfs	<i>amplectens</i> Hust.
<i>Cymbella cucumis</i> A. Schmidt	<i>bacillum</i> Ehr.
<i>grossistriata</i> O. Müll.	cf. <i>bacillum</i>
<i>leptoceros</i> (Ehr.) Kütz.	<i>barbarica</i> Hust.
cf. <i>mendosa</i> VanLandingham	cf. <i>barbarica</i>
	cf. <i>bryophila</i> Petersen

THE GLOBAL CARBON CYCLE AND THE FUTURE LEVEL OF ATMOSPHERIC CO₂

UNIVERSITÉ DE LIÈGE
INSTITUT D'ASTROPHYSIQUE ET GÉOPHYSIQUE
Allée du 6 août, 17
B-4000 LIÈGE
Jean-Claude GERARD (coordinator CG/DD11A)
Louis FRANÇOIS
Anne MOUCHET
Bernard NEMRY
Pierre WARNANT

VITO
Boeretang 200
B-2400 MOL
Frank VEROUSTRÆTE (promoter CG/DD/11B)
Herman EERENS
Bart DERONDE
Gil LISSENS
Yves VERHEIJEN

UNIVERSITÉ LIBRE DE BRUXELLES (ULB)
FACULTÉ DES SCIENCES - SCIENCES DE LA TERRE (UNITÉ ULB187)
OCÉANOGRAPHIE CHIMIQUE ET GÉOCHIMIE DES EAUX
CAMPUS DE LA PLAINE
Boulevard du Triomphe
B-1050 BRUXELLES
Roland WOLLAST (promoter CG/DD/11C)
Victor MARTINEZ
Jean-Pierre VANDERBORGHT
Michèle LOIJENS
Lei CHOU

TABLE OF CONTENTS

ABSTRACT	1
1. INTRODUCTION	1
2. NUMERICAL MODELING OF THE PRESENT GLOBAL CARBON CYCLE	4
2.1 Development of the models	5
2.1.1 Continental carbon: the CARAIB model	5
2.1.1.1 <i>Biospheric model adaptations</i>	5
2.1.1.2 <i>Vegetation</i>	7
2.1.1.3 <i>Soils, radiative transfer and vegetation maps</i>	8
2.1.2 The LOCH Oceanic carbon model	9
2.1.2.1 <i>Dynamics</i>	9
2.1.2.2 <i>Carbon cycle</i>	10
2.1.2.3 <i>Atmosphere and air-sea gas exchange</i>	10
2.1.2.4 <i>Soft tissue production and organic carbon</i>	11
2.1.2.5 <i>Silica cycle and the rain ratio</i>	12
2.2 Validation of the CARAIB Biospheric model	13
2.2.1 Material and method	13
2.2.1.1 <i>Simulation of isotopic composition of atmospheric CO₂</i>	13
2.2.1.2 <i>POTSDAM Intercomparison</i>	14
2.2.1.3 <i>DURHAM Intercomparison</i>	16
2.2.2 Results	17
2.2.2.1 <i>Simulation of isotopic composition of atmospheric CO₂</i>	17
2.2.2.2 <i>POTSDAM Intercomparison</i>	17
<i>Seasonal cycle of biospheric fluxes</i>	17
<i>Annual values, seasonal amplitudes and phases</i>	18
2.2.2.3 <i>DURHAM Intercomparison</i>	25
2.3 Impact of future levels of atmospheric CO₂ on vegetation and climate: results and discussion	27
2.3.1 Global scale	27
2.3.1.1 <i>Impact of crops on biomass and soil carbon: steady state stimulations</i>	27
2.3.1.2 <i>Atmospheric General Circulation Models</i>	30
2.3.2 Local scale: simulated response of Belgian forests to transient change in climate	34
2.3.2.1 <i>Introduction</i>	34
2.3.2.2 <i>Forested site measurements</i>	34
2.3.2.3 <i>Spatial downscaling</i>	34
2.3.2.4 <i>Time downscaling</i>	35
2.3.2.5 <i>Emission scenario</i>	36
2.3.2.6 <i>Response of Net Ecosystem Productivity to the emission scenario</i>	37
2.4 The biosphere during glacial-interglacial periods	37

2.5	Interannual variation of biosphere-atmosphere exchanges	41
2.6	Oceanic carbon and its evolution	43
2.6.1	Pre-industrial and LGM runs	43
2.6.2	Advection scheme and biogeochemical tracers	47
2.6.3	Industrial era and radiocarbon	49
2.6.3.1	<i>Method</i>	50
2.6.3.2	<i>Experiments</i>	51
2.6.3.3	<i>Results</i>	52
2.7	Future trends	54
2.7.1	Doubling the atmospheric CO ₂	54
2.7.2	The industrial area	55
3.	REMOTE SENSING OF BIOSPHERICAL PROCESSES	57
3.1	Processing chains and image data (AVHRR, VGT)	58
3.1.1	Pre-processing	60
3.1.1.1	<i>NOAA-AVHRR</i>	60
3.1.1.2	<i>Spot-Vegetation (VGT)</i>	64
3.1.2	Creation of Composite Images & Global Data Sets	65
3.1.2.1	<i>Principles of the NDVI-MDV compositing</i>	65
3.1.2.2	<i>Global data sets used in this project</i>	66
3.1.3	Further enhancements	69
3.1.3.1	<i>Detection and replacement of cloudy measurements</i>	69
3.1.3.2	<i>Extraction of phenological variables</i>	73
3.1.3.3	<i>Enhancement of global imagery via a dedicated data reduction</i>	76
3.2	Global biome classification	82
3.2.1	Legend & Upscaling	82
3.2.2	IGBP-Classifications derived from the Path Finder Image Set	84
3.2.2.1	<i>Methodology</i>	85
3.2.2.2	<i>Results and discussion</i>	87
3.3	fAPAR-comparison: Caraib-predictions vs. image estimate	92
3.3.1	Estimations of fAPAR from NDVI	92
3.3.2	fAPAR-comparison by means of the EROS Image Set of 1992/3	94
3.3.2.1	<i>Methodology</i>	94
3.3.2.2	<i>Results and discussion</i>	95
3.4	Additional studies	98
3.4.1	Extension of the Canopy Reflectance Model SAIL	98
3.4.2	Analysis of AVHRR-signals over the Euroflux Forest Site in Brasschaat	100
3.4.3	DAIS Hyperspectral Imagery over the Euroflux Forest Site in Brasschaat	101
3.4.4	Estimation of the Carbon Balance of Terrestrial Vegetations (C-Fix model)	101
3.4.5	Crop Yield Forecasting with 1 km-Resolution Imagery (AVHRR, VGT)	101
3.4.6	Global Biome Classification	102
3.4.7	A new vegetation map of Central Africa, derived from VGT-imagery of 1998	103
3.5	Conclusions	103

4. CONTRIBUTION OF OCEANIC PROCESSES TO THE GLOBAL CARBON CYCLE	106
4.1 Introduction	106
4.2 Relative importance of the coastal zone in the global ocean carbon cycle	107
4.3 The 1-D coupled hydrodynamical ecological model of the ocean margin system	115
4.3.1 The physical model	116
4.3.1.1 <i>Objectives and theoretical background</i>	116
4.3.1.2 <i>Implementation of the physical model at La Chapelle Bank</i>	120
4.3.1.3 <i>Model results and validation</i>	122
4.3.1.4 <i>Heat budget</i>	123
4.3.2 The biological model	126
REFERENCES	133

ABSTRACT

This final report describes the results obtained during the period January 1997-November 2000 in the framework of the Belgian Federal research programme "Sustainable development – global change". It resulted from the efforts of three laboratories: the Laboratory for Planetary and Atmospheric Research (LPAP-UIg), the Expertisecentrum voor Teledetectie en Atmosferische Processen (VITO-TAP) and the Laboratoire d'Océanographie Chimique (ULB). This research focused on the role played in the past, present and future by the oceans and the biosphere as sources or sinks of atmospheric CO₂. It presents some of the tools developed to monitor the current state of the global carbon cycle based on measurements of key quantities.

Conclusions concerning the role of vegetation and the biomass changes in the past obtained with the CARAIB biospheric global model are presented. Results from intercomparisons of CARAIB with other global models in the framework of the IGBP-GAIM project and other validations are described. A three-dimensional model of the ocean carbon cycle has been developed. Results of sensitivity tests to the transport and biological schemes are summarised. New approaches developed for the analysis and the interpretation of vegetation data collected with remote sensing satellites are described and applied to the interpretation of vegetation indices. A particular attention was given to the construction of vegetation maps and determination of the phenology. A synthesis of data collected recently has been compiled to evaluate more precisely the relative importance of the continental margins in the global ocean carbon cycle and compare it to the open ocean. A one-dimensional model of the carbon fluxes in the area of the Gulf of Biscay is described. It provides many profiles of the important physical, chemical and biological parameters in the description of the carbon cycle. Experiments were also conducted to determine the influence of basic parameters on primary production and new production in the same area.

1. INTRODUCTION: THE GLOBAL CARBON CYCLE

A number of factors, most notably the Kyoto Protocol, are focusing the attention of both the policy and scientific communities on the global carbon cycle. There is increasing interest in understanding the potential future levels of atmospheric CO₂ levels and possible direct and indirect feedbacks of the increasing concentration on climate, terrestrial, oceanic and human ecosystems. The response of the Earth's system to human and natural phenomenon is an emergent property of multiple

interacting factors from human societies, terrestrial, oceanic, atmospheric systems as well as current and past climate events. As such, the metabolism of the Earth's system may well be as important an indicator of global change as shifting temperatures. In a recent document entitled IGBP Global Carbon Project - *Integrated Terrestrial/Ocean Carbon Planning Workshop Report*, three main questions were raised:

- a) Where, geographically and physically/ecologically, are the current sources and sinks and why? What are the natural patterns of temporal variability in the carbon cycle?
- b) What is the nature of human alterations of the carbon cycle?
- c) What are the likely dynamics of the carbon cycle in the future?

The purpose of this study was mostly to address several aspects of the first question.

Over the last few decades, the observed growth rates of atmospheric CO₂ concentrations have varied widely. The magnitude of these variations, associated with changes in the ocean and terrestrial exchange, has been as high as [6 Gt.C/yr], of the same order of magnitude as the gross fossil fuel emissions. Results from several globally integrating studies suggest that a large portion of excess anthropogenic atmospheric CO₂ is assimilated to a greater extent in the northern relative to the southern hemisphere and it is the terrestrial rather than the oceanic biosphere that is likely responsible for excess uptake. Global observations and inversion models, however, are currently unable to resolve carbon sources or sinks at regional, continental or interannual scales.

While there may be a general consensus towards *global* carbon fluxes from observations and models from terrestrial, atmospheric, or oceanic systems, there are large uncertainties in the geographic and temporal distribution of those fluxes at local to regional scales. Strong globally correlative relationships between processes and their driving mechanisms are not necessarily robust, nor do they translate linearly to local and regional answers. However, global-scale observations, from atmospheric CO₂ to satellite observations of the Earth's surface, make it clear that there are consistencies in the response of the biosphere to natural cycles including El Niño Southern Oscillation (ENSO), as well as to anthropogenic forcings such as increased atmospheric CO₂ or nutrient deposition.

The interannual and seasonal variations of carbon fluxes between the terrestrial biosphere and atmosphere are largely driven by the interaction between climate variability and disturbance at local scales. The net effect of observed carbon fluxes

are the result of complex interactions between physical and biological phenomenon. For instance, carbon uptake at the ecosystem level can vary by as much as 1-2 t.C ha⁻¹ in response to interannual variability of climate, atmospheric chemistry (CO₂, N) and/or land use disturbances. In addition, significant differences in carbon fluxes can emerge in response to extreme events such as drought or large shifts in seasonal temperatures. Remote sensing is a promising tool toward providing information on vegetation phenology and net carbon exchange. However, biospheric models are the only integrative tool that can simulate future carbon fluxes under global environmental change.

Exchange of CO₂ between the atmosphere and ocean surface and the transport of carbon from the surface to deep oceans are driven by a combination of physical and biological processes. There is currently a consensus that both the strictly physical-mechanical solubility pump as well as the biological pump play major roles in global carbon fluxes. Major questions that are unresolved include the response of marine ecosystems to a changing climate and the role of continental margins as an interface between terrestrial and open ocean ecosystems.

The rising CO₂ is well established to be an anthropogenic effect, largely driven by emissions of fossil fuel CO₂ and partially offset by absorption of CO₂ into the biosphere. The terrestrial biosphere has played a complex role in changing atmospheric CO₂, with emissions from changing land use, largely in the tropics, regrowth by northern temperate forests, and some additional (still unresolved) terrestrial sinks. The terrestrial sources and sinks of CO₂ are either direct or indirect responses to human activities. A large and growing fraction of the carbon in the atmosphere, oceans and land is directly impacted by human activities. The two major pools of carbon in the terrestrial biosphere, soil carbon and tree biomass, both include a large component of long-lived (slow turnover) materials. This introduces a memory into the terrestrial portions of the C cycle, and requires that analysis of the cycle be extended back to about 300 y BP.

Increasing atmospheric CO₂ content will result in significant changes in ocean chemistry, and these changes in ocean chemistry could have significant ecosystem impacts which could, in turn, affect air-sea CO₂ fluxes. For example, increasing atmospheric CO₂ will result in increased concentrations of dissolved aqueous CO₂ (CO₂(aq)). There is some evidence that calcareous plankton are favored in environments in which calcification is an effective strategy for increasing cellular absorption of CO₂. With increasing [CO₂(aq)], calcareous organisms could be outcompeted by other planktonic groups. This would result in greater alkalinity in surface waters, which could lead to increased oceanic carbon uptake. The study of the effect of the impacts of chemical changes in the marine environment has been

largely unexplored, but could prove to be important both in terms of direct environmental impacts and for its impact on the global carbon cycle. In a broader view, the change due to acidification of nutrient and carbonate utilization by marine life must be taken into account. Humans may impact the marine carbon cycle not only by altering climate and atmospheric CO₂ content but also through activities that directly affect ocean biogeochemistry, such as human-induced changes in river fluxes, coastal pollution, and fish stocks.

In this research, we focused on a few key aspects important in the understanding of the global carbon cycle and its perturbation by human activities. In particular, our efforts concentrated on a few key points:

The ability of remote sensing techniques to build vegetation cover maps and to derive quantitative information on the carbon content of the biosphere;

The role played by coastal regions as sources or sink of CO₂ and in the balance of the global carbon budget;

The past and future evolution of the biosphere in conditions of changing climate conditions and CO₂ level;

The role of the open ocean in the exchange of CO₂ with the atmosphere.

This report will be divided into three chapters corresponding to the global modeling aspects (chapter I), the application of remote sensing to the study of vegetation cover (chapter II) and the role of coastal regions in the global C cycle (chapter III).

2. NUMERICAL MODELING OF THE PRESENT GLOBAL CARBON CYCLE

Since the beginning of the industrial era, the atmospheric CO₂ partial pressure has increased from 280 ppmv to ~360 ppmv today and is expected to reach 700 ppmv before the end of the 21st century (Schimel et al., 1996). The climatic implications of these changes in radiative forcing of the planet are still under debate, but it is likely that they will significantly alter the spatial distribution and temporal variability of most climate variables (temperature, precipitation, air humidity, winds, etc) at the Earth's surface.

While gross primary productivity (GPP) is the input carbon flux to living biomass by photosynthetic production, autotrophic respiration (R_A) and mortality remove carbon from this pool. Dead matter accumulates in litter and deep soil layers and is decomposed by bacterial colonies which release carbon to the atmosphere through

the heterotrophic respiration (R_H). All these carbon fluxes depend on the seasonal and interannual changes in climate variables. Photosynthesis is also enhanced by increased levels of atmospheric CO_2 concentration, provided water and nutrients are available (IPCC, 1995). Due to anthropogenic changes in land use, atmospheric CO_2 concentration and climate, the present amounts of carbon in the continental biospheric pools are thus transient. In particular, increase in net primary productivity ($NPP = GPP - R_A$) by CO_2 fertilization induces a rise in the amount of carbon contained in living biomass. The subsequent increase in litter and soil carbon contents intensifies R_H . During such a transient episode, change in NPP leads change in R_H and this flux difference results in a net annual exchange of carbon between the biosphere and the atmosphere. As a consequence, pools of continental carbon contained in biomass, litter and soil are changing from year to year. A new steady state will be reached when climate, land use and atmospheric CO_2 concentration stabilize.

2.1 Development of the models

2.1.1 Continental carbon: the CARAIB Model

The standard version of the terrestrial biospheric model CARAIB was described by Warnant et al. (1994). The continental cover is divided into grid boxes of fixed longitudinal and latitudinal extensions. Fractional areas of functional plant types (FPTs) are ascribed to each grid box: C_3 and C_4 grasslands, C_3 and C_4 crops, needleleaf forests (evergreen and deciduous) and broadleaf forests (evergreen and deciduous). GPP is calculated from the models of Farquhar et al. (1980) and Collatz et al. (1992) for C_3 and C_4 plants, respectively. Both R_A and R_H depend exponentially on temperature. Carbon budget is calculated in biomass, litter and soil for each FPT. Heterotrophic respiration results from the bacterial oxidation of litter and soil organic carbon. A steady state simulation consists in determining the amounts of carbon contained in the pools of biomass, litter and soil in such a way that annual values of NPP and R_H balance each other (Nemry et al., 1996).

2.1.1.1 Biospheric model adaptations

The main changes to model CARAIB carried out during this project concern its adaptation into a non steady state version to make it suitable for use in transient situations. Another major improvement of the model is the determination of natural vegetation in steady state with climate by CARAIB itself. Other changes were made as well. They mainly concern the improvement of the radiation transfer module, the implementation of a calculation of the $\delta^{13}C$ fractionation and improvements in the model coding.

In the current version of CARAIB, biospheric carbon is redistributed between five reservoirs (figure 1). Two reservoirs represent the standing biomass. The first one, GC (green carbon) only includes green leaves, the second one RC (remaining carbon) corresponds to the rest of the plant. The leaves are responsible for the only carbon flux entering the system (photosynthesis); this is why they are treated separately from the rest of the plant. In the framework of this model, the rest of the plant essentially consists in a carbon sink.

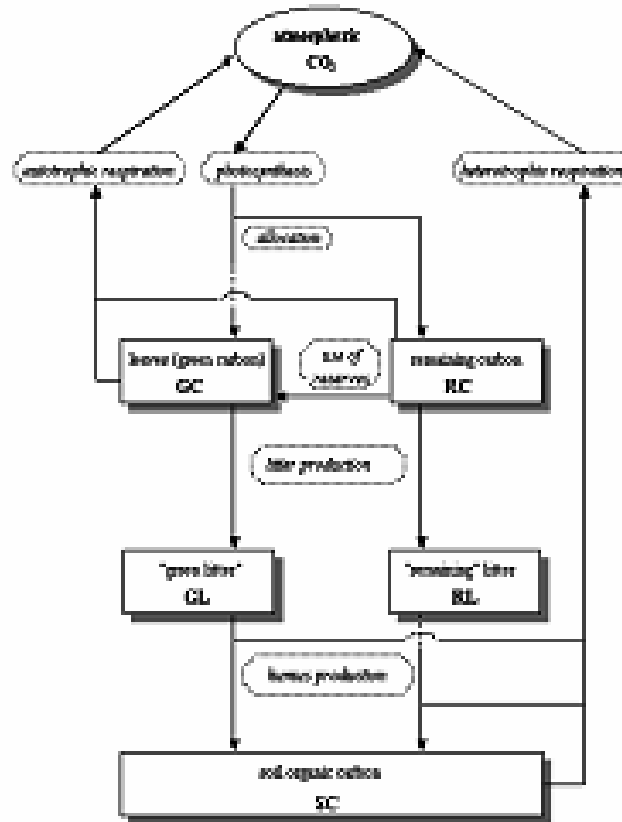


Figure 1: General scheme of the time-dependent reservoir model included in CARAIB in 1998.

A fraction of the content of these reservoirs disappears by mortality and produces litter. The difference between the litter from leaves, GL (green litter) and from the rest of the plant, RL (remaining litter) is *conserved* to take into account differences between decomposition times in these two reservoirs. Finally, litter decomposition produces humus. It is taking into account in a fifth reservoir, SC (soil carbon), containing soil organic carbon. An estimation of the fluxes and the calculation of the resulting carbon content for each reservoir are updated daily from each grid element

and for each plant type present on this element. The differential equation describing each reservoir content may be written:

$$\frac{dC}{dt} = F_{in} - F_{out}$$

where C is the content of the reservoir considered (gC m^{-2}), t is time (day), F_{in} the sum of the incoming flux into the reservoir considered in one day ($\text{gC m}^{-2} \text{ j}^{-1}$), and F_{out} the sum of the outgoing flux from the reservoir considered in one day ($\text{gC m}^{-2} \text{ day}^{-1}$).

2.1.1.2 *Vegetation*

The vegetation pool is divided into two reservoirs. The input flux into these reservoirs is due to photosynthesis. The daily GPP is distributed between two plant reservoirs; a fraction S of this GPP being allocated to leaves.

$S = 0$, if external conditions (temperature, amount of sunshine and available water) do not reach prescribed levels;

$S = S_{max}$ if the leaf biomass has not reached its maximum;

$S < S_{max}$ if the increase of leaf biomass can make this biomass exceed its maximum value. The output fluxes are maintenance respiration, growth respiration and mortality. These three fluxes are assumed proportional to the corresponding pool content. Respirations are calculated in a way consistent with the implementation in the previous CARAIB version but the calculation of the respiring wood fraction has been improved (Warnant, 1999):

$$\text{frac} = \xi C_2^{-0.375}$$

where, frac is the sapwood fraction (dimensionless);

ξ is a parameter depending on tree type ($(\text{gC m}^{-2})^{0.375}$);

C_2 is the carbon content of the RC reservoir (gC m^{-2}).

$\xi = 16.0$ for needle leaved trees and 8. for broadleaf trees.

Mortality is proportional to the carbon content of the reservoir and it depends on plant type and also of the stress exerted by external factors. When those conditions reach a threshold plant begin to die with a time constant of one week. Threshold values are listed in table I Note that the same thresholds are use for leave death and for allocation of assimilated carbon to the RC pool ($S = 0$).

Table I: Thresholds used for stress condition determination. Index 1 corresponds to the GC pool and 2 to the RC pool. Soil water is expressed in fraction of the field capacity limited to the wilting point.

<i>Plant type</i>	<i>SW</i>	<i>SW</i>	<i>T_{min,1}</i>	<i>T_{min,2}</i>	<i>T_{max,1}</i>	<i>T_{max,2}</i>	<i>PAR₁</i>	<i>PAR₂</i>
C3 grass	0.1	0.0	-45	-45	45	45	-	-
C4 grass	0.1	0.0	0	0	45	45	-	-
C3 crop	0.1	0.1	0	0	40	40	5	5
C4 crop	0.1	0.1	0	0	40	40	5	5
Needleleaved evergreen	0.1	0.1	-40	-40	30	30	-	-
Needleleaved deciduous	0.1	0.0	-40	-45	30	35	5	5
Broadleaf evergreen tree	0.1	0.1	0	0	40	40	-	-
Broadleaf deciduous tree	0.1	0.0	0	-25	40	45	5	5

2.1.1.3 Soils, radiative transfer and vegetation maps

The input fluxes into the litter pool are the fluxes of mortality corresponding to the vegetation. The output fluxes are on one hand heterotrophic respiration and humus production on the other hand. These fluxes are assumed proportional to the parameterization of the total heterotrophic respiration adjusted following Nemry et al. (1996). Humus production is assumed to be five times less than the total output flux from the litter reservoirs. Humus respiration is 100 little than litter ones.

The radiative transfer module has also be modified. Each layer has been divided in 3 components: one part is directly irradiated by the sun beam (+ diffuse radiation), another one is irradiated by diffuse radiation from the sky or the other layers, and the last fraction is irradiated by diffuse radiation from clouds or other layers under cloudy conditions. This partitioning yield more accurate calculations of the photosynthesis rate of the different layers including different behaviors due to different light conditions. This modification makes it possible to increase the thickness of the leaf layers. It is a first step toward the inclusion of a one-leaf layer model of radiative transfer into CARAIB. In the latest version of CARAIB, the canopy is divided into two layers to take the light limitation of photosynthesis in herbaceous plant into account (see also next paragraph).

We initially planned to use new vegetation maps derived from remote sensing studies to improve our results. Due to important international efforts in this field, it appeared more efficient to use existing data files rather than building new ones. Consequently,

VITO provided us with us files for 6 internationally recognized classifications. Analysis of these files has begun. But, since classifications differ drastically it has been possible to build a really improved map of the vegetation distribution for present day. More over the choice of a new vegetation type list depends on the study of natural biome determination not yet totally ended. It thus seems a non sense to follow in this direction at this stage.

2.1.2 *The LOCH Oceanic carbon model*

2.1.2.1 *Dynamics*

LOCH, the ocean carbon cycle model developed at LPAP is an off-line 3D transport model. The dynamics driving it is either provided by the LSG-OGCM from the Max-Planck Institute for Meteorology (Maier-Reimer et al., 1993) or by OM, the 3D ocean model developed at ASTR, Louvain-la-Neuve (Campin and Goosse, 1999). In the following the circulation fields from these OGCMs will respectively be referred to by the acronyms MPI-OM and LLN-OM.

The conservation form of the transport equation for a scalar quantity C given per unit volume is (Hirsch, 1988)

$$\frac{\partial C}{\partial t} + H(C) = Q_v(C) + \nabla \cdot \vec{Q}_s(C) \quad (1)$$

$$H(C) = \nabla \cdot \left[\vec{u} - \bar{\kappa} \nabla C + \vec{E}_s \right]$$

In equation (1) Q_v represent the volume sources or sinks and Q_s the surface fluxes of C , both resulting from biogeochemical processes. The 3D transport operator H includes the effects of advective and convective transports, diffusive fluxes due to sub-grid scale eddy mixing and convection (with $\bar{\kappa}$ the diffusivity tensor), as well as surface fluxes due to evaporation and precipitation (E_s). The fields intervening in H are provided by the OGCMs.

The resolution of the whole equation (1) is achieved within one time step ensuring the consistency of the solutions. The horizontal and source terms are explicit in time while vertical and sink processes are treated implicitly. Stability of the numerical schemes requires a time step of 5 days with LLN-OM and of 10 days with MPI-OM, resulting in average CPU times of 3 and 1 hour per variable per kyr respectively. The additional factor comes from the fact that LLN-OM contains twice as much grid points as does MPI-OM, which has a lower resolution.

2.1.2.2 *Carbon cycle*

LOCH computes the evolution of total inorganic carbon, C_t , total alkalinity, A_t , phosphate, PO_4 , oxygen, O_2 , organic matter, OM, and silica, SiO_2 , together with the isotopes 13 and 14 for all carbon species. Atmospheric values of carbon dioxide, oxygen and carbon isotopes are also among the prognostic variables. The main processes considered are the evolution of plankton biomass leading to new production, remineralization and sequestration of organic matter, calcium carbonate or silicate shells formation and their subsequent dissolution or sedimentation.

2.1.2.3 *Atmosphere and air-sea gas exchange*

The atmospheric values of any of the gases or their isotopic ratio may either be imposed or predicted. In the latter case, oceanic, biospheric, and anthropogenic fluxes make up the sources or sinks terms of a 1D diffusive transport equation. This system is solved for the latitudinal direction, as mixing in the zonal direction may be described as occurring instantaneously on the decadal or centennial timescales.

The air-sea CO_2 and O_2 fluxes are computed from the gas concentrations in each media with the help of the formulations from Wanninkhof (1992) and Wanninkhof and Knox (1996) for the gas transfer velocity. This velocity is a function of the long-term average of the squared wind speed, whose values are taken from the climatology by Trenberth et al. (1989) and Trenberth et al. (1990). The gas exchange rate is also affected by the presence of sea-ice. We use the annual average of the ice cover seasonal fields from the Ocean Carbon Model Intercomparison Project (OCMIP). CO_2 and O_2 solubilities are evaluated with the model surface temperatures and salinities according to the formula of Weiss (Unesco, 1987) and Wanninkhof (1992) respectively. The seawater partial pressure of CO_2 is set by the total dissolved inorganic carbon and alkalinity concentrations. An iterative procedure is used to solve the 3^d order pH equation with the dissociation constants for carbonate of Roy et al. (1993). Dissociation constants for borate and water are respectively taken from Dickson (1990) and Millero (1995), with the borate concentration being a linear function of salinity (Millero, 1995). A tunable coefficient in the formulation of the gas transfer velocity was then adjusted for each of the OGCMs so as to obtain a CO_2 invasion rate of $0.061 \text{ mol } \mu\text{atm}^{-1} \text{ m}^{-2} \text{ yr}^{-1}$ for pre-industrial times (Siegenthaler, 1986; Watson and Liss, 1998).

The formulations of air-sea exchange for the carbon isotopes are similar to that for $^{12}CO_2$ with dynamic and equilibrium fractionation factors to account for the tendency of these heavier elements to accumulate in the liquid phase with respect to ^{12}C . The dynamic fractionation factor is calculated after Siegenthaler and Munnich (1981) and

the equilibrium fractionation relation between dissolved carbon species after Mook et al. (1974) and Vogel et al. (1970) with the model sea surface temperature.

2.1.2.4 *Soft tissue production and organic carbon*

Soft tissues production by the marine biota in the surface layers and the subsequent export of organic matter (export or new production) to great depths, by maintaining a significant vertical gradient of carbon are responsible for the low atmospheric CO₂ partial pressure. The horizontal gradients are also controlled by the biological activity. The organic carbon cycle component in LOCH is a simplified version of fully comprehensive NPZD (Nutrients-Phytoplankton-Zooplankton-Detritus) models (e.g. Fasham et al., 1990; Fasham, 1993; Carrada et al., 1983), that is it takes into account nutrient limitation and regulation of the population (grazing and mortality) with a limited number of state variables. This formulation has the advantage of retaining enough complexity while leading to a model that is low CPU consuming and hence fit for simulations over long time period. This model is aimed at describing how fluxes between different reservoirs evolve but not at giving an exact description of the marine biota.

The growth of phytoplankton responsible for the export production, in the surface layers, is driven by phosphate and light availability (Michaelis-Menten law with slight effect of the temperature on growth efficiency). Phytoplankton decay occurs through mortality and grazing. There is no explicit zooplankton population. It is assumed that the zooplankton biomass is directly related to that of the phytoplankton with very low grazing efficiency at low values of the latter. While being prognostic the phytoplankton biomass is not a state variable as it is not transported. Global models rely on the Redfield ratios giving the relative composition of organic matter in the primary elements (C, N, P, ...). We use the classical ratio C:N:P:O₂:A_t=116:16:1:138:18.

Detrital sinking is modeled by specifying a simple sinking rate and the resulting flux is considered to be exported from the mixed layer in the sense that no remineralization is allowed in the productive layer. The organic matter is degraded through two pathways: oxic and anoxic remineralization, the latter occurring only at very low oxygen concentrations. The remineralization rate is only determined by oxygen availability and does not include any temperature effect on bacterial efficiency, as this effect is questioned (Jahnke, 1996). After its transit through the water column organic matter may be indefinitely included in sediments. Sequestration is reproduced by way of an OM flux at the water-sediment boundary with a rate that was tuned so as to meet the observed global quantities (approximately 1.3TmolCyr⁻¹ in the open ocean; Hedges and Keil, 1995; Jahnke, 1996). In the standard version of

the model, inputs from the main river compensate for the imbalance so produced in state variables, though it is also possible to prescribe the river loads (in order to analyze the role of weathering in the carbon cycle by example). The contribution of each river is proportional to the ratio of its discharge to the total amount of freshwater brought yearly to the ocean. These values were computed after the data from Berner and Berner (1987) and Amiotte Suchet (1994).

2.1.2.5 *Silica cycle and the rain ratio*

Together with soft tissue, many living organisms develop shells made either out of silicate or of calcium carbonate. Opal test building has no consequence on the air-sea exchange of CO_2 while CaCO_3 precipitation results in an increase of CO_2 partial pressure. The ratio of carbon in CaCO_3 to organic carbon in exported matter (the rain ratio) is highly non-homogeneous (Tsunogai and Noriki, 1991). In oligotrophic areas this ratio ranges from 0.5 up to 1.0, while in the polar oceans it drops down to less than 0.1. In coastal and upwelling regions the mean ratio is comprised between 0.1 and 0.5. Diatoms, the dominant group of opal building organisms, contribute to approximately half the net oceanic primary production and their relative abundance in the phytoplankton increases as primary productivity increases (Nelson et al., 1995).

The implicit assumption in LOCH is that silica shells are preferentially built. A constant Si:P ratio of 45 (Jacques and Treguer, 1986; Nelson et al., 1995) and a half saturation constant for silica uptake of 1mMSi are used to determine from the actual Si concentrations the fraction of export production that result in opal test growth.

The fraction of soft tissue production not supported by opal building organisms is attributed to CaCO_3 shell formation (calcium is not among the limiting elements in seawater). An additional temperature-dependent term accounts for calcareous organisms (e.g., corals, foraminifera) which preferentially grow in warm waters.

After the death of organisms the tests are transferred immediately to the deepest layer where conditional dissolution occurs. CaCO_3 shell dissolution is driven by the level of seawater saturation computed in the same way as surface seawater pH taking into account the effect of pressure on dissociation constants (Millero, 1995). On the contrary to calcite or aragonite, sea water is everywhere undersaturated with respect to amorphous silica and no such limitation intervenes in the dissolution of opal shells (Edmond, 1974; Wollast, 1974), hence a constant dissolution rate is used.

The amount of silica, carbon and alkalinity lost to the sediments are subsequently brought back to the ocean by the main world rivers when the model is run in a conservative mode.

All the parameters intervening in shell formation and dissolution tuned under the constraint of reproducing the observed North Atlantic to North Pacific horizontal and vertical gradients in C_t and A_t .

2.2 Validation of the CARAIB Biospheric model

Validating large-scale models of terrestrial net primary productivity (NPP) is thoroughly difficult. Site-based measurements provide critical data, but do not effectively address key components of scaling problem. Specifically, they are rarely consistent with the simulation scales (e.g. 0.5° by 0.5° for the Potsdam intercomparison described below), and they are never spatially comprehensive (Cramer *et al.*, 1999). Analyses based on the spatial distribution of the concentration of CO_2 and other tracers in the global atmosphere can provide a complementary approach to site-based validation, but with some important caveats. First, methods based on the spatial distribution of CO_2 concentration provide information on the net carbon exchange or the difference between NPP and heterotrophic respiration (R_H). Thus, the validation of NPP estimate from this approach is never stronger than the confidence in the model of R_H . Second, the analysis depends on net exchanges from all sources, including ocean exchanges, fossil fuel combustion, and land use change. Third, patterns in the global atmosphere do not constrain the distribution of surface sources and sinks at a very high spatial resolution. They tend to reveal patterns at the scale of entire continents or broad latitude zones (e.g. Enting, 1987; Tans *et al.*, 1990). Even with these caveats, analyses of the carbon cycle based on patterns of atmospheric CO_2 play a central role in our current understanding. They were critical in demonstrating the link between the seasonality of NDVI and the seasonality of atmospheric CO_2 (Fung *et al.*, 1987; Heimann and Keeling, 1989; Knorr and Heimann, 1995) and the existence of a northern temperate terrestrial sink (Tans *et al.*, 1990; Ciais *et al.*, 1995; Randerson *et al.*, 1997).

2.2.1 Material and method

2.2.1.1 Simulation of isotopic composition of atmospheric CO_2

The isotopic composition of atmospheric CO_2 is influenced by biospheric, oceanic and industrial carbon fluxes. At seasonal scale, it provides a mean to validate CARAIB because the atmospheric $^{12}CO_2$ and $^{13}CO_2$ concentrations vary seasonally due mainly to the fractionation in the photosynthetic flux in the terrestrial biosphere. CARAIB calculates the dependence of this fractionation on the intercellular CO_2 concentration and takes into account the differences between the C_3 and C_4 plants. We simulated the seasonal atmospheric signal of $\delta^{13}C$ with the atmospheric transport

model TM2 driven by weekly fluxes of GPP, autotrophic and heterotrophic respirations calculated by CARAIB.

2.2.1.2 POTSDAM Intercomparison

Analysis of the seasonal atmospheric CO₂ concentration was the LPAP contribution to the Potsdam'95 intercomparison workshop devoted to the comparison of global models of terrestrial net primary productivity (Cramer et al., 1999; Nemry et al., 1999). We conducted experiments with eight terrestrial models, using the TM2 atmospheric tracer transport model to transform surface fluxes into concentration fields. The overall approach was similar to that used by Heimann et al. (1998), though we used a different suite of terrestrial models and added a Fourier analysis to strengthen the interpretation of seasonality and the relative contributions of individual source regions to the concentration patterns in various parts of the atmosphere.

For this study, we analyzed eight TBMs participating in the workshop. All of these models calculate both NPP and R_H, allowing studies based on NEP. One of them, SDBM, holds a special position since it was calibrated with the help of the satellite-derived normalized-difference-vegetation index (NDVI, from Gallo, 1992) to calculate the photosynthetically active radiation absorbed by the canopy. The other TBMs are prognostic models that calculate the vegetation phenology from climatic conditions instead of prescribing it from the satellite observations of surface reflectance. A complete description of the NPP models is in Cramer *et al.* (1999) and references therein. We added a general description of the various ways followed by the TBMs to model litter production and R_H flux. These carbon fluxes increase and decrease soil carbon content, respectively.

The monthly net carbon fluxes R_H - NPP supplied by the TBMs can be used as boundary conditions in a transport model. The transport simulations were run with a time step of four hours. We used meteorological fields updated every 12 hours for 1987. Several monitoring stations have supplied measured atmospheric CO₂ for several years (Conway et al., 1994). A total of 25 monitoring stations were considered in the present analysis. Application of criteria allows us to reject stations where the interannual variability is not well known or where episodic CO₂ sources have too much importance. For example, tropical fires appear during only a few months in the year and generate an atmospheric CO₂ signal of about 1 ppmv, including high harmonics in addition to the fundamental mode. This contribution is perceptible at Ascension Island but not dominating.

To estimate the ocean contribution to the seasonal atmospheric signal, we add the fluxes calculated by Six and Maier-Reimer (1996) with the Hamburg Model of the Ocean Carbon Cycle (HAMOCC3). The seasonal amplitude of ocean CO₂ fluxes

ranges from approximately $15 \text{ g C m}^{-2} \text{ mo}^{-1}$ in the equatorial region to 70 and $120 \text{ g C m}^{-2} \text{ mo}^{-1}$ in the northern and southern temperate zones respectively. These values are comparable to the seasonal amplitude of the terrestrial biospheric fluxes. Nevertheless, the seasonal amplitude of the ocean CO_2 emissions, the product of the ocean fluxes and areas in each band, does not exceed $0.15 \text{ Gt C mo}^{-1}$ while the terrestrial biospheric emissions exceed 1 Gt C mo^{-1} northward of the Tropic of Capricorn. This proportion limits the potential influence of the ocean on the atmospheric CO_2 signals to the southern extratropical latitudes.

Due to transport, the time series of CO_2 concentrations at any point in the atmosphere is influenced by fluxes from a number of regions. To isolate the role of various geographic regions, we performed simulations with seasonal carbon fluxes limited to selected regions of the terrestrial biosphere. The Fourier analysis of results from these geographically restricted simulations allows us to estimate the relative influence of each region on the CO_2 signal at all others (Nemry *et al.* 1996; François *et al.* 1996). For this analysis, we divide the globe into eight zones with southern limits at latitudes 90° S , 70.5° S , 47° S , 23.5° S , 0° , 23.5° N , 47° N and 70.5° N . Each of these bands contains 3 latitudinal bands of the TM2 grid. They define 8 tropospheric zones "a" and cover the 7 biospheric zones "b" defined in section 3.1. The entire land biosphere is labeled zone "B". With each TBM, we ran eight four-year transport simulations, limiting terrestrial biospheric fluxes to one on the 8 biospheric zones for each simulation. TM2 provides a CO_2 concentration in the tropospheric zones "a" every four hours. We combined these into monthly averages to produce a seasonal signal, which was then detrended as described in section 5.3. Using a period $T = 1$ year to define the frequency $\omega = 2\pi/T$, we calculated the fundamental Fourier amplitudes $C_{a,B}$ and $C_{a,b}$ and phases $\gamma_{a,B}$ and $\gamma_{a,b}$ of the detrended signals from the whole biosphere "B" and each biospheric zone "b". The fundamental Fourier mode in any tropospheric zone "a" from biospheric zone $z = \text{"b" or "B"}$ is

$$S_{a,z}(t) = C_{a,z} \sin _a,z(t) \quad (1)$$

where $_a,z(t) = \omega t + \gamma_{a,z}$. The Fourier modes of the partial signals can be written

$$S_{a,b}(t) = P_{a,b} \sin _a,B(t) + Q_{a,b} \cos _a,B(t) \quad (2)$$

where $P_{a,b}$ and $Q_{a,b}$ are the amplitudes of fundamental Fourier modes of the partial signals respectively in phase and in quadrature with the fundamental Fourier modes of the total signal:

$$P_{a,b} = C_{a,b} \cos(\gamma_{a,b} - \gamma_{a,B}) \quad (3)$$

$$Q_{a,b} = C_{a,b} \sin(\gamma_{a,b} - \gamma_{a,B}) \quad (4)$$

Because of the linearity of the atmospheric transport model, the sum of the 7 amplitudes $P_{a,b}$ in any zone "a" is equal to $C_{a,B}$ while the sum of the 7 amplitudes $Q_{a,b}$ is zero. The amplitude $P_{a,b}$ is negative if the fundamental modes of the partial and total signals $S_{a,b}(t)$ and $S_{a,B}(t)$ in the tropospheric zone "a" are out of phase by more than 3 months.

2.2.1.3 *DURHAM Intercomparison*

LPAP participated in the international workshop organized by the Global Analysis, Interpretation and Modelling (GAIM) task force office at the New England Center Conference in University of New Hampshire (UNH, Durham, USA), on 5-8 December, 1999. Each participating group started the workshop preparation in July 1999 by simulating NPP from monthly climatic measurements at various sites in the world. Once our results were provided to UNH, we got the annual values of the observed NPP. UNH separated the observations between Class I/II and Class III. Class I/II is composed of around 150 well-documented sites, where values of above-ground and below-ground NPP are available, as well as climatic records. Class III is composed of around 1600 sites. Most of the sites are located in the Northern Hemisphere. About 30 sites are spread in Australia, Southern America and Africa. Fourteen land cover types were provided for each class I/II site, while only the dominant type was provided with the Class III sites. Hereafter, we focus on the Class I/II sites. In any cell of the continental grid of CARAIB, fractional cover areas (FCARs) are defined for eight Plant Functional Types (PFTs).

The land cover types were converted into PFTs in any cell as follows: (i) WATER and URBAN covers were added to BARE cover. (ii) MIXED, WOODLAND, SHRUB-CLOSE and SHRUB-OPEN covers were added to the forested covers (types 1 to 4) present in the cell. (iii) WOODGRASS cover was added to the GRASSLAND cover (type 10). (iv) distinction between C3 and C4 plants was performed in the GRASS and CROP covers according to the proportion used in the CARAIB grid.

Annual NPP values were simulated at each site as a combination (COMB) from the various functional types of the site, weighted by their FCARs. The NPP was actually calculated for each of the eight PFTs in any site, even if the FCAR was zero. Two sites from class I/II, located close to each other on the Eastern coast of Australia near the tropics, illustrate to which extent vegetation composition can differ despite similar climatic conditions (figure 2). At site 1, grasslands account for 55 % of NPP, while each of the four forest types contributes by 10 %. At site 2, only grasslands and broadleaf evergreen forest are present.

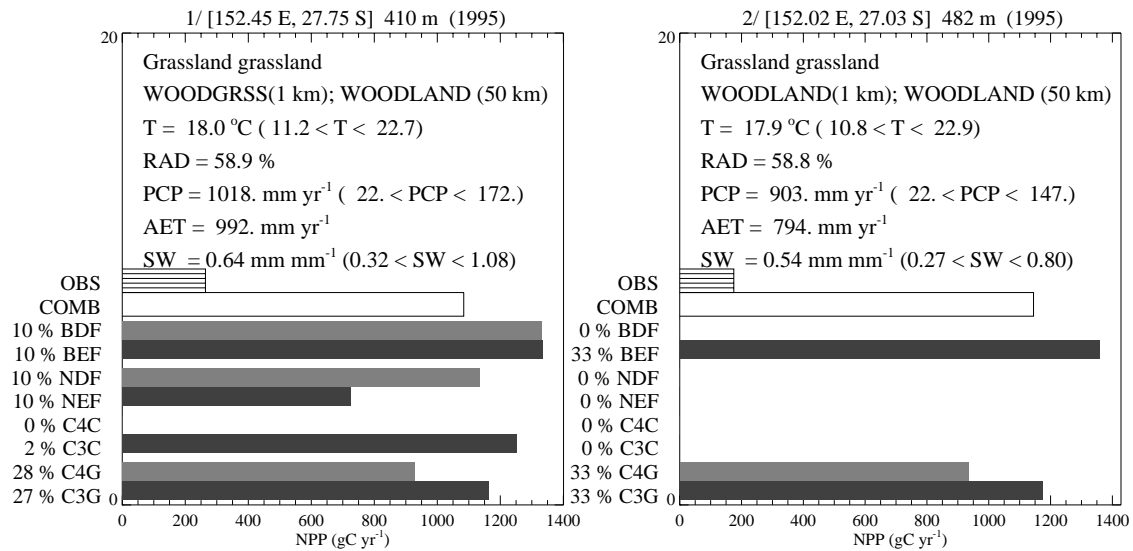


Figure 2: Comparison of 2 sites from the Eastern Australian coast. The climatic conditions are similar, but the vegetation distributions are different. The eight PFTs of CARAIB were simulated: C3 and C4 grasslands, C3 and C4 crops, needleleaf evergreen and deciduous forests (NEF - NDF), broadleaf evergreen and deciduous forests (BEF - BDF). Their contributions to the site NPP were weighted by the fractional areas into the COMB values, to be compared with the observed values of annual NPP.

2.2.2 Results

2.2.2.1 Simulation of isotopic composition of atmospheric CO₂

The mean seasonal cycles of CO₂ concentrations and δ¹³C over the period 1980-1993 were calculated for four monitoring stations. A good agreement is found between the observed and simulated seasonal cycles. Simulations of atmospheric CO₂ transport performed on the basis of monthly fluxes from several terrestrial biospheric models and net monthly fluxes from the ocean carbon model HAMMOC of Max-Planck Institute (Maier Reimer, personal communication) do not reveal substantial influence of the oceanic carbon fluxes on the seasonal atmospheric signal (Nemry et al., 1999). Isotopic simulations carried out after replacing the net ocean fluxes with the gross ocean fluxes, that is the fluxes of ¹²CO₂ and ¹³CO₂ from ocean to atmosphere and from atmosphere to ocean did not get additional information.

2.2.2.2 POTSDAM Intercomparison

Seasonal cycle of biospheric fluxes

Figure 3 summarizes the seasonality of NPP, R_H and R_H - NPP (g C m⁻² mo⁻¹) calculated by the various TBMs. The zonal averages of these fluxes are presented in

the tropical bands [23.5° S, 0°] and [0°, 23.5° N], two inner temperate bands [47° S, 23.5° S] and [23.5° N, 47° N], two outer temperate bands [70.5° S, 47° S] and [47° N, 70.5° N], and the arctic band [70.5° N, 90° N]. FBM, HYBRID and PLAI simulate negative NPP during winter in the temperate latitudes. The seasonality of the R_H signal is particularly small in the south temperate and arctic bands. In those bands, NPP has a greater amplitude. Elsewhere, the seasonal amplitude is generally lower for R_H than for NPP but not negligible.

The seasonal signature of the terrestrial biosphere in atmospheric CO₂ is influenced by the latitudinal distribution of the continental area. Among the five dominant zones, the contrast in area reduces the seasonal influence of the inner south temperate zone. Moreover, the seasonality of the fluxes themselves in these latitudes is low due to the effectiveness of thermal inertia of the ocean in preventing the soil from freezing and mitigating the seasonal amplitude of continental temperatures. As a consequence, the simulated seasonality in atmospheric CO₂ is mainly influenced by the four zones located between the Tropic of Capricorn and 70° N.

Annual values, seasonal amplitudes and phases

Figure 4 presents latitudinal profiles for the annual integrals and the seasonal amplitudes of the modeled biospheric fluxes.

Each TBM produces a latitudinal profile of the annual R_H which is nearly identical to the annual NPP profile. This is a consequence of the steady-state assumption. BIOME-BGC, which does not make a steady-state assumption, simulates a sink of 11 gigatons of carbon per year (Gt C/yr) in the north temperate zones, a source of 18 Gt C/yr from the intertropical band, and a sink of about 0.8 Gt C/yr in the south temperate bands. These sources and sinks are clear in the latitudinal profile of R_H - NPP (figure 2.4.). The annual carbon exchange between the atmosphere and the biosphere from HYBRID is also not at steady state, but to a much lesser extent (source of around 0.9 Gt C/yr).

Most of the TBMs predict that the seasonal amplitude of NPP varies dramatically with latitude, while the pattern in R_H is more muted. CARAIB and FBM simulate little seasonal R_H amplitude south of 40° N. BIOME-BGC and HYBRID simulate maximum seasonal amplitude of R_H at the equator. The remaining models (HRBM, PLAI, SDBM and SILVAN) produce latitudinal distributions of seasonal amplitude close to each other and similar to the seasonal profiles of NPP.

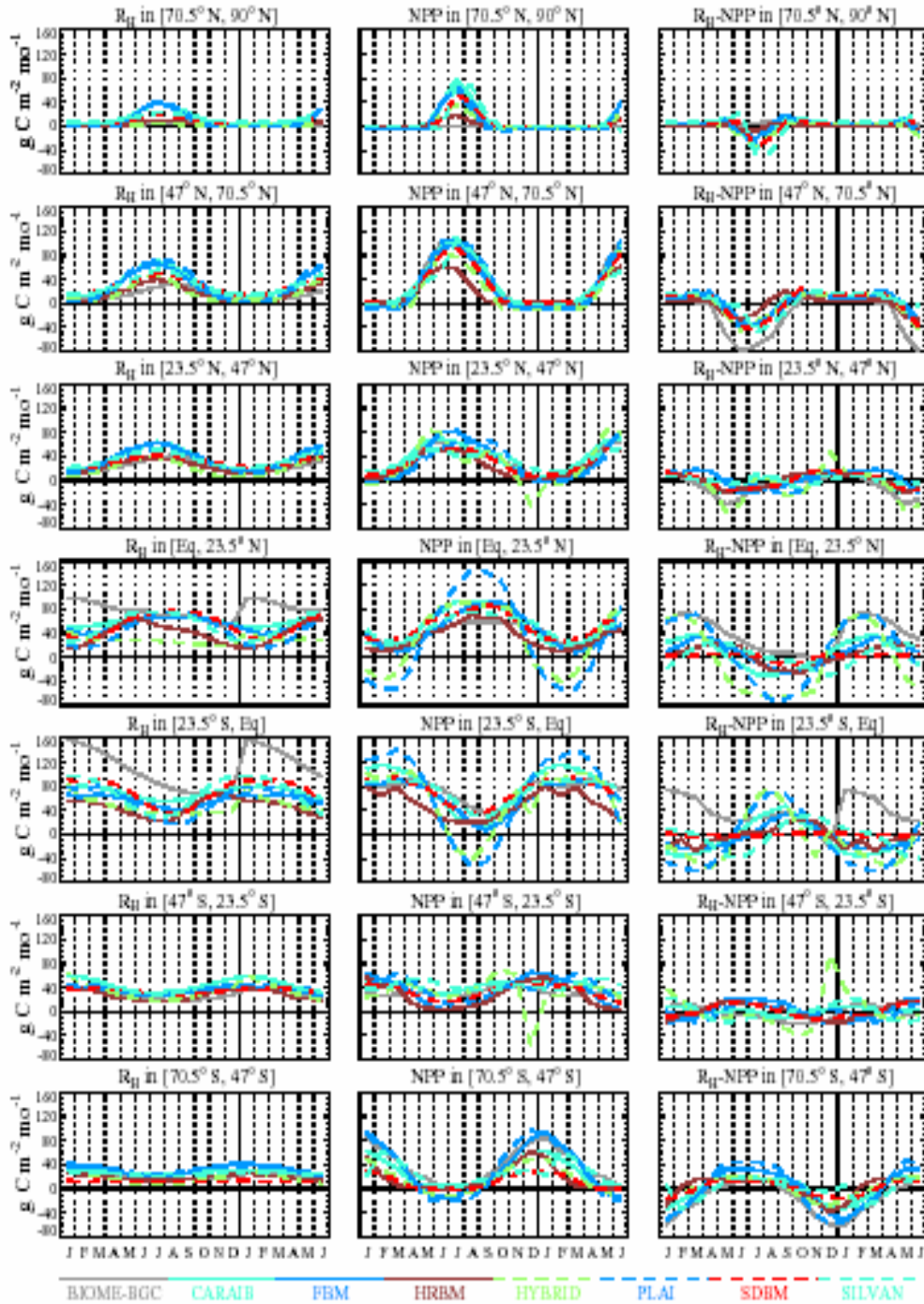


Figure 3: Zonal continental averages of the seasonal biospheric fluxes ($\text{g C m}^{-2} \text{mo}^{-1}$) calculated by eight Terrestrial Biosphere Models. R_H : heterotrophic respiration; NPP: net primary productivity.

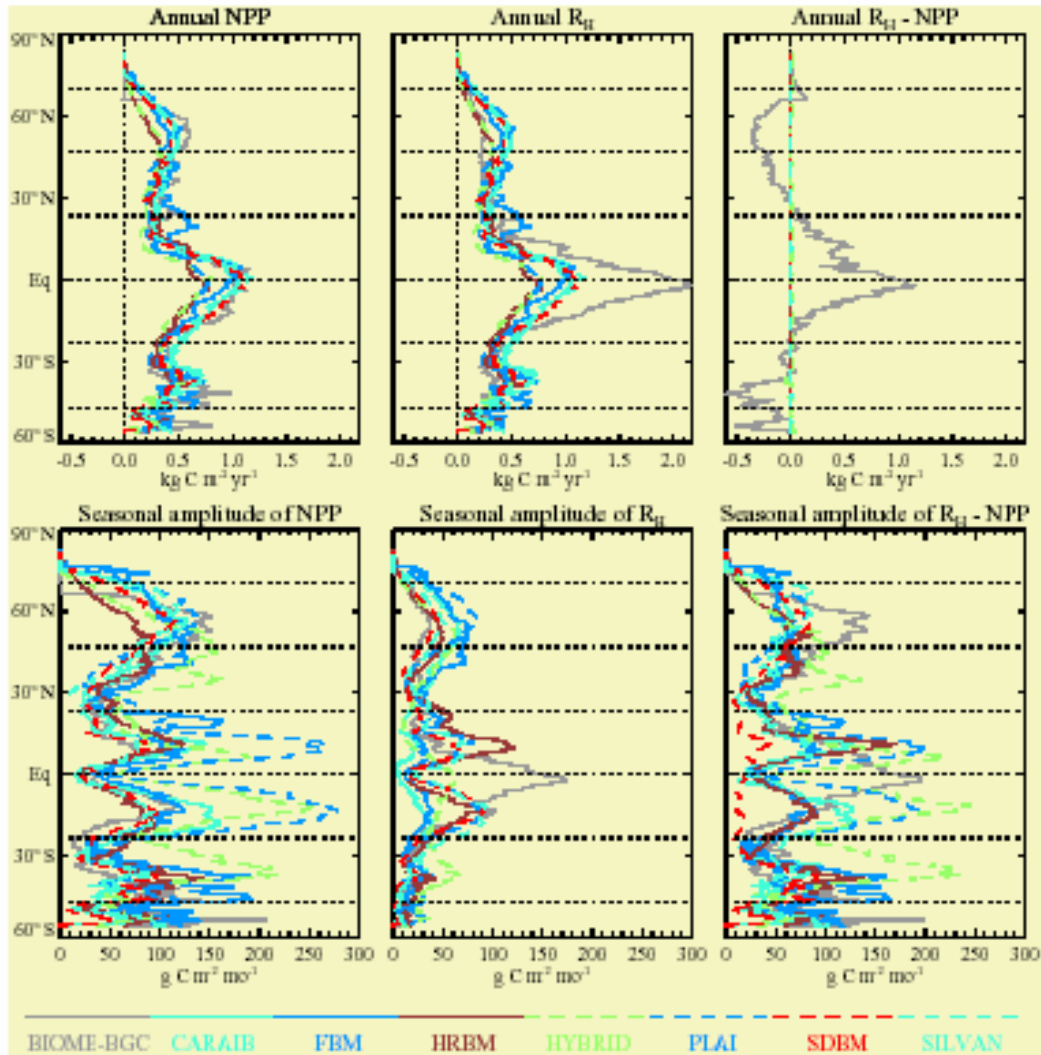


Figure 4: Annual values and seasonal amplitudes of the biospheric fluxes from eight Terrestrial Biosphere Models. R_H : heterotrophic respiration; NPP: net primary productivity.

All of the TBMs agree relatively well on the phasing of NPP and R_H in the north temperate zones (figure 3). All the models simulate their maximum NPP in June or July and maximum R_H in July or August. Minimum R_H in these latitudes is in January except for HYBRID (one to two months earlier), BIOME-BGC, and SDBM (both one month later). The month of minimum NPP in these temperate regions falls between October (FBM and HYBRID) and January (SDBM and HRBM). In the tropics, the maximum NPP from all models lags the maximum precipitation, which occurs in August and January in the northern and southern tropical bands respectively. Similarly, the minimum NPP from all the models lags the minimum precipitation, which occurs around six months after the humid season. Comparison with selected monitoring stations.

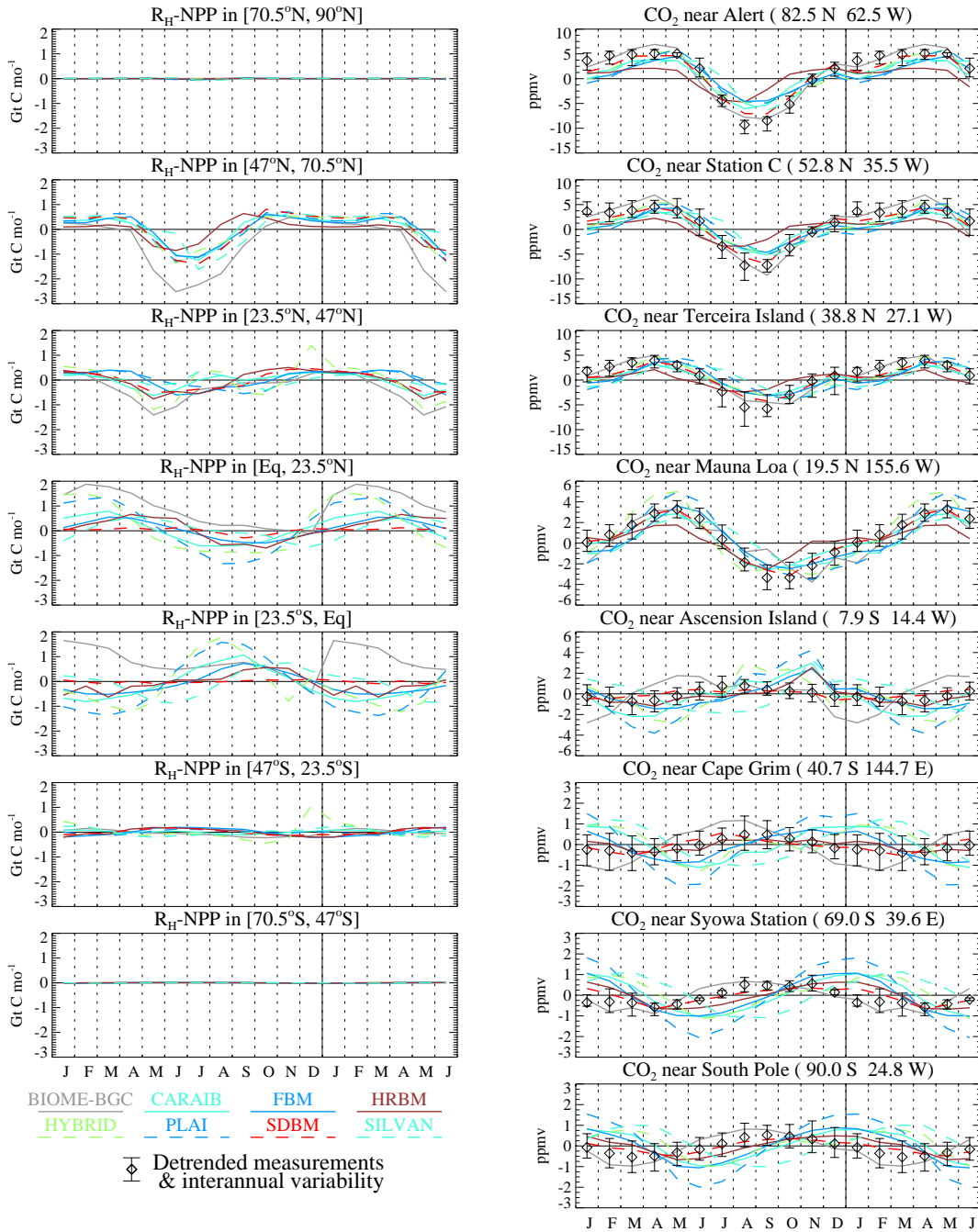


Figure 5: Zonal continental averages of simulated seasonal biospheric emissions (Gt C mo^{-1}) simulated by eight Terrestrial Biosphere Models (TBMs), and corresponding seasonal atmospheric CO_2 signals (ppmv) simulated near monitoring stations. The simulated atmospheric signals result from the TM2 transport model (Heimann et al., 1989) coupled to a TBM, simulated CO_2 emissions from ocean (Six and Maier-Reimer, 1996) and fossil fuel burning (Andres and Marland, 1996). The CO_2 measurements (Conway et al, 1994) have been detrended and the observed interannual variability is indicated by error bars.

Figure 5 presents the zonal net carbon exchanges of the terrestrial biosphere (Gt C mo^{-1}) obtained by multiplying the R_H - NPP fluxes from figure 3 by the continental areas in each latitude zone. The monthly averages of atmospheric CO_2 concentration simulated by TM2 are also presented for one monitoring station selected in each band. The interannual variability around each monthly value of the reference cycle is represented by the extremes found in the detrended series. At the four stations selected in the northern hemisphere (Alert, 82.5° N ; Station C, 52.8° N ; Terceira Island, 38.8° N ; Mauna Loa, 19.5° N), the TBMs overestimate CO_2 concentration in the summer trough.

Comparison with all monitoring stations

The fundamental Fourier modes (those with a period of one year) provide a compact way to summarize the seasonal dynamics at the 25 selected monitoring stations and to evaluate the influence of the ocean and the fossil fuel burning. Figure 6 displays the amplitudes and the time of the seasonal minimum of the fundamental Fourier modes based on measured and simulated CO_2 concentrations at the 25 selected stations. The interannual variability of the measured values was obtained at each station from the Fourier analysis of the individual detrended seasonal cycles used to construct the reference seasonal cycle. The latitudinal profiles are calculated with the biospheric seasonality alone, then with the ocean influence included and finally with both the ocean and the fossil fuel burning contributions.

The seasonal amplitudes in the north are generally too low except with BIOME-BGC and SDBM (figure 6). This is particularly true with HRBM as already noted in figure I.5. The effect of the ocean and fossil fuel burning is weak. The simulated phase in the northern hemisphere ranges from a lag of 2 months, mainly with PLAI and SILVAN in the northern temperate latitudes, to a lead of 2 months with HRBM in the extra-tropical northern regions (figure 6). The phases of CARAIB and HYBRID in the northern hemisphere are generally close to the observations, but not as close as that of SDBM, which was calibrated to match the seasonality of the atmospheric CO_2 signal. In the tropics, the effect of the ocean and the fossil fuel burning on the month of the CO_2 minimum varies among the TBMs. The effect of the ocean is generally larger than that of fossil fuel. Predicted CO_2 minima in the southern extra-tropical zones from the TBMs except BIOME-BGC and SDBM lag observations by one to five months. Adding the ocean and fossil fuel seasonality does not improve the match between the simulations and the observations in these regions.

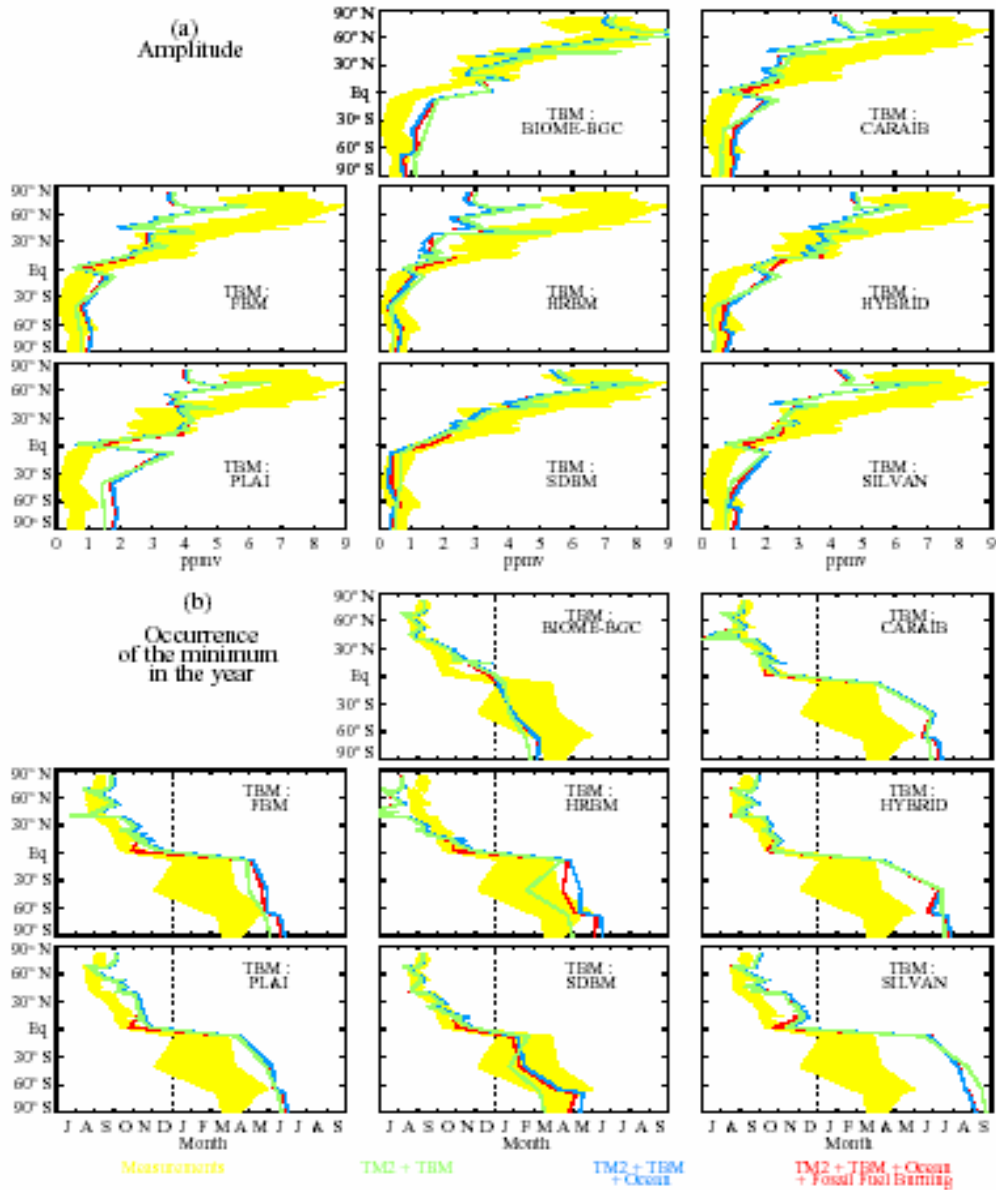


Figure 6: Latitudinal distribution of (a) amplitude (b) phase of the fundamental Fourier modes (period of one year) from observed and simulated detrended seasonal atmospheric CO₂ concentrations. Yellow: observation (Conway et al., 1994); Green: atmospheric transport model TM2 (Heimann et al., 1989) coupled to a Terrestrial Biospheric Model (TBM); Blue: TM2 coupled to a TBM and an ocean carbon model (Six and Maier-Reimer, 1996); Red: same as blue, with fossil fuel burning (Andres and Marland, 1996) included.

As explained in section 5.4, the seasonal tropospheric signal in any zone "a" is the sum of the partial seasonal signals from the biospheric regions located in the different zones "b". Each of the partial signals may be split into two seasonal components, one in phase with the signal of the whole biosphere, and the other one out of phase. The amplitude $P_{a,b}$ of the first component is displayed in figure 7.

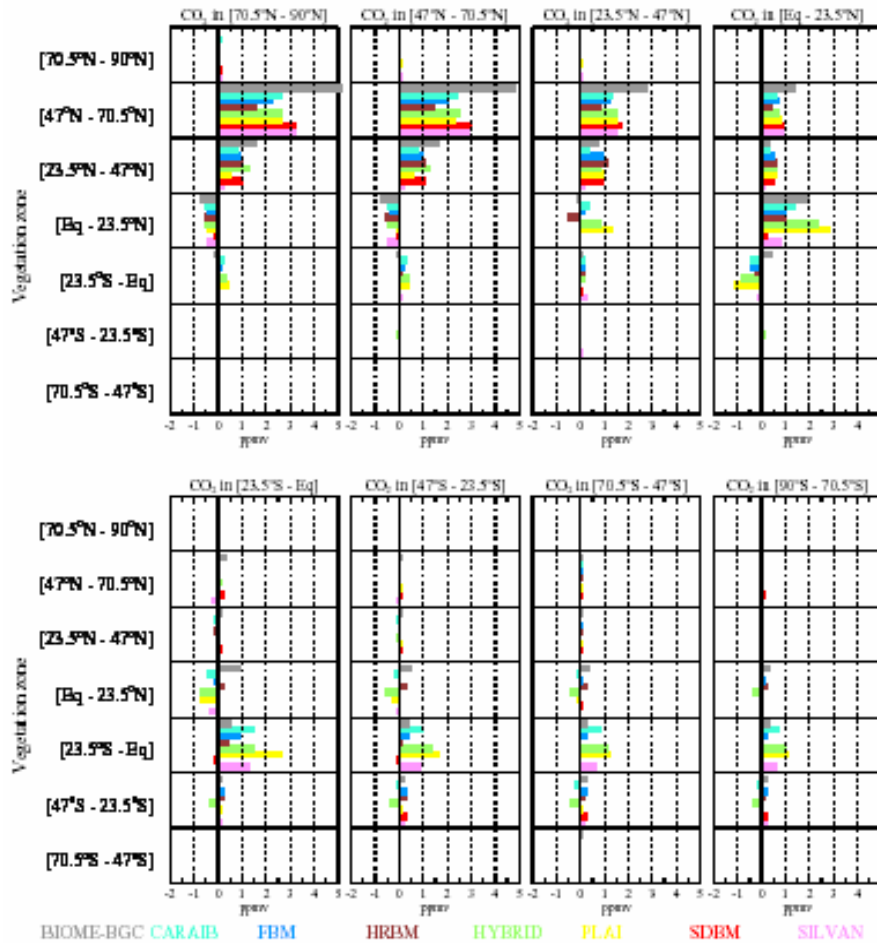


Figure 7: Influence of the vegetation zones on the seasonal tropospheric CO₂ concentration according to eight Terrestrial Biosphere Models. The fundamental Fourier modes have been calculated in each zone and their amplitudes projected onto the direction of the fundamental mode of the signal from the total biosphere.

The seasonal dynamics of atmospheric CO₂ in **the arctic and the northern temperate zones** is dominated by the biospheric fluxes in the northern temperate bands, mainly the outer one. In **the northern tropics**, contributions to the seasonal CO₂ dynamics are divided approximately equally between local influence and inputs from more northern zones for all models except SDBM, where local influences are very minor. In **the southern tropics**, the northern temperate biosphere has virtually no impact. The local vegetation is the main biospheric source of atmospheric seasonality. It produces a positive signal while the northern tropical biosphere has a slightly negative influence except in the results of HRBM and BIOME-BGC. In **the extratropical southern zones**, the latitudinal distribution of the biospheric influences on the atmospheric seasonal cycle is close to the simulated cycle in the southern tropical zones, with a progressive decrease of the amplitudes towards the South Pole and without change in the signs.

2.2.2.3 *Durham Intercomparison*

CARAIB simulation was run from 1901 to 1995, based on monthly climatic values of temperature, maximum and minimum daily temperatures, precipitation and insolation. Atmospheric CO₂ concentration was considered to increase from 296 ppmv to 361 ppmv over this period. The model was first spun up over 1901 in order to simulate the pre-industrial steady state of the biosphere. Then the following years until 1995 were used to simulate the transient response of the biosphere to the interannual changes in climate and atmospheric CO₂ concentration. Annual NPP values (COMB) simulated at each site in 1995 were usually smaller than the observed values (OBS) by a factor 2 at least (figure 8). The COMB value is the sum of the contributions from the PFTs weighted by their FCARs. The NPP was actually calculated for each of the eight PFTs in any site, even if the FCAR was zero.

At first sight, simulated annual NPP values do not match measurements. Most of the simulated NPP values are too large, especially where annual precipitation exceeds 600 mm/yr. The project is still in progress. Measurements have been analyzed and some of them have been rejected. Further exercises are scheduled in the next years.

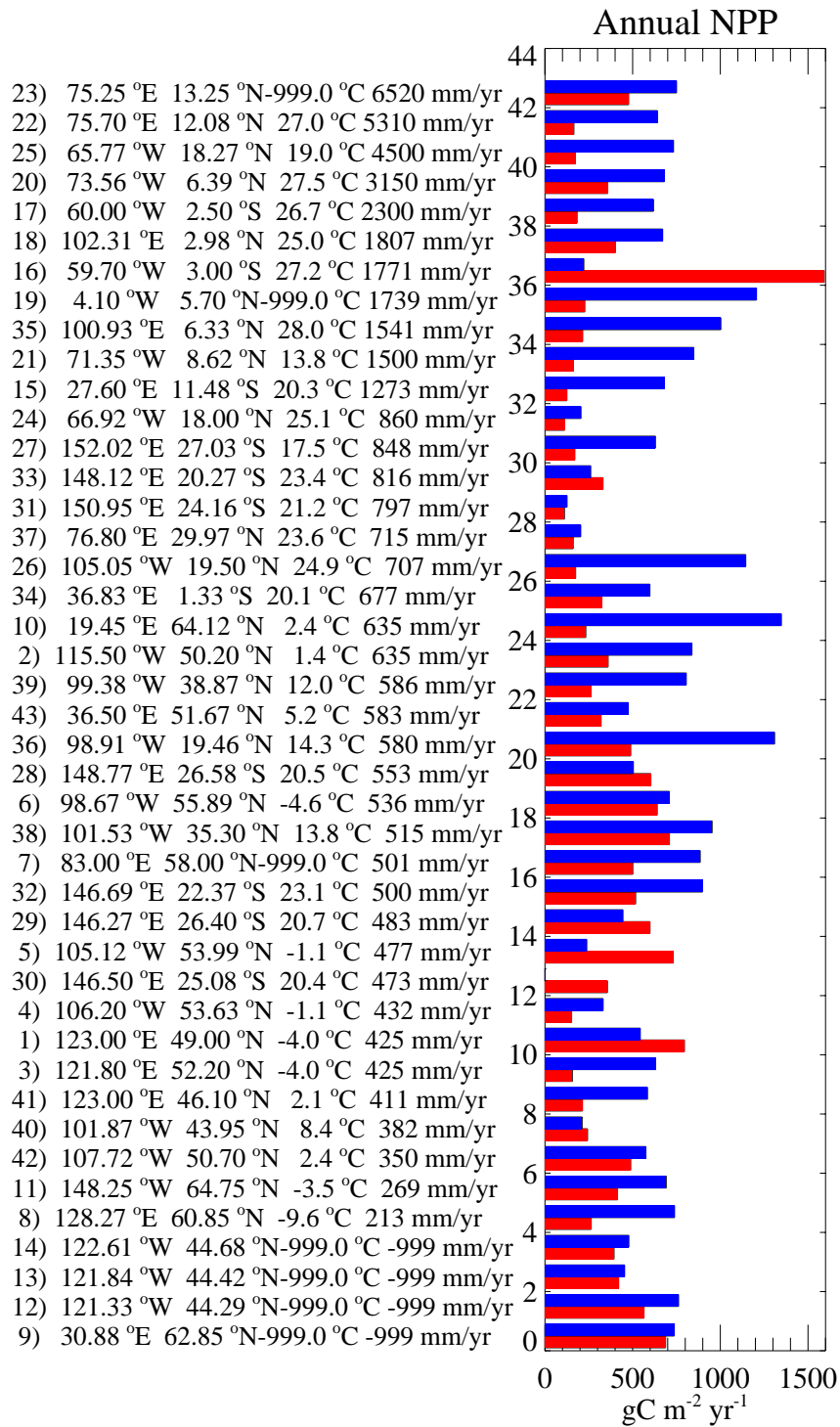


Figure 8: Comparison of 2 sites from the Eastern Australian coast. The vegetation distributions are different despite similar climatic conditions. The eight PFTs of CARAIB were simulated: C3 and C4 grasslands, C3 and C4 crops, needleleaf evergreen and deciduous forests (NEF - NDF), broadleaf evergreen and deciduous forests (BEF - BDF). Their contributions to the site NPP were weighted by the fractional areas into the COMB values, to be compared with the observed values of annual NPP.

2.3 Impact of Future levels of atmospheric CO₂ on vegetation and climate: results and discussion

2.3.1 Global scale

2.3.1.1 Impact of crops on biomass and soil carbon: steady state simulations

LPAP participated in the ECLAT-2 workshop held in Potsdam (Germany, October 13-15, 1999). The theme was "Climate scenarios for agricultural, ecosystem and biological impacts". Several working groups were defined. In order to estimate the influence of crops on the biospheric carbon budget, we analyzed more specifically the differences between simulated steady states of the present vegetation and a vegetation without crops (Nemry et al., 2000). Impact of CO₂ fertilization was also estimated.

A 'no crop world' scenario was built from the present vegetation distribution, by replacing crops with neighbouring forests. The grassland areas were not modified. Present contributions of C₃ and C₄ crops to the continental vegetation cover (127.41 10⁶ km²) are 11.60 10⁶ km² and 2.06 10⁶ km², respectively (figure 9). Together, they have reduced the area of needleleaf evergreen forests by 2.38 10⁶ km² between 40°N and 60°N, and the area of broadleaf deciduous forests by 9.44 10⁶ km², between 0° and 60°N. Other forested areas have been reduced to a lesser extent: broadleaf evergreen forests and needleleaf deciduous forests have lost 1.49 10⁶ km² and 0.35 10⁶ km², respectively.

Fertilization of the biosphere by increasing atmospheric CO₂ concentration was estimated by comparing biospheric steady states simulated at two levels of CO₂ concentration. François et al. (1996) and Gérard et al. (1999) used CARAIB to analyze the influence of interannual climate changes on the biosphere. In the assessment of the present results, we focussed on the direct impacts of crops and CO₂ fertilization and deliberately neglected any interannual climatic change, including greenhouse warming. All the simulations were performed on the basis of the average seasonal climatology from Cramer and Leemans (personal communication). Nevertheless, two daily weather inputs were considered. A standard distribution of daily temperature and precipitation was produced by the stochastic weather generator included in CARAIB (Hubert et al., 1998). In an alternative weather distribution, temperature was changed linearly from day to day between two successive months, while precipitation did not change during any month.

A global annual value of 67 Gt C yr⁻¹ was calculated for the sink of carbon associated with the NPP flux under an atmospheric CO₂ concentration of 360 ppmv. Under 280 ppmv, the estimated global annual NPP sink was reduced by 21%; a value of 53 Gt

$C\text{ yr}^{-1}$ was calculated whether the considered biosphere was the ‘no crop world’ or the present vegetation (figure 2.10). When atmospheric CO_2 concentration was doubled from 330 ppmv to 660 ppmv, the simulated NPP increase by 67% (Warnant, 1999). This biospheric response to a doubling in atmospheric CO_2 exceeds the 20 to 40% range measured in small scale experiments. This range can be reduced due to unavailability in water or nutrient (IPCC, 1995).

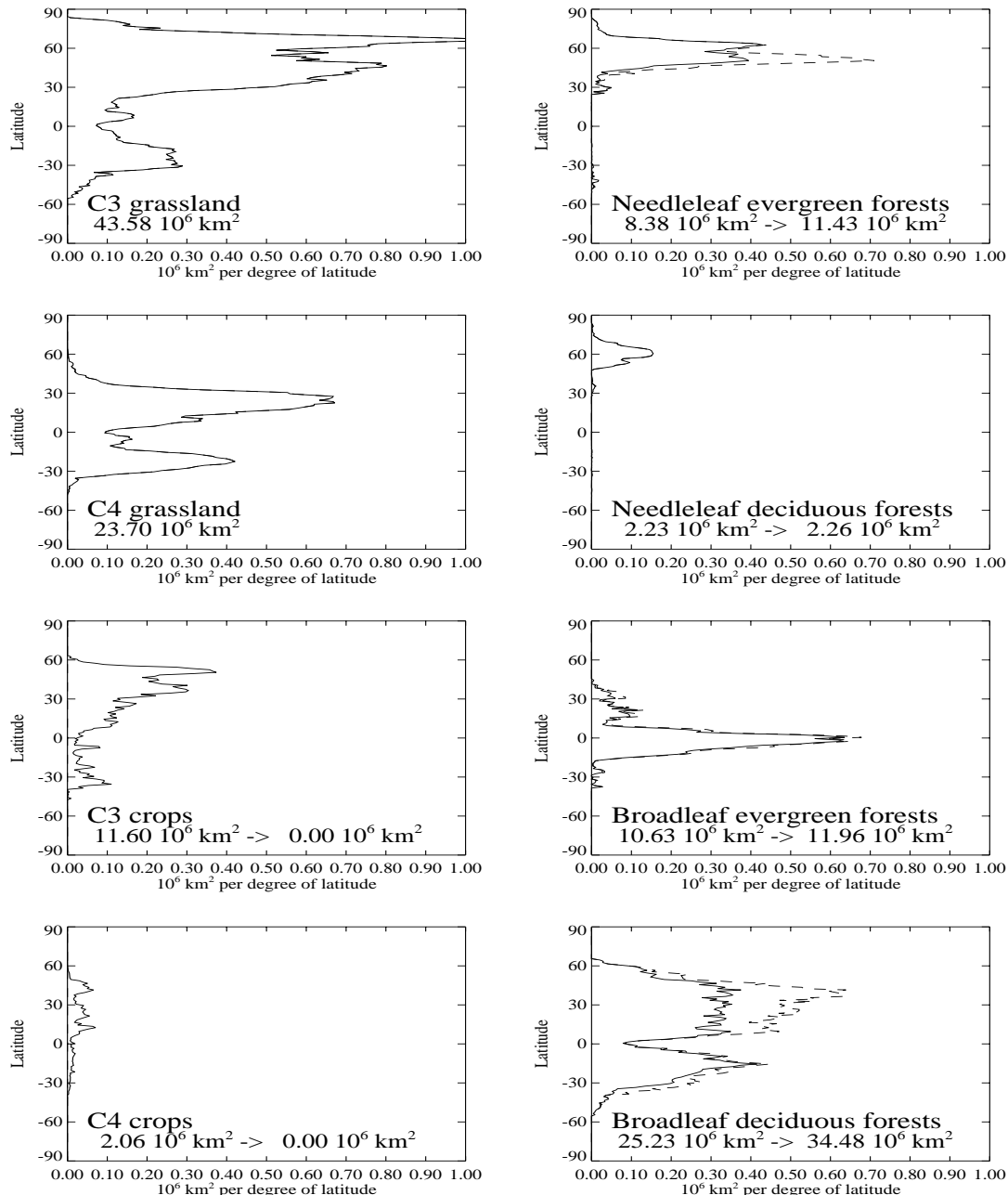


Figure 9: Latitudinal distribution of the annual carbon sink associated with the NPP flux simulated by CARAIB. Three steady states are compared. Vegetation is considered to include crops (‘now’) or not (‘no crop world’). Two atmospheric CO_2 concentrations have been used.

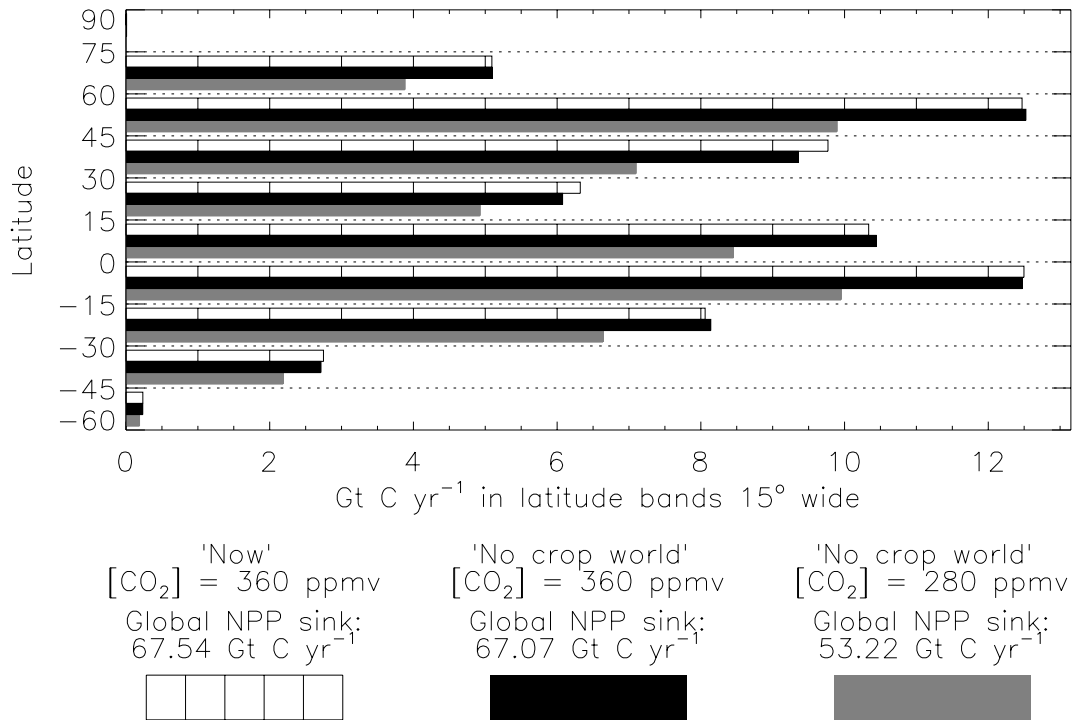


Figure 10: Latitudinal distribution of the annual carbon sink associated with the NPP flux simulated by CARAIB. Three steady states are compared. Vegetation is considered to include crops ('now') or not ('no crop world'). Two atmospheric CO₂ concentrations have been used.

As far as latitudinal distribution was considered in bands 30° wide, our results were rather insensitive to the spatial resolution. Sensitivity to temporal resolution was higher. When the stochastic sequence of daily weather was replaced with the linear sequence, the global annual amount of carbon absorbed by NPP flux was reduced by 30%. As a consequence, stochastic daily weather can be a cause of overestimation in NPP values. The transition from the 'no crop world' at 280 ppmv to the present vegetation at 360 ppmv can be decomposed into two transitions: (i) an « atmospheric carbon change » (ACC) transition of the 'no crop world' from 280 ppmv to 360 ppmv ; (ii) a « land use change » (LUC) transition from the 'no crop world' to the present vegetation at the constant CO₂ concentration of 360 ppmv. In the ACC transition, the carbon content increased by 175 Gt C in the biomass, 60 Gt C in the litter pools and 492 Gt C in the soil. Fertilization of the 'no crop world' induced a total increase in biospheric carbon of 727 Gt C. These results were produced with stochastic daily weather (figure 11). In the LUC transition, the loss of woody biomass associated with the substitution of crops for forested areas amounted to 160 Gt C. All latitudes were affected, especially in the northern temperate regions. Green biomass was lost to a lesser extent (around 1 Gt C). It happened mainly between 45°N and 60°N, where the largest areas of crops have been planted at the

expense of needleleaf evergreen and broadleaf deciduous forests. Non green litter carbon decreased by 3 Gt C while green litter carbon increased by an equivalent quantity. Soil organic carbon increased by 146 Gt C. The global budget of the biospheric carbon pools was a loss of about 15 Gt C.

According to ACC and LUC transitions, the biospheric carbon increase induced by CO₂ fertilization prevailed on the loss of carbon due to the substitution of crops for forests. The net result of these transitions was an increase of 712 Gt in the global amount of biospheric carbon. The increase in carbon contents from the 'no crop world' at 280 ppmv to the present vegetation at 360 ppmv occurred in all pools at all latitudes, except for the northern temperate latitudes where the loss of woody biomass dominated the fertilization effect by about 30 Gt C.

2.3.1.2 *Atmospheric General Circulation Models*

We analyzed the results from three Atmospheric General Circulation Models (AGCMs) available at the Data Distribution Center of the Intergovernmental Panel on Climate Change (DDC-IPCC). They were run to simulate the response of the Earth climate to a standard increase in the concentration of atmospheric carbon dioxide (CO₂) over the 20th and 21st centuries. We focussed on simulations where the radiative forcing of the climate system included a greenhouse warming and a cooling by sulfate aerosols: (i) Canadian Global Coupled Model (CGCM1) from the Canadian Center for Climate Modeling and Analysis (CCCMA); (ii) the HadCM2 from the Hadley Center (iii) the GFDL-R15 from the Geophysical Fluid Dynamics Laboratory (GFDL). The equilibrium climate sensitivity of CGCM1 and HadCM2, that is the global-mean temperature response to a doubling of effective CO₂ concentration, is about 2.5°C. This is 1°C lower than the sensitivity of GFDL-R15. In the three simulations, the negative forcing from sulfate aerosols is added to the forcing of all the greenhouse gases combined as an equivalent CO₂ concentration. The global distribution of the average temperature over the period 1900-1909 is compared between the three AGCMs in figure 2.12., as well as the temperature increment from this decade to 2090-2099. Signification differences are observed concerning the amplitude and spatial distribution of the warmings.

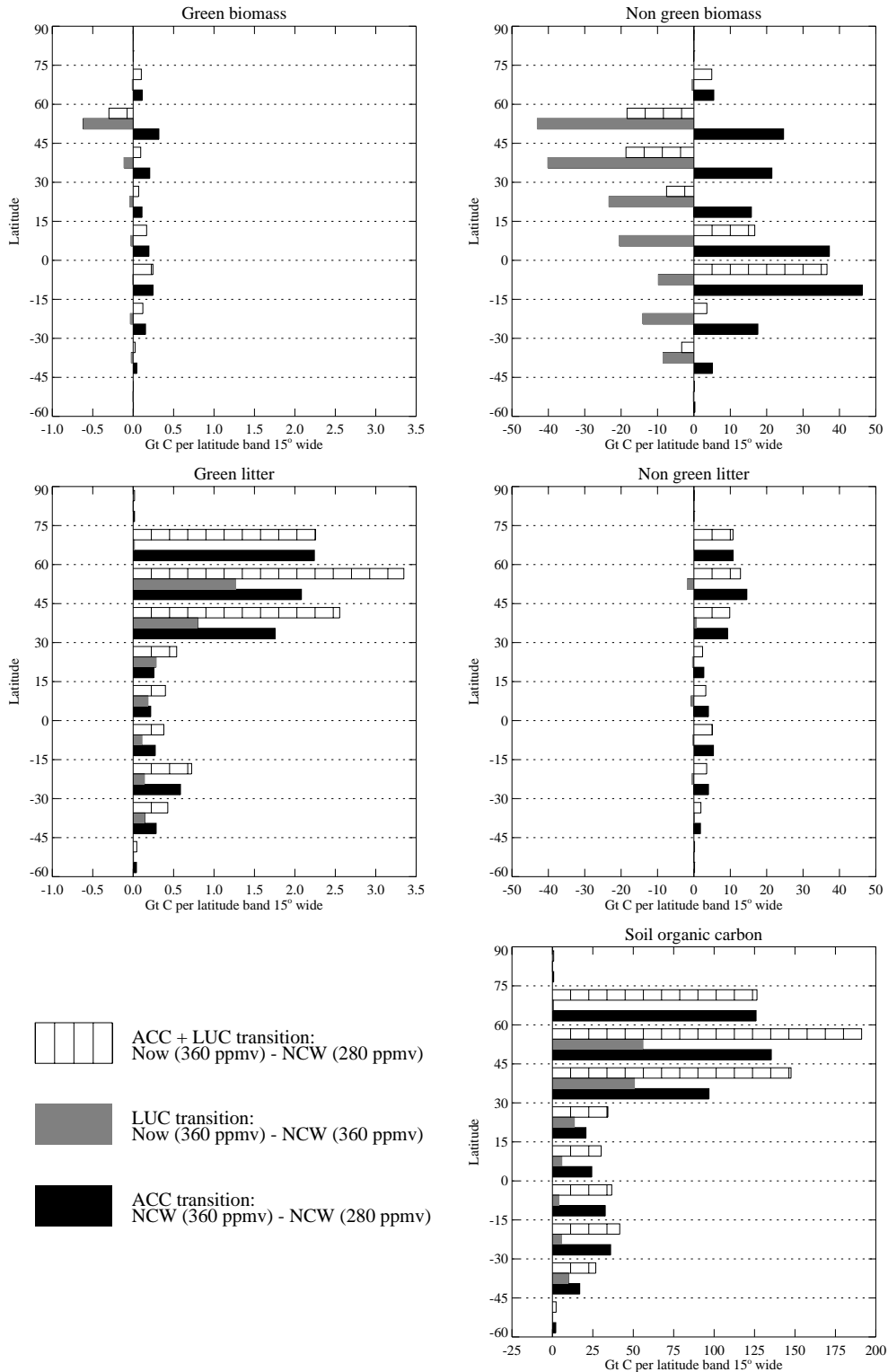


Figure 11: Latitudinal distribution of the carbon increments simulated by CARAIB in five pools: green and non green biomass, green and non green litter, and soil. Three transitions are considered: (i) Atmospheric CO₂ Change (ACC) transition: 'no crop world' (NCW) from 280 ppmv to 360 ppmv; (ii) Land Use Change (LUC) transition: from NCW to now, at 360 ppmv; (iii) ACC + LUC transition: from NCW at 280 ppmv to now at 360 ppmv.

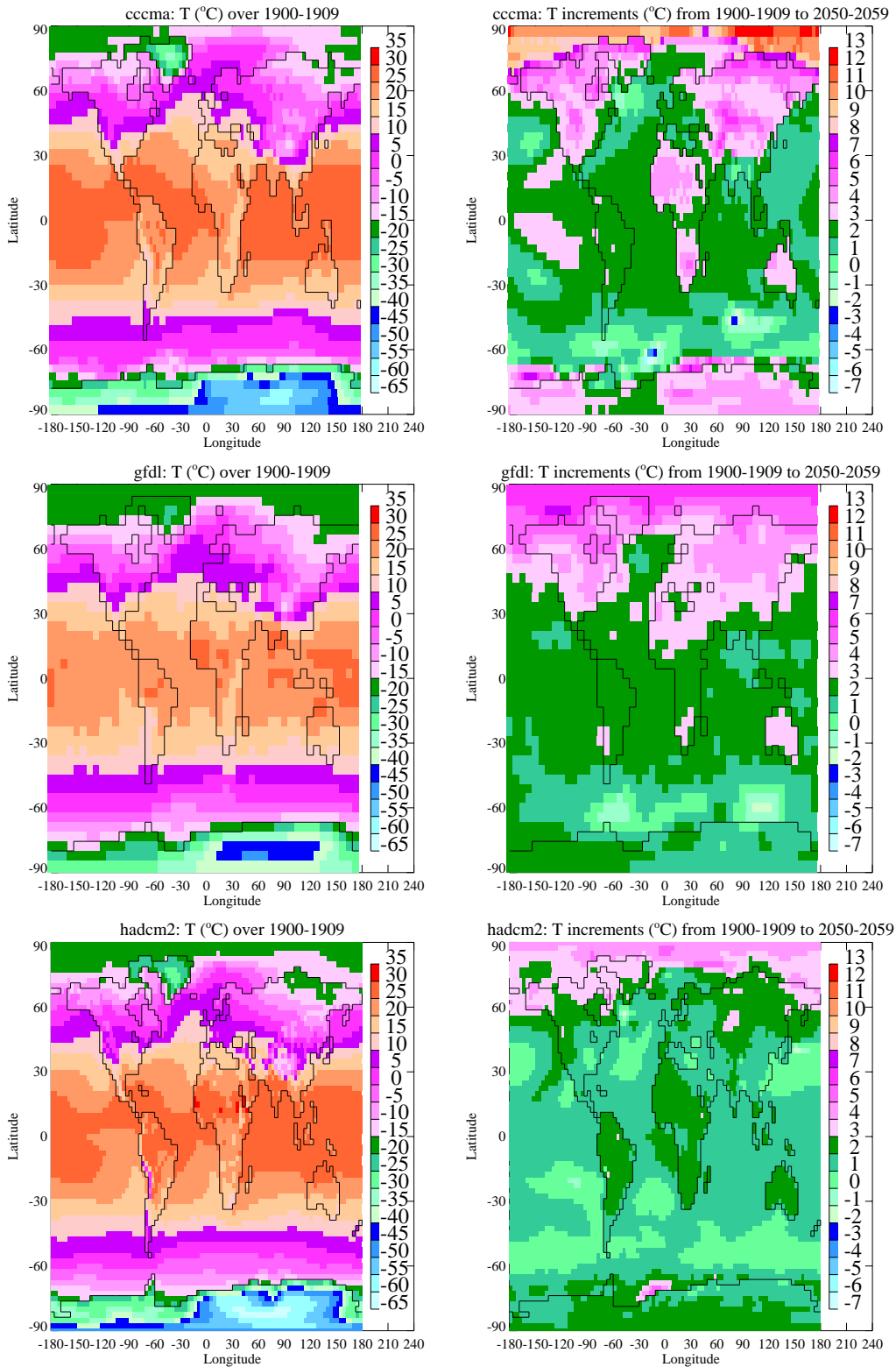


Figure 12: Comparison of simulated temperature from 3 AGCMs. The simulated change in climate is due to an increase in atmospheric CO₂ concentration by 1%/yr. Left: mean climate over 1900-1909; Right: mean increment of temperature from 1900-1909 to 2050-2059.

We compared the AGCM results with the gridded datasets of temperature (Jones, 1994) and precipitation (Hulmes *et al.*, 1998). The mean annual values of precipitation simulated over the period 1900-1994 in the grid cells close to Belgium look more realistic with GFDL-R15 and HadCM2 than with CCCMA when they are compared with the Hulmes gridded dataset (table II). The largest values of precipitation are simulated during the whole year by CCCMA. Interannual variability of the annual precipitation over this period depends on the choice of the grid cell with various sensitivities between the GCMs and the Hulmes dataset.

Table II: Average (left of /) and standard deviation (right of /) of annual precipitation values over the period 1900-1994 in two grid cells from three AGCMs and from gridded observations.

Origin	Grid cell 1	Grid cell 2
CCCMA	1267 / 35.2	1223 / 33.2
GFDL-R15	750 / 27.5	680 / 28.3
HadCM2	891 / 29.3	882 / 26.9
Hulmes <i>et al.</i> (1998)	871 / 32.4	715 / 25.2

The Jones dataset provides temperature anomalies with respect to the period 1961-1990 for each month of the years 1900-1994. We compared these temperature anomalies with those calculated from the GCM simulations (table III). While the positive values from the Jones dataset correspond to a cooling of the years 1961-1990, the negative values predicted by the GCMs correspond to a warming of this period by at least 1°C. This difference between the Jones dataset and the GCMs has not the same magnitude from grid cell to grid cell. in the GCM simulations than in this dataset.

Table III: Average (left of /) and standard deviation (right of /) of annual temperature anomalies over the period 1900-1994 in two grid cells from three AGCMs and from gridded observations.

Origin	Grid cell 1	Grid cell 2
CCCMA	-1.542 / 1.092	-1.542 / 1.133
GFDL-R15	-1.959 / 1.699	-2.703 / 1.780
HadCM2	-1.082 / 1.919	-0.769 / 2.122
Jones (1994)	0.287 / 0.907	1.667 / 1.305

2.3.2 Local scale: Simulated response of Belgian forests to transient change in climate

2.3.2.1 Introduction

We estimated the impact of climate and meteorology on vegetation at two monitoring Belgian sites 150 km apart. We used the monthly results of three AGCMs analyzed in a previous section. These models had been run to simulate the response of the global climate to an increase in equivalent greenhouse gas over the period 1900-2100. We downscaled their monthly climatic results to subdaily meteorologies on the basis of site measured series of semi-hourly meteorological variables.

2.3.2.2 Forested site measurements

Six meteorological variables were measured every half-hour during 1997 and 1998 at two Belgian forested sites. The first site, Brasschaat, is located at 51.18°N, 4.37°E at a height of 16 meters. The second site, Vielsalm, is situated around 150 km away at 50.17°N, 6.00°E, with an elevation of 490 meters. The annual values of the six meteorological variables, solar radiation ($W m^{-2}$), air temperature ($^{\circ}C$), precipitation ($mm day^{-1}$), relative humidity ($kg kg^{-1}$), wind ($m s^{-1}$) and atmospheric pressure (Pa) are listed in Table IV.

Table IV: Annual values of six meteorological variables measured every half-hour in 1997 and 1998 at Brasschaat and Vielsalm: solar radiation (Rad), air temperature (T), precipitation (PCP), relative humidity (RH), wind (W) and atmospheric pressure (P_{atm}).

Site of measurements	Year	Rad W/m ²	T °C	PCP mm/yr	RH kg/kg	W m/s	P _{atm} 10 ² Pa
Brasschaat	1997	202	10.4	671	0.84	2.67	1016
51°18'N, 4°37'E, 16 m	1998	180	10.7	1041	0.82	2.53	1014
Vielsalm	1997	211	7.6	785	0.83	2.35	963
50°17'N, 6°00'E, 490 m	1998	176	7.4	1246	0.86	2.60	961

2.3.2.3 Spatial downscaling

The monthly climatic variables simulated by each AGCM at the grid cells including the sites were corrected to account for the spatial subgrid variability and the characteristics of each site, unknown at the scale of the GCM resolutions. Differences in downscaled variables were larger between these GCM simulations

than between two periods simulated by the Hadley GCM, because of its low sensitivity to greenhouse gas forcing. We decided to base our spatial downscaling on simple algebra to reconcile the interannual averages of the seasonal cycles simulated and observed during 1997-1998. Monthly correction factors were calculated as

$$\phi_V(m) = \frac{\underline{V}_{obs}(m)}{\underline{V}_{GCM}(m)}$$

where $\underline{V}_{obs}(m)$ and $\underline{V}_{GCM}(m)$ are the interannual averages over 1997-1998 of variable V observed and simulated by GCM at month m , respectively. The monthly corrections $\Phi_V(m)$ were applied over the whole industrial era so that variable $V_{GCM}(m,k)$ simulated at month m of any year $y = k + 1900$ was corrected into

$$V_{corr}^x(m, k) = V_{GCM}(m, k) \cdot \phi_V(m)$$

Alternatively, monthly correction terms were calculated as differences between observed and simulated averages:

$$\delta_V(m) = \underline{V}_{obs}(m) - \underline{V}_{GCM}(m)$$

These differential corrections were used as additional terms to convert the original GCM simulated variables into corrected variables consistent with the measurements:

$$V_{corr}^+(m, k) = V_{GCM}(m, k) + \delta_V(m)$$

Since the monthly corrections $\Phi_V(m)$ and $\delta_V(m)$ do not vary from year to year, the interannual variability of the GCM simulations is not affected by the spatial downscaling.

2.3.2.4 Time downscaling

Time downscaling consisted in adding semi-hourly variability to each corrected variable $V_{corr}(m,k)$ calculated as $V_{corr}^x(m,k)$ or $V_{corr}^+(m,k)$ at each month m of year k of the industrial period. Several estimation methods were tested.

In a first estimation method, the selection of year k_{opt} between 1997 and 1998 was carried out each month m of year k to minimize the absolute value of the relative difference between $V_{corr}(m,k)$ and $V_{obs}(m, k_{opt})$. Then the subdaily values at instant h of day d were estimated as

$$V_{EM1}(h, d, m, k) = \frac{V_{corr}(m, k)}{V_{obs}(m, k_{opt})} \cdot V_{obs}(h, d, m, k_{opt})$$

To protect these estimates from unrealistic values, limitations were defined for every instant h of any month m as the extremes found at this instant of any day in the month. The estimated values $V_{EM1}(h,d,m,k)$ were thus constrained to lay between

$$V_{\max}(h,m) = \max_{d,k_o} \{V_{obs}(h,d,m,k_o)\}$$

and

$$V_{\min}(h,m) = \min_{d,k_o} \{V_{obs}(h,d,m,k_o)\}$$

where d covers the days in month m and k_o points to the years 1997 and 1998.

Other estimation methods were tested, but no significant differences were obtained.

2.3.2.5 Emission scenario

We built an atmospheric CO₂ forcing similar to the forcing used in the GCM simulations, that is an increase based on historical records from 1900 to 1990 followed by a projection until 2100. The annual values of atmospheric CO₂ concentration were assumed to increase exponentially during both these periods. As a consequence, annual atmospheric concentration [CO₂(y)] at year y between y_1 and y_2 is given by

$$[CO_2(y)] = [CO_2(y_1)] \exp(K_{12} \cdot (y - y_1))$$

with

$$K_{12} = \frac{\ln \left[\frac{[CO_2(y_2)]}{[CO_2(y_1)]} \right]}{y_2 - y_1}$$

The annual value of atmospheric CO₂ concentration was set to 300 ppmv in 1900, a mean value found in the air enclosed between 1883 and 1925 in the ice core of Siple Station, and to 355 ppmv in 1990, close to measurements at various sites in the Northern Hemisphere. The level of atmospheric CO₂ concentration reached in 2100 was estimated to 700 ppmv, as calculated from the scenario IS92a with the Bern model (Houghton *et al.*, 1995). As a consequence, the values of K_{12} are 0.19 % yr⁻¹ and 0.62 % yr⁻¹ for the periods 1900-1990 and 1990-2100, respectively. The last value is lower than the rate used in the GCM simulations (1 % yr⁻¹). Such a rate, used for the combination of an equivalent greenhouse gas combined with aerosols, looks too high because the resulting concentration calculated in 2100 is 1066 ppmv, larger

than 900 ppmv, the maximum CO₂ concentration predicted in any of the IS92 scenarios.

2.3.2.6 Response of Net Ecosystem Productivity to the emission scenario

Since the monthly AGCM climatic fields were corrected and downscaled on the basis of the same site measurements, they converged to similar meteorologies. Nevertheless, they influenced the biospheric results with their own interannual variabilities over the period 1900-2100 (figure 13). The simulations were performed with a version of CARAIB specialized to biospheric aspects that can be accounted for at local scale (Rasse et al., 2000). The annual growth of branches, stems and coarse roots was reset to zero every year so that their initial state did not change from year to year. Leafs and fine roots were limited to maximum values.

According to these simulations, the simulated net ecosystem productivity (NEP) is positive and increases over the whole period 1900-2100, from 200 g C m⁻² yr⁻¹ to about 300 g C m⁻² yr⁻¹. Consequently, the activity of the forest as a sink of carbon is amplified by the increase in atmospheric CO₂ concentration.

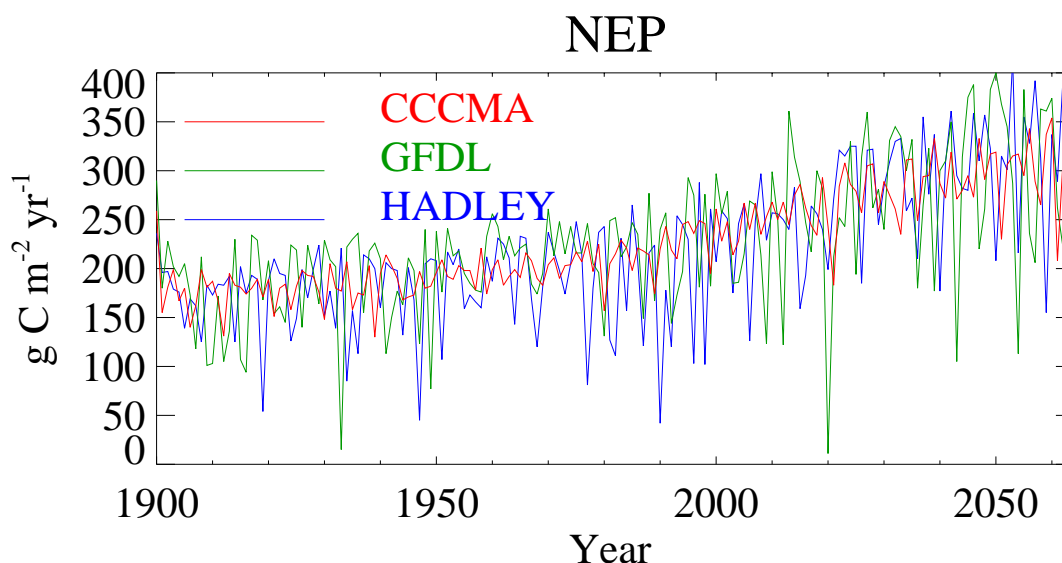


Figure 13.

2.4 The biosphere during glacial-interglacial periods

Ice-core measurements have revealed significant fluctuations of the CO₂ atmospheric level during glacial-interglacial cycles. Indications show that, at the time of these transitions, a significant amount of carbon is redistributed between the atmosphere, the ocean and the continental biosphere. It is important to understand the role played

by the vegetation as a sink or a source of atmospheric CO₂ during the climate changes. For this purpose, a study of carbon flows, stocks and isotope balances at the time of the last glacial maximum (-21.000 years) and mid-Holocene (-6.000 years) was carried out using the CARAIB model (François *et al.*, 1998).

The last glacial maximum (LGM) was characterized by a weak atmospheric CO₂ concentration in parallel to a colder and generally drier climate than today, an extended north polar cap and an ocean level significantly lower than today. In order to simulate these climates, two different general circulation models (GCM) were used: the ECHAM model of the Max Planck Institute at Hamburg and the model of the LMD (Laboratoire de Météorologie Dynamique). The study showed that the trends calculated with the two models for a same climate are convergent, although quantitative differences appear. The calculated changes compared to present vary from -132 to +92 GtC for the mid-Holocene and from -710 to +70 GtC for the LGM. A significant share of the range of values is related to the consideration or not of the fertilization effect by CO₂.

The study also concludes that the organic fraction of material synthesized by C₄ plants was higher at the LGM and mid-Holocene than today. This change in the relative importance of the plants in C₃ and C₄ induced modifications in ¹³C fractionation of the continental biosphere. These changes in the fractionation efficiency due to the redistribution between C₃ and C₄ plants was partly *compensated* by differences in the efficiency of the fractionation by C₃ plants generated by the change in the CO₂ intercellular pressure in the leaves. The combination of the two factors reduced the CO₂ discrimination of the continental vegetation by 0.03 (to 0.032 ‰) at mid-holocene and 0.30 (to 1.86 ‰) during the LGM.

Figure 14 illustrates the distribution between biomes of the change of total carbon stocks (vegetation + litter + soil) calculated by CARAIB for mid-holocene (6 ka) and LGM (21 ka). The fertilization effect by CO₂ is illustrated by comparing the results without fertilization (ECHAM and LMD-LSCE). These changes mainly reflect those of the global integrated vegetation productivity. When the fertilization effect is taking into account, the model indicated an increase of the biospheric carbon stock between 70 GtC (LMD-LSCE) and 250 GtC (ECHAM) for today compared to the LGM.

The terrestrial biosphere model CARAIB (CARbon Assimilation In the Biosphere) (Warnant *et al.*, 1994; Warnant, 1999) was improved by introducing two vegetation storeys and implementing a new module which simulates the equilibrium distribution of the vegetation inferred from physiological processes and climatic constraints. In this fourth version of CARAIB, we differentiate ground-level grasses from tree canopies, which allows us to determine the light available to grasses as a direct function of the leaf area index (LAI) of the forest canopy. Both of these storeys are

potentially composed of several plant functional types (PFTs). The cover fraction of each PFT within each storey is estimated according to its respective net primary productivity (NPP). A biome is assigned to each grid cell on the basis of three physiological criteria: 1. the cover fraction, 2. the NPP, and 3. the LAI, and two climatic constraints: 1. the growing degree-days (GDD) and 2. the lowest temperature reached during the cold season (T_{min}), which are well-known indices of vegetation expansion boundaries. Total biospheric carbon stocks (vegetation + soil) and fluxes are reconstructed by forcing the model with eight climatic scenarios of the last glacial maximum (LGM, 21 kyr bp), which were obtained from the Paleo Modelling Intercomparison Project (PMIP) from four general circulation models (MRI2, UGAMP, LMD4, and GEN2) using prescribed and computed sea surface temperatures (SSTs). The model was also forced with a current climate together with a preindustrial atmospheric CO_2 level of 280 ppm as reference simulation.

The results indicate an increase in NPP from the LGM to the present of 16.0 - 21.8 $Gt\ C\ yr^{-1}$, and an increase in the total biospheric carbon stock of 827.8 - 1106.1 $Gt\ C$. To validate the model, current biome distribution is reconstructed and compared, for the modern climate, with two distributions of potential natural vegetation : the map simulated by the TEM (Melillo et al., 1993) adapted from Haxeltine and Prentice (1996), and the map of Matthews (1983) (figure 14). At a comparison scale of $1^\circ \times 1^\circ$, the overall agreements are respectively of 61% and 52%. A comparison between the two natural maps has also been performed and shows an intermediate agreement of 55%. Two types of SSTs reconstructions are available: prescribed on deep-sea cores data (CLIMAP Project Members, 1981), and computed with an atmosphere-mixed layer ocean model. These reconstructions provide respectively tropical SSTs on average $1^\circ C$ and $2^\circ C$ cooler than present-day. Computed SSTs reconstructions are thus closer to recent geochemical studies, which indicate that the tropical cooling during glaciation was of 4 to $5^\circ C$. The eight vegetation distributions simulated for the LGM have been compared with pollen data from Crowley (1995). The model shows a mean global agreement of 47% for the prescribed SST versions and 52 % for the computed ones. These results comfort us in the idea that computed SSTs are closer to the reality than prescribed ones.

The main characteristic of the LGM vegetation distribution as simulated by CARAIB is the extension of desertic and semi-desertic area at the detriment of forests and grasslands. Sensitivity analyses were performed to discriminate the relative effects of the atmospheric CO_2 level increase ("fertilization effect"), the climate variation, and the sea level drop since the LGM. Our results suggest that the CO_2 fertilization effect is mostly responsible for the total increase in NPP, vegetation and soil carbon stocks.

Present vegetation distribution

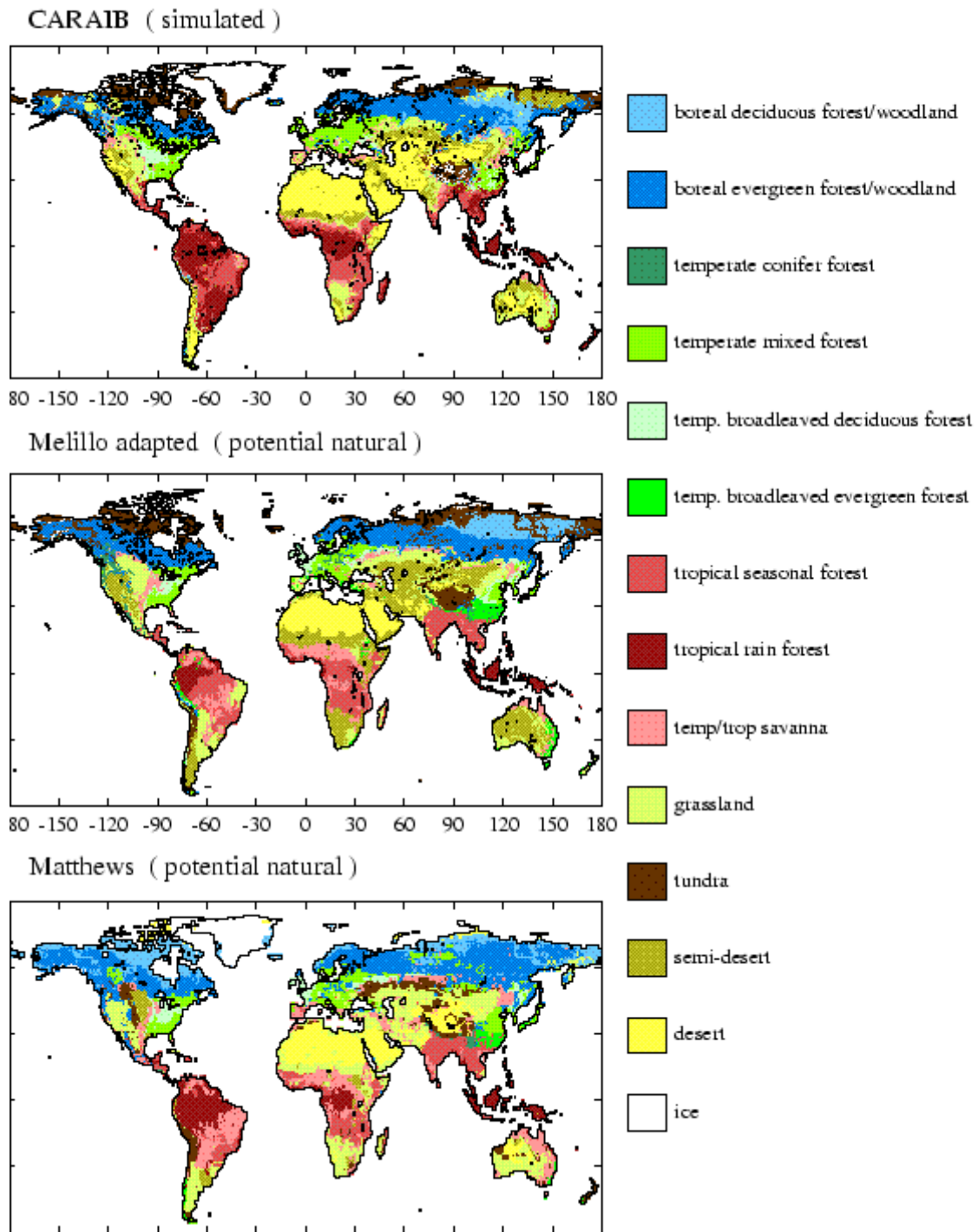


Figure 14.

2.5 Interannual variation of biosphere-atmosphere exchanges

The total increase of the atmospheric CO₂ level due to the use of fossil fuels shows year-to-year variations. This "anomaly" in CO₂ increase is, on the average, about 2 Gt C/year. The combination of measurement of the CO₂ concentration and ¹³C/¹²C isotopic ratio makes it possible to show that a significant part of this anomaly is due to some variation temporal of the CO₂ net exchange flux between the atmosphere and the biosphere. We used the CARAIB model in order to assess the importance relative of the gross productivity primary (GPP), autotrophic (AR) and heterotrophic respiration (HR) during the period 1980-1993. Moreover, our analysis also evaluated the contribution of the main ecosystems types to the total anomaly.

For this study, the new non-steady state version of the CARAIB model was used jointly with global measurements of temperature, precipitation and total insolation during the 14-year period. Our simulations are based on two independent meteorological data sets collected using different techniques [Christy et al., 1994; Jones, 1994; Hulme, 1994; Bishop et al., 1997]. Figure 15 shows the anomalies of the CO₂ flux to the atmosphere calculated by forcing the model while including:

- the change of temperature only (curve T1)
- the change of temperature and of pressure (TP1)
- the change of temperature, of pressure and insolation (TPS1)
- another time series of climatic variations (TP2)

The comparison with the values computed on the basis of Keeling et al.'s (1995) measurements shows a good agreement for the amplitude of the CO₂ biospheric fluxes as well as their time evolution. It also shows that temperature is the most significant forcing controlling the anomalies of the CO₂ flux from the biosphere. The model predicts the largest value of the flux anomaly to the atmosphere for El Nino years 1983 and 1987 corresponding to positive annual temperature anomalies. Conversely, the calculated assimilation by the biosphere is maximum in 1989, 1992 and 1993. The last two years are characterized by negative temperature anomalies, probably related to the global cooling due to the aerosols released by the Pinatubo eruption in June 1991.

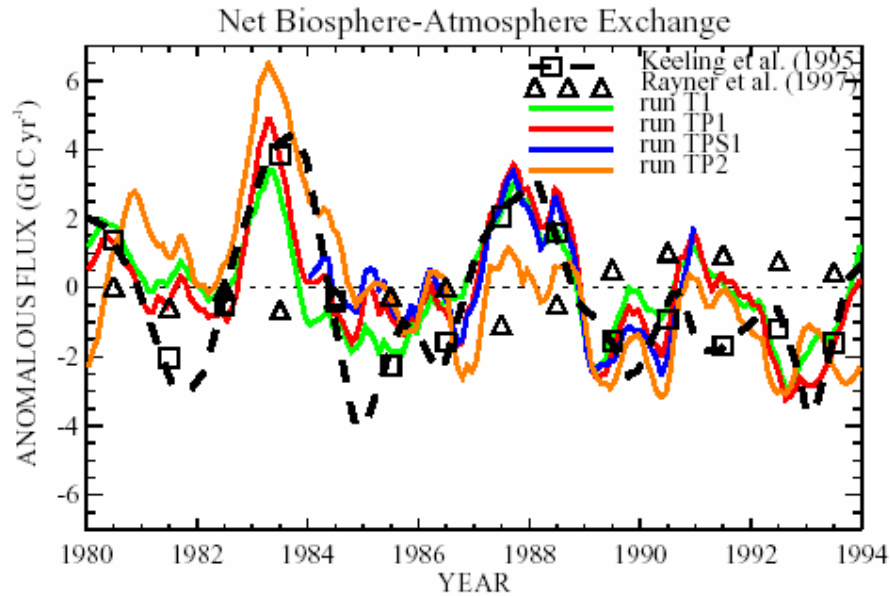


Figure 15: Calculated anomaly of the biospheric CO₂ flux to the atmosphere. Four cases are illustrated: T1 (temperature anomaly only), TP1 (T1 + precipitation anomaly), TPS1 (TP1+ solar irradiance anomaly) and TP2 (TP1 with alternative anomaly data sets). The result of the deconvolution by Keeling et al. [1995] and Rayner et al. [1997] are also shown for comparison.

An analysis of the contribution of the exchange flux of CO₂ by zone of latitude and ecosystem was carried out (figure 16). It indicates that the tropical zones make the dominant contribution to the CO₂ anomaly. Moreover, tropical rain forests and savannas play a dominant role both in the positive and negative contributions to the global CO₂ flux anomalies. Our results indicate that in savannas the interannual changes are, to a large extent, exerted by the control of the amount of available soil water on the gross primary productivity. In rain forest, the variations of the CO₂ exchange fluxes are due to changes in the GPP as well as in the respiration rate.

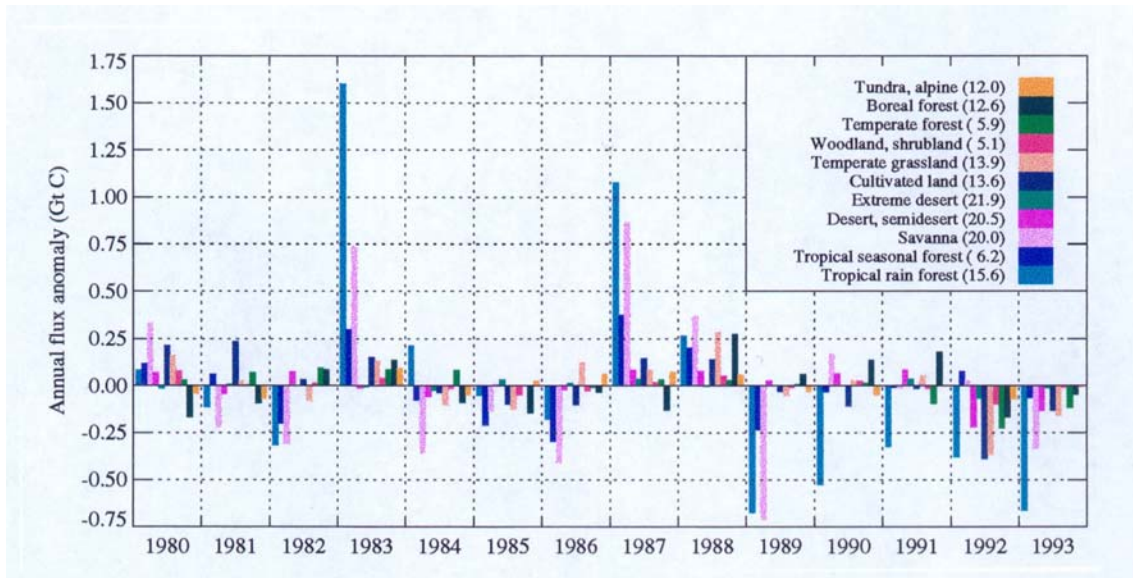


Figure 16: Contribution from various ecosystems to the interannual anomalies of CO₂ exchange between atmosphere and biosphere calculated with the CARAIB model (Gérard et al., in press). The numbers in parentheses in the inset indicate the area covered by each vegetation class in 10⁶ km².

2.6 Oceanic carbon and its evolution

2.6.1 Pre-industrial and LGM runs

The carbon model driven by MPI-OM fields was run for 4000 years, a duration sufficient to achieve a good equilibrium state as attested by net air-sea gas fluxes. Biogeochemical parameters were tuned so as to achieve an atmospheric partial pressure of CO₂ as close as possible to the pre-industrial value of 280 μatm while obtaining reasonable values for global fluxes and variables. Global results for this standard run compare favorably with experimental values (Table V). The amount of precipitated CaCO₃ in the model is lower than that from data but is within the given range for river inputs. As no net loss of matter occurs in the model the amount of carbon included in sediments must be exactly compensated for, while in the real ocean it seems that CaCO₃ preservation exceeds external inputs (Wollast, 1994). Vertical and horizontal distributions of state variables (Figures 17 and 18) illustrate the general agreement between data and model results. Shortcomings in the hydrodynamic fields might explain some of the discrepancies: e.g., the annual mean fields do not take into account the specific monsoon driven circulation in the Indian Ocean, the upwelling in the eastern equatorial Pacific Ocean seems to be overestimated. On the other hand, biological activity is modeled in a very simplified way, no account being taken of species distribution nor of processes within the sediments.

World ocean mean values

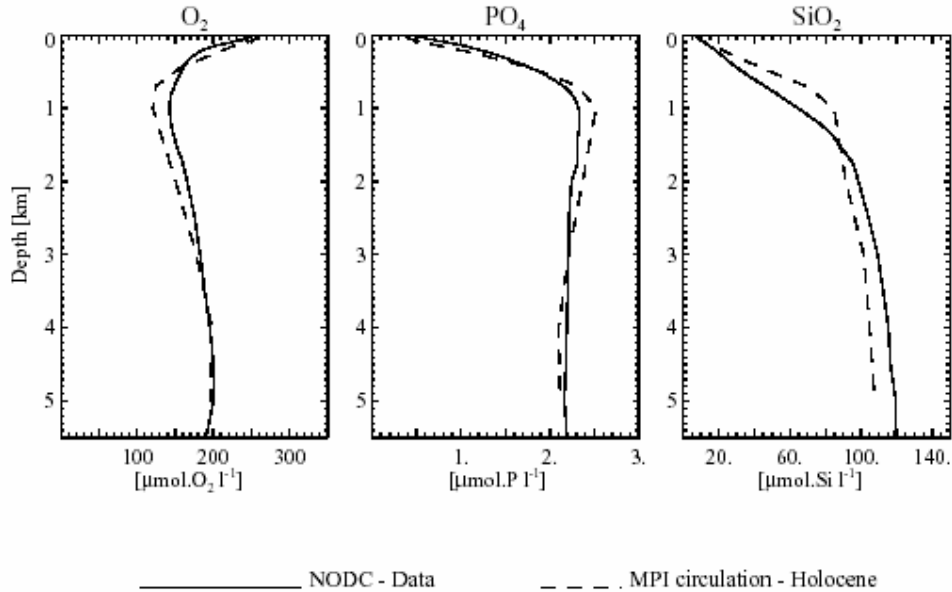


Figure 17: Global mean values of O_2 , PO_4 and SiO_2 obtained from the model standard run (dashed) and from data (solid).

The hydrodynamic fields for the LGM were obtained by running the Hamburg LSG-OGCM with the boundary conditions provided by CLIMAP SST and by surface salinities derived from planktonic foraminifera $\delta^{18}O$ (Winguth et al., 1996). This reconstructed circulation was tested against $\delta^{13}C$ in benthic foraminifera shells. The main differences with the Holocene fields are:

- a reduced southward transport of the North Atlantic Deep Water (10 Sv. instead of 20 Sv.);
- an enhanced circumpolar transport around Antarctica;
- a lower upwelling below the euphotic layer in the equatorial Pacific.

The results of three experiments are presented (Table V and Figure 19). In the first one (LMG_1) everything was kept to the same values as for the standard run. The resulting atmospheric CO_2 partial pressure is slightly higher than in the standard run case. The effect of salinity on concentrations and on solubility counterbalances the increase in solubility resulting from lower sea surface temperatures. The reasons for the higher export production are to be found in higher vertical upwelling rates in the Northern Pacific and the Equatorial Atlantic and Indian. A second element is the higher oceanic oxygen content leading to a faster recycling of the organic matter. Opal production increases accordingly.

Table V: Global mean values for fluxes and variables as from data, model standard run and three different experiments for the LGM. (1)Broecker and Peng, (1982); (2)Longhurst (1991); Shaffer(1993); (3)Tsunogai and Noriki (1991); (4)Wollast (1994); (5)Nelson et al. (1995).

	Pre-industrial		Last Glacial Maximum		
	Data	Model	LGM 1	LGM 2	LGM 3
CO ₂ ^{atm} (μatm)	280 ⁽¹⁾	280.7	284.2	204.1	202.5
Export Production (GtC yr ⁻¹)	5-12 ⁽²⁾	6.4	7.1	7.1	7.1
Rain ratio	0.133-0.286 ⁽³⁾	0.190	0.181	0.181	0.127
CaCO ₃ production (TmolCyr ⁻¹)	52-64 ⁽³⁾	88.7	96.7	96.7	62.5
Preserved CaCO ₃ (TmolCyr ⁻¹)	18-29 ⁽⁴⁾	14.4	10.9	47.5	27.7
River inputs (TmolCyr ⁻¹)	13-15 ⁽⁴⁾	14.4	10.9	47.5	27.7
SiO ₂ production (TmolSiyr ⁻¹)	100-140 ⁽⁵⁾	136.	154.	154.	154.
Preserved SiO ₂ (%)	3-11 ⁽⁵⁾	13.5	12.7	12.7	12.7

Spatial distribution of PO₄ corresponds well to estimates from deep sea sediment studies showing a smaller contrast between the deep Atlantic and Pacific Oceans during LGM (Yu et al., 1994) together with an increase in nutrient concentrations in the deep Atlantic (Sarnthein et al., 1994). In the second and the third experiments the total amount of carbon in the ocean-atmosphere system was slightly lowered while alkalinity was raised. The percentage of change was chosen so as to obtain an atmospheric pressure very close to the 200 μatm recorded for LGM while keeping other parameters as in the LGM_1 run. For the LGM_3 run a further modification was introduced by decreasing the temperature influence on the rain ratio. In figure 19 and in table V it can be seen that these modifications lead to a higher amount of preserved CaCO₃ and to a smaller surface-to-deep alkalinity gradient. Results of experiment LGM_3 as shown in figure 19 are consistent with the analysis of Howard and Prell (1994) and their observation of a lower accumulation rate of CaCO₃ in Southern Ocean sediments. Zonal air-sea fluxes (not illustrated) show that during the LGM the North Atlantic and the Equatorial Pacific were respectively a stronger sink and a smaller source for atmospheric CO₂. While the result for the North Atlantic agrees with other studies (Maslin et al., 1996), it had been concluded that net sea to air CO₂ fluxes in the Equatorial Pacific were much stronger at LGM than present day values (Sanyal et al., 1997).

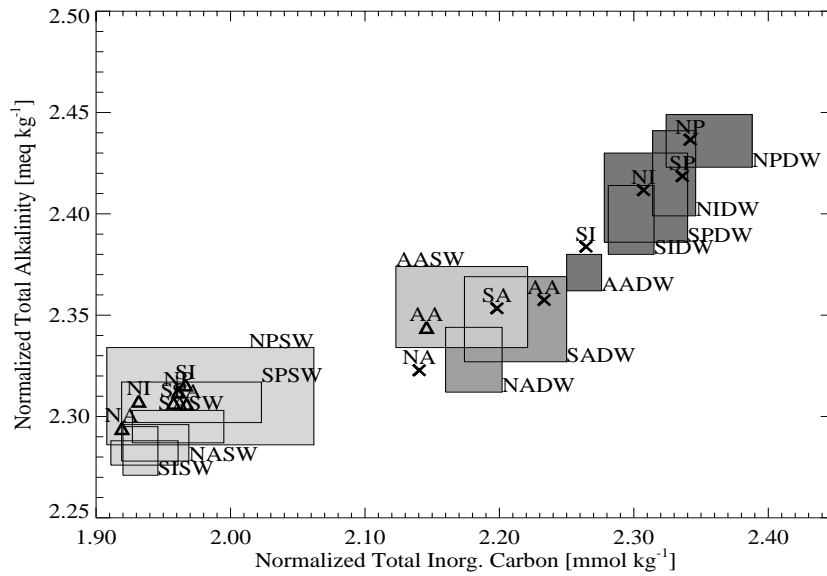


Figure 18: Values of normalized carbon and alkalinity averaged for the different ocean basins (AA=Antarctica, NA and SA = North and South Atlantic, NP and SP = North and South Pacific, NI and SI = North and South Indian). Standard run results are represented by triangles for surface waters and by crosses for deep waters. Data from GEOSECS with their standard deviation are represented by shaded areas. SW and DW stand for surface and deep waters respectively.

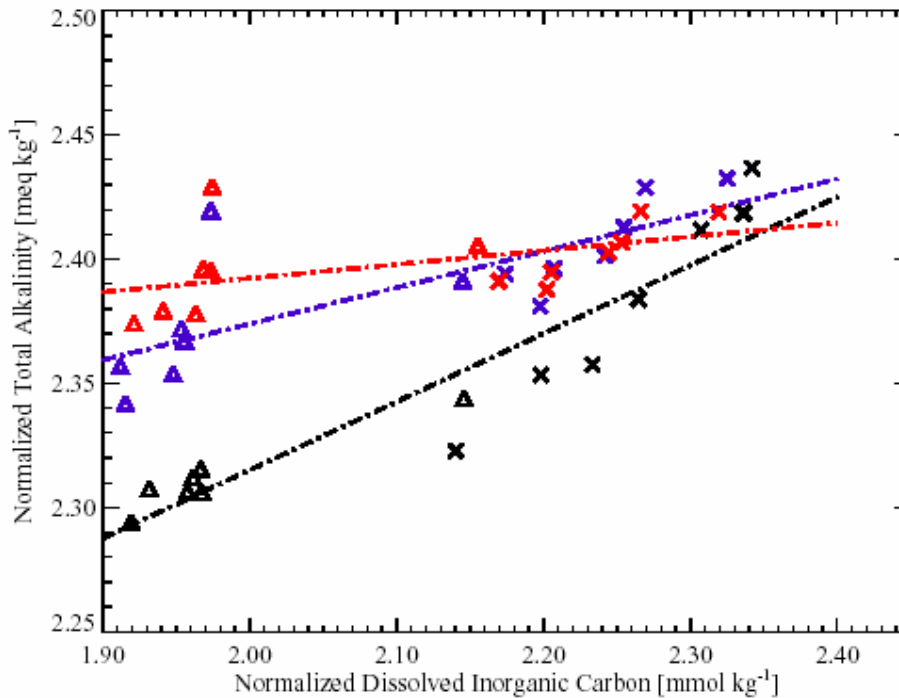


Figure 19: Same as previous, this time for LGM experiments (black symbols and line are for LGM_1, blue for LGM_2 and red ones for LGM_3). Dash-dotted lines result from a linear fit through each result sets and are used for illustrative purpose. As in the previous figure triangles and crosses represent basin averages of surface and deep values respectively.

2.6.2 *Advection scheme and biogeochemical tracers*

Different numerical schemes, through differences in implicit diffusion, may result in differing ventilation rates. For the sake of consistency the transport equation in LOCH should be discretized in exactly the same way as in the 3D OGCM. However expected properties of a transport model include conservation and positivity (a weaker constraint than monotonicity) together with reasonable computing time. As these properties were not readily met by the original numerical schemes in LLN-OM, the numerics differ somehow in LOCH. The way of representing convection in the off-line model by a diffusion term differs also from the on-line practice of water exchanges between the different cells of a water column as applied in MPI-OM. Due to the different time steps used in both cases it was not possible to adopt the same method in the off-line model.

Simple tracer distributions (water age, passive tracer, *quick- $\Delta^{14}\text{C}$*) were then computed in order to assess the effect of changes in the numerical schemes (time step, convective and advective schemes, no variability in the off-line driving fields).

In the case of MPI-OM, no significant differences appeared between the distributions of simple tracers obtained on-line or off-line.

In LLN-OM the advection is performed with a centred scheme along the vertical while a low-diffusion hybrid scheme is used along the horizontal. These schemes, hereafter referred to as LD scheme, are non positive and when used for transporting fields that can naturally reach depletion, such as O_2 and PO_4 , very quickly produce negative values leading to inconsistency in the model. On the one hand, restoring to zero in case of negative values artificially adds matter to the system, and on the other hand, the corrections to be applied may be of the same order of magnitude as seasonal changes in phosphate fields.

For modelling the full carbon cycle it was decided at first to replace the LD-scheme by a first order upwind scheme (U) for transporting BGC state variables. All our tests lead to the conclusion that the chosen vertical advection scheme is of critical importance. Indeed, changes in the predicted fields when switching from the LD to the U scheme are quite completely explained by the sole modification in the vertical advection scheme. The influence of the horizontal advection scheme is much smaller while differences in time steps (1 day in LLN-OM, 7 days in LOCH) and in the convection parameterization have negligible effects.

To reduce departures from the original scheme, a correction is then applied to the U scheme, i.e. reducing the explicit diffusion coefficient when feasible by the amount of implicit numerical diffusion which is easily computed from the velocity field. This latter

scheme (named RU) is the one used in LOCH with the LLN-OM fields for all carbon cycle-related runs.

The conclusions derived from simple tracers simulations revealed their general significance in the study of O₂ ventilation of the deep ocean, a critical aspect for the fate of organic carbon in the ocean. The model was run twice with the same biology but with a different advection scheme: the U scheme in one case, the RU one in the other. The PO₄ field was imposed and the same in both cases, so that the primary production and, as a consequence, the organic matter production rate were identical in the two experiments. Any change in the oxygen distribution may then be attributed to a change in ventilation and not to a reorganisation of the PO₄ field.

Higher O₂ concentrations are obtained in the deep ocean with the RU scheme than with the U scheme, while intermediate waters are more depleted with the former scheme (Figure 20). The numerical dispersion, k^{num} , of the upwind schemes increases as the modulus of the velocity (Hirsch, 1988). A detailed analysis of the amplitude of k^{num} shows that while for horizontal velocities the extreme values of k^{num} are restricted to the upper 200m, maximum values of k^{num} associated to the vertical transport occur on a larger depth range (from 150 to 2000m). In the U-scheme experiment the larger vertical diffusivity more efficiently distributes the O₂ depletion associated with the remineralization of organic matter under very productive areas. This is why the deep ocean is less O₂ depleted in the RU case.

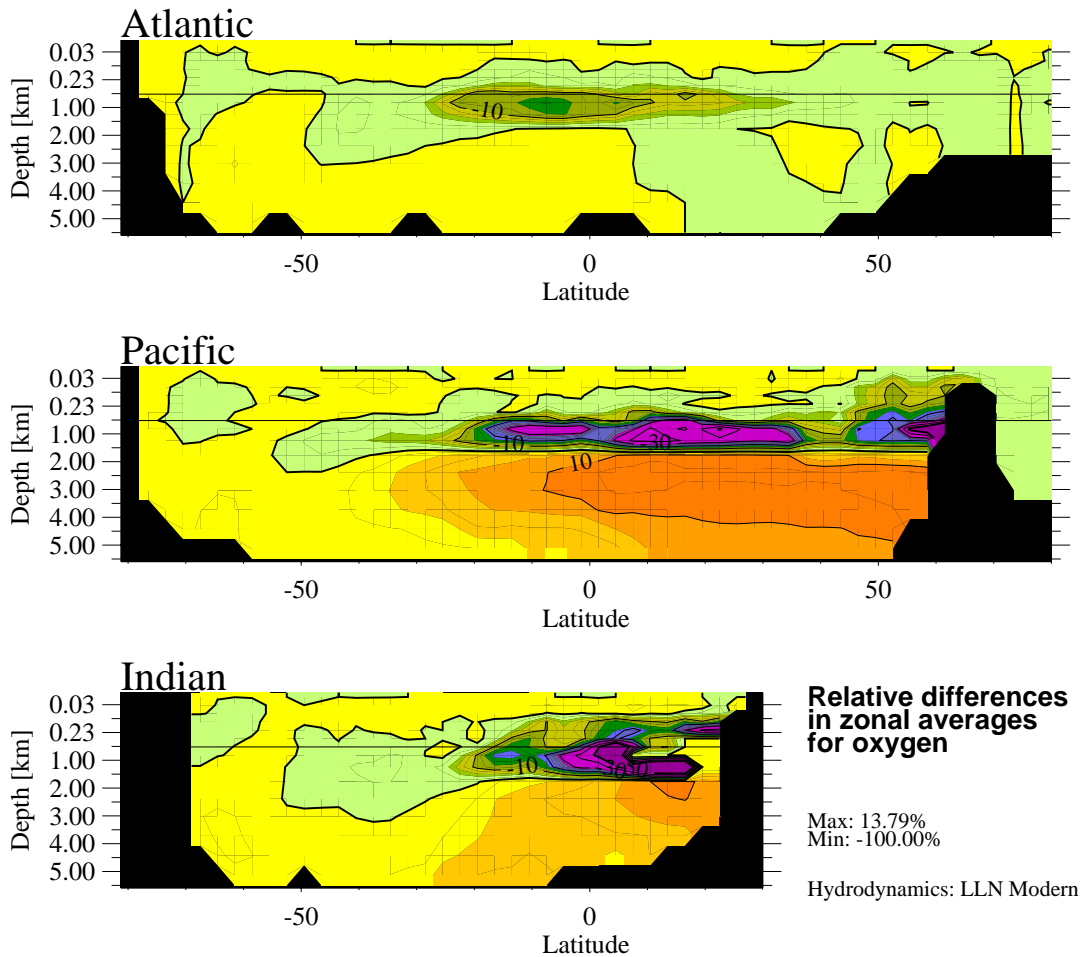


Figure 20: Relative differences in zonal averages of O_2 concentrations obtained with the RU and U advection schemes. Positive values correspond to higher ventilation by the RU scheme. The U scheme leads to increased concentrations in intermediate waters. The maximum value in deep North Pacific corresponds to an increase of $22.3 \mu\text{mol.l}^{-1}$ for a background value of $162 \mu\text{mol.l}^{-1}$. In intermediate waters depletion can reach up to $20 \mu\text{mol.l}^{-1}$ with respect to mean values of the order of $40 \mu\text{mol.l}^{-1}$.

2.6.3 Industrial era and radiocarbon

The present day atmospheric abundance of radiocarbon results from natural (cosmic rays interaction with ^{14}N , ocean overturning rates) and anthropogenic processes (Suess effect, nuclear bomb testing). The different timescales of these processes make of radiocarbon a useful tool for testing OGCMs and OCCMs (Duffy and Caldeira, 1995; Jain et al., 1995; Joos et al., 1997; Toggweiler et al., 1989a,b).

Model estimates of the oceanic bomb ^{14}C uptake in 1990 encompass a wide range, from 286 to $486 \cdot 10^{26}$ atoms (Joos, 1994; Duffy and Caldeira, 1995; Joos and Bruno,

1998). Among the documented causes of discrepancies are differences in gas exchange coefficient (Joos et al., 1997; Joos and Bruno, 1998), surface salinity boundary conditions in the Southern Ocean (Toggweiler and Samuels, 1993), numerical scheme used in the OGCMs and OCCMs (Bryan, 1987; Duffy et al., 1997). The latter two causes affect directly the distribution and renewal rates of oceanic water masses. An additional reason for the wide range in the predicted uptake may lie in the method adopted for computing the ocean ^{14}C concentrations. Several of the previous model studies adopted a simplified formulation to describe the transport of radiocarbon in the ocean (Toggweiler et al., 1989a,b; Duffy and Caldeira, 1995; Stocker et al., 1994; Maier-Reimer et al., 1993). As will be shown below, this way of doing significantly affects the air-sea exchange rate of radiocarbon.

We studied the sensitivity of the stationary and transient distributions of ^{14}C towards the forcing function or air-sea fluxes and the deep ocean ventilation rate by driving LOCH with the two circulation fields (LLN-OM and MPI-OM). The natural and bomb radiocarbon distributions in the ocean are then calculated for both circulations by two different methods, one in which all three carbon isotopes are transported and the simplified method in which $\Delta^{14}\text{C}$ is the state variable.

2.6.3.1 Method

The radiocarbon content of a sample is expressed with the following quantities $^{14}\text{R}_x = ^{14}\text{C}_x / \text{C}_x$ and $\Delta^{14}\text{C}_x = (^{14}\text{R}_x / ^{14}\text{R}_{\text{OXA}} (0.9751 + \delta^{13}\text{C}_x)^2 - 1) \cdot 10^3$ where C_x is the total carbon content in x , $\delta^{13}\text{C}_x$ a measure of the $^{13}\text{C} / ^{12}\text{C}$ ratio in x and $^{14}\text{R}_{\text{OXA}}$ the oxalic acid standard (Stuiver and Pollach, 1977; Keeling, 1981). The $\Delta^{14}\text{C}_x$ value represents the ratio that would have been observed if isotopic fractionation did not occur.

In what follows the contributions from biological activity to the volume sources will be neglected. This elimination produces an error that is globally negligible (Stuiver et al., 1981; Bacastow and Maier-Reimer, 1990; Joos et al., 1997). Biotic transport significantly contributes to the ^{14}C content of the deep Pacific Ocean (Craig, 1969) with an effect on $\Delta^{14}\text{C}$ less than 10% (Stuiver et al., 1981).

Combining the transport equations for the individual species, one obtains the equation governing the ratio, $^{14}\text{R}_{\text{Ct}}$, for the total dissolved inorganic carbon, C_t , in the ocean,

$$\frac{\partial}{\partial t} ^{14}\text{R}_{\text{Ct}} + \text{H}(^{14}\text{R}_{\text{Ct}}) = \frac{2}{\text{C}_t} \nabla \text{C}_t \cdot \mathbf{K} \cdot \nabla ^{14}\text{R}_{\text{Ct}} - \lambda ^{14}\text{R}_{\text{Ct}} + (^{14}\alpha_{\text{aw}} ^{14}\text{R}_{\text{a}} - ^{14}\text{R}_{\text{Ct}}) \frac{F_{\text{a}}^{\text{aw}}}{\Delta z \text{C}_t} + (^{14}\alpha_{\text{wa}} - 1) ^{14}\text{R}_{\text{Ct}} \frac{F_{\text{Ct}}^{\text{wa}}}{\Delta z \text{C}_t}$$

with H and K, the hydrodynamic operators previously defined, $^{14}\lambda$ the rate of radioactive decay, $^{14}R_a$ the radiocarbon ratio in atmospheric CO₂, $F_{C_t}^{aw}$ and $F_{C_t}^{wa}$ the gross CO₂ fluxes between air and sea, $^{14}\alpha_{aw}$ and $^{14}\alpha_{wa}$ kinetic and equilibrium isotopic fractionation factors in both directions, and Δz the mixed layer depth [m].

The first term on the right hand side of this last equation is generated by mixing processes and has no equivalent in the equation governing concentrations. Ordinary numerical schemes are not fit for solving it, and a full treatment of the problem, that is the determination of oceanic $\Delta^{14}C_t$, demands that the three individual equations be solved, that is one for C_t and each of its isotopes. Several model studies adopted a simplified version of that equation in which the ratio $\Delta^{14}C_t$ is transported rather than the individual species. This version demands that the mixed product in the former equation vanishes, that is that the C_t field be stationary and homogeneous (Toggweiler et al., 1989a). The further hypothesis that no fractionation occurs, that is $^{14}\alpha_x=1$, results in the simplified form,

$$\frac{\partial}{\partial t} \Delta^{14}C_t + H(\Delta^{14}C_t) = -^{14}\lambda \Delta^{14}C_t + (\Delta^{14}C_a - \Delta^{14}C_t) \frac{F_{C_t}^{aw}}{\Delta z C_t}$$

In this method \bar{C}_t is determined from the average surface DIC distribution and remains constant over time and space as does the gross air-to-sea flux $F_{C_t}^{aw}$. This is equivalent to the assumption of local rather than global air-sea equilibrium for CO₂.

We used both methods to estimate the natural and anthropogenic distributions in the ocean. The method in which the ratio is transported will be referred to as *quick* method while the use of *full* means that transport equations for each of the three carbon species were solved.

2.6.3.2 Experiments

Atmospheric isotopic ratios and partial pressure need to be specified. For equilibrium experiment that will serve afterward as initial conditions to the transient ones we proceeded as follows. The atmospheric $\Delta^{14}C$ is forced to be zero, while atmospheric carbon dioxide and its $\delta^{13}C$ are left free to evolve. The total amount of carbon in the coupled atmosphere-ocean system is adjusted so as to obtain a p_{CO_2} close to the 278 ppmv pre-industrial value. That value was used in the quick method for the evaluation of $F_{C_t}^{aw}$.

For runs over the industrial period the atmospheric concentrations of carbon dioxide and of its two isotopes are imposed. In this purpose we need reconstructed series

of these quantities from 1765 to present. While such series are available for CO_2 and $\Delta^{14}\text{C}$ (Enting et al., 1994) nothing similar exists for $\delta^{13}\text{C}$. We then reconstructed the temporal evolution of atmospheric $\delta^{13}\text{C}$ by using all the available data sets that included measurements of atmospheric CO_2 and $\delta^{13}\text{C}$ performed at the same time and location.

Gas exchange coefficients depend only weakly on the temperature as the effect of solubility decrease with temperature is nearly compensated for by the Schmidt number increase (Bard, 1988; Wanninkhof, 1992). The use of the same wind and ice cover fields for both models hence guarantees that gas air-sea exchange will be as similar as possible in both case and that the results should only be interpreted in terms of water masses exchange rates.

2.6.3.3 Results

Several experiments were performed in which various aspects were tested. The lowest uptake of radiocarbon was observed when using the *quick* method (about $310 \cdot 10^{26}$ at. ^{14}C) while the highest resulted from the *full* method (on average $430 \cdot 10^{26}$ at. ^{14}C). The effects of fractionation and of the reconstructed atmospheric $\delta^{13}\text{C}$ were also assessed. The influence of such factors is nearly negligible (variations of the order of $5 \cdot 10^{26}$ at. ^{14}C in inventories). A last set of experiments consisted in questioning the role of the increasing atmospheric CO_2 pressure in the actual value of radiocarbon inventories. All these tests lead to the conclusion that while the global mean oceanic $\Delta^{14}\text{C}$ does not change much from one experiment to the other (4 to 6 permil) the uptake of radiocarbon is strongly sensitive to the method adopted and so is the spatial distribution of $\Delta^{14}\text{C}$ (difference of several permil in basin averages). The reason for such dramatic changes in inventories among methods lies in the magnitude and distribution of radiocarbon net air-to-sea fluxes (see Fig. 2.21). The larger atmospheric inputs occur at high latitudes where intense downwelling exists. On the contrary near the equator, where the oldest surface waters are found, air-to-sea fluxes are weaker. The full formulation is the one with the largest input rate in the downwelling areas, as it fully includes the local disequilibrium between the CO_2 partial pressure in the atmosphere and in the ocean. In these experiments no biology intervenes. While the influence of the ocean biosphere is expected to be low on the actual $\Delta^{14}\text{C}$ values, its role is far from negligible in determining the distribution of air-to-sea CO_2 partial pressure differences. In a near future this aspect will carefully be examined.

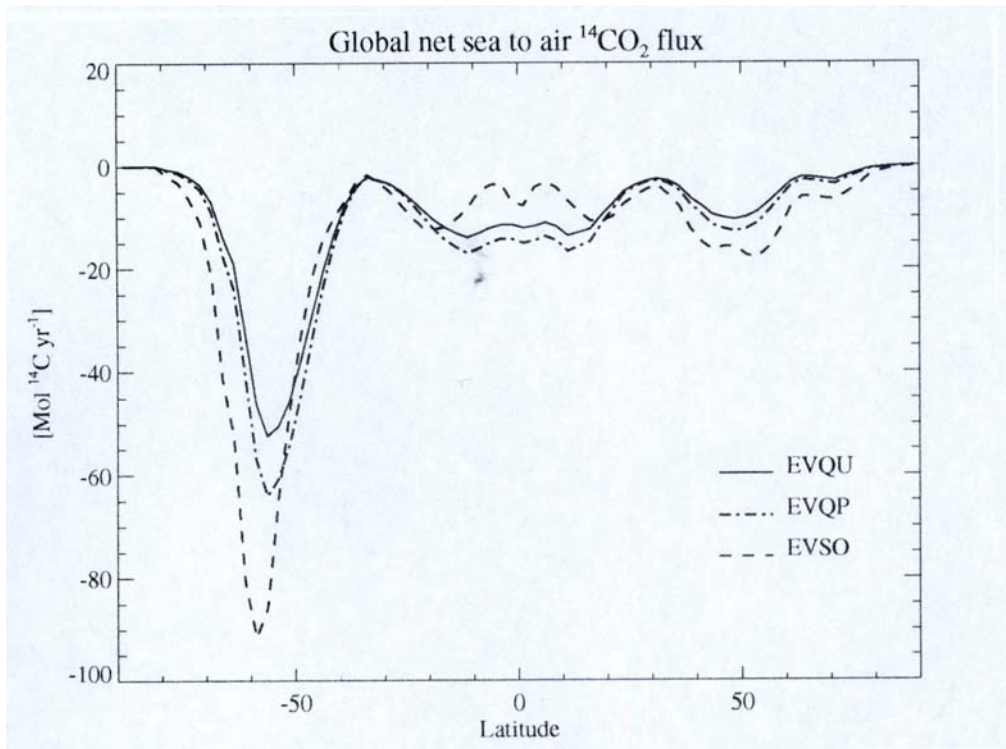


Figure 21: Zonal averages of net air-to-sea fluxes in the last year of the transient experiments (1990). Values for the full and quick methods correspond respectively to the dashed and solid lines. A third experiment with the quick formulation but in which the atmospheric CO_2 partial pressure was allowed to evolve is illustrated by the dot-dashed line. The surface chemistry of CO_2 explains the fluxes differences among methods.

Atmospheric CO_2 net uptake in the last year of experiment (1990) is 2.4GtC for LLN-OM and 2.1GtC for MPI-OM. Also the bomb radiocarbon inventory in 1990 with MPI-OM always lags behind that of LLN-OM; for the full method experiment the inventories are respectively of 425×10^{26} at. ^{14}C .

On the other hand, mean values of $\Delta^{14}\text{C}$ with LLN-OM are much smaller than with MPI-OM, especially in the deep North Pacific where the waters in LLN-OM are about 500 yr older than in MPI-OM. This ageing of waters originates in the much slower renewal rate of deep Pacific waters from the Antarctic area. In the Atlantic ocean both fields behave very similarly.

The uptake of bomb radiocarbon is very sensitive to the method adopted for computing air-sea exchange and to a lower extent to the circulation. Indeed, driving the model with another OGCM produces a change in inventory of at most 23×10^{26} at. ^{14}C while switching from the *quick* to the *full* method produces an increase of 137×10^{26} at. ^{14}C . This shows the strong sensitivity of the equilibration time of isotopic ratio to the gas exchange formulation.

2.7 Future trends

2.7.1 *Doubling the atmospheric CO₂ concentration*

Simulations have been performed with an atmosphere containing two times more CO₂ than the present value. In this case a value of 660 ppmv of CO₂ is chosen to correspond to the climatic simulations that are available to us (runs of the GCMII model of the CCMA).

In a first time, we test the influence of a doubling of the atmospheric CO₂ concentration alone. Since CO₂ is the first nutrient for vegetation, an increase of it conduct to an enhancement of the photosynthetic assimilation. The global gross primary productivity (GPP) increases of about 56 % while the global NPP increases even more drastically (67 %). The increase of productivity is particularly important in less productive ecotypes (98 % for GPP in tundras, 116 % in semi-deserts and 126 % in extreme deserts). In productive biomes, the relative increase is lower (for example, the GPP of the tropical rain forest increases of 38 %). In this extreme case, the biosphere already absorbs the main fraction of the photosynthetic active radiation (PAR) and the excess CO₂ is less easily absorbed since no light energy is available. This increase of the productivity due to an increase of available carbon for photosynthesis is classically called: CO₂ fertilization effect. It has clearly be demonstrated that this type of effect exist at very short term. A long term exposure to high CO₂ concentration can however have less effect due to some other limitations or to plant adaptation. The extent of such an effect probably depend on plant type and external conditions but it existence itself is still under debate when long term exposure to high CO₂ is concerned. In every case, the amplitude of this effect is certainly over estimated in the run presented here.

A second simulation has thus been performed with high (doubled) CO₂ concentration and climate changes. Available data gives mean monthly temperature and precipitation from a 20 years run of an atmospheric GCM (GCMII of the CCCMA). It gives a mean increase of the temperature of about 4°C over continental areas with very little changes of the annual mean temperature in equatorial regions and up to 6 (or more) increase of it mostly at high continental latitudes. Precipitation anomalies are more complex to analyze with positive changes compensating more or less negative ones (global anomaly of only 3%). The effect of climate on continental biosphere is principally a decrease of the CO₂ fertilization effect. In fact an increase of temperature produces an increase of the evapotranspiration and thus an enhancement of the water stresses. The reverse effect exists however. In high latitude regions the increase of the temperature induces a lenghtening of the growing season and thus an higher productivity for example in tundras. On another hand, some very hot regions receive more precipitation. Since in those cases water

availability is the more important limitation to plant growth, climate changes can enhance the simple CO₂ fertilization.

These two simulation experiences lead to two major conclusions:

- CARAIB certainly overestimates the CO₂ fertilization effect.
- Coupling CARAIB and IBM (water module) will certainly lead to a better estimation of carbon fluxes by our model. In the same way, the inclusion of a nutriment (Nitrogen in particular) module would certainly improve the present results.

Finally a general remark can be made on this type of experiences. These runs assume the steady state between vegetation and the atmosphere. A doubling of the atmospheric CO₂ level due to man impact will likely be reached during the next century. With this celerity of the carbon content growth, vegetation will certainly not have the possibility to adapt rapidly enough. Some regions may become desert if plants are not replaced by new species adapted to the new climate conditions. Moreover, tree biomass and even more soil carbon will take decades or centuries to reach an equilibrium due to their long characteristic times.

2.7.2 The industrial era

The previous paragraph shows that CARAIB is able to reproduce transient simulation over relatively short periods (one or two decades) and that it can be used to analyze the variations of the biosphere behavior in those cases. Now we test the performance of CARAIB over a longer period. Transient runs are performed over 200 years beginning in 1800 and ending in 1994. The initialization estimate assume an atmospheric CO₂ concentration of 280 ppmv and the run is performed until an equilibrium is reached (a new year simulation gives the same results as the previous one).

In a first case, climate is kept constant and classical climatic fields are used (Leemans and Cramer,...). Atmospheric CO₂ concentration increases progressively according to measured values and reaches a value of 350 ppmv in the early 90ies. As described before, CARAIB shows an important CO₂ fertilization effect. This leads to a huge sink of carbon in the biosphere. In fact, if the biosphere was able to assimilate carbon as it makes in this simulation, the atmospheric CO₂ level would not have change since the vegetation pump all the carbon released by man activities. This experience teaches us two things:

At the present rate, the atmospheric CO₂ increases slow enough to allow an equilibrium of the plant productivities. In fact, as productivities are concerned, results

stay the same for a transient run or a steady state run if the atmospheric CO₂ concentration is the same. It has to be noted however that in this version CARAIB do not include biome migration. Even if this process will certainly be more critical in the future than in the previous 2 centuries it may have some importance.

As expected, in this transient run soil carbon reservoir has not the time to equilibrate with the rest of the system. The present day value of this pool is no more realistically comparable with other estimates. One parameter of the model (the fraction of the respiration coming from the soil due to root and not to soil carbon) has to be tuned to give again realistic soil carbon content. The new value (0.4) of this parameter seems more appropriate than the previous one. However we can ask ourselves about the validity of steady state runs and their results concerning soil carbon.

In a second step, temperature variations are taken into account. There is some lack in those climatic data sets and an interpolation from the nearest neighbour is performed to get complete monthly fields. For year before 1950, the number of missing data is too big and only the global mean temperature anomaly is added to present climate data. Finally before 1854, the temperature is kept constant.

Compared to the previous run the biospheric carbon sink is more or less divided by a factor of two. It is however even two times too great. Once again the coupling with the water module would certainly improve the CARAIB results.

3. REMOTE SENSING OF BIOSPHERIC PROCESSES

Vito's contribution to this project mainly comprises two tasks. First, by classifying low-resolution satellite images global land-cover maps will be produced which can serve as input for the CARAIB-model. And second, the CARAIB-model will be validated, by comparing its *f*APAR-predictions (fraction of Absorbed Photosynthetically Active Radiation) with the *f*APAR-values derived from the satellite data.

Optical low-resolution imaging sensors ($\pm 1\text{km}^2$) with spectral bands in the RED and Near-Infrared (NIR) spectrum prove to be very useful for the study of vegetation dynamics in the spatial and temporal domain. Especially the well-known Normalized Difference Vegetation Index (NDVI), which combines the information of the RED and NIR reflectance bands, is strongly correlated with the photosynthetic activity of green plants (Sellers, 1985).

Initially, it was planned to use images of the POLDER-sensor on-board of the ADEOS-satellite. This 12-band optical sensor had a coarse resolution of $6\times 7\text{ km}^2$ but its innovative scanning technique allowed to investigate the bidirectional reflectance behaviour of the natural targets. Unfortunately, the ADEOS-system was lost in space shortly after launch (exactly on June 30, 1997), so an alternative solution had to be found.

During the 1980's, pioneering research was conducted to explore the potentials of mapping and monitoring vegetation on subcontinental and continental scales, primarily with data acquired by the U.S. National Oceanographic and Atmospheric Administration's (NOAA) meteorological satellites, equipped with the Advanced Very High Resolution Radiometer (AVHRR). The systematic monitoring of the earth surface with NOAA-AVHRR started in 1979, and resulted in the largest stockpile of historical geo- and biophysical information on the earth's vegetation cover. Unfortunately, the imagery was not stored in one central archive, because everybody can capture AVHRR-data with the appropriate antenna. This has resulted in hundreds of small archives with data of local coverage and heterogeneous quality. Such images serve a good purpose for regional and continental vegetation studies but fail for global research. However, some institutes like the USGS-EROS Data Centre (United States Geological Survey, Earth Resources Observation System) did – and still do – a tremendous effort in centralising all AVHRR-imagery and creating a historical, global archive. These global, long time image series are especially useful in the discussion on Global Change, because they allow a detailed follow-up of the world's vegetation cover during the last two decades, the period with the heaviest human pressure on the natural environment in history.

Recently, with the launch of the VEGETATION instrument (VGT) on-board SPOT4 in 1998, a new source of constant and high quality optical remote sensing data came into being. Since these data are produced on an operational basis and centrally archived, interesting perspectives and new opportunities for global scale environmental monitoring at the 1km spatial level were opened. Moreover, the VGT-data are quite comparable and compatible with the imagery of AVHRR: both systems have identical spatial and temporal resolution (daily global coverage, 1km² pixel size), and they both share the most important spectral bands (RED and NIR).

This chapter contains four major topics. The first section explains how raw images of NOAA-AVHRR and SPOT-VGT are processed to obtain more manageable, synthetic and global information. In this context it also presents the 1km²-resolution image sets which were used in practice. Section 3.2 discusses the production of the land cover maps, to be used as input for CARAIB. Section 3.3 then continues with the extraction of the fAPAR information and the comparison of these image-derived values with the ones predicted by the model. At the end, section 3.4 describes some additional or parallel studies, which were also executed in the course of the project.

We finally want to remark, that it would be impossible to present all the results obtained in the course of this 4-years project within the limits of this document. Therefore, the focus will be placed here on the most recent analysis of the Pathfinder-data (see § 3.1.2.2). For the other results, mainly related to the data sets of USGS-EROS and SPOT-VGT, the reader is referred to previous reports and publications.

Processing chains & image data (AVHRR, VGT)

This section presents the AVHRR and VGT image sets which were used in this study. At the same time it also describes the processing steps needed to upgrade the raw data into high quality image products, which then can be used as inputs for the “real” processing – such as the qualitative and quantitative image analyses, described in the later sections.

We first give a brief overview of the main characteristics of (and similarities between) both earth observation systems. The NOAA-AVHRR instrument was described in depth by Cracknell (1997), while more information on SPOT-VGT can be found on the URL <http://www.vgt.vito.be>.

Orbit: Both platforms (NOAA and SPOT) follow a quasi-circular, near-polar and heliosynchronous orbit at a height of ±850km, with an inclination of ±99°. Every day both satellites circle 14.1 times around the globe. However, the true local time of

passage over Belgium is 13h30' for NOAA (NOAA11 and -14), but 10h45' for SPOT4. From a statistical point of view the morning passage of SPOT results in more cloud-free images.

Spatial characteristics: Both sensors have a nominal resolution of ± 1.1 km and a very broad swath width of about 2500 km, which enables a global coverage once a day (at higher latitudes the registration frequency is even higher). In the along track direction the image is formed by the movement of the satellite, while in the across track direction both sensors use a different scanning method. The AVHRR-sensor uses a rotating mirror which reflects the incident radiation on one single detector (per band). Due to perspective effects, the actual pixel size rapidly increases with scan angle, especially near the scene edges. These deformations are largely avoided by the VGT-sensor which makes use of the "push-broom" principle: this is a linear array (one per band) of ± 2000 detectors, which simultaneously register one entire scanline.

Spectral characteristics: The spectral bands of AVHRR and VGT are listed in table VI. Both sensors contain the most important RED and NIR bands. The VGT-instrument permanently monitors the calibration (i.e. the band-specific conversion of raw voltages to radiances) by means of an on-board calibration lamp. Unfortunately, this is not the case for the optical bands (RED, NIR) of the AVHRR-sensor. Here, the calibration can only be based on less reliable equations, which are experimentally derived from the image data over certain reference surfaces (water, deserts,...). This method of course results in a less accurate calibration.

Data transmission and distribution: The RAM of the VGT-system is sufficiently large to store the data captured during one entire orbit. When the satellite passes over Sweden all these data are transmitted to the (one and only) receiving station in Kiruna. The data are then sent to the "Centre de Traitement des Images VEGETATION" (CTIV) in Mol, Belgium, where they are pre-processed (with standard procedures), archived and distributed to the user community. The story of AVHRR is completely different. With the right antenna everyone can freely download AVHRR data. But, since on-board memory is limited (at least for the 1 km²-data), the captured imagery is restricted to the areas surrounding the antenna. The compilation of global AVHRR-sets thus requires close co-operation between several receiving stations, spread over the world. This explains the existence of many different AVHRR data sets and pre-processing chains.

As outlined in figure 22, the entire processing chain comprises three well-separated steps:

The **pre-processing** applies a number of geometric, radiometric and atmospheric corrections on each individual track or segment (raw data).

The **compositing** step then assembles and mosaics a number of individual, pre-processed tracks in the temporal and spatial domain to form global and periodic (mostly 10-daily) synthesis images. The image data used in this project were mostly of this type.

Finally, some **further enhancements** are required, primarily the elimination and re-interpolation of noisy measurements (mostly due to clouds), and the extraction of new images with more informative, phenological variables. These operations are realized on a per-pixel base through a longitudinal or time-series analysis, and as such they already give rise to a very significant data reduction. In § 3.1. C. c), we also describe an alternative and more efficient way, where the data are first submitted to a transversal reduction.

These three steps will be described in more detail in the following paragraphs.

Table VI: Spectral bands of NOAA-AVHRR and SPOT-VGT
(NIR, SWIR, MIR and TIR = Near, ShortWave, Mid and Thermal InfraRed)

NOAA-AVHRR			SPOT-VGT		
N	Band	Range [μm]	N	Band	Range [μm]
1	RED	0.58 – 0.68	1	BLUE	0.43 – 0.47
2	NIR	0.73 – 1.10	2	RED	0.61 – 0.68
3	MIR	3.55 – 3.93	3	NIR	0.78 – 0.89
4	TIR1	10.3 – 11.3	4	SWIR	1.58 – 1.75
5	TIR2	11.5 – 12.5			

3.1.1 Pre-Processing

3.1.1.1 NOAA-AVHRR

AVHRR-receiving stations distribute raw data in the form of Level1B-files (exact format specifications are provided by Kidwell, 1997). The pre-processing chain developed in the course of this project, is a menu-driven system which upgrades a raw Level1B-registration into a fully corrected product. The general flowchart of the chain is outlined in figure 23, while the subsequent operations are detailed below (same numbers as in the figure):

The Level1B-file (10-bit pixel-interleaved format) is thoroughly tested and unpacked into five 16-bit spectral images. All ancillary information is stored in a separate binary file, i.e. the scan-times, calibration data, and the geo-locations (longitude λ , latitude β) of a subset of pixels, as estimated with an elementary orbital model.

The relation between the geographical system (λ , β) and the raw image system (column, record) is quantified by application of a polynomial regression on the subsample of pixels with known geo-location. By means of this relation, one can quickly register existing vector-files with main landmarks (coasts, rivers) and national boundaries over the image.

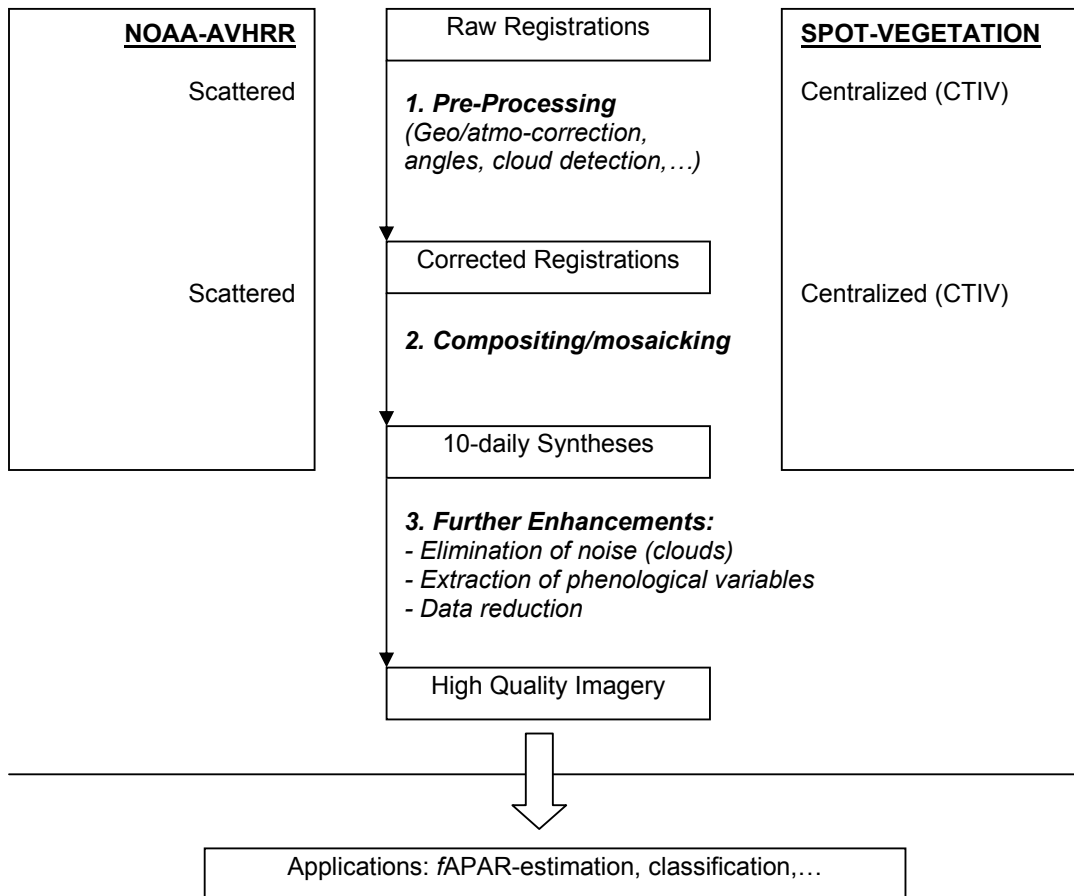


Figure 22: Components of the processing chain for AVHRR and VGT imagery.

In this optional step, the unpacked images can be visualized with the registered vectors in overlay. If desired, the cloudy scenes can be withdrawn and the processing can only be continued for the scenes of sufficient quality.

Many later operations might require the input of the zenith angle (θ) and azimuth (φ) of the sun (θ_s , φ_s) and the sensor (θ_v , φ_v) at registration time. These angles are computed here on a per-pixel base and stored in 4 additional images. The required geo-locations (λ , β) and registration times are derived from the ancillary information file (see step 1).

Intermezzo: In order to get rid of the never-ending burden of spatial incompatibilities between different geographical data sets, it was decided to elaborate an independent software which performs the conversion between different geodetical datums and/or cartographic projections. This program works for any type of geographical data: points (with interactive input), vector-files, and raster-images. The package contains all current datums (new ones can be added interactively) and about 20 projections (always in the direct and inverse modes, i.e. from/to the unprojected Lon/Lat-system), inclusive some more exotic ones which are ignored by commercial software, such as the Interrupted Goode Homolosine (see figure II.4), the Miller Oblate Stereographic, and even the Belgian Conic Conform. Because of the availability of the code, new projections can easily be added as to the needs. The main source for this work was the unsurpassed manual of Snyder (1987). The program was also incorporated into the AVHRR-chain, such that the raw images can directly be projected into any selected georeference system.

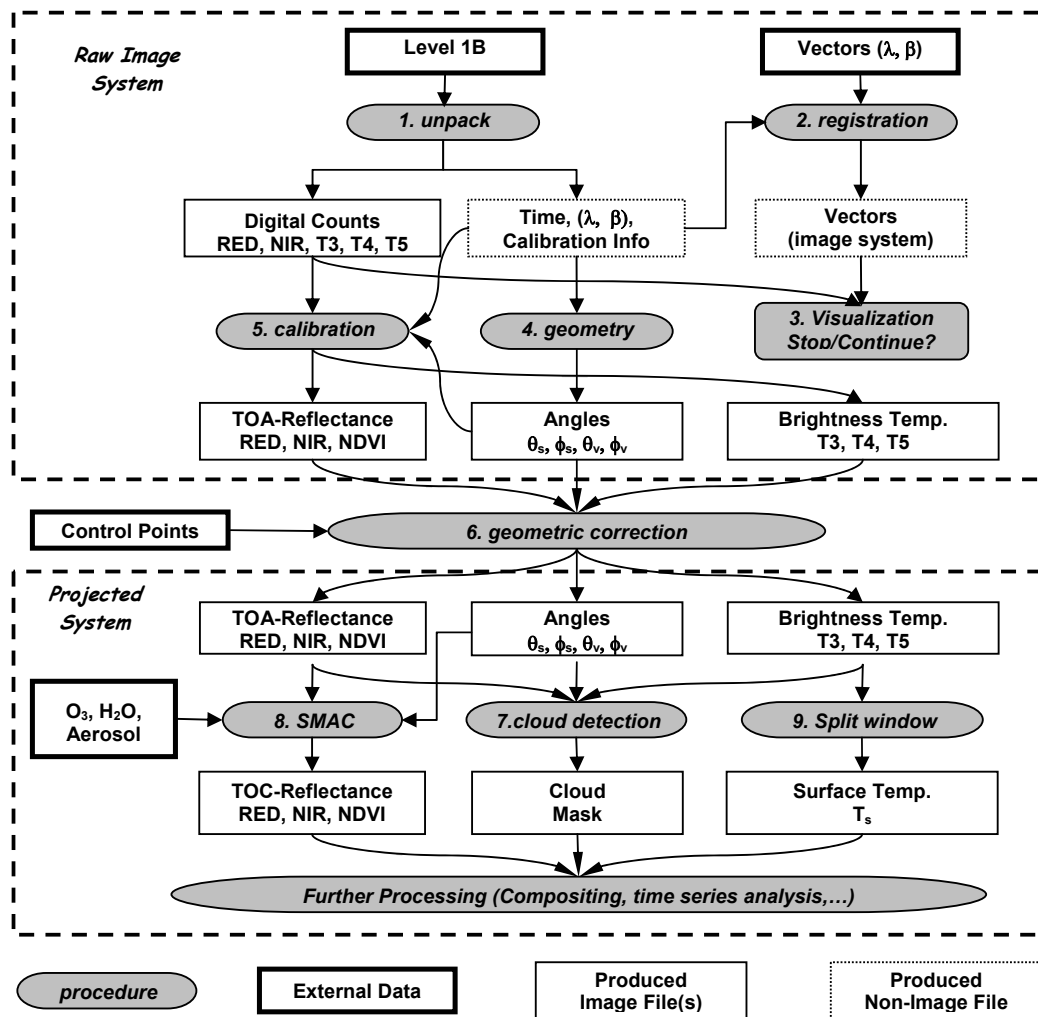


Figure 23: Flowchart of the NOAA-AVHRR pre-processing chain.

The digital counts in the unpacked images are converted into physical units. The MIR and TIR-bands are calibrated into brightness temperatures (T3, T4, T5) by means of Planck's law (in inverse mode), the known spectral response of the sensors, and the

ancillary measurements of the on-board internal calibration standards. For the shortwave bands (RED, NIR), 'top of atmosphere' reflectances (R_{toa}) are computed, based on published and regularly updated calibration equations which cope with sensor ageing effects (Rao & Chen, 1995). This calibration also involves a correction for the solar zenith angle θ_s and for the actual distance between earth and sun.

All the images (R_{toa} , brightness temperatures, 4 angles) are now reprojected (with a nearest neighbour resampling) towards a user-defined "output-frame". This output-frame must be defined in advance (see the intermezzo) by the following specifications: geodetical datum, projection (+ appropriate parameters), pixel resolution (mostly 1km²), and cartographic extension. For this geometric correction, the polynomials of step 2 have to be improved, because the geo-locations of the Level1B-file were only computed with a simple orbital model and hence slightly biased. The bias is removed here by means of control points, whose position has to be defined in a manual way on a screen visualization of the imagery.

A 0/1 cloud mask is elaborated by means of an interactive version of the classical scheme of Saunders and Kriebel (1988), which is based on thresholds in the available spectral bands (separately for land and sea).

The well known SMAC-algorithm (Rahman & Dedieu, 1994) is used to eliminate the atmospheric influences on the shortwave bands (RED, NIR) and to convert the 'top of atmosphere' reflectances (R_{toa}) into surface or 'top of canopy' reflectances (R_{toc}). The effects of the varying atmospheric pathlengths are quantified via the previously computed solar and viewing angles. In addition, SMAC requires the input of the vertically integrated amounts of ozone (which causes a weak absorption in the RED) and water vapour (strong absorption in the NIR), and of the optical depth at 550 nm related to the absorption and scattering of the aerosols (important effect on both bands). Each of these three external data can be input, either as a fixed parameter holding for the entire image area, or in the form of an image to account for local (per-pixel) variations.

As usual, the obtained R_{toc} -values are combined into an NDVI-image (the TOC-subscript is dropped): $NDVI = [R_{NIR} - R_{RED}] / [R_{NIR} + R_{RED}]$. This NDVI is a good indicator of the amount of living vegetation. Although it potentially ranges between -1 and +1, the NDVI normally varies from about 0.15 for built-up areas and bare soils up to 0.75 for the densest vegetations. Clouds and snow have values around zero, while negative figures mostly represent water.

Land surface temperatures are estimated from the brightness temperatures T4 and T5 with the method of Coll & Caselles (1997), which requires the input of the total amount of water vapour (same as for SMAC) and of the emissivities in both bands.

These emissivities are derived on a per-pixel base from the NDVI-values by means of the log-linear relations, proposed by Cihlar et al. (1997).

The chain was applied, tested and optimized on a set of about 100 AVHRR-scenes of 1996/7, registered by DLR-Oberpfaffenhofen. More details on this analysis are provided in §3.4.2. This Vito-software was developed because at the start of the project (around 1997), no real alternatives were available. It was only in recent days, that we could obtain two other AVHRR-chains: VTT of the Finnish meteorological institute, and SpacePC of the EU Joint Research Centre (JRC) in Italy. Nevertheless, this programming effort gave us a lot of experience, which in the future can easily be transferred to other earth observation systems.

3.1.1.2 *Spot-vegetation (VGT)*

As mentioned before, all VGT-data is registered by the receiving station of Kiruna (Sweden), while the pre-processing is centralized in the CTIV which is hosted at Vito (Belgium). This pre-processing obviously must comprise more or less the same operations as for AVHRR. We only mention some of the main differences:

Thanks to the large RAM-facilities on-board the satellite, all registered data can be memorized and transmitted to the antenna of Kiruna. For NOAA-AVHRR much information is lost in zones without antennas.

At the level of spatial accuracy, VGT-products are superior to those of AVHRR for different reasons: the push-broom sensor shows less deformations near the scanline edges; the navigation (tracking of satellite position and sensor view direction) uses a better orbital model, includes the most recent knowledge on the geoid, and accounts for the local relief (DEM); the sensor's attitude (pitch, yaw, roll) is permanently monitored (and transmitted as ancillary info) which drastically facilitates the estimation of the view directions; remaining errors are removed by means of control points, which are defined for each track (or segment) by a team of skilled operators.

In a spectral sense, the calibration of the VGT-products is more accurate thanks to the on-board calibration lamps. As for AVHRR, the atmospheric correction is also performed with the SMAC-algorithm, but the CTIV has better parameter values to its disposal (ozone, water vapour, aerosols – all delivered on-line by Meteo-France).

On the other hand the VGT-system is limited to the shortwave range and lacks thermal bands. This not only excludes the monitoring of surface temperatures, but it also hampers the cloud detection.

3.1.2 Creation of Composite Images & Global Data Sets

3.1.2.1 Principles of the NDVI-MVC compositing

Working with individual, pre-processed tracks is not optimal. For instance, with 2 or 3 registrations per day (for Europe), it is not exceptional to end up with a collection of ± 1000 images per year. In practice, most of them will be cloudy, while the remainder often contains redundant information. Moreover, the individual tracks do not cover exactly the same regions.

The classical approach to overcome these problems consists in the creation of periodic, "synthesis" or "mosaic" images, by means of the NDVI-MVC algorithm (NDVI-Maximum Value Compositing). Beforehand, the user must specify the composition period, and the output region of interest (ROI). Most often, a period of 1 decade is selected (10 days, or for the last decade of the month: 8 - 11 days). Figure 3.3 explains the MVC-procedure for the creation of a decadal, global (world-wide) mosaic.

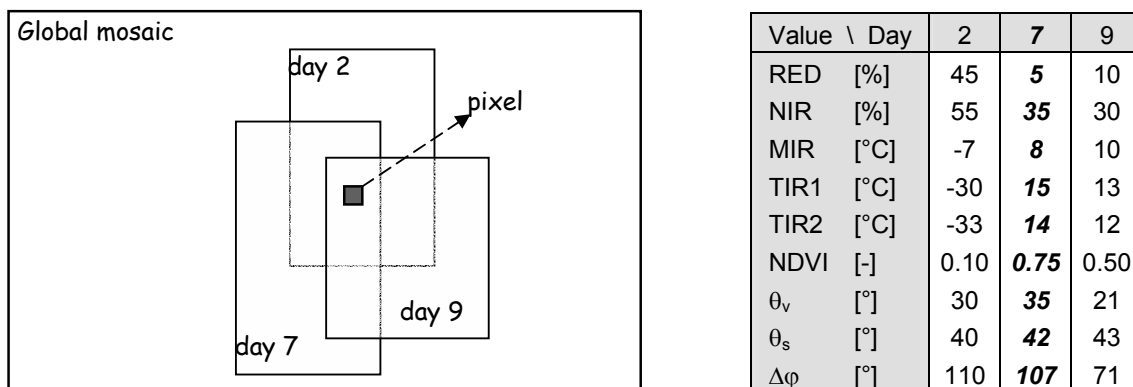


Figure 24: Production of a decadal, global mosaic with the NDVI-MVC algorithm (fictive example, for AVHRR). For the shown pixel, three different measurements are available within the concerned decade (from registrations at days 2, 7 and 9). The MVC selects day 7 because the NDVI is maximal (probably cloudfree) at that moment. All values of that registration (reflectances, temperatures, angles) are copied to the global synthesis. The low NDVI- and temperature-values on day 2 suggest the pixel was overcast at that moment.

The produced mosaic will (at least) contain as many image layers as the underlying, pre-processed tracks (AVHRR: 5 spectral, 4 angles; VGT: 5 spectral, 4 angles, 1 status mask). In a first stage, all the original pre-processed tracks are searched, which were registered in the concerned decade and over the specified ROI. For each pixel in the output frame, several measurements are available registered at different moments in the decade. The MVC-algorithms now selects the registration with the

highest NDVI. All the values and attributes of this registration (not only NDVI, but also the reflectances, temperatures, angles, quality labels) are copied to the corresponding pixel position in the output frames.

Since this selection procedure is repeated for every individual pixel in the ROI, it happens that in the created syntheses the values of neighbouring pixels often originate from different registrations/dates (and hence different atmospheric conditions, geometries, etc). However, the main goal of the MVC consists in the elimination of clouds: since clouds have low NDVI, the MVC indeed generally favours cloudfree measurements.

In spite of the criticism of some authors against the MVC (concerning the introduction of artificial speckle noise in the reflectance bands), it can not be denied that the compositing is an essential step in the entire processing: it introduces an enormous data reduction (only 36 syntheses remain per year) and the resulting synthetic images are of better quality than the original tracks. Moreover, it is the only way to obtain satellite imagery with global coverage.

3.1.2.2 *Global data sets used in this project*

The remote sensing part of this project was mainly performed with the three data sets listed in table VII. These are all global, 10-daily syntheses created with the NDVI-MVC method. We first give a brief description:

The **Pathfinder data set** is freely available on the Internet, and was elaborated by a team of specialists of NOAA, NASA and the University of Maryland. The imagery was acquired by different NOAA-platforms (7, 9, 11 and 14), with AVHRR in the GAC-mode (Global Area Coverage), i.e. with a deteriorated resolution of about $5 \times 3 \text{ km}^2$. The data were submitted to a standard pre-processing and converted to the IGH-projection (see figure 25) with an output-resolution of $8 \times 8 \text{ km}^2$. The 6 image layers, comprised in each decadal MVC-composite, are listed in table VIII. Although it's fully recognized that the Pathfinder images suffer from a lot of errors (data gaps, different versions,...), it remains an extremely valuable data set, because it represents the longest series of global and pre-processed AVHRR-data available so far. Actually, we only received this data set at the end of the project. To save disk space, only the NDVI-layers were downloaded. Total required space (see table VII) amounted to 17 year \times 373 Mb/year = 6 341 Mb (\approx 6 Gb).

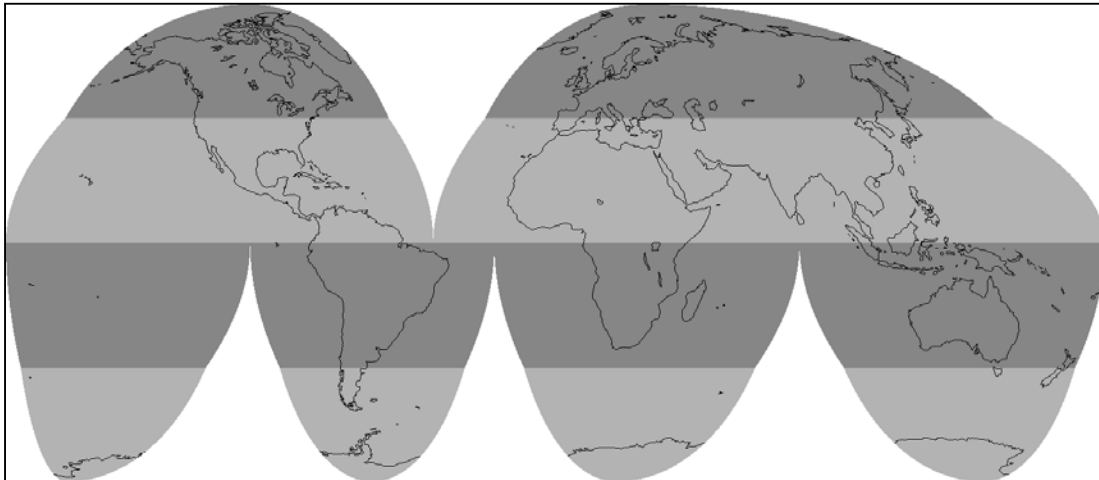


Figure 25: The “Interrupted Goode Homolosine” projection (IGH – see Steinwand) partitions the globe in 12 zones. The 6 equatorial zones ($\beta \leq \pm 45^\circ$) follow the Sinusoidal projection, the 6 boreal ones (2 north of 45° , 4 south of -45°) the projection of Mollweide. To reduce local deformations, each zone receives appropriate projection parameters (central meridian, etc.). All these projections (Sinusoidal, Mollweide, IGH) are equal-area, i.e. all surfaces are represented in a correct, proportional way. For IGH-images, all pixels cover exactly the same surface – which is not the case for most other projections. The pixel distribution in the IGH global mosaics is as follows: 53% is covered with water, 21.5% with terrestrial surfaces, and the remaining 25.5% are “void” pixels which fill the areas between the IGH-zones. These void pixels do not correspond with any real, physical surface on the globe.

Table VII: The three global image sets used in this project.

Data Set	PathFinder	EROS	VGT
Sensor	NOAA-AVHRR	NOAA-AVHRR	SPOT-VEGETATION
Period	Jan. 1983 – Dec. 1999 17 year (612 decades)	April 1992 - March 1993 1 year (36 decades)	April 1998 – March 1999 1 year (36 decades)
Pre-processing	NOAA/NASA	USGS-EROS	CTIV-CNES
Projection & Resolution	Interrupted Goode Homolosine (8x8km) ²	Interrupted Goode Homolosine (1x1km) ²	Geographic Lat/Lon (1°/112) ²
Acquired from	Internet	Internet	JRC-SAI
More Info on URL	http://daac.gsfc.nasa.gov/ CAMPAIGN_DOCS/FTP SITE/readmes/pal.html	http://edcwww.cr.usgs.gov /landdaac/1KM /1kmhomepage.html	http://www.vgt.vito.be
Bands / BPP ^o	6 / 11	10 / 15	11 / 16
$N_{col} \times N_{rec} = N_{pix}$	5004 x 2168 = 10 848 672	40031x17347=694 417 757	40320x14673=591 615 360
Mb/decade*	114 (10)	9 934 (662)	9 027 (564)
Mb/year*	4 097 (373)	357 614 (23 841)	324 984 (20 312)

(^o) BPP = total bytes per pixel in one synthesis (sum of BPP-values in tables below).

(*) Values between parentheses indicate the disk space in Megabyte (Mb) occupied by only the NDVI-layers.

Table VIII: Overview of the 6 image layers comprised in each decadal PathFinder synthesis. BPP=Bytes-per-Pixel (1=BYTE, 2=INTEGER)
NB: The images contain 3 special W-codes: 0=Missing data over land, 1=Sea, 2=IGH-void.

N	FILE	BPP	CONTENTS / SCALING	(W = digital number in image)
1	Ch1	2	Red Surface reflectance (0.58-0.68 μ m)	$R_r = (W-10)/50000$ [-]
2	Ch2	2	NIR Surface reflectance (0.73-1.10 μ m)	$R_n = (W-10)/50000$ [-]
3	Ch3	2	MIR Brightness temperature (3.55-3.93 μ m)	$T_3 = (W+31990)/200$ [K]
4	Ch4	2	TIR1 Brightness temperature (10.3-11.3 μ m)	$T_4 = (W+31990)/200$ [K]
5	Ch5	2	TIR2 Brightness temperature (11.5-12.5 μ m)	$T_5 = (W+31990)/200$ [K]
6	NDVI	1	Surface NDVI = $(R_n - R_r)/(R_n + R_r)$	NDVI = $(W-128)/125$ [-]

Table IX: Overview of the 11 image layers comprised in each decadal VGT-synthesis. BPP=Bytes-per-Pixel (1=BYTE, 2=INTEGER).

N	FILE	BPP	CONTENTS / SCALING	(W = digital number in image)
1	X_B0	2	Blue Surface reflectance (0.43-0.47 μ m)	$R_b = W/2000$ [-]
2	X_B2	2	Red Surface reflectance (0.61-0.68 μ m)	$R_r = W/2000$ [-]
3	X_B3	2	NIR Surface reflectance (0.78-0.89 μ m)	$R_n = W/2000$ [-]
4	X_MIR	2	SWIR Surface reflectance (1.58-1.75 μ m)	$R_s = W/2000$ [-]
5	X_NDV	1	Surface NDVI = $(R_n - R_r)/(R_n + R_r)$	NDVI = $W/250 - 0.1$ [-]
6	X_SZA	1	Solar zenith angle	$\theta_s = W/2$ [°]
7	X_VZA	1	View zenith angle	$\theta_v = W/2$ [°]
8	X_SAA	1	Solar azimuth angle	$\phi_s = 1.5W$ [°]
9	X_VAA	1	View azimuth angle	$\phi_v = 1.5W$ [°]
10	X_TG	2	Time grid : minutes between pixel registration and start of synthesis (LOG-file)	
11	X_SM	1	Status mask (bit 1=Most Significant, bit 8=Least Significant) Bit 1-4 : 1=ok 5 : 1=land 6 : 1=ice/snow 7 : 1=cloud 8 : unused (always 0)	0=data error in spectral bands 1=Blue... 4=SWIR 0=water (wide rim along the coasts) 0=no ice/snow 0=no cloud

In the beginning of the project most time was devoted to the “Global Land 1 km AVHRR Data Set”, elaborated by the USGS-EROS Data Centre (Eidenshink & Faundeen, 1994). This **EROS data set** comprises decadal global mosaics of NOAA11-AVHRR, derived from HRPT-data (full resolution) registered between April 1992 and December 1995 by an international network of antennas. The pre-processing was similar to the one of PathFinder. The MVC-composites are also warped to the IGH-projection, but with the full 1x1km²-resolution. And each synthesis now contains 10 layers: the 5 spectral bands (Integer), the NDVI (Byte), 3 Byte-images with angular information (θ_s , θ_v , $\Delta\phi = |\phi_v - \phi_s|$), and a last Byte-layer with the registration day (1-11) within the decade. Here again, the data set was too large (see table VII), so a data reduction was necessary. In the spectral sense, we only selected the most informative NDVI-layers, while in the temporal sense the analysis was limited to the 36 decades from April 1992 till March 1993 (one year). But since the remaining data set still occupied ± 23 Gb, we also had to apply a spatial reduction: the images were systematically sub-sampled with a thinning factor of 3x3. No spatial

averaging was applied, such that the retained pixels still possess all the spectral characteristics of an original 1x1km² pixel. By repeated sub-sampling, several global image sets (each with 36 NDVI-layers) were derived with different resolutions (3x3km², 9x9km², 27x27km², ...). Thanks to their limited size, the most degraded sets proved very useful for general data inspection, program development, and quick evaluation of new procedures.

The **VGT data set** was delivered by JRC-SAI (Space Applications Institute, Italy) in the frame of an informal collaboration with Vito. It comprises the first full year cycle (April 98-March 99) of global, 10-daily composites, produced by CTIV. These so-called S10-products are delivered in the "Plane Carré" projection (more correct: unprojected Lon/Lat) with a resolution of 1°/112 in both directions. Actually, the term "global" is a bit misleading here, because the S10-syntheses only comprise the latitude belt between -56° and +75° and hence do not cover the poles (PathFinder and EROS cover the entire range from -90° ... +90°). Each decadal VGT-synthesis is delivered in the form of 11 image layers, stored in 11 separate binary HDF-files (Hierarchical Data Format). The characteristics of these image layers are summarized in table IX. In addition, all ancillary information (geo-referencing, period, quality labels, etc.) is described in a separate ASCII/text file (X_LOG.TXT). As usual with this type of global data, the disk space requirements are overwhelming (± 320Gb/year). In § 3.1.3.3, we describe a procedure to tackle this always-recurring problem.

3.1.3 Further Enhancements

3.1.3.1 Detection and replacement of cloudy measurements

In spite of all efforts made to obtain high quality products, decadal syntheses still contain a lot of perturbations. Sharp edge lines appear in regions where insufficient registrations were available for the MVC compositing process. Missing values occur, especially in winter at higher latitudes due to the polar night. However, the most important source of noise are clouds, because clouds often persist longer than 10 days, such that the decadal NDVI-MVC can not eliminate them. In the temporal NDVI-profiles, shown in figure 26, clouds can be recognized as irregular dips. These perturbations are so prevalent that any attempt to perform an analysis on the original composites is condemned to fail. Therefore, a procedure was developed for the cleaning of the 10-daily NDVI time series. This algorithm was inspired by the famous BISE (Viovy e.a., 1992). It inspects each pixel's profile and removes all abrupt local minima (supposedly clouds), as far as they don't persist longer than 4 decades (40 days - a longer period would eliminate too much significant fluctuations).

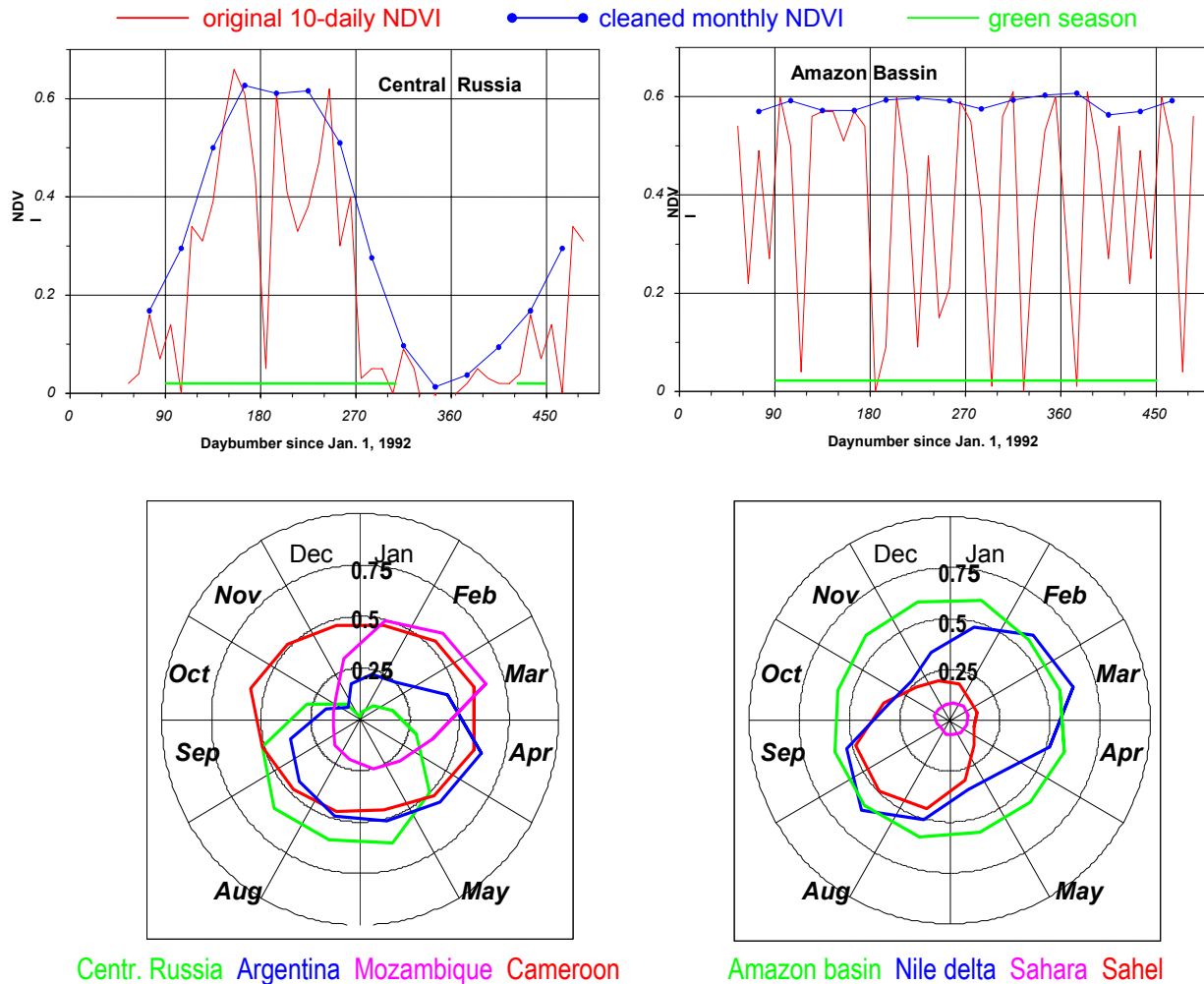


Figure 26: NDVI-profiles of some representative pixels, extracted from the EROS data set. The concerned year ranges from day 90 (start of April 1992) till day 450 (end of March 1993). Top figure: The original 10-daily NDVI-series (red) are severely perturbed by clouds (V-dips). The cleaned profiles with monthly means (blue) have a more logic and fluent course. From these, phenological attributes are computed such as the length of the growing season (green). Bottom figure: Alternative representation of the monthly NDVI-evolution of 8 pixels in the form of time roses or “phenograms”.

We first remark that this kind of cleaning operations is rather experimental and not really based on scientific grounds. The procedure comprises a number of often cryptic (though important) tests and sideways, which are hard to explain. Below, we only explain the major elements of the method. We assume the data set comprises 36 decadal syntheses (1 year).

- **Initialization:** The 36 NDVI-values of the pixel to be cleaned, are read from the correct positions in the MVC-composites. These byte-values are immediately scaled to the real NDVI-range (-1 ... +1) with the appropriate equation (e.g. for VGT: $NDVI = W/250 - 0.1$, see table IV) and stored in the

vector $Y(1 \text{ TO } 36)$, i.e. in the rows 1 to 36 of a RAM-table with the name Y . This table contains 4 additional places at the bottom in $Y(-3 \text{ TO } 0)$ and 4 more at the top in $Y(37 \text{ TO } 40)$. Initially, these additional places are "empty".

- **Test on missing values:** Cloudfree land surfaces always have NDVI's greater than a pre-defined value (say 0.1). All decades (D) with NDVI below this threshold are traced and labelled with the special code $Y(D) = -1$ (which means: measurement rejected). In principle such withdrawals can only occur for water pixels, or for land pixels covered by clouds or snow. If the number of refused measurements is larger than 27 (75% of 36), the entire pixel is rejected and flagged in the output imagery with special code 255 (sea or insufficient data). In the other case (at least 9 good NDVI-measurements), we probably deal with a terrestrial pixel and the cleaning operation can start.
- **Circularization:** First, the profile is made "circular": the values of the last four decades in $Y(33 \text{ TO } 36)$ are copied to the four empty places $Y(-3 \text{ TO } 0)$ at the beginning of the table, and the first four real values $Y(1 \text{ TO } 4)$ are copied to the end in $Y(37 \text{ to } 40)$. These "profile-tails" will serve as starting and ending strips for the cleaning operation.
- **First elimination of unreliable values:** This step searches and eliminates the unreliable NDVI-values. This is technically realized by means of a second table $Y_s(-3 \text{ to } 40)$, a duplicate of table Y but with all values initialized to -1 (i.e. the code for rejected measurement/decade). Then the NDVI-profile is scanned (table Y) and only the reliable NDVI-values are copied to the corresponding positions in table Y_s . The procedure tries to find the best compromise between two opposite goals: maximal conservation of the good measurements and maximal elimination of unreliable values. The procedure begins with the search of a measurement which is certainly reliable, and not contaminated by clouds or snow (this initial search is explained further on). Starting from this 'clean' decade, the four following decades are examined, i.e. the NDVI-values of the 40 following days. Within this group of four values, the program actually searches the two decades which respectively have the highest NDVI-value and the steepest slope with respect to the starting point. Amongst these two –most often they occur in the same decade– the value closest (in time) to the starting decade is retained. This value is considered reliable, its value is copied to Y_s , and the concerned decade will serve as new starting point for the following iteration. In other words, all measurements (at most 3) between the starting point and the retained decade are considered unreliable and hence rejected (code -1 in Y_s). This process is repeated until the end of the time series ($Y(40)$) is reached. The rationale of this method is

that clouds can indeed be very persistent, but that within a period of 40 days at least one clear-sky registration may be assumed.

- As mentioned before, the procedure is partly based on the BISE-algorithm. However, there are some important differences. BISE only looks for the neighbour with the highest value and does not account for the slopes. This results in the undesired withdrawal of a considerable number of pertinently reliable points (mostly inflection points). Another problem concerns the start of the search method. BISE simply begins with the first decade in the profile $Y(1)$, whose NDVI-value is always considered reliable, without proof. Our variant initially searches the decade with the highest NDVI-value, and from this (certainly reliable) point the cleaning operation is performed in both directions: first to the right (progressive), then to the left (back in time). A last problem is raised by the pixels near the poles, whose profiles often show long periods of missing values (longer than 40 days) as a result of the polar night. Under certain conditions these periods are not rejected, but rather labelled with the special output-code 0 (meaning: snow, ice or no light).
- **Second elimination of unreliable values:** A number of unreliable measurements seems to slip through the net, and after the first elimination step there often remain some abrupt and unlikely V-dips in the profile. This is quite a tricky matter, because these local minima can also be due to relevant phenomena on the ground (for example, the harvest of an important culture). However, we only want to eliminate those V-dips where the abrupt descent and rise of the NDVI surpasses the potential growth dynamics of the vegetation. This step scans the retained points in the profile (table Y_s) and searches the decades with local minima (V-dips). For each such decade, the slopes are computed w.r.t. the 2 retained neighbours (which by definition have higher NDVI). If the mean of the absolute value of both slopes exceeds a certain threshold, the concerned decade is eliminated (again, by resetting its value in Y_s to -1). Best results were obtained with a threshold of 0.1. Implicitly, this assumes that the NDVI of vegetations can not change faster than by 0.1 units per decade.
- **Interpolation:** This step replaces all eliminated values (those with code -1 in table Y_s) by means of a simple linear interpolation on the base of the surrounding decades with reliable measurements (value ≥ 0). First, the Y_s -profile is however "circularized" again, as described above for table Y . This avoids many unrealistic extrapolations at the start and end of the time-series. At this stage, table Y_s only contains NDVI's greater than or equal to zero.

- **Computation of monthly means & output:** The cleaned profile $Y_s(1 \text{ TO } 36)$ is divided in 12 months of 3 decades, and for each month the mean NDVI is computed. The 12 NDVI-values are then again scaled to the BYTE-range ($W[0-200] = 200 \cdot \text{NDVI}[0.0...1.0]$). Finally, the 12 digital values W are written to the correct position (of the concerned pixel) in the output-image(s) (either 12 separate single-band image-files, or 1 global file with 12 layers).

This procedure is of course repeated for each pixel in the imagery. It's also very simple to adapt the method for data sets which contain more than 36 decades (e.g. PathFinder). It's not easy to provide a scientific validation of the method. We could only evaluate it in a visual way, i.e. by inspection of the results for hundreds of test-pixels selected from different parts of the globe. In this way, the examples in figure 3.5 indeed confirm that the cleaned, monthly NDVI-profiles follow a more fluent and (pheno-)logical course than the original time series. The noise provoked by clouds (and other effects) is clearly eliminated to a large extent. The method thus seems efficient, but it is certainly not perfect. In a number of cases, the cleaning is too drastic, when low NDVI-values are by mistake interpreted as clouds. Of course, this effect may possibly lead to a systematic over-estimation of the NDVI at the global scale. Apart from that, it is clear that by the transition from 10-daily to monthly mean values, a number of temporal details are sacrificed. However, the resulting data-reduction with a factor 3 can also be regarded as a positive measure.

3.1.3.2 *Extraction of phenological variables*

The above images with monthly mean NDVI's can be used as such for the validation of the CARAIB-model (see § 3.3). It only remains to translate the NDVI-data into fAPAR-values, the parameter which is also predicted by the model. However, for other applications such as land cover classification (see §3.2), the image information is still expressed in a sub-optimal form. Key point is that the data set still contains a lot of redundancy. Typically, a full year cycle of MVC-composites can be reduced to only 3 independent, principal components. This not only causes an unnecessary overload as to the disk space requirements and processing time, but it also excludes the application of statistically-based classification algorithms such as the Maximum Likelihood (covariance matrix inversion errors!). Another problem is that due to the equatorial anti-symmetry in the occurrence of the seasons, a same land cover type may follow the same growth phenology and NDVI-evolution on both hemispheres, but with a phase shift of about 6 months. Without precautions, the classification algorithms thus would divide most biomes into two sub-classes, one for each hemisphere. However, in this context such a climatologically defined subdivision is irrelevant and undesirable.

These problems can be eliminated to a certain extent, by the computation of a number of new rasters with more condensed, quantitative and phenological information. In practice, the following phenological attributes are derived on a yearly base, by inspection of each pixel's profile of 12 monthly mean NDVI's:

- Mean: the mean annual NDVI (average of the 12 monthly values)
- Min: the minimum annual NDVI (lowest of the 12 monthly values)
- Max: the maximum annual NDVI (highest of the 12 monthly values)
- Range: the annual NDVI-range (Max – Min)
- SI: Seasonality Index $SI = (Range - Mean)/(Range + Mean)$, a relative measure for the seasonal fluctuations (often better than Range)
- S_{nr} : the number of growing seasons per year (0, 1, or at most 2)
- S_{len} : the length in months of the 1 or 2 growing seasons (0 for deserts, 12 for evergreen vegetations)
- S_{ini} : the relative length of the initial growing stage, in % of S_{len}
- S_{st} : the startdate (in months from January 1) of the (principal) growing season.

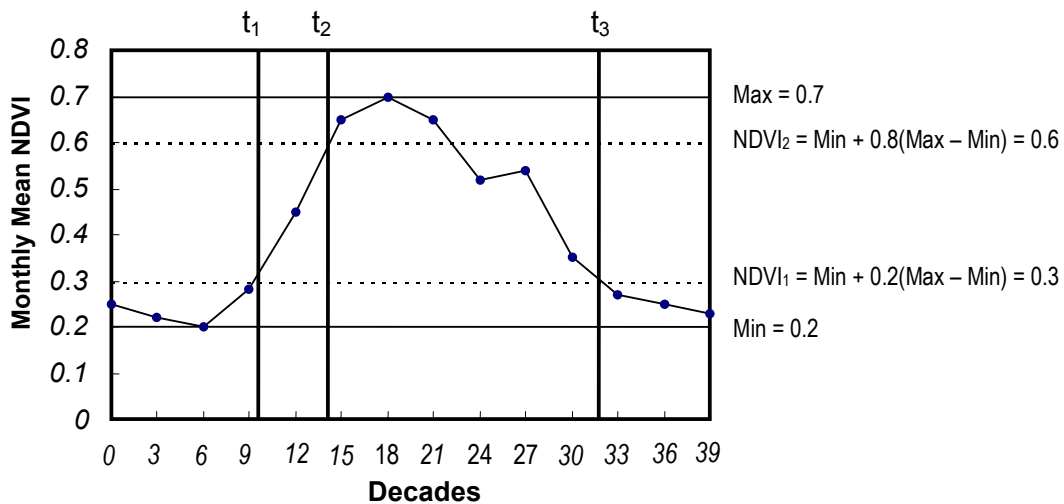


Figure 27: Computation of phenological attributes from the monthly NDVI-profile, for a (fictive) pixel with one growth cycle (green season + dead season). Min/Max = annual NDVI-extremes; t_1 = start of green season; t_2 = end of initial growth stage; t_3 = end of green season. According to our convention, the 3 dates occur when the NDVI-curve crosses the critical levels $NDVI_1$ and $NDVI_2$. Attributes: $S_{nr}=1$, $S_{len}=t_3-t_1$, $S_{ini}=(t_2-t_1)/(t_3-t_1)$, $S_{st}=t_1$. NB: the small local minimum around decade 24 is considered irrelevant.

The first five attributes (Mean, Min, Max, Range, SI) are straightforward and can be easily computed for each pixel from its 12 monthly values. As the annual Mean decreases, the Range obviously has to decline as well. This correlation is taken into account by the Seasonality Index SI, which represents an alternative measure for the seasonal fluctuations (often better than the Range). On the other hand, the latter four attributes (S_{nr} , S_{len} , S_{ini} , S_{st}) require the positioning of the growing season. The principle is outlined and explained in figure 3.6, for a (most common) pixel with one growth cycle (NDVI maximum and minimum) per year. For pixels with two distinct cycles (e.g. in the Nile delta), S_{len} represents the length of both green seasons, while S_{ini} and S_{st} hold for the principal (longest) season. For biomes without noticeable NDVI-dynamics (deserts, evergreen forests), S_{ini} and S_{st} are undefined. These land cover types are isolated from the beginning and labelled with a special code in the images S_{ini} and S_{st} . Figure 28 shows some examples of the obtained phenological images S_{len} and S_{st} , extracted from the EROS data set.

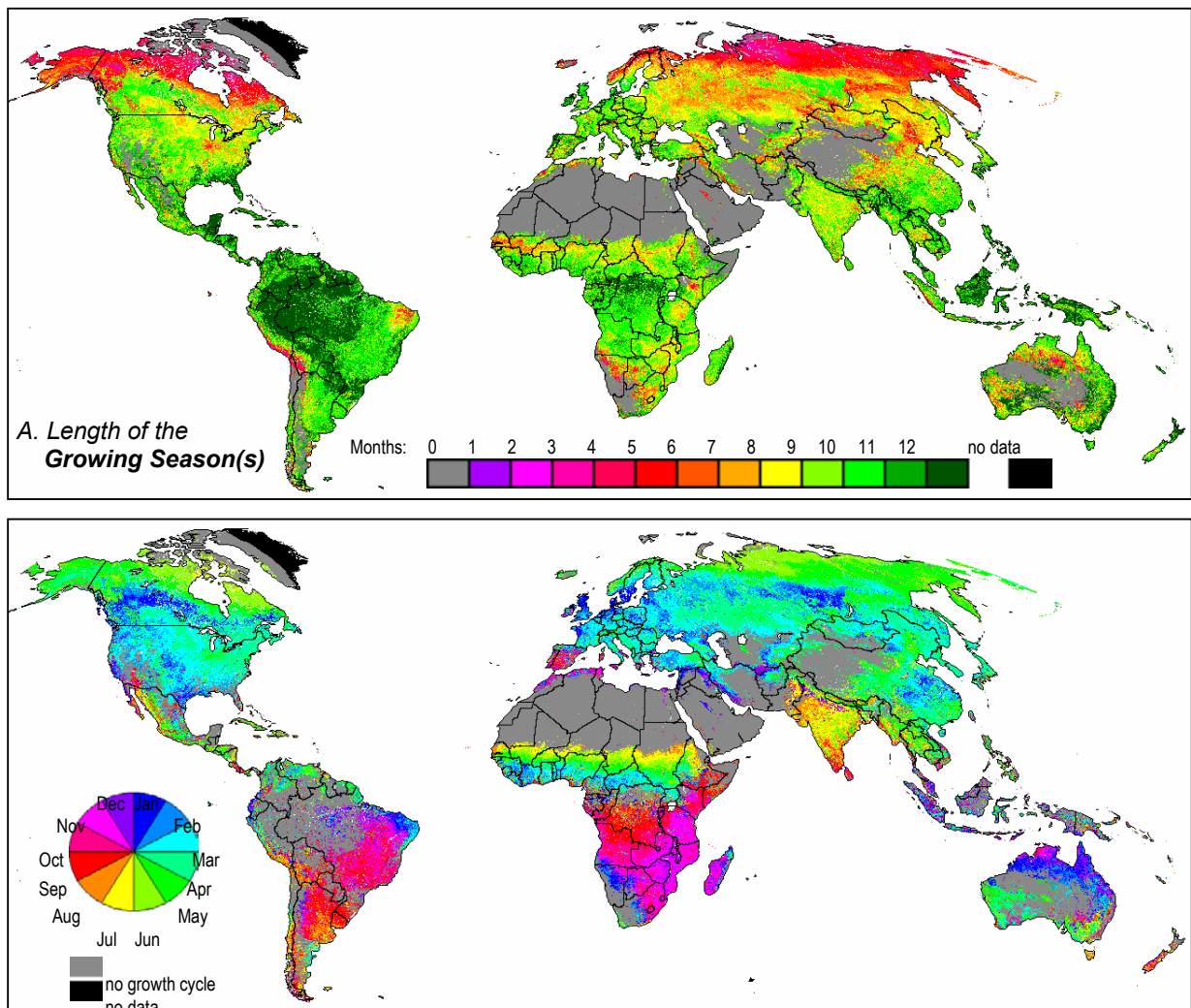


Figure 28: Phenological images derived from the EROS data set (year 1992/3).

These 9 images with phenological attributes – and especially Mean, SI, S_{len} and S_{st} – can be considered as valuable stand-alone products, because of their high diagnostic power. As their mutual correlation is lower than for the group of 12 monthly NDVI-means, they will be used (or at least, a subset of them) as the starting point for the biome classification (see §3.2). Moreover, all information concerning the timing of the growing season is now compressed into one single attribute: the start of the green season (S_{st}). By deliberately excluding this image variable from the classification process, one can by-pass the problems of the equatorial anti-symmetry and achieve a biome classification, which is purely based on the intrinsic features of each biome.

3.1.3.3 *Enhancement of global imagery via a dedicated data reduction*

Some important lessons were learned from our experience with the analysis of global, 1km²-resolution image sets. First of all, the data sets are enormous. As pointed out by table VII, the EROS and VGT data sets both occupy more than 300 Gb for one year of decadal composites. Nobody is able to consider (store and process) such a vast amount of data in its full integrity, except maybe some of the biggest organizations – which thus achieve a kind of scientific monopoly. In practice, most researchers are forced to treat only a fragmentary part of the data, and to make a selection in one or more of the following dimensions:

- *Temporal*: Instead of investigating all data, only a limited period is selected.
- *Spectral*: Most often only the NDVI is used, and all the other information is skipped (reflectances, temperatures, angles,...). This of course excludes the computation of more performant vegetation indices instead of the NDVI, and –more important– the application of up-to-date, model-based techniques for the estimation of biophysical parameters (LAI, soil cover, *f*APAR).
- *Spatial*: In most studies the analysis is restricted to one specific study area (say one country or continent). Rather exceptional is the approach where the global coverage is retained by spatial degradation of the imagery.

We also experienced that in the long term the analysis per continent – the most commonly applied solution – is extremely time-consuming: for every new analysis, the original syntheses must be reloaded (one by one) from hardly accessible media such as DLT or ExaByte, and unzipped. Actually to our opinion, the astronomic and unmanageable nature of these data sets forms the main bottleneck for this type of global scale image investigations.

The previous paragraphs also evidenced that the decadal MVC-syntheses should only be considered as intermediary products and that at the end of the process only a

limited number (though highly informative) images remain. However, the latter can only be produced if at a given moment, all the information (all bands, angles,...., global, at 1km²) is available in readily accessible formats. And this can only be achieved if we manage to economize on the size of the MVC-files – of course without sacrificing too much information. This goal is indeed feasible, if we consider that $\pm 75\%$ of the pixels in the global syntheses are sea pixels which can be dropped (in the syntheses they are just labelled with special codes). Moreover some spectral bands can be dropped because of their high mutual correlation, while also a lot of space can be gained by applying a radiometric compression.

The strategy for data reduction and enhancement, described below, was specifically developed for the global MVC-syntheses of VGT. These are by default delivered in the unprojected Lon/Lat-system, which is not equal-area (a prerequisite for global scale analyses) and space-consuming (drastic oversampling at higher latitudes). Here, the conversion towards an equal area projection leads to an improvement of the data set and a reduction of the image size. Preference was given to the IGH-projection (see figure 25), because most existing global data sets are expressed in this system. The main elements of the data reduction strategy are outlined in figure II.8 and they can be grouped in five stages.

In the **preliminary stage** (to be performed only once, at the start) we first created an improved, global land/sea mask. The standard VGT land/sea mask indeed overestimates the water-bodies: along the coasts, the syntheses contain a rim of 5 to 10 water pixels. The new mask was achieved by applying a 0/1-classification on the buffer zones along the coasts, based on the NIR-bands of two (summer/winter) global syntheses (water can be easily identified by its very low NIR-reflectance). Once so far, the land pixels were labelled with the unique ID-codes of the country to which they belong. To this goal, we used the territorial boundaries in vector format, provided by the ArcView data set "ESRI Data & Maps". Finally, the resulting raster with the country ID-numbers was converted, from the unprojected Lon/Lat-system to the equal-area IGH-projection with a resolution of 1km² (see figure 25). The pixel values in this raster thus indicate the country-ID (e.g. 1=Canada, 2=USA,...), while all water pixels have the special code 0 (see the Country-ID raster in figure 29, topleft part).

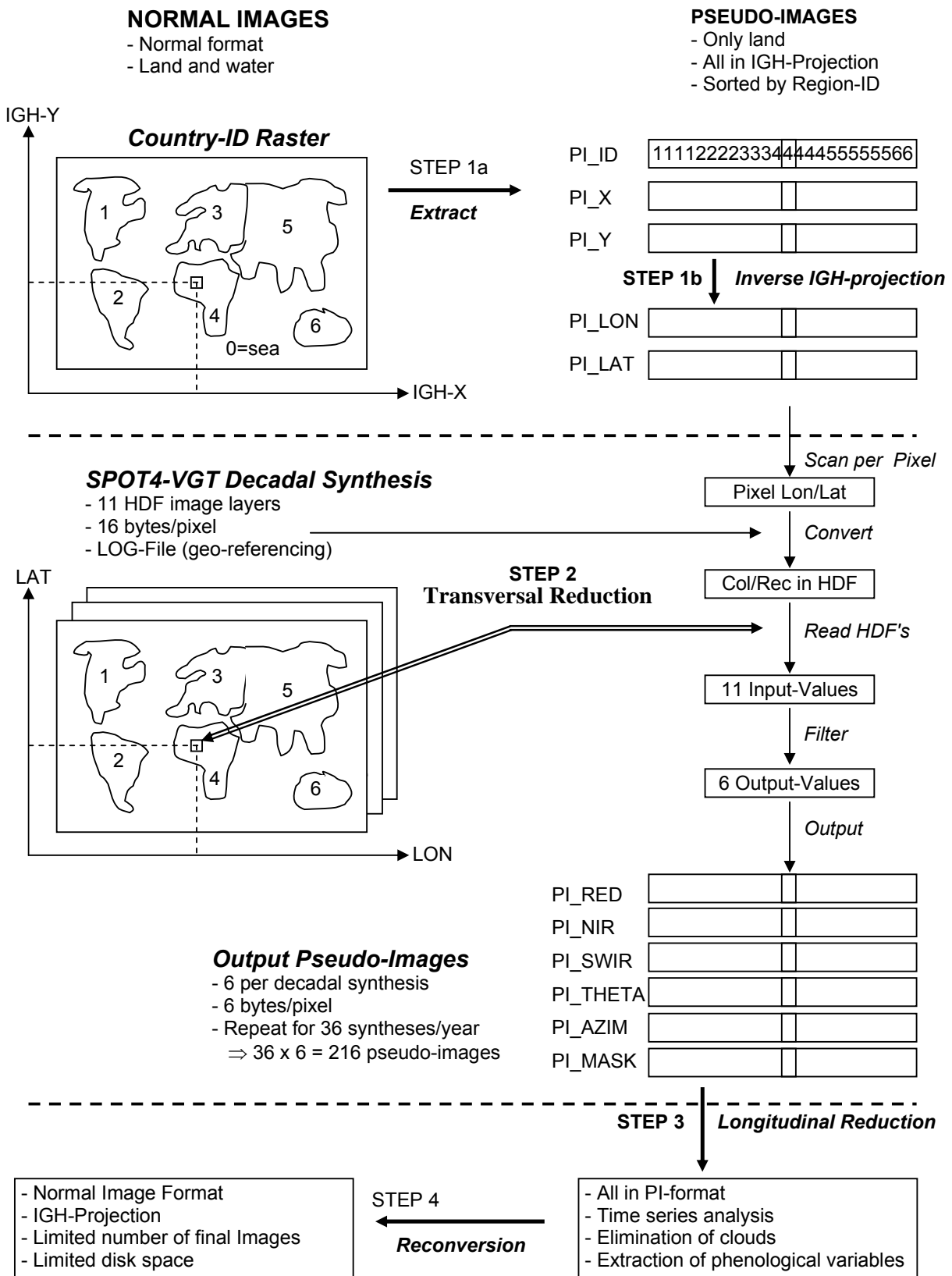


Figure 29: The data reduction scheme elaborated for the decadal syntheses of SPOT-VGT (IGH = Interrupted Goode Homolosine, see figure 25).

The following stage (step 1 in the figure) concerns the **creation of the "master" pseudo-images**. These pseudo-images (or PI's) are binary files which only contain the image information of the land pixels. Because all the sea pixels are skipped, each PI thus only contains the data of the ± 135 million 1km^2 terrestrial pixels of the globe (the true land surface on the earth). First, 3 separate PI's were extracted with the country-ID, and the IGH co-ordinates (IGH-X, IGH-Y in meters) of the pixel centres (step 1a). From the very beginning, in these PI's, all pixels are sorted as to the country to which they belong. For instance: first come all the pixels of Canada, then those of the USA, etc. By application of the equations of the inverse IGH-projection, two more PI's were then produced providing for each pixel the corresponding longitude λ and latitude β (step 1b). These 5 "master PI's" (which have to be created only once in the beginning) are of crucial importance for the further extraction of the VGT-imagery, and for the later reconversion of the PI's to normal image format.

The **transversal reduction** is outlined in step 2 of figure 29, and it must be repeated once again for each individual, decadal synthesis. The terrestrial pixels included in the PI's, are scanned one by one, and for each individual pixel the Lon/Lat-values are read from the latter two master-PI's. By means of the geo-reference information of the VGT-synthesis (mentioned in the LOG-file), the program localizes the corresponding pixel (record, column) in the synthesis, and reads its values from the 11 synthesis layers. These 11 values (together 16 bytes, i.e. the sum of BPP in table IV) are then compressed to 6 byte-values, which are written to 6 output pseudo-images. This process is repeated for each pixel in the PI's (± 135 million land pixels). The radiometric compression (from 16 to 6 bytes) is achieved as follows:

- Two values are skipped: the Blue reflectance because it is highly correlated with the Red, and the NDVI because it can easily be recomputed later when necessary.
- The other three reflectances are scaled from Integer to the Byte-range 0-250, where 250 corresponds with a band-specific maximum reflectance: 62.5% for the Red and SWIR (reflectances vary in discrete steps of 0.25%), 83.33% for the NIR (steps of 0.33%). The values 251-255 are special codes (reflectance above maximum, data error,...).
- The two zenith angles (θ_s , θ_v) are scaled in steps of 5° , with 19 levels for θ_s and 13 levels for θ_v . Both are combined in 1 byte-value ($19 \times 13 = 247$ levels).
- Both azimuths are combined in a "relative azimuth" $\Delta\varphi = |\varphi_v - \varphi_s|$ (byte-range: $0^\circ - 180^\circ$).

- The sixth and last byte value contains miscellaneous information: bits 1-4 (range 0-15) contain the registration day since the start of the synthesis (derived from the time grid and log-file), bits 5-6 are copies of the snow/cloud labels of the status mask, while bits 7-8 are unused.

The application of this transversal reduction to each of the 36 syntheses of one year has a number of important consequences. First, the data set is freed of redundant information. Thanks to the elimination of the sea pixels (and the improved land/sea mask), it only contains land pixels. The PI-data conform to the equal-area IGH-projection and each pixel now really covers exactly 1km². The radiometric compression is achieved with a minimal loss of information. Second, the disk space is drastically reduced because we only deal with the ± 135 Mb of land pixels. In PI-form, each synthesis (6 Byte-layers) now occupies 135 Mb x 6 = 810 Mb (instead of 9 027 Mb, see table VII), and the entire yearly set covers 810 Mb x 36 ≈ 29 Gb (instead of ±320 Gb). Hence, the data set shrank to about 9% of its original size.

Once the transversal reduction has been applied to a full year cycle of VGT-syntheses, one can start with the **longitudinal reduction** (step 3 in figure 29). Actually, this common denominator may cover a whole family of procedures, which involve time series analysis on a per-pixel base. This also includes the previously discussed enhancement techniques for the elimination of cloud perturbations and extraction of phenological variables. But as the entire image set now covers a more manageable size (29 Gb), more interesting procedures can be applied (new vegetation indices, etc.). Even the classification can directly be performed on the PI data set, because classification is a typical per-pixel operation!

The final step (step 4 in figure 29) concerns the **reconversion to normal image format**. This operation requires the presence of the original master-PI's and can be applied for any selected PI. This is for instance useful if one wants to visualize a certain spectral band in the normal way. But as this reconversion implies an "explosion" of the file sizes, in practice it will only be applied to the most useful end products of the analysis (e.g. derived classifications). This program also allows to reconvert only a specific geographic block (e.g. one continent).

The above procedure is fully operational: it has been programmed (mostly in C, the longitudinal reduction in IDL) and applied on the 36 global VGT-composites of 1998/9 (see table VII). At this moment (December 2000) we are preparing the first global 1km²-resolution classification, made with VGT-imagery. Some remarks:

- Most important is that the derived pseudo-images (which aren't but binary pixel databases) actually are stored here in normal image format following the

IDL-ENVI standards. That is: for each PI (*.IMG) a corresponding header-file (*.HDR) is created with all necessary info, just as for normal images. However, the number of columns (samples) and records (lines) are specified as 5000 x 27000, which indeed gives a total number of pixels of 135 million. As a consequence, the PI-data can still be manipulated with standard image processing software (ENVI). Of course, as the spatial context is removed, spatial operations (visualization, filters,...) are no longer meaningful. But the more important spectral operations (analysis of temporal profiles, classification,...) still can directly be performed on these PI's. This implies that all previously developed programs, which of course acted on normal images, (cloud removal, phenological variables) can be used as such on the pseudo-images without adaptations.

- Because the pixels are sorted and grouped per country, tables with national statistics (on land cover or specific spectral variables) can easily be derived directly from the PI's,
- We also added a procedure by which external raster information (DTM, ground truth data, ...) can be extracted and converted to PI-format, for overlay with the PI's with the VGT-data.
- Another program reconverts the PI's to normal image format but with degraded resolution (systematic thinning). In this way, we established a 33x33km²-resolution image set, which contains all the information on a global scale (36 decades x 6 layers). This degraded set (all together still 125 Mb) proved extremely useful for the testing and validation of new procedures.
- At last, it's evident that the entire strategy can very easily be adapted for application on similar imagery, such as the EROS-AVHRR data set.

To our opinion, it would be a significant improvement if this data reduction and enhancement scheme could be integrated in the standard processing chains (for SPOT-VGT: the CTIV), and especially if the "longitudinal reduction" would be extended with a number of procedures for the assessment of biophysical parameters (LAI, soil cover). This would free the user community with the burden of "cleaning" and further processing the global composites. And everybody would have the opportunity to directly order the thematic products needed for his specific application.

3.2 GLOBAL BIOME CLASSIFICATION

3.2.1 Legend & Upscaling

One of the main contributions of remote sensing to the modelling of the carbon balance of terrestrial surfaces consists in the delivery of global scale maps with the distribution of the broad land cover types (biomes). Models for vegetation carbon budgeting such as CARAIB indeed require this type of input (Warnant, 1999). However, the link between the remote sensing maps and the CARAIB-input is hampered by two incompatibilities.

First, CARAIB works with cells of ($1^{\circ} \times 1^{\circ}$)-resolution, whereas the imagery of AVHRR and VGT has a pixel size of about 1km^2 (at the equator, 1 CARAIB-cell thus corresponds with about $111 \times 111 = 12321$ image pixels). This incompatibility can be solved by means of an appropriate "upscaling" method: based on the 1km^2 -map, the acreage fractions occupied by each land cover class are computed for each CARAIB-cell (see further).

Second, the land cover types in image-derived maps mostly refer to relatively detailed and widely recognized classification legends, whereas CARAIB works with 8 "functional vegetation types". These functional types are based on 3 dichotomies (herbaceous/trees, evergreen/deciduous, C3/C4) which are indeed important for the modelling of carbon exchange. So far, the "sub-cell" surface proportions of the 8 functional vegetation types were mainly derived by combining the ecosystem map of Wilson and Henderson-Sellers (WHS) and the FAO national-level statistics of 1992 (Warnant, 1999). However, classifications of AVHRR or VGT imagery can not yield land cover maps which directly conform to one of these CARAIB-keys (functional types or WHS): it's impossible to distinguish the 8 functional types on spectral grounds, and the WHS-map can not be used for the calibration of the image classification due to its coarse resolution. This problem can only be solved by establishing the link between the CARAIB-legend and one of the common keys used in image classification.

Via the Internet (see: <http://edcdaac.usgs.gov/glcc/>), the USGS-EROS Data Centre freely provides a set of global land cover maps at 1km^2 -resolution, which were derived from the "Global Land 1km AVHRR Data Set" of the year 1992/3 (see table VII). These six land cover maps follow as many different legends or "keys":

- SiB1 : Simple Biosphere Model
- SiB2 : Simple Biosphere 2 Model
- IGBP : International Geosphere Biosphere Programme

BATS : Biosphere-Atmosphere Transfer Scheme
 USGS : USGS Land Use/Land Cover System (Modified Level 2)
 OLGE : Olson Global Ecosystems Legend

In principle, each of these maps can be used to calibrate and produce new classifications with imagery of other years. In order to select the most appropriate legend, the six biome maps were "upscaled" and converted to CARAIB-compatible format in the following ways:

- The raw product (± 700 Mb per map) was transformed from the original IGH-projection (figure 3.4) with 1km^2 -resolution into the unprojected Lon/Lat-system with an output resolution of $0.05^\circ \times 0.05^\circ$ ($20 \times 20 = 400$ pixels per CARAIB-cell). The involved resampling was performed with the "nearest neighbour" method.
- A CARAIB-compatible and ASCII-formatted database was computed which provides for each of the 15347 terrestrial $1^\circ \times 1^\circ$ -cells considered by the model, the acreage proportions covered by the different classes discerned by the key in question.

Figure 30 shows a partial example (only Europe-Africa, only a few classes) of the results derived from the SiB1-classification. On the base of these upscaled land cover data, it was decided to continue the further classification efforts with the IGBP-legend (Belward et al., 1996). The 17 broad land cover classes or "biomes" of the IGBP-key are listed in table X.

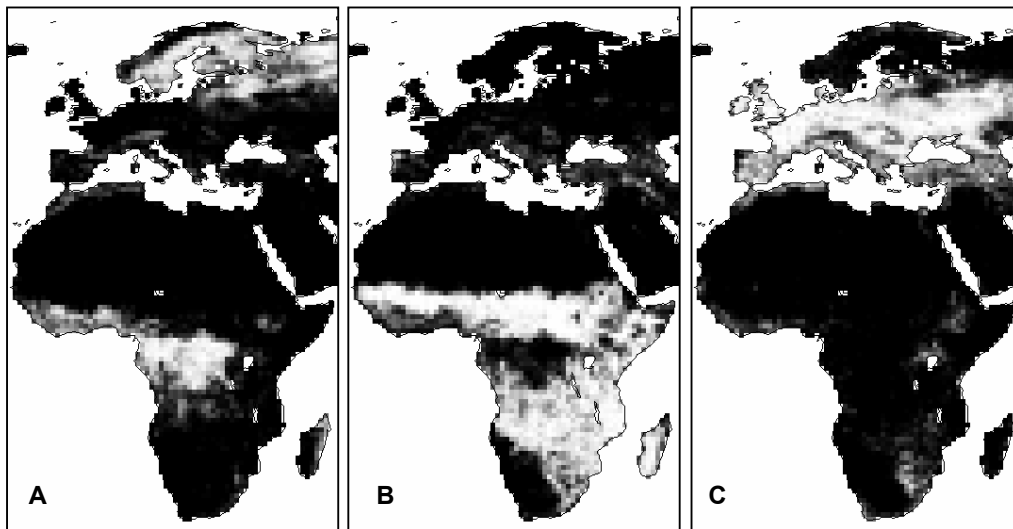


Figure 30: Acreage fractions (black=0%,..., white=100%) per CARAIB-cell ($1^\circ \times 1^\circ$), occupied by 3 different land cover classes in the SiB1-key: A.Evergreen forests (deciduous+coniferous), B.Ground cover with trees and shrubs, C.Agriculture and C3-grasslands.

Table X: The 17 land cover classes (biomes) of the IGBP-legend (Belward et al., 1996).

1	Evergreen needleleaf forests	Land dominated by trees with canopy cover > 60% and height > 2 meters. Needleleaf trees. Almost all trees remain green throughout the year. Canopy is never without green foliage.
2	Evergreen broadleaf forests	Land dominated by trees with canopy cover > 60% and height > 2 meters. Broadleaved trees. Almost all trees remain green throughout the year. Canopy is never without green foliage.
3	Deciduous needleleaf forests	Land dominated by trees with canopy cover > 60% and height > 2 meters. Seasonal needleleaf tree communities with an annual cycle of leaf-on and leaf-off periods.
4	Deciduous broadleaf forests	Land dominated by trees with canopy cover > 60% and height > 2 meters. Seasonal broadleaf tree communities with an annual cycle of leaf-on and leaf-off periods.
5	Mixed forests	Land dominated by trees with canopy cover > 60% and height > 2 meters. Interspersed mixtures or mosaics of the above 4 forest types. None of these has cover > 60%.
6	Closed shrublands	Land with woody vegetation less than 2 meters tall and with shrub canopy cover > 60%. The shrub foliage can be either evergreen or deciduous.
7	Open shrublands	Land with woody vegetation less than 2 meters tall and with shrub canopy cover between 10-60%. The shrub foliage can be either evergreen or deciduous.
8	Woody savannahs	Land with herbaceous and other understorey systems, and forest canopy cover between 30-60%. The forest cover height exceeds 2 meters.
9	Savannahs	Land with herbaceous and other understorey systems, and forest canopy cover between 10-30%. The forest cover height exceeds 2 meters.
10	Grasslands	Land with herbaceous types of cover. Tree and shrub cover is less than 10%.
11	Permanent Wetlands	Land with a permanent mixture of water and herbaceous or woody vegetation that cover extensive areas. The vegetation can be present in either salt, brackish, or fresh water.
12	Croplands	Land covered with temporary crops followed by harvest and a bare soil period (e.g. single and multiple cropping systems). Note that perennial woody crops will be classified as the appropriate forest or shrub land cover type.
13	Urban & built-up	Land covered by buildings and other man-made structures.
14	Cropland & natural vegetation mosaic	Land with a mosaic of croplands, forests, shrublands, and grasslands in which no one component comprises more than 60% of the landscape.
15	Snow & ice	Land under snow and/or ice cover throughout the year.
16	Barren or sparsely vegetated	Land with exposed soil, sand, rocks, or snow. Vegetation cover is always less than 10% throughout the year.
17	Water bodies	Oceans, seas, lakes, reservoirs, and rivers. Can be either fresh or salt water bodies.

3.2.2 IGBP-Classifications derived from the PathFinder Image Set

In the course of the project much attention was paid to the problematic of land cover mapping. At first, the EROS-AVHRR data set was tackled with an unsupervised approach (ISODATA). But the results were quite disappointing, because the resulting spectral clusters are arbitrary in number and difficult to interpret in terms of biomes. Therefore, we quickly moved to the supervised approach where the algorithms must

be calibrated (trained) with reference data ("ground truth") which must be available in advance. In this way, different classifications could be extracted from the EROS data set over Africa (in different degradations). Later we also established a new vegetation map over Central-Africa by means of the VGT-imagery of 1998/9. These classifications were realized by application of the classical Maximum Likelihood (ML) and/or a newly developed Non-Parametric Bayes classifier (NPB), on the phenological images extracted from the original MVC-syntheses. The NPB-classifier reaches similar results as the ML, but it doesn't require any assumption on the distribution of the data and it is much faster. However, in this section the focus is placed on the PathFinder data set, which was recently classified by means of a neural network approach (NN).

3.2.2.1 *Methodology*

As explained in § 3.1.2.2, the PathFinder set contains the decadal, global MVC-syntheses of the last 17 years (1983-1999), in the IGH-projection and with a resolution of 8x8km². In this analysis we only used the NDVI-layers (± 6 Gb). These were first cleaned with the procedure described in § 3.3.3.1, which resulted in a series of 204 images (17 years x 12 months) with monthly mean NDVI's. As the dynamics of land cover change are relatively slow, it was decided to produce only 3 different land cover maps, valid for the 3 subsequent periods of 5 years centred around 1987 (1985-1989), 1992 (1990-1994), and 1997 (1995-1999). For each period, a series of 12 monthly NDVI-images was compiled, by averaging the values of the 5 corresponding years. As land cover obviously varies with latitude, two additional images were created, providing for each 8x8km² "cell" the absolute value and the sign of the latitude.

The USGS-IGBP classification of 1992 (see § 3.2.1) was used as reference data. This 1x1km²-raster was made compatible with the PathFinder imagery, by computation of 17 "fraction images" with the acreage distribution of the 17 IGBP-classes (over the 64 1km²-pixels) in each 8x8km²-cell. An additional raster contained the code (1-17) of the predominant class in each 8x8km²-cell (hard classification). Then a fuzzy training set was extracted, valid for the year 1992 and with equal proportions with respect to the dominant class (i.e. for every class, 400 cells were randomly chosen amongst the cells labelled dominant for that class). The training database contained (for each of the 17 x 400 retained cells) the 12 monthly NDVI-averages of the period 1992 and the 2 latitude-variables (input-side), as well as the corresponding acreage fractions of the 17 classes (output-side).

As to the classification algorithm, preference was given to a neural network (NN). An excellent review on this subject is provided by Paola & Schowengerdt (1995). The

NN-classifiers are robust, non-parametric (no assumptions on the distribution of the classes) and fast (as to the application, the training can be quite slow), but on the other hand they do not provide any insight (black-box!) and are very susceptible to over-training, which can result in misleadingly high accuracies. Nevertheless, the NN was selected because it's the only algorithm which can also be calibrated with fuzzy data (as is the case with our training set).

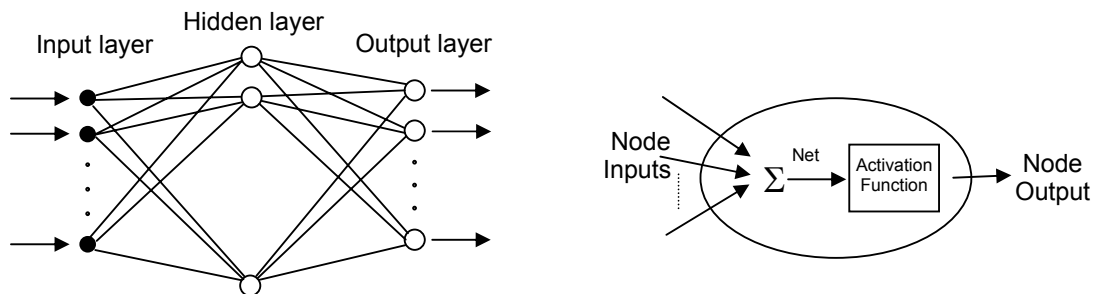


Figure 31: Principles of the Neural Network (adapted from Paola & Schowengerdt, 1995).
 Left: a 3-layer NN-structure (each circle represents a node).
 Right: internal structure of a processing node.

As outlined in figure 31, the basic element of a neural network is the processing node. Each node mimics the biological neurone and performs two functions. First it sums the values of its inputs. This sum is then passed through an activation function (mostly the sigmoid function) to produce the node's output value. The nodes are organized in layers. Each node is fully interconnected with all the nodes in the previous and the following layers, but amongst the nodes of a same layer there are no interconnections. The *input layer* only serves as a distribution structure for the data being presented to the network. No processing is done at this layer. One or more processing layers follow the input layer. The final processing layer is called the *output layer*. Any layers between the input and output layers are termed *hidden layers*. The interconnections between each pair of nodes have an associated weight. When a value is passed down that interconnection, it is multiplied by the weight. These weight values contain the distributed knowledge of the network. Before the NN can be applied in practice ("extrapolation"), these weights have to be assessed from the training data set ("calibration").

In practice, a 3-layer NN was elaborated with 14 nodes in the input layer (12 NDVI's, 2 latitude-variables), 45 nodes in the single hidden layer, and 17 in the output layer (surface fractions of the 17 classes). The net was calibrated with the mentioned training database (valid for the situation around 1992), and then extrapolated on the image sets of the three periods (1987, 1992, 1997). In this way, we obtained for each period a fuzzy classification, i.e. a set of 17 image layers with the estimated acreage proportions.

As usual, these initial surface fractions or class probabilities f_k are still biased and require some adjustments. According to the classical Bayesian approach, one can obtain for each class k a more reliable "aposteriori probability" P_k by multiplying its image-derived probability f_k with an "apriori probability" or specific class weight A_k , whose value has to be defined on the base of external knowledge. For this analysis we developed a new scheme, in which the aprioris A_k of the 17 classes were locally adapted on a per-pixel base and in function of the reference situation of 1992. In practice, for each pixel to be classified an apriori of 50% was assigned to the dominant class in the reference raster of 1992, while the remaining 16 biomes received much lower but equal weights $A_k = 50\%/16 = 3.125\%$. By applying Bayes' rule ($P_k = f_k \cdot A_k$) for each period, three improved fuzzy classifications were established, this time with the aposteriori probabilities P_k of the 17 classes.

At that stage, for each period a hard classification was derived, containing for each pixel the code of the predominant class (i.e. the one with the highest aposteriori probability). And at last, the three resulting biome maps were "upscaled" and converted into a CARAIB-compatible format, in the same way as applied for the USGS reference data (see §3.2.1).

3.2.2.2 *Results and discussion*

Two of the final, hard classifications (1987 and 1997) are shown in figure 32, while the estimated acreage distributions of the land cover classes in the three periods are listed in table XI. Inspection of these results immediately points out that there are no striking differences and that land cover remained nearly stable during this 15-year period. This also proves the stability of the PathFinder data and the robustness of the classification procedure.

This robustness is certainly due to some extent to the adopted scheme for the apriori probabilities, which favoured the true class of 1992. This scheme tuned the decision process in such a way that the classification was based for 50% on the image-information (PathFinder) and for 50% on the previous situation in 1992 (as depicted by the USGS-IGBP-classification). In other words, before a pixel was assigned to another class than the one of 1992, the imagery had to provide quite convincing evidence.

The three hard classifications were also compared with the underlying USGS reference raster of 1992. The agreement (or "accuracy") only amounted to about 75% of the pixels. However this low number should be relativized. Visual comparison shows a fairly good agreement, and an additional analysis with confusion matrices clearly indicated that the large majority of the observed deviations in land cover (on 25% of the pixels) are certainly irrelevant, because they relate to confusions between

very similar classes (e.g. deciduous forest vs. mixed forest, different savannah types, etc.).

We thus conclude that the three biome maps, derived from the PathFinder image set, are certainly useful and that it makes sense to include them in the carbon cycle model CARAIB. Below, we briefly summarize the geographical distribution of the IGBP-biomes, as observed in these classifications.

The **evergreen needleleaf forests**, which are typical for the boreal Taiga zone, count for 5.5 to 5.8% of the total classified land area. They are found in large parts of Scandinavia, Northern Russia, Canada, and some regions of Alaska, spreading south to the Northwest-coast of the United States. They are also found in some high mountain ranges like the Alps, and the Rocky Mountains. The three classifications indicate a slight increase in area of this biome.

Evergreen broadleaf forests are typical for the moist tropical belt. In America they occupy almost the entire Amazon-basin, but they extend as far North as the flat plains of the Yucatan-peninsula in Mexico. Southwards they extend to Paraguay and northern Argentina, while in the west they are limited by the Andes range. At certain altitudes (2000-3000m) this vegetation type forms the so-called 'cloud forest', i.e. the mountain variant of the evergreen tropical forest of the lowlands. It is an extremely interesting forest type because of the species-richness and the high rate of endemism. In Africa the largest evergreen broadleaf forests are found in the Congo basin on both sides of the equator. Some other areas are situated along the coast of the gulf of Guinea, especially in Ghana, Ivory Coast, Liberia and Sierra Leone. In the highlands of Ethiopia and Eastern Madagascar one can find respectively the most northern and southern remnants of the evergreen broadleaf forest of Africa. In Asia, evergreen broadleaf forests are found on the Indonesian islands and on Papua New Guinea, but also on the continent, especially in Myanmar, Thailand, and Vietnam.

The **deciduous needleleaf forests** are mainly situated in northeastern Russia. As to table XI they cover about 2% of the land and showed a slight increase in the last 15 years. But the confusion matrices learn that this type is largely confused with the mixed forest class.

Deciduous broadleaf forests also cover about 2% of the area but they are more spread over the globe. This biome is mainly represented in Europe, the eastern United States, along the west coast of Mexico and in Myanmar.

The **mixed forests** are widespread in northern Russia and Canada, limiting the evergreen needleleaf forests to the South. Their total coverage is $\pm 4.7\%$, but there is a lot of confusion with the other forest types.

Closed shrublands appear almost uniquely in Somalia and East-Ethiopia, and represent less than 1% of the total land cover.

The **open shrublands** are much more common. They cover large parts of central-Australia, the Kalahari region, Somalia, Yemen and the Sahel, as well as the northern border of the Sahara in Morocco and Algeria. In Asia this biome can be seen from Israel, over Iraq, Iran, Pakistan to Mongolia. In the new world open shrublands appear in the western part of the United States, Mexico (including Baja California), on the Altiplano and on the dry west side of the Andes, and in Patagonia. Open shrublands are often found on the border of deserts in the semi-arid regions. According to our classifications there are no major changes in the global extent of the open shrublands ($\pm 12.4\%$). However, an analysis per continent showed that over the last 15 years the surface of this biome slightly increased in Africa (8,5% to 9,3%) and decreased in Australia (from 62,2% to 60,9%).

Woody savannahs represent about 3.4% of the total global land cover, and form the transition from evergreen broadleaf forests to savannahs. They are typical for Africa, but less important zones of this biome also occur in South-America.

As the climate gets drier, the forest canopy cover decreases, trees become smaller and the herbaceous layer gets more developed. This kind of vegetation is well known as the **savannahs**. They are very common in sub-Saharan Africa, occupying 24% of the entire continent (as compared to 7.5% on a global scale). A particular type of the African savannahs is the Miombo, a savannah ecosystem dominated by *Brachistegia*, *Jubelnardia* and *Isobertinia* (Fabaceae-trees). The Miombo extends across ± 2.8 million km² of the southern subhumid tropical zone, from Tanzania and Congo in the north, through Zambia, Malawi and eastern Angola, down to Zimbabwe and Mozambique in the south. In South-America several savannah types (Campos Cerrado, Chaco, Llanos) occur in the rim of the Amazon forest. In Australia, the main savannah areas are situated in the east and the north of the country.

The **grasslands** are mainly found in the Sahel, Central-Asia and in the western United States. Table XI suggests a slight decline: from 6,8% in 1987 to 6,4% in 1997.

Permanent wetlands are rather difficult to classify with low-resolution imagery, because they don't form a well-defined vegetation type but rather an amalgam of ecosystems which are characterized by water-saturated soils all year round, and which can be dominated by herbaceous vegetation but also by forests. As a consequence, large parts of the tundra in northern Russia and Canada were misclassified as permanent wetlands. However, this is not illogical and not explicitly wrong, because the upper layer of the permafrost melts in summer, which results in very swampy soils.

The three "anthropic" biomes together cover about 20% of the global land area: **croplands** (9.3%), **urban & built-up areas** (0.1%), and **cropland & natural vegetation mosaic** (10.1%). Here again, some confusion can not be avoided because we deal with a complex mixture of different elements (vegetation, construction materials, bare soils,...), each with a different spatial extension and spectral behaviour.

In practice, large parts of China and India, the wheat and corn belts in the USA and Canada, as well as the southwestern and southeastern corners of Australia are classified as croplands.

On the other hand, the more densely populated areas such as western Europe, southeastern China, and southeastern Brazil are assigned to the mosaic class. Here, the landscape is highly fragmented with alternating patches of agriculture, pastures and forests.

Snow and ice cover about 10.6% of the land, mainly in the arctic regions (Antarctica, Greenland, Nova-Zembla, Spitsbergen,...) but also in high mountain ranges (glaciers).

Table XI: Acreage distribution of the IGBP land cover classes (with exclusion of water) in the three global classifications derived from the PathFinder data set (five-year periods around 1987, 1992, and 1997) – All values in % of the total land surface.

IGBP Land Cover Class	1987	1992	1997
1. Evergreen needleleaf forests	5.536	5.477	5.820
2. Evergreen broadleaf forests	9.477	9.079	9.689
3. Deciduous needleleaf forests	1.861	2.009	2.015
4. Deciduous broadleaf forests	2.153	2.123	2.258
5. Mixed forests	4.619	4.712	4.676
6. Closed shrublands	0.750	0.831	0.769
7. Open shrublands	12.463	12.439	12.360
8. Woody savannahs	3.361	3.500	3.298
9. Savannahs	7.500	7.621	7.344
10. Grasslands	6.775	6.519	6.421
11. Permanent Wetlands	1.821	1.906	1.789
12. Croplands	9.187	9.587	9.139
13. Urban & built-up	0.100	0.095	0.092
14. Cropland & natural vegetation mosaic	9.943	10.246	10.283
15. Snow & ice	10.618	10.585	10.594
16. Barren or sparsely vegetated	13.834	13.268	13.453
<i>TOTAL LAND</i>	<i>100.000</i>	<i>100.000</i>	<i>100.000</i>

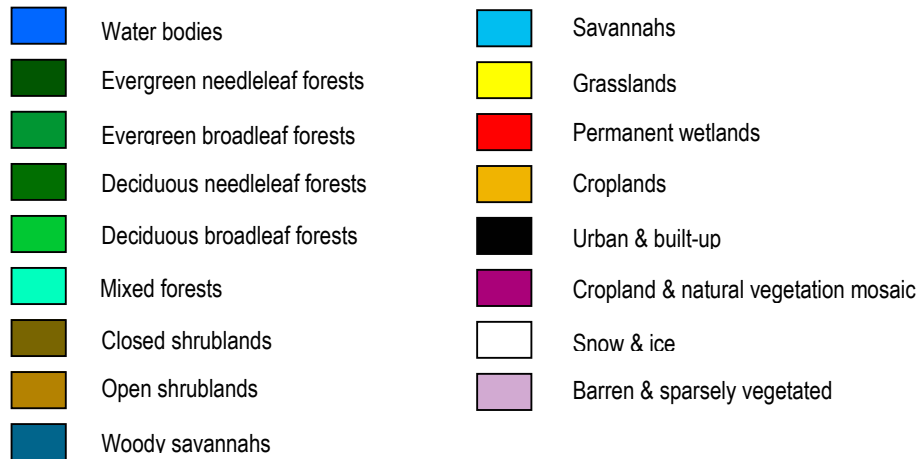
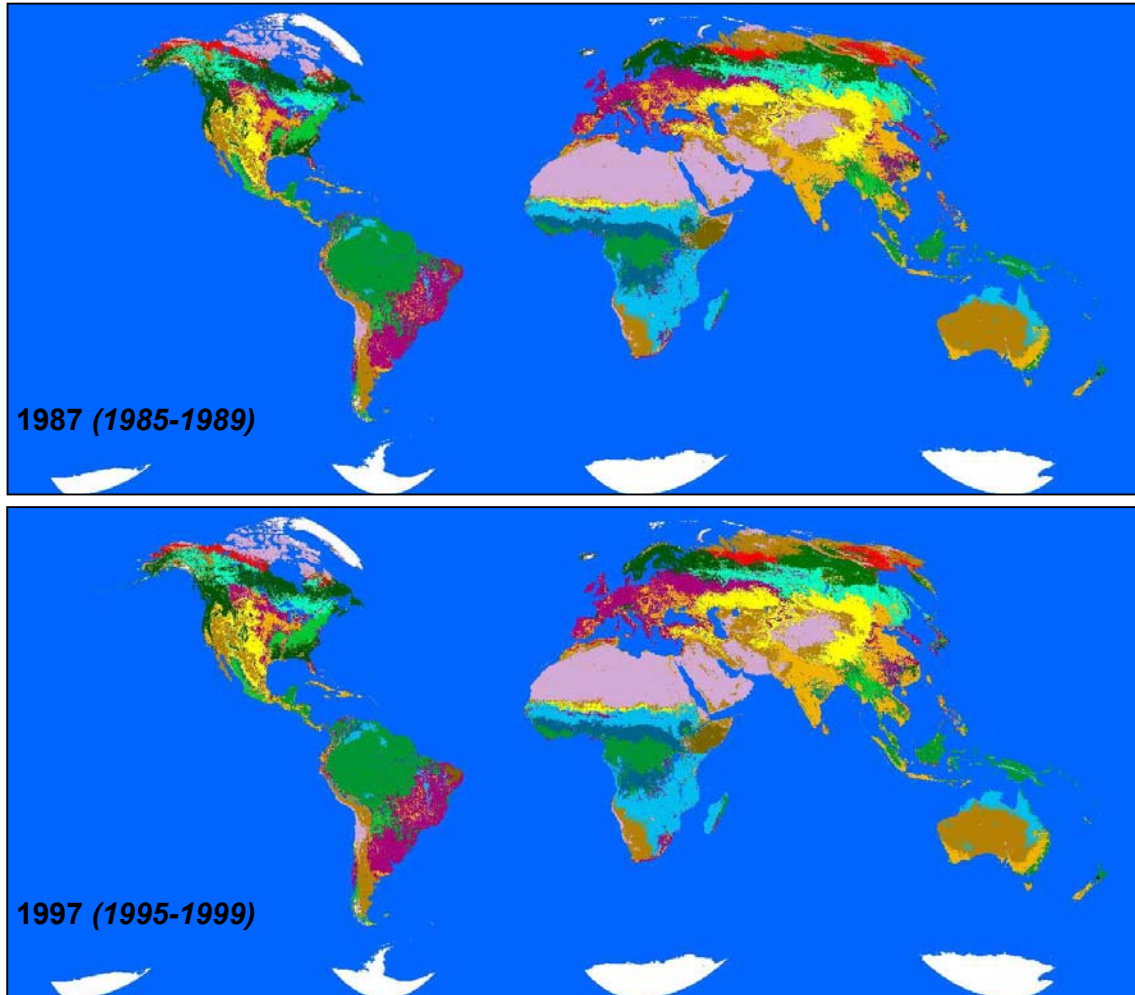


Figure 32: Global IGBP classifications derived from the Pathfinder AVHRR-imagery of two different periods (IGH-projection, $8 \times 8 \text{ km}^2$ -resolution).

The last class, **barren land & sparse vegetation**, covers the about 13.5% of the land. It comprises all deserts, hot (Atacama, Sahara, Namib, Arabia) or cold (Gobi, Tibetan plateau, northern tundra).

3.3 **fAPAR-COMPARISON: CARAIB-PREDICTIONS vs. IMAGE ESTIMATES**

From the very beginning, it was decided to perform the confrontation CARAIB vs. Remote Sensing at the level of *fAPAR* (fraction of Absorbed Photosynthetically Active Radiation – 400-700nm), and not on any other parameter such as LAI, biomass or NPP. For the model, *fAPAR* is a quite important intermediary variable, which correlates well with the amount and the state of the vegetation. From the viewpoint of remote sensing, *fAPAR* is the biophysical parameter which can be retrieved most easily from the imagery.

3.3.1 **Estimation of fAPAR from NDVI**

In literature, much attention has been paid to this subject (see for instance Bartlett et al., 1990). Most authors agree that there is a strong linear relationship between *fAPAR* and NDVI:

$$fAPAR = A + B \cdot NDVI \quad [-]$$

However, difficulties arise with the exact definition of the intercept A and slope B. For instance, Myneni published a number of quite different A/B-sets, all derived from simulation studies. In our first tests, we used the values of Myneni & Williams (1994; A = -0.1426, B = 1.1638), but these apparently resulted in a drastic and world-wide underestimation of *fAPAR*. The reason for this could be revealed by means of a separate study of canopy reflectance models (see §3.4.1.). It's commonly known that the reflectance R of green vegetations is largely determined by the optical parameters of the individual leaves, i.e. leaf reflectance ρ and transmittance τ . But so far most modellers (inclusive Myneni) used monospectral values observed at the absolute extremes of the Red and NIR bands – i.e. very low values for the Red (say at 650nm: $\rho < 5\%$, $\tau < 8\%$) and high ones for the NIR (at 840nm: $\rho > 40\%$, $\tau > 40\%$). At these "pure" Red and NIR wavelengths, the canopy reflectances show large fluctuations and mutual contrast. As a consequence, the NDVI will also show high dynamics with values varying between 0.15 and a maximum of 0.90 or even more. However, recent measurements of Asner et al. (1998) pointed out that for the broad AVHRR-bands more moderate parameter values should be used (e.g. Red: $\rho = 8\%$, $\tau = 15\%$; NIR: $\rho = 35\%$, $\tau = 38\%$). With these broad radiometric values, the simulated canopy reflectances agree far better with the AVHRR-observations and show far less variation and contrast. This explains the relatively low dynamics of the AVHRR-NDVI:

the world-wide maximum NDVI in both global AVHRR image sets (PathFinder and EROS) only balances around 0.75. The Red and NIR-bands of the SPOT-VEGETATION sensor (VGT) are somewhat narrower and better positioned in the spectrum than those of AVHRR. This results in a higher NDVI-dynamics with maxima of about 0.85.

The $fAPAR \approx NDVI$ -relation is thus sensor-specific, but it's quite difficult to reveal reliable parameter values (A,B) via modelling. Therefore, we later adopted the experimental approach of Sellers (1985), where A and B are derived from the position of two points on the line. These points can easily be defined on the NDVI-histograms of a representative sample of pixels. This simple approach (see Eerens at al., 2000c) yielded the following values:

AVHRR: (NDVI=0.16, $fAPAR=0.0$) and (NDVI=0.725, $fAPAR=0.95$) \Rightarrow A = -0.269, B = 1.68
VGT: (NDVI=0.16, $fAPAR=0.0$) and (NDVI=0.775, $fAPAR=0.95$) \Rightarrow A = -0.247, B = 1.54

Figure 33 shows the multi-annual $fAPAR$ -evolution of some selected pixels, as calculated with the above AVHRR-equation from the NDVI-layers of the PathFinder image set.

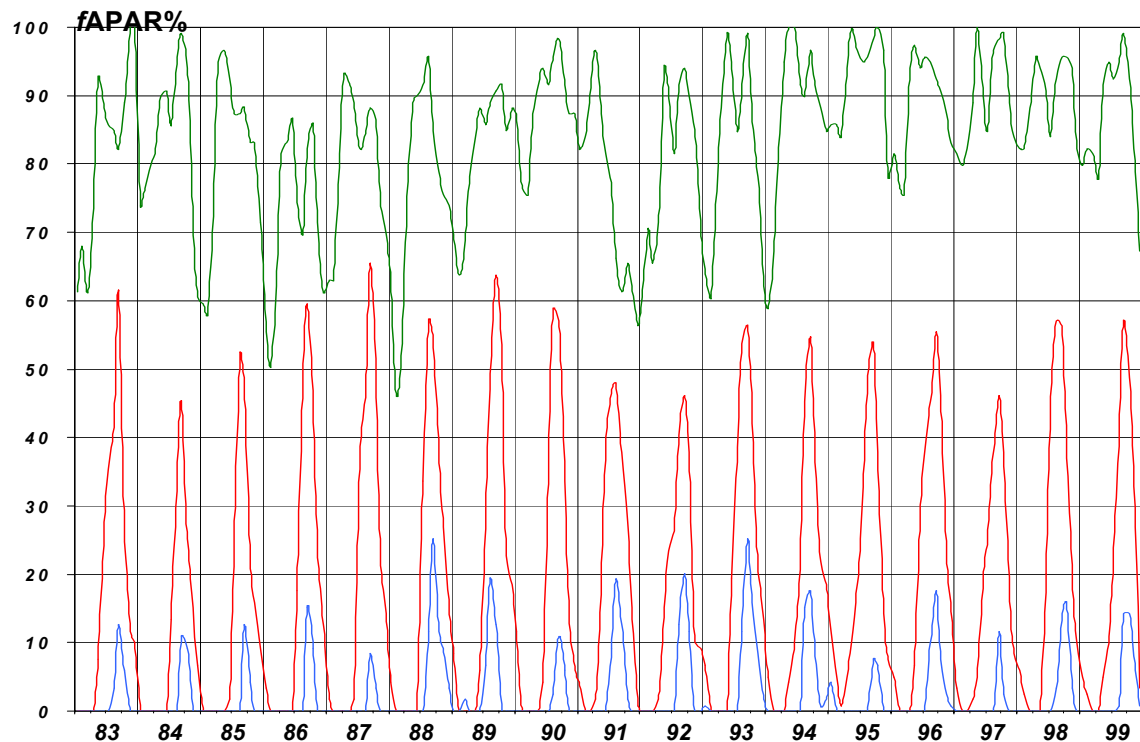


Figure 33: $fAPAR$ time series of three different pixels over the years 1983-1999, derived from the PathFinder AVHRR image set, with the equation: $fAPAR = 1.68 \cdot NDVI - 0.269$. A=evergreen equatorial forest, B=Sahelian open shrubland, C=sparse vegetation (steppe at transition Sahel-Sahara).

3.3.2 *f*APAR-Comparison by means of the EROS Image Set of 1992/3

3.3.2.1 *Methodology*

For this comparison LPAP only provided us with one single data set of CARAIB-predicted *f*APAR's. Unfortunately, it only covered one "standard" year, because the simulations were based on climatological data (long term meteorological averages). A long-term and multi-annual comparison with the PathFinder data was thus excluded. As a consequence, we could only confront the CARAIB-simulations with the *f*APAR's extracted from the EROS image set of 1992/3.

This CARAIB-database contained the 12 monthly *f*APAR-means for each of the 15347 terrestrial 1°x1°-resolution cells discerned by the model. To facilitate the further operations, this database was immediately converted to the normal image format (unprojected Lon/Lat, 1°-resolution, 360 columns x 180 records, 12 image layers with *f*APAR).

As to the part of remote sensing, the 36 global NDVI-mosaics of the EROS data set (see table VII) were first spatially degraded to a resolution of 27x27km² by systematic subsampling. The degraded pictures were then cleaned with the procedure described in §3.1.3.3), which resulted in 12 images with monthly mean NDVI's. These were transformed from the IGH-projection into the unprojected Lon/Lat system and then degraded with a mean filter to the CARAIB-resolution of 1°x1°. Finally, the 12 NDVI-images were converted into *f*APAR-scenes with the AVHRR-equation specified above: $fAPAR = 1.68 \cdot NDVI - 0.269$ (of course, negative *f*APAR's are reset to zero, and values greater than 1 to 1).

In this way, we ended up with two spatially and thematically compatible sets of 12 monthly *f*APAR-images, one derived from the EROS-imagery of 1992/3, the other with model-predicted values.

In order to condense the results, we computed –for both cases– the four images with the seasonal *f*APAR-means, as well as one image with the annual mean. Finally, for each period (4 seasons, 1 year) a "difference image" was computed containing for each land pixel the result of the operation $fAPAR\%(CARAIB) - fAPAR\%(AVHRR)$. The difference images of the summer and winter months are shown in figure 34, while the relative distributions of all five difference images are listed in table XII. The values of this difference operator are of course limited to the range –100% (CARAIB-predictions lower than the image estimates) to +100% (higher). Obviously, we hope that the majority of pixels are situated in the middle group (with a negligible difference of only ±5%).

In another comparison, both image sets with monthly *f*APAR's were further degraded with a mean filter to 5°x5° resolution. Figure 14 shows the CARAIB- and image-derived *f*APAR-values along the meridian of 27.5° East (from South Africa to Finland), for the months of January and July and for the entire year (April 92 - March 93). For 4 pixels along this transect, the monthly *f*APAR-profiles according to both methods are presented at the bottom of the same figure 35.

3.3.2.2 *Results and discussion*

Obviously both approaches have their drawbacks and limitations. The final AVHRR-images are the result of a large number of often complex procedures, (calibration, atmo-/geo-correction, cloud removal, *f*APAR-estimation, ...) which all may introduce some errors. Also the upscaling (data degradation from 1x1km² to 1°x1°) might have biased the results. As to the modelling side, like all man-made models CARAIB is only a rude simplification of reality, which merely aims to provide general insights in the mechanisms of carbon fixation. Moreover, the actual exercise is a bit hampered because we have to compare a specific year of images (April 92 – March 93) with model-predictions valid for a climatological year. As a consequence, this analysis should not be considered as a real validation but rather as a simple comparison.

Whatever be, the inspection of the above-mentioned results brings about the following observations:

According to figure 34 and table XII, the CARAIB-predictions are in general higher than the image-derived *f*APAR-values. There are however some geographical and temporal tendencies.

In barren regions without vegetation (deserts, poles) both methods correctly retrieve *f*APAR=0%, such that the correspondence is perfect.

Very important discrepancies (CARAIB >> AVHRR) occur at higher latitudes during the winter months. This is probably due to the twilight regime (very low levels of solar irradiance) which rules out all possibilities for remote sensing (hence *f*APAR=NDVI=0), but not for photosynthesis (CARAIB: *f*APAR>0).

In these situations, the image-derived *f*APAR-values thus systematically underestimate reality. Note that during summer (more light) the discrepancies in these regions are much more moderate.

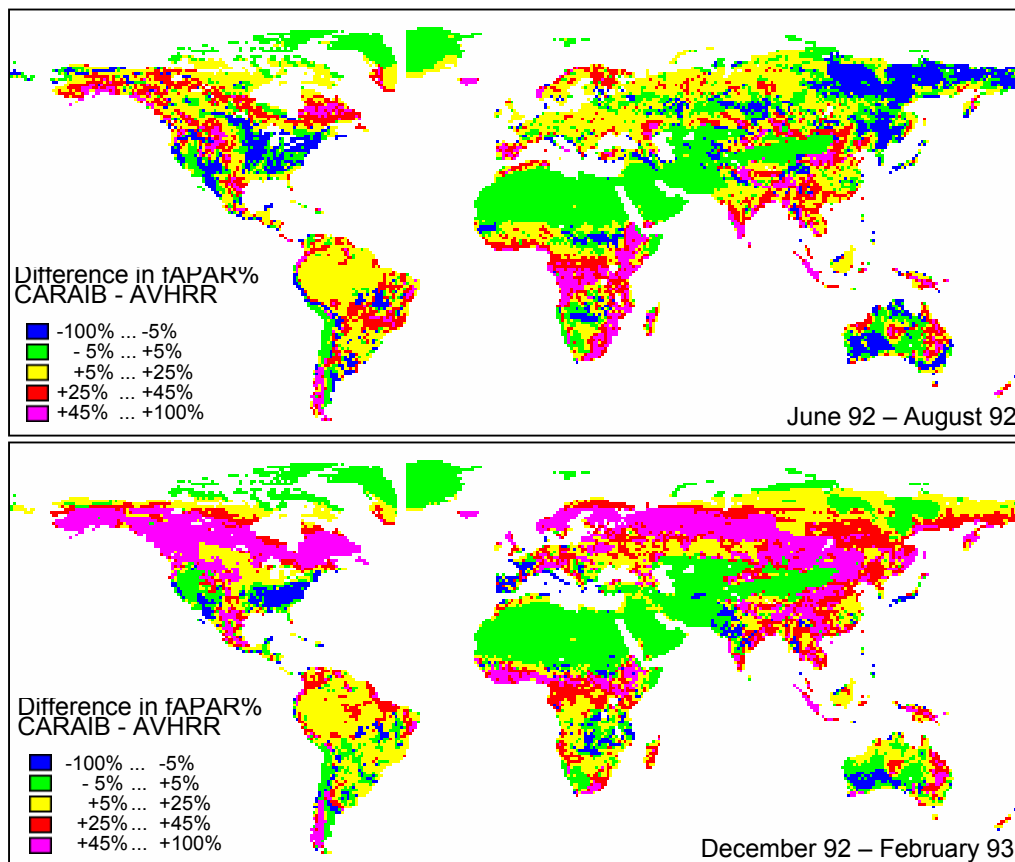


Figure 34: Absolute difference between the fAPAR-values (always in %), predicted by the CARAIB-model and observed from the EROS-AVHRR imagery of 1992/3. Mean values for the summer and the winter of 1992/3, reclassified in 5 broad difference classes.

Table XII: Relative distribution amongst the land pixels (=100%) of the difference between the fAPAR's, predicted by the CARAIB-model and observed from the EROS-AVHRR imagery of 1992/3. Values (in %) for the entire year and for each of the 4 seasons.

Difference fAPAR% CARAIB–AVHRR	Year June-May	Summer June-Aug	Autumn Sep-Nov	Winter Dec-Feb	Spring Mar-May
–100% ... –85%	0.000	0.000	0.000	0.000	0.000
–85% ... –65%	0.007	0.020	0.002	0.005	0.003
–65% ... –45%	0.154	0.330	0.023	0.020	0.242
–45% ... –25%	0.885	0.784	0.812	1.534	0.412
–25% ... –5%	6.881	10.549	7.346	4.321	5.307
–5% ... +5%	27.105	23.177	20.179	23.921	41.144
+5% ... +25%	34.553	24.772	40.427	45.225	27.789
+25% ... +45%	20.884	34.060	20.375	13.819	15.281
+45% ... +65%	6.218	4.040	7.968	6.418	6.444
+65% ... +85%	3.129	2.261	2.860	4.171	3.225
+85% ... +100%	0.183	0.006	0.009	0.565	0.153

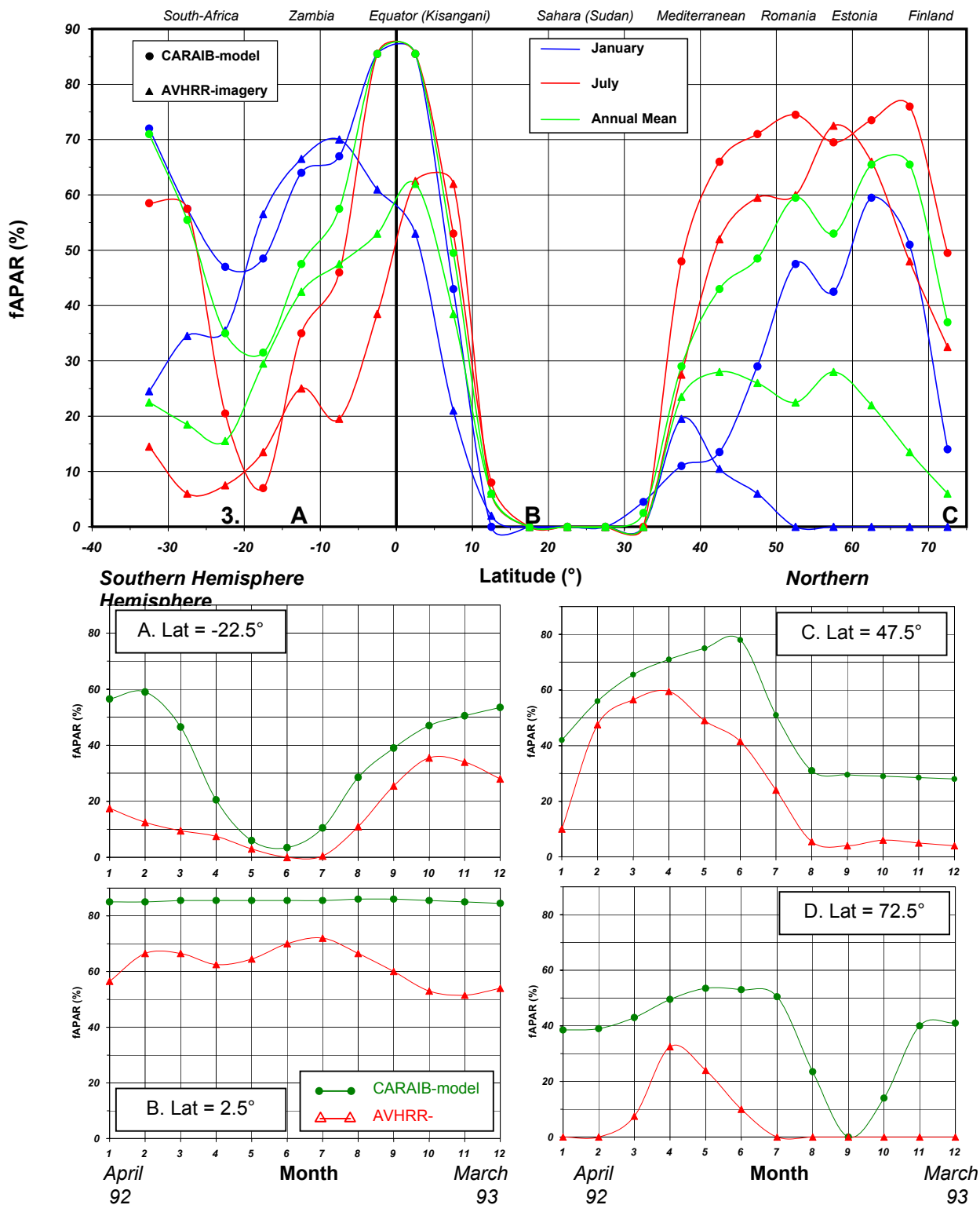


Figure 35: Comparison of fAPAR-values, upscaled to 5°x5°-resolution cells, predicted by the CARAIB-model and extracted from the EROS-AVHRR data set (year: April92-March93). **Top:** South-North transect along the meridian of 27.5° East, from South Africa to Finland, showing the fAPAR-values in 3 different periods (July 92, January 93, entire year 1992/3). **Bottom:** Monthly fAPAR-profiles for 4 selected 5°x5°-cells (A-D) at different latitudes along the same transect (the 4 positions A-D are also indicated in the top figure).

In mid-latitude and equatorial regions where the above image artefact doesn't play, the $fAPAR$ -difference between CARAIB and AVHRR clearly augments with the amount of vegetation. In this case, we believe it is rather the model which overestimates the true (green) $fAPAR$. The carbon assimilation module of CARAIB assumes the real vegetation is composed of one single layer of green leaves. This might be appropriate for agricultural crops but not for tropical forests, where a significant fraction of the PAR-radiation is lost to non-productive components such as stems and branches.

For some exceptional regions (SE-USA, California, SW-Australia,...) CARAIB yields throughout the year lower $fAPAR$ -values than AVHRR. This might be due to errors in the land cover map used by the model (e.g. overestimation of the desert class).

In spite of the significant differences in $fAPAR$, the agreement is certainly much better at the phenological level (see for instance the 4 graphs at the bottom of figure 35). As to the length and the phasing in time of the growing seasons, there is in general a fairly good correspondence between both approaches (CARAIB, AVHRR).

In summary, we see two main sources of error, the first related to remote sensing (boreal regions in winter), the other to the modelling of the radiation flux (and $fAPAR$) in multi-layered vegetations (forests). In future developments, both teams involved in this research (Vito, LPAP) will try to adapt their methodologies in order to solve these problems.

3.4 ADDITIONAL STUDIES

This section briefly describes the additional studies which were performed in parallel to the current project. More information on these studies can be found in the mentioned references.

3.4.1 *Extension of the Canopy Reflectance Model SAIL*

SAIL (Scattering by Arbitrarily Inclined Leaves) is a 1-dimensional model which predicts the shortwave reflectance behaviour of homogeneous vegetations (Verhoef, 1984, 1998). The model is widely used in the remote sensing world, especially for agricultural crops, and nearly always in its elementary form. In that case, the vegetation is considered as being built up only by green leaves (1 component), distributed in a uniform way (in vertical and azimuthal sense) over one single layer, which is delimited on top by the sky and at the bottom by the soil. For this elementary form, the following 10 input-parameters are required: the angles describing the position of the sun (θ_s , φ_s) and sensor (θ_v , φ_v), the leaf area index LAI, the leaf zenith

angle distribution LAD, the optical parameters of the leaves (reflectance ρ , transmittance τ), the reflectance of the soil background σ , and the contribution P of the direct sunlight in the global irradiance. The model then provides a full description of the radiation fluxes throughout the canopy, inclusive the BRDF (Bidirectional Reflectance Distribution Function) at the top. In this project, we developed an extended SAIL-version with the following characteristics:

- Output is simultaneously retrieved for the 3 spectral bands, relevant for our specific purpose: Red, NIR (remote sensing observations) and PAR (photosynthesis).
- For the Red and NIR-reflectance bands, the model now deals with the "hot spot" effect, i.e. the (experimentally observed) phenomenon by which the reflectance shows an abrupt maximum in the backscatter direction ($\theta_v = \theta_s$, $\varphi_v = \varphi_s$).
- The new SAIL-version can take into account the presence of different vegetation layers (e.g. lower, medium, upper stratum), each comprising different components (e.g. green leaves, dead leaves, stems,...). This approach multiplies the number of input-parameters and excludes a full inversion, but it explains a lot of experimental observations, unpredicted by the classical models. For instance the unexpectedly low NIR-reflectance of forests (due to black stems/branches) or the odd behaviour of crops in the ripening stage (mixture of green and yellow leaves).
- The extended SAIL-version now also provides a full bookkeeping of the $fAPAR$, i.e. the fractions of PAR-radiation, absorbed by the soil and by the different layers/components. Logically, only the $fAPAR$ of the green components contributes to photosynthesis. Depending on the canopy composition, significant fractions of the overall $fAPAR$ are indeed lost to non-active components (stems, dead leaves, and soil). Some simulations pointed out that the relation $fAPAR \approx NDVI$ is less linear than often presumed, and certainly dependent on canopy composition and soil background.
- At last, also the gross carbon assimilation or GPP (gross primary production) of the canopy can be retrieved. Therefore, one also has to specify (for each component) the radiation use efficiency and maximum assimilation rate. To this goal, we incorporated the assimilation principles of the crop growth model SUCROS/WOFOST (Spitters et al., 1989) into the SAIL-model. These equations take into account the non-linear response of carbon uptake to

green $fAPAR$, the variation of $fAPAR$ with the depth in the canopy, and the presence of directly illuminated sunflecks.

All the above extensions were merged into a single general-purpose program subroutine, which can be used to improve existing production models (WOFOST, CARAIB,...) or to perform sensitivity analyses.

3.4.2 Analysis of AVHRR-Signals over the EUROFLUX Forest Site in Brasschaat

Reference: Gond et al. (1999)

Our own-developed AVHRR-chain (see §3.1.1.1) was used to pre-process about 100 raw AVHRR-scenes over Western Europe. These images were registered in the course of 1996/7 by the antenna of DLR in Oberpfaffenhofen. The geometric corrections were performed with about 30 (manually indicated) control points per scene, and resulted in a multitemporal, 1km²-resolution image set over Belgium in the IGH-projection. The quasi-perfect match of the individual layers confirmed the sub-pixel accuracy of the geo-rectification. The necessary inputs for the atmospheric correction (SMAC) were obtained from the Royal Meteorological Institute in Brussels: total ozone was derived from Brewer measurements, water vapour from balloon soundings, but for the aerosol optical depth a fixed “clear sky” value was used ($\tau_{550nm}=0.2$). Our initial attempt to use the (spatially interpolated) horizontal visibilities measured at 15 weather stations, did not yield the expected results. In the resulting image set one can inspect the multitemporal profiles of the ‘top of canopy’ reflectances and NDVI for each 1km²-pixel in Belgium.

This study actually focused on the EUROFLUX site of Brasschaat. In this pine/oak forest, a lot of measurements were executed (by other teams) in 1997, for instance: species composition, LAI and chlorophyll content per species, etc. The overall reflectance behaviour of the forest was estimated by means of an upscaling approach, in which the collected field data were input to the coupled models PROSPECT (leaf reflectance) and SAIL (canopy reflectance). This analysis thus also retrieved the multitemporal NDVI-evolution of the forest as a whole. A comparison study pointed out that this upscaled time series agreed fairly well with the NDVI-profile of the Brasschaat-pixel in the pre-processed AVHRR-imagery of 1997.

3.4.3 DAIS Hyperspectral Imagery over the EUROFLUX Forest Site in Brasschaat

Reference: Debruyn et al.(1999)

On July, 20, 1998, the airborne, hyperspectral sensor DAIS was flown over the wide surroundings of the same experimental forest of Brasschaat. We also participated in the preparation and execution of this campaign, as well as in the analysis of the 5m-resolution imagery set (10 tracks, 79 bands). The imagery was geometrically rectified and atmospherically corrected by means of ground reflectances, measured (with a portable LICOR spectrometer) during the DAIS-overflight on three reference targets (15mx15m sheets with different colours). On the base of the multi-angular image registrations, the BRDF of some cover land types could be reconstructed.

3.4.4 Estimation of the Carbon Balance of Terrestrial Vegetations (C-Fix model)

Reference: Sabbe et al. (1999)

Assimilation of atmospheric carbon by terrestrial ecosystems is driven by photosynthesis. However, part of this gross uptake is re-emitted by autotrophic and heterotrophic (soil) respiration. Depending on the flux balance between uptake and release, vegetations can act as carbon sinks or sources. The reliable quantification of this balance is one of the main scientific challenges within the context of global warming. The C-Fix procedure, developed by Veroustraete et al. (1996) combines the elementary model of Monteith (1972) with remotely sensed imagery and easily obtainable meteorological inputs (solar irradiance, temperature on a daily base), to estimate the temporal evolution and geographical distribution of the relevant carbon flux parameters.

Assistance was provided on behalf of this C-Fix project, at several levels: re-designing of the software, improvement of the spatial interpolation technique, delivery of the fully corrected *f*APAR-imagery over Europe and Africa for the years 1992 (AVHRR) and 1998 (VGT), etc.

3.4.5 Crop Yield Forecasting with 1km²-Resolution Imagery (AVHRR, VGT)

Reference: Eerens et al. (2000b, 2000c)

This B-CGMS project was performed in collaboration with FUL (Fondation Universitaire Luxembourgeoise-Arlon) and CRA (Centre de Recherches Agronomiques-Gembloux), and it tried to adapt the EU Crop Growth Monitoring System to Belgian conditions. This CGMS is a model-based tool to predict the yields

of the main crops. Our task consisted in the improvement of the forecasts by means of 1km²-resolution imagery. In practice, the analysis was based on 4 years of AHVRR-images, pre-processed by the Space-software of the EU-JRC, and on 2 years of VGT-data.

By application of a linear unmixing technique on a regional base, the mixed 1km²-measurements were at first unraveled into the pure NDVI-responses of the individual crops. The required knowledge on the surface fractions of each crop, were extracted from the SIGEC-system of the Ministry of Agriculture (yearly updated vectorial map with all parcels in the country). The multitemporal NDVI-data were then converted to crop-specific fAPAR-profiles. Daily dry matter productions (per region x crop) were then assessed by means of the approach of Monteith (1972) which combines the fAPAR-data with elementary meteorological information (irradiance, temperature). By accumulating these daily productions over certain periods (months, phenological stages), one obtains useful yield indicators, which indeed have a significant contribution to the yield forecasting. The procedure was calibrated and validated with official yield statistics.

3.4.6 Global Biome Classification

Reference: Canters et al. (1998a, 1998b).

This collaboration with VUB (Vrije Universiteit Brussel) aims at the development of improved strategies for the production of global land cover maps with the 1km²-resolution imagery of NOAA-AVHRR and/or SPOT-VGT. The first phase of the project only used AVHRR-imagery and focused on Africa. Particular attention was paid to the optimization of phenology-based classification techniques ('hard' and 'soft'), and on the development of methods for the removal of areal bias present in coarse-scale estimates of biome proportions. In the currently running second phase of the project, the AVHRR-imagery is substituted by VGT-data and the classifications are extended over the globe. The main improvements are situated in the incorporation of a dedicated data reduction chain (indispensable for global mapping at 1km²- see §3.1.3.3), and in the estimation of sub-pixel acreage proportions of the considered classes. This however requires a preliminary calibration with high-resolution classifications.

3.4.7 A new Vegetation Map of Central Africa, derived from VGT-imagery of 1998

Reference: Eerens et al. (1999, 2000a).

On behalf of METAFRO InfoSys, the on-line information system of the Royal Museum of Central Africa (Tervuren, Belgium), a new vegetation map of Central Africa was produced, valid for the year 1998 and covering 10 general land cover classes. The map was derived from a full year cycle of 10-daily syntheses of SPOT4-VGT. The image pre-processing included the following operations: elimination of the cloud perturbations, extraction of time series with the Soil Adjusted Vegetation Index (SAVI), and computation of images with more informative phenological variables such as the annual SAVI-mean, the annual SAVI-extremes, a seasonality index and the length of the growing season.

The new vegetation map was realized by applying a Maximum Likelihood classifier on this set of phenological images. The algorithm was calibrated with ground truth extracted from the well-known JRC TREES-map which depicts the land cover situation around the year 1992 (Mayaux et al., 1997). The a priori probabilities were tuned in such a way, that the classification was based for 50% on the situation in 1992 (TREES) and for 50% on the image-derived phenological information of 1998. In this light, the present map should not be considered as a "new", stand-alone product but rather as an update of the JRC TREES-map.

The updated map was incorporated in a GIS, plotted on A0-sheets on a scale of 1/4 000 000, and tables were derived with the national and regional land cover statistics for both years (TREES 1992, Update 1998). The correspondence between both years amounts to 89%. Although part of the deviations observed on the remaining 11% of the area are probably due to mis-classifications, a lot of deforestation "hot spots" are manifested which deserve further inspection, either by field controls or by the analysis of high resolution imagery.

3.5 CONCLUSIONS

As to the contribution of remote sensing, it must be admitted that the initial targets could only be achieved in a partial way. We indeed delivered a number of image-derived land cover maps, even at the global scale, but so far they couldn't be incorporated into the CARAIB-model (as a substitute for the Henderson-Sellers map). The CARAIB-validation, which consisted in the comparison of model-predicted and image-derived *f*APAR-values, had to be restricted to the EROS-data set of 1992. Unfortunately, a more stringent multi-annual comparison with the PathFinder imagery

couldn't be performed, partly because this data set was acquired too late in the project.

On the other hand it can't be denied that the initial targets were a bit unrealistic, especially with regard to the global coverage of the image data. Around the start of the project (March 1997), it was nearly inconceivable that one had to acquire, store and process such huge amounts of data (330 Gb per year!). As a consequence, we permanently had to struggle with new (and mostly unforeseeable) technical problems. This also explains why far less attention could be devoted to the (maybe more relevant) thematic aspects of the research.

On the positive side of the balance, four groups of achievements can be discerned:

- We now master most of the links in the processing chain of low-resolution image data: the pre-processing of individual registrations, the compositing and creation of global mosaics, and the further enhancements. The "enhancements" mainly comprise the elimination of cloud perturbations and the extraction of phenological or biophysical information (e.g. length of the growing season, *f*APAR,...).
- Much experience was acquired in the fields of image classification and global land cover mapping. This experience concerns many different aspects: biome legends and reference data sets, classification algorithms, training and application modes (unsupervised/supervised, hard/fuzzy), post-classification enhancements (filtering, combination classification + segmentation), upscaling issues, GIS-integration, etc.
- Another group of applications tries to assess the productivity of vegetations by combining image-derived *f*APAR information with solar irradiance and temperature data (Monteith approach). The main activity here consisted in the development and validation of image-based crop yield indicators. Besides, we also assisted in the C-Fix project, which rather deals with natural vegetations. At this level, we also mention the development of an extended version of the reflectance model SAIL. This version copes with multi-layer and multi-component vegetations, and it simultaneously retrieves the BRDF in the Red and NIR bands (remote sensing) as well as the *f*APAR and dry matter productions (growth and productivity models).
- The data reduction procedure, described in § 3.1.3.3) and developed in the course of the project, is quite unique. Without significant losses, the disk size of the global MVC-composites is first reduced from about 330 Gb/year to 30 Gb/year. All the above-mentioned procedures (enhancements, classification,

productivity assessment) can directly be applied on this more manageable data set – yet still on a global scale. To our opinion, this data reduction scheme is even a "conditio sine qua non" for the future implementation of global-scale procedures for the extraction of vegetation parameters (LAI, $fAPAR$, soil cover) which are no longer based on the NDVI but rather on a combination of all the available spectral, temporal and angular information.

Thanks to the research activities performed in the frame of this project, Vito is now better armed than before (at all levels: storage capacity, procedures, software,...) for the analysis and interpretation of global scale earth observation data.

4. CONTRIBUTION OF OCEANIC PROCESSES TO THE GLOBAL CARBON CYCLE

Introduction

According to the IPCC report of 1995, the anthropogenic flux of CO₂ to the atmosphere represented $7.1 \pm 1.1 \text{ GtC.yr}^{-1}$ in the early nineties of which $2.0 \pm 0.8 \text{ GtC}$ was annually transferred to the ocean. This transfer is partly related to the marine primary production which transforms CO₂ into organic carbon in the surface waters depending on the supply of sunlit and nutrients. Total primary production can be partitioned into two fractions:

- a) the recycled production supported by nutrients released in the euphotic zone by remineralization of organic matter
- b) the new production supported by nutrients entering the euphotic zone primarily from the deep ocean, but also from the atmosphere and from land in the coastal zone.

The biological carbon pump is thus the process by which carbon from the ocean surface layer is removed as organic matter and settled to the deeper water, reducing the total carbon dioxide in the surface layer. It is estimated that this biological pump contribute to a flux around 1 GtC.yr^{-1} . The settling carbon may be remineralized at depth except a small fraction which may be deposited and buried in the sediments. Considering the properties of the general circulation model (GCM) of the ocean, one may assume that carbon transferred below 500 m depth, will not be restored to the surface ocean before several hundred years and can thus be considered as scavenged at this time scale.

In the open ocean, the primary production is low due to the reduced vertical mixing which transfers only limited amounts of nutrients from the deep water to the euphotic zone. Under nutrient depleted conditions, the phytoplankton produced is small and the food web long; most of the primary production (80-90%) is recycled and a small fraction only is settling to deeper waters. As a consequence, the open ocean contributes only slightly to the biological pump. On the contrary, the global pattern of primary production suggests that the largest values of the marine production are found along the continental margins, resulting from coastal upwelling and vertical mixing at the shelf break. The 1995 IPCC report recognized that *“the contribution of continental margins to global estimates of total export oceanic production, may not have been properly estimated”*.

This is largely due to the widespread heterogeneities of the margins and to the strong seasonality of the processes responsible for the transfer of nutrients from the deep ocean to the shelf break.

The first step of our research was to collect the recent data published in the literature which could allow to evaluate more precisely the relative importance of the continental margins in the global ocean carbon cycle. A synthesis of the existing data concerning both the total production and new production for the shelf area will be presented and compared to those of the open ocean. The second goal of our project was to develop a coupled 1-D hydrodynamical/ecological model describing the carbon fluxes in the area of the Gulf of Biscay, where previous field work was conducted by our group (contract n°GC/11/009) This research provided many profiles of physical, chemical and biological parameters of importance in the description of the carbon cycle. Furthermore, experiments were conducted in order to determine the influence of basic parameters on primary production and new production in the same area. These measurements were extended during opportunity cruises during the present research contract. The final objective of this approach was to provide a model which could be applied to similar situations at a global scale and to allow a better evaluation of the biological carbon pump at the boundaries of the open ocean.

4.2 Relative importance of the coastal zone in the global ocean carbon cycle

It is a well-established fact, that the coastal zone is characterized by a high primary productivity as compared to that of the open ocean (Berger et al., 1989; Walsh, 1991; Wollast, 1991). It is also recognized that the new production and thus the export production, is larger on the shelf than in the pelagic zone (Berger et al., 1989). This area contributes thus significantly to the biological pump in the ocean and a better quantification of the fluxes is required to decrease the existing uncertainties in the role of the ocean as an atmospheric CO₂ sink at the present time (IPCC, 1995). There are mainly two sources of discrepancies in the evaluation of the role of the coastal zone. The first are the input fluxes of nutrients from various sources which, compared to the recycling fluxes, defines the f-ratio (fraction of new production versus total production). The other subject of controversies is the fate of the new production which is partly preserved by burial in the sediments and partly exported across the shelf break, to the slope and open ocean.

Besides light, which is the main factor controlling photosynthesis, primary production in oceanic systems is most often limited by the availability of nutrients. The input flux of nutrients in the euphotic zone is thus a basic parameter which can be used to evaluate the potential photosynthetic capacity of the system. It is, however, important to keep in mind that a significant fraction of the primary production is fuelled by

nutrients recycled in the euphotic zone by remineralization of organic matter. The new production is related to nutrient input at the boundaries of the system. The nutrient fluxes in the coastal ocean are very complex and include river discharge, wet and dry atmospheric deposition, diagenetic processes in the sediments and transfer of deep ocean water across the shelf break by upwelling or vertical mixing. It is the importance of these various fluxes which controls the relative fertility of the shelf compared to the open ocean. The nutrient fluxes at the boundaries of the coastal zone are also responsible for the high values of new production versus recycled production and thus for the ability of the shelf seas to export organic carbon to the open ocean. Our discussion will be limited here to the nitrogen fluxes because this element is probably the limiting nutrient in most parts of the ocean. Nitrogen is also an interesting element because, in the open ocean at least, ammonia is the nitrogen species resulting from the respiration of organic matter. In the absence of nitrification in the euphotic zone, it might serve as a tracer to evaluate the recycled production. In contrast, nitrate provided by deep water to the photic zones sustains the new production. As indicated previously, the nitrogen cycle is in fact complicated. N_2 can be fixed by specialized organisms in systems highly depleted in nutrients. Oxidation of ammonia to nitrate can occur in surface waters and compete with phytoplankton uptake. Nitrate can be used by denitrifying bacteria and transformed into N_2 under anoxic conditions, mainly occurring in the sediments. Finally, phytoplankton can use some dissolved organic nitrogen compound as N nutrient source. Unfortunately, most of these processes are enhanced in the coastal zone and complicate the interpretation of the data. Thus there are large uncertainties associated with the fluxes related to these processes. We have attempted to quantify the global N cycle for the coastal zone, based on the C cycle and on existing reviews of the processes affecting nitrogen fluxes at the boundaries (Wollast, 1991 and 1998). The nitrogen fluxes associated with planktonic activity can be easily evaluated from the carbon fluxes by imposing the classical Redfield ratio. We have assumed that the composition of the phytoplankton and that of the detrital organic matter in the euphotic zone is similar and constant (C:N = 6.6). The nitrogen fluxes required to sustain total primary production and new production are then easily calculated, as well as the deposition flux to the sediments and the export of organic particulate N to the open ocean (Table XIII and Figure 36). The present day river input has been carefully estimated by Meybeck (1993) and the atmospheric deposition evaluated by GESAMP (1989). The latter values show that the continental inputs, through either river discharge or atmospheric deposition, are totally insufficient to maintain the nitrogen requirements of the planktonic activity. There is in addition, a consensus concerning the low capacity of nitrogen fixation in the coastal zone where the concentrations of ammonia or nitrate are rarely sufficiently exhausted.

There are, in contrast, large disagreements in the literature concerning the importance of the import flux of N from the open ocean and the denitrifying activity in the coastal sediments. In figure 1 the evaluation of the denitrification flux is based on model calculations which take into account the rate of deposition of organic matter as the main controlling factor (Wollast, 1998). The model indicates that about 20% of the N deposited is lost as N₂ by denitrification, most of the depositional flux being recycled as NO₃ and NH₄ and restored to the water column. Only a negligible fraction of N is stored in the sediments by burial. This figure shows the important role of the coupling of pelagic and benthic biological processes on the shelf in the N cycle. In the budget shown in figure 36., the input flux of N nutrients was calculated to fulfil the mass balance requirements for the N cycle.

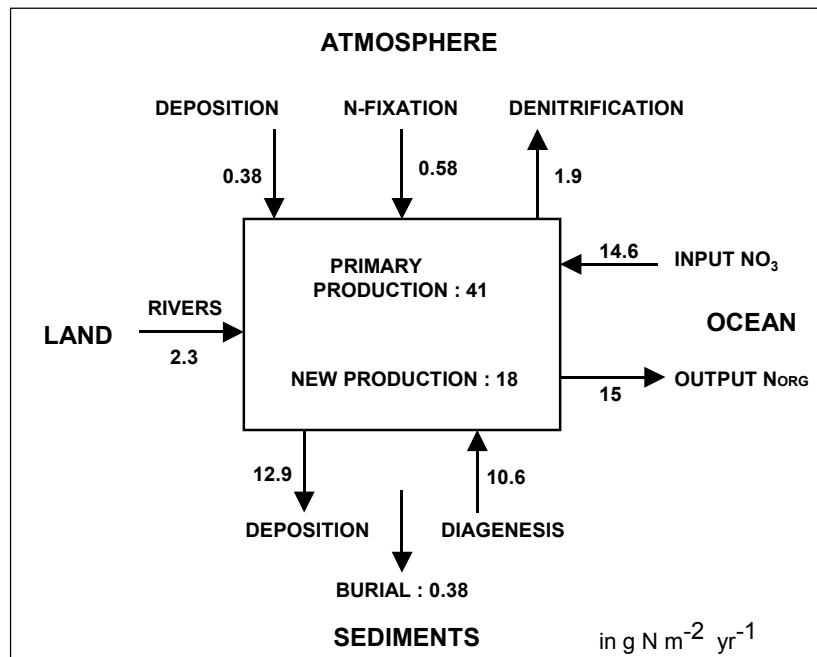


Figure 36: Global mean fluxes of nitrogen in the coastal zone.

Table XIII: Averaged fluxes of nitrogen (in $\text{g N m}^{-2} \text{yr}^{-1}$) in the coastal zone.

	Walsh (1991) Global	Wollast (1998) Global	Howarth (1996) North Atlantic
Primary production	40	41	57
New production	22	18	29
River discharge	2.3	2.3	1.6
Atmospheric deposition	-	0.38	0.32
N fixation	-	0.58	0.05
N burial	-	0.38	0.29
Denitrification	1.9	1.9	3.4
Offshore export	22	15	neg.
Deep ocean water input	21	14.6	5

Walsh (1991) did a similar exercise but attempted to estimate the N fluxes from the deep ocean to the shelf, by distinguishing and assessing the transfer due to various physical processes. His global budget is thus based on areas dominated by upwelling, western boundary currents and estuarine circulation where fresh water input occurs. These estimates are however affected by a large degree of uncertainty due to the variability of the physical processes involved. Walsh (1991) estimated a global N input flux from the ocean across the shelf break of about $560 \times 10^{12} \text{ g N yr}^{-1}$ (or $21 \text{ g N m}^{-2} \text{ yr}$) and assumed that there is no significant accumulation of N in the sediments. To fulfil the mass balance constraints for N, the input is compensated by export of organic N both as particulate and dissolved species. Considering the fact that the value of Walsh (1991) for primary production on the shelf is similar to ours and corresponds to an uptake of $40 \text{ g N m}^{-2} \text{ yr}^{-1}$ Walsh assumes that the f-ratio is 0.52, a value in the upper range of the observations. Even if there are differences in the absolute values, they agree with ours in a sense that the new production and productivity of the coastal zone are mainly supported by the transfer of nutrients from the open ocean. The river input and atmospheric deposition, further enhanced by anthropogenic activities, are secondary sources for the shelf, which are roughly compensated by denitrification and N burial in the sediments.

An attempt to establish a detailed nitrogen cycle in the North Atlantic has been published recently in a special issue of Biogeochemistry (Howarth, 1996). The authors first estimate that the rivers carry an equivalent of $3.55 \text{ g N m}^{-2} \text{ yr}^{-1}$ but that a large fraction of the nitrogen is lost by denitrification in the estuaries and thus only $1.6 \text{ g N m}^{-2} \text{ yr}^{-1}$ reaches the coastal zone (Table XIII.). Atmospheric deposition ($0.32 \text{ g N m}^{-2} \text{ yr}^{-1}$)

$\text{m}^2 \text{yr}^{-1}$) is very similar to our global estimate, but Howarth (1996) assume that the nitrogen fixation is negligible ($0.05 \text{ g N m}^{-2} \text{ yr}^{-1}$). Burial on the shelf and slope ($0.29 \text{ g N m}^{-2} \text{ yr}^{-1}$) is similar to our global mean but denitrification in the sediment is equivalent to a loss of $3.4 \text{ g N m}^{-2} \text{ yr}^{-1}$, almost twice our value. The authors have based this value on a model and recognize that the denitrification flux is high compared to the experimental observations of Seitzinger and Giblin (in Howarth, 1996). Export of organic nitrogen from the shelf to the open ocean is considered by the authors as negligible ($< 2\%$ of the primary production), mainly based on the results of the SEEP experiment (Anderson *et al.*, 1994). An interesting paragraph in the review is devoted to the input of dissolved inorganic nitrogen (DIN) from the deep oceanic waters (Nixon *et al.*, in Howarth, 1996). The authors first report several estimates of the nitrate flux from slope waters onto various regions of the North Atlantic continental shelf. They vary by a factor of 20, but Nixon *et al.* (in Howarth, 1996) suggest that most often the fluxes are between 4 and $15 \text{ g N m}^{-2} \text{ yr}^{-1}$ with a few special areas more intensively enriched such as the Georges Bank. They have used, on the other hand, a relation between primary production and DIN input for various areas of the world. These authors obtain a total flux of $7 \text{ g N m}^{-2} \text{ yr}^{-1}$, which gives an input of deep water at the shelf break of $5 \text{ g N m}^{-2} \text{ yr}^{-1}$, if the river and atmospheric inputs are subtracted. A simple calculation suggests that a total N input equal to $7 \text{ g N m}^{-2} \text{ yr}^{-1}$ corresponds to a f-ratio of 0.24 for a primary production of $165 \text{ g C m}^{-2} \text{ yr}^{-1}$, assumed by the authors. This gives a very low value for the new production for the shelf area. In this nitrogen budget, the export of nitrogen from the deep ocean is compensated by the rates of nitrogen fixation in the pelagic North Atlantic ocean and not by the export of particulate organic N from the shelf.

More recently Soetaert *et al.* (2001) developed within the OMEX project a coupled biogeochemical -1D hydrodynamic model describing the N cycle at the margins in the Northern part of the Gulf of Biscay. There is no river in the area and the new production of this very broad shelf is only sustained only by import of nutrients from the deep waters at the shelf break. These authors obtain an N input from the deep water equal to $14 \text{ g N m}^{-2} \text{ yr}^{-1}$ with a f-ratio of 0.40. Interestingly, their model shows that about 20% of the nitrate consumed by the phytoplankton results from nitrification of ammonia in the euphotic zone.

The discussion here presented on the nitrogen cycle shows that there are large discrepancies concerning the importance of the nutrient fluxes at the margins. Yet the lowest estimates of the N transfer through the shelf break in the North Atlantic ocean exceeds the sum of river discharge and atmospheric deposition, even for an ocean subjected to a large continental supply of fresh water. In other words, the fertility of the coastal zone is largely due to nutrients provided by deep ocean waters and not by continental input.

Another approach to evaluate the f-ratio is to consider the export flux of carbon out of the euphotic zone. On sufficiently long time scales (10 - 100 years), the new production must obviously be compensated by an equal export flux to maintain steady state conditions in the system, and thus to avoid depletion or accumulation of nutrients in the coastal zone. There are however some discrepancies in the way how this export flux is estimated. Evaluations are often based on fluxes of organic matter in a sediment trap moored across the slope, but they do not take into account losses by respiration during settling. The same comment is valid for deposition fluxes below the mixing depth. In shallow areas, the export of organic matter to the sediments should take into account the fact that the export flux is not equal to the deposition rate, but to the burial rate. In deeper parts of the margins, the vertical export of organic matter should be estimated from the fluxes across the pycnocline, and the horizontal export to the slope and to the open ocean from the fluxes across the shelf break. Both fluxes are usually inaccessible, except however by modelling or indirectly by mass balance calculations.

Taking into account all the limitations discussed here above and the geographical variability of the ocean margins, it is surprising to see that the values suggested for global primary production and new production by various authors are not that different. They indicate, in any case, the same trends with similar values for the fluxes. Table 4.2. shows the mean value and variance of primary and new production calculated by Liu *et al.* (2000a) from published data in the literature. The values were selected by the authors after a critical analysis of the estimations obtained during recent large international programs on the margins carried out in various parts of the world.. These authors have also included in their data set, evaluations of the new production and of the export flux. The export flux is systematically lower by a factor of 2-3 than the new production. This is because the export fluxes are mostly measured with sediment traps moored at various depth (often below 500m) or estimated from deposition rates on the slope. These values do not take into account the respiration of organic matter during settling through intermediate and deep waters that must be included necessarily in the export term. Berger *et al.* (1987) have proposed to estimate the f-ratio by using an empirical relation based on observation that there is an obvious relation between the primary production PP (in $\text{g C m}^{-2} \text{ yr}^{-1}$) and the f-ratio:

$$f = PP/400 - PP^2/340000$$

For the mean primary production of $215 \text{ g C m}^{-2} \text{ yr}^{-1}$ proposed by Liu *et al.* (2000a) as typical for the shelf, the f-ratio would be equal to 0.40.

Table XIV: Estimates of primary production and new production in the global ocean and margins.

Zone	Primary Production		New Production		f-ratio	Reference
	gCm ⁻² yr ⁻¹	GtCyr ⁻¹	gCm ⁻² yr ⁻¹	GtCyr ⁻¹		
Shelf (mean)	195	7.2	89	2.7	0.35	Liu et al (2000a)
variance	75	2.5	50	1.5	0.23	“
selected value	215	7.8		see text		“
Open Ocean (mean)	93	31	12.3	4.1	0.13	Liu et al (2000a)
variance	30	10	6	2	0.20	“
selected value	96	32	12	4	0.13	“
Shelf	230	6.0	83	2.4	0.40	Wollast (1998)
Slope	150	4.8	30	1.0	0.20	“
Open Ocean	94	28	14	3.8	0.15	“

The values of Liu *et al.* (2000a) in Table XIV. are compared to values estimated during this study and where a distinction has been made between the shelf and slope, besides the open ocean (Wollast, 1998). Our C fluxes are based on data collected during a dozen of detailed coastal studies as well as on a synthesis of the C fluxes in the open ocean. The agreement with the selected values of Liu *et al.* (2000a) are surprisingly good. This gives us more confidence in the tentative global carbon cycle that we have published earlier and which is reproduced in figure 37. In fact, very little information is available concerning the fluxes across the boundaries between the shelf, the slope and the open ocean. Therefore, a hypothetical flux of 2.2 GtC yr⁻¹ has been estimated between the shelf and the slope area from mass balance requirements. This represents roughly one third of the primary production and appears to be overestimated. Fluxes of organic matter recorded in sediment traps along the slope deployed during various recent ocean margin studies (Liu *et al.*, 2000b) all suggest that only a small fraction of the shelf primary production is exported to the slope. These studies also show, however, that there is a well-established lateral transport across the slope, which complicates the evaluation of the export fluxes.

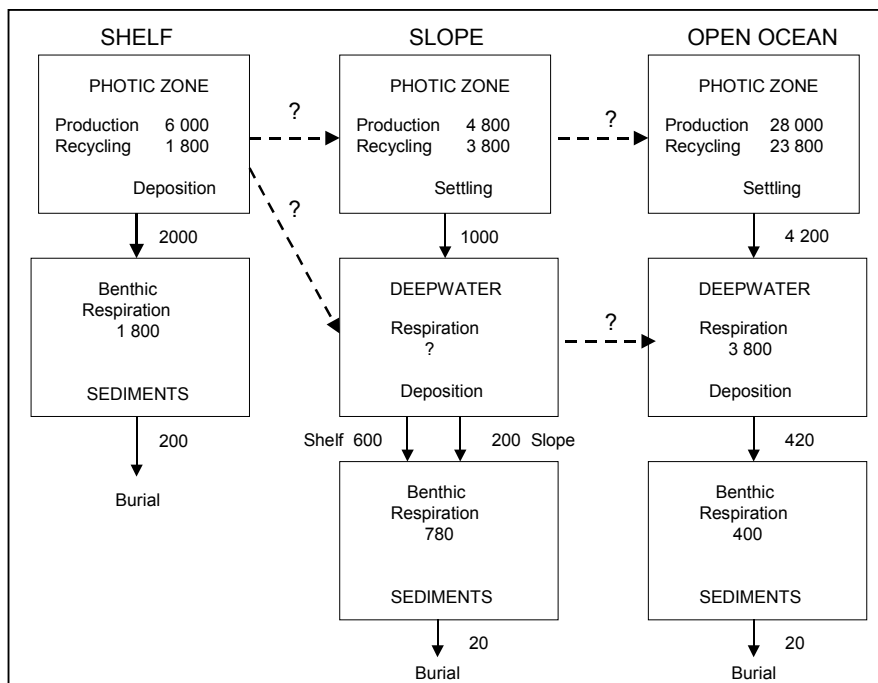


Figure 37: Tentative global cycle of organic carbon in the oceanic system (in MtC. Yr⁻¹).

From their review of the literature, Liu *et al.* (2000a) have suggested that only 0.9 GtC of organic matter are exported from the shelf, which represents only 12% of the coastal primary production. Here again this value may be underestimated, because it does not take into account the respiration of settling organic particles. In a recent study of the carbon cycle in the Gulf of Biscay, we found a primary production of 200 g C m⁻² yr⁻¹ at the shelf break with a respiration in the water column below the mixing depth of 50 g C m⁻² yr⁻¹. An additional respiration of 20 g C m⁻² yr⁻¹ occurs in the sediments and the export flux to the slope is about 30 g C m⁻² yr⁻¹ (Wollast and Chou, 2001). This export represents thus 15% of the primary production at the shelf break but 50% of that primary production leaving the euphotic zone is already respired below the mixing depth. In the adjacent area above the slope, 54 g C m⁻² yr⁻¹ representing 34% of the primary production there, is transferred to deeper waters. It is believed that some of this organic matter may have been transported from the surface water of the shelf to that of the slope. In the upwelling area of the Iberian margin, covered during the second phase of the European project OMEX, the preliminary results show that the primary production on the shelf is about 360 g C m⁻² yr⁻¹ and about 270 g C m⁻² yr⁻¹ over the slope, of which 200 g C m⁻² yr⁻¹ is recycled production fed mainly by organic matter exported from this narrow shelf.

4.3 The 1-D coupled hydrodynamical/ecological model of the ocean margin system

The area selected for the application of the 1-D model is the *La Chapelle Bank*, in the Gulf of Biscay, which is situated at the shelf break of the Celtic sea at 47°24'N - 07°16'W (Figure 38). This area is known to be under the influence of strong internal waves due to the interaction of tidal currents with the steep topography of the slope (Pingree, 1982). The internal waves are transporting a substantial amount of energy which is dissipated as turbulent kinetic energy and makes an important contribution to vertical mixing in the region of the shelf break. This vertical mixing is responsible for the transfer of nutrients in the euphotic zone and for the enhanced phytoplankton activity. The position of the shelf break front can be easily detected by remote sensing by the presence of a narrow band of cold water along the 200m isobaths (Figure 39).

We have in addition covered intensively the area during cruises of the R.V. Belgica in the course of a previous Global Change Project and during the phase I and II of OMEX which was devoted to the Gulf of Biscay. A station situated above the slope of La Chapelle Bank, now known as the Belgica station in the international literature, has been also visited by our team during opportunity cruise of the Belgica en route for the Iberian margin. We have thus collected a broad range of data covering the vertical distribution of physical, chemical and biological parameters from spring to fall. We have also performed incubation experiments using ^{14}C , ^{32}P (ULB) and ^{15}N (VUB) in order to estimate the activity of the phytoplankton.

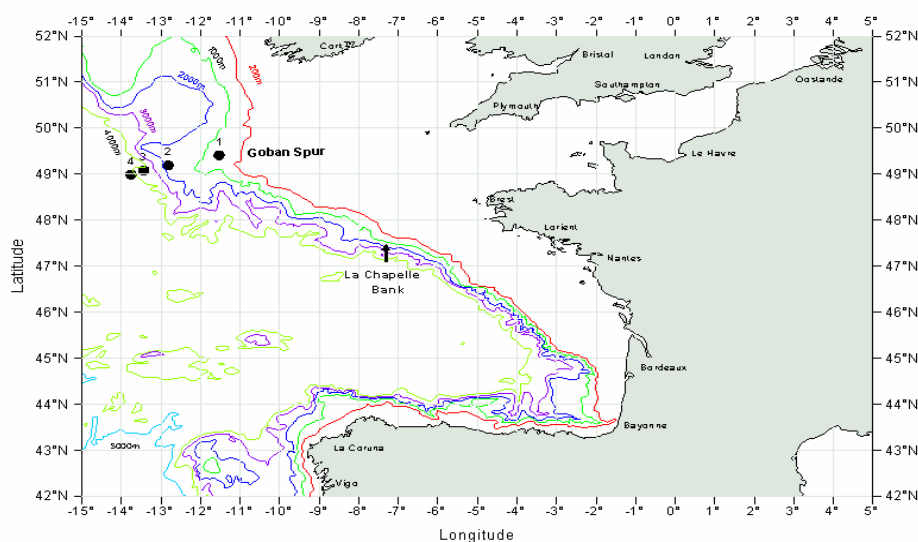


Figure 38: Map of the Gulf of Biscay showing the position of La Chapelle Bank for which the 1-D model was run. The Goban Spur area was covered by the 1-D model of Soetaert et al. (2001).

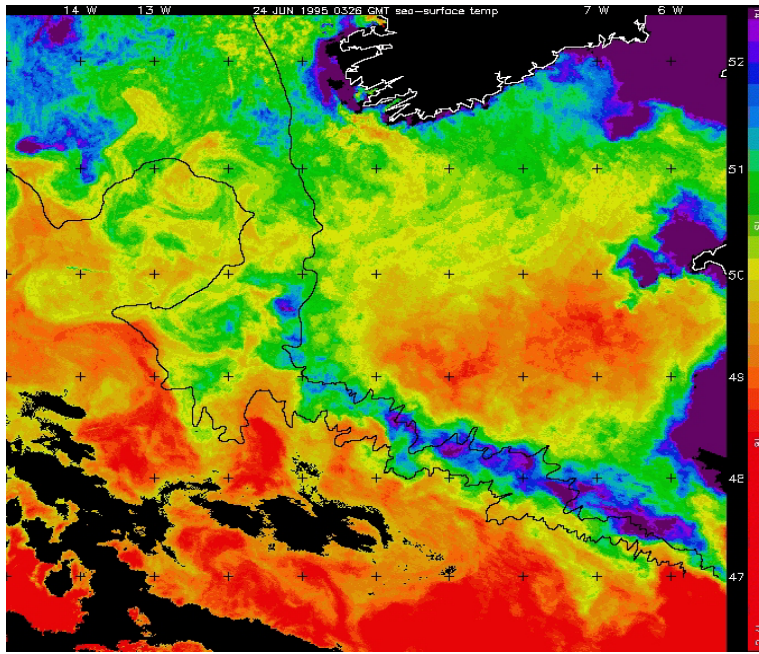


Figure 39: See surface temperature distribution along the margin of the Gulf of Biscay AVHRR data were received at the NERC Dundee University Receiving Station and processed by the Remote Sensing Group, Plymouth Marine Laboratory.

Finally, a similar 1-D model has been developed by Soetaert *et al.* (2001) for the area of Goban Spur, situated at about 500 km North-East of La Chapelle Bank, where vertical mixing also due to tidal waves occurs, however, with a significantly lower energy. It will be interesting to compare their results to ours.

4.3.1 The physical model

4.3.1.1 Objectives and theoretical background

Our central objective in setting up a coupled physical and ecological model of the ocean-margin system is to differentiate between the new and the recycled primary production. Because new production is basically driven by the supply of fresh nutrients from the deep water layers, the description and quantification of vertical exchanges in the water column is a first necessary step in order to account for nitrate inputs into the euphotic zone. The vertical mixing is inhibited by thermal stratification, which can be destroyed by a number of physical processes. The mechanisms that lead to thermal instabilities may vary in importance for the different areas of the ocean: upwelling in coastal zones, eddies, fronts, internal waves, etc, at continental margins (Huthnance, 1995). But in the open ocean, or where the influence of these phenomena is reduced, turbulent mixing due to wind stress and surface cooling becomes important. A numerical 1-D (vertical) model has therefore been developed

for the purpose of simulating the vertical turbulent mixing, and its main features are presented below. It was developed in collaboration with the Department of Mechanical Engineering at the Instituto Superior Tecnico of Lisbon (Prof. R. Neves).

This 1-D model is based on the turbulent-closure formulation presented by Bougeault and Lacarrère (1989) and adapted to marine systems by Gaspar *et al.* (1990). It aims at a full description of turbulence-induced exchanges along the vertical, leaning on the concepts of local turbulent kinetic energy (TKE or e) and momentum diffusivity (K_m). The inclusion of eddy diffusivity (and its relation with eddy diffusivities of other properties such as heat, salinity or nutrients) is a convenient way to account for the variability of exchange processes along the depth. This is especially the case at the lower frontier of the euphotic zone, where the most relevant information on mass fluxes is sought. The basic equations used in the physical model are briefly presented below. For a detailed discussion, the reader is invited to refer to the original paper by Gaspar *et al.* (1990).

In a one-dimensional approach, the equations for the conservation of momentum, heat and salinity are respectively:

$$\frac{\partial \bar{U}}{\partial t} = -\frac{\partial \overline{w'U'}}{\partial z} - f(k \times \bar{U}) \quad (1)$$

$$\frac{\partial \bar{T}}{\partial t} = \frac{F_{sol}}{\rho_0 C_p} \frac{\partial I}{\partial z} - \frac{\partial \overline{w'T'}}{\partial z} \quad (2)$$

$$\frac{\partial \bar{S}}{\partial t} = -\frac{\partial \overline{w'S'}}{\partial z} \quad (3)$$

where U , w , T and S respectively stand for the horizontal and vertical velocities ($m.s^{-1}$), the temperature (K) and the salinity. \bar{X} denotes mean values and X' (or x') the corresponding fluctuations around these mean values. k is the unit vector in the vertical direction and f the Coriolis parameter (s^{-1}); F_{sol} is the solar radiation flux crossing the ocean surface (W/m^2) and $I(z)$ is the fraction of F_{sol} effectively reaching depth z ; C_p is the specific heat of seawater ($J.kg^{-1}.K^{-1}$). The underwater light field $I(z)$ is described by a double exponential dependence with depth according to the traditional approach by Kraus (1972), in which the numerical coefficients proposed by Paulson and Simpson (1977) for seawater of Type I have been used, according to the classification of Jerlov (1968):

$$I(z) = I_1 \exp\left(-\frac{z}{\lambda_1}\right) + I_2 \exp\left(-\frac{z}{\lambda_2}\right) \quad \text{with } I_1 + I_2 = 1 \quad (4)$$

It should already be noted that the coupling between the physical and the ecological part of the model does not include yet the effect of the phytoplankton concentration on the underwater light distribution (no self-shading effect).

The turbulent vertical fluxes appearing in the above conservation equations (1 to 3) are parameterized using the classical concept of eddy diffusivity:

$$-\overline{w'U'} = K_m \frac{\partial \bar{U}}{\partial z} \quad (5)$$

$$-\overline{w'T'} = K_h \frac{\partial \bar{T}}{\partial z} \quad (6)$$

$$-\overline{w'S'} = K_s \frac{\partial \bar{S}}{\partial z} \quad (7)$$

As initially suggested by Prandl (1945), the eddy diffusivity of momentum is related to the local TKE according to:

$$K_m = C_m l_m \sqrt{e} \quad (8)$$

with TKE expressed, by definition, by:

$$e = \frac{1}{2} (u'^2 + v'^2 + w'^2) \quad (9)$$

In equation 8, l_m is a characteristic mixing length (Hinze, 1975) and C_m is a dimensional coefficient whose value is usually taken equal to 0.1. The turbulent kinetic energy is determined from its budget equation, taken here in its one-dimensional form (*i.e.* neglecting the horizontal advection and diffusion):

$$\frac{\partial \bar{e}}{\partial t} = -\frac{\partial}{\partial z} \left(\overline{e w'} + \frac{\overline{p' w'}}{\rho_0} \right) - \overline{U' w'} \frac{\partial \bar{U}}{\partial z} + \overline{b' w'} - \varepsilon \quad (10)$$

where p is the hydrostatic pressure (N.m^{-2}), ε is the dissipation rate of turbulent kinetic energy ($\text{m}^2.\text{s}^{-3}$) and b the buoyancy (m.s^{-2}):

$$b = \frac{\rho - \rho_0}{\rho_0} g \quad (11)$$

ρ is the seawater density (kg.m^{-3}) at temperature T , and ρ_0 this density at the reference temperature T_0 . A simplified linear equation of state:

$$\rho = \rho_0 [1 - \alpha_T (T - T_0) + \alpha_S (S - S_0)] \quad (12)$$

is applied to predict seawater density, with values for α_T (thermal expansion coefficient,

K^{-1}) and α_S (haline contraction coefficient, $\%_o^{-1}$) from Bryan & Cox (1972). The vertical flux of TKE in the above budget (eq. 10) is again parameterized using the concept of eddy diffusivity:

$$-\left(\overline{e w'} + \frac{\overline{p' w'}}{\rho_0} \right) = K_e \frac{\partial \bar{e}}{\partial z} \quad (13)$$

with the assumption:

$$K_e = K_m \quad (14)$$

Finally, the dissipation rate ε is parameterized according to Kolmogorov (1942):

$$\varepsilon = \frac{C_\varepsilon \bar{e}^{-1.5}}{I_\varepsilon} \quad (15)$$

where I_ε is a characteristic dissipation length and C_ε a factor whose value is taken equal to 0.7 in the oceanic environment (Bougeault & Lacarrère, 1989). Two primary turbulent length scales, I_u (upwards) and I_d (downwards) are introduced to compute the value of the mixing and dissipation lengths l_m and I_ε according to:

$$l_m = \min(I_u, I_d) \quad (16)$$

and

$$I_\varepsilon = \sqrt{I_u I_d} \quad (17)$$

l_u and l_d are themselves computed from the integral equations:

$$\frac{g}{\rho_0} \int_z^{z+l_u} [\bar{\rho}(z) - \bar{\rho}(z')] dz' = \bar{e}(z) \quad (18)$$

and

$$\frac{g}{\rho_0} \int_z^{z-l_d} [\bar{\rho}(z) - \bar{\rho}(z')] dz' = \bar{e}(z) \quad (19)$$

When the stratification is stable (density gradient close to constant), these expressions reduce, as a first approximation, to:

$$l_m = I_\varepsilon = \sqrt{2} I_b \quad (20)$$

where the buoyancy scale I_b is parameterized from its relation to the stratification parameter N^2 (the square of Brunt-Väisälä frequency) and to the local value of the TKE:

$$N^2 = \frac{\bar{e}}{l_b^2} \quad (21)$$

with, by definition:

$$N^2 = \frac{\partial b}{\partial z} = \frac{g}{\rho_0} \frac{\partial \rho}{\partial z} \quad (22)$$

Eddy diffusivities for other properties (*i.e.* heat and salinity) are all set equal and estimated from the eddy diffusivity of momentum by way of the turbulent Prandtl number Pr , according to:

$$K_h = K_s = \frac{K_m}{Pr} \quad (23)$$

Pr is usually taken equal to 1, assuming that scalar variables diffuse at the same rate than vectorial variables.

The advantage of linking K_m and ε to the local value of the TKE in the 1-D model should again be emphasized: e can act as a “memory” of the turbulence pattern in the stratified flow and helps therefore to the full continuity of information along the vertical. This would not be the case if the mixing layer approach had been selected (e.g. Price et al, 1986), in which case the information along the vertical is discontinuous in essence.

4.3.1.2 Implementation of the physical model at La Chapelle Bank

Initial and boundary conditions

The vertical turbulent mixing is controlled, at the seasonal scale, by the balance between heating (which leads to stratification) and wind mixing (which tends to homogenize the water column) at the atmosphere-ocean interface. These factors are introduced into the model via forcing conditions, which must be carefully adapted to the area of study (Gaspar *et al.* 1990).

The surface turbulent fluxes are specified in the model as follows (for layer 0):

$$-\rho_0 \overline{U'w'}(0) = \tau \quad (20)$$

$$-\rho_0 C_p \overline{T'w'}(0) = F_{\text{nsol}} = H + LE + F_{\text{ir}} \quad (21)$$

$$-\rho_0 \overline{S'w'}(0) = E - P \quad (22)$$

where τ is the surface wind stress (N.m^{-2}), F_{nsol} is the non-solar surface heat flux defined as the sum of the surface sensible heat flux (H), plus the latent heat fluxes

(LE), plus the long wave re-emission (F_{ir}) (all in $W.m^{-2}$, with heat fluxes positive downwards); E and P are the evaporation and the precipitation rates ($kg.m^{-2}.s^{-1}$).

For bottom boundary conditions (at 300 m depth), a no-flux condition (zero gradient) is imposed for heat, salinity and TKE.

Atmospheric data from the ECMWF (European Center for Medium-Range Weather Forecast) "Initialized Analysis" data-files have been used for the estimation of surface boundary conditions for the simulation period. These data include near-surface air temperature and humidity, wind speed and direction, barometric pressure, wet bulb temperature, dew point temperature, sea surface temperature and cloud coverage, with an horizontal resolution of $0.5^{\circ} \times 0.5^{\circ}$ and a temporal resolution of 6 hours. F_{sol} values were taken from Da Silva (1994).

In order to determine the most effective formulation for estimating the parameters of equations 20 to 22 from the available atmospheric data, several *bulk formula* have been tested, leading to results similar to those of Blanc (1985). In particular, as the estimation of evaporation and precipitation fluxes showed a high degree of uncertainty, we have decided to impose a zero net flux condition for these two processes (*i.e.* constant salinity).

For the various simulations conducted, the initial condition for temperature was the January 1993 climatic temperature from Levitus *et al.* (1994a). Initial velocity in x and y directions were set to zero.

All simulations were conducted over three years (1993 – 1995), for a water column of 300 m. The time-step for the simulations was 3600 seconds and the spatial grid 1 m.

Internal parameters adjustment

Vertical mixing at the ocean margin is not only due to eddy diffusivity, but also to the existence of internal waves, pole-ward current, fronts and up-welling which contributes to vertical mixing but also to lateral advection. One pragmatic way to include the enhanced mixing in a 1-D model is by adjusting the parameters that control the eddy diffusivity, the only tunable parameter in the model formulation being the minimum value of the turbulent kinetic energy e_{min} . It is important to note that a minimum value of TKE should be arbitrarily imposed to avoid mixing to become zero. This value can be parameterized as a function of wind speed or internal waves (Gaspar *et al.* 1990), and its range of variation lies in the range 10^{-6} to $10^{-7} m^2/s^2$ (Gargett, 1984).

4.3.1.3 Model results and validation

The computation of seawater temperature and its comparison with *in situ* data is a convenient way to verify and validate the model ability to reproduce a realistic spatial (vertical) and temporal distribution of the turbulent kinetic energy field. The resulting pattern of K_m can then be in a subsequent ecological model, taking advantage of its postulated relation with the turbulent diffusion coefficients of scalar variables such as chemical constituents or phytoplankton. Two main sets of results will be briefly presented here: (1) simulation of sea surface temperature, (2) monthly evolution of the vertical temperature profile. A complementary check of the model validity can be obtained by computing time-integrated heat fluxes budgets. These results are also presented hereunder, together with an estimation of how the frequency of meteorological data forcing influence the heat flux balance closure.

Sea surface temperature

Figure 40. shows the results of sea surface temperature (SST) computation for different values of the minimum turbulent kinetic energy e_{min} . These results are compared with SST data from the ECMWF database. Satisfactory results are obtained for e_{min} comprised between 2 and $5 \cdot 10^{-6} \text{ m}^2 \cdot \text{s}^{-2}$, including the inter-annual increasing trend that can be noticed for this 3-year period. A value of $5 \cdot 10^{-6} \text{ m}^2 \cdot \text{s}^{-2}$ has been selected for the simulations.

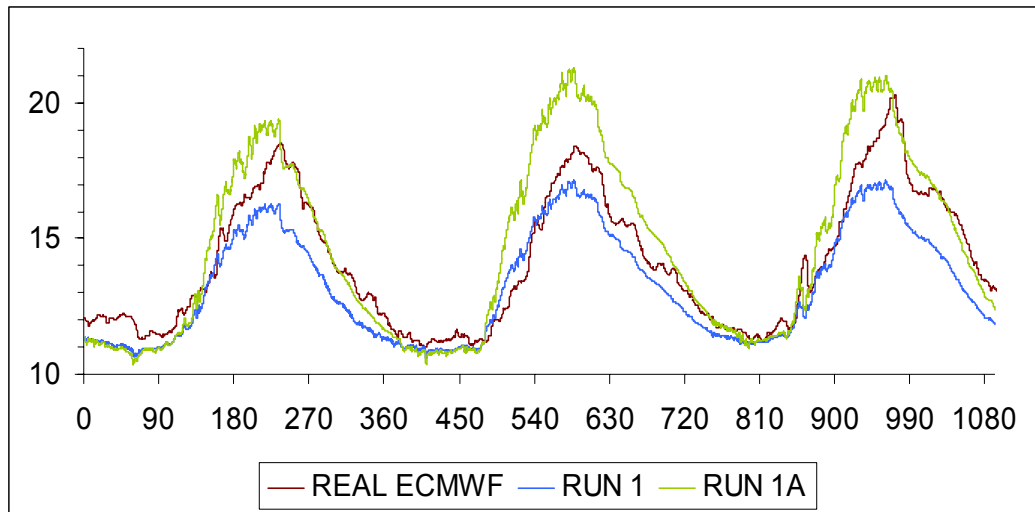


Figure 40: Simulation of the surface temperature evolution, 1993-1995. Field data from ECMWF.

Run 1: $e_{min} = 5 \cdot 10^{-6} \text{ m}^2 \cdot \text{s}^{-2}$ Run 1A: $e_{min} = 2 \cdot 10^{-6} \text{ m}^2 \cdot \text{s}^{-2}$

Vertical temperature profiles

Figure 41 presents the results of vertical temperature profiles computation for 12 selected days between January and December 1995. These results are compared with the data from the ICES database, including the results acquired at nearby sites during various OMEX and other opportunity cruises. (This database covers the period 1960-1998, and the following stations have been retained: (a) coordinates between $47^{\circ}2-47^{\circ}8N$ and $7^{\circ}0-7^{\circ}5W$ and (b) depth in the range 200 to 2000 m.) The temperature distribution, both in time and space, is very correctly described in the first 200m of the water column, with a clear stratification occurring between May and the end of October.

4.3.1.4 Heat budget

The results of heat flux balances integrated over one year are reported in Table 4.3. The net heat budget, using the ECMWF 6-hour forcing conditions, is balanced within less than 6% of the incoming solar energy flux. This discrepancy can be, at least partly, attributed to the heat removal by advective processes.

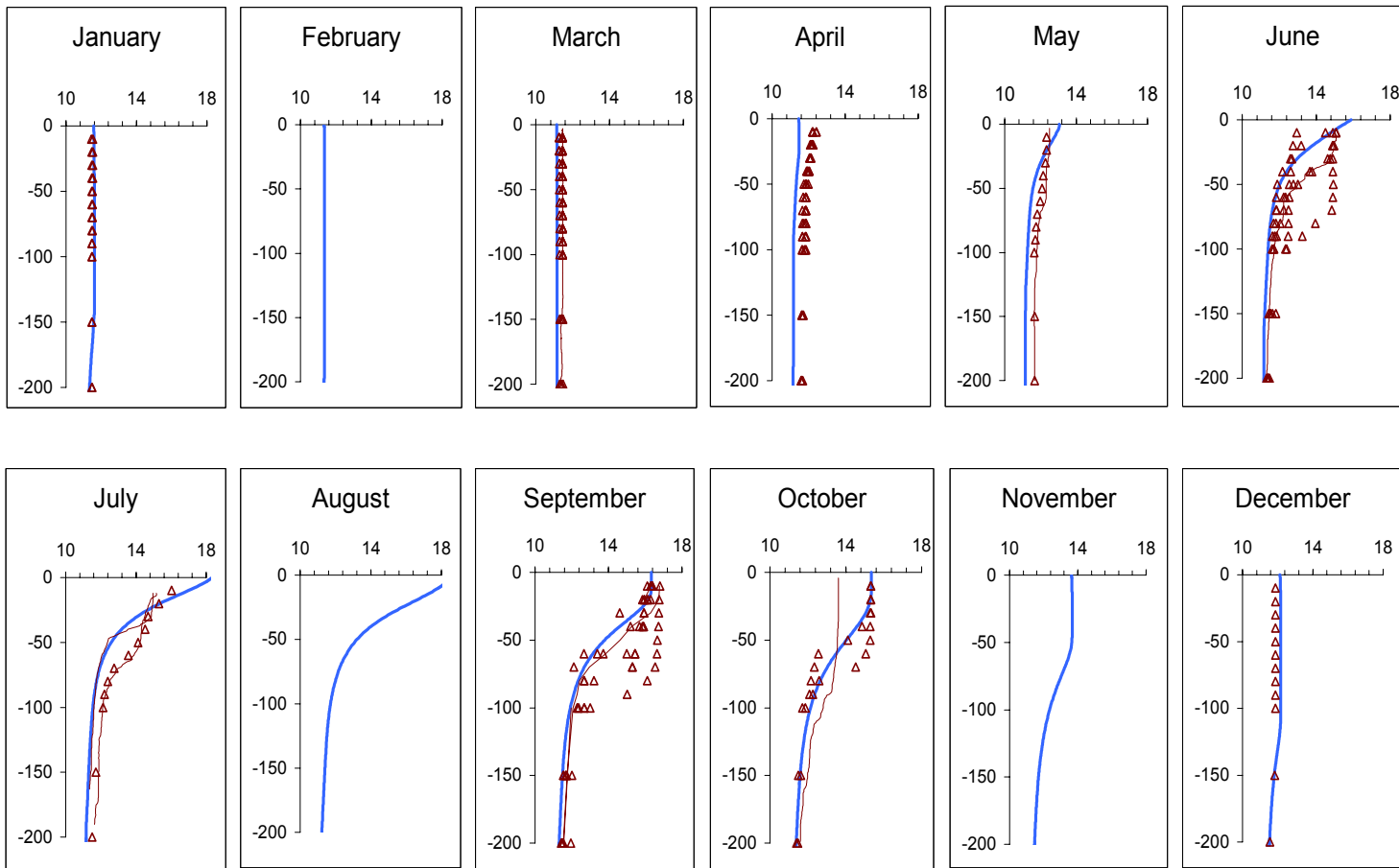


Figure 41: Monthly evolution of the computed temperature profiles (thick line) compared to measured profiles (thin line: Belgica data, triangles ICES and other OMEX data).

Table XV: Heat fluxes balance for various atmospheric forcing. (All fluxes are annual mean in $W.m^{-2}$).

Data frequency	1 month DaSilva 94 (47.25°N-7.25°W)	1 month Esbensen 81 (46°N-5°W)	ECMWF (47.25°N-7.16°W)		
			6-hour	3-hour + stoch wmax=4.8m/s	1-hour + stoch wmax=4.8m/s
Solar Radiation	134.28	135.41	134.39	134.39	134.39
Sensible Heat	-9.13	-4.54	-4.89	-4.95	-5.42
Latent Heat	-59.45	-56.18	-42.45	-43.01	-46.76
Net Longwave	-53.05	-58.55	-79.14	-79.14	-79.14
Net Heat	12.65	16.13	7.91	7.29	3.07

To determine how the frequency of the meteorological data used for forcing influences the model results, complementary simulations have been made, using 1-month averaged values (Da Silva, 1994 and Esbensen, 1981) and 6-hour ECMWF data with a super-imposed stochastic contribution. This allows the simulation of 3-hour and 1-hour wind data frequency, and shows that the benefit of increasing the time-resolution of meteorological data is rather small. As a consequence, 6-hour ECMWF data have been used for the simulations.

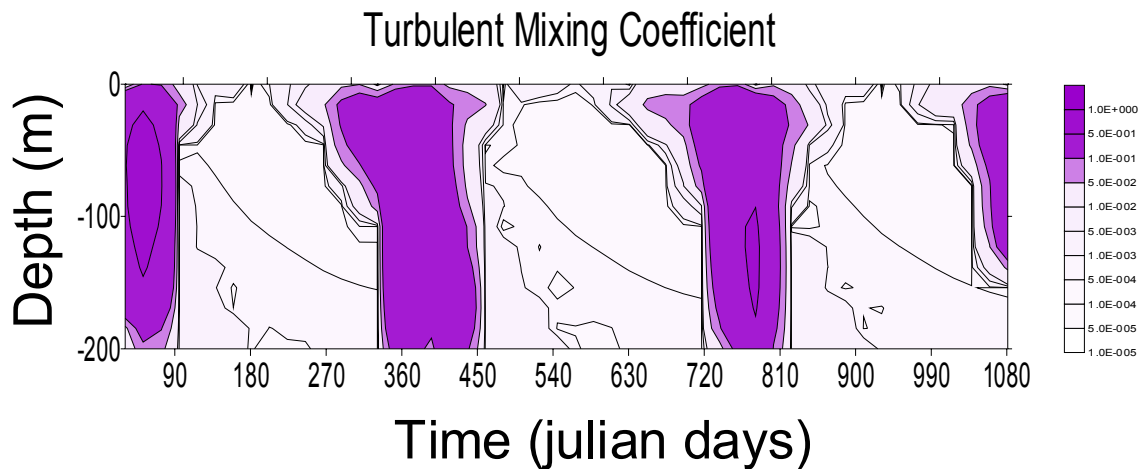


Figure 42: Evolution of the turbulent diffusivity $K_m (m^2.s^{-1})$, 1993-1995.

Eddy diffusivity

The eddy diffusivity K_m is the central “coupling” variable between the physical and the ecological models. Results show (figure 4.7) that eddy diffusivity is large enough to mix the first 200 m of the water column during the winter month, with values in the range 0.1 to 0.2 $m^2.s^{-1}$. As already illustrated by the temperature profiles, stratification appears in spring (April-May) and remains during all summer and part of fall.

4.3.2 The biological model

The biological model that we are proposing here has been kept simple in order to derive informations which can be used later in more complex global models. It is limited to five reservoirs representing the amounts of phytoplankton, zooplankton, nutrients, fast and slow sinking detrital organic matter.

The fluxes of carbon and nutrients between these reservoirs are represented schematically by the arrows between the reservoirs in the figure 43. The parameters used in the following equation are listed in table XVI.

Table XVI: List of symbols.

C_{ph}	concentration of phytoplankton
C_{zoo}	concentration of zooplankton
C_N	concentration of nutrient
C_{de}	concentration of detrital organic matter
∇	photosynthesis efficiency
μ_{max}	maximum of specific photosynthetic capacity
I_k	light adaptation parameter
$($	Redfield C:N ratio of the phytoplankton
μ	rate of photosynthesis
Gr	rate of grazing
k_{pz}	zooplankton grazing rate constant
k_{mph}	phytoplankton mortality rate constant
k_{mzo}	zooplankton mortality rate constant
k_{resp}	zooplankton respiration rate constant
$k_{f,p}$	bacterial respiration rate constant
k_{diff}	vertical turbulent diffusion coefficient
k_N	Menten-Michaelis constant for the nutrient
I	light intensity
z	depth
t	time

In equation (23) I is the intensity of the light at a given time and a given depth and is calculated according to

$$I = I_0 e^{-k_z z} \quad (27)$$

The grazing of phytoplankton by zooplankton depends on both the biomass of phytoplankton and zooplankton:

$$Gr = k_{p-z} C_{ph} \cdot C_{zoo} \quad (28)$$

where k_{p-z} expresses the specific rate of filtration of water by the zooplankton.

The phytoplankton is also affected by its natural mortality and can be transported to the deep water by vertical mixing. The evolution of its biomass is thus given by:

$$\frac{dC_{ph}}{dt} = \mu - Gr - k_{mph} C_{ph} - k_{diff} \frac{dC_{ph}}{dz} \quad (29)$$

The evolution of the zooplankton biomass depends on its growth rate minus its respiration, the excretion of fecal pellets and its mortality, all considered as first order rates with respect to the zooplankton biomass:

$$\frac{dC_{zoo}}{dt} = Gr(1 - f_{resp} - f_{f,p}) - k_{mzoo} C_{zoo} \quad (30)$$

The fecal pellets as well as the dead bodies of zooplankton are rapidly sinking to deeper waters (100-200 m day⁻¹).

The detrital organic carbon is produced by the mortality of the phytoplankton. It is degraded by bacterial respiration which regenerates the nutrients. It can further be exported to deeper waters by slow settling or turbulent diffusion

$$\frac{dC_{det}}{dt} = k_{mzoo} C_{zoo} + k_{mph} C_{ph} - k_s C_{det} - k_{diff} \frac{dC_{det}}{dz} \quad (31)$$

Finally nutrients are either transferred from deep waters to the euphotic zone by turbulent mixing or regenerated by consumption of phytoplankton by zooplankton and degradation of detrital organic matter by bacteria. They are consumed during photosynthesis at a rate depending on the Redfield C:N ration of the phytoplankton.

$$\frac{dC_N}{dt} = k_{diff} \frac{dC_N}{dz} + k_{resp} C_{zoo} + k_b C_{det} - \frac{\mu}{\gamma} \quad (32)$$

A set of similar equation can be written for each nutrient, taking into account the fact that the phytoplankton has a relatively constant composition with C:N:P given by the Redfield ration 106:16:1: in molar units. In our numerical calculations, we have used nitrogen rather than carbon because the recycled production can then be

immediately associated with the ammonium flux and new production to the nitrate flux.

Several runs were performed by changing the parameters within the limits of the values obtained during field experiments or of the range of values published in the literature. These runs allowed to test the sensitivity of the model to these parameters. We will first briefly summarize the main results. The start of the spring bloom is a very critical phenomenon which is strongly dependant on the photosynthetic parameters of the phytoplankton and especially of μ_{\max} and I_k . The evolution with time of the phytoplankton biomass is mainly controlled by the rate of grazing by zooplankton but also by its mortality rate and vertical mixing. All these processes are influencing the concentration of dissolved matter which in turn controls the rate of supply of nitrate from the deep water and thus the f-ratio. All this model is extremely sensitive and small fluctuation of μ_{\max} for example has a drastic influence both on the beginning of the bloom and on the accumulation of the phytoplankton biomass in the system over the rest of the year.

We will show below as an example the results obtained with the coupled 1-D model and a given set of biological parameters, whose values are indicated in table XVII.

Table XVII: Numerical values for the selected run of the biological model.

Symbol	Selected Value	Unit
μ_{\max}	0.125	h^{-1}
k_{pZ}	0.02	$\text{m}^3 (\text{mmolN} \cdot \text{h})^{-1}$
k_{mph}	0.0041	h^{-1}
k_{mzo}	0.0031	h^{-1}
f_{resp}	0.4	
f_{fp}	0.2	
k_{b}	0.0045	h^{-1}
K_{N}	2.0	mmolN m^{-3}

The validity of the model was tested by comparing the vertical distribution of the various variables (c_i) with the observed values. However, the latter values are covering several years (1992-1995) and the calculated profiles correspond to one selected year (1995), which may introduce some discrepancies due to inter-annual climatological variations. Figure 44 shows as an example a comparison between the

computed and the observed values for nitrate. The agreement is reasonably good except for the month of April. The discrepancies correspond to the fact that the phytoplankton bloom started later than predicted by the model in 1994.

The annual fluxes between the reservoirs are shown in figure 45. The vertical fluxes are calculated at a depth of 50 m corresponding roughly to the depth of the euphotic zone. Another way to check the validity of the model is to calculate the input/output balance for each reservoir. The results of these calculations are shown in table XVIII.

Table XVIII: *Input/output balance for the various reservoirs of the biological model corresponding to year 1995 (in moles N m⁻².yr⁻¹).*

Reservoir	In	Out	Balance
Dissolved N	2.07	1.87	+ 0.20
Phytoplankton	1.87	1.94	- 0.07
Zooplankton	0.78	0.74	+ 0.04
Detrital N	0.78	0.75	+ 0.03

The input/output balance for all the reservoirs is satisfactory. The small imbalances are due to the fact that the system is not exactly at steady-state which is related to the inter-annual variations. In 1995, nitrogen accumulated mainly as dissolved nitrogen and the biomass of phytoplankton slightly decreased. This reflects the fact that during 1995 there has been more wind and less sun than in the previous year.

The total primary production corresponds to 148 g C m² yr⁻¹ which is a typical value for the area above the slope (see Table XIV). The new production fuelled by nitrogen imported to the euphotic zone from the deep ocean (nitrate) is equal to 89 g C m² yr⁻¹, which corresponds to a f-ratio equal to 0.60. However, the recycled production supported by ammonium resulting from the respiration of zooplankton and bacteria amounts to 74 g C m² yr⁻¹ which gives an f-ratio equal to 0.50. The discrepancy between the two values is due to the fact that the system is not exactly at steady state and that during the year 1995. In any case the values of the f-ratio given by our model is very close to the value obtained by Soetaert *et al.* (2001) (f = 0.48), who used a similar model applied to the area of Goban Spur during the OMEX I project. The high values of the f-ratio are not surprising in the area of the shelf break where intensive vertical mixing occurs.

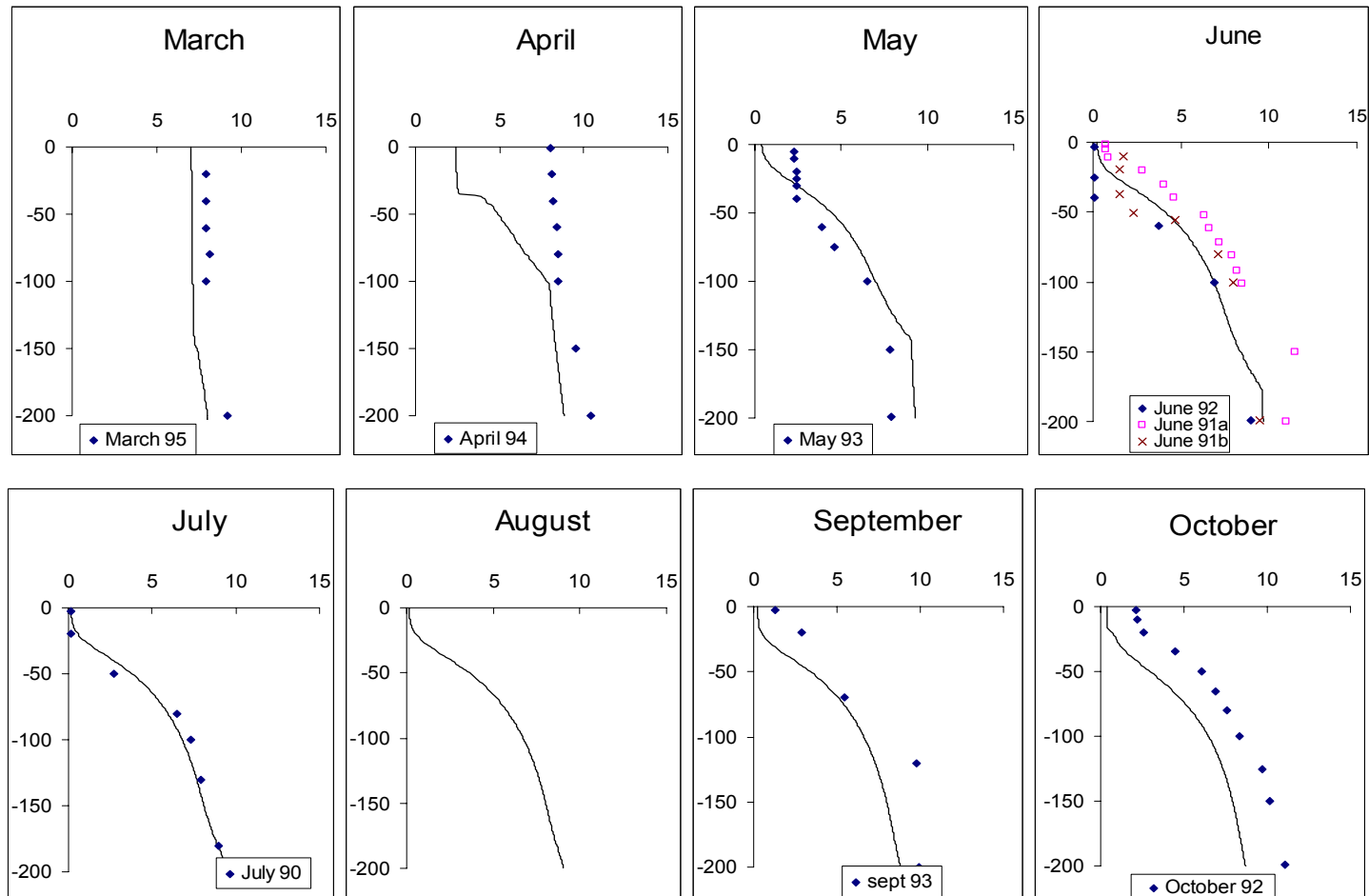


Figure 44: Comparison of the vertical distribution of dissolved nitrogen computed by the model (line) and the concentration of nitrate measured during the same month (points).

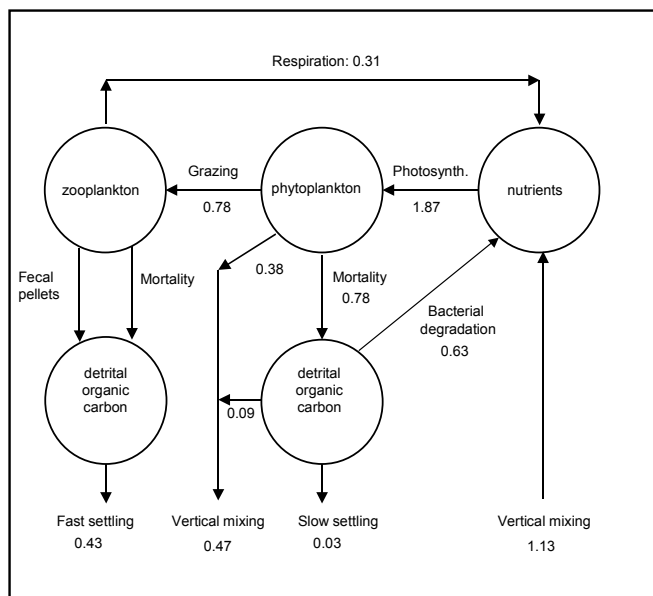


Figure 45: Fluxes of nitrogen between the various reservoirs according to the biological model (in moles $N\ m^{-2}\ yr^{-1}$).

According to the model, roughly 40% of the phytoplankton production is used by the zooplankton and included in a higher trophic food level. A similar value was calculated for the mean fraction of grazing of phytoplankton by zooplankton in the coastal zone on a global scale (Wollast, 1998). This agreement is not surprising for an area with a high nutrient input.

Interestingly, according to the model 20% of the phytoplankton is lost by vertical mixing of surface water with deep water. This export is relatively high and explains probably why the primary production is not even greater than the one observed. Some slow sinking particles of dead phytoplankton are also transferred to the deep water by the same process. Finally, less than 50% of the vertical flux of particles is due to the sinking of large particles (fecal pellets and dead bodies of zooplankton). It is now well established that the sediment traps collect only the fast sinking particles. Sediment traps are usually considered as measuring the main export flux and the contribution of fine particles to the vertical sinking flux is therefore neglected. This may well be one of the reasons why the export flux is systematically underestimated in the slope area.

It would be interesting in the future to extend the biological model by subdividing the nutrient box into two reservoirs: one for ammonia and one for nitrate, with different uptake rates of the nitrogen species by the phytoplankton. This would probably improve the agreement between the calculated and vertical profile of nitrate in the water column.

REFERENCES

Amiotte Suchet P., Cycle du carbone, Erosion chimique des continents et transferts vers les océans. PhD thesis, Université Louis Pasteur, Strasbourg, France, 1994.

Anderson, R.F., G.T. Rowe, P.F. Kempe, S. Trumbore and P.E. Biscaye, Carbon budget for the mid-slope depocenter of the Middle Atlantic Bight. *Deep-sea Res. II*, 41 (2/3), 669-703, 1994.

Andres R and G. Marland, A $1^{\circ} \times 1^{\circ}$ distribution of carbon dioxide emissions from fossil fuel consumption and cement manufacture, 1950-1990. *Global Biogeochemical Cycles*, 10, 419-429, 1996.

Asner G, C. Wessman, D. Schimel and S. Archer, Variability in leaf and litter optical properties: implications for BRDF model inversions using AVHRR, MODIS and MISR, *Remote Sensing of Environment*, 63, 243-257, 1998.

Bacastow R., and E. Maier-Reimer, Ocean-circulation model of the carbon cycle, *Climate Dynamics*, 4, 95-125, 1990.

Bard E., Correction of accelerator mass spectrometry ^{14}C ages measured in planktonic foraminifera: paleoceanographic implications, *Paleoceanography*, 3, 635-645, 1988.

Bartlett D, G. Whiting and J. Hartman, Use of vegetation indices to estimate intercepted solar radiation and net carbon dioxide exchange of a grass canopy, *Remote Sensing of Environment*, 30, 115-128, 1990.

Belward A (editor), The IGBP-DIS Global 1km Land Cover Data Set (DISCover): proposal and implementation plans, IGBP-DIS Working Paper 13, International Geosphere-Biosphere Programme Data and Information System Office, Toulouse, France, 1996.

Berger W.H., K. Fisher, C. Lai and G. Wu. Ocean Productivity and Organic Carbon Flux. *Part I. Overview and maps of primary Production and export production*. SIO Reference Series, Scripps Inst. of Oceanography, La Jolla, CA. 67p, 1987.

Berger W.H., V.S. Smetacek and G. Wefer. Ocean Productivity and paleoproductivity: an overview. *In: Productivity of the Ocean: Present and Past*. W.H. Berger, V.S. Smetacek and G. Wefer eds. Dahlem workshop Report. Wiley, Chichester, West Sussex, England. PP. 1-34. Blanc T. V., 1985. Variation of bulk-derived surface flux, stability, and roughness results due to the use of different transfer coefficient schemes. *J. Phys. Oceanogr.*, 15, 650-669, 1989.

- Berner E. K. and R. A. Berner. The global water cycle. Geochemistry and Environment. Prentice Hall, London, 1987.
- Bondeau A., J. Kaduk, Kicklighter D. and participants of "POTSDAM 95" Comparing global models of terrestrial net primary productivity (NPP): Analysis of the seasonal behaviour of NPP, LAI, FPAR along climatic gradients across ecotones, 1999.
- Bougeault P. and P. Lacarrère, Parametrisation of orography-induced turbulence in a meso-beta scale model. *Mon. Weather Rev.*, 117, 1872-1890, 1989.
- Broecker W. S. and T.-H. Peng, Tracers in the sea, Lamont Doherty Geological Observatory, Columbia University, New York, 1982.
- Broecker W. S., and T.-H. Peng, Tracers in the sea, Lamont Doherty Geological Observatory, Columbia University, New York, 1982, 690p.
- Bryan F. and M.D Cox, An approximate equation of state for numerical models of ocean circulation. *J. Phys. Oceanogr.*, 2, 970-985, 1972.
- Bryan F., Parameter sensitivity of primitive equation OGCMs, *Journal of Physical Oceanography*, 17, 970-985, 1987.
- Campin J.-M. and H. Goosse, Parameterization of density-driven downsloping flow for a coarse-resolution ocean model in z-coordinate, *Tellus*, 51, 412-430, 1999.
- Canter F., H. Eerens and F. Veroustraete, Land-cover classificatie en schatting van land-cover proporties op globale schaal, Final report OSTC-contract T4/DD/002-003, December 1998, 141p, 1998a.
- Canter F., H. Eerens and F. Veroustraete, Estimation of land-cover proportions from aggregated medium-resolution satellite data, In: 'Spatial accuracy assessment: land information uncertainty in natural resources', eds. Lowell K. & Jaton A., Ann Arbor Press, Chelsea, Michigan, 263-270, 1998b.
- Carrada, G. T. Hopkins, Lj. Jeftić, and S. Morcos, editors. Quantitative analysis and simulation of Mediterranean coastal ecosystems: The Gulf of Naples, a case study, volume 20 of *UNESCO reports in marine science*. UNESCO, 1983.
- Ciais P., P.P. Tans, J.W.C. White *et al.*, Partitioning of ocean and land uptake of CO₂ as inferred by $\delta^{13}\text{C}$ measurements from the NOAA Climate Monitoring and Diagnostics Laboratory Global Air Sampling Network. *J. Geophys. Res.*, 100, 5051-5070, 1995.

- Cihlar J, H. Ly, Z. Li, J. Chen, H. Pokrant and F. Huang, Multitemporal, multichannel AVHRR data sets for land biosphere studies – artifacts and corrections, *Remote Sensing of Environment*, 60, 35-57, 1997.
- CLIMAP Project Members, Seasonal reconstruction of the Earth's surface at the last glacial maximum. *Geol. Soc. Am. Map Chart Ser. MC*, 36, 1981.
- Coll C. and V. Caselles, A split-window algorithm for land surface temperature from AVHRR-data : validation and algorithm comparison, *J. Geophys. Res.*, 102, D14, 16697-16713, 1997.
- Collatz G.J., M. Ribas-Carbo and J.A. Berry. Coupled photosynthesis-stomatal conductance model for leaves of C₄ plants. *Aust. J. Plant Physiol.*, 19, 519-538, 1992.
- Conway TJ, P.P. Tans and L.S. Waterman, Atmospheric CO₂ records from sites in the NOAA/CMDL air sampling network. In T.A. Boden, D.P. Kaiser, R.J. Sepanski and F.W. Stoss (eds), *Trends'93 : A Compendium of Data on Global Change*. ORNL/CDIAC-65. Carbon dioxide Information Analysis Center, Oak Ridge National Laboratory, Oak Ridge, Tenn., U.S.A, 1994.
- Cracknell A, The Advanced Very High Resolution Radiometer, Taylor & Francis, ISBN 0-7484-0209-8, 1997.
- Craig H., Abyssal carbon and radiocarbon in the Pacific, *J. Geophys. Res.*, 74, 5491–5506, 1969.
- Cramer W., D.W. Kicklighter, A. Bondeau, B. Moore III, G. Churkina, B. Nemry, A. Ruimy, A.L. Schloss and the participants of the Potsdam NPP Model Intercomparison. Comparing global models of terrestrial net primary productivity (NPP): Overview and key results. *Global Change Biology*, 5 (Suppl. 1), 1-15, 1999.
- Crowley T.J., Ice age terrestrial carbon changes revisited. *Global Biogeochemical Cycles* 9(3), 377-389, 1995.
- Crutzen P.J., W.M. Bao, M.H. Liu, J.M. Lobert, D. Scharffe, Emissions of CO₂ and other trace gases to the atmosphere from fires in the Tropics, in Crutzen P.J., J.C. Gérard and R. Zander (eds), *Our changing atmosphere*. Proceedings of the 28th Liège International Colloquium, 449-472, 1989.
- Da Silva, A. C. Young and S. Levitus, Atlas of Surface Marine Data 1994, *Volume 1: Algorithms and Procedures*. NOAA Atlas NESDIS 6, U.S. Department of Commerce, Washington. D.C. 1994.

Debruyne W., H. Eerens, V. Gond, Y. Verheijen, K. Wouters K and F. Veroustraete, An evaluation of bi-directional Models using airborne imaging spectroscopy, In: 'Forest ecosystem modelling, up-scaling and remote sensing', Eds. Ceulemans R. et al., SPB Academic Publishing The Hague, 235-242, 1999.

Dickson A. G., Thermodynamics of the dissociation of boric acid in synthetic seawater from 273.15 to 318.15 K. *Deep-Sea Research*, 37, 755–766, 1990.

Duffy P. B., and K. Caldeira, Three-dimensional model calculation of ocean uptake of bomb ^{14}C and implications for the global budget of bomb ^{14}C , *Global Biogeochemical Cycles*, 9, 373–375, 1995.

Duffy P. B., K. Caldeira, J. Selvaggi and M. I. Hoffert, Effect of subgrid-scale mixing parameterizations on simulated distributions of natural ^{14}C , temperature, and salinity in a three-dimensional ocean general circulation model, *Journal of Physical Oceanography*, 27, 498–523, 1997.

Edmond J. M., On the dissolution of carbonate and silicate in the deep ocean. *Deep-Sea Research*, 21, 455–480, 1974.

Eerens H, B. Deronde and J. Van Rensbergen, A new land cover map of Central Africa derived from SPOT4-VEGETATION imagery, Proc. Conf. VEGETATION-2000, 3-6 April 2000, Belgirate, Italy, 3p., 2000a, in press.

Eerens H, B. Deronde and J. Van Rensbergen, A land cover map of Central Africa derived from SPOT4-VEGETATION imagery, Feasibility study, OSTC-contract T4/67/57, 33p, 1999.

Eerens H, K. Wouters, D. Buffet, R. Oger, D. Dehem and B. Tychon, Use of 1km²-resolution imagery in the Belgian Crop Growth Monitoring System (B-CGMS), Proc. Conf. VEGETATION-2000, 3-6 April, 2000, Belgirate, Italy, 6 p., 2000b, in press.

Eerens H, Y. Verheijen, F. Veroustraete, K. Wouters, D. Buffet, R. Oger, D. Dehem and B. Tychon, Prévision des productions végétales à l'échelle nationale basée sur un système intégré 'Modèle Agrométéorologique – Télédétection': Analyse de sensibilité et domaine de validité en tant qu'outil d'aide à la décision en politique agricole, Final report OSTC+Min. of Agriculture+Vito, 2000c, 145p. + annexes.

Eidenshink J and J. Faundeen, The 1km AVHRR global land data set: first stages in implementation, *Int. J. Rem. Sens.*, 15, 3443-3482, 1994.

Enting I.G., The interannual variation in the seasonal cycle of carbon dioxide concentration at Mauna Loa. *J. Geophys. Res.*, 92, 5497-5504, 1987.

Enting, I. G., T. M. L. Wigley, and M. Heimann, Future emissions and concentrations of carbon dioxide : Key ocean/atmosphere/land analyses, Tech. Rep. 31, CSIRO, 1994.

Esbensen, S. K. and V. Kushnir. The heat budget of the global ocean: An atlas based on estimates from surface marine observations. Tech. Rep. 29, Clim. Res. Inst., Oreg. State Univ., Corvallis, 1981.

Esser G., Hoffstadt J., Mack F., Wittenberg U., *High Resolution Biosphere Model: Documentation Model version 3.00.00*. Institut für Pflanzenökologie, Justus-Liebig-Universität Gießen, 1994.

Farquhar G.D., S. von Caemmerer and J.A. Berry., A biochemical model of photosynthesis CO₂ assimilation in leaves of C₃ species. *Planta*, 149, 78-90, 1980.

Fasham M. J., H. W. Ducklow, and S. M. McKelvie. A nitrogen-based model of plankton dynamics in the oceanic mixed layer. *Journal of Marine Research*, 48, 591–639, 1990.

Fasham M. J., Modelling the marine biota. In M. Heimann, editor, *The Global Carbon Cycle*, volume 115 of *NATO ASI Series*, pages 457–504. Springer Verlag, Berlin Heidelberg, 1993.

François L., B. Nemry, P. Warnant and J.-C. Gérard. Seasonal and interannual influences of the terrestrial ecosystems on atmospheric CO₂ : A model study, *Phys. Chem. Earth*, 21, 537-544, 1996.

Friend AD, Stevens AK, Knox RG, Cannell MGR. A process-based, terrestrial biosphere model of ecosystem dynamics (Hybrid 3.0). *Ecological Modelling* 95, 249-287, 1997.

Friend AD. PGEN: An integrated model of leaf photosynthesis, transpiration, and conductance. *Ecological Modelling*, 77, 233-255, 1995.

Fung I.Y., Tucker C.J. and Prentice K.C., Application of advanced very high resolution radiometer vegetation index to study atmosphere-biosphere exchange of CO₂. *J. Geophys. Res.*, 92, 2999-3015, 1987.

Gallo K.P., Experimental global vegetation index from AVHRR utilizing pre-launch calibration, cloud and sun-angle screening. Digital data, National Oceanic and Atmospheric Administration, National Geophysical Data Center, Boulder, Colorado, 1992.

Gargett A.E., Vertical eddy diffusivity in the ocean interior. *J. Mar. Res.*, 42, 359-393, 1984.

Gaspar P., Grégoris Y. and Lefevre J-M. A simple eddy kinetic energy model for simulations of the oceanic vertical mixing: tests at Station Papa and Long-Term Upper Ocean Study Site. *J. Geophys. Res.*, 195, C9, 16.179 -16.193, 1990.

Gérard J.-C., B. Nemry, L. François and P. Warnant. The interannual change of atmospheric CO₂: contribution of subtropical ecosystems ? *J. Geophys. Res.*, 26, 243-246, 1999.

GESAMP. 1989. Atmospheric input of trace species to world ocean. Reports and studies, 38. World Meteorological Organization, Geneva, 111 p.

Gond V, D. de Pury, H. Eerens, F. Veroustraete and R. Ceulemans, The Brasschaat pixel: interpretation of multitemporal NOAA-AVHRR reflectances of a multi-layer mixed forest, In: 'Forest ecosystem modelling, up-scaling and remote sensing', Eds. Ceulemans R. et al., SPB Academic Publishing The Hague, 221-234, 1999.

Haxeltine, A., and I., Prentice, Biome3 : an equilibrium terrestrial biosphere model based on ecophysiological constraints, resource availability, and competition among plant functional types, *Global Biogeochemical Cycles* 10(4), 693-709, 1996.

Hedges J. I. and R. G. Keil. Sedimentary organic matter preservation: an assessment and speculative synthesis. *Marine Chemistry*, 49, 81-115, 1995.

Heimann M. and C.D. Keeling, A three dimensional model of atmospheric CO₂ transport based on observed winds, 2, Model description and simulated tracer experiments. *Geophys. Monogr.*, 55, 237-275, edited by AGU, Washington, 1989.

Heimann M., G. Esser, A. Haxeltine, et al, Evaluation of terrestrial carbon cycle models through simulations of the seasonal cycle of atmospheric CO₂ : first results of a model intercomparison study. *Global Biogeochemical Cycles*, 12, 1-24, 1998.

Hinze J.O. 1975. Turbulence. 2nd edition, McGraw Hill, New York, N.Y. 790pp.

Hirsch C. Numerical computation of internal and external flows, Volume 1. Fundamentals of numerical discretization. Wiley, Chichester, 1988. 515p.

Hirsch C., Numerical computation of internal and external flows. Volume 1. Fundamentals of numerical discretization, Wiley, Chichester, 1988, 515p.

Howard W. R., and W. L. Prell, Late Quaternary CaCO₃ production and preservation in the Southern Ocean: implications for oceanic and atmospheric carbon cycling, *Paleoceanography*, 9, 453–482, 1994.

Howarth R., Editor of Nitrogen Cycling in the North Atlantic Ocean and its Watersheds. Special issue, *Biogeochemistry*, 35, n°1, 304p, 1996.

Hubert B., L. François, P. Warnant and D. Strivay. Stochastic generation of meteorological variables effects on global models of water and carbon cycles in vegetation and soils, *J. of Hydrol.*, 212-213, 318-334, 1998.

Huthnance J. Circulation, exchange and water masses at the ocean margin: the role of physical processes at the shelf edge. *Prog. Oceanogr.* 35, 353-431, 1995.

Iacobellis S.F., R. Frouin, H. Razafimpanilo, R.C.J. Somerville and S.C. Piper, North African savanna fires and atmospheric carbon dioxide. *J. Geophys. Res.*, 99D, 8321-8334, 1994.

IPCC (Intergovernmental Panel on Climate Change), Climate Change 1995, The Science of Climate Change. Cambridge University Press, Cambridge, 572p.

IPCC (Intergovernmental Panel on Climate Change). Radiative Forcing of Climate Change and An Evaluation of the IPCC IS92 Emission Scenarios. Edited by Houghton J.T., L.G. Meira Filho, J. Bruce, Hoesung Lee, B. A. Callander, E. Haites, N. Harris and K. Maskell, Cambridge University Press, 1995.

Jacques G. and P. Tréguer. Ecosystèmes pélagiques marins, volume 19 of Collection d'écologie. Masson, Paris, 1986. 243p.

Jahnke R. A.. The global ocean flux of particulate organic carbon: areal distribution and magnitude. *Global Biogeochemical Cycles*, 10, 71–88, 1996.

Jain A. K., H. S. Kheshgi, M. I. Hoffert, and D. J. Wuebbles, Distribution of radiocarbon as a test of global carbon cycle models, *Global Biogeochemical Cycles*, 9, 153–166, 1995.

Jerlov, N.G. 1976. Marine Optics. Elsevier, New York, 231p, 1995.

Joos F., and M. Bruno, Long-term variability of the terrestrial and oceanic carbon sinks and the budgets of carbon isotopes ¹³C and ¹⁴C, *Global Biogeochemical Cycles*, 12, 277–295, 1998.

Joos F., Imbalance in the budget, *Nature*, 370, 181–182, 1994.

Joos F., J. C. Orr, and U. Siegenthaler, Ocean carbon transport in a box-diffusion versus a general circulation model, *Journal of Geophysical Research*, 102, 12367–12388, 1997.

Kaduk J. and M. Heimann, A prognostic phenology scheme for global terrestrial carbon cycle models. *Climate Research*, 6(1), 1-19, 1989.

Keeling C. D., Standardization of notations and procedures. 3.3 The modelling of rare isotopic carbon with regards to notation, in *Carbon Cycle Modelling*, edited by B. Bolin, pp. 89–101, John Wiley & Sons, New York, 1981.

Kidwell K, NOAA polar orbiter data user's guide, US Department of Commerce, National Oceanic and Atmospheric Administration, National Environmental Satellite, Data and Information Service, Washington, DC 20233, Revision January 1997.

Kindermann J., M.K.B. Lüdeke, F-W Badeck *et al.*, Structure of a global and seasonal carbon exchange model for the terrestrial biosphere - The Frankfurt Biosphere Model (FBM). *Wat. Air and Soil Poll.*, 70(1-4), 675-684, 1993.

Knorr W. and M. Heimann, Impact of drought stress and other factors on seasonal land biosphere CO₂ exchange studied through an atmospheric tracer transport model. *Tellus 47B*, 471-489, 1995.

Kohlmaier G.H., F-W Badeck, R.D. Otto, *et al.*, The Frankfurt Biosphere Model: a global process-oriented model of seasonal and long-term CO₂ exchange between terrestrial ecosystems and the atmosphere. Part II. Global results for potential vegetation in an assumed equilibrium state. *Climate Research*, 8, 61-87, 1997.

Kolmogorov A.N., The equation of turbulent motion in an incompressible fluid. *Izv. Akad. Nauk. SSSR, Ser. Fiz.*, 6, pp. 56-58, 1942.

Kraus E.B., *Atmosphere Ocean Interaction*. Claredon Press, Oxford, England. 275pp, 1972.

Law R.M., Rayner P.J., A.S. Denning *et al.*, Variations in modeled atmospheric transport of carbon dioxide and the consequences for CO₂. *Global Biogeochemical Cycles*, 10, 783-796, 1996.

Leuenberger, M., U. Siegenthaler, and C. C. Langway, Carbon isotope composition of atmospheric CO₂ during the last ice age from an Antarctic ice core, *Nature*, 357, 488–490, 1992.

Levitus S. and T.P. Boyer,. World Ocean Atlas 1994 - Volume 4: Temperature. NOAA Atlas NESDIS 4. U.S. Department of Commerce, Washington, D.C, 117 pp, 1994a.

Levitus S., R. Burgett and T.P. Boyer, World Ocean Atlas 1994 - Volume 3: Salinity. NOAA Atlas NESDIS 3. U.S. Department of Commerce, Washington, D.C., 99 pp, 1994b.

Liu K.K., K. Iseki and S.-Y. Chao, Continental margin carbon fluxes. In: The Changing Carbon Cycle: A midterm synthesis of the Joint Global Ocean Flux Study, R.B. Hanson, H.W. Ducklow and J.G. Field eds., pp. 187-239. International Geosphere-Biosphere Programme Book Series, Cambridge: Cambridge University Press, 2000a.

Liu K.K., L. Atkinson, C.T.A. Chen, S. Gao, J. Hall, R.W. McDonald, L. Talaue McManus, R. Quiñones, 2000b. Submitted to Eos, Transactions, American Geophysical Union.

Longhurst, A. R., Role of the marine biosphere in the global carbon cycle, *Limnology and Oceanography*, 36, 1507–1526, 1991.

Lüdeke M.K.B., F.W. Badeck, R.D. Otto, *et al.*, The Frankfurt Biosphere Model: a global process oriented model for the seasonal and longterm CO₂ exchange between terrestrial ecosystems and the atmosphere. Part 1: Model description and illustrating results for the vegetation types cold deciduous and boreal forests. *Climate Research* 4, 143-166, 1994.

Maier-Reimer E. , U. Mikolajewicz, and K. Hasselmann. Mean circulation of the Hamburg LSG OGCM and its sensitivity to the thermohaline surface forcing. *Journal of Physical Oceanography*, 23, 731–757, 1993.

Maier-Reimer E., U. Mikolajewicz, and K. Hasselmann, Mean circulation of the Hamburg LSG OGCM and its sensitivity to the thermohaline surface forcing, *Journal of Physical Oceanography*, 23, 731–757, 1993.

Maslin M. A., M. A. Hall, N. J. Shackleton, and E. Thomas, Calculating surface water pCO₂ from foraminiferal organic $\delta^{13}\text{C}$, *Geochimica et Cosmochimica Acta*, 60, 5089–5100, 1996.

Matthews E., Global vegetation and land use: new high-resolution data bases for climate studies. *J. Clim. Appl. Met.* 22, 474-487, 1983.

Matthews E., Global vegetation and land use : new high resolution data bases for climate studies. *J. Clim. And applied meteor.* 22, 474-487, 1983.

- Mayaux P, E. Janodet, C. Blair-Myers and P. Legeay-Janvier, 1997, Vegetation map of Central Africa at 1 :5.000.000, TREES series D : Thematic outputs N° 1, Space Applications Institute, EC-JRC, EUR 17322 EN.
- Melillo J., A. McGuire, D. Kicklighter III, B.M., C. Vorosmarty, A. Schloss, Global climate change and terrestrial net primary production. *Nature* 363, 234-240, 1993.
- Meybeck M. C, N, P and S in rivers: from sources to global inputs. In: *Interactions of C, N, P and S Biogeochemical Cycles and Global Change*, R. Wollast, F.T. Mackenzie and L. Chou, eds. NATO ASI Series, Vol. 14. Springer_Verlag, Berlin, pp. 163-193, 1993.
- Millero F. J.. Thermodynamics of the carbon dioxide system in the oceans. *Geochimica et Cosmochimica Acta*, 59, 661–677, 1995.
- Monteith J, Solar radiation and productivity in tropical ecosystems, *Journal of Applied Ecology*, 9, 747-766, 1972.
- Mook W. G., J. C. Bommerson, and W. H. Staverman. Carbon isotope fractionation between dissolved bicarbonate and gaseous carbon dioxide. *Earth and Planetary Science Letters*, 22, 169–176, 1974.
- Myneni R and D. Williams, On the relationship between fAPAR and NDVI, *Remote Sensing of Environment*, 49, 200-211, 1994.
- Nelson D. M., P. Tréguer, M. A. Brzezinski, A. Leynaert, and B. Quéguiner. Production and dissolution of biogenic silica in the ocean: revised global estimates, comparison with regional data and relationship to biogenic sedimentation. *Global Biogeochemical Cycles*, 9, 359–372, 1995.
- Nelson, D. M., P. Tréguer, M. A. Brzezinski, A. Leynaert, and B. Quéguiner, Production and dissolution of biogenic silica in the ocean: revised global estimates, comparison with regional data and relationship to biogenic sedimentation, *Global Biogeochemical Cycles*, 9, 359–372, 1995.
- Nemry B., François L., Gérard J.-C., Bondeau A., M. Heimann and the participants of the Potsdam NPP Model Intercomparison. Comparing global models of terrestrial net primary productivity (NPP): Analysis of the seasonal atmospheric CO₂ signal. *Global Change Biology*, 5 (Suppl. 1), 65-76, 1999.
- Nemry B., François L., Gérard J.-C., Otto D., Rasse D., Warnant P. Impact of crops on biomass and soil carbon: steady state simulations. In: Climate scenarios for agricultural, forest and ecosystem impacts. Proceedings of the ECLAT-2 Potsdam

Workshop 13-15 October, 1999. Published by the Climatic Research Unit of East Anglia, Norwich, July 2000.

Nemry B., L. François, P. Warnant, F. Robinet and J.-C. Gérard. The seasonality of the CO₂ exchange between the atmosphere and the land biosphere : A study with a global mechanistic vegetation model, *J. Geophys. Res.*, 101, 7111-7125, 1996.

Nixon, S.W., J.W. Ammerman, L.P. Atkinson, V.M. Berounsky, G. Billen, W.C. Boicourt, W.R. Boynton, T.M. Church, D.M. Ditoro, R. Elmgren, J.H. Garber, A.E. Giblin, R.A. Jahnke, N.J.P. Owens, M.E.Q. Pilson and S.P. Seitzinger, 1996. The fate of nitrogen and phosphorus at land-sea margin of the North Atlantic Ocean. In: Nitrogen Cycling in the North Atlantic Ocean and its Watersheds. R.W. Howarth, ed. Special issue, *Biogeochemistry*, 35, n°1, 141-180.

Otto R., E.R. Hunt and G.H. Kohlmaier (manuscript) Static and dynamic input data of Terrestrial Biogeochemical Models.

Paola J. and R. Schowengerdt, , A review and analysis of backpropagation neural networks for classification of remotely-sensed multi-spectral imagery, Review article, *Int. J. Remote Sensing*, 16, 3033-3058, 1995.

Paulson C.A. and J.J. Simpson, Irradiance measurements in the upper ocean. *J. Phys. Oceanogr.*, 7, 952-956, 1977.

Platt, T. C.L. Gallegos and W.G. Harrison, Photoinhibition of photosynthesis in natural assemblages of marine phytoplankton. *J. Mar. Res.*, 38, pp. 687-701, 1980.

Plöchl M. and W. Cramer, Possible impacts of global warming on tundra and boreal forest ecosystems: Comparison of some biogeochemical models. *Journal of Biogeography*, 22, 775-783, 1995b.

Plöchl M. and Cramer W., Coupling global models of vegetation structure and ecosystem processes. *Tellus*, 47B, 240-250, 1995a.

Prandtl L., Über ein neues Formelsystem für die ausgebildete Turbulenz. *Nachrichten der Akademie der Wissenschaften zu Göttingen, Math.-Phys. Kl.*, 6-19, 1945.

Prentice I.C., W. Cramer, S.P. Harrison, R. Leemans, R.A. Monserud., A.M. Solomon, A global biome model based on plant physiology and dominance, soil properties and climate. *Journal of Biogeography*, 19, 117-134, 1992.

Price J.F., Weller R.A. and Pinkel R., Diurnal cycling: observations and models of the upper ocean response to diurnal heating, cooling and mixing. *J. Geophys. Res.*, 91,

8411-8427, 1986.

Rahman H and G. Dedieu, SMAC: A simplified method for the atmospheric correction of satellite measurements in the solar spectrum, *Int. J. Remote Sensing*, 15, 123-143, 1994.

Randerson J.T., M.V. Thompson., T.J. Conway, I.Y. Fung, C.B. Field, The contribution of terrestrial sources and sinks to trends in the seasonal cycle. *Global Biogeochemical Cycles*, 11, 535-560, 1997.

Rao C and J. Chen, Inter-satellite calibration linkages for the visible and near-infrared channels of the Advanced Very High Resolution Radiometer on the NOAA-7, -9, and -11 spacecraft, *Int. J. Remote Sensing*, 16 (11), 1931-1942, 1995.

Roy R. N., L. N. Roy, K. M. Vogel, C. Porter-Moore, T. Pearson, C. E. Good, F. J. Millero, and D. M. Campbell. The dissociation constants of carbonic acid in seawater at salinities 5 to 45 and temperatures 0 to 45 °C. *Marine Chemistry*, 44, 249–267, 1993.

Ruimy A, Kergoat L, Bondeau A and participants of "POTSDAM 95" (1999) Results of the Potsdam '95 IGBP NPP model intercomparison workshop: Analysis of differences in light absorption, light-use efficiency, and whole plant respiration costs.

Running SW, Hunt ER (1993) Generalization of a forest ecosystem process model for other biomes, BIOME-BGC, and an application for global-scale models. In: *Scaling Processes Between Leaf and Landscape Levels* (eds Ehleringer JR, Field C), pp. 141-158. Academic Press, Orlando.

Russell G and Lerner J (1981) A new finite-differencing scheme for the tracer transport equation. *J. Appl. Meteor.*, 20, 1483-1498.

Sabbe H, H. Eerens and F. Veroustraete, *Estimation of the carbon balance of European terrestrial ecosystems by means of the C-Fix model*, Proc. "1999 EUMETSAT Meteorological Satellite Data Users' Conference", 6-10 Sept. 1999, Copenhagen, Denmark, 271-278, 1999.

Sanyal, A., N. G. Hemming, and W. S. Broecker, Changes in ph in the eastern equatorial Pacific across stage 5–6 boundary based on boron isotopes in foraminifera, *Global Biogeochemical Cycles*, 11, 125–133, 1997.

Sarnthein, M., K. Winn, S. J. Jung, J.-C. Duplessy, L. Labeyrie, H. Erlenkeuser, and G. Ganssen, Changes in east Atlantic deepwater circulation over the last 30000 years: eight time slice reconstructions, *Paleoceanography*, 9, 209–267, 1994.

Saunders R and K. Kriebel, An improved method for detecting clear sky and cloudy radiances from AVHRR data, *Int. J. Remote Sensing*, Vol. 9(1), 123-150, 1988.

Schloss A, Wittenberg U, Kicklighter DW and participants of "POTSDAM 95" (1999) Results of the '94 and '95 IGBP NPP model intercomparison: comparison of annual net primary productivity and climate drivers.

Sellers P, Canopy reflectance, photosynthesis and respiration, *Int. J. Remote Sensing*, 6, 1335-1372, 1985.

Shaffer, G., Effects of the marine biota on global carbon cycling, in *The Global Carbon Cycle*, edited by M. Heimann, vol. 115 of NATO ASI Series, pp. 431–455, Springer Verlag, Berlin Heidelberg, 1993.

Siegenthaler U. and K. O. Münnich. $^{13}\text{C}/^{12}\text{C}$ fractionation during CO_2 transfer from air to sea. In B. Bolin, editor, *Carbon Cycle Modelling*, pages 249–257. John Wiley & Sons, New York, 1981.

Siegenthaler U. . Carbon dioxide: its natural cycle and anthropogenic perturbation. In P. Buat-Ménard, editor, *The Role of Air-Sea Exchange in Geochemical Cycling*, volume C185 of *NATO ASI Series*, pages 209–247. D. Reidel Publishing Company, Dordrecht, Holland, 1986.

Six KD, Maier-Reimer E (1996) Effects of plankton dynamics on seasonal carbon fluxes in an ocean general circulation model. *Global Biogeochemical Cycles*, 10, 559-583.

Snyder J, Map projections - a working manual, USGS Professional Paper 1395, 1987.

Soetaert K., P.M.J. Herman, J.J. Middelburg, C. Heip, C.L. Smith, P. Tett and K. Wild-Allen, Numerical modelling the shelf break ecosystem: integrating field measurements of chlorophyll, primary production, zooplankton, nitrate, ammonium, oxygen and sediment properties. Submitted and accepted to *Deep-Sea Research II, Special Issue on OMEG*, 2001.

Spitters Van Keulen and Van Kraalingen, A simple and universal crop growth simulation: SUCROS87, In: "Simulation and systems management in crop protection", Eds. Rabbinge et al., Simulation Monographs, PUDOC, Wageningen, The Netherlands, 1989.

Steinwand D, Mapping raster imagery to the Interrupted Goode Homolosine projection, USGS-EROS Data Center, Sioux Falls, USA,

<http://edcwww.cr.usgs.gov/landdaac/1KM/goodesarticle.html>

Stocker T. F., W. S. Broecker, and D. G. Wright, Carbon uptake experiments with a zonally-averaged global ocean circulation model, *Tellus*, 46B, 103–122, 1994.

Stuiver, M., and H. A. Polach, Reporting of ^{14}C data, *Radiocarbon*, 19, 355–363, 1977.

Stuiver, M., H. Sturmer, and T. McConnaughey, GEOSECS Atlantic and Pacific ^{14}C distribution, in *Carbon Cycle Modelling*, edited by B. Bolin, pp. 201–221, John Wiley & Sons, New York, 1981.

Tans PP, Thoning KW, W.P. Elliott, T.J. Conway, Error estimates of background atmospheric CO_2 patterns from weekly flask samples. *J. Geophys. Res.*, 95, 14063–14070, 1990.

Toggweiler J. R., and B. Samuels, New radiocarbon constraints on the upwelling of abyssal water to the ocean's surface, in *The Global Carbon Cycle*, edited by M. Heimann, vol. 115 of NATO ASI Series, pp. 333–366, Springer Verlag, Berlin Heidelberg, 1993.

Toggweiler J. R., K. Dixon, and K. Bryan, Simulations of radiocarbon in a coarse-resolution world ocean model. 1. Steady state prebomb distributions, *J. Geophys. Res.*, 94, 8217–8242, 1989a.

Toggweiler J. R., K. Dixon, and K. Bryan, Simulations of radiocarbon in a coarse-resolution world ocean model. 2. Distributions of bomb-produced carbon 14, *J. Geophys. Res.*, 94, 8243–8264, 1989b.

Trenberth K. E., J. G. Olson, and W. G. Large. A global ocean wind stress climatology based on ECMWF analyses. Technical Report NCAR/TN-338+STR, National Center for Atmospheric Research, Boulder, Colorado, 1989b.

Trenberth K. E., W. G. Large, and J. G. Olson. The effective Drag coefficient for evaluating wind stress over the oceans. *Journal of Climate*, 2, 1507–1516, 1989a.

Trenberth K. E., W. G. Large, and J. G. Olson. The mean annual cycle in global ocean wind stress. *Journal of Physical Oceanography*, 20, 1742–1760, 1990.

Tsunogai S. and S. Noriki. Particulate fluxes of carbonate and organic carbon in the ocean. is the marine biological activity working as a sink of the atmospheric carbon? *Tellus*, 43:256–266, 1991.

Tsunogai, S., and S. Noriki, Particulate fluxes of carbonate and organic carbon in the

ocean. is the marine biological activity working as a sink of the atmospheric carbon?, *Tellus*, 43, 256–266, 1991.

UNESCO. *Thermodynamics of the carbon dioxide system in seawater*, volume 51 of UNESCO technical papers in marine science. UNESCO, 1987. 21p.

Verhoef W, Light scattering by leaf layers with application to canopy reflectance modelling: the SAIL-model, *Remote Sensing of Environment*, 16, 125-141, 1984.

Verhoef W, Theory of radiative transfer models applied in optical remote sensing of vegetation canopies, PhD-dissertation, Landbouwwuniversiteit Wageningen, The Netherlands, ISBN 90-5485-804-4, 310 p, 1998.

Veroustraete F, J. Patyn and R. Myneni, Estimating net ecosystem exchange of carbon using the Normalised Difference Vegetation Index and an ecosystem model. *Remote Sens. of Environment*, 58, 115-130, 1996.

Viovy N, O. Arino and A. Belward, The Best Index Slope Extraction (BISE): a method for reducing noise in NDVI time-series, *Int. J. Remote Sensing*, 13, 1585-1590, 1992.

Vogel J. C., P. M. Grootes, and W. G. Mook. Isotopic fractionation between gaseous and dissolved carbon dioxide. *Zeitschrift für Physik*, 230, 225–238, 1970.

Walsh, J.J. Importance of continental margins in the marine biogeochemical cycling of carbon and nitrogen. *Nature*, vol. 350, 53-55, 1991.

Wanninkhof R. Relationship between wind speed and gas exchange over the ocean. *Journal of Geophysical Research*, 97, 7373–7382, 1992.

Wanninkhof R. and M. Knox. Chemical enhancement of CO₂ exchange in natural waters. *Limnology and Oceanography*, 41, 689–697, 1996.

Wanninkhof, R., Relationship between wind speed and gas exchange over the ocean, *Journal of Geophysical Research*, 97, 7373–7382, 1992.

Warnant P, Modélisation du cycle du carbone dans la biosphère continentale à l'échelle globale, PhD-dissertation, Univ. de Liège, Laboratoire de Physique Atmosphérique et Planétaire, 276 p, 1999.

Warnant P. Modélisation du cycle du carbone dans la biosphère continentale à l'échelle globale. Ph. D. Université de Liège, Belgique, 1999.

Warnant P., L. François, B. Nemry, B. Hubert, N. Molitor, G. Colinet and J.-C. Gérard. A new distribution of vegetation types and its inclusion on a global biosphere

model. Proceedings of the International Colloquium Photosynthesis and Remote Sensing, 28-30 August 1995, Montpellier. G. Guyot, EARSeL, Paris, 1995.

Warnant P., L. François, D. Strivay and J.-C. Gérard. CARAIB: A global model of terrestrial biological productivity. *Global Biogeochemical Cycles*, 8, 255-270, 1994.

Warnant, P., 1999. Modélisation du cycle du carbone dans la biosphère continentale à l'échelle globale. Ph.D. thesis, Université de Liège, Liège. (In French).

Warnant, P., L.M. François, D. Strivay, J.-C., Gérard, CARAIB : a global model of terrestrial biological productivity,. *Global Biogeochemical Cycles* 8(3), 255-270, 1994.

Watson A. J. and P. S. Liss. Marine biological controls on climate via the carbon and sulfur geochemical cycles. *Philosophical Transactions of the Royal Society of London*, 353, 41–51, 1998.

Winguth, A. M. E., E. Maier-Reimer, U. Mikolajewicz, and J.-C. Duplessy, On the sensitivity of an ocean general circulation model to glacial boundary conditions, Tech. Rep. 203, Max-Planck-Institut für Meteorologie, Hamburg, Germany, 1996.

Wollast R. and Chou L. The carbon cycle at the ocean margin in the Northern Gulf of Biscay. Submitted and accepted to *Deep-Sea Research II, Special Issue on OMEX*, 2001.

Wollast R. The silica problem. In E. D. Goldberg, editor, *The Sea*, volume 5, pages 359–392. Wiley Interscience, New York, 1974.

Wollast, R. Evaluation and comparison of the global carbon cycle in the coastal zone and in the open ocean. In: "The Sea: The Global Coastal Ocean: Processes and Methods". Brink, K.H. and A. R. Robinson, eds. Vol. 10. John Wiley & Sons, Inc. N.Y. pp. 213-252, 1998.

Wollast, R. The coastal Organic Carbon cycle: Fluxes, sources, and sinks. In: *Ocean margin processes in global change*, R.F.C.Mantoura, J.M. Martin and R. Wollast,eds. Dahlem Workshop Report, J. Wiley & sons, Chichester, pp. 365-381, 1991.

Wollast, R., The relative importance of biomineralization and dissolution of CaCO₃ in the global carbon cycle, in *Past and Present Biomineralization Processes*, edited by F. Doumenge, pp. 13–35, Monaco, Institut Océanographique, 1994.

Yu, E.-F., R. Francois, and M. P. Bacon, Similar rates of modern and last-glacial ocean thermohaline circulation inferred from radiochemical data, *Nature*, 379, 689–694, 1996.

**NATURAL HOLOCENE CLIMATE VARIABILITY
AND RECENT ANTHROPIC IMPACT IN
BELGIUM**

UNIVERSITÉ CATHOLIQUE DE LOUVAIN (UCL)
INSTITUT GÉOLOGIQUE
UNITÉ PAGE
Place L. Pasteur 3
B-1348 LOUVAIN-LA-NEUVE
G. SERET (coordinator CG/DD/12)
G. WANSARD

TABLE OF CONTENTS

ABSTRACT	1
1. INTRODUCTION	1
2. OSTRACOD GEOCHEMISTRY: LABORATORY EXPERIMENTS	2
3. THE TRAVERTINE ANNEVOIE-ROUILLON SEQUENCE	2
3.1 Statistical analyses	2
3.2 Ostracod geochemistry	3
4. THE TREIGNES SEQUENCE	3
REFERENCES	4

ABSTRACT

The main objective of the project is the reconstruction of the natural climate variability during the Holocene from the study of travertine sequences located in Belgium.

Pollen, ostracod paleoecology and geochemistry are the main proxy data used for paleoenvironmental reconstitution. Statistical analyses have been performed using the ostracod assemblages of the travertine sequence located at Annevoie-Rouillon, near Namur. These results show past changes in the hydrodynamic of the system. The Mg contents in three fossil ostracod species were determined. In this state of the research, we hypothesise that the observed variation in the ostracod Mg/Ca ratios mainly reflect precipitation changes. On the other hand, the end of the travertine edification should be related to a drastic increase of the precipitation, both with an increase of an erosion activity. Such reconstruction is now in progress for an other travertine sequence, located at Treignes.

The project involves the development of the ostracod geochemistry method. Several laboratory experiments and field collections provided a better understanding of the variability of partition coefficients.

1. INTRODUCTION

The main objective of the project is the reconstruction of the natural climate variability during the Holocene, and the detection of a possible human impact on the environment.

To achieve this goal, two travertine sequences located in south of Belgium were sampled. The study of the Annevoie-Rouillon sequence, located between Namur and Dinant along the Meuse, is finished. The work is in progress for the travertine located at Treignes (Viroin valley).

In Belgium, travertine deposits are important archives for reconstructing past hydrology and environmental changes during the Holocene. Travertine are built by calcium carbonate precipitation mainly due to CO₂ degassing. The decrease of CO₂ content in water is linked to physico-chemical (temperature and pressure) and biological (photosynthetic activity) processes.

In this project, mainly two proxy-data are used: pollen and ostracods (aquatic micro crustaceans). Pollen is used to reconstruct past vegetation landscapes and may be useful for detecting human activities such as farming, forest clearance,... The study of ostracod assemblages may provides local and regional information linked to the hydrological conditions (precipitation) and water temperature.

Moreover, geochemical study of trace-element contents incorporated in the calcite of the ostracod shells offers the opportunity to quantify water chemistry and temperature changes. As this method is relatively new, laboratory experiments and field collections of ostracods are driven in order to provide a better understanding of the links between trace-element contents of ostracods and physical, chemical, and biological factors.

2. OSTRACOD GEOCHEMISTRY: LABORATORY EXPERIMENTS

Several studies have shown that the trace-element composition of the ostracod valves is controlled by the chemistry and the temperature of the water in which calcification occurs (Chivas et al., 1986; Wansard et al., 1999). Newly-identified factors modifying the traceelement partitioning between ostracod shells and water have been recently reported (Xia et al., 1997; Wansard et al., 1998). Particularly, we hypothesised that typical freshwater species do not show a Mg-temperature relationship (Wansard & Roca, 1997; Wansard et al., 1999).

In order to test this hypothesis, several experiments have been realised in controlled laboratory conditions. To assess our preliminary results (cf. annual SSTC report 1998), new experiments using *Candona neglecta* and *Heterocypris incongruens* species were recently achieved.

3. THE TRAVERTINE ANNEVOIE-ROUILLON SEQUENCE

Preliminary results based on ostracod and pollen data were provided in the two first annual reports. Here we provide new results based on statistical analysis of ostracod assemblages and trace-element contents in ostracod shells (Figure 1).

3.1 Statistical analyses

Correspondence analysis (CA) is used in treating ostracod distribution. The results of the CA analysis shows that axis 1 separates species and samples (Figure. 1A) in a gradient that can be interpreted in terms of environmental conditions. The species - *P. zenkeri*, *C. neglecta*, *C. candida* and *Herpetocypris sp.* are present at one end of the first axis, and *Pseudocandona zschokkei*, *S. triquetra*, *F. brevicomis*, *C. vavrai* and *E. Pigra* are present at the other end of the axis 1 (Figure. 1A).

The plot of the percentage of each species in each sample as a function of the coordinate on the first axis reveals the quality of the gradient or relay index (RI) (Figure 1 B). According to the ecological preference of the species, the RI depicts the changes in the ostracod habitat:

- low RI values characterise a slow, or even stagnant, water regime;
- medium RI values correspond to a typical spring regime;
- high RI values depicts an hyporheique habitat.

Theses habitats can be related to the level of energy in the environment, and partially to the hydrological regime. An other evidence is the increase of the grain size of the sediment with the RI. Past changes in the hydrodynamic of the system is illustrated by the RI variations along the whole studied sequence (Figure. 1 C).

3.2 Ostracod geochemistry

Figure 1 C shows the variation in the ostracod Mg/Ca ratio for three species along the whole section. The ostracod Mg/Ca ratio is mainly a function of the water Mg/Ca ratio (Mansard et al., 1998). The Mg/Ca curve shows several fluctuations, with the lowest Mg/Ca ratios in ostracods corresponding to the higher flow regime (RI). Generally, the changes in the water chemistry is mainly due to the aquifer discharge in the travertine system, and hence to the precipitation regime. The greater the discharge (precipitation), the more diluted the water. In this state of the research, we hypothesise that variation in ostracod Mg/Ca ratios reflect precipitation changes. On the other hand, the end of the travertine edification should be related to a drastic increase of the precipitation, both with an increase of an erosion activity.

Several datations are necessary to quantify the apparent cyclicity observed in the Mg/Ca curve. Until now, only one date (14C) is available: 7290 ± 50 y BP at 1.4 m depth (Cors et al., 1998).

4. THE TREIGNES SEQUENCE

The study of the travertine deposited at Treignes started two months ago. The stratigraphic log of a 4 m long sequence and the sampling were realised. One datation is submitted. This travertine sequence is characterised by the presence of peat layers, and charcoals. This should let to a good chronological framework.

REFERENCES

Chivas, A. R., De Deckker, P. & Shelley, J. M. G. (1986): Magnesium and strontium in non-marine ostracod shells as indicators of palaeo-salinity and palaeo-temperature. *Hydrobiologia* 143: 135-142.

Cors M., Wansard G. & Rekk S. (1998). Etude du pollen et des ostracodes du travertin d'Annevoie - Rouillon (Belgique): reconstitution de l'évolution paléo-environnementale au cours du Boreale et de l'Atlantique. *Acta Geogr. Lov.*, 37: 47-61.

Wansard, G. & Roca, J. R. (1997): Etude experimentale de l'incorporation du strontium et du magnesium dans les valves d'un ostracode d'eau douce, *Herpetocypris brevicaudata* (Crustacea, Ostracoda). *C. R. Acad. Sci. Paris* 325: 403-409.

Wansard, G., De Deckker, P. & Julia, R. (1998): Variability in ostracod partition coefficients $D(\text{Sr})$ and $D(\text{Mg})$. Implications for lacustrine palaeo-environmental reconstructions. *Chem. Geol.* 146: 39-54.

Wansard, G., Mezquita, F. & Roca, J. R. (1999). Experimental determination of strontium and magnesium partitioning in calcite of the freshwater ostracod *Herpetocypris internaedia*. *Archiv Hydrobiology*, 145: 237-253.

Xia, J., Engstrom, D. R. & Ito, E. (1997): Geochemistry of ostracode calcite: Part 2. The effects of water chemistry and seasonal temperature variation on *Candona rawsoni*. *Geochim. Cosmochim. Acta* 61: 383-391.

Programme SSTC CG/DD/1 2

Variabilite Naturelle du Climat Holocene et impact anthropique recent en Belgique.

La recherche prevue dans le programme reposait essentiellement sur ('analyse de travertins de fonds de vallees en Belgique par la mise en oeuvre de deux disciplines complementaires: la palynologie et l'ostracodologie.

En outre, 7 datations ^{14}C ont ete effectuees afin de bien positionner ('evolution environnementale repertoriee par ('etude. Ces datations etablissent que l' evolution est finement detaillee pour la partie inferieure de ('Holocene entre 9190 (± 50) y. BP et 7290 (± 50) y. BP.

Un premier resultat a ete de confirmer que l'arret de l'edification des massifs de travertin de fonds de vallees, en Belgique, etait lie a une forte augmentation des precipitations.

Dans le cadre du programme, ce resultat devait titre precise, et notamment quantifie. Cet objectif a du titre abandonne en raison du non-renouvellement inopine du contrat de Mme Cors responsable des analyses et interpretations palynologiques.

Il faut encore ajouter qu'a [l'occasion du projet etaient aussi prevues implicitement plusieurs experimentations en laboratoire sur le comportement d'especes selectionnees d'ostracodes cultives dans de conditions rigoureusement controlees de temperature et de chimie des eaux. Cette partie du programme a ete largement developpee ainsi que l'indiquent plusieurs publications soumisees a des revues scientifiques ou en preparation. Il s'agit, pour l'essentiel, d'ostracodes preleves en region mediterraneenne et etudies avec des collaborateurs espagnols. Le texte de deux articles est joint au dossier:

- Guy Wansard, Josep Roca and Francesc Mesquita - Experimental determination of strontium and magnesium partitioning in calcite of the freshwater ostracod *Herpetocypris intermedia*. Arch. Hydrobiol. 145 2 237-253 - May 1999.
- Francesc Mezquita, Josep Roca and Guy Wansard - Moulting, survival and calcification: the effect of temperature and water chemistry of an ostracod crustacean (*Herpetocypris intermedia*) under experimental conditions. Arch. Hydrobiol. 146 2 219-238 - Sept 1999.

En bref sont observees et quantifiees les conditions controlant la calcification des coquilles de l'*Herpetocypris intermedia*.

Il se revele que cet ostracode est relativement peu sensible aux fluctuations de la temperature. Par contre, la vitesse et l'intensite de l'edification de la coquille sont tres influencees par la chimie de l'eau, et en particulier par les teneurs en bicarbonates (Ca, Mg, Sr) mais aussi en chlore et en sodium.

UNDERSTANDING THE DECADAL-CENTURY- TO MILLENNIA CLIMATE VARIABILITY BY SIMULATING EXTREME PALEOCLIMATIC SITUATIONS

UNIVERSITÉ CATHOLIQUE DE LOUVAIN (UCL)
INSTITUT D'ASTRONOMIE ET DE GÉOPHYSQUE G. LEMAÎTRE
Chemin du Cyclotron, 2
B-1348 LOUVAIN-LA-NEUVE
A. BERGER (coordinator CG/DD/13)
M.F. LOUTRE
M. CRUCIFIX
P. TULKENS¹
C. BERTRAND²
J.M. CAMPIN²

¹ NOW AT TASK FORCE SUSTAINABLE DEVELOPMENT - FEDERAL PLANNING BUREAU

² NOW AT MASSACHUSETTS INSTITUTE OF TECHNOLOGY (MIT)
EARTH, ATMOSPHERE AND PLANETARY SCIENCES DEPARTMENT
(EAPS), CAMBRIDGE (USA)

TABLE OF CONTENTS

ABSTRACT	1
1. INTRODUCTION	2
1.1 Rationale	2
1.2 Strategy	3
2. THE CLIMATE MODEL	3
2.1 General description	3
2.2 Ocean_sea-ice model	4
2.3 Vegetation component	4
3. CLIMATE CHANGE IN THE PAST	7
3.1 The last millennium	7
3.2 Climate evolution during the Holocene	9
3.3 Abrupt events during the last glaciation	11
3.4 The climate during the Eemian	13
4. CONCLUSION	14
ACKNOWLEDGEMENTS	14
REFERENCES	15
LIST OF ABBREVIATIONS	18

ABSTRACT

The climate model designed in Louvain-la-Neuve for palaeoclimate purposes (Gallée et al., 1991; 1992) has been improved in two different directions. It has been coupled to a model representing the dynamics of the vegetation. Two types of vegetation are represented, i.e. tree and grass. Desert is a potential third type of land cover. Vegetation change is determined according to climate, more precisely temperature (growing degree-day, GDD0) and precipitation. Vegetation impacts on climate through the surface albedo.

The second improvement is related to the ocean representation. The ocean was represented by its upper mixed layer in the original version of the climate model. This representation has been replaced by a dynamic ocean model.

This new version of the model, called MoBidiC, allows us to investigate the short-term climate variability in the climate system. Therefore we studied the climate changes during the last millennium and more specially the impact of different origin for this variability either natural sources (volcanic activity, solar forcing) or human activities (greenhouse gases, sulphate emission, land cover change). Before the industrial period climate variability can largely be explained by the natural forcing effect. In particular, the temperature reconstruction can largely be explained by the variation in total solar irradiance. However during the industrial period (from 1765 up to now) the natural forcing alone is not able to explain the climate change and the anthropogenic forcing must be taken into account to simulate the observed climate changes.

Second we investigated climate change during older periods. We studied the conditions under which abrupt climate change can be simulated by the model either in interglacial or glacial periods. We derived the timing and amplitude of the different events following an initial freshwater input. In particular it is shown that after a freshwater input in the North Atlantic thermohaline circulation first shuts down and then resumes in one step during interglacial periods and in two steps in glacial periods.

At last, we analysed the stability of the climate through the Holocene. This study highlights the importance of the vegetation, especially in the high latitudes. Indeed it can induce there a further temperature change of a few degrees during the spring time over the Holocene.

1. INTRODUCTION

1.1 Rationale

There is a large concern about our future climate. This problem is made up of at least two components, i.e. the natural climate variability and the man-induced changes. Moreover different time and space scales should be taken into account. The understanding of climate changes and its mid-and long-term variability still needs to be improved before getting reliable climate predictions for the future. Therefore past climate still needs to be studied either through data collecting or through climate modelling. This second approach was used in this work, which goes beyond the simulation of past climate but tried to understand the processes and feedback leading it.

According to the astronomical theory of paleoclimate the solar energy available on the Earth is the main driver of the major long-term climate changes such as the Glacial-interglacial cycles. Moreover a large part of the climatic changes identified on shorter periods can also be related to insolation variations. However during periods such as the Holocene different feedbacks such as the vegetation-albedo-temperature feedback are playing a fundamental role.

Greenland ice cores have recorded rather rapid and strong climate changes, called Dansgaard-Oeschger (DO). Similarly, rapid climate changes were also recorded during Heinrich Events (HE) in the marine sediments. Simulation of rapid events of this kind can help first to better understand the chain of processes that lead to these events and second to determine whether the global warming could modify the occurrence of such events.

The last millennium is a key period for climate change because it experienced the beginning of the major human impact on its environment and therefore also on climate. It is of the utmost importance for predicting future climate to be able to distinguish between the natural climate variability and the anthropogenic impact on climate.

All these different time-scales (from millennium to several thousand of years and geological time scale) with their relevance, were investigated with the climate model developed and improved in Louvain-la-Neuve.

Coupled general circulation models of the atmosphere and the ocean are often considered as the most complete type of climate models currently available. Moreover recent progress in modelling the geosphere and the biosphere leads to attempts to built comprehensive 'climate system models'. The major limitation of

these models for long-term climate studies arises from their high computational cost. Therefore Earth system Models of Intermediate Complexity (EMICs) are very efficient and suited tools to perform transient climate experiments and to analyse feedbacks at work.

1.2 Strategy

The research undertaken during this project was twofold. First we improved the climate model already available mainly by adding a more comprehensive representation of the ocean dynamics (Hovine and Fichefet, 1994). A vegetation component was also included which was based on a continuous bioclimatic classification (Brovkin et al., 1997). Secondly climatic simulations were performed on different time scale from the millennium to 10,000 years in order to put forward the potential climatic variability and to explain their origin.

2. THE CLIMATE MODEL

2.1 General description

MoBidiC links the atmosphere, the terrestrial surface, the oceans and sea-ice. The surface is represented on a 5° latitudinal grid and each latitudinal band is divided in 2 continental sectors (one for Eurasia and Africa, one for America) and 3 oceans (Atlantic, Pacific and Indian). Each continental sector can be partly covered by snow and each ocean sector can be partly covered by sea-ice. The atmosphere dynamics is represented by a zonally averaged two-level quasi-geostrophic (QG) system of equations written in pressure coordinates (Sela and Wiin-Nielsen, 1971) and applied independently over each hemisphere. The numerical implementation is extended to the whole Earth from Gallée et al (1991). The radiative transfer is computed by dividing the model atmosphere into 10-15 layers, the exact number of which depends on the surface pressure over each surface type (Bertrand, 1998).

In each latitude belt each continent is divided into snow-free land, snow-covered land and ice sheets. Moreover it is characterised by a relative cover of trees, grass and potential desert. The albedo of the snow free continental areas is the weighted average of the desert, tree and grass albedo. The albedo of snow covered area is a function of snow precipitation frequency, snow surface temperature, zenith angle and underlying vegetation. The continental surface temperature is derived from the surface heat balance parameterised as in Taylor (1976).

The ocean representation of each basin is based on the zonally averaged form of the multi-level primitive equation ocean model described in Hovine and Fichefet (1994) and Crucifix et al (2001a).

2.2 Ocean_sea-ice model

This model of ocean circulation considers three zonally averaged ocean basins representing the Atlantic, Indian and Pacific oceans. In the North, lateral exchanges of heat and salt between the Atlantic and Pacific basins are allowed between 85 and 90°N. The Bering Strait connects the North Pacific with the Arctic Ocean. In the South lateral exchanges of heat and salt between the three oceans basins are allowed between 40 and 65°S to account for the Antarctic Circumpolar Current (ACC). Within each individual basin, the model formulation is based on the zonally averaged form of the multi-level primitive equation ocean model described in Bryan (1969) and Semtner (1986) (see also Tulkens, 1998 for a full description).

A simple thermodynamic-dynamic sea-ice model is coupled to the ocean model. It is based on the 0-layer thermodynamic model of Semtner (1976), with the modifications introduced by Harvey (1988, 1992). Leads are taken into account following the approach of Parkinson and Washington (1979). The one-dimension meridional ice advection scheme of Prather (1986) is also implemented with prescribed velocities from Harvey (1988).

The ocean model is able to simulate a rather realistic ocean circulation and a rather realistic conveyor belt pattern. The vertical diffusion parameter is playing a fundamental role for a realistic simulation of the global overturning circulation and meridional heat transport. It was also shown that the general underestimation of the wind has an important influence on the simulated thermohaline circulation and on the meridional heat transport.

The representation of sea ice and surface exchanges of heat and freshwater increases the realism of the model. The ocean_sea-ice model is able to simulate very nicely the NADW circulation, the water export from the Atlantic into the ACC, the main Pacific and Indian Ocean patterns. Antarctic Bottom Water (AABW) recirculates below NADW up to 30°N in the North Atlantic, in agreement with the description of water mass distribution in the global ocean given by Schmitz (1995).

2.3 Vegetation component

The dynamical vegetation model VECODE (Brovkin et al., 1997) is based on a continuous bioclimatic classification which describes vegetation as a composition of simple plant functional types (trees and grass). Equilibrium tree and grass fractions

are parameterised as a function of climate expressed as a sum of degree-days (GDD0) and annual precipitation. The characteristic time scale of the living biomass is determined from the carbon-cycle component of the model (about 80 to 100 years for trees in the northern high latitudes).

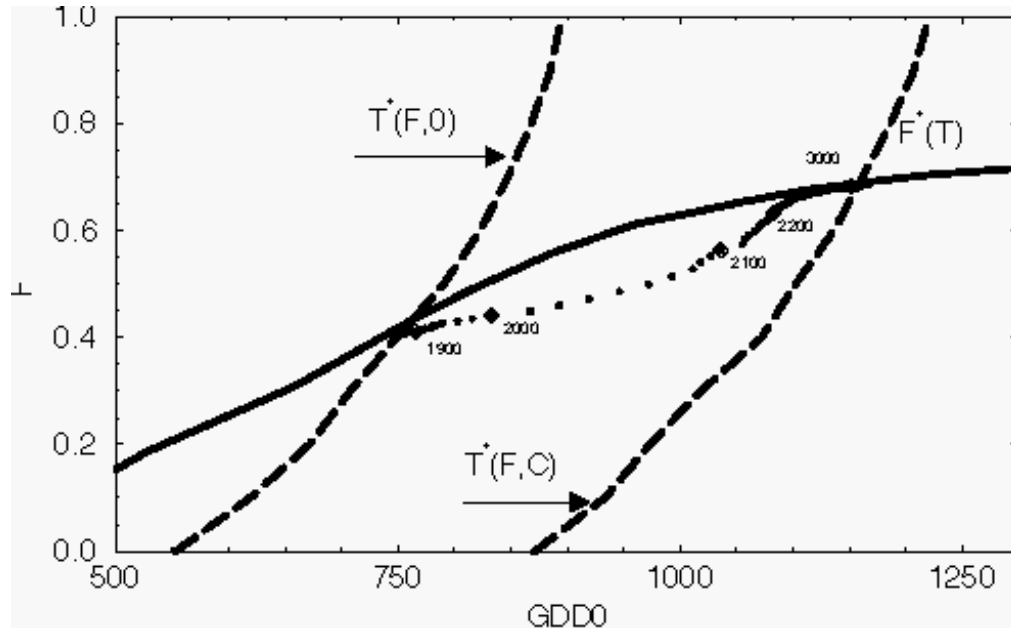


Figure 1: Representation of the system dynamics under transient CO_2 forcing with MoBidiC. Points 1 and 2 are for initial and final states, respectively. Dots show decadal averages, arrows are for dynamics during the years 1990-2060. The solid curve represents the tree fraction in equilibrium with a given climate state ($F^*(T)$), dashed lines are the climate in equilibrium with a prescribed climate state ($T^*(F,E)$) for present-day (0) and double CO_2 (C).

The stability of the climate-vegetation model in the northern high latitudes has been studied with MoBidiC, including the VECODE model. A strong positive climate-vegetation feedback can be put forward, i.e. the initial climate change induced by an external forcing is amplified through the vegetation change. However this amplification does not support multiple steady states. In other words there is a single equilibrium between climate and vegetation, even though the external forcings are modified, at least in the vicinity of the present climate state. With the dynamical ocean the climate sensitivity to the change in external forcing is rather small (compared to other model) and only very slightly higher for a cooler (low tree fraction) and a warmer climate (high tree fraction). This behaviour is related to the fact that snow decreases with increasing tree fraction and hence the forest-temperature feedback becomes less effective. In mixed-layer configuration the model exhibits a considerably higher sensitivity to climate change than with the dynamic ocean. This suggests that ocean dynamics exert a significant negative feedback through the thermohaline circulation. Indeed for large tree fraction the increase in SST and

precipitation in the high latitudes contribute to a weakening of the ocean circulation. As less heat is supplied to the 60-70°N zone, this compensates at least partly for the sea-ice albedo feedback. On the contrary, the diffusive parameterisation used in mixed layer circulation cannot account properly for the circulation effect. Therefore, sea-ice albedo feedback, which is no longer compensated for by an ocean circulation change, leads to overestimate climate sensitivity.

The response of the climate model to a transient increase in CO₂ concentration was then studied. For this simulation atmospheric CO₂ concentration grows from its pre-industrial value (280 ppmv at 1800AD) to its double level (560ppmv in 2065 AD). The scenario is based on ice core data (Neftel et al, 1990), observations (Keeling, 1993) and IPCC emission scenarios (Svirezhev et al, 1999; Houghton et al, 1992). After 2065 the CO₂ atmospheric concentration is assumed to be constant for the next 2000 years while climate-vegetation system relaxes towards equilibrium. The increase in global annual mean temperature due to a double CO₂ concentration is experiencing an additional increase of 0.1°C with interactive vegetation (compared to the response when vegetation is fixed to its present-day value). This further increase of temperature is mainly related to the northward extent of the forest and the subsequent positive albedo-temperature feedback. However the forest is simultaneously decreasing in the middle and low latitude. Therefore the global increase in temperature between the fixed and the interactive vegetation cases is in fact a balance between two opposite effects. Three steps can be identified in the response of the climate model to the increase in CO₂ concentration: (i) a slow temperature increase at nearly constant tree fraction until double CO₂ concentration is reached, (ii) a faster vegetation change, and (iii) a slow temperature increase towards equilibrium. Each step can be interpreted as the response of each sub-system: (i) corresponds to the increase in temperature due to the increased CO₂ concentration, (ii) records the response of vegetation, while (iii) is related to the response of the deep ocean. This transient experiment with MoBidiC shows a significant imbalance between vegetation cover and climate in the northern high latitudes for the present decade. The rate of vegetation cover changes doubles in the next two decades due to the delayed response of the climate system under accelerated CO₂ forcing. This simulation is in line with recent observation in the northern high latitude environment including decline in Arctic sea-ice cover, increase in surface air temperature and photosynthetic activity of plants, and even some indications of northward dynamics of the tree line (Serreze et al., 2000).

3. CLIMATE CHANGE IN THE PAST

3.1 The last millennium

The climate of the last millennium is simulated with MoBidiC in order to assess the potential impact of six different factors, i.e. natural (solar and volcanism) and human-induced (deforestation, additional greenhouse gases and tropospheric aerosol burden) forcings. All these factors are required to simulate the Earth temperature evolution over the last millennium. However a significant part of the low frequency temperature signal can be explained by the solar forcing (i.e. the change in the total solar irradiance) but the amplitude of the reconstructed temperature is larger than the simulated one. The greenhouse gas forcing allows the model to simulate an accelerated warming rate during the last 150 years and in particular during the last three decades. Deforestation, tropospheric sulphate and change in the insolation geometry over the last century only constrain the amplitude of the twentieth century warming to better fit the observations. Moreover taking into account the volcanic perturbation help to better match some recorded cooling events. More precisely, the analysis of the impact of each individual factor shows that only the greenhouse gas and the total solar forcing (TSI) have contributed to a long-term trend. The largest warming is induced by greenhouse gases and amounts to 0.79°C (0.56°C) to 1.17°C (0.79°C) in the Northern (Southern) Hemisphere over the last millennium according to the climate sensitivity to CO₂. On the other hand the model response to the TSI variations scaled to Reid reconstruction (1997) exhibits a substantial net warming of 0.62°C (0.44°C) in the Northern (Southern) hemisphere over the same time interval. Deforestation, volcanism and tropospheric sulphates contribute to a long-term cooling of less than 0.3°C for each of them. However none of the individual forcings appear to be sufficient to generate alone a climate response similar to the reconstructed temperature time series.

When all the natural forcings are combined together the model accounts for up to 29% of the decadal-scale variance of the Northern Hemisphere temperature over the pre-industrial period (1000 to 1765 AD). Moreover the long-term cooling trend exhibited by the temperature reconstruction can be largely explained by the variation in total solar irradiance. During the industrial period (from 1765 to now) the correlation between the simulated climate under natural forcing and reconstructed temperatures can reach up to 0.7. However, although the joint effects of the TSI and the volcanism fit well the major features of the recorded temperature of the first two thirds of the industrial interval the model fails to reproduce the accelerated warming rate which started after 1970. Moreover the resumption of volcanic activity over the last three decades of the 20th century leads to a simulated cooling trend and therefore induces a decrease in the correlation between simulation and observation.

Anthropogenic forcings (i.e. deforestation, greenhouse gases and sulphate) does not impact climate significantly before the industrial period. Since the beginning of the industrialisation they explain up to 67% (47%) of the Northern (Southern) decadal-scale temperature variations. The simulations forced by anthropogenic forcings only reproduce well the warming trend of the last decades but underestimate the early 20th century warming and the long-term warming trend of the last 150 years. Moreover the model suggests that the global warming accelerates as soon as the greenhouse intensification begins to dominate over the combined effect of the anthropogenic sulphate aerosols and the land surface change.

Combining all the forcings (solar, volcanism, vegetation change, tropospheric sulphate aerosols and greenhouse gases) results in the largest agreement between model and data. Over the industrial period the model captures up to 77% of the decadal Northern Hemisphere temperature variations. The agreement between the observed and the simulated smoothed temperature variations strongly supports the contention that forcing from anthropogenic activities, modulated by variations in solar and volcanic forcing has been the main driver of climate change during the past century.

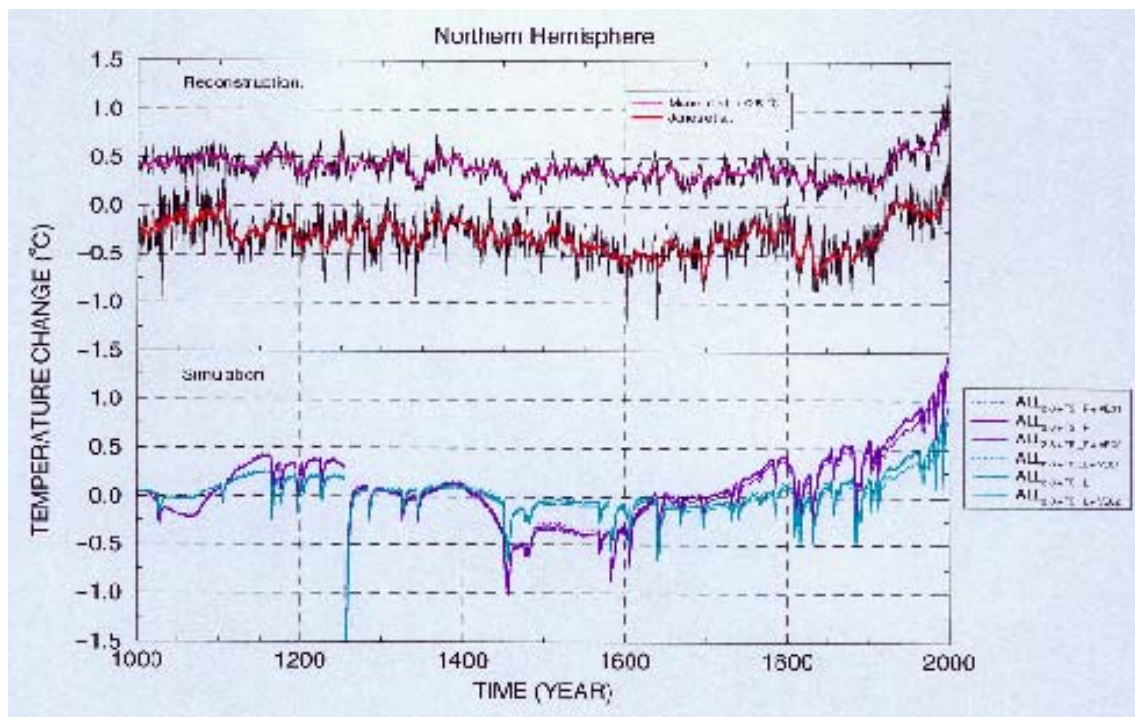


Figure 2: Transient response of the annual and hemispherical mean surface air temperature to both natural and anthropogenic forcings. Vegetation is included or not and the model sensitivity for a doubling CO_2 concentration has been set to $2.8^\circ C$. This simulated temperature is compared to the reconstructed temperature variations from Mann et al (1999) and Jones et al (1998).

3.2 Climate evolution during the Holocene

MoBidiC has been used to simulate the transient variations of continent temperature, sea surface temperature (SST), thermohaline circulation (THC) and sea-ice cover in response to the computed astronomical forcing (Berger, 1978) and the CO₂ concentration changes (Indermühle et al, 1999) over the last 9kyr. Two experiments were performed. The vegetation cover is fixed in the first one, and it is computed interactively with the dynamical vegetation model in the second one. In both experiments the present-day topography of the ice sheets is prescribed and kept fixed throughout the simulation. No other ice sheet is considered.

The latitudinal and seasonal distribution of continental temperature simulated under fixed vegetation changes mainly in response to insolation changes. For example summer temperatures at 50°N decreases by 2 to 3°C from the early Holocene to the present in response to the summer insolation drop of 26W/m² over that period. On the other hand the latitudinal distribution of seasonally averaged SST appears to respond to the insolation of the previous season. However winter SST varies only slightly in the northern polar regions because the ocean remains ice-covered, so that the water temperature remains close to the freezing point. Moreover the changes in annual mean insolation have virtually no impact in the low and mid-latitudes compared to the impact of the CO₂ increase. In the polar region the decrease in annual mean insolation compensates for the CO₂ increase so that the annual mean temperature remains constant.

The study highlights the important role played by the southward treeline shift in the Northern Hemisphere during the Holocene. This shift is linked to the decrease in summer insolation, the treeline being shown to follow roughly the 11°C surface isotherm over the continent. Its impact on surface temperature is strongest during spring, where it can induce a temperature increase up to 5°C at 9 kyr BP. In fact the forest increase, which is mainly controlled by summer temperature, induces a local warming because the albedo of a snow-covered forest is much smaller than the albedo of a snow-covered tundra. This process takes place mainly during winter and early spring but also strengthen the summer warming trend. In particular, vegetation appears as a key feature to explain the winter cooling observed in Scandinavia since the early Holocene, while southern Europe experiences a winter warming. The results also confirm paleoceanographic evidence that the meridional gradient of summer SST has increased during the Holocene. In the simulations, this behaviour is mainly due to variations in obliquity and precession that impact differently on temperature at low and high latitude, but in the Northern Hemisphere, vegetation changes further strengthened this trend.

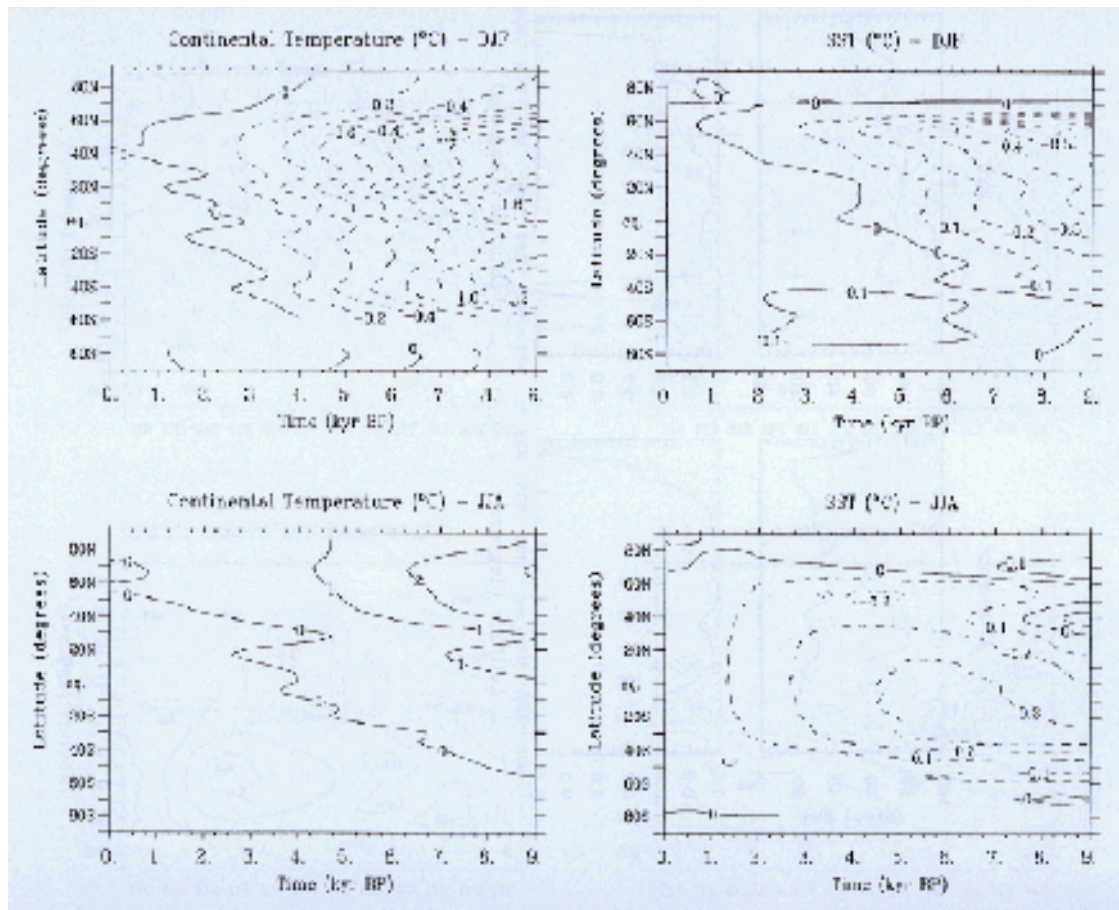


Figure 3: Transient simulation with fixed vegetation: latitude distribution of the zonally averaged (a) DJF surface continental temperature, (b) DJF SST, (c) JJA surface continental temperature and (d) JJA SST. The values represent differences with respect to the distribution obtained at the end of the experiment. Units are °C.

In both experiments the model predicts a gradual decrease in the amount of North Atlantic Deep water exported towards the Southern Ocean, in response to the winter SST increase in the northern North Atlantic. The effective area of September Arctic sea ice is doubling over the Holocene in response to the decrease in summer insolation. This further contributes to the summer cooling through ice-albedo feedback. The model does not simulate any significant variation in sea-ice coverage in the Southern Ocean.

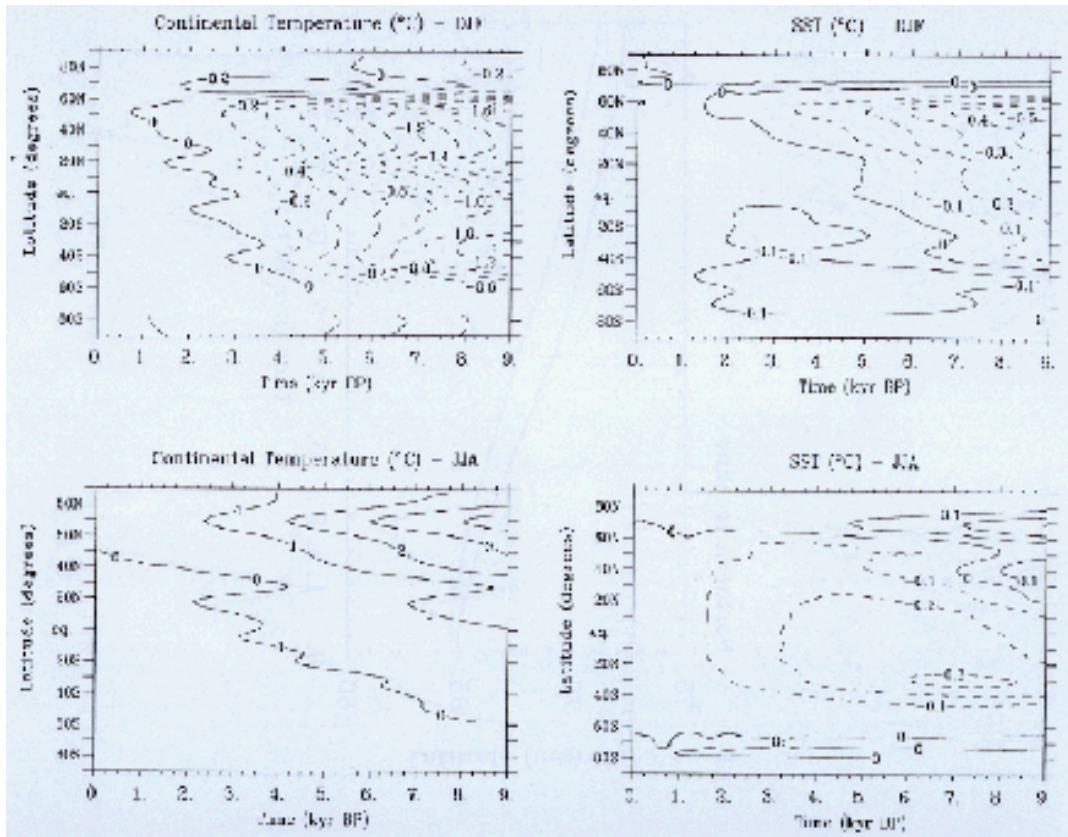


Figure 4: Transient simulation with interactive vegetation: latitude distribution of the zonally averaged (a) DJF surface continental temperature, (b) DJF SST, (c) JJA surface continental temperature and (d) JJA SST. The values represent differences with respect to the distribution obtained at the end of the experiment. Units are °C.

3.3 Abrupt events during the last glaciation

MoBidiC was used to compare the climatic impacts of a freshwater input (FI) in the North Atlantic ocean in pre-industrial (interglacial) and glacial climates. The freshwater input (duration, amplitude and location) is designed in order to be compatible with palaeoceanographic evidence about Heinrich events (HE) 4 and 5. A parameterisation for the sub-polar gyre between 50 and 75N was added to improve the representation of the NADW. On the other hand freshwater is transferred from 72.5S to 67.5S to improve the properties of the Antarctic bottom water and its recirculation in the Atlantic ocean. The inter-glacial equilibrium is obtained from a simulation forced by present-day insolation and a CO₂ concentration of 280ppmv. For the glacial climate the atmospheric CO₂ concentration is fixed at 200 ppmv, insolation at the top of the atmosphere is computed for 21 kyr BP (Berger, 1978), the topography of the Northern American, Eurasian and Greenland ice sheets are fixed according to the ice sheets simulated at 21kyr BP by the LLN 2-D NH model (Gallée et al; 1992).

A first glacial experiment was started from the interglacial equilibrium. It shows a strong enhancement of convection in the North Atlantic driven by cold SST and relatively large SSS. The southward flow of NADW is stronger than today and recirculation of AABW in the Atlantic almost completely vanished. Although these results are similar to those obtained from OGCM (Winguth et al, 1999) they disagree with some reconstructions (Duplessy et al., 1998; Boyle, 1995; Sarnthein et al, 2000). Reducing the sub-polar gyre intensity or starting with a weak ocean circulation allows to simulate a glacial ocean flow in better agreement with the reconstruction.

In agreement with previous studies performed in **interglacial** conditions the model shows that the THC shuts down after ~ 300 year and it resumes along with the HE ~ 300 year later. This is likely to be responsible for the Antarctic warmings observed during some of the Heinrich events, as well as the subsequent Dansgaard-Oeschger abrupt warmings recorded in Greenland ice cores. However in a **glacial** the response time for shutdown and resumption are shorter than in an interglacial climate. Moreover, the thermohaline circulation recovers its initial state in two steps separated by about 1470 years. Both steps correspond to abrupt increase in Greenland temperature by about $4\text{-}5^\circ\text{C}$ induced by a massive release of the heat accumulated at intermediate depth in the Atlantic ocean. In addition to changes in the THC and in the surface temperature the FI induces changes in SSS, and in temperature and salinity in the ocean (Crucifix et al, 2001).

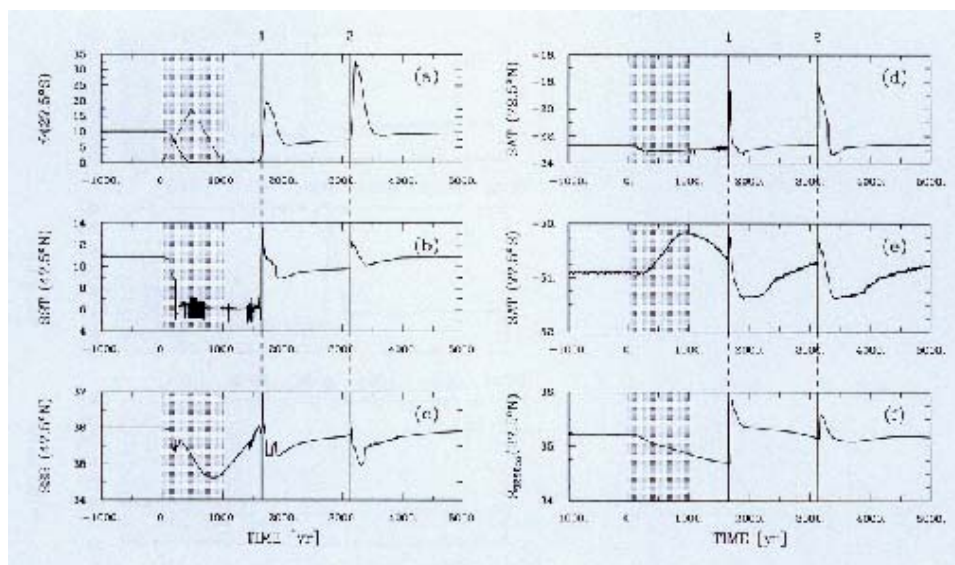


Figure 5: Fresh water input simulation during an interglacial climate. Time evolution of (a) NADW outflow towards the Southern ocean at 27.5S ; (b) zonally averaged Atlantic SST at 47.5N [$^\circ\text{C}$]; (c) zonally averaged Atlantic SSS at 47.5N [psu]; (d) zonally averaged surface air temperature at 72.5N [$^\circ\text{C}$]; (e) zonally averaged surface air temperature at 77.5N [$^\circ\text{C}$]; (f) zonally averaged Atlantic salinity at 3250m depth at 37.5N . The shaded area corresponds to the period of freshwater input and the vertical lines refer to the overshoot.

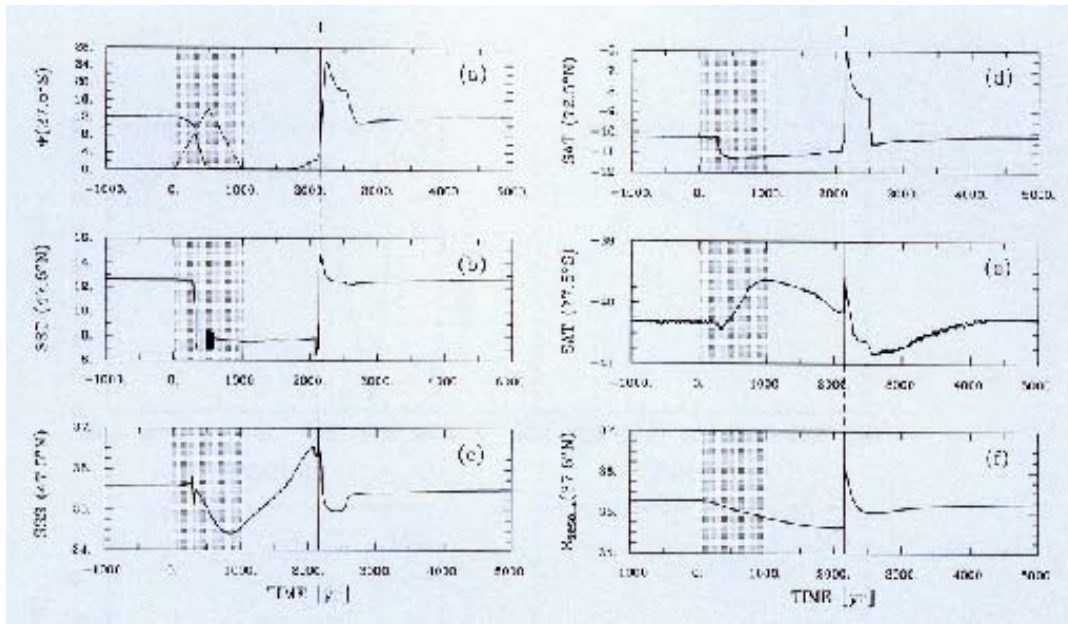


Figure 6: Fresh water input simulation during a glacial climate. Time evolution of (a) NADW outflow towards the Southern ocean at 27.5S; (b) zonally averaged Atlantic SST at 47.5N [$^{\circ}\text{C}$]; (c) zonally averaged Atlantic SSS at 47.5N [psu]; (d) zonally averaged surface air temperature at 72.5N [$^{\circ}\text{C}$]; (e) zonally averaged surface air temperature at 77.5N [$^{\circ}\text{C}$]; (f) zonally averaged Atlantic salinity at 3250m depth at 37.5N. The shaded area corresponds to the period of freshwater input and the vertical lines refer to the overshoot.

3.4 The climate during the Eemian

A set of experiments was design to study the climate during the Eemian, more precisely from 130 to 115 kyr BP. The simulations were started at 130 kyr BP from an equilibrium state. This equilibrium is obtained from a simulation forced by insolation computed for 130 kyr BP and a CO_2 concentration of 261ppmv. It is assumed that the Northern Hemisphere ice sheets are completely melted then. Transient experiments are then performed from this equilibrium using computed insolation (Berger, 1978) and CO_2 concentration changes reconstructed from the Vostok ice core (Petit et al, 1999) from 130 to 115 kyrBP. The dynamical vegetation is allowed to adjust according to climate but the ice sheets are kept unchanged. The Eemian can be divided into two time intervals. In the first one (until 122kyr) climate is very strongly marked by the change in CO_2 concentration while in the second one the vegetation change is playing a more important role.

The latitudinal and seasonal distribution of temperature shows features similar to those put forward for the Holocene. The continental surface temperature changes mainly in response to insolation with a time lag of roughly one month while the SST appears to respond to the insolation of the previous season. However this is mainly the case for the summer SST. During the Eemian the model simulates a cooling in

the mid and high latitudes, especially in the northern summer season and in the southern winter season. This is in good agreement with obliquity changes.

4. CONCLUSION

The improved version of the 2D climate model developed in Louvain-la-Neuve MoBidiC now include the whole globe with a representation for the vegetation change and for the dynamics of the ocean. This model allowed us to study the stability of the climate in the past. For example our simulations are showing a rather stable Holocene, although climate variations related to either natural or anthropogenic factors can be simulated. Our simulations also show the consequences of a freshwater flux on the climate. In particular it shows that the response is different depending whether the fresh water input is applied in an interglacial or a glacial climate, i.e. either a one step or a two step recovery of the thermohaline circulation after the initial shutdown.

ACKNOWLEDGEMENTS

C. Bertrand is scientific collaborator and M. Crucifix is research fellow with the Belgian National Fund for Scientific Research (FNRS). This work was done, in part, within the scope of the Environment and Climate Program of the European Commission (ENV4-CT97-0643) and the impulse Program 'Global Change' (GC/DD/13, Belgian State, Prime Minister's Office, Federal Office for Scientific, Technical and Cultural Affairs). This research has benefited from computer time provided by the Belgian Research Programme on Information Technology (IT/SC/20).

REFERENCES

- Berger A. 1978. Long-term variations of daily insolation and Quaternary climatic changes. *J. Atmos.Sci.*, 35, 2362-2367.
- Bertrand C. 1998. Climate simulation at the secular time scale. PhD thesis. Université catholique de Louvain, Louvain-la-Neuve.
- Bertrand C., Loutre M.F., Crucifix M., Berger A. 2001. Climate of the last millennium: a sensitivity study. *Tellus* (submitted).
- Brovkin V., Ganopolski A., Svirezhev Y. 1997. A continuous climate-vegetation classification for use in climate-biosphere studies. *Ecological Modelling*, 102, 251-261.
- Brovkin V., Levis S., Loutre M.F., Crucifix M., Claussen M., Ganopolski A., Kubatzki C., Petoukhov V. 2001. Stability analysis of the climate-vegetation system in the northern high latitudes (submitted).
- Bryan K. 1969. A numerical method for the study of the circulation of the world ocean. *J.Comp.Phys.*, 4, 347-376.
- Crucifix M., Loutre M.F., Tulkens P., Fichefet T., Berger A. 2001a. Climate evolution during the Holocene: a study with an Earth model of intermediate complexity (submitted).
- Crucifix M., Tulkens P., Berger A. 2001b. Modelling abrupt climatic change during the last glaciation (submitted).
- Duplessy J.-C., Shackleton N.J., Fairbanks R.G., Labeyrie L., Oppo D. and Kallel N. 1988. Deepwater source variations during the last climatic cycle and their impact on the global deepwater circulation. *Paleoceanogr.* 3, 343-360.
- Gallée H., van Ypersele J.P., Fichefet T., Tricot C., Berger A. 1991. Simulation of the last glacial cycle by a coupled sectorially averaged climate ice sheet model I. The climate model. *J. Geophys. Res.*, 96(D7), 13139-13161.
- Gallée H., van Ypersele J.P., Fichefet T., Marsiat I., Tricot C., Berger A., 1992. Simulation of the last glacial cycle by a coupled sectorially averaged climate ice sheet model II. Response to insolation and CO₂ variations. *J. Geophys. Res.*, 97(D14), 15713-15740.

Harvey L.D.D. 1988. Development of a sea-ice model for use in zonally averaged energy balance models. *J.Clim.* 1, 1221-1238.

Harvey L.D.D. 1992. A two dimensional ocean model for long-term climatic simulations: stability and coupling to atmospheric and sea-ice models. *J.Geophys. Res.*, 97, 9435-9453.

Houghton J.T., Callander B.A. and Varney S.K. (Eds) *Climate change 1992 : supplementary report to the IPCC Scientific assessment*, Cambridge Univ. Press, New York.

Hovine S. and Fichefet T. 1994. A zonally averaged, three-basin ocean circulation model for climate studies. *Clim.Dyn.*, 10, 313-331.

Indermühle A., Stocker T.F., Fisher H., Smith H., Wahlen M., Deck B., Mastroianni D., Tschumi T., Blunier T., Meyer R. and Stauffer B. 1999. Holocene carbon-cycle dynamics based on CO₂ trapped in ice at Taylor Dome, Antarctica, *Nature*. 398, 121-125.

Keeling C.D. 1993. *Atmospheric CO₂ concentrations – Mauna Loa Observatory, Hawaii, 1958-1993*. NDP-001, CDIAC, ORNL, Oak Ridge.

Neftel A., Moor E., Oeschger H., Stauffer B., Friedli H., Lüscher H. and Siegenthaler U. 1990. In: *Atmospheric carbon dioxide concentration – historical record, Siple Station, trends 90: A compendium of data on global change*, Rep. 36, CDIAC, ORNL, Oak Ridge.

Parkinson C.L. and Washington W.M. 1979. A large scale numerical model of sea ice. *J.Geophys.Res.* 84(C1), 311-336.

Petit J.R., Jouzel J., Raynaud D., Barkov N.I., Barnola J.-M., Basile I., Benders M., Chappellaz J., Davis M., Delaygue G., Delmotte M., Kotlyakov V., Legrand M., Lipenkov V.Y., Lorius C., Pépin L., Ritz C., Saltzman, E., Stievenard M. 1999. Climate and atmospheric history of the past 420,000 years from the Vostok ice core, Antarctica. *Nature*, 399, 429-436.

Reid G.C. 1997. Solar forcing of global climate change since the mid-17th century. *Clim Change*. 37, 391-405.

Schmitz W.J. 1995. On the interbasin-scale thermohaline circulation. *Rev.Geophys.* 33, 151-173.

Serreze M.C. Walsh J.E., Chapin F.S., Osterkamp T., Dyurgerov M., Romanovsky V., Oechel W.C., Morison J., Zhang T., Barry R.G. 2000. Observational evidence of recent change in the northern high-latitude environment. *Climatic Change*, 46, 159-207.

Trather M.C. 1986. Numerical advection by conservation of second order moments. *J.Geophys.Res.* 91(D6), 6671-6681.

Sarnthein M., Statterger K., Dreger D., Erlenkeuser H., Grootes P., Haupt B., Jung S., Kiefer T., Kuhnt W., Pflaumann U., Schäfer-Neth C., Schulz H., Schulz M., Seidov D., Simstich J., van Kreveland S., Vogelsang E., Völker A. and Weinelt M. 2000. Fundamental modes and abrupt changes in North Atlantic circulation and climate over the last 60ky—concepts, reconstruction, and numerical modelling. In : *The Northern North Atlantic: a changing environment*. Schäfer P. (Ed), Springer Verlag, Berlin, 45-66.

Sela J. and Wiin-Nielsen A. 1971. Simulation of the atmospheric annual energy cycle. *Mon.Wea.Rev.*, 99, 460-468.

Semtner A.J. 1976. A model for the thermodynamic growth of sea ice in numerical investigations of climate. *J.Phys.Oceanogr.* 6, 379-389.

Semtner A.J. 1986. Finite-difference formulation of a world ocean model. In: *Advanced physical oceanographic numerical modelling*, O'Brien, J.J. (Ed), D. Reidel, Dordrecht: 187-202.

Svirezhev Yu, Brovkin V., von Bloh W., Schellnhuber H.-J. and Petschel-Held G. 1999. Optimization of global CO₂ emission based on a simple model of the carbon cycle. *Environmental modeling and assessment*, 4, 23-33.

Taylor K. The influence of subsurface energy storage on seasonal temperature variations. *J.Appl.Meteor.*, 15, 1129-1138.

Tulkens P. 1998. A zonally averaged model of coupled atmosphere-ocean-sea ice system for climate study. PhD thesis. Université catholique de Louvain, Louvain-la-Neuve.

Winguth A.M.E., Archer D., Duplessy J.-C., Maier-Raimer E. and Mikolajewicz U. 1999. Sensitivity of paleonutrient tracer distributions and deep-sea circulation to glacial boundary conditions. *Paleoceanogr.*, 14(3), 304-323.

LIST OF ABBREVIATIONS

AABW	Antarctic Bottom Water
ACC	Antarctic Circumpolar Current
AD	Anno Domini
BP	Before Present
CO ₂	Carbon dioxide
DJF	December-January-February
DO	Dansgard Oeschger event
EMIC	Earth system Model of Intermediate Complexity
FI	Freshwater Input
GDD0	Growing Degree Day above 0
HE	Heinrich Event
JJA	June-July-August
kyr	Thousand of years
NADW	North Atlantic Deep Water
NH	Northern Hemisphere
OGCM	Ocean General Circulation Model
QG	Quasi-Geostrophic
SST	Sea Surface Temperature
SSS	Sea Surface Salinity
THC	Thermohaline circulation
TSI	Total Solar Irradiance